HORIZONS IN MATERIALS

EDITED BY: N. M. Pugno, V. Cannillo, D. Cazorla-Amoros, H. Chen, J.-S. Chen, J. P. Chu, L. Dai, D. S. Galvao, V. G. Harris, W. Li, A. Pegoretti, J. L. Provis, G.-L. Song and P. Ye

PUBLISHED IN: Frontiers in Materials

frontiers Research Topics

ISSN 1664-8714
ISBN 978-2-88976-163-0
DOI 10.3389/978-2-88976-163-0

About Frontiers

Frontiers is more than just an open-access publisher of scholarly articles: it is a pioneering approach to the world of academia, radically improving the way scholarly research is managed. The grand vision of Frontiers is a world where all people have an equal opportunity to seek, share and generate knowledge. Frontiers provides immediate and permanent online open access to all its publications, but this alone is not enough to realize our grand goals.

Frontiers Journal Series

The Frontiers Journal Series is a multi-tier and interdisciplinary set of open-access, online journals, promising a paradigm shift from the current review, selection and dissemination processes in academic publishing. All Frontiers journals are driven by researchers for researchers; therefore, they constitute a service to the scholarly community. At the same time, the Frontiers Journal Series operates on a revolutionary invention, the tiered publishing system, initially addressing specific communities of scholars, and gradually climbing up to broader public understanding, thus serving the interests of the lay society, too.

Dedication to Quality

Each Frontiers article is a landmark of the highest quality, thanks to genuinely collaborative interactions between authors and review editors, who include some of the world's best academicians. Research must be certified by peers before entering a stream of knowledge that may eventually reach the public - and shape society; therefore, Frontiers only applies the most rigorous and unbiased reviews.
Frontiers revolutionizes research publishing by freely delivering the most outstanding research, evaluated with no bias from both the academic and social point of view. By applying the most advanced information technologies, Frontiers is catapulting scholarly publishing into a new generation.

What are Frontiers Research Topics?

Frontiers Research Topics are very popular trademarks of the Frontiers Journals Series: they are collections of at least ten articles, all centered on a particular subject. With their unique mix of varied contributions from Original Research to Review Articles, Frontiers Research Topics unify the most influential researchers, the latest key findings and historical advances in a hot research area! Find out more on how to host your own Frontiers Research Topic or contribute to one as an author by contacting the Frontiers Editorial Office: frontiersin.org/about/contact

HORIZONS IN MATERIALS

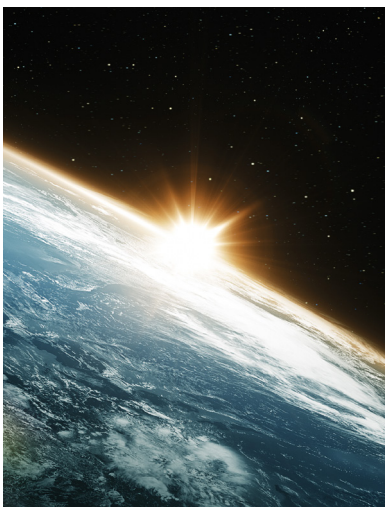

Cover image: spainter_vfx/Shutterstock.com

The *Frontiers in Materials* Editorial Office team are delighted to present the "Horizons in Materials" article collection, showcasing high-impact, authoritative, and accessible Review articles covering important topics at the forefront of the materials science and engineering field.

All contributing authors were nominated by the Chief Editors and Editorial Office in recognition of their prominence and influence in their respective fields. The cutting-edge work presented in this article collection highlights the diversity of research performed across the entire breadth of the materials science and engineering field and reflects on the latest advances in theory, experiment, and methodology with applications to compelling problems.

This Editorial features the corresponding author(s) of each paper published within this important collection, ordered by section alphabetically, highlighting them as the great researchers of the future.

The *Frontiers in Materials* Chief Editors and Editorial Office team would like to thank each researcher who contributed their work to this collection. We are excited to see each article gain the deserved visibility and traction within the wider community, ensuring the collection's truly global impact and success.

Emily Young
Journal Manager

Huanyang Chen

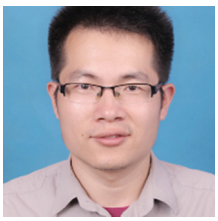

Huanyang Chen was a Professor in Soochow University (2009 – 2016) and in Xiamen University since 2016. His research covers photonic and phononic crystals, metamaterial designs, and transformation optics and acoustics. Prof. Chen has authored or coauthored more than 150 papers, including review articles for Nature Photonics/Nature Materials/Nature Review Materials, and his papers have been cited for over 6000 times. His work on transformation acoustics and cloaking has been selected into the list of "best of 2008" by IOP.

Claude Esling

Claude Esling is Professor Emeritus of University of Lorraine, France. He has worked on crystallographic textures in the first part of his career, then for thirty years with Northeastern University Shenyang on material treatment under high magnetic field. He centered his research interests on the alloy phase diagram in high-intensity magnetic field, the study of solid-state transformation and recrystallization, and materials preparation technology controlled by high-intensity magnetic field.

Vanessa Fierro

Prof. Vanessa Fierro is a CNRS Research Professor at Institut Jean Lamour, France, a joint laboratory of the University of Lorraine and the CNRS, where she heads the Bio-sourced Materials Research Team. Vanessa has over 300 scientific publications and an extensive background in porous materials for energy and environmental applications. She received the Charles E. Pettinos Award from the American Carbon Society in 2019 and the CNRS Silver Medal in 2020.

Surya Kalidindi

Surya Kalidindi is a Regents Professor in Woodruff School of Mechanical Engineering at Georgia Institute of Technology. He earned a Ph.D. in Mechanical Engineering from Massachusetts Institute of Technology in 1992. In 2016, Prof. Kalidindi and his group members were awarded the top prize as well as one of the runner-up prizes in the national Materials Science and Engineering Data Challenge sponsored by the Air Force Research Lab in partnership with the National Institute of Standards and Technology and the U.S. National Science Foundation.

Barbara Lothenbach

Barbara Lothenbach is the Head of the Cement Chemistry and Thermodynamics Group at Empa – Laboratory Concrete & Asphalt. Her research focuses on cement hydration, alternative cementitious materials, and thermodynamic data. She is also Associate Professor at the Institute of Geology, University of Bern, Switzerland, and she is member of various national and international committees.

Véronique Michaud

Prof. Véronique Michaud is currently Associate Professor, Head of the Laboratory for Processing of Advanced Composites and Associate Dean of Engineering for Education, at the Ecole Polytechnique Fédérale de Lausanne, Switzerland. Her research focuses on fundamental aspects of composite materials processing, as well as the development of smart materials and structures including self-healing, shape and vibration control and tailored damping. She is also the co-founder of CompPair Technologies SA, which was created in 2020.

Debora Puglia

Debora Puglia is currently a Researcher of Engineering in Materials Science and Technology. To date, she has participated in over 30 national and international congresses and is co-author of at least 70 papers published in international journals. Additionally, she works as a reviewer for international scientific journals in the field of polymeric and composite materials.

Gaurav Sant

Gaurav Sant is the Pritzker Professor of Sustainability and Henry Samueli Fellow at the UCLA Henry Samueli School of Engineering and Applied Science. His research interests include cementitious materials and porous media, with a focus on their chemistry-microstructure-engineering properties and reducing the carbon footprint of construction materials. Sant has published more than 100 peer-reviewed scientific publications and his work has been supported by federal and state agencies, foundations, and Fortune 500 corporations.

Mei Yu

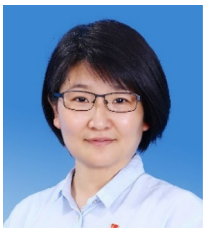

Dr Mei Yu is Professor at Beihang University, Materials Science and Engineering. Her research looks at corrosion science and protection technology for key aerospace materials, including corrosion mechanism and protection methods of aluminum alloys. She has published more than 50 papers, including 30 SCI papers as the first or corresponding author and 14 papers in authoritative journals such as Corrosion Science. She has 15 national invention patents and won 1 second prize of provincial and ministerial level scientific and technological progress.

Yonghao Zhao

Yonghao Zhao is a Professor at Nanjing University of Science and Technology, High Entropy Alloys and Nanometals. He is the deputy director of Nanostructural Materials Research Center, School of Materials Science and Engineering, Nanjing University of Science and Technology since 2011. He has published more than 140 papers in reputed journals and his papers have been cited over 6000 times. His research interests include Mechanical and thermal properties as well as deformation mechanisms of nanostructured metals and alloys, high entropy alloys.

Citation: Pugno, N. M., Cannillo, V., Cazorla-Amoros, D., Chen, H., Chen, J.-S., Chu, J. P., Dai, L., Galvao, D. S., Harris, V. G., Li, W., Pegoretti, A., Provis, J. L., Song, G.-L., Ye, P., eds. (2022). Horizons in Materials. Lausanne: Frontiers Media SA. doi: 10.3389/978-2-88976-163-0

Table of Contents

frontiers in Materials

REVIEW
published: 03 January 2022
doi: 10.3389/fmats.2021.792359

Mechanical Properties and Deformation Mechanisms of Heterostructured High-Entropy and Medium-Entropy Alloys: A Review

Wei Jiang[1], *Yuntian Zhu*[1,2] *and Yonghao Zhao*[1]*

[1]Nano and Heterogeneous Materials Center, School of Materials Science and Engineering, Nanjing University of Science and Technology, Nanjing, China, [2]Department of Materials Science and Engineering, City University of Hong Kong, Hong Kong, China

Recently, heterostructured (HS) materials, consisting of hard and soft zones with dramatically different strengths, have been developed and received extensive attention because they have been reported to exhibit superior mechanical properties over those predicted by the rule of mixtures. Due to the accumulation of geometrically necessary dislocations during plastic deformation, a back stress is developed in the soft zones to increase the yield strength of HS materials, which also induce forward stress in the hard zones, and a global hetero-deformation induced (HDI) hardening to retain ductility. High-entropy alloys (HEAs) and medium-entropy alloys (MEAs) or multicomponent alloys usually contain three or more principal elements in near-equal atomic ratios and have been widely studied in the world. This review paper first introduces concepts of HS materials and HEAs/MEAs, respectively, and then reviewed emphatically the mechanical properties and deformation mechanisms of HS HEAs/MEAs. Finally, we discuss the prospect for industrial applications of the HS HEAs and MEAs.

Keywords: high-entropy alloy, heterostructured material, microstructure, mechanical property, strength, ductility

OPEN ACCESS

Edited by:
John L. Provis,
The University of Sheffield,
United Kingdom

Reviewed by:
Zhiming Li,
Central South University, China
Bo Song,
Southwest University, China

***Correspondence:**
Yonghao Zhao
yhzhao@njust.edu.cn

Specialty section:
This article was submitted to Structural Materials, a section of the journal Frontiers in Materials

Received: *10 October 2021*
Accepted: *12 November 2021*
Published: *03 January 2022*

Citation:
Jiang W, Zhu Y and Zhao Y (2022) Mechanical Properties and Deformation Mechanisms of Heterostructured High-Entropy and Medium-Entropy Alloys: A Review. Front. Mater. 8:792359. doi: 10.3389/fmats.2021.792359

INTRODUCTION

Heterostructured Materials

Metallic materials with outstanding mechanical properties, especially high strength and ductility, are widely used in many engineering fields such as transportation, spacecraft, and industrial manufacture (Bouaziz et al., 2013; He et al., 2017; Zhao and Jiang, 2018). For example, super strong metallic materials can significantly reduce the weight of transport vehicles, thus improving their energy efficiency (Zhao and Jiang, 2018). Therefore, the development of metallic materials with high strength and ductility is an unremitting research subject for material scientists (Gao et al., 2020). Nowadays, the challenge for the industrial application of metallic materials is that the strength of most metallic materials is limited and needs to be further improved to meet the industrial requirements. Considering the internal mechanism that affects the strength and ductility of metallic materials, the strength of metallic materials depends on the hindrance of dislocation motion, while the ductility depends on the ability of dislocation activity, such as dislocation generation, accumulation, and movement (Hughes et al., 2003; Meyers and Chawla, 2008). Therefore, one of the traditional strengthening strategies for high-strength materials is to produce nanostructured materials by grain refinement through severe plastic deformation, such as equal-channel angular pressing (ECAP) and high-pressure torsion (HPT) (Cao et al., 2018).

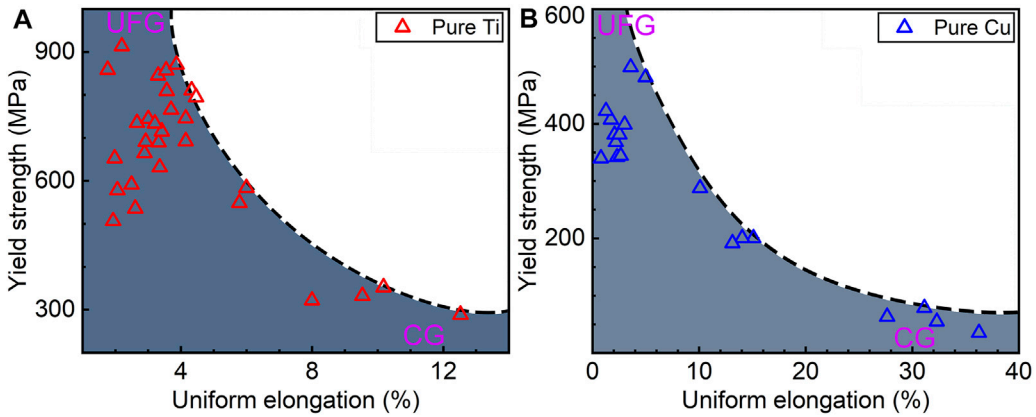

FIGURE 1 | Traditional strength–ductility trade-off relationship in pure **(A)** Ti and **(B)** Cu (Wang et al., 2002; Ritchie, 2011; Wu et al., 2015; Shahmir et al., 2016).

According to the empirical Hall–Petch relationship and classic Taylor hardening model, the strength of metallic materials monotonically increases with reducing grain size and increasing dislocation density (Taylor, 1934; Hansen, 2004). The introduction of substantial grain boundaries and high density of dislocations is a powerful approach for blocking dislocation movement and thus significantly enhances the strength of metallic materials (He et al., 2017; Jiang et al., 2021a). Moreover, the introduction of precipitates and solute atoms to induce precipitation hardening and solid solution strengthening are also effective means of strengthening (Zhao et al., 2004; Li et al., 2015; Jiang et al., 2021a).

Unfortunately, these traditional methods of introducing obstacles, e.g., grain boundaries, dislocations, precipitation, and solute atoms, to improve strength inevitably limit the multiplication and accumulation of dislocations. According to the Hart's theory (Hart, 1967) and the Considère criterion (Wei et al., 2004), higher dislocation storage capacity associated with dislocation multiplication and accumulation means higher strain hardening, which can help delay the onset of necking during plastic deformation and prolong ductility. Consequently, the enhancement of strength through the traditional strengthening mechanisms always leads to a degradation of ductility, which is referred to as the strength-ductility trade-off, as shown in **Figure 1** (Wang et al., 2002; Ritchie, 2011; Wu et al., 2015; Shahmir et al., 2016). Actually, the strength-ductility trade-off has always been a problem in the materials science community, because good ductility is simultaneously required for high-strength materials to prevent catastrophic failure during service (Wang and Ma, 2004; Ma and Zhu, 2017). Over the centuries, engineers have been forced to choose either strength or ductile of metallic materials, not both as desired (Zhu and Li, 2010).

Previous efforts to resolve this trade-off problem have been focused on boundary engineering such as coherent twin boundaries (Lu et al., 2004; Lu K. et al., 2009; Gutierrez-Urrutia and Raabe, 2011) and phase boundaries (Byun et al., 2004); the associated strengthening mechanisms are known as twinning-induced plasticity (TWIP) effect (Gutierrez-Urrutia and Raabe, 2011) and transformation-induced plasticity

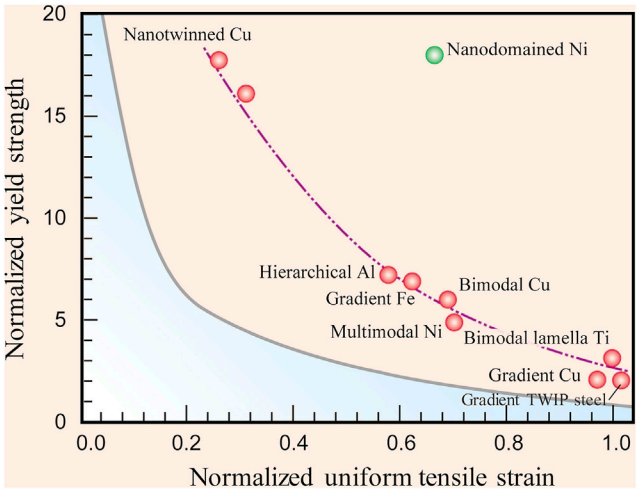

FIGURE 2 | Normalized yield strength versus normalized uniform tensile strain of metallic materials with homogeneous (banana-shaped shaded regions) and heterogeneous (solid circle) microstructures. Image adopted from Ref. Ma and Zhu (2017). with permission from Elsevier.

(TRIP) effect (Byun et al., 2004), respectively. TWIP and TRIP effects generate additional boundaries *in-situ* for dislocation storage and significantly reduce the effective grain size, resulting in secondary strain hardening (Byun et al., 2004; Gutierrez-Urrutia and Raabe, 2011, 2012; Zhu et al., 2012; Su et al., 2019) and enhanced ductility. Moreover, the preexisting twin boundaries can act as both obstacles to dislocation movement and pathways to dislocation slip and cross-slip, simultaneously enhancing the strength and ductility (Ming et al., 2019). However, there are still shortcomings: 1) their strength may reach a limit with reducing boundary spacing to nanometers (Lu L. et al., 2009; Li et al., 2010); 2) both the TWIP and TRIP effects are confined in materials with low stacking-fault energy (SFE) (Grässel et al., 2000; An et al., 2012); and 3) the yield strength is low, and a further increase in yield strength will still lead to a degradation of ductility (Bouaziz et al., 2011).

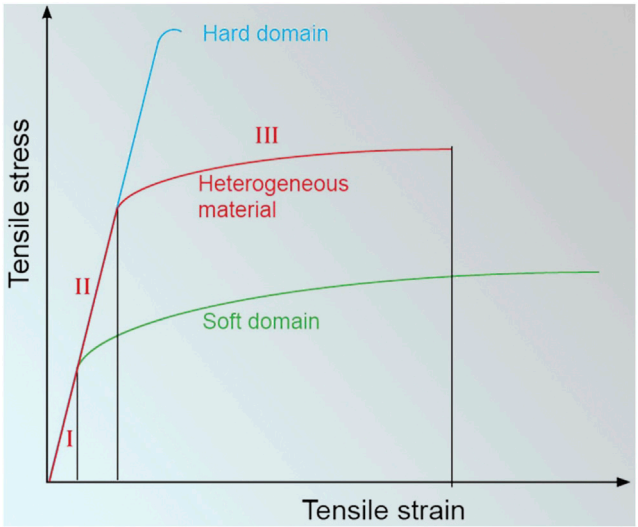

FIGURE 3 | The plastic deformation process of heterogeneous materials during tension. Image adopted from Ref. Wu and Zhu (2017) with permission from Taylor and Francis.

More recently, a novel concept of heterostructured (HS) materials has attracted increasing attention due to their superior strength-ductility combination (Zhu et al., 2020), as shown in **Figure 2**. After years of development, there are several types of HS materials, including bimodal grain structures (Wang et al., 2002; Han et al., 2005; Zhao et al., 2008), heterogeneous lamella structures (HLSs) (Wu et al., 2015; Li J. et al., 2019), gradient grain structures (Wu X. et al., 2014; Lu, 2014; Wei et al., 2014; Qin et al., 2019), laminate structures (Qin et al., 2019), dual-phase structures (Li et al., 2016), harmonic structures (Sawangrat et al., 2014), and metal matrix composites (Choudhuri et al., 2018; Liu et al., 2018). What they have in common is that all these HS materials consist of very diverse microstructures: the mixture of hard and soft zones with dramatically different strengths (Wu and Zhu, 2017). The strength difference between the hard and soft zones can be achieved by adjusting the crystal structures (Zhao et al., 2017), defect concentration (Yang M. et al., 2018; Ming et al., 2019), and just the grain size ranging from nanometers to millimeters (Wang et al., 2002). For example, a simple thermomechanical treatment of Cu skillfully avoids the traditional strength–ductility paradox through the bimodal grain structures, in which a small amount of micron-size grains randomly distribute in nanocrystalline (NC) and ultrafine grain (UFG) matrices (Wang et al., 2002).

The key concept for HS materials to increase strength while retaining ductility is to enhance the strain hardening ability and thus in turn delay plastic instability. As shown in **Figure 3**, HS materials experience a unique deformation process during tension, compared to homogeneous materials. Once loaded, both the hard and soft zones start elastic deformation first (Wu and Zhu, 2017). After the simultaneous elastic deformation stage, the soft zones begin plastic deformation, while the hard zones are still in elastic status. Constraints resulting from the hard zones will be imposed on the soft zones to inhibit its free plastic deformation. Consequently, geometrically necessary dislocations (GNDs) will be generated and pile up against zone interfaces due to mechanical incompatibility of hard and soft zones. The induced GNDs can produce long-range internal stress, i.e., back stress, in soft zones to offset the applied shear stress, making them appear stronger to withstand higher shear stress (Wu and Zhu, 2017; Zhu and Wu, 2019). Meanwhile, the stress concentration caused by dislocation piling up at zone interfaces induces forward stress in hard zones to make hard zones appear weaker (Zhu and Wu, 2019). As evidenced by the increasing works in recent years, the hetero-deformation-induced (HDI) hardening effect (Zhu and Wu, 2019), induced by the interaction between back stresses and forward stresses, exert extra strain hardening in HS materials and thus enhanced the yield strength and ductility (Zhu and Wu, 2019; Liu et al., 2020). With the flow stress further increasing, the hard zones start yielding to accommodate the stress concentration (Zhu and Wu, 2019). Finally, both the hard and soft zones are deforming plastically, while the soft zones bear higher plastic strain, leading to a strain partitioning. However, the continuity of zone boundaries requires the same plastic strain for adjacent soft and hard zones. Thus, strain gradient is necessary near the zone interface to accommodate the strain partitioning (Zhu and Wu, 2019). There is clear evidence that rapid accumulation of GNDs in the hetero-zone boundary-affected regions (HBARs) (Wu and Zhu, 2021) will result in a significant HDI effect at low strain (>4.5%), while dislocation hardening dominates at higher strain levels (Fang et al., 2020).

There is no doubt that the HS materials have microstructural requirements for the optimum mechanical properties, such as volume fraction of soft zones, interface spacing, and distribution of hard zones (Ma et al., 2016; Huang et al., 2018; Liu et al., 2020). For instance, thinner interface spacing results in a synergetic improvement of strength and ductility in copper/bronze laminates (Ma et al., 2016). In the vicinity of zone boundaries, the accumulation of GNDs results in a (HBAR) of a few micrometers. The optimum spacing is that the adjacent HBARs begin to overlap to maximize the hardening capacity, after which the strength–ductility trade-off occurred (Huang et al., 2018). Likewise, the volume fractions of the gradient structure have a significant influence on the strength and ductility of gradient structural pure copper (Yang et al., 2015). The optimum gradient structure volume fraction of 0.08–0.1 produces an excellent strength–ductility combination (Yang et al., 2015). Moreover, the strength–ductility combination in HS materials can be optimized by adjusting the volume and density of boundaries between the hard and soft zones to maximize the strain/stress partitioning and strain gradient between the zones (Ma and Zhu, 2017; Wu and Zhu, 2017). For guidance of material design, Zhu et al. have made numerous efforts to systematically study the effectiveness of various HS structural materials (Wu and Zhu, 2017). With regard to the gradient structures, the dynamic migration of interfaces from the coarse-grained core to the nanograined layer makes the successive deformation over the sample and suppresses strain localization (Lu, 2014). However, the limited interface density of

gradient structures weakens the density of accumulated dislocation and thus their capability of back-stress work hardening (Wu X. et al., 2014; Lu, 2014). For bimodal structures (Wang et al., 2002; Han et al., 2005; Zhao et al., 2008), the problem that still exists is that the limited interface density cannot effectively maximize the HDI stress strengthening potential. For dual-phase steels with hard zones embedded in the soft matrix, the continuous soft matrix induces high ductility but relatively low yield strength (Calcagnotto et al., 2011; Li et al., 2016). For harmonic structures with soft zones surrounded by hard zones, strength can be further improved by tuning the interface spacing and volume fraction of hard zones (Sawangrat et al., 2014). In contrast, the heterogeneous lamella structures (HLSs) present the best strength–ductility combination (Wu et al., 2015). By asymmetric rolling and partial recrystallization, HLS Ti featured with soft lamellae zones embedded in the hard lamella matrix was architected (Wu et al., 2015). The high constraint of the soft zones by the hard matrix renders high strength, and the strong strain partitioning also renders extraordinary strain hardening and consequent increased ductility (Wu et al., 2015).

High Entropy Alloy

While alloys of dilute solid solutions are still being researched, there is a continuous surge worldwide in developing alloys of concentrated solid solutions—medium-entropy alloys (MEAs) and high-entropy alloys (HEAs) (Zhang et al., 2014; Gludovatz et al., 2016; Ding et al., 2019). Different from traditional dilute solid solution alloys with only one principal element and some other elements in minor quantity, the MEAs/HEAs are nominally equiatomic or near-equimolar multicomponent alloys typically with three or more principal elements. This concept, first pointed out by Yeh et al. (Yeh et al., 2004) and Cantor et al. (Cantor et al., 2004), results in a paradigm shift in the alloy design concept toward the unexplored center region of the phase diagram and broadens the field of scope on alloy design (Miracle and Senkov, 2017; Sathiyamoorthi and Kim, 2020; Jiang et al., 2021b). MEAs are composed of three or more principal elements with near-equal atomic percentages (Gludovatz et al., 2016), and their configurational entropies are in the range of 1–1.5R (R = 8.314 mol−1·K−1). HEAs are comprised of five or more principal elements with near-equal atomic percentages (Zhang et al., 2014), and their configurational entropies are larger than 1.5R (Miracle et al., 2014). Due to the high mixing entropy associated with a disordered solution of several elements, both MEAs and HEAs can form stable single-phase solid solutions, in which atoms with different sizes are homogeneously distributed in the ideal situation. However, enthalpic interactions unavoidably change the local chemical order (LCO) in MEAs and HEAs, leading to short-range ordering (SRO) and/or incipient concentration waves. Notwithstanding the uncertainty of LCO, a mixture of atoms of diverse sizes results in severe lattice distortion, presenting frequent short-range resistance to dislocation slip, in this manner to maximize the solid solution strengthening effect in MEAs and HEAs (Yeh et al., 2007; Tsai et al., 2013; Li Q.-J. et al., 2019; Jiang et al., 2021c). Thus, the MEAs/HEAs exhibit remarkable properties and spark a lot of research interests among materials scientists.

After years of research, there are four unique core effects summarized in HEAs, which are relatively unusual in conventional alloys: high entropy effect, sluggish diffusion effect, lattice distortion effect, and cocktail effect (Tsai et al., 2013; Tsai and Yeh, 2014; Song et al., 2017; Li et al., 2021). These effects are closely related to the phase stability, microstructures, and mechanical properties of MEAs/HEAs. Nevertheless, the high entropy effect is still debatable. In some research, the high mixing entropy was confirmed that can stabilize MEA/HEA solution phases rather than intermetallic and complex phases (Yeh et al., 2004; Tsai and Yeh, 2014). Works on CoCrFeNi HEA argue the absence of long-range ordering, indicating the formation of really disordered solid solutions (Lucas et al., 2012). However, both first-principle density functional theory (DFT)-based simulations and direct experimental observation also verify the presence of LCO in MEAs/HEAs (Ding et al., 2018; Li Q.-J. et al., 2019; Chen et al., 2021).

Hitherto, it has been broadly demonstrated that both MEAs and HEAs have extraordinary mechanical properties over a wide temperature range from elevated to cryogenic temperatures (Jo et al., 2017; Yang M. et al., 2019; Gao et al., 2019; Jiang et al., 2021c). For instance, almost all the traditional high-temperature alloys tend to lose both strength and ductility at high temperatures, while equiatomic NbMoTaW and VNbMoTaW refractory HEAs sustain high strength at elevated temperatures more than 1,000°C (Senkov et al., 2011). At room and cryogenic temperatures, researchers attempt to introduce deformation substructures of stacking faults, deformation twins, and hexagonal close-packed (HCP) phase into MEAs/HEAs by tailoring the SFE (Zaddach et al., 2013). As evidenced by first-principle electronic structure calculations, the SFEs of MEAs/HEAs can be tuned by tailoring the atomic proportions of individual components. For example, the SFE of CrMnFeCoNi HEA is determined as approximately 25.5–27.3 mJm^{-2}, and that of $Cr_{26}Mn_{20}Fe_{20}Co_{20}Ni_{14}$ HEA is as low as 3.5 mJm^{-2} (Zaddach et al., 2013). These induced deformation substructures contribute to improve the strain hardening ability and leads to high tensile strength and ductility. As exemplified, Li et al. designed a metastable $Fe_{50}Mn_{30}Co_{10}Cr_{10}$ HEA to induce interface hardening and dynamic transformation induced hardening effects and consequently overcome the traditional strength–ductility trade-off (Li et al., 2016). Moreover, the prototypical Cantor alloy (CoCrFeMnNi) and its variants and subsets such as $Cr_{26}Mn_{20}Fe_{20}Co_{20}Ni_{14}$ HEA, CoCrFeNi HEA, and CoCrNi MEA are proven to possess remarkable cryogenic properties such as enhanced strength and ductility and superior fracture toughness, which are ascribed to their low SFEs and high propensity for twinning and phase transformation (Zaddach et al., 2013; Gludovatz et al., 2014; Gludovatz et al., 2016). More recently, LCO is confirmed to have significant influence on the SFE, which results in the increase of the SFE with the increase of the LCO (Ding et al., 2018). Furthermore, LCO affects the critical stress for dislocation slip and dislocation storage capacity in the bulk material, thus in turn affecting strain

hardening in single phase MEAs/HEAs (Jiang et al., 2021c). The dislocation slip in MEAs/HEAs has to continuously overcome the activation barriers created by LCO. In turn, MEAs/HEAs with LCO may exhibit higher strength.

Unfortunately, the yield strength of MEAs/HEAs is relatively low, especially for those with single-phase face-centered cubic (FCC) structures, which will greatly limit their industrial application prospects. Traditional methods to improve yield strength, such as solid solution strengthening (He et al., 2020), precipitation strengthening (Ming et al., 2017), and grain boundary strengthening (Sathiyamoorthi et al., 2019b), inevitably cause a degradation of ductility. The simple MEAs/HEAs are not exempted from the dilemma of the strength–ductility trade-off. Therefore, based on the novel alloy design concept with multi-principal elements, it is anticipated to achieve superior mechanical properties by further tuning the microstructures of HEAs/MEAs to fabricate HS structures. This review paper introduces the concept of HS MEAs/HEAs and then emphatically overviews the mechanical properties and deformation mechanisms of HS MEAs/HEAs. Finally, we discuss the prospects and industrial applications of the HS MEAs/HEAs.

HS HEAS

Heterogeneous Gradient Structure

A typical gradient structure is featured by a microstructural gradient at a macroscopic scale, which shows gradually increased grain size, increased substructure size, and reduced defect density from the surface layer to the interior layer (Wu X. L. et al., 2014; Yang et al., 2016; Bian et al., 2017; Pan et al., 2021). Due to the existing grain size gradient and/or the defect density gradient, the gradient structures possess prominent mechanical incompatibility, thus in turn leading to a macroscopic strain gradient and complex stress state, which needs to be accommodated by accumulated GNDs. The gradient structural materials usually show superior strength–ductility synergy, which are ascribed to either mechanically driven grain growth of the unstable nanostructured surface layer (Fang et al., 2011) or extra strain hardening caused by the presence of the strain gradient combined with the stress state change for the mechanically stable gradient structure (Wu X. et al., 2014; Wu X. L. et al., 2014; Bian et al., 2017). The intrinsic synergetic strengthening effect induced by the gradient structure is even much higher than the sum of the strength of individual layers, as calculated by the rule of mixtures (Wu X. L. et al., 2014).

The common methods for producing gradient materials include surface mechanical grinding treatment (SMGT) (Li et al., 2008), surface mechanical rolling treatment (SMRT) (Chen et al., 2020), surface mechanical attrition treatment (SMAT) (Yang et al., 2016), and rotationally accelerated shot peening (RASP) (Hasan et al., 2019; Liang et al., 2020). However, these surface treatment techniques produce only thin nanostructured surface layers with a depth of a few hundred micrometers (~200 μm) along the thickness direction of materials. In contrast, torsion, especially the HPT process, can produce larger-scale gradient structures along the diameter of the samples (Cao et al., 2011; Cao et al., 2014).

RASP was used to prepare gradient structural CoCrFeNiMn HEA (Hasan et al., 2019). Along the thickness direction, there exist gradient microstructures (**Figure 4**), such as gradients in twin and dislocation densities, and hierarchical nanotwin, which contribute to the strain hardening capability and mechanical properties (Hasan et al., 2019). Compared to the coarse grain (CG), the CoCrFeNiMn HEA with gradient structures (RASP1) shows enhanced strength (418 MPa) and ductility (45%) (**Figure 4**) (Hasan et al., 2019). However, an appropriate gradient structure profile is essential for the effective improvement of mechanical properties. Simultaneously enhanced strength and ductility can be realized in a gradient structure with an undeformed core sandwiched between two thin deformed surface layers (RASP1), while the fully deformed gradient structure profile (RASP3) will double the yield strength but sacrifice ductility (Hasan et al., 2019). This is due to the higher strain gradient in the gradient samples with the thin gradient structure profile, thus in turn promoting the generation and accumulation of GNDs to enhance the yield strength and strain hardening.

Gradient structures produced by SMRT are closely related to the processing passes, in which the depth of the surface gradient layer increases with increasing SMRT passes. For the $(Fe_{40}Mn_{40}Co_{10}Cr_{10})_{96.7}C_{3.3}$ HEA with a gradient structure, enhanced strength (from 429 to 765 MPa) together with considerable ductility (20.5%) is achieved, due to the high HDI hardening (Chen et al., 2020). The gradient structure containing dislocations and twins produces multiaxial stress state and strain gradient under tensile deformation, which contributes to the accumulation of GNDs, leading to the improvement of strength higher than the prediction of the rule of mixture.

Cyclic dynamic torsion (CDT) processing was used to obtain a gradient microstructural $Al_{0.1}$CoCrFeNi HEA (Chen et al., 2019a; Chen et al., 2019b). Along the radial direction, grain size gradually decreases from CG (~130 μm) at the center to fine grain (FG, ~8 μm) at the surface layer, as shown in **Figure 5**. Moreover, numerous deformation structures, such as deformation twins, dislocations, and microbands, form due to the torsional strain. The gradient structure results in a gradient distribution of hardness, which decreases from 3.4 GPa in surface layers to 2.6 GPa at the center (Chen et al., 2019a). A combination of high yield strength (850 MPa) and ductility (19%) indicates the important role of gradient microstructures (Chen et al., 2019b). More recently, Pan et al. designed a novel gradient nanoscaled dislocation–cell structures in $Al_{0.1}$CoCrFeNi HEA, which lead to enhanced strength (539 MPa) and little sacrificed ductility (42.6%) (Pan et al., 2021). Numerous low-angle dislocation cells provide nucleation sites for the formation of stacking faults and deformation twins, thereby contributing to extra strengthening, work hardening, and ductility (Pan et al., 2021).

Asymmetric rolling (ASR) followed by annealing is a novel strategy for producing CoCrFeMnNi HEA with gradient microstructures (Han et al., 2018). Different from the homogeneous structures achieved by symmetric rolling and

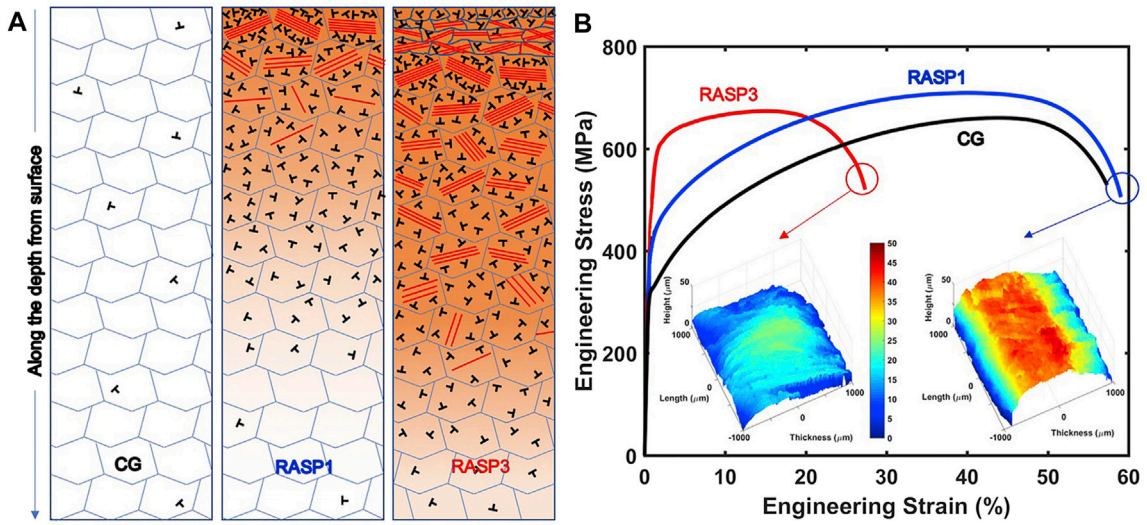

FIGURE 4 | (A) Gradient microstructures of CG, RASP1, and RASP3 samples along depths from the surface. **(B)** Engineering stress–strain curves for CG, RASP1, and RASP3 samples. Insets are the 3D surface topography for RASP1 and RASP3 after tensile deformation. Image adopted from Ref. Hasan et al. (2019) with permission from Elsevier.

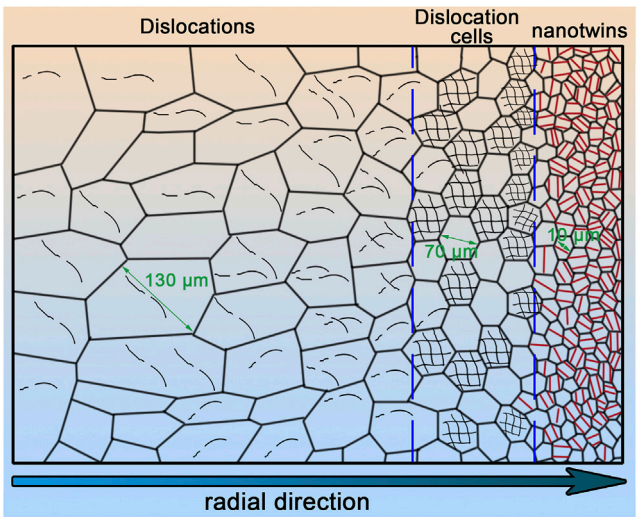

FIGURE 5 | A schematic diagram of the gradient microstructural $Al_{0.1}CoCrFeNi$ HEA after DT processing, showing coarse grain area, intermediate area, and the fine grain area along the radial direction (Chen et al., 2019b; Mao et al., 2021).

annealing treatment, ASR and subsequent annealing processing produce a gradient structure. The surface layers contain UFGs (~500 nm), while the center consists of FGs (~2 μm) (Han et al., 2018). The combined effects of fine-grain strengthening and HDI hardening induced by the gradient microstructure give rise to a superior combination of strength (930 MPa) and ductility (42%).

During the tensile deformation of gradient structures, elastic–plastic deformation occurs immediately after the initial elastic deformation between the center CG regions and the gradient surface layer, thus in turn resulting in an elastic–plastic interface. As the deformation continues, the grains in the inner gradient layer gradually reach the yielding state and begin to deform plastically, leading to the dynamic movement of the elastic–plastic interface toward the surface. Due to the mechanical incompatibility between the center CG regions and the gradient surface layer, they significantly constrain each other during tensile deformation (Yang et al., 2015; Li et al., 2017). The CG core is subjected to tensile stresses laterally, while the gradient surface layer is subjected to compressive stresses along the gradient direction. These biaxial stress states can effectively activate more slip systems and improve the dislocation activities. Moreover, the mutual constraint between the central CG region and the gradient layer during the plastic deformation results in strain gradients near the interfaces to sustain the strain continuity, causing the generation and accumulation of GNDs at the interface. Some surface treatment processes, e.g., SMAT and SMRT, will also introduce the compressive stress, developing multiaxial stress states (Moering et al., 2016). The combined effect of the piling-up of GNDs and multiaxial stress states results in the superior strength–ductility combination in gradient structural materials (**Table 1**).

It has been substantiated that there exist optimal gradient thickness condition and microstructures within the gradient layer to optimize the strain hardening capacity and mechanical properties. Hasan et al. (Hasan et al., 2019) used different RASP parameters to produce a series of gradient structural CoCrFeNiMn HEAs with different gradient structural profiles. This accordingly results in different mechanical properties. Among the gradient structural CoCrFeNiMn HEAs, samples subjected to more severe deformation exhibit an obvious fine-grained layer, while those subjected to mild deformation only exhibit TBs, high-angle grain boundaries, and low-angle grain boundaries distributed along the gradient direction (Hasan et al.,

TABLE 1 | List of the processing steps (P), yield strength (YS), ultimate tensile strength (UTS), and uniform elongation (UE) of MEAs/HEAs reported with gradient structure. AN—annealing; EP-USR—electropulsing-assisted ultrasonic surface rolling; SP—shot peening.

Alloys	P	YS (MPa)	UTS (MPa)	UE (%)	References
CoCrFeMnNi	ASR, AN	700	930	42	Han et al. (2018)
$Al_{0.1}$CoCrFeNi	CDT	510	850	19	Chen et al. (2019b)
$Al_{0.1}$CoCrFeNi	CT	539	690	42	Pan et al. (2021)
$(Fe_{40}Mn_{40}Co_{10}Cr_{10})_{96.7}C_{3.3}$	SMRT	587	885	40.4	Chen et al. (2020)
$(Fe_{40}Mn_{40}Co_{10}Cr_{10})_{96.7}C_{3.3}$	SMRT	765	956	20.5	Chen et al. (2020)
CrCoFeNiMn	RASP	418	720	45	Hasan et al. (2019)
CrCoFeNiMn	RASP	610	680	15	Hasan et al. (2019)
CoCrFeMnNi	EP-USR	750	802	21.9	Xie et al. (2020a)
$CoCrFeNiMo_{0.15}$	Torsion	724	904	27	Wu et al. (2017)
$FeCoCrNiMo_{0.15}$	SP	486	855	46.8	Guo et al. (2020)
CoCrNi	Torsion	760	880	31	Liu et al. (2021a)
CoCrNi	Torsion, AN	930	1,050	27	Liu et al. (2021b)

TABLE 2 | List of the heterogeneous structures (H) and mechanical properties of MEAs/HEAs reported with heterogeneous grain structure. "-" represents the compressive test.

Alloys	H	YS (MPa)	UTS (MPa)	UE (%)	References
$Co_{25}Ni_{25}Fe_{25}Al_{7.5}Cu_{17.5}$	NG + UFG	-1795	-1936	-10.6	Fu et al. (2016)
$Ti_{10}Fe_{30}Co_{30}Ni_{30}$	NG + CG	-1830	-2024	-18.7	Fu et al. (2018)
$Cr_{20}Fe_6Co_{34}Ni_{34}Mo_6$	FG + UFG	1,100	1,300	29	Ming et al. (2019)
$V_{10}Cr_{15}Mn_5Fe_{35}Co_{10}Ni_{25}$	FG + CG	761	936	28.3	Jo et al. (2017)
$Al_{0.1}$CoCrFeNi	UFG + FG + CG	711	928	30.3	Wu et al. (2019b)
$Al_{0.1}$CoCrFeNi	FG + CG	525	784	37	Wang et al. (2019)
CrMnFeCoNi	FG + UFG	625	855	50.7	Bae et al. (2017)
CoCrFeNiMn	UFG + CG	1,298	1,390	9.4	Xie et al. (2020b)
CoCrNi	NG + UFG + FG	1,150	1,320	22	Yang et al. (2018a)
CoCrNi	UFG + FG	797	1,360	19	Slone et al. (2019)
CoCrNi	FG + UFG	928	1,191	28	Sathiyamoorthi et al. (2019a)
CrCoNi	CG + NG	1,452	1,520	10	Schuh et al. (2019)
CoCrNi	UFG + FG	1,435	1,580	24	Sathiyamoorthi et al. (2019b)

2019). The former shows the dramatic improvement of yield strength but scarified ductility, while the latter shows the simultaneously enhanced strength and ductility (**Figure 4**). This is attributed to the optimal gradient structures of a sandwich structure with a CG core and a thin layer of gradient structure on each side of the surface, improving mechanical properties due to the hierarchical twin structures in the gradient structural layers and the prominent strain gradient induced during the subsequent tensile deformation (Hasan et al., 2019). Besides, the surface treatment processes and the geometry of the tensile samples will lead to the difference in stress state and thus in turn influence the mechanical properties of the materials with gradient structures (Moering et al., 2016). For example, the SMAT and RASP processes can produce rod and flat samples, respectively. For the former, the ductile core is fully confined by the hard-outer surface and subjected to complex stress states, while for the latter, the ductile core is not confined in the lateral surface and subjected to biaxial stress states (Hasan et al., 2019; Chen et al., 2020).

Heterogeneous Grain Structure

"Smaller is stronger" means that grain refinement from CG to nano-grain (NG) results in extreme improvement in strength for conventional materials. However, low ductility has always been a problem for NG materials. Scientists are always looking for materials that have both the strength of NG and the ductility of CG. Recently, a heterogeneous material with bimodal and/or multimodal grain structures is a novel material design strategy to unite the advantages of both CG materials and NG materials, which present high strain hardening rate and superior strength and ductility combination (Wang et al., 2002).

Inspired by this concept, many strategies are explored to produce bimodal structural materials (**Table 2**). Both bimodal $Fe_{30}Co_{30}Ni_{30}Ti_{10}$ MEA and $Fe_{25}Co_{25}Ni_{25}Al_{7.5}Cu_{17.5}$ HEA produced by mechanical alloying and following spark plasma sintering exhibit high compressive strength (>1.7 GPa) and enhanced plasticity, as compared to their CG counterparts (Fu et al., 2016; Fu et al., 2018). The combined effect of local temperature gradient in SPS processing and sluggish diffusion effect of MEAs/HEAs results in the inhomogeneous grain size, where the $Fe_{30}Co_{30}Ni_{30}Ti_{10}$ MEA consists of CGs (>1 μm) and NGs and the $Fe_{25}Co_{25}Ni_{25}Al_{7.5}Cu_{17.5}$ HEA is comprised of NGs and UFGs (>200 nm) (Olevsky and Froyen, 2009; Tsai et al., 2013). HPT followed by annealing processing successfully produces bimodal microstructures in CoCrNi MEA (Sathiyamoorthi et al., 2019b; Schuh et al., 2019). Annealing parameters such as temperature and time play an important role in the ratio of bimodal grains and thus in turn influence the

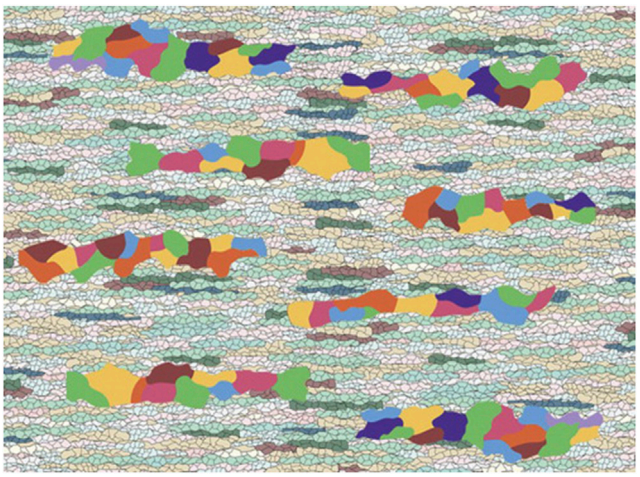

FIGURE 6 | Schematics of the lamella structure with elongated soft coarse-grained domains embedded in an ultrafine-grained matrix. Image adopted from Ref. Wu and Zhu (2017) with permission from Taylor and Francis.

mechanical properties. For the CoCrNi MEA annealed at 500°C/100 h, the mixture of NG and FG structures gains the ultra-high strength (1,500 MPa) and decent ductility (10%) combination (Schuh et al., 2019). By contrast, Sathiyamoorthi et al. (Sathiyamoorthi et al., 2019b) doubled the ductility (24%) of CoCrNi MEA with comparable strength (1,580 MPa) *via* HPT and followed annealing processing (600°C/1 h). Bimodal grain structures comprised of UFGs and FGs are responsible for the superior strength–ductility synergy. This observation indicates that the bimodal grain structure with UFGs and FGs seems to be better than that with NGs and FGs.

More strikingly, material design strategies for fabricating three-level heterogeneous grain structures, characterized by mixture of NGs, UFGs, and FGs, are successfully controlled (**Table 2**). Through partial recrystallization, Yang et al. (Yang M. et al., 2018) produced a HS CoCrNi MEA with a large span of grain size from NG to FG, imparting gigapascal yield strength (1,150 MPa) and high ductility (22%). Similarly, the $CoCrFeNiAl_{0.1}$ HEA with multiscale grains was produced by cold-rolling and intermediate temperature annealing, which is featured by three types of grains consisting of stretched grains (~20 μm), deformed grains (1–20 μm), and recrystallized grains (0.2–5 μm) (Wu S. W. et al., 2019). The thermomechanical treatments induced a difference in grain sizes, and dislocation density leads to a superior combination of yield strength (711 MPa) ductility (30.3%) (Wu S. W. et al., 2019).

According to the "smaller is stronger," NGs and/or UFGs in either bimodal or multimodal MEAs/HEAs serve as hard zones, while CGs serve as soft zones. Such HS materials present extra strain hardening ability, attributing to the generation and accumulation of GNDs to accommodate the strain gradient at zone interface (Wang et al., 2002). Moreover, partitioning of stress and strain comes into being at the zone interface, inducing a high stress concentration upon plastic deformation. Such stress concentration will achieve the critical resolved shear stress (CRSS) for twinning and generate twinned NGs, which in turn results in greater inhomogeneity (Yang M. et al., 2018). Significant HDI hardening effects together with the TWIP effects result in the superior strength–ductility synergy.

HLS

The HLS is featured by the soft micro-grained lamellae embedded in the hard UFG/NG lamella matrix (**Figure 6**). This material design strategies can also effectively unite the advantages of both CG materials and nanostructured materials to achieve excellent mechanical properties. Wu et al. (Wu et al., 2015) produced an HLS Ti, which presents an unprecedented property combination: as strong as UFG metals and as ductile as CG metals (Wu et al., 2015). HDI stress results in the unusual high strength, while HDI hardening and dislocation hardening lead to the high ductility (Wu et al., 2015).

For fabricating the HLSs, some approaches are typically employed, such as powder metallurgy with different size particles and asymmetrical rolling followed by annealing to obtain recrystallization with laminar distribution (Wu et al., 2015; Huang et al., 2017). Zhang et al. (Zhang et al., 2018; Zhang et al., 2019) successfully produced two kinds of MEAs with HLSs through thermomechanical processing (rolling and annealing). After cold rolling, numerous deformed structures, such as deformation bands, shear bands, and microbands, are formed, which depends on the original grain size (Zhang et al., 2019). After subsequent annealing, these deformed structures evolve into different annealing structures, forming HLSs. Partial recrystallization occurs to form recrystallized grains with sizes between 3 and 7 μm in the shear bands due to the high dislocation density (Zhang et al., 2019), while some UFGs with sizes less than 1 μm form in the large deformation bands (Zhang et al., 2019). The difference in the fraction of precipitates between the large deformation bands and shear bands has great influence on the behavior of recrystallization and grain growth. With increasing annealing time, the recrystallization and grain growth in large deformation bands occur, while these behaviors are much slower in shear bands due to the much more precipitate-induced Zener pinning effect (Zhang et al., 2018; Zhang et al., 2019). Thus, the rolling and subsequent annealing process results in the nonuniform grain size and the formation of the HLSs comprising of a UFG-FG lamella structure or FG-CG lamella structure (Zhang et al., 2019). The HS structure leads to a good combination of strength and ductility compared to simple FG and CG samples (Zhang et al., 2018).

The key advantage of materials with HLSs is the enhanced strain hardening ability (Wu et al., 2015; Wu and Zhu, 2017), which can prevent the early onset of necking (Hart, 1967). Due to the distribution of soft and hard lamella structures, corresponding to the CG and UFG grains, lots of GNDs are introduced to accommodate the strain gradients in order to avoid the formation of voids during the loading process. UFG lamellae with higher yield strength surround and constrain the soft CG lamellae, leading to the accumulation and block of dislocations in the CGs. Thus, yielding occurs in CG lamellae first due to the higher resolved shear stress from dislocation pile-

TABLE 3 | List of the heterogeneous structures and mechanical properties of MEAs/HEAs reported with HLSs.

Alloys	H	YS (MPa)	UTS (MPa)	UE (%)	References
FeNiCoAlTaB	FG + UFG	586	1,050	23	Zhang et al. (2019)
FeNiCoAlTaB	FG + CG	484	890	43	Zhang et al. (2019)
FeNiCoAlCrB	FG + CG	330	690	34	Zhang et al. (2018)
FeNiCoAlTaB	FG + CG	851	1,400	30	Zhang et al. (2020)
FeNiCoAlTaB	FG + CG	1,100	1700	10	Zhang et al. (2020)

TABLE 4 | A collection of reported HEAs with completely eutectic microstructure.

Alloys	Eutectic structure	YS (MPa)	UTS (MPa)	UE (%)	References
$AlCrFeNi_3$	(FeCrNi)-FCC + (AlNi)-B2	626	1,200	10.1	Dong et al. (2020)
$CrFeNi_{2.2}Al_{0.8}$	(FeCrNi)-FCC + (AlNi)-B2	479	956	12.7	Jin et al. (2019)
$Ni_{30}Co_{30}Cr_{10}Fe_{10}Al_{18}W_2$	(FeCoCrNi)-FCC + (AlNi)-B2	700	1,266	20.3	Wu et al. (2019a)
$Fe_{20}Co_{20}Ni_{41}Al_{19}$	(Fe, Co)-rich $L1_2$ + (AlNi)-B2	577	1,103	18.7	Jin et al. (2018b)
$Fe_{28.2}Ni_{18.8}Mn_{32.9}Al_{14.1}Cr_6$	(Fe, Mn, Ni)-FCC + (AlNi)-B2	599	868	19.5	Baker et al. (2016)
$Fe_{36}Ni_{18}Mn_{33}Al_{13}$	(Fe, Mn, Ni)-FCC + (AlNi)-B2	270	578	22.8	Wang et al. (2016)
$Al_{17}Co_{14.3}Cr_{14.3}Fe_{14.3}Ni_{40.1}$	$L1_2$ + B2	479	1,067	14	Jin et al. (2018a)
$Al_{17}Co_{28.6}Cr_{14.3}Fe_{14.3}Ni_{25.8}$	FCC + B2	476	1,001	14.8	Jin et al. (2018a)
$Al_{17}Co_{14.3}Cr_{14.3}Fe_{28.6}Ni_{25.8}$	FCC + B2	731	1,145	10.3	Jin et al. (2018a)

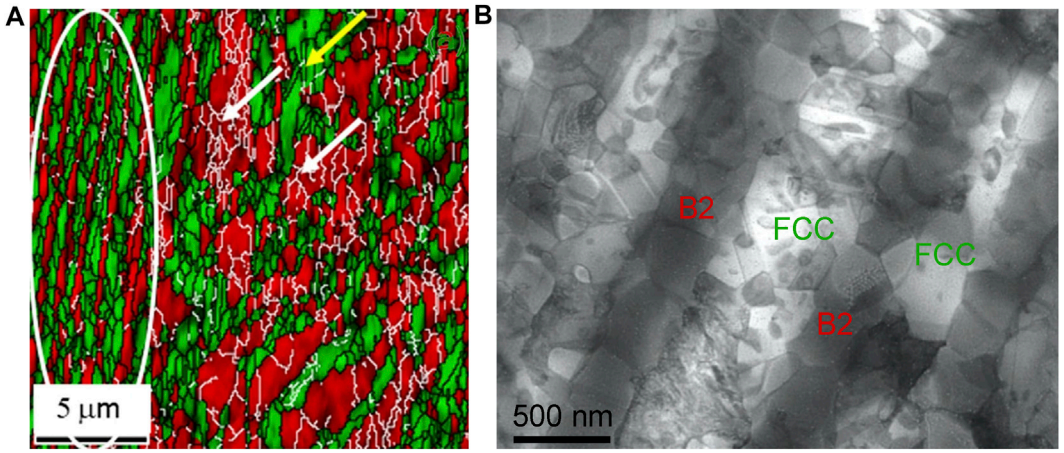

FIGURE 7 | Eutectic lamellate structures in $AlCoCrFeNi_{2.1}$ HEA by thermomechanical treatments. **(A)** Cryo-rolling and annealing (Bhattacharjee et al., 2018), **(B)** cold-rolling and annealing (Shi et al., 2019). Image adopted with permission under the terms of Creative Common License.

ups at the CG/UFG interface (Eshelby et al., 1951). Pile-ups of GNDs will also induce the long-range back stress, which resists the movement of dislocations in the CG lamellae and thus enhance strain hardening (Wu et al., 2015). With further increase in tensile load, the UFG lamellae begin plastic deformation, and hence the overall strength is enhanced by the HDI stress. The MEAs/HEAs with HLSs present remarkable mechanical properties, as shown in **Table 3**.

Heterogeneous Phase Structure

Eutectic structure

The approach of introducing two phases has been successfully used in MEAs/HEAs such as eutectic HEAs (Lu et al., 2014; Gao et al., 2017). Generally, the eutectic HEAs consist of alternate layers of soft FCC and hard B_2 phases (Baker et al., 2016; Wang et al., 2016; Jin et al., 2018b; a; Jin et al., 2019; Wu Q. et al., 2019; Dong et al., 2020), which possess a dramatic difference in strength and hardness. Like conventional dual-phase steel, the eutectic HEAs are typical HS materials that present a superior combination of strength and ductility, as shown in **Table 4**.

Among the numerous eutectic HEAs, $AlCoCrFeNi_{2.1}$ is the most widely investigated. Through different thermomechanical treatments, such as warm-rolling, cryo-rolling, cold-rolling, and subsequent annealing process, the heterogeneous microstructures of the $AlCoCrFeNi_{2.1}$ eutectic HEA can be further tuned to achieve superior mechanical properties, as shown in **Figure 7** (Bhattacharjee et al., 2018; Shukla et al., 2018; Reddy et al., 2019; Shi et al., 2019). Warm-rolled (750°C) $AlCoCrFeNi_{2.1}$ eutectic

TABLE 5 | List of the processing steps (P), eutectic structure (S) and mechanical properties of reported eutectic HEAs. AC—as cast, WR—warm rolling, CR—cold rolling, CryoR—cryo rolling, AN—annealing, A—aging.

Alloys	P	S	YS (MPa)	UTS (MPa)	UE (%)	References
$AlCoCrFeNi_{2.1}$ eutectic HEA	AC	FCC + B2		1,100	18	Gao et al. (2017)
	WR		1,192	1,635	18	Reddy et al. (2019)
	50%CR, AN		1,110	1,340	10	Shukla et al. (2018)
	84%CR, AN		1,490	1,638	16	Shi et al. (2019)
	CryoR, AN		1,437	1,562	14	Bhattacharjee et al. (2018)
	70%CR, AN, A		1,009	1,476	19	Xiong et al. (2020)

HEA presents a heterogeneous microstructure characterized by the mixture of the retained lamellar region of B2 and FCC with B2 phases inside the FCC lamellar and non-lamellar regions consisting of disordered FCC, precipitated B2, and Cr-rich sigma phases (Reddy et al., 2019). The heterogeneous microstructures produced by cold-rolling and cryo-rolling and subsequent annealing are quite different. Through cold-rolling and following annealing, the $AlCoCrFeNi_{2.1}$ eutectic HEA consists of hard and soft lamellae with recrystallized grains and substantial B2 precipitates (Shukla et al., 2018; Shi et al., 2019). The cryo-rolling and subsequent annealing result in an HLS comprising of fine alternative FCC and B2 lamellar structures and coarse non-lamellar regions (Bhattacharjee et al., 2018). The fine FCC and B2 lamellae are filled with recrystallized UFGs (~200–250 nm) and low-angle grain boundaries, respectively, while the coarse non-lamellar regions are featured by ultrafine FCC (~200–250 nm), coarse recrystallized FCC grains, and coarse uncrystallized B2 phase (~2.5 μm) (Bhattacharjee et al., 2018). However, the Cr-rich sigma phases observed in the warm-rolled (750°C) $AlCoCrFeNi_{2.1}$ eutectic HEA were not observed in the HEA processed by cold-rolling and cryo-rolling.

Despite of the difference in thermomechanical treatments, all these remarkable HS $AlCoCrFeNi_{2.1}$ eutectic HEAs with high lamella density obtain an outstanding strength–ductility combination with gigapascal yield strength and ductility of over 15% (**Table 5**). This is attributed to the constraint effect originated from the lamellae. Upon plastic deformation, the hard B2 lamellae and the intergranular B2 precipitates provide rigid deformation constraint to FCC lamellae, resulting in generation and accumulation of GNDs at the lamellar interface and at the FCC-B2 interphase. This in turn makes the soft FCC lamellae stronger and improves the overall yield strength of $AlCoCrFeNi_{2.1}$ eutectic HEAs. Further plastic deformation results in the synergistic deformation of both hard and soft lamellae, with soft FCC lamellae bearing a higher strain, leading to the more substantial HDI hardening effect. Moreover, the aligned lamellar structure and ductile FCC matrix can delay crack propagation and coalescence, thereby delaying the onset of global necking (Shi et al., 2019; Shi et al., 2021).

Precipitation structure

As utilized in traditional materials, precipitations can be introduced in the grain interior to enhance the accumulation of dislocations when they intersect or bypass precipitations. This will result in strain hardening and consequently higher ductility. Moreover, the precipitations will impede the slip of dislocations and increase the stress required for dislocation movement. Thus, precipitation strengthening is an important strategy for improving the yield strength of MEAs/HEAs. This approach has been reported by several groups with the addition of Al, Cu, and Mo alloying elements to produce multiphase structures. Various kinds of precipitations, such as σ, μ, B2, BCC, and $L1_2$ phases, have been compounded in MEAs/HEAs to achieve superior mechanical properties (**Table 6**). It should be noted that, in order for this approach to be effective, the concentration of the alloying elements and the thermomechanical processing need to be optimized (Shahmir et al., 2016).

A multiphase hierarchical microstructure in $Al_{0.3}CoCrNi$ MEA was achieved by cold-rolling and annealing (Sathiyamoorthi et al., 2019c). After annealing, the multiphase hierarchical microstructure features non-recrystallized regions, partial recrystallized regions with fine (3 ± 2 μm) and coarse (14 ± 3 μm) grains, and hierarchical distribution of σ phase (100–500 nm) and B2 precipitates (300–400 nm). This $Al_{0.3}CoCrNi$ MEA with a multiphase hierarchical microstructure presents an excellent combination of high yield strength (1 GPa), high tensile strength (1.2 GPa), and high ductility (~28%). Similarly, the $CoCrFeNiMo_{0.3}$ HEA strengthened by σ and μ particles presents a yield strength of 816 MPa and a ductility of ~19% (Liu et al., 2016). By using different thermomechanical processings, Choudhuri et al. fabricated a three-phase microstructure consisting of FG FCC, ordered B2, and σ phase in $Al_{0.3}CoCrFeNi$ HEA (Choudhuri et al., 2019). Strikingly, the $Al_{0.3}CoCrFeNi$ HEA with a three-phase microstructure shows a fourfold increase in yield strength and more significant work hardening ability compared to that with only the FCC microstructure.

The thermomechanical processing-induced precipitations have significant effects on the mechanical properties of MEAs/HEAs. First, the precipitations promote the formation of heterogeneous grain structures. The difference in dislocation density and interface energy induced by plastic deformation results in heterogeneous nucleation and distribution of precipitation (Gwalani et al., 2018; Sathiyamoorthi et al., 2019c). Meanwhile, the heterogeneous precipitations can delay the recrystallization process and facilitate partial recrystallization with formation of fine and coarse recrystallized grains (Sathiyamoorthi et al., 2019c; He et al., 2020). Second, precipitations offer an important strengthening effect. Both the experiments by transmission electron microscopy and molecular

TABLE 6 | List of the strengthening phase (P) and mechanical properties of MEAs/HEAs reported with multiphase hierarchical microstructure.

Alloys	P	YS (MPa)	UTS (MPa)	UE (%)	References
$(FeCoNiCr)_{94}Ti_2Al_4$	$L1_2$, Ni_2AlTi	645	1,094	39	He et al. (2016)
$CoCrFeNiMo_{0.3}$	σ, μ	816	1,187	19	Liu et al. (2016)
$Al_{0.5}Cr_{0.9}FeNi_{2.5}V_{0.2}$	Ni_3Al, BCC	1800	1900	9	Liang et al. (2018)
$Al_{0.3}CrFeNi$	$L1_2$, B2	1,074	1,302	8	Dasari et al. (2020)
$Ni_{30}Co_{30}Fe_{13}Cr_{15}Al_6Ti_6$	$L1_2$	925	1,310	35	Yang et al. (2019b)
$(CoCrNi)_{94}Al_3Ti_3$	$L1_2$	750	1,300	40	Zhao et al. (2017)
$Al_{0.5}CrFeCoNiCu$	$L1_2$	850	1,300	35	Yang et al. (2018b)
$Al_7Co_{23.26}Cr_{23.26}Fe_{23.26}Ni_{23.26}$	$L1_2$, B2	490	825	48	Borkar et al. (2016)
$(Fe_{25}Co_{25}Ni_{25}Cr_{25})_{94}Ti_2Al_4$	$L1_2$, $L2_1$	645	1,094	39	He et al. (2016)
$Al_{3.7}Cr_{18.5}Fe_{18.5}Co_{18.5}Ni_{37}Cu_{3.7}$	$L1_2$	719	1,048	30.4	Wang et al. (2017)
$Al_{3.64}Co_{40.9}Cr_{27.27}Fe_{27.27}Ni_{40.9}Ti_{5.45}$	$L1_2$	640	830	10	Kuo and Tsai, (2018)
$Al_{3.31}Co_{27}Cr_{18}Fe_{18}Ni_{27.27}Ti_{5.78}$	$L1_2$	952	1,306	20.5	Chang and Yeh, (2018)
$Al_{10}Co_{25}Cr_8Fe_{15}Ni_{36}Ti_6$	$L1_2$	596	1,039	20	Daoud et al. (2015)

dynamic simulations have demonstrated that the ordered B2 and σ phases will raise the local stress levels to facilitate deformation twinning (Choudhuri et al., 2019). Furthermore, direct observation by EBSD shows the heterogeneous distribution of strain induced by the heterogeneous microstructures, with higher strain accumulation in uncrystallized regions and FGs (Sathiyamoorthi et al., 2019c). The outstanding mechanical properties of MEAs/HEAs with multiphase hierarchical microstructure are attributed to the combined effect of hierarchical constraints to the deformation of the major phase. The combination of strengthening from HDI stress induced by heterogeneous structures and effective stress induced by nano-precipitates results in high strength, while the GNDs and twins lead to a remarkable strain hardening rate and thus high ductility.

Dynamic phase transformation

It has been documented that the deformation mechanisms in FCC materials perform as a function of SFE, which can be summarized as the following: 1) SFEs for dislocation slip are higher than 60 mJm^{-2}; 2) SFEs for twinning are in the range of 20–60 mJm^{-2}; and 3) SFEs for transformation from the FCC to HCP phases are lower than 20 mJm^{-2} (Remy and Pineau, 1977; Saeed-Akbari et al., 2012). The low SFE promotes the dissociation of unit dislocation into partial dislocations and suppresses the unit dislocation slip. Furthermore, the low SFE reduces the CRSS for phase transformation, and hence it enhances the TRIP effects, leading to dynamically accumulating dislocations and hardening of alloys during deformation. Therefore, MEAs/HEAs with extremely low SFE usually experience dynamic phase transformation from FCC to HCP and achieve simultaneously enhanced strength and ductility.

Utilizing this concept, metastable dual-phase $Fe_{80-x}Mn_xCo_{10}Cr_{10}$ (at%) HEAs were developed, which overcome the traditional strength–ductility trade-off (Li et al., 2016). By tuning the Mn content, the authors realized the transition of dominating deformation mechanisms from dislocation slip to the TWIP effect in metastable HEAs, due to the lower Mn content-induced reduction of SFE. Finally, the $Fe_{50}Mn_{30}Co_{10}Cr_{10}$ HEA is composed of the dual-phase microstructure with ~28% HCP phase and ~72% FCC phase (Li et al., 2016). Upon plastic deformation, sustaining phase transformation from the FCC to HCP phases is realized through the formation of stacking faults on alternative slip planes. The phase transformation-induced high-phase boundary density creates additional obstacles for dislocation slip, thereby contributing to higher strain hardening in the dual-phase $Fe_{50}Mn_{30}Co_{10}Cr_{10}$ HEA than in the single-phase HEAs (Li et al., 2016). In conclusion, the increased interface density and the massive solid solution strengthening result in greatly improved strength, while at the same time the dislocation plasticity and transformation-induced hardening lead to enhanced ductility. The synergic deformation of the two phases leads to a highly beneficial dynamic strain–stress partitioning effect, and thus the combined increase in strength and ductility (Li et al., 2016).

Similarly, Su et al. developed an HS interstitial carbon-doped HEA ($Fe_{49.5}Mn_{30}Co_{10}Cr_{10}C_{0.5}$ (at%), which exhibits excellent mechanical properties (Su et al., 2019). Through a thermomechanical process (cold-rolling and annealing at 600°C), the authors can fine-tune the microstructures of the HEAs to form a trimodal grain structures featured by fine recrystallized grains (<1 μm) related to shear bands, medium-sized grain (1–6 μm) recrystallized from the retained FCC phase, and large non-recrystallized grains from the reverted FCC phase (**Figure 8**) (Su et al., 2019). The tri-modal grain structure shows superior combination of yield strength and ductility compared to the fully recrystallized coarse and FGs. Nano-twins and grain refinement account for the improvement in yield strength, and multistage work hardening associated with the TWIP and TRIP effects accounts for the enhanced ductility (Su et al., 2019).

The transformation nucleus of FCC usually occurs in the SF–SF intersections, which has been revealed in the FCC/BCC transformation in $Co_{25}Ni_{25}Fe_{25}Al_{7.5}Cu_{17.5}$ HEA by molecular dynamic simulation (Li et al., 2018). In addition, the nano-HCP laths may form in the presence of nano-twins, leading to the formation of nano-twin–HCP composite lamellae. The nanocomposite of the dual-phase mixture offers an optimal balance of strain and stress benefits and decreases the possibility of damage nucleation due to their elastic compliance. Without the adjustment to the deformation *via* twinning and/or dislocation slip, the deformation attributed solely to the single HCP phase transformation is prone to produce damage to the tensile specimen, thereby leading to a

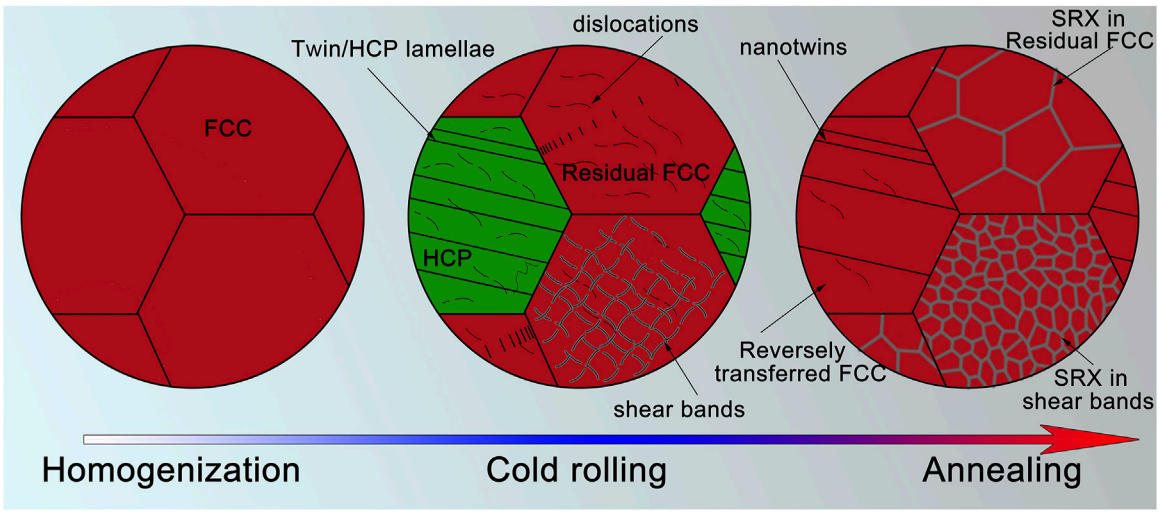

FIGURE 8 | A schematic diagram of producing $Fe_{49.5}Mn_{30}Co_{10}Cr_{10}C_{0.5}$ with bimodal and trimodal microstructures (Su et al., 2019).

premature fracture even though the TRIP effect is contributed to a high strain hardening effect. When compared with the hardening effect from TBs, the HCP lamellar structure would be an effective barrier for dislocation slip since the transmission of edge-component dislocations into the HCP phase would require the activation of either <c> or < c + a> dislocation with a component along (0001) (Miao et al., 2017; Lu et al., 2018). The <c> or < c + a> dislocation typically exhibits extremely high CRSS in HCP materials.

Heterogeneous Structure by Additive Manufacturing

The additive manufacturing technique, including selective laser melting and direct laser deposition, can also produce bulk heterogeneous structures in HEAs/MEAs, without any post-processing (e.g., homogenization, severe plastic deformation, and annealing). The additive manufacturing technique possesses unique forming mode (e.g., melt pool connection, layer-by-layer deposition, high cooling rate, and nonequilibrium solidification). Thus, the produced heterogeneous structures are usually featured by melt pools, columnar grains, cellular dislocation structures, twinning, solute heterogeneity, and precipitation (Zhu et al., 2018; Park et al., 2019; Kim et al., 2020; Luo et al., 2020; Wang et al., 2020).

In the single-phase CoCrFeMnNi HEA produced by selective laser melting, the three-dimensional dislocation network structures are observed (Zhu et al., 2018). Such unique dislocation networks generate by the substantial interaction between dislocation slip bands and cellular dislocation walls and show no misorientation with the matrix. These cellular dislocation structures can efficiently accommodate and trap dislocations to bring about remarkably dislocation hardening, thereby resulting in an outstanding combination of high strength (609 MPa) and excellent ductility (34%) (Zhu et al., 2018).

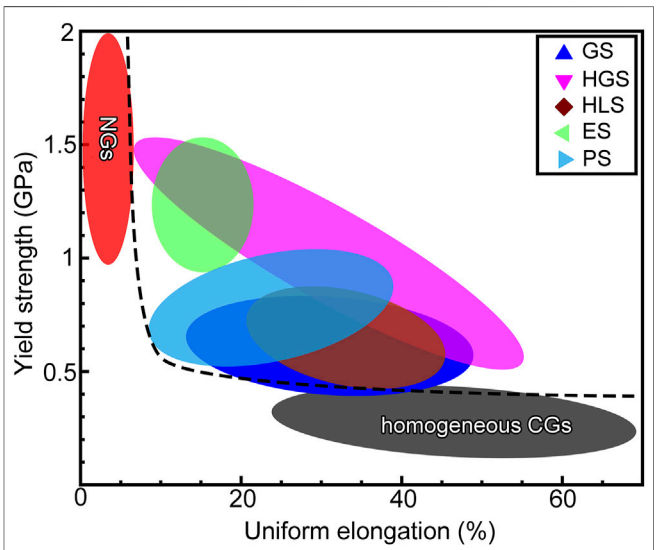

FIGURE 9 | Yield strength versus uniform elongation of MEAs/HEAs with homogeneous structures (below banana-shaped region) and various heterostructures. (GS, HGS, HLS, ES, and PS are gradient structure, heterogeneous grain structure, heterogeneous lamella structure, eutectic structure, and precipitation structure, respectively).

Luo et al. fabricate a dual-phase AlCrCuFeNix (x = 2.0, 2.5, 2.75, 3.0) HEA with BCC and FCC structures using selective laser melting (Luo et al., 2020). The AlCrCuFeNix HEA exhibits an excellent combination of strength (957 MPa) and ductility (14.3%), which is attributed to the heterogeneous microstructures and distinct deformation mechanisms in FCC and BCC phases (Luo et al., 2020). The deformation of FCC phases is carried by planar dislocation slip and stacking faults, while high densities of Cr-rich nano-precipitates promote the formation of deformation twins and stacking faults in BCC

phases. Moreover, the strain-induced phase transition from BCC to FCC contributes to the strain hardening and ductility.

However, there remains a paucity of studies on the nature and the inherent formation mechanisms of the heterogeneous structures in additively manufactured materials. Much more effort is required to understand the influence of processing parameters to design HEAs/MEAs with superior mechanical properties.

SUMMARY AND FUTURE ISSUES

This review paper introduces HS and HEA concepts and emphatically reviews the microstructure, mechanical properties, and deformation mechanisms of HS MEAs/HEAs. The HS design can enhance strain hardening capacity and delay plastic instability, effectively evading the paradox between strength and ductility observed in metallic materials with conventional strengthening strategies. The introduction of HS into MEAs/HEAs helps to achieve a superior strength–ductility synergy, as shown in **Figure 9**. The HS MEAs/HEAs should be comprised of different microstructures characterized by large strength difference, which induces stress and strain partitioning upon tensile deformation and thus leads to GND pile-up and HDI-stress effects.

From the previous reported mechanical properties of MEAs/HEAs with heterostructure, the field is still in its incipient stage and the great potential in next-generation structural and functional applications spanning diverse fields remains to be explored, such as transportation, energy sustainability (nuclear reactors and hydrogen storage), aerospace applications, and biomedical applications. Meanwhile, the shortcomings in the field of high-entropy alloy research must be faced up to, which is the transition from laboratory explorations to practical engineering applications. For example, strength and ductility are the concern for laboratory investigations whereas a complex application environment must be considered for practical applications. In this sense, more application-driven and building-up of benchmarking for commercial application is also a crucial step in exploring MEAs/HEAs. Most importantly, the expense could by and large be a decisive issue for utilizations of MEAs/HEAs, which requires careful contemplations.

AUTHOR CONTRIBUTIONS

WJ wrote the first draft of the manuscript. YTZ and YHZ reviewed and edited the manuscript. All authors contributed to the article and agreed to the submitted version of the manuscript.

FUNDING

The authors acknowledge financial support from the National Key R and D Program of China (Grant No. 2017YFA0204403), the National Natural Science Foundation of China (Grant No. 51971112 and 51225102), the Fundamental Research Funds for the Central Universities (Grant No. 30919011405), and the Hong Kong Research Grants Council (GRF 11214121).

REFERENCES

An, X. H., Wu, S. D., Zhang, Z. F., Figueiredo, R. B., Gao, N., and Langdon, T. G. (2012). Enhanced Strength-Ductility Synergy in Nanostructured Cu and Cu-Al Alloys Processed by High-Pressure Torsion and Subsequent Annealing. *Scripta Materialia* 66, 227–230. doi:10.1016/j.scriptamat.2011.10.043

Bae, J. W., Moon, J., Jang, M. J., Yim, D., Kim, D., Lee, S., et al. (2017). Trade-off between Tensile Property and Formability by Partial Recrystallization of CrMnFeCoNi High-Entropy alloy. *Mater. Sci. Eng. A* 703, 324–330. doi:10.1016/j.msea.2017.07.079

Baker, I., Meng, F., Wu, M., and Brandenberg, A. (2016). Recrystallization of a Novel Two-phase FeNiMnAlCr High Entropy alloy. *J. Alloys Compd.* 656, 458–464. doi:10.1016/j.jallcom.2015.09.264

Bhattacharjee, T., Wani, I. S., Sheikh, S., Clark, I. T., Okawa, T., Guo, S., et al. (2018). Simultaneous Strength-Ductility Enhancement of a Nano-Lamellar AlCoCrFeNi2.1 Eutectic High Entropy Alloy by Cryo-Rolling and Annealing. *Sci. Rep.* 8, 3276. doi:10.1038/s41598-018-21385-y

Bian, X., Yuan, F., Zhu, Y., and Wu, X. (2017). Gradient Structure Produces superior Dynamic Shear Properties. *Mater. Res. Lett.* 5, 501–507. doi:10.1080/21663831.2017.1334715

Borkar, T., Gwalani, B., Choudhuri, D., Mikler, C. V., Yannetta, C. J., Chen, X., et al. (2016). A Combinatorial Assessment of AlxCrCuFeNi2 (0. *Acta Materialia* 116, 63–76. doi:10.1016/j.actamat.2016.06.025

Bouaziz, O., Allain, S., Scott, C. P., Cugy, P., and Barbier, D. (2011). High Manganese Austenitic Twinning Induced Plasticity Steels: A Review of the Microstructure Properties Relationships. *Curr. Opin. Solid State. Mater. Sci.* 15, 141–168. doi:10.1016/j.cossms.2011.04.002

Bouaziz, O., Zurob, H., and Huang, M. (2013). Driving Force and Logic of Development of Advanced High Strength Steels for Automotive Applications. *Steel Research Int.* 84, a–n. doi:10.1002/srin.201200288

Byun, T. S., Hashimoto, N., and Farrell, K. (2004). Temperature Dependence of Strain Hardening and Plastic Instability Behaviors in Austenitic Stainless Steels. *Acta Materialia* 52, 3889–3899. doi:10.1016/j.actamat.2004.05.003

Calcagnotto, M., Adachi, Y., Ponge, D., and Raabe, D. (2011). Deformation and Fracture Mechanisms in fine- and Ultrafine-Grained Ferrite/martensite Dual-phase Steels and the Effect of Aging. *Acta Materialia* 59, 658–670. doi:10.1016/j.actamat.2010.10.002

Cantor, B., Chang, I. T. H., Knight, P., and Vincent, A. J. B. (2004). Microstructural Development in Equiatomic Multicomponent Alloys. *Mater. Sci. Eng. A* 375-377, 213–218. doi:10.1016/j.msea.2003.10.257

Cao, Y., Ni, S., Liao, X., Song, M., and Zhu, Y. (2018). Structural Evolutions of Metallic Materials Processed by Severe Plastic Deformation. *Mater. Sci. Eng. R: Rep.* 133, 1–59. doi:10.1016/j.mser.2018.06.001

Cao, Y., Wang, Y. B., An, X. H., Liao, X. Z., Kawasaki, M., Ringer, S. P., et al. (2014). Concurrent Microstructural Evolution of Ferrite and Austenite in a Duplex Stainless Steel Processed by High-Pressure Torsion. *Acta Materialia* 63, 16–29. doi:10.1016/j.actamat.2013.09.030

Cao, Y., Wang, Y. B., Figueiredo, R. B., Chang, L., Liao, X. Z., Kawasaki, M., et al. (2011). Three-dimensional Shear-Strain Patterns Induced by High-Pressure Torsion and Their Impact on Hardness Evolution. *Acta Materialia* 59, 3903–3914. doi:10.1016/j.actamat.2011.03.015

Chang, Y.-J., and Yeh, A.-C. (2018). The Formation of Cellular Precipitate and its Effect on the Tensile Properties of a Precipitation Strengthened High Entropy alloy. *Mater. Chem. Phys.* 210, 111–119. doi:10.1016/j.matchemphys.2017.09.057

Chen, G., Li, L. T., Qiao, J. W., Jiao, Z. M., Ma, S. G., Ng, F. L., et al. (2019a). Gradient Hierarchical Grain Structures of Al0.1CoCrFeNi High-Entropy Alloys through Dynamic Torsion. *Mater. Lett.* 238, 163–166. doi:10.1016/j.matlet.2018.11.176

Chen, G., Qiao, J. W., Jiao, Z. M., Zhao, D., Zhang, T. W., Ma, S. G., et al. (2019b). Strength-ductility Synergy of Al0.1CoCrFeNi High-Entropy Alloys with

Gradient Hierarchical Structures. *Scripta Materialia* 167, 95–100. doi:10.1016/j.scriptamat.2019.04.002

Chen, L., Cao, T., Wei, R., Tang, K., Xin, C., Jiang, F., et al. (2020). Gradient Structure Design to Strengthen Carbon Interstitial Fe40Mn40Co10Cr10 High Entropy Alloys. *Mater. Sci. Eng. A* 772, 138661. doi:10.1016/j.msea.2019.138661

Chen, X., Wang, Q., Cheng, Z., Zhu, M., Zhou, H., Jiang, P., et al. (2021). Direct Observation of Chemical Short-Range Order in a Medium-Entropy alloy. *Nature* 592, 712–716. doi:10.1038/s41586-021-03428-z

Choudhuri, D., Gwalani, B., Gorsse, S., Komarasamy, M., Mantri, S. A., Srinivasan, S. G., et al. (2019). Enhancing Strength and Strain Hardenability via Deformation Twinning in Fcc-Based High Entropy Alloys Reinforced with Intermetallic Compounds. *Acta Materialia* 165, 420–430. doi:10.1016/j.actamat.2018.12.010

Choudhuri, D., Shukla, S., Green, W. B., Gwalani, B., Ageh, V., Banerjee, R., et al. (2018). Crystallographically Degenerate B2 Precipitation in a Plastically Deformed Fcc-Based Complex Concentrated alloy. *Mater. Res. Lett.* 6, 171–177. doi:10.1080/21663831.2018.1426649

Daoud, H. M., Manzoni, A. M., Wanderka, N., and Glatzel, U. (2015). High-Temperature Tensile Strength of Al10Co25Cr8Fe15Ni36Ti6 Compositionally Complex Alloy (High-Entropy Alloy). *JOM* 67, 2271–2277. doi:10.1007/s11837-015-1484-7

Dasari, S., Gwalani, B., Jagetia, A., Soni, V., Gorsse, S., and Banerjee, R. (2020). Hierarchical Eutectoid Nano-Lamellar Decomposition in an Al0.3CoFeNi Complex Concentrated Alloy. *Sci. Rep.* 10, 4836. doi:10.1038/s41598-020-61538-6

Ding, J., Yu, Q., Asta, M., and Ritchie, R. O. (2018). Tunable Stacking Fault Energies by Tailoring Local Chemical Order in CrCoNi Medium-Entropy Alloys. *Proc. Natl. Acad. Sci. USA* 115, 8919–8924. doi:10.1073/pnas.1808660115

Ding, Q., Zhang, Y., Chen, X., Fu, X., Chen, D., Chen, S., et al. (2019). Tuning Element Distribution, Structure and Properties by Composition in High-Entropy Alloys. *Nature* 574, 223–227. doi:10.1038/s41586-019-1617-1

Dong, Y., Yao, Z., Huang, X., Du, F., Li, C., Chen, A., et al. (2020). Microstructure and Mechanical Properties of AlCoxCrFeNi3-X Eutectic High-Entropy-alloy System. *J. Alloys Compd.* 823, 153886. doi:10.1016/j.jallcom.2020.153886

Eshelby, J. D., Frank, F. C., and Nabarro, F. R. N. (1951). XLI. The Equilibrium of Linear Arrays of Dislocations. *Lond. Edinb. Dublin Philos. Mag. J. Sci.* 42, 351–364. doi:10.1080/14786445108561060

Fang, T. H., Li, W. L., Tao, N. R., and Lu, K. (2011). Revealing Extraordinary Intrinsic Tensile Plasticity in Gradient Nano-Grained Copper. *Science* 331, 1587–1590. doi:10.1126/science.1200177

Fang, X. T., He, G. Z., Zheng, C., Ma, X. L., Kaoumi, D., Li, Y. S., et al. (2020). Effect of Heterostructure and Hetero-Deformation Induced Hardening on the Strength and Ductility of Brass. *Acta Materialia* 186, 644–655. doi:10.1016/j.actamat.2020.01.037

Fu, Z., Chen, W., Wen, H., Zhang, D., Chen, Z., Zheng, B., et al. (2016). Microstructure and Strengthening Mechanisms in an FCC Structured Single-phase Nanocrystalline Co25Ni25Fe25Al7.5Cu17.5 High-Entropy alloy. *Acta Materialia* 107, 59–71. doi:10.1016/j.actamat.2016.01.050

Fu, Z., MacDonald, B. E., Zhang, D., Wu, B., Chen, W., Ivanisenko, J., et al. (2018). Fcc Nanostructured TiFeCoNi alloy with Multi-Scale Grains and Enhanced Plasticity. *Scripta Materialia* 143, 108–112. doi:10.1016/j.scriptamat.2017.09.023

Gao, B., Lai, Q., Cao, Y., Hu, R., Xiao, L., Pan, Z., et al. (2020). Ultrastrong Low-Carbon Nanosteel Produced by Heterostructure and Interstitial Mediated Warm Rolling. *Sci. Adv.* 6, eaba8169. doi:10.1126/sciadv.aba8169

Gao, X., Lu, Y., Liu, J., Wang, J., Wang, T., and Zhao, Y. (2019). Extraordinary Ductility and Strain Hardening of Cr26Mn20Fe20Co20Ni14 TWIP High-Entropy alloy by Cooperative Planar Slipping and Twinning. *Materialia* 8, 100485. doi:10.1016/j.mtla.2019.100485

Gao, X., Lu, Y., Zhang, B., Liang, N., Wu, G., Sha, G., et al. (2017). Microstructural Origins of High Strength and High Ductility in an AlCoCrFeNi2.1 Eutectic High-Entropy alloy. *Acta Materialia* 141, 59–66. doi:10.1016/j.actamat.2017.07.041

Gludovatz, B., Hohenwarter, A., Catoor, D., Chang, E. H., George, E. P., and Ritchie, R. O. (2014). A Fracture-Resistant High-Entropy alloy for Cryogenic Applications. *Science* 345, 1153–1158. doi:10.1126/science.1254581

Gludovatz, B., Hohenwarter, A., Thurston, K. V. S., Bei, H., Wu, Z., George, E. P., et al. (2016). Exceptional Damage-Tolerance of a Medium-Entropy alloy CrCoNi at Cryogenic Temperatures. *Nat. Commun.* 7, 10602. doi:10.1038/ncomms10602

Grässel, O., Krüger, L., Frommeyer, G., and Meyer, L. W. (2000). High Strength Fe–Mn–(Al, Si) TRIP/TWIP Steels Development — Properties — Application. *Int. J. Plast.* 16, 1391–1409. doi:10.1016/S0749-6419(00)00015-2

Guo, L., Wu, W., Ni, S., Yuan, Z., Cao, Y., Wang, Z., et al. (2020). Strengthening the FeCoCrNiMo0.15 High Entropy alloy by a Gradient Structure. *J. Alloys Compd.* 841, 155688. doi:10.1016/j.jallcom.2020.155688

Gutierrez-Urrutia, I., and Raabe, D. (2011). Dislocation and Twin Substructure Evolution during Strain Hardening of an Fe–22wt.% Mn–0.6wt.% C TWIP Steel Observed by Electron Channeling Contrast Imaging. *Acta Mater.* 59, 6449–6462. doi:10.1016/j.actamat.2011.07.009

Gutierrez-Urrutia, I., and Raabe, D. (2012). Grain Size Effect on Strain Hardening in Twinning-Induced Plasticity Steels. *Scripta Materialia* 66, 992–996. doi:10.1016/j.scriptamat.2012.01.037

Gwalani, B., Gorsse, S., Choudhuri, D., Styles, M., Zheng, Y., Mishra, R. S., et al. (2018). Modifying Transformation Pathways in High Entropy Alloys or Complex Concentrated Alloys via Thermo-Mechanical Processing. *Acta Materialia* 153, 169–185. doi:10.1016/j.actamat.2018.05.009

Han, B. O., Lavernia, E. J., Lee, Z., Nutt, S., and Witkin, D. (2005). Deformation Behavior of Bimodal Nanostructured 5083 Al Alloys. *Metall. Mat Trans. A.* 36, 957–965. doi:10.1007/s11661-005-0289-7

Han, Z. H., Liang, S., Yang, J., Wei, R., and Zhang, C. J. (2018). A superior Combination of Strength-Ductility in CoCrFeNiMn High-Entropy alloy Induced by Asymmetric Rolling and Subsequent Annealing Treatment. *Mater. Characterization* 145, 619–626. doi:10.1016/j.matchar.2018.09.029

Hansen, N. (2004). Hall-Petch Relation and Boundary Strengthening. *Scripta Materialia* 51, 801–806. doi:10.1016/j.scriptamat.2004.06.002

Hart, E. W. (1967). Theory of the Tensile Test. *Acta Metallurgica* 15, 351–355. doi:10.1016/0001-6160(67)90211-8

Hasan, M. N., Liu, Y. F., An, X. H., Gu, J., Song, M., Cao, Y., et al. (2019). Simultaneously Enhancing Strength and Ductility of a High-Entropy alloy via Gradient Hierarchical Microstructures. *Int. J. Plasticity* 123, 178–195. doi:10.1016/j.ijplas.2019.07.017

He, B. B., Hu, B., Yen, H. W., Cheng, G. J., Wang, Z. K., Luo, H. W., et al. (2017). High Dislocation Density-Induced Large Ductility in Deformed and Partitioned Steels. *Science* 357, 1029–1032. doi:10.1126/science.aan0177

He, J., Makineni, S. K., Lu, W., Shang, Y., Lu, Z., Li, Z., et al. (2020). On the Formation of Hierarchical Microstructure in a Mo-Doped NiCoCr Medium-Entropy alloy with Enhanced Strength-Ductility Synergy. *Scripta Materialia* 175, 1–6. doi:10.1016/j.scriptamat.2019.08.036

He, J. Y., Wang, H., Wu, Y., Liu, X. J., Mao, H. H., Nieh, T. G., et al. (2016). Precipitation Behavior and its Effects on Tensile Properties of FeCoNiCr High-Entropy Alloys. *Intermetallics* 79, 41–52. doi:10.1016/j.intermet.2016.09.005

Huang, C. X., Wang, Y. F., Ma, X. L., Yin, S., Höppel, H. W., Göken, M., et al. (2018). Interface Affected Zone for Optimal Strength and Ductility in Heterogeneous Laminate. *Mater. Today* 21, 713–719. doi:10.1016/j.mattod.2018.03.006

Huang, K., Zhang, K., Marthinsen, K., and Logé, R. E. (2017). Controlling Grain Structure and Texture in Al-Mn from the Competition between Precipitation and Recrystallization. *Acta Materialia* 141, 360–373. doi:10.1016/j.actamat.2017.09.032

Hughes, D. A., Hansen, N., and Bammann, D. J. (2003). Geometrically Necessary Boundaries, Incidental Dislocation Boundaries and Geometrically Necessary Dislocations. *Scripta Materialia* 48, 147–153. doi:10.1016/S1359-6462(02)00358-5

Jiang, W., Cao, Y., Jiang, Y., Liu, Y., Mao, Q., Zhou, H., et al. (2021a). Effects of Nanostructural Hierarchy on the Hardness and thermal Stability of an Austenitic Stainless Steel. *J. Mater. Res. Techn.* 12, 376–384. doi:10.1016/j.jmrt.2021.02.100

Jiang, W., Gao, X., Guo, Y., Chen, X., and Zhao, Y. (2021b). Dynamic Impact Behavior and Deformation Mechanisms of Cr26Mn20Fe20Co20Ni14 High-Entropy alloy. *Mater. Sci. Eng. A* 824, 141858. doi:10.1016/j.msea.2021.141858

Jiang, W., Yuan, S., Cao, Y., Zhang, Y., and Zhao, Y. (2021c). Mechanical Properties and Deformation Mechanisms of a Ni2Co1Fe1V0.5Mo0.2 Medium-Entropy

alloy at Elevated Temperatures. *Acta Materialia* 213, 116982. doi:10.1016/j.actamat.2021.116982

Jin, X., Bi, J., Zhang, L., Zhou, Y., Du, X., Liang, Y., et al. (2019). A New CrFeNi2Al Eutectic High Entropy alloy System with Excellent Mechanical Properties. *J. Alloys Compd.* 770, 655–661. doi:10.1016/j.jallcom.2018.08.176

Jin, X., Zhou, Y., Zhang, L., Du, X., and Li, B. (2018a). A New Pseudo Binary Strategy to Design Eutectic High Entropy Alloys Using Mixing Enthalpy and Valence Electron Concentration. *Mater. Des.* 143, 49–55. doi:10.1016/j.matdes.2018.01.057

Jin, X., Zhou, Y., Zhang, L., Du, X., and Li, B. (2018b). A Novel Fe 20 Co 20 Ni 41 Al 19 Eutectic High Entropy alloy with Excellent Tensile Properties. *Mater. Lett.* 216, 144–146. doi:10.1016/j.matlet.2018.01.017

Jo, Y. H., Jung, S., Choi, W. M., Sohn, S. S., Kim, H. S., Lee, B. J., et al. (2017). Cryogenic Strength Improvement by Utilizing Room-Temperature Deformation Twinning in a Partially Recrystallized VCrMnFeCoNi High-Entropy alloy. *Nat. Commun.* 8, 15719. doi:10.1038/ncomms15719

Kim, J. G., Park, J. M., Seol, J. B., Choe, J., Yu, J.-H., Yang, S., et al. (2020). Nano-scale Solute Heterogeneities in the Ultrastrong Selectively Laser Melted Carbon-Doped CoCrFeMnNi alloy. *Mater. Sci. Eng. A* 773, 138726. doi:10.1016/j.msea.2019.138726

Kuo, C.-M., and Tsai, C.-W. (2018). Effect of Cellular Structure on the Mechanical Property of Al0.2Co1.5CrFeNi1.5Ti0.3 High-Entropy alloy. *Mater. Chem. Phys.* 210, 103–110. doi:10.1016/j.matchemphys.2017.10.064

Li, H., Mao, Q., Wang, Z., Miao, F., Fang, B., and Zheng, Z. (2015). Enhancing Mechanical Properties of Al-Mg-Si-Cu Sheets by Solution Treatment Substituting for Recrystallization Annealing before the Final Cold-Rolling. *Mater. Sci. Eng. A* 620, 204–212. doi:10.1016/j.msea.2014.10.012

Li, J., Fang, C., Liu, Y., Huang, Z., Wang, S., Mao, Q., et al. (2019a). Deformation Mechanisms of 304L Stainless Steel with Heterogeneous Lamella Structure. *Mater. Sci. Eng. A* 742, 409–413. doi:10.1016/j.msea.2018.11.047

Li, J., Fang, Q., Liu, B., and Liu, Y. (2018). Transformation Induced Softening and Plasticity in High Entropy Alloys. *Acta Materialia* 147, 35–41. doi:10.1016/j.actamat.2018.01.002

Li, J., Weng, G. J., Chen, S., and Wu, X. (2017). On Strain Hardening Mechanism in Gradient Nanostructures. *Int. J. Plasticity* 88, 89–107. doi:10.1016/j.ijplas.2016.10.003

Li, Q.-J., Sheng, H., and Ma, E. (2019b). Strengthening in Multi-Principal Element Alloys with Local-Chemical-Order Roughened Dislocation Pathways. *Nat. Commun.* 10, 3563. doi:10.1038/s41467-019-11464-7

Li, W. L., Tao, N. R., and Lu, K. (2008). Fabrication of a Gradient Nano-Micro-Structured Surface Layer on Bulk Copper by Means of a Surface Mechanical Grinding Treatment. *Scripta Materialia* 59, 546–549. doi:10.1016/j.scriptamat.2008.05.003

Li, W., Xie, D., Li, D., Zhang, Y., Gao, Y., and Liaw, P. K. (2021). Mechanical Behavior of High-Entropy Alloys. *Prog. Mater. Sci.* 118, 100777. doi:10.1016/j.pmatsci.2021.100777

Li, X., Wei, Y., Lu, L., Lu, K., and Gao, H. (2010). Dislocation Nucleation Governed Softening and Maximum Strength in Nano-Twinned Metals. *Nature* 464, 877–880. doi:10.1038/nature08929

Li, Z., Pradeep, K. G., Deng, Y., Raabe, D., and Tasan, C. C. (2016). Metastable High-Entropy Dual-phase Alloys Overcome the Strength-Ductility Trade-Off. *Nature* 534, 227–230. doi:10.1038/nature17981

Liang, N., Wang, X., Cao, Y., Li, Y., Zhu, Y., and Zhao, Y. (2020). Effective Surface Nano-Crystallization of Ni2FeCoMo0.5V0.2 Medium Entropy Alloy by Rotationally Accelerated Shot Peening (RASP). *Entropy* 22, 1074. doi:10.3390/e22101074

Liang, Y.-J., Wang, L., Wen, Y., Cheng, B., Wu, Q., Cao, T., et al. (2018). High-content Ductile Coherent Nanoprecipitates Achieve Ultrastrong High-Entropy Alloys. *Nat. Commun.* 9, 4063. doi:10.1038/s41467-018-06600-8

Liu, J., Chen, Z., Zhang, F., Ji, G., Wang, M., Ma, Y., et al. (2018). Simultaneously Increasing Strength and Ductility of Nanoparticles Reinforced Al Composites via Accumulative Orthogonal Extrusion Process. *Mater. Res. Lett.* 6, 406–412. doi:10.1080/21663831.2018.1471421

Liu, W. H., Lu, Z. P., He, J. Y., Luan, J. H., Wang, Z. J., Liu, B., et al. (2016). Ductile CoCrFeNiMox High Entropy Alloys Strengthened by Hard Intermetallic Phases. *Acta Materialia* 116, 332–342. doi:10.1016/j.actamat.2016.06.063

Liu, Y., Cao, Y., Mao, Q., Zhou, H., Zhao, Y., Jiang, W., et al. (2020). Critical Microstructures and Defects in Heterostructured Materials and Their Effects on Mechanical Properties. *Acta Materialia* 189, 129–144. doi:10.1016/j.actamat.2020.03.001

Liu, Y., He, Y., and Cai, S. (2021a). Effect of Gradient Microstructure on the Strength and Ductility of Medium-Entropy alloy Processed by Severe Torsion Deformation. *Mater. Sci. Eng. A* 801, 140429. doi:10.1016/j.msea.2020.140429

Liu, Y., He, Y., and Cai, S. (2021b). Gradient Recrystallization to Improve Strength and Ductility of Medium-Entropy alloy. *J. Alloys Compd.* 853, 157388. doi:10.1016/j.jallcom.2020.157388

Lu, K., Lu, L., and Suresh, S. (2009a). Strengthening Materials by Engineering Coherent Internal Boundaries at the Nanoscale. *Science* 324, 349–352. doi:10.1126/science.1159610

Lu, K. (2014). Making strong Nanomaterials Ductile with Gradients. *Science* 345, 1455–1456. doi:10.1126/science.1255940

Lu, L., Chen, X., Huang, X., and Lu, K. (2009b). Revealing the Maximum Strength in Nanotwinned Copper. *Science* 323, 607–610. doi:10.1126/science.1167641

Lu, L., Shen, Y., Chen, X., Qian, L., and Lu, K. (2004). Ultrahigh Strength and High Electrical Conductivity in Copper. *Science* 304, 422–426. doi:10.1126/science.1092905

Lu, W., Liebscher, C. H., Dehm, G., Raabe, D., and Li, Z. (2018). Bidirectional Transformation Enables Hierarchical Nanolaminate Dual-phase High-Entropy Alloys. *Adv. Mater.* 30, 1804727. doi:10.1002/adma.201804727

Lu, Y., Dong, Y., Guo, S., Jiang, L., Kang, H., Wang, T., et al. (2014). A Promising New Class of High-Temperature Alloys: Eutectic High-Entropy Alloys. *Sci. Rep.* 4, 6200. doi:10.1038/srep06200

Lucas, M. S., Wilks, G. B., Mauger, L., Muñoz, J. A., Senkov, O. N., Michel, E., et al. (2012). Absence of Long-Range Chemical Ordering in Equimolar FeCoCrNi. *Appl. Phys. Lett.* 100, 251907. doi:10.1063/1.4730327

Luo, S., Zhao, C., Su, Y., Liu, Q., and Wang, Z. (2020). Selective Laser Melting of Dual Phase AlCrCuFeNix High Entropy Alloys: Formability, Heterogeneous Microstructures and Deformation Mechanisms. *Additive Manufacturing* 31, 100925. doi:10.1016/j.addma.2019.100925

Ma, E., and Zhu, T. (2017). Towards Strength-Ductility Synergy through the Design of Heterogeneous Nanostructures in Metals. *Mater. Today* 20, 323–331. doi:10.1016/j.mattod.2017.02.003

Ma, X., Huang, C., Moering, J., Ruppert, M., Höppel, H. W., Göken, M., et al. (2016). Mechanical Properties of Copper/bronze Laminates: Role of Interfaces. *Acta Materialia* 116, 43–52. doi:10.1016/j.actamat.2016.06.023

Mao, Q., Chen, X., Li, J., and Zhao, Y. (2021). Nano-Gradient Materials Prepared by Rotary Swaging. *Nanomaterials* 11, 2223. doi:10.3390/nano11092223

Meyers, M. A., and Chawla, K. K. (2008). *Mechanical Behavior of Materials*. Cambridge University Press. doi:10.1016/S1369-7021(09)70086-0

Miao, J., Slone, C. E., Smith, T. M., Niu, C., Bei, H., Ghazisaeidi, M., et al. (2017). The Evolution of the Deformation Substructure in a Ni-Co-Cr Equiatomic Solid Solution alloy. *Acta Materialia* 132, 35–48. doi:10.1016/j.actamat.2017.04.033

Ming, K., Bi, X., and Wang, J. (2017). Precipitation Strengthening of Ductile Cr 15 Fe 20 Co 35 Ni 20 Mo 10 Alloys. *Scripta Materialia* 137, 88–93. doi:10.1016/j.scriptamat.2017.05.019

Ming, K., Bi, X., and Wang, J. (2019). Strength and Ductility of CrFeCoNiMo alloy with Hierarchical Microstructures. *Int. J. Plasticity* 113, 255–268. doi:10.1016/j.ijplas.2018.10.005

Miracle, D. B., and Senkov, O. N. (2017). A Critical Review of High Entropy Alloys and Related Concepts. *Acta Materialia* 122, 448–511. doi:10.1016/j.actamat.2016.08.081

Miracle, D., Miller, J., Senkov, O., Woodward, C., Uchic, M., and Tiley, J. (2014). Exploration and Development of High Entropy Alloys for Structural Applications. *Entropy* 16, 494–525. doi:10.3390/e16010494

Moering, J., Ma, X., Malkin, J., Yang, M., Zhu, Y., and Mathaudhu, S. (2016). Synergetic Strengthening Far beyond Rule of Mixtures in Gradient Structured Aluminum Rod. *Scripta Materialia* 122, 106–109. doi:10.1016/j.scriptamat.2016.05.006

Olevsky, E. A., and Froyen, L. (2009). Impact of Thermal Diffusion on Densification during SPS. *J. Am. Ceram. Soc.* 92, S122–S132. doi:10.1111/j.1551-2916.2008.02705.x

Pan, Q., Zhang, L., Feng, R., Lu, Q., An, K., Chuang, A. C., et al. (2021). Gradientcell-Structured High-Entropy Alloy with Exceptional Strength and Ductility. *Science* 374, 984–989. doi:10.1126/science.abj8114

Park, J. M., Choe, J., Kim, J. G., Bae, J. W., Moon, J., Yang, S., et al. (2019). Superior Tensile Properties of 1%C-CoCrFeMnNi High-Entropy alloy Additively

Manufactured by Selective Laser Melting. *Mater. Res. Lett.* 8, 1–7. doi:10.1080/21663831.2019.1638844

Qin, W., Mao, Q., Kang, J., Liu, Y., Shu, D., She, D., et al. (2019). Superior Impact Property and Fracture Mechanism of a Multilayered Copper/bronze Laminate. *Mater. Lett.* 250, 60–63. doi:10.1016/j.matlet.2019.04.119

Reddy, S. R., Yoshida, S., Sunkari, U., Lozinko, A., Joseph, J., Saha, R., et al. (2019). Engineering Heterogeneous Microstructure by Severe Warm-Rolling for Enhancing Strength-Ductility Synergy in Eutectic High Entropy Alloys. *Mater. Sci. Eng. A* 764, 138226. doi:10.1016/j.msea.2019.138226

Remy, L., and Pineau, A. (1977). Twinning and Strain-Induced F.C.C. → H.C.P. Transformation in the Fe Mn Cr C System. *Mater. Sci. Eng.* 28, 99–107. doi:10.1016/0025-5416(77)90093-3

Ritchie, R. O. (2011). The Conflicts between Strength and Toughness. *Nat. Mater* 10, 817–822. doi:10.1038/nmat3115

Saeed-Akbari, A., Mosecker, L., Schwedt, A., and Bleck, W. (2012). Characterization and Prediction of Flow Behavior in High-Manganese Twinning Induced Plasticity Steels: Part I. Mechanism Maps and Work-Hardening Behavior. *Metall. Mat Trans. A.* 43, 1688–1704. doi:10.1007/s11661-011-0993-4

Sathiyamoorthi, P., Asghari-Rad, P., Bae, J. W., and Kim, H. S. (2019a). Fine Tuning of Tensile Properties in CrCoNi Medium Entropy alloy through Cold Rolling and Annealing. *Intermetallics* 113, 106578. doi:10.1016/j.intermet.2019.106578

Sathiyamoorthi, P., and Kim, H. S. (2022). High-entropy Alloys with Heterogeneous Microstructure: Processing and Mechanical Properties. *Prog. Mater. Sci.* 123, 100709. doi:10.1016/j.pmatsci.2020.100709

Sathiyamoorthi, P., Moon, J., Bae, J. W., Asghari-Rad, P., and Kim, H. S. (2019b). Superior Cryogenic Tensile Properties of Ultrafine-Grained CoCrNi Medium-Entropy alloy Produced by High-Pressure Torsion and Annealing. *Scripta Materialia* 163, 152–156. doi:10.1016/j.scriptamat.2019.01.016

Sathiyamoorthi, P., Park, J. M., Moon, J., Bae, J. W., Asghari-Rad, P., Zargaran, A., et al. (2019c). Achieving High Strength and High Ductility in Al0.3CoCrNi Medium-Entropy alloy through Multi-phase Hierarchical Microstructure. *Materialia* 8, 100442. doi:10.1016/j.mtla.2019.100442

Sawangrat, C., Kato, S., Orlov, D., and Ameyama, K. (2014). Harmonic-structured Copper: Performance and Proof of Fabrication Concept Based on Severe Plastic Deformation of Powders. *J. Mater. Sci.* 49, 6579–6585. doi:10.1007/s10853-014-8258-4

Schuh, B., Pippan, R., and Hohenwarter, A. (2019). Tailoring Bimodal Grain Size Structures in Nanocrystalline Compositionally Complex Alloys to Improve Ductility. *Mater. Sci. Eng. A* 748, 379–385. doi:10.1016/j.msea.2019.01.073

Senkov, O. N., Wilks, G. B., Scott, J. M., and Miracle, D. B. (2011). Mechanical Properties of Nb25Mo25Ta25W25 and V20Nb20Mo20Ta20W20 Refractory High Entropy Alloys. *Intermetallics* 19, 698–706. doi:10.1016/j.intermet.2011.01.004

Shahmir, H., He, J., Lu, Z., Kawasaki, M., and Langdon, T. G. (2016). Effect of Annealing on Mechanical Properties of a Nanocrystalline CoCrFeNiMn High-Entropy alloy Processed by High-Pressure Torsion. *Mater. Sci. Eng. A* 676, 294–303. doi:10.1016/j.msea.2016.08.118

Shi, P., Li, R., Li, Y., Wen, Y., Zhong, Y., Ren, W., et al. (2021). Hierarchical Crack Buffering Triples Ductility in Eutectic Herringbone High-Entropy Alloys. *Science* 373, 912–918. doi:10.1126/science.abf6986

Shi, P., Ren, W., Zheng, T., Ren, Z., Hou, X., Peng, J., et al. (2019). Enhanced Strength-Ductility Synergy in Ultrafine-Grained Eutectic High-Entropy Alloys by Inheriting Microstructural Lamellae. *Nat. Commun.* 10, 489. doi:10.1038/s41467-019-08460-2

Shukla, S., Wang, T., Cotton, S., and Mishra, R. S. (2018). Hierarchical Microstructure for Improved Fatigue Properties in a Eutectic High Entropy alloy. *Scripta Materialia* 156, 105–109. doi:10.1016/j.scriptamat.2018.07.022

Slone, C. E., Miao, J., George, E. P., and Mills, M. J. (2019). Achieving Ultra-high Strength and Ductility in Equiatomic CrCoNi with Partially Recrystallized Microstructures. *Acta Materialia* 165, 496–507. doi:10.1016/j.actamat.2018.12.015

Song, H., Tian, F., Hu, Q.-M., Vitos, L., Wang, Y., Shen, J., et al. (2017). Local Lattice Distortion in High-Entropy Alloys. *Phys. Rev. Mater.* 1, 023404. doi:10.1103/PhysRevMaterials.1.023404

Su, J., Raabe, D., and Li, Z. (2019). Hierarchical Microstructure Design to Tune the Mechanical Behavior of an Interstitial TRIP-TWIP High-Entropy alloy. *Acta Materialia* 163, 40–54. doi:10.1016/j.actamat.2018.10.017

Taylor, G. I. (1934). The Mechanism of Plastic Deformation of Crystals. Part I. Theoretical. *Proc. R. Soc. A.* 145, 362–387. doi:10.1016/0001-6160(81)90112-7

Tsai, K.-Y., Tsai, M.-H., and Yeh, J.-W. (2013). Sluggish Diffusion in Co-cr-fe-mn-ni High-Entropy Alloys. *Acta Materialia* 61, 4887–4897. doi:10.1016/j.actamat.2013.04.058

Tsai, M.-H., and Yeh, J.-W. (2014). High-Entropy Alloys: A Critical Review. *Mater. Res. Lett.* 2, 107–123. doi:10.1080/21663831.2014.912690

Wang, H., Zhu, Z. G., Chen, H., Wang, A. G., Liu, J. Q., Liu, H. W., et al. (2020). Effect of Cyclic Rapid thermal Loadings on the Microstructural Evolution of a CrMnFeCoNi High-Entropy alloy Manufactured by Selective Laser Melting. *Acta Materialia* 196, 609–625. doi:10.1016/j.actamat.2020.07.006

Wang, T., Shukla, S., Komarasamy, M., Liu, K., and Mishra, R. S. (2019). Towards Heterogeneous AlxCoCrFeNi High Entropy alloy via Friction Stir Processing. *Mater. Lett.* 236, 472–475. doi:10.1016/j.matlet.2018.10.161

Wang, Y., Chen, M., Zhou, F., and Ma, E. (2002). High Tensile Ductility in a Nanostructured Metal. *Nature* 419, 912–915. doi:10.1038/nature01133

Wang, Y. M., and Ma, E. (2004). Three Strategies to Achieve Uniform Tensile Deformation in a Nanostructured Metal. *Acta Materialia* 52, 1699–1709. doi:10.1016/j.actamat.2003.12.022

Wang, Z. G., Zhou, W., Fu, L. M., Wang, J. F., Luo, R. C., Han, X. C., et al. (2017). Effect of Coherent L12 Nanoprecipitates on the Tensile Behavior of a Fcc-Based High-Entropy alloy. *Mater. Sci. Eng. A* 696, 503–510. doi:10.1016/j.msea.2017.04.111

Wang, Z., Wu, M., Cai, Z., Chen, S., and Baker, I. (2016). Effect of Ti Content on the Microstructure and Mechanical Behavior of (Fe36Ni18Mn33Al13)100−xTix High Entropy Alloys. *Intermetallics* 75, 79–87. doi:10.1016/j.intermet.2016.06.001

Wei, Q., Cheng, S., Ramesh, K. T., and Ma, E. (2004). Effect of Nanocrystalline and Ultrafine Grain Sizes on the Strain Rate Sensitivity and Activation Volume: Fcc versus Bcc Metals. *Mater. Sci. Eng. A* 381, 71–79. doi:10.1016/j.msea.2004.03.064

Wei, Y., Li, Y., Zhu, L., Liu, Y., Lei, X., Wang, G., et al. (2014). Evading the Strength-Ductility Trade-Off Dilemma in Steel through Gradient Hierarchical Nanotwins. *Nat. Commun.* 5, 3580. doi:10.1038/ncomms4580

Wu, Q., Wang, Z., Zheng, T., Chen, D., Yang, Z., Li, J., et al. (2019a). A Casting Eutectic High Entropy alloy with superior Strength-Ductility Combination. *Mater. Lett.* 253, 268–271. doi:10.1016/j.matlet.2019.06.067

Wu, S. W., Wang, G., Wang, Q., Jia, Y. D., Yi, J., Zhai, Q. J., et al. (2019b). Enhancement of Strength-Ductility Trade-Off in a High-Entropy alloy through a Heterogeneous Structure. *Acta Materialia* 165, 444–458. doi:10.1016/j.actamat.2018.12.012

Wu, W., Guo, L., Liu, B., Ni, S., Liu, Y., and Song, M. (2017). Effects of Torsional Deformation on the Microstructures and Mechanical Properties of a CoCrFeNiMo0.15 High-Entropy alloy. *Philos. Mag.* 97, 3229–3245. doi:10.1080/14786435.2017.1369191

Wu, X., Jiang, P., Chen, L., Yuan, F., and Zhu, Y. T. (2014a). Extraordinary Strain Hardening by Gradient Structure. *Proc. Natl. Acad. Sci.* 111, 7197–7201. doi:10.1073/pnas.1324069111

Wu, X. L., Jiang, P., Chen, L., Zhang, J. F., Yuan, F. P., and Zhu, Y. T. (2014b). Synergetic Strengthening by Gradient Structure. *Mater. Res. Lett.* 2, 185–191. doi:10.1080/21663831.2014.935821

Wu, X., Yang, M., Yuan, F., Wu, G., Wei, Y., Huang, X., et al. (2015). Heterogeneous Lamella Structure Unites Ultrafine-Grain Strength with Coarse-Grain Ductility. *Proc. Natl. Acad. Sci. USA* 112, 14501–14505. doi:10.1073/pnas.1517193112

Wu, X., and Zhu, Y. (2021). Gradient and Lamellar Heterostructures for superior Mechanical Properties. *MRS Bull.* 46, 244–249. doi:10.1557/s43577-021-00056-w

Wu, X., and Zhu, Y. (2017). Heterogeneous Materials: a New Class of Materials with Unprecedented Mechanical Properties. *Mater. Res. Lett.* 5, 527–532. doi:10.1080/21663831.2017.1343208

Xie, J., Zhang, S., Sun, Y., Hao, Y., An, B., Li, Q., et al. (2020a). Microstructure and Mechanical Properties of High Entropy CrMnFeCoNi alloy Processed by Electopulsing-Assisted Ultrasonic Surface Rolling. *Mater. Sci. Eng. A* 795, 140004. doi:10.1016/j.msea.2020.140004

Xie, Y., Liang, J., Zhang, D., Luo, Y., Zhang, Z., Liu, Y., et al. (2020b). Sustaining Strength-Ductility Synergy of CoCrFeNiMn High Entropy alloy by a Multilevel

Heterogeneity Associated with Nanoparticles. *Scripta Materialia* 187, 390–394. doi:10.1016/j.scriptamat.2020.06.054

Xiong, T., Zheng, S., Pang, J., and Ma, X. (2020). High-strength and High-Ductility AlCoCrFeNi2.1 Eutectic High-Entropy alloy Achieved via Precipitation Strengthening in a Heterogeneous Structure. *Scripta Materialia* 186, 336–340. doi:10.1016/j.scriptamat.2020.04.035

Yang, M., Pan, Y., Yuan, F., Zhu, Y., and Wu, X. (2016). Back Stress Strengthening and Strain Hardening in Gradient Structure. *Mater. Res. Lett.* 4, 145–151. doi:10.1080/21663831.2016.1153004

Yang, M., Yan, D., Yuan, F., Jiang, P., Ma, E., and Wu, X. (2018a). Dynamically Reinforced Heterogeneous Grain Structure Prolongs Ductility in a Medium-Entropy alloy with Gigapascal Yield Strength. *Proc. Natl. Acad. Sci. USA* 115, 7224–7229. doi:10.1073/pnas.1807817115

Yang, M., Zhou, L., Wang, C., Jiang, P., Yuan, F., Ma, E., et al. (2019a). High Impact Toughness of CrCoNi Medium-Entropy alloy at Liquid-Helium Temperature. *Scripta Materialia* 172, 66–71. doi:10.1016/j.scriptamat.2019.07.010

Yang, T., Zhao, Y., Liu, W., Kai, J., and Liu, C. (2018b). L12-strengthened High-Entropy Alloys for Advanced Structural Applications. *J. Mater. Res.* 33, 2983–2997. doi:10.1557/jmr.2018.186

Yang, T., Zhao, Y. L., Luan, J. H., Han, B., Wei, J., Kai, J. J., et al. (2019b). Nanoparticles-strengthened High-Entropy Alloys for Cryogenic Applications Showing an Exceptional Strength-Ductility Synergy. *Scripta Materialia* 164, 30–35. doi:10.1016/j.scriptamat.2019.01.034

Yang, X., Ma, X., Moering, J., Zhou, H., Wang, W., Gong, Y., et al. (2015). Influence of Gradient Structure Volume Fraction on the Mechanical Properties of Pure Copper. *Mater. Sci. Eng. A* 645, 280–285. doi:10.1016/j.msea.2015.08.037

Yeh, J.-W., Chang, S.-Y., Hong, Y.-D., Chen, S.-K., and Lin, S.-J. (2007). Anomalous Decrease in X-ray Diffraction Intensities of Cu-Ni-Al-Co-Cr-Fe-Si alloy Systems with Multi-Principal Elements. *Mater. Chem. Phys.* 103, 41–46. doi:10.1016/j.matchemphys.2007.01.003

Yeh, J.-W., Chen, S.-K., Lin, S.-J., Gan, J.-Y., Chin, T.-S., Shun, T.-T., et al. (2004). Nanostructured High-Entropy Alloys with Multiple Principal Elements: Novel Alloy Design Concepts and Outcomes. *Adv. Eng. Mater.* 6, 299–303. doi:10.1002/adem.200300567

Zaddach, A. J., Niu, C., Koch, C. C., and Irving, D. L. (2013). Mechanical Properties and Stacking Fault Energies of NiFeCrCoMn High-Entropy alloy. *JOM* 65, 1780–1789. doi:10.1007/s11837-013-0771-4

Zhang, C., Zhu, C., Cao, P., Wang, X., Ye, F., Kaufmann, K., et al. (2020). Aged Metastable High-Entropy Alloys with Heterogeneous Lamella Structure for superior Strength-Ductility Synergy. *Acta Materialia* 199, 602–612. doi:10.1016/j.actamat.2020.08.043

Zhang, C., Zhu, C., Harrington, T., and Vecchio, K. (2018). Design of Non-equiatomic High Entropy Alloys with Heterogeneous Lamella Structure towards Strength-Ductility Synergy. *Scripta Materialia* 154, 78–82. doi:10.1016/j.scriptamat.2018.05.020

Zhang, C., Zhu, C., and Vecchio, K. (2019). Non-equiatomic FeNiCoAl-Based High Entropy Alloys with Multiscale Heterogeneous Lamella Structure for Strength and Ductility. *Mater. Sci. Eng. A* 743, 361–371. doi:10.1016/j.msea.2018.11.073

Zhang, Y., Zuo, T. T., Tang, Z., Gao, M. C., Dahmen, K. A., Liaw, P. K., et al. (2014). Microstructures and Properties of High-Entropy Alloys. *Prog. Mater. Sci.* 61, 1–93. doi:10.1016/j.pmatsci.2013.10.001

Zhao, J., and Jiang, Z. (2018). Thermomechanical Processing of Advanced High Strength Steels. *Prog. Mater. Sci.* 94, 174–242. doi:10.1016/j.pmatsci.2018.01.006

Zhao, Y. H., Liao, X. Z., Jin, Z., Valiev, R. Z., and Zhu, Y. T. (2004). Microstructures and Mechanical Properties of Ultrafine Grained 7075 Al alloy Processed by ECAP and Their Evolutions during Annealing. *Acta Materialia* 52, 4589–4599. doi:10.1016/j.actamat.2004.06.017

Zhao, Y. L., Yang, T., Tong, Y., Wang, J., Luan, J. H., Jiao, Z. B., et al. (2017). Heterogeneous Precipitation Behavior and Stacking-Fault-Mediated Deformation in a CoCrNi-Based Medium-Entropy alloy. *Acta Materialia* 138, 72–82. doi:10.1016/j.actamat.2017.07.029

Zhao, Y., Topping, T., Bingert, J. F., Thornton, J. J., Dangelewicz, A. M., Li, Y., et al. (2008). High Tensile Ductility and Strength in Bulk Nanostructured Nickel. *Adv. Mater.* 20, 3028–3033. doi:10.1002/adma.200800214

Zhu, T., and Li, J. (2010). Ultra-strength Materials. *Prog. Mater. Sci.* 55, 710–757. doi:10.1016/j.pmatsci.2010.04.001

Zhu, Y., Ameyama, K., Anderson, P. M., Beyerlein, I. J., Gao, H., Kim, H. S., et al. (2020). Heterostructured Materials: superior Properties from Hetero-Zone Interaction. *Mater. Res. Lett.* 9, 1–31. doi:10.1080/21663831.2020.1796836

Zhu, Y. T., Liao, X. Z., and Wu, X. L. (2012). Deformation Twinning in Nanocrystalline Materials. *Prog. Mater. Sci.* 57, 1–62. doi:10.1016/j.pmatsci.2011.05.001

Zhu, Y., and Wu, X. (2019). Perspective on Hetero-Deformation Induced (HDI) Hardening and Back Stress. *Mater. Res. Lett.* 7, 393–398. doi:10.1080/21663831.2019.1616331

Zhu, Z. G., Nguyen, Q. B., Ng, F. L., An, X. H., Liao, X. Z., Liaw, P. K., et al. (2018). Hierarchical Microstructure and Strengthening Mechanisms of a CoCrFeNiMn High Entropy alloy Additively Manufactured by Selective Laser Melting. *Scripta Materialia* 154, 20–24. doi:10.1016/j.scriptamat.2018.05.015

Conflict of Interest: The authors declare that the research was conducted in the absence of any commercial or financial relationships that could be construed as a potential conflict of interest.

Publisher's Note: All claims expressed in this article are solely those of the authors and do not necessarily represent those of their affiliated organizations, or those of the publisher, the editors and the reviewers. Any product that may be evaluated in this article, or claim that may be made by its manufacturer, is not guaranteed or endorsed by the publisher.

frontiers in Materials

REVIEW
published: 04 January 2022
doi: 10.3389/fmats.2021.796476

A Deep Learning Approach to Design and Discover Sustainable Cementitious Binders: Strategies to Learn From Small Databases and Develop Closed-form Analytical Models

Taihao Han[1], Sai Akshay Ponduru[1], Rachel Cook[1], Jie Huang[2], Gaurav Sant[3] and Aditya Kumar[1]**

[1]Materials Science and Engineering, Missouri University of Science and Technology, Rolla, MO, United States, [2]Electrical and Computer Engineering, Missouri University of Science and Technology, Rolla, MO, United States, [3]Civil and Environmental Engineering, University of California, Los Angeles, Los Angeles, CA, United States

OPEN ACCESS

Edited by:
John L. Provis,
The University of Sheffield,
United Kingdom

Reviewed by:
Neven Ukrainczyk,
Darmstadt University of Technology,
Germany
Qiu Li,
Wuhan University of Technology,
China

***Correspondence:**
Aditya Kumar
kumarad@mst.edu
Gaurav Sant
gsant@ucla.edu

Specialty section:
This article was submitted to Structural Materials, a section of the journal Frontiers in Materials

Received: 16 October 2021
Accepted: 02 December 2021
Published: 04 January 2022

Citation:
Han T, Ponduru SA, Cook R, Huang J, Sant G and Kumar A (2022) A Deep Learning Approach to Design and Discover Sustainable Cementitious Binders: Strategies to Learn From Small Databases and Develop Closed-form Analytical Models. Front. Mater. 8:796476. doi: 10.3389/fmats.2021.796476

To reduce the energy-intensity and carbon footprint of Portland cement (PC), the prevailing practice embraced by concrete technologists is to partially replace the PC in concrete with supplementary cementitious materials [SCMs: geological materials (e.g., limestone); industrial by-products (e.g., fly ash); and processed materials (e.g., calcined clay)]. Chemistry and content of the SCM profoundly affect PC hydration kinetics; which, in turn, dictates the evolutions of microstructure and properties of the [PC + SCM] binder. Owing to the substantial diversity in SCMs' compositions–plus the massive combinatorial spaces, and the highly nonlinear and mutually-interacting processes that arise from SCM-PC interactions–state-of-the-art computational models are unable to produce *a priori* predictions of hydration kinetics or properties of [PC + SCM] binders. In the past 2 decades, the combination of Big data and machine learning (ML)—commonly referred to as the *fourth paradigm of science*–has emerged as a promising approach to learn composition-property correlations in materials (e.g., concrete), and capitalize on such learnings to produce *a priori* predictions of properties of materials with new compositions. Notwithstanding these merits, widespread use of ML models is hindered because they: 1) Require *Big data* to learn composition-property correlations, and, in general, large databases for concrete are not publicly available; and 2) Function as black-boxes, thus providing little-to-no insights into the materials laws like theory-based analytical models do. This study presents a deep learning (DL) model capable of producing *a priori*, high-fidelity predictions of composition- and time-dependent hydration kinetics and phase assemblage development in [PC + SCM] pastes. The DL is coupled with: 1) A fast Fourier transformation algorithm that reduces the dimensionality of training datasets (e.g., kinetic datasets), thus allowing the model to learn intrinsic composition-property correlations from a small database; and 2) A thermodynamic model that constrains the model, thus ensuring that predictions do not violate fundamental materials laws. The

training and outcomes of the DL are ultimately leveraged to develop a simple, easy-to-use, closed-form analytical model capable of predicting hydration kinetics and phase assemblage development in [PC + SCM] pastes, using their initial composition and mixture design as inputs.

Keywords: deep learning, sustaianability, hydration kinetic, prediction, thermodynamics

INTRODUCTION

Concrete–a mixture of Portland cement (PC); water; sand; and stone–is the principal material used in the construction of all forms of physical infrastructure; and, more generally, the built environment. At the current global level of production—~4.5 gigatonnes (Gt) every year (Lange and Clare, 2013; Gartner and Hirao, 2015; Biernacki et al., 2017; Scrivener et al., 2018)—PC requires $11 \bullet 10^{18}$J of thermal energy; (Gartner and Hirao, 2015; Ludwig and Zhang, 2015; Schneider, 2015; Biernacki et al., 2017; He et al., 2019); which is equivalent to the energy generated from the combustion of ~1.3 billion barrels of crude oil. (Schneider et al., 2011; Schneider, 2015; Cadavid-Giraldo et al., 2020; Ighalo and Adeniyi, 2020). When we account for emission of greenhouse gases, especially CO_2, the statistics exacerbate alarmingly: (Gartner and Hirao, 2015; Ludwig and Zhang, 2015; Schneider, 2015): PC's production-and-use accounts for ~9% of all anthropogenic CO_2 emissions. (Miller, 2013; Schorcht, 2013; Dowling et al., 2015). As the global population rises to 10 billion by 2050, (United Nations, 2019), the demand for PC concrete infrastructure–and, thus, the concomitant energy demand and CO_2 emissions–are expected to continually increase in the future.

To alleviate the energy-intensity and carbon footprint of PC's production-and-use, the construction community has emphasized partial substitution of PC (up to $60\%_{mass}$) with supplementary cementitious materials (SCMs: limestone; quartz; metakaolin; fly ash; slag; etc. (Mehta and Monteiro, 1976; Johari et al., 2011; Juenger et al., 2012; Juenger and Siddique, 2015; Biernacki et al., 2017; Juenger et al., 2019)). However, much research is still required to comprehensively understand and describe the underlying composition-reaction-microstructure-property correlations in low-PC or [PC + SCM] binders (i.e., pastes; mortars; and concretes). Such understanding–when distilled down to theories, and subsequently, as closed-form mathematical equations–would offer the ability to produce *a priori* predictions of binders' properties, just using their compositions (plus a few other easy-to-measure attributes, e.g., mixture proportion and fineness of precursor materials) as inputs. This would be greatly beneficial, as it would substantially reduce the time and cost of conducting experiments to determine the binders' properties; and would allow end-users to manipulate (e.g., enhance) the binders' properties by simply finetuning their composition.

While the needs and benefits of *a priori* predictions of cementitious binders' properties (from their compositions) are clear, developing theory-based models that are actually capable of producing accurate predictions is not straightforward. This is largely because, in all PC-based binders (e.g., plain paste [PC + SCM] paste; etc.), the development of properties (e.g., strength) is dictated by the hydration of PC, a complex process involving the reaction of PC with water. (Taylor, 1997). The aforesaid complexity–which has, in effect, stymied the development of accurate, predictive models–arises from the presence of numerous anhydrous (i.e., unreacted) and hydrated phases (i.e., hydration products) within the binder at any given age (Mehta and Monteiro, 1976; Thomas et al., 2011; Cook et al., 2021a). A typical, commercial PC comprises C_3S, C_2S, C_3A, and C_4AF (plus $C\$H_2$)—where: C = CaO; S = SiO_2; A = Al_2O_3; \$ = SO_3; F = Fe_2O_3; and H = H_2O–and all of these phases concurrently undergo hydration at distinct rates upon contact with water, and produce distinct sets of hydrates. (Bullard et al., 2011; Cook et al., 2019a). Many past studies (Breval, 1976; Vovk, 2000; Chen and Juenger, 2011; Kumar et al., 2012; Quennoz and Scrivener, 2012; Lapeyre et al., 2020; Cook et al., 2021a) have attempted to describe PC hydration by investigating simpler variants of PC pastes; for example, pure C_3S and C_3S-C_3A-gypsum pastes. While these studies have provided foundational understanding of intrinsic composition-reaction-microstructure-property correlations in simpler systems, this understanding falls short of explaining hydration (and the ensuing development of microstructure and properties) in low-PC binders. For instance, in [PC + SCM] binders, chemical interactions of the SCM with anhydrous cementitious phases (e.g., C_3S; and C_3A) and hydrates–that occur alongside the hydration of the anhydrous phases–can be difficult to explain or predict based on our knowledge gained from simpler systems. Complexities resulting from metakaolin–for example–are well-documented in both binary (Lapeyre and Kumar, 2018; Lapeyre et al., 2019) and ternary pastes; (Cook et al., 2021b); as it can act as both a pozzolan and a filler, (Lapeyre and Kumar, 2018; Lapeyre et al., 2019), as well as contribute to carboaluminate hydrate formation. (De Weerdt et al., 2011; Antoni et al., 2012; Vance et al., 2013a; Ramezanianpour and Hooton, 2014).

To predict the properties of a given (PC + SCM) binder (e.g., paste) at a specific age, it is critical to know the binder's phase assemblage [i.e., volume fractions of anhydrous PC; anhydrous SCMs; hydrates; and capillary pores]; which, in turn, depends on the rate and extent of hydration of PC in the binder. Isothermal calorimetry has emerged as the dominant technique among cement chemists to measure the rate and extent (degree) of hydration of PC in cementitious binders. This technique measures time-resolved exothermic heat release from the hydration of PC (and other endothermic and exothermic reactions, if any). This heat–generally speaking–is much larger in magnitude compared to minor amounts of thermal energy associated with interactions of SCMs with other components of

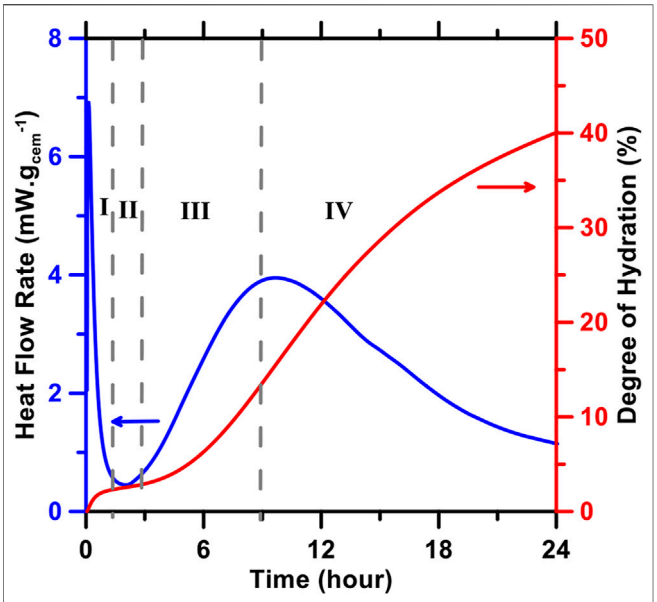

FIGURE 1 | Heat flow rate profile (blue), depicting the kinetics of PC hydration during four stages that manifest within the first 24 h after mixing (I) *initial period* (II) *induction period* (III) *acceleration period*; and (IV) *deceleration period* (Bullard et al., 2011; Cook, 2020; Cook et al., 2021b). The *initial period* corresponds to wetting of PC particulates (upon contact with water) and their rapid dissolution. The *induction period* corresponds to a period of slow dissolution of PC particulates, and precipitation of small amounts of hydrates (Bullard et al., 2011; Scrivener et al., 2015). The *acceleration* and *deceleration periods* are associated with a short burst of nucleation and subsequent growth of hydrates (Bullard, 2008; Bazzoni, 2014; Bazzoni et al., 2014; Bullard et al., 2015; Scrivener et al., 2015). The heat flow rate profile can be used to estimate the time-dependent extent/degree of reaction of PC (red).

the binder (Cook et al., 2021b). The heat evolution (or calorimetry) profiles thus obtained can be processed to determine the degree of reaction (or hydration) of PC in the binder as a function of time. (Bullard et al., 2011; Cook et al., 2021b). **Figure 1** shows representative isothermal calorimetry profiles (i.e., time-resolved heat flow rate; and cumulative heat release) of a type I/II PC paste. These heat evolution profiles can be coupled with thermodynamic simulations to describe the evolution of a binder's phase assemblage (i.e., volume fractions of anhydrous PC and SCMs; hydrates; and capillary pores) with respect to time or the degree of hydration of PC. Gibbs Energy Minimization Software (GEMS)—designed for geochemical modeling (Wagner et al., 2012; Kulik et al., 2013)—has become a popular tool for such thermodynamic simulations. (Lothenbach and Winnefeld, 2006; Lothenbach et al., 2008; De Weerdt et al., 2011). More specifically: isothermal calorimetry results and GEMS simulations–when combined–can describe, with reasonable accuracy, the phase assemblage of a PC-based binder with respect to time; which can be further analyzed to qualitatively or quantitively predict the properties of the binder. With that said, the combination of isothermal calorimetry and GEMS still cannot produce *a priori* predictions of time-resolved phase assemblage of a new binder. This is because experimental measurement of the new binder's heat evolution profiles, or PC's hydration kinetics, would still be required. And, to reiterate the point made earlier, due to our lack of understanding of underlying composition-reaction correlations, state-of-the-art kinetic models (e.g., phase boundary nucleation and growth models with constant, (Thomas, 2007), or variable growth rate (Oey et al., 2016; Ley-Hernandez et al., 2018; Lapeyre et al., 2019)) are unable to produce reliable predictions of heat evolution profiles of PC-based systems. Furthermore, although these kinetic models can reproduce heat evolution profiles, experiments are required to determine key parameters (e.g., constant or time-dependent growth rate of CSH) for the models. Consequently, these models are unable to produce *a priori* predictions of calorimetry profiles of cementitious systems.

Recent studies (Cook et al., 2021b; Lapeyre et al., 2021) have shown that machine learning (ML) models–once trained from a sufficiently large calorimetry database–can produce *a priori* predictions of heat evolution profiles (i.e., time-dependent heat flow rate and cumulative heat release) of PC-based binders, including binary and ternary [PC + SCM] pastes. Despite the successes of these studies, there are still few challenges that need to be addressed. 1) In both studies, (Cook et al., 2021b; Lapeyre et al., 2021), relatively *homogenous* databases were used to train and test the prediction performance of the ML model. To better explain the aforesaid *homogeneous* nature of the databases: in one study, (Lapeyre et al., 2021), a database comprised of calorimetry profiles of (synthetic PC + SCM) pastes was used; whereas, in the other, (Cook et al., 2021c), a database comprised of calorimetry profiles of (commercial PC + SCM) pastes was used. It is unclear if the prediction performance of the ML models would decline if the two databases were to be combined to produce a singular, highly *heterogeneous*–yet a moderately low-volume–database. The authors hypothesize that for such a highly *heterogeneous* database, it is important to reduce the dimensionality (complexity) of the database; to make it easier for the ML models to learn the intrinsic input-output correlations during their training. Fourier transformation–which has historically been used for signal processing, and processing of 2D and 3D images obtained from various techniques (e.g., spectroscopy; (Fromherz and Guenther, 2005); microstructures generated from micro- and nano-indentation apparatuses; (Passoja and Psioda, 1981; Hao et al., 1993); electron microscopy; (Buseck et al., 1988; Zeng et al., 2016) etc.;)—is a promising tool for dimensionality-reduction of numerical databases. This is because of Fourier transformation's innate ability to maintain most of the information–except for the redundant ones–contained within the database of interest, but in a much simpler, *near loss-less* format (Duhamel and Vetterli, 1990). Preservation of pertinent information in the database–while reducing the redundancies–not only simplifies the initial transformation, but also the reverse transformation (i.e., from the reduced to the original dimensional form) (Duhamel and Vetterli, 1990). Although Fourier transformation has never been used to treat or process calorimetry databases, the authors hypothesize that its use could substantially enhance the prediction performance of ML models, especially when working with complex, highly *heterogeneous* database with a relatively small volume. This hypothesis will be tested in this study. 2) The ML models used

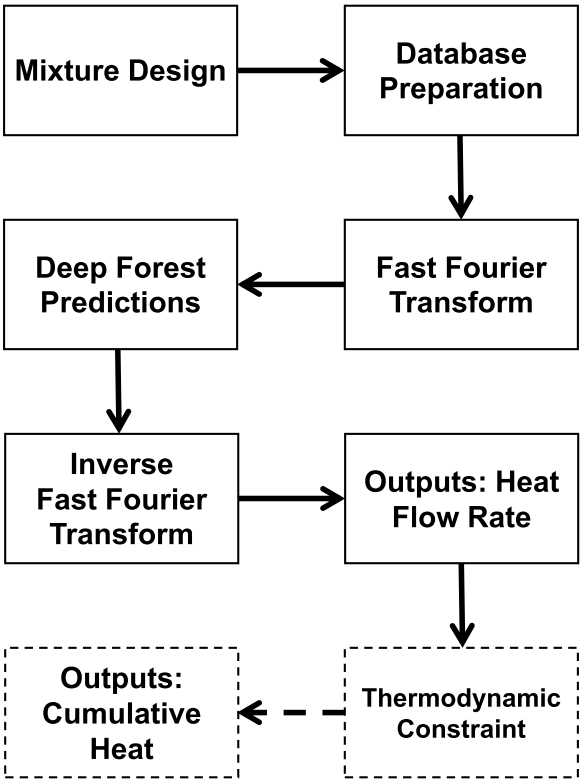

FIGURE 2 | Schematic of the original FT-DL model, developed in this study, to predict hydration kinetics (i.e., heat flow rate and cumulative heat release) of (PC + SCM) pastes. For prediction of cumulative heat release, thermodynamic constraint–obtained from simulations of phase assemblages in the pastes–is used to provide guidance to the model, and constrain its outputs.

in the two studies (Cook et al., 2021b; Lapeyre et al., 2021) cited above–while good at producing *a priori* predictions of heat evolution profiles of [PC + SCM] pastes–were not constrained in any way. The authors hypothesize that if these ML models are constrained–e.g., using thermodynamic rules as constraints–their prediction performance would improve. Importantly, it would be less likely for the models' predictions to violate basic thermodynamic rules. Testing this hypothesis is another focus of this study. 3) The studies (Cook et al., 2021b; Lapeyre et al., 2021) cited above used ML models that function–more or less–as *black-boxes*; providing little-to-no insights into the materials laws like closed-form analytical models do. This is a problem, because end-users–who do not have access to ML models–would not gain any benefits from such ML models. It is, thus, important to capitalize on the training of the ML models–and the cause-effect correlations established by them–to develop simple, closed-form analytical models that are accessible to all end-users, irrespective of their knowledge of, or access to, ML models.

In this study, a deep learning (DL) model–trained from a *heterogenous*, low-volume database of heat evolution profiles of [PC + SCM] pastes–is implemented to produce *a priori*, high-fidelity predictions of composition- and time-dependent hydration kinetics, and phase assemblage development in (PC + SCM) pastes. The SCMs used in this study include permutations-and-combinations of limestone; quartz; silica fume; and metakaolin. To enhance the prediction performance, the DL model is coupled with: 1) A fast Fourier transformation (FFT) algorithm that reduces the dimensionality of database; and 2) A thermodynamic constraint (obtained from thermodynamic simulations of phase assemblages) that ensures that the predictions do not violate fundamental materials laws. The DL model is used to quantify the influence of each input variable (e.g., contents of SCMs and C_3S in the binder) on the resultant properties of the binder; thereby allowing the distinction between consequential and inconsequential variables (in terms of their influence on hydration kinetics). On the premise of this understanding, an easy-to-use, closed-form analytical model is developed; and it is shown that this model–despite its simplicity and fewer input requirements–can produce reliable, *a priori* predictions of hydration kinetics and phase assemblage development in (PC + SCM) pastes.

MODELING METHODS

An original Fourier transform-deep learning (FT-DL) model was developed in this study. The model was trained: first, using a synthetic database for benchmarking and validation (described in **section 3.1**); and second, using database of isothermal calorimetry profiles of (PC + SCM) pastes (described in **section 3.2**). The trained model was subsequently employed to produce predictions of outputs in blank data-domains of the synthetic database, and hydration kinetics of new (PC + SCM) pastes. Prediction performance of the model was rigorously appraised by comparing its predictions against actual values. **Figure 2** shows the architecture of the FT-DL model. As can be seen, this model unites the fast Fourier transformation (FFT) algorithm with the deep learning (DL) model. Details of the DL model–which is premised on the random forests model that has been in our previous studies (Cook et al., 2021b; Lapeyre et al., 2021; Xu et al., 2021)—can be found in **Supplementary Section S1** of **Supplementary Information S1**

The calorimetry database used for training and validation of FT-DL model is composed of: 1) Input variables: physicochemical properties of (PC + SCM) pastes (e.g., mixture design; and physical attributes such as specific surface areas (SSAs) of the PC and SCM measured using static light scattering); and 2) Output: time-resolved heat flow rate profiles, obtained from isothermal calorimetry. First, the model is trained using a large fraction of the database. Prior to the training, dimensionality of the heat flow rate profiles (in the training database) is reduced using the FFT algorithm. Next, during the training, the model finds the underlying correlations between input variables and the FFT-transformed heat flow rate profiles. The trained FT-DL model is then validated against a testing database (the remaining minor fraction of the database that is kept hidden from the model during its training). The model leverages its training to predict the FFT-transformed heat flow rate profiles in relation to physicochemical properties of

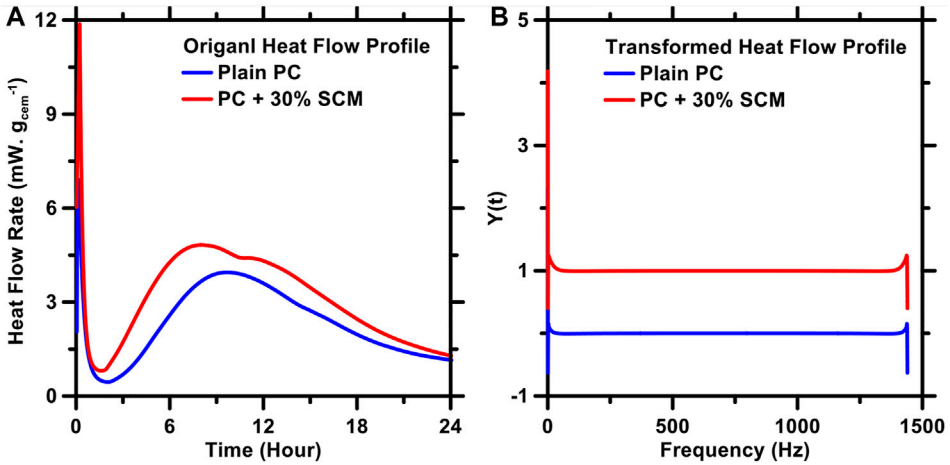

FIGURE 3 | (A) Original and **(B)** FFT-transformed heat flow rate profiles of representative plain and (PC + SCM) pastes. As can be seen, FFT transformation significantly reduces the dimensionality (complexity) of the profile; thereby making is easier and more (computationally) efficient for the FT-DL model to statistically analyze the datasets–and learn input-output correlations–during its training.

pastes in the testing database. Finally, the model's predictions are reverse-transformed, back to time-dependent heat flow rate profiles–akin to those obtained from isothermal calorimetry–using the inverse FFT algorithm. In select cases (e.g., to predict the cumulative heat release of pastes at 24 h; see **section 3.3**), thermodynamic simulations of phase assemblages in the pastes are used to provide theoretical guidance to the FT-DL model, and to constrain its outputs. These predictions are then compared against experiments. To evaluate the accuracy of predictions produced by the FT-DL model, five statistical parameters–mean absolute error (*MAE*); mean absolute percentage error (*MAPE*); root mean squared error (*RMSE*); Person correlation coefficient (*R*); and coefficient of determination (R^2)—are used. Relevant equations that describe these parameters–the measures of errors in the model's predictions–can be found in our previous studies. (Cook et al., 2019b; Cai et al., 2020).

Fourier transform (FT) is a signal-processing technique that is used to convert a complex waveform from its original domain (e.g., time) to a representation in the frequency domain, and vice versa. (Cochran et al., 1967; Bergland, 1969; Higgins, 1976). Time-to-frequency domain conversion, when done for a dataset comprising a finite number of data-records spanning a finite range (as opposed to functions, e.g., sin *(x)*, that are continuous over an infinite domain) (Duhamel and Vetterli, 1990), is called discrete-time Fourier transform (DFT; shown in)

$$A_r = \sum_{k=0}^{N-1} X_k e^{-2\pi i r k/N} \qquad r = 0, \cdots, N-1 \tag{1}$$

where A_r is the r^{th} coefficient of the DFT; X_k represents the k^{th} sample of the time series which consists of N samples; $i = \sqrt{-1}$; and N is the number of data points.

In this study, FFT algorithm–a simple and efficient algorithm, designed to obtain discrete-time Fourier transformations of complex datasets–is used to reduce the dimensionality (or complexity) of heat flow rate profiles of [PC + SCM] pastes. (Cooley and Tukey, 1965). Compared to competing algorithms (e.g., conventional DFT), FFT is computationally more efficient. This is because the number of required operations is reduced from N^2 to $N\ log_2 N$. In general, the FFT algorithm splits the N-point transformation into 2 N/2-point transformations in each step. Then, in an iterative manner, each subset is bifurcated, until the final subset only has a 1-point transformation. Overall, each point requires $log_2 N$ splits, resulting in $N log_2 N$ operations for generating N-point transformations. The FFT algorithm is described in **Eq. (2)**. **Figure 3** shows representative examples of FFT transformation of heat flow rate profiles of pastes. As can be seen, the transformed profiles are much simpler than their original counterparts. Information contained within the transformed profiles (**Figure 3B**) can be expressed using far fewer number of datapoints than the corresponding original versions (**Figure 3A**). This is important because such reduction in number of datapoints substantially reduces the time and computational resources (e.g., memory) needed for the FT-DL model's training. Furthermore, as the number of inflection (i.e., non-differentiable) points in the transformed profiles are significantly lower than in the original ones, it is much easier for the FT-DL model to establish input-output correlations from the transformed profiles as compared to the original ones.

$$A_r = \sum_{k=0}^{N/2-1} X_{2k} e^{-4\pi i r k/N} + X_{2k-1} e^{-2\pi i r (2k+1)/N} \qquad k = 0, \cdots, \frac{N}{2} - 1; \qquad r = 0, \cdots, N-1 \tag{2}$$

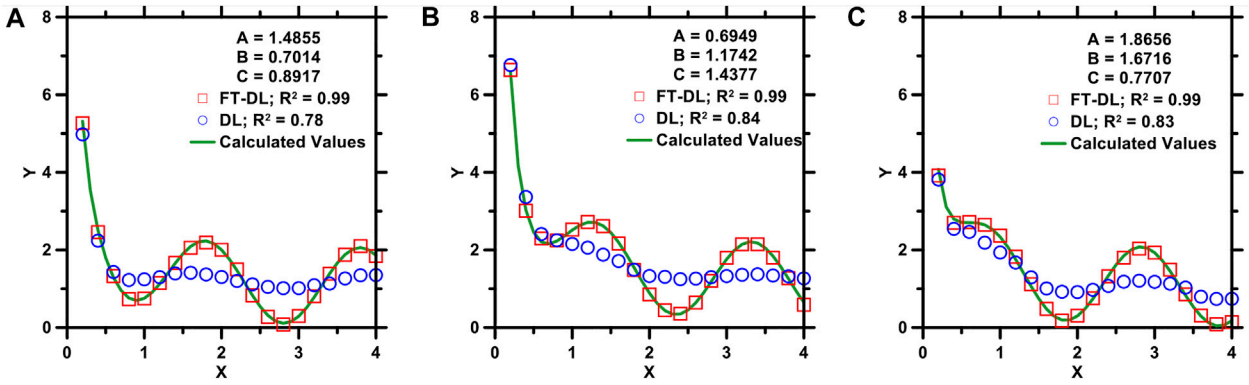

FIGURE 4 | Representative predictions of *Y* of mathematical functions produced by the DL and FT-DL models plotted against calculated *Y* values. The input, *X*, ranges from 0.2 to 2.0. The coefficients **(A–C)** used in the functions, and the models' prediction accuracies (R^2), are shown in the legends.

RESULTS AND DISCUSSION

Validation of the FT-DL Model

The FT-DL model described in section 2.0 differs from the ML models used in our previous studies (Cook et al., 2021b; Lapeyre et al., 2021; Xu et al., 2021) (i.e., DL model based on random forests) in one key respect: In the FT-DL model, the database is FFT-transformed, prior to the model's training, so as to reduce the database's dimensionality; whereas in the DL model, the database is used in its pristine form. In section 2.0, it was argued that the FFT-transformation of the database ensures better training of FT-DL model; thereby, resulting in improvement of its prediction performance. To justify this argument, the prediction performance of the FT-DL model was compared against that of the DL model; using a synthetic database featuring a highly nonlinear, and non-monotonous relationship between the input (*X*) and the output (*Y*). Within the database, the complex input-output relationships are represented by a composite mathematical function (**Eq. (3)**). This function consists of three separate functions: exponential; trigonometric; and hyperbolic. Here, *X* is the input; *Y* is the output; and *A*, *B*, and *C* are coefficients ranging from 0-to-2. The synthetic database was populated with ~20,000 data-series (i.e., *Y* as a function of *X*), created by randomly assigning an independent set of coefficients (i.e., randomly chosen values of *A*, *B*, and *C* within the pre-selected range of 0-to-2); while varying *X* from 0.2 to 4.0 with a step-size of 0.2.75% of data-series were randomly selected from the database, and used to train the FT-DL and DL models. The remaining 25% were used to probe and compare the prediction performances of the two models.

$$Y = \exp\left(\frac{-1}{X + A}\right) + \sin\left[\pi\left(B + x\right)\right] + \frac{C}{X} \tag{3}$$

Figure 4 shows representative predictions (of data-series included in the testing database) produced by the DL and FT-DL models; the actual data-series, calculated directly from **Eq. (3)**, are also shown. As can be seen, the prediction performance of the FT-DL model is clearly superior to that of the DL model. This result is in agreement with our previous studies, (Cook et al., 2019b; Han et al., 2020a; Han et al., 2020b), wherein we have shown that standalone ML models–including the random forests-based DL model–generally exhibit moderate-to-poor prediction performance over datasets that feature highly nonlinear and non-monotonous input-output correlations. The FT-DL model–in which the database is FFT-transformed prior to the model's training–produces accurate predictions; because the FFT transformation substantially reduces the nonlinearity and non-monotonicity of the database, by transforming it from the original domain to the frequency domain (see **Figure 3**). Put in another way: the FFT algorithm converts each data-series to a simple, *broadly* monotonic *Y-X* relationship; thereby, making it easier for the FT-DL model to establish the underlying mathematical relationship between the output and input. The DL model–on the other hand–must employ *brute-force* statistical methods to establish *Y-X* relationship from the highly complex data-series; and, consequently, is susceptible to missing key inflection points (peaks and troughs) and other vicissitudes (e.g., sharp changes in *Y* occurring over small ranges of *X*) in the data-series.

Prediction of Heat Flow Rate Profiles of Pastes

Results in **section 3.1** demonstrate that the FT-DL model can produce accurate predictions; even in data-domains featuring complex input-output correlations. Since *Y-X* relationships shown in **Figure 4** are similar in nature to heat flow rate profiles of (PC + SCM) pastes, it is reasonable to posit that the FT-DL model would produce more accurate predictions of PC hydration kinetics compared to those produced by the DL model. To test this hypothesis, a calorimetry database–comprising heat flow rate profiles of (PC + SCM) pastes–was consolidated from our two prior studies. (Cook et al., 2021b; Lapeyre et al., 2021). The combined database consists of eight types of PCs: one commercial cement (CC; type I/II PC); and seven synthetic cements (SCs). Phase compositions of the 8 PCs are shown in

TABLE 1 | Compositions of commercial cement (CC) and synthetic cements (SCs) 1–7.

Cement type	C_3S ($\%_{mass}$)	C_2S ($\%_{mass}$)	C_3A ($\%_{mass}$)	C_4AF ($\%_{mass}$)	$C\$H_2$ ($\%_{mass}$)
CC	62.37	19.35	6.24	9.35	2.69
SC 1	90	0	4	0	6
SC 2	92	0	4	0	4
SC 3	88	0	8	0	4
SC 4	80	0	8	0	12
SC 5	70	0	12	0	18
SC 6	82	0	12	0	6
SC 7	100	0	0	0	0

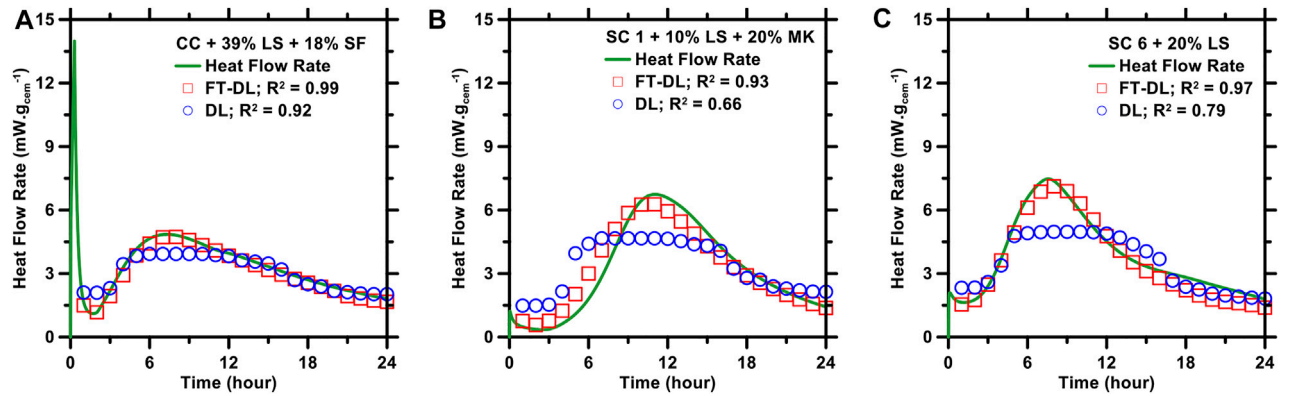

FIGURE 5 | The FT-DL and DL models' predictions of heat flow rate profiles of: **(A)** (commercial cement (CC) + limestone (LS) + silica fume (SF)])paste; **(B)** [synthetic cement 1 (SC 1) + limestone (LS) + metakaolin (MK)] paste; and **(C)** [synthetic cement 6 (SC 6) + limestone (LS)] paste compared against experimental measurements. Coefficient of determination (R^2) of each prediction is shown in the legends.

TABLE 2 | Statistical parameters describing the mean prediction errors (i.e., averaged over a period of 24 h) of DL and FT-DL models. Errors were estimated by comparing predicted heat flow rate profiles of (PC + SCM) pastes against experimentally-measured ones. Time-solved prediction errors are descried in **Supplemetary Information**.

ML model	R	R^2	MAE	MAPE	RMSE
	Unitless	*Unitless*	mW. g_{cem}^{-1}	%	mW. g_{cem}^{-1}
DL	0.8935	0.7983	0.5852	41.07	0.8211
FT-DL	0.9454	0.8937	0.3188	18.36	0.5289

Table 1. The SCMs comprise permutations-and-combinations of quartz (QZ); limestone (LS); metakaolin (MK); and silica fume (SF). Other details of this database are described in **Supplementary Section S2.0**. The parent database was split into training and testing databases. The training database consisted of 13,416 data-records from 559 (PC + SCM) pastes; and the testing database consisted of 960 data-records from 40 (PC + SCM) pastes. The training database was used for training the FT-DL model (and the DL model for comparison), and optimizing the models' hyperparameters. The testing database was used to evaluate the prediction performance of the trained models against experimental measurements. Both databases include physicochemical attributes of the pastes as inputs: C_3S content ($\%_{mass}$); C_2S content ($\%_{mass}$); C_3A content ($\%_{mass}$); C_4AF content ($\%_{mass}$); $C\$H_2$ content ($\%_{mass}$); types (integers) and contents ($\%_{mass}$) of SCMs; specific surface area (SSA) of PC and SCMs (cm (Biernacki et al., 2017). g^{-1}); and time (hour). The output is time-dependent heat flow rate (mW. g_{Cem}^{-1}) from 0-to-24 h, with a 1-h time-interval between successive steps. Pertinent statistical variations in the inputs and outputs of the training and testing databases are shown in **Supplemetary Table S1** and **Supplemetary Table S2**.

Figure 5 shows representative predictions of heat flow rate profiles produced by the DL and FT-DL models compared against experimental (isothermal calorimetry) measurements. Prediction errors are summarized in **Table 2**; and depicted graphically in **Supplemetary Figure S1**. As shown in **Figure 5** and **Table 2**, both DL and FT-DL models produce accurate predictions of heat flow rate profiles of (PC + SCM) pastes; with R^2 ranging from 0.79 to 0.89, and *MAE* ranging from 0.32 to 0.58 mW g_{Cem}^{-1}. The FT-DL model–across the board–produces more accurate predictions compared to the DL model; validating the hypothesis made earlier in this section. Importantly, the FT-DL model is able to produce accurate *a priori* predictions of heat flow rates of new (PC + SCM) pastes (i.e., new to the model); even during early ages (i.e., between 1 h and ±2 h of the main hydration peak) when the heat flow rates change rapidly from very high values (during stage I) to very low values (during stage II), and then again to high values (during stage III). Each SCM–depending on its content;

physical properties (mainly fineness); and composition–casts unique influence on the heat flow rate profile. For example, fine limestone and fine quartz cause leftward shift of the heat flow rate profile; (Cook et al., 2019a); resulting in steeper rise to, and earlier occurrence of, the main hydration peak. In contrast, fine metakaolin, when used to replace $\geqslant 20\%_{mass}$ of PC, causes deceleration of PC's hydration kinetics; (Lapeyre and Kumar, 2018; Cook et al., 2019a; Lapeyre et al., 2019); which manifests as delayed occurrence of the main hydration peak (although the peak's intensity is comparable to, and sometimes greater than, that of its plain paste counterpart). Coarse metakaolin also causes deceleration of PC's hydration rates; but–owing to metakaolin's slow dissolution kinetics–the deceleration is minor, sometimes imperceptible (Lapeyre et al., 2019). Notwithstanding these disparate influences of SCMs, **Figure 5** and **Table 2** demonstrate that the FT-DL model can capture the effects of SCM type and physicochemical attributes during its training; and capitalize on this *knowledge* to produce reliable predictions of hydration behavior of new [PC + SCM] pastes. The DL model–on the other hand–fails to capture the critical inflection points of the heat flow rate profiles. As can be seen in **Figure 5**, for each of the three (PC + SCM) pastes, DL model's predictions of the time of occurrence and intensity of the main hydration peak are not accurate. The main hydration peak is a critical juncture of the hydration process; as it is indicative of the period that generally occurs a few hours after the paste sets, and begins to gain strength at a rapid rate due to massive precipitation of hydrates. (Mehta and Monteiro, 1976; Taylor, 1997; Bullard et al., 2011; Mehdipour et al., 2017). Because of the significance of the main hydration peak, in many prior studies, (Kumar et al., 2012; Scherer et al., 2012; Oey et al., 2013; Masoero et al., 2014; Ley-Hernandez et al., 2018), the accuracies of kinetic models (and the underlying mechanisms that were implemented within the models) have been adjudicated–almost exclusively–on the basis of whether or not they were able to capture the experimentally-observed main hydration peak. Since the DL model was unable to capture the main hydration peak–whereas the FT-DL model was–it is justified to say that the FT-DL model is the more reliable tool to produce *a priori* predictions of heat evolution profiles of cementitious binders.

As stated earlier in **section 3.1**, the disparity in the prediction performance of the DL model vis-à-vis the FT-DL model arises, mainly, from the FFT algorithm; which is integrated in the latter model, but not in the former. In the FT-DL model, the FFT algorithm–which is used to preprocess the training database prior to the model's training–substantially reduces the nonlinearity and non-monotonicity of heat flow rate profiles; thereby, reducing their complexity (see **Figure 3**). This reduction in complexity becomes particularly important when the volume of the training database is low (e.g., the database used in this study, which comprises heat flow rate profiles of only ~600 pastes). If a large database were used, most ML models–including the DL model–would be able to statistically (i.e., by brute-force) process input-output maps–with both inputs and outputs spanning a wide range of magnitudes–and establish a sufficiently-accurate mathematical correlation between them. But, in a small but complex database, establishing such correlation is not easy. Furthermore, the FFT-transformed heat flow rate profiles contain fewer data-records compared to the original ones; this ensures that the computational resources (e.g., number of processing threads; memory; etc.) required to train the FT-DL model are substantially less than the DL model.

Prediction of Cumulative Heat Release

Results in **section 3.2** show that the FT-DL model is a reliable tool for *a priori* predictions of time-dependent heat flow rate profiles–or hydration kinetics–of (PC + SCM) pastes. These predicted heat flow rate profiles can simply be processed (i.e., integrated with respect to time) to obtain time-dependent cumulative heat release profiles. Cumulative heat release profiles are important for a practical standpoint; as several past studies have shown that the cumulative heat released from PC's hydration in a binder is directly correlated with the binder's rheological properties, (Mehdipour et al., 2017; Meng et al., 2019; Ferraz et al., 2020), setting time, (Vance et al., 2013b; Lootens and Bentz, 2016), and compressive strength. (Bentz et al., 2012; Kumar et al., 2013a; Kumar et al., 2013b; Mehdipour et al., 2017). Put in another way: cumulative heat release profiles can be used to roughly estimate important compliance-relevant properties of binders; thus, eliminating the need for costly, cumbersome, and time-consuming experiments. For instance, if the 24-h cumulative heat releases of [PC + SCM] pastes are known, this information can be used to rank and order the pastes on the basis of their 24-h compressive strengths. (Bentz et al., 2012; Mehdipour et al., 2017).

In this study, the predicted heat flow rate profiles of all (PC + SCM) pastes (in the testing database) were processed to obtain cumulative heat release profiles; which were then compared against experiments. It was found–expectedly, as discussed in **section 3.1**—that the FT-DL model's predictions were more accurate than those produced by the DL model. However, the prediction errors–as evaluated using the five statistical parameters discussed in section 2.0—were, in general, greater than those associated with predictions of heat flow rate profiles. This is because the prediction errors of heat flow rate profiles accrue as they are integrated to obtain the cumulative heat release profiles. Therefore, to obtain reliable predictions of cumulative heat release–especially at critical ages (e.g., at 24 h, at which the paste's strength is used as a qualification criterion for use in construction of infrastructure (Taylor et al., 2015))—it is important to further finetune the FT-DL model. Towards this end, thermodynamic simulations of phase assemblages in the pastes (summarized below; and in **Supplementary Section S3.0** of **Supplementary Information S1**) were used to provide theoretical guidance to the FT-DL model, and to constrain its outputs.

GEMS (Lothenbach et al., 2019; Kulik et al., 2012) was used to produce thermodynamic simulations of phase assemblage evolution in (PC + SCM) pastes in relation to their mixture design (i.e., composition and mixture proportions of precursors used to formulate the binders). Phase assemblages obtained from the simulations (see **Figures 6A,B**) reveal the volumes of all reactants (i.e., PC; and SCMs) and products (i.e., hydration products such as C-S-H and ettringite) at increasing degrees of

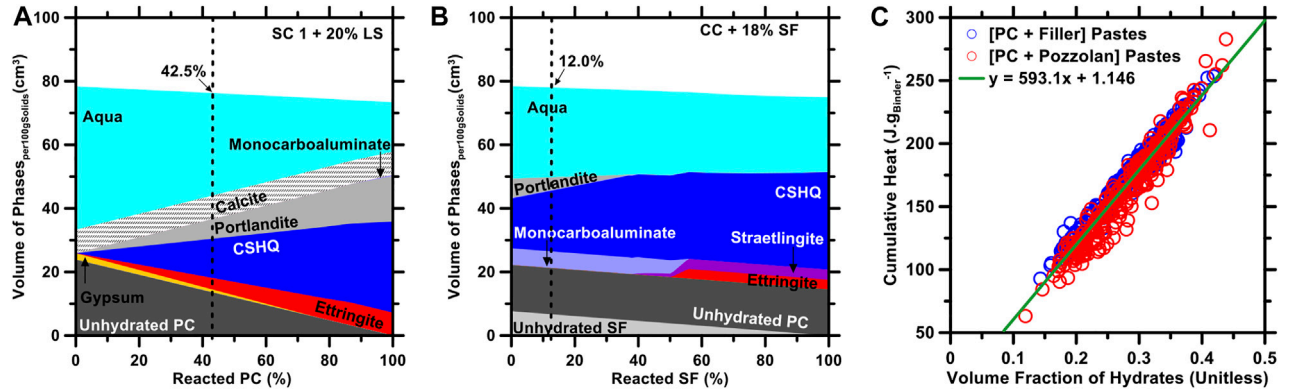

FIGURE 6 | (A) Equilibrium phase assemblage, estimated using GEMS, of a representative (synthetic cement 1 + limestone (LS) paste at 24 h. The vertical dashed line indicates the phase assemblage at 24 h based on the degree of hydration of PC as estimated from the cumulative heat release. **(B)** Equilibrium phase assemblage of a representative [commercial cement + silica fume (SF)] paste at the age of 24 h. Here, the degree of hydration of PC at 24 h is estimated from isothermal calorimetry. The vertical dashed line represents the degree of reaction of silica fume. **(C)** A linear correlation between volume fraction of hydrates and cumulative heat release at 24 h of ~600 [PC + SCM] pastes used in this study (PC + pozzolan) pastes are silica fume- and metakaolin-containing pastes; and (PC + filler) pastes are either plain pastes, or pastes that contain limestone or quartz.

reaction of the main reactant (PC or SCM). (Lothenbach and Winnefeld, 2006; Lothenbach et al., 2008). To obtain accurate phase assemblages, it is important to specify the degree of reaction of PC and of the SCM (if it is reactive). PC's degree of reaction at any given age–for example, at 24 h–can be estimated directly from the cumulative heat release at that age. More specifically: PC's degree of reaction in each paste at 24 h is equivalent to the ratio of cumulative heat release at 24 h to the enthalpy of hydration of PC. The enthalpy of hydration of each PC (i.e., either the commercial PC, or one of the seven synthetic ones) is calculated as the sum of enthalpies of hydration of each of its constituent phases [$C_3S \approx 500\ J\ g^{-1}$; $C_2S \approx 260\ J\ g^{-1}$; C_3A (reacting with $C\$H_2$) $\approx 1160\ J\ g^{-1}$; and $C_4AF \approx 725\ J\ g^{-1}$ (Taylor, 1997; Kurdowski, 2014).] multiplied to its respective mass fraction. In this study, four different types of SCMs were used: quartz; limestone; silica fume; and metakaolin. Quartz and limestone dissolve at very slow rates; as, as such, in the thermodynamic simulations, they were assumed to be inert (i.e., degree of reaction at 24 h = 0.0) (Cook et al., 2019a; Oey et al., 2013; Kumar et al., 2017; Berodier and Scrivener, 2014). Silica fume and metakaolin–on the other hand–dissolve (albeit slowly), and can partake in chemical interactions with anhydrous cementitious phases (e.g., metakaolin can react with C_3A and $C\$H_2$) and hydrates (e.g., metakaolin and silica fume can undergo pozzolanic reaction with portlandite, a hydrate present in the paste). (Cook et al., 2019a; Lapeyre et al., 2019; Lapeyre and Kumar, 2018; Meng et al., 2019). Therefore, to obtain accurate phase assemblages of metakaolin- and silica fume-containing pastes, it is important to determine their degrees of reaction. In a series of prior studies, (Cook et al., 2019a; Lapeyre et al., 2019; Lapeyre and Kumar, 2018; Meng et al., 2019), it has been shown that the degrees of reaction of silica fume and metakaolin range between 5-and-15% within the first 24 h. To determine the precise degrees of reaction at 24 h, GEMS simulations of all [PC + SCM] pastes were employed by varying silica fume's and metakaolin's degree of reaction from 5-to15%; while using PC's degree of reaction at 24 h as calculated from cumulative heat release profiles, and assuming that limestone and quartz are inert. Based on the simulation results (**Figure 6B**), it was found that across all (PC + silica fume) and (PC + metakaolin) pastes, a degree of reaction of 12% for silica fume and degree of reaction of 6% for metakaolin resulted in a *near* linear relationship between the cumulative heat release and the volume fraction of hydrates (**Figure 6C**). We chose specifically to evaluate this relationship to estimate the pozzolanic SCMs' degrees of reaction, because cumulative heat release of any (PC + SCM) paste is correlated with the extents of reaction of the reactants (i.e., PC and SCM); which, in turn, dictates the amounts (or volume fractions) of the hydrates. In **Figure 6C**, it should be noted that results pertaining to plain pastes [PC + quartz] pastes, and (PC + limestone) pastes are also included; which justify our assumption that limestone and quartz are inert in the first 24 h. An important aspect of **Figure 6C** is the generic mathematical equation that describes the relationship between cumulative heat release and volume fraction of hydrates in ~600 (PC + SCM) pastes. It should be noted that both the cumulative heat and volume fraction of hydrates account for not just the hydration of cement but also cement-SCM interactions. This relationship–in and of itself–is an important outcome; since, it allows researchers to promptly estimate the volume fraction of hydrates in any given (PC + SCM) paste using its 24 h cumulative heat release as the sole input. The volume fraction of hydrates–which is a crude measure of the solid-to-solid connectivity within the paste (Zalzale and McDonald, 2012; Zalzale et al., 2013; Lootens and Bentz, 2016; Banala and Kumar, 2017)—can be used to roughly estimate the compressive strength and porosity of the paste. The authors would like to clarify that the volume fractions of hydrates in (PC + SCM) pastes–shown in **Figure 6C**–can be predicted directly from the FT-DL model; as opposed to deriving them from GEMS simulations. For this, the FT-DL model needs to be trained using a new database; comprising the same input variables as those described in **section 3.2**, and the volume fraction of hydrates

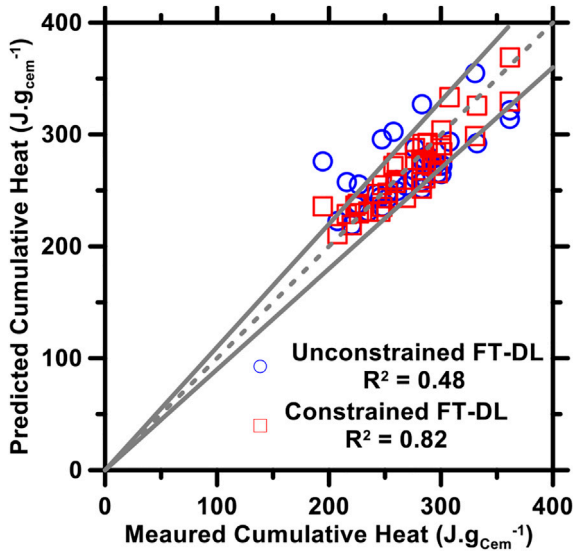

FIGURE 7 | Predictions of cumulative heat at 24 h produced by the FT-DL model–with and without thermodynamic constraint–compared against experimental measurements. The coefficients of determination (R^2) of the predictions are shown in the legends. The dashed and solid lines represent the line of ideality and ±10% error bounds, respectively.

(estimated from GEMs simulations) as the output. Once trained, the FT-DL model can predict the volume fraction of hydrates in a new (PC + SCM) paste using its mixture proportion and physiochemical attributes as inputs. Therefore, it can be said that the FT-DL model can not only produce reliable, *a priori* predictions of hydration kinetics but also of phase assemblages of (PC + SCM) pastes.

Outcomes of thermodynamic simulations–shown in **Figure 6C**–allow us to correlate the cumulative heat release (at 24 h) with the volume fraction of hydrates in (PC + SCM) pastes. In this study, this correlation was used as a *thermodynamic constraint* to guide and regulate the predictions of 24 h cumulative heat release of (PC + SCM) pastes. More specifically, for any given (PC + SCM) paste, the heat flow rate profile–and then the cumulative heat release at 24 h–was predicted using the FT-DL model described in **sections 3.1** and 3.2. Next, the predicted value of the 24 h cumulative heat release was compared with the cumulative heat release derived from **Figure 6C** (using the paste's phase assemblage (i.e., volume fraction of hydrates at 24 h), calculated from thermodynamic simulations (GEMS), as input]. If the deviation between the two predictions was found to be smaller than 10 J. g_{cem}^{-1}, the prediction from the FT-DL model was selected as the final output. Otherwise, the cumulative heat release from the thermodynamic simulations was selected as final output. **Figure 7** compares the predictions of 24-h cumulative release of (PC + SCM) pastes obtained using the *unconstrained* FT-DL model and the thermodynamically-constrained FT-DL model. The corresponding prediction errors are summarized in **Table 3**. As can be seen, predictions of 24 h cumulative heat release from the thermodynamically-constrained FT-DL model are

TABLE 3 | Statistical parameters describing the errors in predictions of 24 h cumulative heat release, as produced by the unconstrained and thermodynamically-constrained FT-DL models.

ML model	R	R^2	MAE	MAPE	RMSE
	Unitless	*Unitless*	J. g_{cem}^{-1}	%	J. g_{cem}^{-1}
Unconstrained FT-DL	0.6935	0.4809	21.63	8.087	27.64
Constrained FT-DL	0.9033	0.8161	13.24	4.887	16.79

significantly more accurate than the unconstrained FT-DL model. This result clarifies that guidance from thermodynamic simulations significantly boosts the ability of the FT-DL model to predict the hydration kinetics of (PC + SCM) pastes. It must be noted that, in **Figure 7**, the 24 h cumulative heat release of the pastes is used merely as a representative example. The thermodynamically-constrained FT-DL model can be used–in similar fashion–to produce *a priori* predictions of the cumulative heat release at other ages (0 ≤ age ≤24 h) as well.

DISCUSSION

Development of a Closed-form Analytical Model

Results in section 3.0 show that the FT-DL model–especially when integrated with thermodynamic guidance and constraints–can produce reliable, *a priori* predictions of hydration kinetics and phase assemblages (e.g., volume fraction of hydrates at a given age) of (PC + SCM) pastes. It must, however, be acknowledged that the FT-DL model–while powerful–is not accessible to end-users; especially those who have limited background in computer programming. Hence, it is important that the learnings of the FT-DL model be distilled down to simple, closed-form analytical models that can be used by end-users of all expertise and disciplines. Such distillation of the FT-DL model into an analytical model also improves the interpretability of the outcomes; as in an analytical model the correlation between each input (e.g., physicochemical properties of binders' precursors) and the output (i.e., cumulative heat release at 24 h) is clearly outlined in the form of a mathematical equation.

To develop a reliable analytical model, it is crucial to select input variables that cast significant influence on the output, while disregarding those which are largely inconsequential. The "DL" part of the FT-DL model is important in this context; because, it can statistically evaluate–in the form of Gini scores (Xu et al., 2021; Han et al., 2020a; Han et al., 2020b; Breiman, 2001; Menze et al., 2009)—the influence of each variable on the output. Results from this analysis are shown in **Figure 8**. Here, the contents of $C\$H_2$, C_3S, C_3A, and SCM cast the strongest influence on the 24 h cumulative release. C_3S–being the major phase in PC (Taylor, 1997)—is expectedly an influential factor. C_3A and $C\$H_2$ are also influential because these two phases react with each other (and water) vigorously within minutes of mixing; thereby releasing heat at a rapid rate for few hours, followed by relatively slow, near-constant rate of heat release. (Taylor, 1997; Bullard et al.,

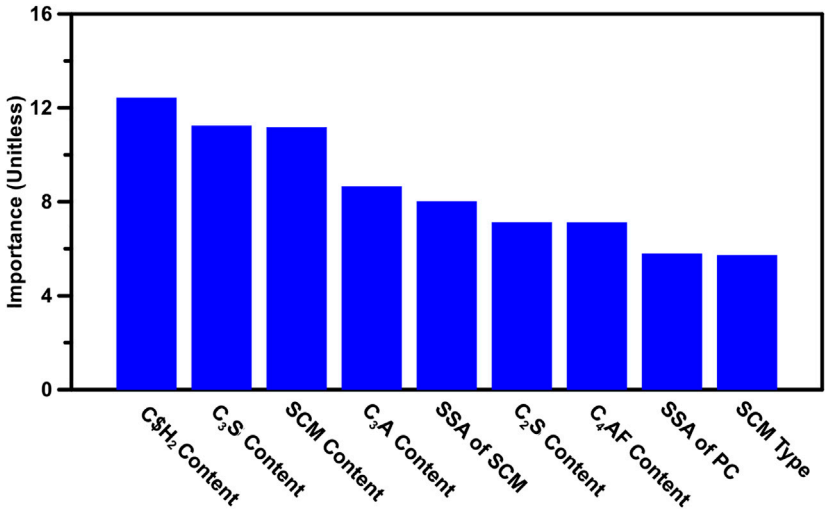

FIGURE 8 | Ranking of input variables (descending order of variable importance), based on their abilities to influence the 24-h cumulative release of (PC + SCM) pastes at 24 h.

2011; Kurdowski, 2014). SCM content and specific surface area (SSA) are also influential; as these variables dictate the ability of the SCM to influence the overall hydration kinetics through the filler effect, and/or pozzolanic effect, and/or chemical interactions with other paste components. (Juenger and Siddique, 2015; Lapeyre and Kumar, 2018; Cook et al., 2019a; Lapeyre et al., 2019). C_2S and C_4AF react very slowly with water in the first 24 h; thus, their effects on the overall hydration kinetics are not significant. (Bullard et al., 2011; Cook et al., 2021a). SSA of PC is known to profoundly affect its hydration kinetics (Bullard et al., 2011). However, owing to limited variability in SSA of PC in the database used in this study, it is evaluated as the less influential. SCM type is appraised to be the least important variable. This–once again–is because only two types of SCMs (fillers and pozzolans) were used in this study.

Variable importance, shown in **Figure 8**, was used to guide the mathematical form of the closed-form analytical model. SCM type, C_2S content, and C_4AF content were excluded due to their low variable importance; but the other influential input variables were included. $C\$H_2$ content and C_3S content were assigned greater weight; by raising them to the second power. The general form of the analytical model, thus developed, is shown in **Eq. (3)**. Here, *CH* is the cumulative heat release at 24 h ($J.g_{cem}^{-1}$); C_i is the coefficient for each input variable; M_i is mass percentage of component i ($\%_{mass}$); and A_j is SSA of component j ($cm.g^{-1}$) (Biernacki et al., 2017).

$$CH_{24\,hours} = C_0 + C_1 \times M_{C_3S}^2 + C_2 \times M_{C_3A} + C_3 \times M_{CH_2} + C_4 \times M_{SCM} + C_5 \times A_{PC} + C_6 \times A_{SCM} \quad (4)$$

In the analytical model, six coefficients and one constant need to be optimized. Those coefficients were optimized for two scenarios: 1) (PC + pozzolan) pastes; and 2) (PC + filler) pastes; wherein silica fume and metakaolin are treated as pozzolans, and limestone and quartz are treated as fillers (as discussed in **section 3.3**). A nonlinear, gradient-descent scheme (Han et al., 2020a; Han et al., 2020b; Lapeyre et al., 2021)—based on the Nelder-Mead multi-dimensional simplex algorithm (Nelder and Mead, 1965; McKinnon, 1998)—was used to optimize the coefficients of the analytical model. The optimal coefficients for (PC + pozzolan) pastes and (PC + filler) pastes are shown in **Table 4**. Final predictions of the 24 h cumulative heat release of both types of pastes are shown in **Figure 9**.

TABLE 4 | Optimum values of coefficients and the constant for the analytical model shown in **Eq. 3**. The model can be used to estimate the 24 h cumulative heat release of (PC + pozzolan) pastes and (PC + filler) pastes.

(PC + pozzolan) pastes	C_0	166.2189	C_1	−0.0027	C_2	8.7031
	C_3	−0.5031	C_4	1.4123	C_5	0.0106
	C_6	−0.0001				
[PC + Filler] pastes	C_0	135.243	C_1	0.0044	C_2	5.692
	C_3	−0.3137	C_4	1.8383	C_5	0.0053
	C_6	0.0014				

As can be seen in **Figure 9**, the analytical model–despite being much simpler and easier-to-use than its parent model (FT-DL model)—produces accurate predictions (i.e., margin of error within ±6.3%) of 24 h cumulative heat release of (PC + pozzolan) and (PC + filler) pastes. The values of *R* are 0.81 and 0.90 for (PC + pozzolan) pastes and (PC + filler) pastes, respectively; which are commensurable to that of the FT-DL model ($R \approx 0.90$). Importantly, the analytical model has a simple polynomial form; which can be coded into any spreadsheet software by end-users of all disciplines and expertise to produce *a priori* predictions of heat evolution behavior of

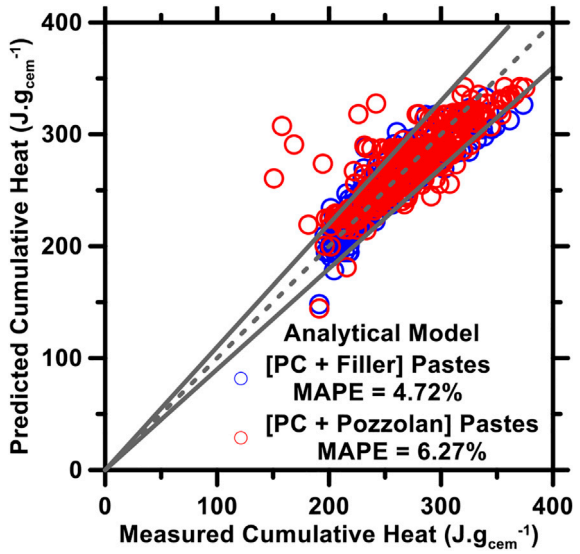

FIGURE 9 | Predictions of 24-h cumulative heat of (PC + pozzolan) pastes and (PC + filler) pastes compared against experimental measurements. Mean absolute percentage errors (*MAPE*) of the predictions are shown in the legends. The dashed and solid lines represent the line of ideality and ±10% error bounds, respectively.

(PC + SCM) pastes; using just a few mixture design parameters as inputs. It is worth pointing out that in **Figure 9**, the 24 h cumulative heat release is used as a representative example. Using the method described in this section, cumulative heat release at other critical ages can also be predicted. Furthermore, the cumulative heat release predictions produced by the analytical model can be plugged into the equation shown in **Figure 6C** to directly estimate the volume fraction of hydrates in the (PC + SCM) pastes. Therefore, as a standalone prediction tool, the analytical model–although not as sophisticated or accurate as the FT-DL model–can be used for *a priori* predictions of important aspects of both hydration kinetics and phase assemblage development in PC-based binders.

Conclusion

Supplementary cementitious materials (SCMs: e.g., limestone; calcined clays; etc.) are typically used to partially replace Portland cement (PC) in concrete to reduce its energy-intensity and carbon footprint. SCMs–depending on their composition; physical properties (e.g., fineness); and content–cast significant influence on PC's hydration behavior; thus, affecting nearly all fresh- and mature-state properties of concrete. For decades, researchers have attempted to develop analytical models–premised on theories and mechanisms learned from classical materials science approaches–that would be able to produce *a priori* predictions of (PC + SCM) binders. While the pursuit of theory-based models is essential for the advancement of our understanding of underlying composition-reaction-microstructure-property correlations in (PC + SCM) binders, our current piecemeal understanding of these correlations has thus far stymied the development of such models.

In recent years, machine learning (ML)—coupled with a large database (i.e., Big data); comprised of experimental measurements, and/or experimentally-validated simulations–has emerged as a promising approach to learn the intrinsic cause-effect correlations in materials, including (PC + SCM) binders (e.g., pastes); and, then, to capitalize on such *learnings* to predict the properties of new materials by simply using their easy-to-measure physicochemical characteristics as inputs. While promising, widespread use of ML models is hindered because they: 1) Require "Big" data for their training (which is difficult to produce, or mine from literature); and 2) Provide little-to-no insights into the origins of the materials' behavior/properties (and, thus, are perceived as *black boxes*).

In this study, an original deep learning (DL) model was developed, with the objective of predicting hydration kinetics (i.e., time-dependent heat flow rate, and cumulative heat release), and phase assemblage development (e.g., volume fraction of hydrates at a specific age) in (PC + SCM) pastes. A fast Fourier transformation (FFT) algorithm was integrated into the model: to reduce the dimensionality of the database used to train the DL model; and to make it easier, and computationally efficient, for the model to learn the input-output correlations from a relatively small database (comprised of reaction behavior of only ~600 distinct [PC + SCM] pastes). Results obtained from extramural thermodynamic simulations (conducted using GEMS: a free-to-use, and publicly accessible, thermodynamic modeling software) were also integrated into the model: to provide theoretical guidance to the model; and to constrain its outputs, to ensure that they do not violate basic thermodynamic rules. It was shown that the model–i.e., thermodynamically-constrained FT-DL model–produced accurate *a priori* predictions of hydration behavior and phase assemblage development of (PC + SCM) pastes. The training and outcomes of the FT-DL model were then used to develop a closed-form analytical model. The analytical model–albeit not as sophisticated or accurate as the FT-DL model–was shown to be a simple, easy-to-use prediction tool to produce reliable *a priori* predictions of important aspects of both hydration kinetics and phase assemblage development in (PC + SCM) binders.

The FT-DL model–and its simpler derivative, the closed-form analytical model–that are presented in this study demonstrate that, even with *small* data (rather than Big data), reliable predictions of reaction behavior and microstructural evolution (phase assemblage) of cementitious systems are possible. As with any ML model, it is expected that the FT-DL model's accuracy would improve if/when it is trained with a larger, more diverse Big Data. Such a Big Data/FT-DL platform–if created and disseminated–would give researchers and end-users unprecedented access to data (information); and empower them with reliable prediction (and optimization) tools to tune locally-available–but often overlooked and/or underutilized–materials (e.g., volcanic, and off-specification ash; waste-to-energy residue produced from incineration of municipal waste) to function as CO_2-efficient SCMs.

DATA AVAILABILITY STATEMENT

The database, machine learning model, thermodynamic model, and code used in this study are available from the corresponding author (AK; kumarad@mst.edu) by request.

AUTHOR CONTRIBUTIONS

SP and RC: Database development and manuscript development TH and JH: Development and validation of ML models; and development of manuscript AK and GS: Manuscript development and review.

FUNDING

Financial support for this research was provided by: the Leonard Wood Institute (LWI: W911NF-07-2-0062); the National Science Foundation (NSF-CMMI: 1661609; NSF-CMMI: 1932690; and NSF-DMR: 2034856); and the Federal Highway Administration (Award no: 693JJ31950021).

SUPPLEMENTARY MATERIAL

The Supplementary Material for this article can be found online at: https://www.frontiersin.org/articles/10.3389/fmats.2021.796476/full#supplementary-material

REFERENCES

Antoni, M., Rossen, J., Martirena, F., and Scrivener, K. (2012). Cement Substitution by a Combination of Metakaolin and limestone. *Cement Concrete Res.* 42, 1579–1589. doi:10.1016/j.cemconres.2012.09.006

Banala, A., and Kumar, A. (2017). Numerical Simulations of Permeability of plain and Blended Cement Pastes. *Int. J. Adv. Eng. Sci. Appl. Math.* 9, 67–86. doi:10.1007/s12572-017-0184-7

Bazzoni, A., Ma, S., Wang, Q., Shen, X., Cantoni, M., and Scrivener, K. L. (2014). The Effect of Magnesium and Zinc Ions on the Hydration Kinetics of C3 S. *J. Am. Ceram. Soc.* 97, 3684–3693. doi:10.1111/jace.13156

Bazzoni, A. (2014). *Study of Early Hydration Mechanisms of Cement by Means of Electron Microscopy*. Lausanne: EPFL.

Bentz, D. P., Barrett, T., De la Varga, I., and Weiss, W. J. (2012). Relating Compressive Strength to Heat Release in Mortars. *Adv. Civ. Eng. Matls.* 1, 20120002. doi:10.1520/acem20120002

Bergland, G. D. (1969). A Guided Tour of the Fast Fourier Transform. *IEEE Spectr.* 6, 41–52. doi:10.1109/mspec.1969.5213896

Berodier, E., and Scrivener, K. (2014). Understanding the Filler Effect on the Nucleation and Growth of C-S-H. *J. Am. Ceram. Soc.* 97, 3764–3773. doi:10.1111/jace.13177

Biernacki, J. J., Bullard, J. W., Sant, G., Brown, K., Glasser, F. P., Jones, S., et al. (2017). Cements in the 21 St century: Challenges, Perspectives, and Opportunities. *J. Am. Ceram. Soc.* 100, 2746–2773. doi:10.1111/jace.14948

Breiman, L. (2001). Random Forests. *Machine Learn.* 45, 5–32. doi:10.1023/a:1010933404324

Breval, E. (1976). C3A Hydration. *Cement Concrete Res.* 6, 129–137. doi:10.1016/0008-8846(76)90057-0

Bullard, J. W. (2008). A Determination of Hydration Mechanisms for Tricalcium Silicate Using a Kinetic Cellular Automaton Model. *J. Am. Ceram. Soc.* 91, 2088–2097. doi:10.1111/j.1551-2916.2008.02419.x

Bullard, J. W., Jennings, H. M., Livingston, R. A., Nonat, A., Scherer, G. W., Schweitzer, J. S., et al. (2011). Mechanisms of Cement Hydration. *Cement Concrete Res.* 41, 1208–1223. doi:10.1016/j.cemconres.2010.09.011

Bullard, J. W., Scherer, G. W., and Thomas, J. J. (2015). Time Dependent Driving Forces and the Kinetics of Tricalcium Silicate Hydration. *Cement Concrete Res.* 74, 26–34. doi:10.1016/j.cemconres.2015.03.016

Buseck, P. R., Epelboin, Y., and Rimsky, A. (1988). Signal Processing of High-Resolution Transmission Electron Microscope Images Using Fourier Transforms. *Acta Cryst. Sect A.* 44, 975–986. doi:10.1107/s0108767388007500

Cadavid-Giraldo, N., Velez-Gallego, M. C., and Restrepo-Boland, A. (2020). Carbon Emissions Reduction and Financial Effects of a Cap and Tax System on an Operating Supply Chain in the Cement Sector. *J. Clean. Prod.* 275, 122583. doi:10.1016/j.jclepro.2020.122583

Cai, R., Han, T., Liao, W., Huang, J., Li, D., Kumar, A., et al. (2020). Prediction of Surface Chloride Concentration of marine concrete Using Ensemble Machine Learning. *Cement Concrete Res.* 136, 106164. doi:10.1016/j.cemconres.2020.106164

Chen, I. A., and Juenger, M. C. G. (2011). Synthesis and Hydration of Calcium Sulfoaluminate-Belite Cements with Varied Phase Compositions. *J. Mater. Sci.* 46, 2568–2577. doi:10.1007/s10853-010-5109-9

Cochran, W. T., Cooley, J. W., Favin, D. L., Helms, H. D., Kaenel, R. A., Lang, W. W., et al. (1967). What Is the Fast Fourier Transform? *Proc. IEEE* 55, 1664–1674. doi:10.1109/proc.1967.5957

Cook, R., Han, T., Childers, A., Ryckman, C., Khayat, K., Ma, H., et al. (2021). Machine Learning for High-Fidelity Prediction of Cement Hydration Kinetics in Blended Systems. *Mater. Des.* 208, 109920. doi:10.1016/j.matdes.2021.109920

Cook, R., Han, T., Childers, A., Ryckman, C., Khayat, K., Ma, H., et al. (2021). Machine Learning for High-Fidelity Prediction of Cement Hydration Kinetics in Blended Systems. *Mater. Des.* 208, 109920. doi:10.1016/j.matdes.2021.109920

Cook, R., Lapeyre, J., Ma, H., and Kumar, A. (2019). Prediction of Compressive Strength of Concrete: Critical Comparison of Performance of a Hybrid Machine Learning Model with Standalone Models. *J. Mater. Civ. Eng.* 31, 04019255. doi:10.1061/(asce)mt.1943-5533.0002902

Cook, R., Ma, H., and Kumar, A. (2019). Influence of Size-classified and Slightly Soluble mineral Additives on Hydration of Tricalcium Silicate. *J. Am. Ceram. Soc.* 103, 2764–2779. doi:10.1111/jace.16936

Cook, R., Ma, H., Okoronkwo, M., Sant, G., and Kumar, A. (2021). Influence of Water Activity on Belite (β-C 2 S) Hydration. *J. Am. Ceram. Soc.* 104, 1831–1840. doi:10.1111/jace.17608

Cook, R. (2020). *Studying the Effects of Various Process Parameters on Early Age Hydration of Single- and Multi-phase Cementitious Systems*. Rolla, MO, USA: Missouri University of Science and Technology.

Cooley, J. W., and Tukey, J. W. (1965). An Algorithm for the Machine Calculation of Complex Fourier Series. *Math. Comp.* 19, 297–301. doi:10.1090/s0025-5718-1965-0178586-1

De Weerdt, K., Haha, M. B., Le Saout, G., Kjellsen, K. O., Justnes, H., and Lothenbach, B. (2011). Hydration Mechanisms of Ternary Portland Cements Containing limestone Powder and Fly Ash. *Cement Concrete Res.* 41, 279–291. doi:10.1016/j.cemconres.2010.11.014

Dowling, A., O'Dwyer, J., and Adley, C. C. (2015). Lime in the Limelight. *J. Clean. Prod.* 92, 13–22. doi:10.1016/j.jclepro.2014.12.047

Duhamel, P., and Vetterli, M. (1990). Fast Fourier Transforms: A Tutorial Review and a State of the Art. *Signal. Process.* 19, 259–299. doi:10.1016/0165-1684(90)90158-u

Ferraz, D. F., Martho, A. C. R., Burns, E. G., Romano, R. C. O., and Pileggi, R. G. (2020). "Effect of Mixing Procedure on the Rheological Properties and Hydration Kinetics of Portland Cement Paste," in *Rheology and Processing of Construction Materials*. Editors V. Mechtcherine, K. Khayat, and E. Secrieru (Manhattan, New York City: Springer International Publishing), 311–319. doi:10.1007/978-3-030-22566-7_36

Fromherz, T. (2005). "SPECTROSCOPY-fourier Transform Spectroscopy," in *Encyclopedia of Modern Optics*. Editor R. D. Guenther (Amsterdam, Netherlands: Elsevier).

Gartner, E., and Hirao, H. (2015). A Review of Alternative Approaches to the Reduction of CO2 Emissions Associated with the Manufacture of the Binder

Phase in concrete. *Cement Concrete Res.* 78 (Part A), 126–142. doi:10.1016/j.cemconres.2015.04.012

Han, T., Siddique, A., Khayat, K., Huang, J., and Kumar, A. (2020). An Ensemble Machine Learning Approach for Prediction and Optimization of Modulus of Elasticity of Recycled Aggregate concrete. *Construction Building Mater.* 244, 118271. doi:10.1016/j.conbuildmat.2020.118271

Han, T., Stone-Weiss, N., Huang, J., Goel, A., and Kumar, A. (2020). Machine Learning as a Tool to Design Glasses with Controlled Dissolution for Healthcare Applications. *Acta Biomater.* 107, 286–298. doi:10.1016/j.actbio.2020.02.037

Hao, Y., Wang, Z. G., and Tian, J. F. (1993). A Quantitative Investigation of Fatigue Fracture Surfaces by Using the Fourier Transform Method. *Mater. Sci. Eng. A* 161, 195–200. doi:10.1016/0921-5093(93)90513-e

He, Z., Zhu, X., Wang, J., Mu, M., and Wang, Y. (2019). Comparison of CO2 Emissions from OPC and Recycled Cement Production. *Construction Building Mater.* 211, 965–973. doi:10.1016/j.conbuildmat.2019.03.289

Higgins, R. J. (1976). Fast Fourier Transform: An Introduction with Some Minicomputer Experiments. *Am. J. Phys.* 44, 766–773. doi:10.1119/1.10128

Ighalo, J. O., and Adeniyi, A. G. (2020). A Perspective on Environmental Sustainability in the Cement Industry. *Waste Disposal Sustain. Energ.* 2, 161–164. doi:10.1007/s42768-020-00043-y

Johari, M. A. M., Brooks, J. J., Kabir, S., and Rivard, P. (2011). Influence of Supplementary Cementitious Materials on Engineering Properties of High Strength concrete. *Construction Building Mater.* 25, 2639–2648. doi:10.1016/j.conbuildmat.2010.12.013

Juenger, M. C. G., and Siddique, R. (2015). Recent Advances in Understanding the Role of Supplementary Cementitious Materials in concrete. *Cement Concrete Res.* 78 (Part A), 71–80. doi:10.1016/j.cemconres.2015.03.018

Juenger, M. C. G., Snellings, R., and Bernal, S. A. (2019). Supplementary Cementitious Materials: New Sources, Characterization, and Performance Insights. *Cement Concrete Res.* 122, 257–273. doi:10.1016/j.cemconres.2019.05.008

Juenger, M., Provis, J. L., Elsen, J., Matthes, W., Hooton, R. D., Duchesne, J., et al. (2012). Supplementary Cementitious Materials for concrete: Characterization Needs. *Mater. Res. Soc. symposia Proc. Mater. Res. Soc.* 1488, imrc12, 2012 . Cambridge Univ Press. doi:10.1557/opl.2012.1536

Kulik, D. A., Wagner, T., Dmytrieva, S. V., Kosakowski, G., Hingerl, F. F., Chudnenko, K. V., et al. (2012). GEM-selektor Geochemical Modeling Package: Revised Algorithm and GEMS3K Numerical Kernel for Coupled Simulation Codes. *Comput. Geosci.* 17, 1–24. doi:10.1007/s10596-012-9310-6

Kulik, D. A., Wagner, T., Dmytrieva, S. V., Kosakowski, G., Hingerl, F. F., Chudnenko, K. V., et al. (2013). GEM-selektor Geochemical Modeling Package: Revised Algorithm and GEMS3K Numerical Kernel for Coupled Simulation Codes. *Comput. Geosciences* 17, 1–24. doi:10.1007/s10596-012-9310-6

Kumar, A., Bishnoi, S., and Scrivener, K. L. (2012). Modelling Early Age Hydration Kinetics of Alite. *Cement Concrete Res.* 42, 903–918. doi:10.1016/j.cemconres.2012.03.003

Kumar, A., Oey, T., Falla, G. P., Henkensiefken, R., Neithalath, N., and Sant, G. (2013). A Comparison of Intergrinding and Blending limestone on Reaction and Strength Evolution in Cementitious Materials. *Construction Building Mater.* 43, 428–435. doi:10.1016/j.conbuildmat.2013.02.032

Kumar, A., Oey, T., Falzone, G., Huang, J., Bauchy, M., Balonis, M., et al. (2017). The Filler Effect: The Influence of Filler Content and Type on the Hydration Rate of C3S and OPC. *J. Am. Chem. Soc.* 100, 3316–3328. doi:10.1111/jace.14859

Kumar, A., Oey, T., Kim, S., Thomas, D., Badran, S., Li, J., et al. (2013). Simple Methods to Estimate the Influence of limestone Fillers on Reaction and Property Evolution in Cementitious Materials. *Cement and Concrete Composites* 42, 20–29. doi:10.1016/j.cemconcomp.2013.05.002

Kurdowski, W. (2014). *Cement and concrete Chemistry*. New York: Springer.

Lange, T., and Clare, S. (2013). "Advancements in concrete Material Sustainability: Supplementary Cementitious Material Development and Pollutant Interaction,". UT Electronic Theses and Dissertations (Austin, USA: The University of Texas at Austin).

Lapeyre, J., Han, T., Wiles, B., Ma, H., Huang, J., Sant, G., et al. (2021). Machine Learning Enables Prompt Prediction of Hydration Kinetics of Multicomponent Cementitious Systems. *Sci. Rep.* 11, 3922. doi:10.1038/s41598-021-83582-6

Lapeyre, J., and Kumar, A. (2018). Influence of Pozzolanic Additives on Hydration Mechanisms of Tricalcium Silicate. *J. Am. Ceram. Soc.* 101, 3557–3574. doi:10.1111/jace.15518

Lapeyre, J., Ma, H., and Kumar, A. (2019). Effect of Particle Size Distribution of Metakaolin on Hydration Kinetics of Tricalcium Silicate. *J. Am. Ceram. Soc.* 102, 5976–5988. doi:10.1111/jace.16467

Lapeyre, J., Ma, H., Okoronkwo, M., Sant, G., and Kumar, A. (2020). Influence of Water Activity on Hydration of Tricalcium Aluminate-calcium Sulfate Systems. *J. Am. Ceram. Soc.* 103, 3851–3870. doi:10.1111/jace.17046

Ley-Hernandez, A. M., Lapeyre, J., Cook, R., Kumar, A., and Feys, D. (2018). Elucidating the Effect of Water-To-Cement Ratio on the Hydration Mechanisms of Cement. *ACS Omega* 3, 5092–5105. doi:10.1021/acsomega.8b00097

Lootens, D., and Bentz, D. P. (2016). On the Relation of Setting and Early-Age Strength Development to Porosity and Hydration in Cement-Based Materials. *Cement and Concrete Composites* 68, 9–14. doi:10.1016/j.cemconcomp.2016.02.010

Lothenbach, B., Kulik, D. A., Matschei, T., Balonis, M., Baquerizo, L., Dilnesa, B., et al. (2019). Cemdata18: A Chemical Thermodynamic Database for Hydrated Portland Cements and Alkali-Activated Materials. *Cement Concrete Res.* 115, 472–506. doi:10.1016/j.cemconres.2018.04.018

Lothenbach, B., Matschei, T., Möschner, G., and Glasser, F. P. (2008). Thermodynamic Modelling of the Effect of Temperature on the Hydration and Porosity of Portland Cement. *Cement Concrete Res.* 38, 1–18. doi:10.1016/j.cemconres.2007.08.017

Lothenbach, B., and Winnefeld, F. (2006). Thermodynamic Modelling of the Hydration of Portland Cement. *Cement Concrete Res.* 36, 209–226. doi:10.1016/j.cemconres.2005.03.001

Ludwig, H.-M., and Zhang, W. (2015). Research Review of Cement Clinker Chemistry. *Cement Concrete Res.* 78 (Part A), 24–37. doi:10.1016/j.cemconres.2015.05.018

Masoero, E., Thomas, J. J., and Jennings, H. M. (2014). A Reaction Zone Hypothesis for the Effects of Particle Size and Water-To-Cement Ratio on the Early Hydration Kinetics of C3 S. *J. Am. Ceram. Soc.* 97, 967–975. doi:10.1111/jace.12713

McKinnon, K. I. M. (1998). Convergence of the Nelder--Mead Simplex Method to a Nonstationary Point. *SIAM J. Optim.* 9, 148–158. doi:10.1137/s1052623496303482

Mehdipour, I., Kumar, A., and Khayat, K. H. (2017). Rheology, Hydration, and Strength Evolution of Interground limestone Cement Containing PCE Dispersant and High Volume Supplementary Cementitious Materials. *Mater. Des.* 127, 54–66. doi:10.1016/j.matdes.2017.04.061

Mehta, P. K., and Monteiro, P. J. (1976). *Concrete-microstructure, Properties and Materials. 2006. Utilization of palm Oil Fuel Ash in concrete: A Review*. Ney York, USA: McGraw Hill Professional.

Meng, W., Kumar, A., and Khayat, K. H. (2019). Effect of Silica Fume and Slump-Retaining Polycarboxylate-Based Dispersant on the Development of Properties of portland Cement Paste. *Cement and Concrete Composites* 99, 181–190. doi:10.1016/j.cemconcomp.2019.03.021

Menze, B. H., Kelm, B. M., Masuch, R., Himmelreich, U., Bachert, P., Petrich, W., et al. (2009). A Comparison of Random forest and its Gini Importance with Standard Chemometric Methods for the Feature Selection and Classification of Spectral Data. *BMC Bioinformatics* 10, 213. doi:10.1186/1471-2105-10-213

Miller, M. M. (2013). *Lime, United States Geological Survey, 2012 minerals Yearbook*. Reston, VA: USGS.

Nelder, J. A., and Mead, R. (1965). A Simplex Method for Function Minimization. *Comput. J.* 7, 308–313. doi:10.1093/comjnl/7.4.308

Oey, T., Kumar, A., Bullard, J. W., Neithalath, N., and Sant, G. (2013). The Filler Effect: The Influence of Filler Content and Surface Area on Cementitious Reaction Rates. *J. Am. Ceram. Soc.* 96, 1978–1990. doi:10.1111/jace.12264

Oey, T., Kumar, A., Falzone, G., Huang, J., Kennison, S., Bauchy, M., et al. (2016). The Influence of Water Activity on the Hydration Rate of Tricalcium Silicate. *J. Am. Ceram. Soc.* 99, 2481–2492. doi:10.1111/jace.14181

Passoja, D., and Psioda, A. (1981). Fourier Transform Techniques- Fracture and Fatigue. *ASTM STP* 733, 355.

Quennoz, A., and Scrivener, K. L. (2012). Hydration of C3A-gypsum Systems. *Cement Concrete Res.* 42, 1032–1041. doi:10.1016/j.cemconres.2012.04.005

Ramezanianpour, A. M., and Hooton, R. D. (2014). A Study on Hydration, Compressive Strength, and Porosity of Portland-limestone Cement Mixes

Containing SCMs. *Cement and Concrete Composites* 51, 1–13. doi:10.1016/j.cemconcomp.2014.03.006

Scherer, G. W., Zhang, J., and Thomas, J. J. (2012). Nucleation and Growth Models for Hydration of Cement. *Cement Concrete Res.* 42, 982–993. doi:10.1016/j.cemconres.2012.03.019

Schneider, M. (2015). Process Technology for Efficient and Sustainable Cement Production. *Cement Concrete Res.* 78 (Part A), 14–23. doi:10.1016/j.cemconres.2015.05.014

Schneider, M., Romer, M., Tschudin, M., and Bolio, H. (2011). Sustainable Cement Production-Present and Future. *Cement Concrete Res.* 41, 642–650. doi:10.1016/j.cemconres.2011.03.019

Schorcht, F. (2013). *Best Available Techniques (BAT) Reference Document for the Production of Cement, Lime and Magnesium Oxide: Industrial Emissions Directive 2010/75/EU: Integrated Pollution Prevention and Control*. Ispra, Italy: EU Science Hub - European Commission. Available at: https://ec.europa.eu/jrc/en/publication/reference-reports/best-available-techniques-bat-reference-document-production-cement-lime-and-magnesium-oxide.

Scrivener, K. L., Juilland, P., and Monteiro, P. J. M. (2015). Advances in Understanding Hydration of Portland Cement. *Cement Concrete Res.* 78, 38–56. doi:10.1016/j.cemconres.2015.05.025

Scrivener, K., Martirena, F., Bishnoi, S., and Maity, S. (2018). Calcined clay limestone Cements (LC3). *Cement Concrete Res.* 114, 49–56. doi:10.1016/j.cemconres.2017.08.017

Taylor, A., Hamilton, T., III, and Nanni, A. (2015). *The Reinforced concrete Design Handbook: A Companion to ACI*. volume 1. Michigan, United States: ACI, 318–414.

Taylor, H. F. (1997). *Cement Chemistry*. London, UK: Thomas Telford.

Thomas, J. J. (2007). A New Approach to Modeling the Nucleation and Growth Kinetics of Tricalcium Silicate Hydration. *J. Am. Ceram. Soc.* 90, 3282–3288. doi:10.1111/j.1551-2916.2007.01858.x

Thomas, J. J., Biernacki, J. J., Bullard, J. W., Bishnoi, S., Dolado, J. S., Scherer, G. W., et al. (2011). Modeling and Simulation of Cement Hydration Kinetics and Microstructure Development. *Cement Concrete Res.* 41, 1257–1278. doi:10.1016/j.cemconres.2010.10.004

United Nations (2019). Growing at a Slower Pace, World Population Is Expected to Reach 9.7 Billion in 2050 and Could Peak at Nearly 11 Billion Around 2100 | UN DESA | United Nations Department of Economic and Social Affairs. Available at: https://www.un.org/development/desa/en/news/population/world-population-prospects-2019.html.

Vance, K., Aguayo, M., Oey, T., Sant, G., and Neithalath, N. (2013). Hydration and Strength Development in Ternary portland Cement Blends Containing limestone and Fly Ash or Metakaolin. *Cement and Concrete Composites* 39, 93–103. doi:10.1016/j.cemconcomp.2013.03.028

Vance, K., Kumar, A., Sant, G., and Neithalath, N. (2013). The Rheological Properties of Ternary Binders Containing Portland Cement, limestone, and Metakaolin or Fly Ash. *Cement Concrete Res.* 52, 196–207. doi:10.1016/j.cemconres.2013.07.007

Vovk, A. I. (2000). Hydration of Tricalcium Aluminate C3A and C3A-gypsum Mixtures in the Presence of Surfacants: Adsorption or Surface Phase Formation? *Colloid J.* 62, 24–31.

Wagner, T., Kulik, D. A., Hingerl, F. F., and Dmytrieva, S. V. (2012). GEM-selektor Geochemical Modeling Package: TSolMod Library and Data Interface for Multicomponent Phase Models. *Can. Mineral.* 50, 1173–1195. doi:10.3749/canmin.50.5.1173

Xu, X., Han, T., Huang, J., Kruger, A. A., Kumar, A., and Goel, A. (2021). Machine Learning Enabled Models to Predict Sulfur Solubility in Nuclear Waste Glasses. *ACS Appl. Mater. Inter.* 13, 53375–53387. doi:10.1021/acsami.1c10359

Zalzale, M., and McDonald, P. J. (2012). Lattice Boltzmann Simulations of the Permeability and Capillary Adsorption of Cement Model Microstructures. *Cement Concrete Res.* 42, 1601–1610. doi:10.1016/j.cemconres.2012.09.003

Zalzale, M., McDonald, P. J., and Scrivener, K. L. (2013). A 3D Lattice Boltzmann Effective media Study: Understanding the Role of C-S-H and Water Saturation on the Permeability of Cement Paste. *Model. Simul. Mater. Sci. Eng.* 21, 085016. doi:10.1088/0965-0393/21/8/085016

Zeng, Y., Liu, Z., Wu, W., Xu, F., and Shi, J. (2016). Combining Scanning Electron Microscopy and Fast Fourier Transform for Characterizing Mesopore and Defect Structures in Mesoporous Materials. *Microporous Mesoporous Mater.* 220, 163–167. doi:10.1016/j.micromeso.2015.09.001

Conflict of Interest: The authors declare that the research was conducted in the absence of any commercial or financial relationships that could be construed as a potential conflict of interest.

Publisher's Note: All claims expressed in this article are solely those of the authors and do not necessarily represent those of their affiliated organizations, or those of the publisher, the editors and the reviewers. Any product that may be evaluated in this article, or claim that may be made by its manufacturer, is not guaranteed or endorsed by the publisher.

frontiers in Materials

REVIEW
published: 05 January 2022
doi: 10.3389/fmats.2021.796396

Role of Aluminum and Lithium in Mitigating Alkali-Silica Reaction—A Review

Zhenguo Shi[1,2] *and Barbara Lothenbach*[2]*

[1]Global R&D, HeidelbergCement AG, Leimen, Germany, [2]Laboratory Concrete and Asphalt, Swiss Federal Laboratories for Materials Science and Technology (Empa), Dübendorf, Switzerland

Effective mitigation of alkali-silica reaction (ASR) is critical for producing durable concrete. The use of alumina-rich supplementary cementitious materials (SCMs) and chemical admixtures such as lithium salts to prevent expansion caused by ASR was first reported 70 years ago, shortly after the discovery of ASR in 1940s. Despite numerous investigations, the understanding of the mechanisms of Al and Li for mitigating ASR remain partially inexplicit in the case of Al, and hardly understood in the case of Li. This paper reviews the available information on the effect of Al and Li on ASR expansion, the influencing factors, possible mechanisms and limitations. The role of Al in mitigating ASR is likely related to the reduction of dissolution rate of reactive silica. Moreover, the presence of Al may alter the structure of crystalline ASR products to zeolite or its precursor, but such effect seems to be not that significant at ambient conditions due to the slow kinetics of zeolite formation. Several mechanisms for the lithium salts in mitigating ASR have been proposed, but most of them are not conclusive primarily due to the lack of knowledge about the formed reaction products. Combination of Al-rich SCMs and lithium salts may be used as an economic solution for ASR mitigation, although systematic studies are necessary prior to the applications.

Keywords: alkali silica reaction, supplementary cementitious materials, expansion, aluminium, lithium salts

OPEN ACCESS

Edited by:
Jie-Sheng Chen,
Shanghai Jiao Tong University, China

Reviewed by:
Linwen Yu,
Chongqing University, China
Neven Ukrainczyk,
Darmstadt University of Technology, Germany

***Correspondence:**
Barbara Lothenbach
barbara.lothenbach@empa.ch

Specialty section:
This article was submitted to Structural Materials, a section of the journal Frontiers in Materials

Received: *16 October 2021*
Accepted: *09 December 2021*
Published: *05 January 2022*

Citation:
Shi Z and Lothenbach B (2022) Role of Aluminum and Lithium in Mitigating Alkali-Silica Reaction—A Review. Front. Mater. 8:796396. doi: 10.3389/fmats.2021.796396

1 INTRODUCTION

Alkali-silica reaction (ASR) is an important durability issue world-wide, which causes significant expansion and deterioration of various concrete infrastructures including dams, pavements, bridges, walls, barriers, and nuclear/power plant structures (Rajabipour et al., 2015; Sims and Poole, 2017). The reaction starts by the dissolution of reactive silica at high pH in presence of alkalis from concrete pore solution followed by formation of alkali-silica gels. With further uptake of Ca, gelation and/or crystallization occur(s) leading to formation of amorphous and/or crystalline ASR products. The nature of the ASR products varies significantly depending on the composition of the pore solution, stage of ASR, and temperature (Shi et al., 2019; Shi et al., 2020a; Shi et al., 2020b). It remains unclear at which steps and by which mechanisms ASR expansion is generated (Shi et al., 2020b). Generally, the expansion due to ASR has been related to swelling of the product in the presence of water as more

Abbreviations: ASR, alkali-silica reaction; C-S-H, calcium-silicate-hydrate; C-A-S-H, calcium-alumina-silicate-hydrate; OPC, ordinary Portland cement; SCMs, supplementary cementitious materials; SEM/EDS, scanning electron microscopy with energy dispersive spectroscopy; TAL, threshold alkali level; DEF, delayed ettringite formation.

damage has been observed at high relative humidity (Olafsson, 1986; Kurihara and Katawaki, 1989; Stark, 1991). However, recent work based on synthetic ASR products (Shi et al., 2019) and field ASR products (Leemann et al., 2020) demonstrated that neither amorphous nor crystalline ASR products based on Na, K, Ca and silica swell upon uptake of water. The uptake of water by these ASR products was lower than that of C-S-H, suggesting that not swelling but rather alternative mechanisms are responsible for ASR expansion, indicating an urgent need for further investigations.

To stop ASR in existing structures is challenging and costly and can involve water proofing by coatings and/or slot cutting to release stresses due to concrete expansion of the affected structure. However, in both cases ASR can continue as there can be sufficient water for the ASR even in coated concrete structures and the concrete will continue expanding after slot cutting. In new structures, the use of non-reactive aggregates is a relatively cheap and efficient solution to avoid ASR. However, local aggregates are often used due to environmental and economic reasons, and in remote locations such as for dams may be the only choice.

Effective mitigation of ASR is critical for safe use of reactive aggregates for producing durable concrete. The use of supplementary cementitious materials (SCMs) and chemical admixtures such as lithium salts to prevent expansion caused by ASR was first reported 70 years ago shortly after the discovery of ASR in 1940s. For freshly produced concrete, use of appropriate cement blends such as Portland cement blended with SCMs to lower the pH and alkali concentration in the concrete pore solution is an efficient solution to minimize damage risk of ASR. Lower pH values decreases the dissolution kinetics of silica-containing minerals within the aggregate (Iler, 1979; Bagheri et al., 2021) and lower pH values together with lower alkali concentrations decrease also the risk of the formation of ASR products (Thomas, 2011; Shi and Lothenbach, 2020). Moreover, alumina-rich SCMs such as fly ash, blast furnace slags or metakaolin are found to be more effective than silica-rich SCMs such as silica fume (Aquino et al., 2001; Duchesne and Bérubé, 2001; Kandasamy and Shehata, 2014).

The role of Al in mitigating ASR has been at least partially related to a slowing down of the dissolution of reactive silica (Chappex and Scrivener, 2012b; Bagheri et al., 2022). The presence of Al may also alter the structure of crystalline ASR products to zeolite or its precursor at 80°C, while their formation kinetics at ambient temperatures seem to be too slow to have a relevant effect (Hünger, 2007; Shi et al., 2018; Shi et al., 2021). Thus despite of numerous investigations, the understanding of the mechanisms of Al mitigating ASR remains at least partially inexplicit (Hünger, 2007; Chappex and Scrivener, 2012a).

In contrast to SCMs, which can only be introduced during concrete production, lithium salt solutions can be applied to an expanding concrete structure in addition to being used as an admixture during production. So far, eleven different types of lithium salts have been studied to mitigate ASR including

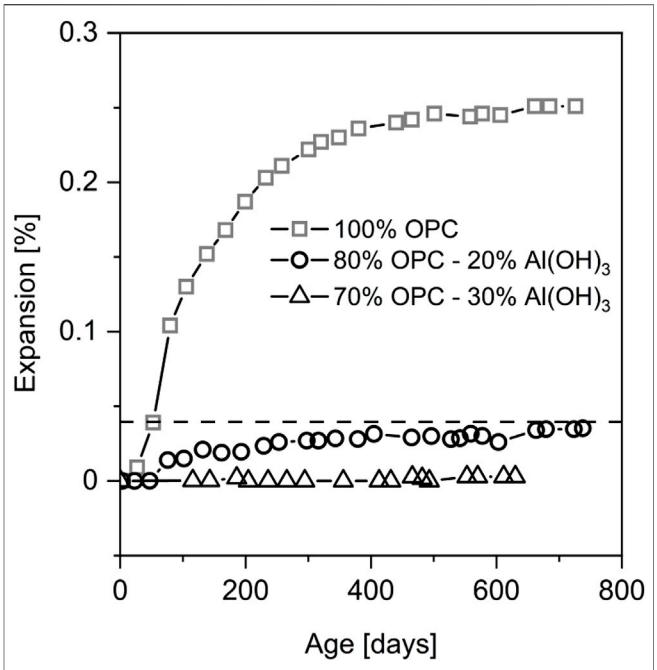

FIGURE 1 | ASR expansion of concrete prisms containing highly reactive Spratt coarse aggregates and binder materials of control cement (OPC) partially replaced with $Al(OH)_3$. Data from (Szeles et al., 2017).

LiCl, Li_2CO_3, LiF, Li_2SiO_3, $LiNO_3$, Li_2SO_4, LiOH, $LiNO_2$, LiBr, $LiOH{\cdot}H_2O$, LiH_2PO_4 (McCoy and Caldwell, 1951; Qinghan et al., 1995; Lumley, 1997; Demir and Arslan, 2013). Some difficulties of using these lithium salts are encountered because the dosage of different types of lithium salts varies significantly depending on several factors such as the type of lithium salts, the mineralogy of reactive aggregates, and the alkali content of the concrete. Moreover, the mechanisms of different types of lithium salts are also complicated, since they may result in formation of different types of Li-bearing ASR products and lithium silicates.

Understanding the precise mechanisms of both Al and Li for mitigating ASR is important for optimizing the use of these materials and for ensuring their long-term efficiency in mitigating ASR. This has been a challenge for many decades, primarily due to the difficulties to characterize the ASR products formed in small amounts and volume with conventional laboratory techniques. Moreover, Li-containing reaction products are difficult to be characterized in particular for their chemical compositions. Recent successful synthesis of ASR products at different temperatures resembling to those formed in concrete aggregates under accelerated and field conditions, provide a new opportunity to re-investigate the mechanisms of Al and Li in mitigating ASR (Shi et al., 2019; Shi et al., 2020a; Shi et al., 2021). This review article summaries and critically discusses the available investigations on the effect of Al and Li on ASR expansion, the influencing factors, possible mechanisms and limitations.

2 ROLE OF AL IN MITIGATING ASR

2.1 Efficiency of Al in Mitigating ASR Expansion

Both Al_2O_3 and SiO_2 from Al-rich SCMs can contribute to the reduction of ASR expansion as addressed in the introduction. In order to differentiate between the influence of SiO_2 and Al_2O_3 in SCMs on ASR expansion, few studies (Szeles et al., 2017; Zhou et al., 2019) have isolated the role of Al on ASR expansion by partially replacing Portland cement with pure $Al(OH)_3$ or γ-Al_2O_3. As demonstrated in **Figure 1**, replacing 20% OPC with $Al(OH)_3$ significantly reduced the ASR expansion below the threshold level 0.04% at 38°C as specified in ASTM C1293-08b (Szeles et al., 2017). The ASR expansion of the concrete prism was completely suppressed by increasing the replacement level up to 30% over 600 days of exposure. In another study (Zhou et al., 2019) the control concrete using different aggregate composed of 10% crushed fused silica (2.36–4.75 mm) and 90% standard sand (0.15–2.36 mm) showed a comparable ASR expansion to the expansion of the control concrete in **Figure 1**. However, incorporation of only 10% γ-Al_2O_3 could already reduce the ASR expansion to the threshold level following either ASTM C227 (at 38°C) or ASTM C1260 (at 80°C). The SEM images from both of the studies demonstrated that the aggregates remain intact for the concrete containing Al in contrast to the reference concrete with significant damage and ASR product formation (Szeles et al., 2017; Zhou et al., 2019). These studies confirmed the role of sole Al in mitigating ASR as previously suggested by other studies based on comparison of the ASR mitigation efficacy between Al-rich SCMs and silica fume (Aquino et al., 2001; Ramlochan et al., 2004). Therefore, it is of significance to elucidate the mechanisms of Al in mitigating ASR in order to predict its long-term efficiency.

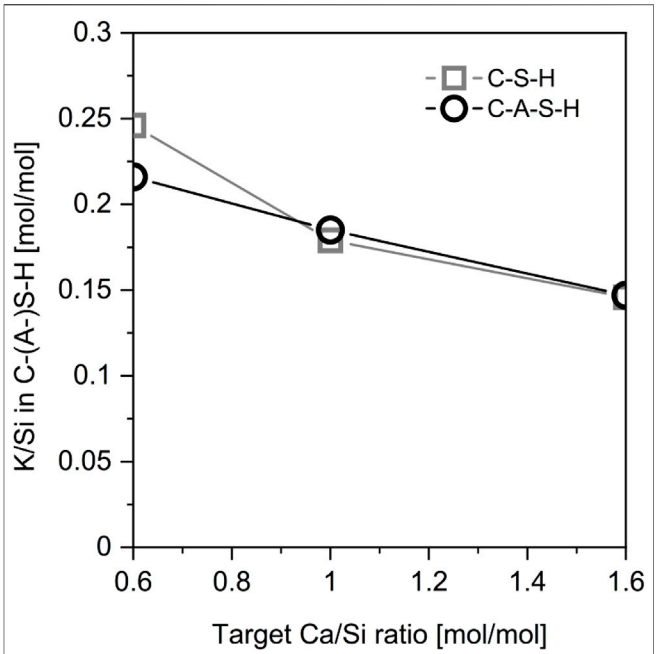

FIGURE 2 | Alkali uptake in C-S-H and C-A-S-H (Al/Si = 0.05, Ca/Si = 0.8) in equilibrium with a solution containing 0.5 mol/L [KOH] equilibrated for 182 days. Reproduced from (L'Hôpital et al., 2016).

2.2 Mechanisms of Al in Mitigating ASR

Several mechanisms of Al in mitigating ASR were proposed in the literature, which include increased alkali fixation, alteration of the ASR products, and reduction of the silica dissolution rates, as discussed in the following.

2.2.1 Increased Alkali Fixation With Subsequent pH Reduction

It was conjectured that the presence of Al in the SCMs possibly enhance the removal of alkalis from the concrete pore solution resulting a reduction of its pH, which would be beneficial for ASR mitigation. Hong and Glasser (Hong and Glasser, 2002) reported that incorporation of Al into C-S-H leads to formation of C-A-S-H phase, which markedly increases its alkali binding capacity. They suggested that this partially contributes to the potential of Al-rich SCMs in reducing pore solution alkalinity and subsequently ASR expansion. Later, Sun et al. (2006) showed significant increases in basal spacings when Al was incorporated into C-S-H phase. They explained that alumina was incorporated into C-S-H and present in the interlayer and that the substitution of Si by Al provides a negative site that must be charge balanced by a net positive charge (e.g., Na^+, K^+) leading to alkali binding. Thomas (Thomas, 2011) also stated that there is evidence that the alumina content of the SCM also affects its alkali-binding capacity as its silica content.

On contrary, an earlier study from Diamond (Diamond, 1981) showed that class F fly ash reduced hydroxyl and alkali ion concentration of the pore solution by a factor equivalent to its OPC replacement level of 30%, indicating a simple dilution effect. This observation is supported by the studies of Chappex and Scrivener (Chappex and Scrivener, 2012a). In their study, they compared an OPC-metakaolin paste with a paste containing silica fume and an inert filler to maintain an equivalent silica fraction and could thus isolate the effect of alumina. They found that the pore solution alkalinity was reduced with increasing the replacement level of OPC. However, such reduction of pore solution alkalinity was a mere dilution effect, and the alumina did not actively consume hydroxyl ions or alkalis.

Most of the aforementioned studies focused on cement mixtures containing Al-rich SCMs, where the joint effects of alumina and silica in SCMs could not be directly separated. To isolate the role of Al in mitigating ASR, Szeles et al. (2017) replaced OPC with 20% $Al(OH)_3$ and measured the pore solution pH of the cement paste mixtures. They observed that the pH of the $Al(OH)_3$ mixture was initially similar to the 80% of the control mixture, indicating a pure dilution effect. At later ages up to 1 year, slight reduction of pH (0.13 pH unit) was observed beyond the dilution effect, the pH reduction was not significant enough to be the sole mechanism for Al to mitigate ASR. A drop of pH from 12.4 to 11.9 was also recently captured by Shi et al. (2021) during the synthesis of ASR products at 40°C containing

SiO_2, CaO, and KOH, where $Al(OH)_3$ precipitated as a separate phase. However, the pH increased at 80°C from 12.1 to 12.8, where the formation of an alumino-silicate phase prevented the formation of ASR products. The influence of Al on formation and structure of ASR products will be discussed in detail in the next section.

The above seeming contradictions has been clarified based on synthetic C-S-H (L'Hôpital et al., 2016), where the uptake of K in C-S-H and C-A-S-H at different Ca/Si ratios were compared as shown in **Figure 2**. The results show that the K/Si ratio in C-S-H is not significantly increased in the presence of aluminum. The scattered results reported in the aforementioned studies was attributed to the experimental error associated with the measurement of alkali concentrations, the synthesis protocol, and equilibration time (L'Hôpital et al., 2016). Therefore, the mechanism of significantly increased alkali fixation with subsequent pH reduction can be excluded.

2.2.2 Alteration of ASR Products or Formation of Alumino-Silicates

For a long period of time, it was debated whether dissolved aluminum ions affect the formation and structure of ASR products or not. Many studies reported the incorporation of Al in ASR products based on scanning electron microscope with energy-dispersive X-ray spectroscopy (SEM/EDS) analysis (Fernandes et al., 2007; Fernandes, 2009; Šachlová et al., 2010; Hagelia and Fernandes, 2012; Leemann and Lura, 2013; Shafaatian et al., 2013; Guo et al., 2018), while many others reported no Al or hardly detectable amounts in ASR products (Aquino et al., 2001; Leemann and Lothenbach, 2008; Katayama, 2012a; Katayama, 2012b; Leemann, 2017). It should be noted that the observation of Al in ASR products could be caused either by the close intermixing with Al-containing phases (hydrated cements or Al-containing minerals within the aggregates) or by cross-contaminations during sample preparation for SEM/EDS analysis. The absence of a significant amount of Al in ASR products was recently confirmed (Shi et al., 2021) based on laboratory synthetized ASR samples, where Al precipitated as a separate phase [gibbsite, $Al(OH)_3$] at 40°C, i.e., under temperatures relevant for field conditions, while the structure and composition of ASR products was not affected by aluminum.

At high temperature (80°C) and high alkali concentration (0.5–1 mol/L NaOH or KOH), however, the formation of zeolites or zeolitic precursors (alkali alumino-silicate phase) was observed in concrete (Hünger, 2007; Shi et al., 2018) as well as in synthetic samples (Shi et al., 2021). Hünger (Hünger, 2007) found an inverse relation between the silica releasing rate of aggregate and the amount of zeolite formed at the same temperature and suggested that the formation of alkali alumino-silicate and zeolite would reduce the concentration of so-called "free" silica available for ASR and thus inhibit ASR. Also laboratory experiments showed the suppression of the formation of ASR products in the presence of sufficient Al. While the formation of alkali alumino-silicate or zeolite could in fact lower the potential to form ASR products at high temperatures (80°C or above), at ambient temperatures the formation of alkali alumino-silicate and zeolite is usually slow (decades) (Sand et al., 1987; Lothenbach et al., 2017). Thus, the formation of alkali alumino-silicate and zeolite is under most conditions too slow to be relevant in suppressing ASR formation in field concretes.

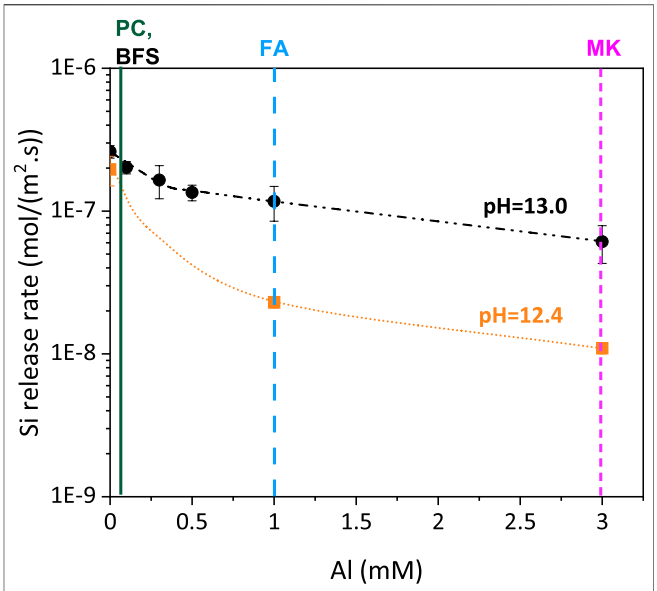

FIGURE 3 | Effect Al concentration on the Si release rate [mol/(m²·s)] of amorphous silica in 100 and 400 mM KOH at 40°C, adapted from (Bagheri et al., 2022). The vertical lines indicate Al concentrations typically observed in the pore solution of Portland cements (≈0.1 mM), in blends with blast furnace slags (≈0.1 mM), with fly ash (≈1 mM) and with metakaolin (≈3 mM) (Deschner et al., 2012; Vollpracht et al., 2016; Avet and Scrivener, 2018).

2.2.3 Slow Down the Dissolution Rate of the Reactive Silica

A possibility to prevent ASR is to suppress or strongly slow down the dissolution of SiO_2 within the aggregate. Aluminum can drastically reduce silica dissolution rates as aluminum sorbs on the silica surface, which passivates the active silica sites and slows down dissolution (Iler, 1973; Bickmore et al., 2006; Nicoleau et al., 2014). Relatively low concentrations of Al (1–5 mM) can reduce the dissolution rate of silica by as much as 90%. However, the sorption of $Al(OH)_4^-$ on the surface of silica and the slowing down of silica dissolution silica is more distinct at intermediate pH values (<12), while at pH 13 and above the sorption of $Al(OH)_4^-$ on silica becomes weak resulting in only feeble suppression of the dissolution rate (Yokoyama et al., 1988; Chappex and Scrivener, 2012b; Nicoleau et al., 2014) as illustrated in **Figure 3** (Bagheri et al., 2022). A comparison with the Al concentration in the pore solution of Portland cement and blended cements, show that blending of Portland cement with fly ash or metakaolin could in fact increase the Al concentration to 1 mM and above, i.e., to Al concentrations efficient in slowing down silica dissolution (see **Figure 3**). Recent study from Zhou et al. (2022) showed that the Al concentration could potentially reach about 80 mM after dissolution of 2 g metakaolin (ca. 1.0 g Al_2O_3) for 100 days in 75 ml simulated pore solution [0.6M NaOH, $Ca(OH)_2$ saturated], although in a concrete pore solution the concentrations might be significantly lower due to the formation of AFt and AFm phases.

In fact, drastic reduction in damage to reactive siliceous aggregates is observed in metakaolin, slag or fly ash blended cements (Chappex and Scrivener, 2012a; Tapas et al., 2021), although this reduction might also relate to the decrease of pH in the pore solution due to the reaction of metakaolin, slag or fly ash.

As Al slows down, but does not prevent silica dissolution, one could expect a slower buildup of ASR with time. However, as demonstrated in **Figure 1**, the presence of $Al(OH)_3$ or Al-rich SCMs seems to prevent ASR completely up to 700 days (Ramlochan et al., 2004; Szeles et al., 2017), indicating that other effects in addition to a slow down of dissolution could play an important role.

3 ROLE OF LI IN MITIGATING ASR

3.1 Factors Influencing the Li Salts on ASR Expansion

3.1.1 Types of Li Salts

Lithium salts to inhibit ASR were first used 70 years ago by McCoy and Caldwell (McCoy and Caldwell, 1951). McCoy and Caldwell investigated the potential of over 100 different compounds to prevent ASR of mortars containing Pyrex glass as reactive aggregate. All the studied lithium salts containing LiCl, Li_2CO_3, LiF, Li_2SiO_3, $LiNO_3$, and Li_2SO_4 were found to be more effective than the other inorganic salts and the other compounds such as acids, oils, organic chemicals, proteins, and proprietary admixtures. Since even the almost insoluble LiF seemed to be beneficial, they also suggested that the nature of the accompanying anion of the lithium salts was not particularly important. Later, Stark (Stark, 1992) confirmed the effectiveness of LiF and Li_2CO_3 in inhibiting ASR expansion, and reported that also LiOH seemed to be effective. Several other studies further reported that also LiBr (Qinghan et al., 1995; Bian et al., 1996; Demir and Arslan, 2013; Demir et al., 2018) and LiH_2PO_4 (Bian et al., 1996) are effective in reducing ASR expansion. Bian et al. (Bian et al., 1996) reported LiCl, LiBr, $LiNO_2$, $LiNO_3$, Li_2SO_4, and LiH_2PO_4 actually produced similar suppressive effects on ASR expansion, whereas Li_2CO_3, LiOH, and LiF only exhibited certain effects at a [Li]/[Na + K] molar ratio of 0.8.

Among all types of lithium salts, $LiNO_3$ emerged as the preferred lithium compound for inhibiting ASR (Diamond, 1999), due to its neutrality, high solubility and good compatibility with other admixtures (Wang et al., 1996). It was also reported that $LiNO_3$ has a benign effect on the concrete properties of strength, electrical resistance, drying shrinkage, and resistance to freezing and thawing, whereas LiOH retard the strength development (Lane and Board, 2002). In Japan the use of lithium nitrite ($LiNO_2$) as an ASR inhibitor has been widely studied (Sakaguchi et al., 1989; Saito et al., 1992; Kobayashi and Takagi, 2020) due to its positive effect on preventing rebar corrosion as well as due to its high solubility.

3.1.2 Li/(K + Na) Ratio and its Influencing Factors

Although lithium salts are used to inhibit ASR expansion, Stark et al. (Stark et al., 1993) also reported that insufficient dosages of lithium compounds may even increase the ASR expansion in some aggregates, known as "pessimum effect". The dosage of lithium salts to be added for inhibiting ASR is commonly expressed as the molar ratio Li/(Na + K). Only at relative high Li/(Na + K) ratio can completely suppress the ASR expansion. A molar ratio of Li/(Na + K) of 0.74 seems to be required to suppress ASR expansion as found in many studies (McCoy and Caldwell, 1951; Bérubé et al., 2004; Leemann et al., 2014), while others also reported that the optimum Li/Na molar ratio is in the range of 0.9–1.2 if LiOH is added (Sakaguchi et al., 1989). In fact, the exact value of the Li/(K + Na) ratio is not fixed but varies depending on the following factors:

a) Type of lithium salts: Thomas et al. (2000) observed that in the case of for $LiNO_3$ a [Li]/[Na + K] molar ratio of 0.74 sufficiently suppressed ASR-induced expansion with most aggregates, whereas higher ratio of [Li]/[Na + K] of 0.85 was required in the case of $LiOH{\cdot}H_2O$ in concrete prisms containing a crushed siltstone aggregate. Collins et al. (2004b) reported that the required minimum threshold $[Li_2O]/[Na_2O_e]$ ratio varies from 0.5 to 1.0 for each additive examined (LiOH, LiCl, or $LiNO_3$), with respect to the particular reactive aggregate used in their work.
b) Equivalent dosage relates to alkali content: Several studies reported that the minimum Li/(K + Na) ratio required to substantially suppress ASR expansion depends also on the amount of alkali present in the cement. Mo et al. (2003) reported that if the cement contained less than 2.5% Na_2O equivalent, a [Li/Na] molar ratio above 0.3 was sufficient to

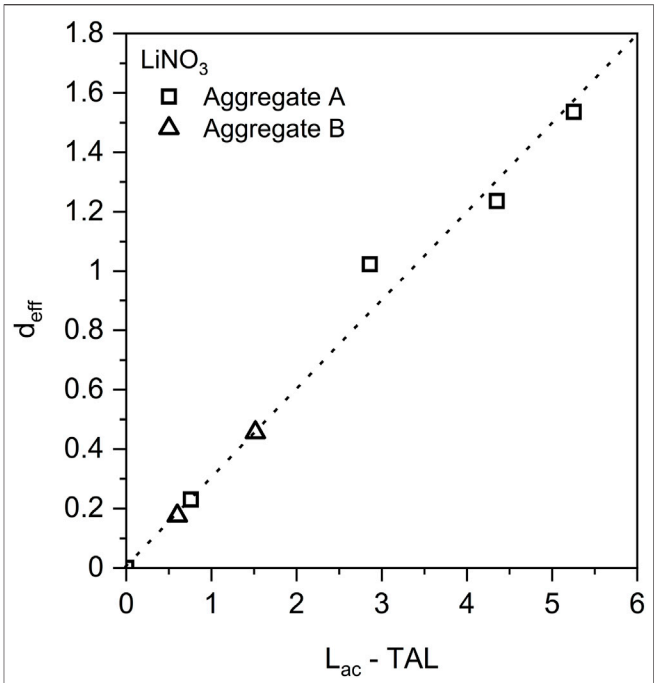

FIGURE 4 | Relationship between the effective dosage of lithium nitrate (d_{eff}), the alkali content of concrete (L_{ac}), and the threshold alkali level (TAL) of the aggregates. Data reproduced from (Berra et al., 2003).

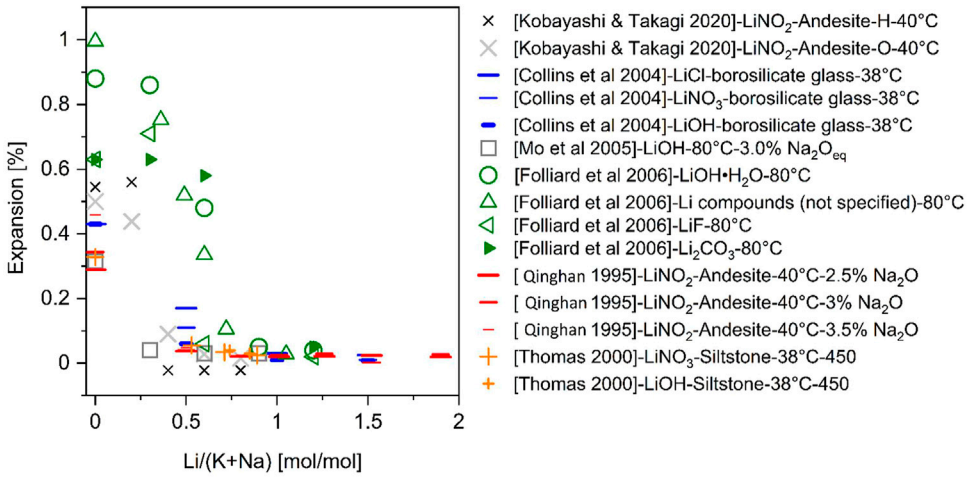

FIGURE 5 | Expansion measured over an extended time frame as it relates to the Li/Na ratio of the product for various lithium treatments (Qinghan et al., 1995; Thomas et al., 2000; Collins et al., 2004b; Mo et al., 2005; Folliard et al., 2006; Kobayashi amd Takagi, 2020).

inhibit ASR in long-term by adding LiOH. However, when the cement contained more than 3% Na_2O equivalent, a Li/Na ratio of at least 0.6 was needed (Mo et al., 2003). Qinghan et al. (1995) studied the suppressive effect of $LiNO_2$ on mortars containing an andesite sand from Japan following an autoclave test procedure, they reported that the required Li/Na ratios were 0.1, 0.3 and 0.5 and 0.8 corresponding to Na_2O equivalent levels of 0.5, 1.0, 1.5%, and 2%. Berra et al. (2003) found a linear relationship between the effective lithium dosage in terms of Li/[Na + K] and the difference between total alkali content and threshold alkali level of the aggregates (alkali reactivity level) as shown in **Figure 4**.

c) Types of reactive aggregates: Several early studies showed that the dosage of lithium depends also on the aggregates (Lane, 2000; Lane and Board, 2002; Collins et al., 2004b). Lane and coworkers (Lane, 2000; Lane and Board, 2002) studied the efficiency of both LiOH and a commercial $LiNO_3$ solution in mitigating ASR for the concrete prisms containing Pyrex glass and some Virginia reactive aggregates composed of microcrystalline and strained quartz. They observed that [Li]/[Na + K] = 0.925 was required for the two aggregates, and also concluded that both lithium compounds were more effective for the highly reactive aggregates than for the less reactive aggregates. Similar observation is also reported in Drimalas et al. (2012) based on a study on the long-term exposed concrete blocks, using different aggregate types and various dosages of lithium-based salts. The concrete blocks exposed for up to 16 years showed a varying response to lithium based on aggregate types. Tremblay and co-workers (Tremblay et al., 2004a; Tremblay et al., 2007) systematically investigated 12 different aggregates and showed that 50% of the reactive aggregates responded well to the commonly used dosage (0.74 molar ratio). For three other aggregates tested, a higher dosage of $LiNO_3$ ranging from 0.75 to 1.04 was required. For the remaining three aggregates, a 1.11 molar ratio was not sufficient to limit ASR below threshold 0.04% of the concrete prism test. Moreover, they also showed that the response of lithium could not be correlated to the aggregate reactivity level and mineralogy.

Regardless of the above-mentioned factors, it is generally accepted that a dosage of Li/(Na + K) of >0.6 is required to inhibit ASR (Collins et al., 2004b; Leemann et al., 2014; Islam and Ghafoori, 2016) as illustrated in **Figure 5** reproduced based on the data from literature (Qinghan et al., 1995; Thomas et al., 2000; Collins et al., 2004b; Mo et al., 2005; Folliard et al., 2006; Kobayashi and Takagi, 2020) and in **Table 1**.

3.1.3 Introducing Lithium Salts to ASR Affected Concrete

The proposed Li/(K + Na) molar ratios from most of the studies discussed above are based on freshly prepared mortars and concretes where lithium salts have been used as admixtures. In practice, lithium salts are often used afterwards to slow down expansion in ASR affected concrete. The determination of the optimum amount of lithium for concrete is thus not straightforward. The even distribution of lithium ions within the entire concrete plays a key role in effectively suppressing ASR expansion. Several methods have been suggested to apply lithium salts to ASR-affected concrete, e.g., sprinkling lithium solution on concrete surface (Zapała-Sławeta and Owsiak, 2018), using electrochemical method by applying voltage at 40 V (Souza et al., 2017), injecting lithium solution into concrete under vacuum (Thomas et al., 2007) or by pressure through drilled holes of a 10–30 mm diameter using a compressor (Kobayashi and Takagi, 2020), or by soaking ASR affected concrete elements in lithium solutions. Most of these methods do not achieve sufficient ingress of the lithium salts into concrete (Thomas et al., 2007). The electrochemical process showed higher Li penetration, but reduced the pH of the pore solution near rebar (cathode) due to electrochemical reduction of water. Surface overlay is commonly used on road and airfield

TABLE 1 | Summary of selected research findings related to the lithium dosage ([Li]/[Na + K] molar ratio) needed to suppress ASR expansion and their test conditions. The table is adapted based on the version published in (Folliard et al., 2006).

References	Test methods	Reactive aggregates	Lithium salts	Parameter studies, i.e., [Li]/[Na + K]
McCoy and Caldwell (1951)	ASTM C 227	Pyrex glass	LiCl Li_2CO_3 LiF Li_2SiO_3 $LiNO_3$ Li_2SO_4	0.74
Lawrence and Vivian (1961)	Mortar prism at 43°C		LiOH	Data not provided to calculate the ratio
Sakaguchi et al. (1989)	Mortar bar at 40°C (standard not specified)	Pyrex glass pyroxene andesite	$LiOH{\cdot}H_2O$ $LiNO_2$ Li_2CO_3	• 0.9 for $LiOH{\cdot}H_2O$ at 1.2 wt.% Na_2O • 0.69 for $LiNO_2$ at 0.8 wt.% Na_2O (expansion not completely suppressed) • 0.56 for $LiNO_2$ at 1.0 wt.% Na_2O (expansion not completely suppressed) • 0.77 for Li_2CO_3 at 0.8 wt.% Na_2O • 0.63 for Li_2CO_3 at 1.0 wt.% Na_2O
Stark (1992)	ASTM C 227 ASTM P 214	Aggregates of andesitic to rhyolitic composition; Granite gneiss	$LiOH{\cdot}H_2O$ LiF Li_2CO_3	• 0.755–1.00 for LiOH • 0.6 for LiF • 0.92 for Li_2CO_3
Diamond and Ong (1992)	ASTM C 227	Cristobalite Beltane opal	LiOH	1.2 (for cristobalite, more for opal)
Qinghan et al. (1995)	Autoclave	Andesite	$LiNO_2$	• 0.8 at higher Na_2O level • 0.1 at 0.5 wt.% Na_2O • 0.3 at 1.0 wt.% Na_2O • 0.5 at 1.5 wt.% Na_2O
Lumley (1997)	ASTM C 1293	Calcined flint cristobalite	$LiOH{\cdot}H_2O$ LiF Li_2CO_3	0.62
Durand (2000)	ASTM C 1293	Canadian aggregates (Sudbury—sandstone quartzwacke; Potsdam—siliceous sandstone, and Sherbrooke—chloritic schist)	$LiOH{\cdot}H_2O$ LiF Li_2CO_3 $LiNO_3$	• 0.72 (for $LiNO_3$ with Sudbury) • 0.82 (for $LiOH{\cdot}H_2O$, LiF, and $LiCO_3$ with Sudbury)
Collins et al. (2004b)	ASTM C 227	Crushed, graded borosilicate glass	LiOH $LiNO_3$ LiCl	• 0.60 (LiOH) • 0.83 ($LiNO_3$) • 0.93 (LiCl) Data taken at threshold expansion: 0.05%
Tremblay et al. (2004a); Tremblay et al. (2004b)	ASTM C 1293	Canadian aggregates (greywacke-argillite, dolostone, polygenic gravels, rhyolite, siliceous limestones, granite-gneiss)	$LiNO_3$	Agg. type (1-year CPT exp. %): Molar ratio • Granite/gneiss (0.029%): 0.56 • Chloritic schist (0.082%): >0.94 • Greywacke/arg. (0.087%): 0.71 • Dolostone (0.100%): 0.61 • Gravel (0.101%): 0.58 • Gravel (0.103%): 0.91 • Gravel (0.113%): 0.97 • Gravel (0.122%): 0.66 • Greywacke (0.142%): >1.11 • Gravel (rhyolite) (0.151%): 0.63 • Siliceous limestone (0.162%): 1.04 • Siliceous limestone (0.199%): >1.11
Mo et al. (2005)	80°C at 95% relative humidity	Zeolitic perlite aggregate, Liuhe aggregate (minerology not mentioned)	LiOH	Zeolitic perlite aggregate • 0.3 at 2.5 wt.% Na_2O_{eq} • 0.3 at 3.0 wt.% Na_2O_{eq}

(Continued on following page)

TABLE 1 | (*Continued*) Summary of selected research findings related to the lithium dosage ([Li]/[Na + K] molar ratio) needed to suppress ASR expansion and their test conditions. The table is adapted based on the version published in (Folliard et al., 2006).

References	Test methods	Reactive aggregates	Lithium salts	Parameter studies, i.e., [Li]/[Na + K]
Kobayashi and Takagi (2020)	35–40°C	Andesite	$LiNO_2$	Liuhe aggregate • 0.6 (expansion 0.05%) at 2.5 wt.% Na_2O_{eq} • 0.3 (expansion 0.04%) at 3.0 wt.% Na_2O_{eq} • 0.4 (Andesite from Hokkaido) • 0.6 (Andesite from Oita)

pavements and on highway dividers. In this case, better penetration of Li can be achieved by several applications of smaller amounts, e.g., 0.06 L/m^2 to 0.40 L/m^2 of 30% $LiNO_3$ solution with multiple applications (Folliard et al., 2003; Thomas et al., 2007). Injection of lithium salts has been applied to almost 100 ASR-affected concrete structures in Japan (Kobayashi and Takagi, 2020). Since it can only prevent further deterioration and not recover the lost performance, Kobayashi and Takagi suggested that it is desirable to perform lithium injection in an as early as possible stage of deterioration (Kobayashi and Takagi, 2020). However, they found that lithium injection into concrete at early deterioration stage, which indeed suppressed the ASR expansion to some extent, resulted in a larger final expansion than that of the concrete treated with lithium after developing ASR cracks. Moreover, injection of lithium also took longer time for concrete at early stage of deterioration, thus the authors suggested that it would be reasonable and economical to apply this treatment only to concrete already suffering ASR with expected further deterioration. Of course, one should avoid over development of ASR cracks, as it will affect the serviceability of concrete structure. An optimization of injection time is therefore very important. For this purpose, precise evaluation of the stage of ASR is critical for lithium treatment.

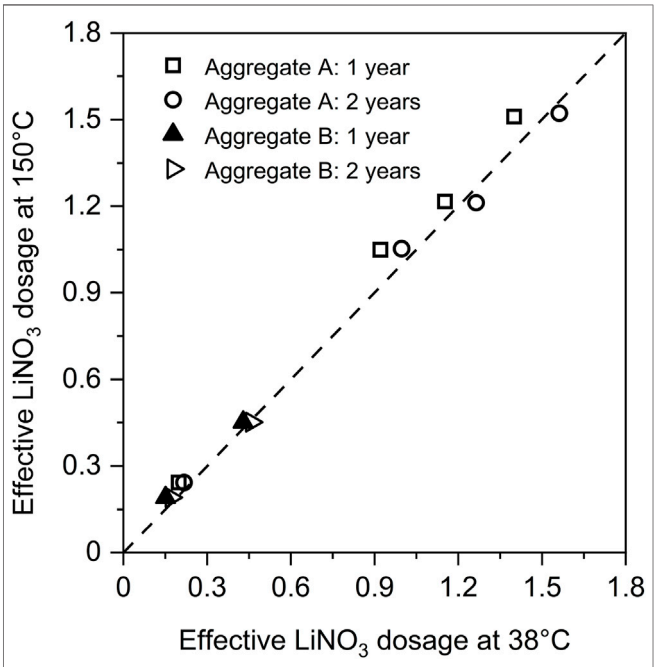

FIGURE 6 | Comparison between the effective dosages of lithium nitrate for mitigating ASR obtained from the ultra-accelerated concrete prism test (150°C) and the concrete prism test at 38°C and 100% RH. Data from (Berra et al., 2003).

3.1.4 Temperature

ASR is a very slow process at ambient temperature, thus many studies applying lithium salts to mitigating ASR expansion are based on accelerated or ultra accelerated (autoclave) testing methods (Ohama et al., 1989; Qinghan et al., 1995; Bian et al., 1996; Mo et al., 2003). Feng et al. (2005) concluded that the results from autoclave methods involving lithium are not directly comparable to those from studies at lower temperatures and pressures. In contrast, Berra et al. (2003) found that $LiNO_3$ was effective at both low (38°C) and high (150°C) temperatures and reported a linear relationship of the effective $LiNO_3$ dosage (Li/[K + Na] molar ratio) between the two temperatures as shown in **Figure 6**. However, they also found that Li_2CO_3 was only effective at 38°C.

3.2 Mitigation Mechanisms

3.2.1 Influence on Dissolution of Silica

Most published studies on ASR with respect to the effect of lithium on silica dissolution is based on the findings of Lawrence and Vivian (Lawrence and Vivian, 1961), who found that the dissolution of reactive silica strongly depended on the type of alkali hydroxides (i.e., NaOH, KOH, or LiOH) following the order LiOH < NaOH < KOH. Twenty years later, Wijnen et al. (1989) reported similar results and suggested that the dissolution rate of reactive silica decreased with an increase in the effective cation radius of the alkaline species following the order $K^+ < Na^+ < Li^+$. While many later studies supported the observation of reduced silica dissolution in the presence of various lithium compounds (Plettinck et al., 1994; Kurtis and Monteiro, 2003; Collins et al., 2004b; Feng et al., 2005; Tremblay et al., 2010; Rajabipour et al., 2015), others also observed no significant influence of Li on silica dissolution (Dove and Nix, 1997; Dove, 1999; Leemann et al., 2014; Oey et al., 2020; Leemann, 2021; Bagheri et al., 2021). In some cases, even an increase in silica dissolution in presence of lithium was observed (Kurtis and Monteiro, 2003; Collins et al., 2004b; Bagheri et al., 2021). Kurtis and Monteiro (Kurtis and Monteiro, 2003) and Collins et al. (2004b) studied the dissolution of silica gel in simulated pore

solutions with and without lithium salts and observed that in the slurries prepared with LiCl and $LiNO_3$, the dissolved Si concentration decreased with increasing lithium dosages, while for LiOH they observed an increase in silica dissolution with increasing lithium dosage. A recent study (Bagheri et al., 2021) indicated that lithium in the absence of calcium could in fact accelerate SiO_2 dissolution rate at high pH values by 20–50%.

The above contradictory observations reported in literature are found to be related to the influence of pH and Ca^{2+} on the effect of Li^+ the dissolution rates (Bagheri et al., 2021). Many studies, which investigated the effect of Li on the dissolution of SiO_2, were carried out under acidic to neutral conditions (Plettinck et al., 1994; Dove and Nix, 1997; Dove, 1999), where no or only a slightly retarding effect of Li^+ in comparison to Na^+ or K^+ was observed and related to the lower tendency of Li^+ to sorb on the SiO_2 surface and faster ligand exchange rate (Dove, 1999). Bagheri et al. (2021) investigated the effect of Li^+ under high pH conditions (in 400 mM KOH) and found a clear acceleration of SiO_2 dissolution in the presence of Li^+, which might be related to the ability of Li^+ to form surface complexes on silica. It should be noted that lithium can precipitate in the presence of silica as Li_2SiO_3 (Zhou et al., 2018; Bagheri et al., 2021), which can lower the measured silicon concentration or mass loss in dissolution experiments (Kurtis and Monteiro, 2003; Tremblay et al., 2010; Leemann et al., 2014; Zhou et al., 2018; Oey et al., 2020; Leemann, 2021), leading to an apparent decrease in the observed dissolution rate. In the presence of calcium, the effect of Li on the dissolutions changes drastically. A significant decrease in SiO_2 dissolution rate in 100 and 1,000 mM NaOH in the presence of both Li and Ca and the formation of a dense C-S-H containing Li were observed (Leemann et al., 2014; Zhou et al., 2018), indicating a destabilization of Li_2SiO_3 in the presence of calcium. It has been speculated that this Li containing C-S-H layer is responsible for the slowdown of the silica dissolution in the presence of both Li and Ca. More detailed discussions on influence of the lithium on the change of ASR products and formation of Li-Si complex are presented in the next sections.

The detailed study of the literature has indicated that Li might somewhat accelerate SiO_2 dissolution, but only in the absence of calcium, while in the presence of Ca and Li a clear decrease of the silica dissolution has been observed (Leemann et al., 2014; Zhou et al., 2018), which might contribute together with other factors to the lower the expansion observed for Li containing concretes.

3.2.2 Non Expansive Reaction Products

Along with the studies on dissolution of silica in presence of lithium, also changes in the ASR product has been reported in many of the studies mentioned above. Several studies reported that presence of lithium lowers the CaO/SiO_2 as well as the (Na + K)/Si ratio in the ASR products (Kawamura and Fuwa, 2003; Feng et al., 2010; Leemann et al., 2014). Feng and co-workers (Feng et al., 2010) observed a dense rigid alkali–silica gel composed of Li with low-Ca contents. The low content of Ca in reaction products was also confirmed in the extensive study by Leemann et al. (2014). They suggested that Ca can be replaced by lithium due to comparable radius of the hydrated cation. It also has been suggested that Li^+, due to its smaller ionic radius and higher charge density, is more readily incorporated in ASR products than K^+ and Na^+ (Kawamura and Fuwa, 2003; Mo, 2005).

In addition to lower the Ca content of ASR products, the precipitation of amorphous Li-Si products has been observed (Sakaguchi et al., 1989; Schneider et al., 2008; Guo et al., 2019). Due to the lack of characterizations of the chemical composition and molecular structure, the amorphous Li-Si products are often described as "Li-Si complex" following the work of Lawrence and Vivian (1961). In some cases, also the precipitation of crystalline Li-containing products has been observed (Mo et al., 2003; Collins et al., 2004a; Feng et al., 2010), generally Li_2SiO_3, which seems to form in the absence of Ca and at low Ca but high Li contents (Zhou et al., 2018; Bagheri et al., 2021). However, so far no systematic investigations about the formation conditions of the amorphous and crystalline Li-containing products have been conducted. Leemann et al. (2014) found no evidence of crystalline Li_2SiO_3 formation and argued that crystalline lithium silicate is unlikely to form under dosages of Li/Na + K < 1.0.

Most studies reported that those Li-containing products are not expansive (Sakaguchi et al., 1989; Diamond, 1992; Kawamura et al., 1994; Leemann et al., 2014), although a minimum proportion of lithium must be reached to be non-expansive (Stark, 1992), which could explain the "pessimum" effect of lithium dosages on controlling ASR expansion. However, a recent study showed that formation of crystalline Li_2SiO_3 could actually cause expansion and cracks in concrete after long periods of exposure (Liu et al., 2019).

Several researchers (Mitchell et al., 2004; Schneider et al., 2008; Leemann et al., 2014) have used nuclear magnetic resonance (NMR) spectroscopy to study the effects of lithium on the chemical structure of ASR gels. The incorporation of Li^+ ions into the ASR gel changes its structure from a product with a layered structure (containing mainly Q^3 sites) to a product with more disordered networks containing mainly Q^1 and Q^2 sites. This was put forward as a possible reason, why Li based ASR products show little expansion. It was claimed that expansive gels are typically characterized by large presence of Q^3 sites as layered silicates, while the depolymerized products containing mainly Q^1 and Q^2 sites are not considered to swell upon contact with water (Kirkpatrick et al., 2005; Tambelli et al., 2006). Also Kurtis and coworkers (Kurtis et al., 2000; Kurtis and Monteiro, 2003) suggested that the suppressive effect of lithium on ASR expansion should be attributed to the limitation of ASR gel re-polymerization, rather than reduced dissolution of silica. By dispersing the ASR gel extracted from ASR-affected structure to NaOH solution alone, they observed that ASR is partially dissolved and re-polymerized as a potentially expansive gel. However, when the ASR gel was exposed to the mixture NaOH and LiCl solution, re-polymerization into an expansive gel was limited.

The understanding of ASR mitigation mechanisms by Li is simply based on the assumption that conventional ASR products, which have a layered silicate structure, will swell upon uptake of water while Li-containing ASR products with mainly Q^1 and Q^2

sites will not swell. However, as recent work based on synthetic ASR products (Shi et al., 2019) and field ASR products (Leemann et al., 2020) demonstrated that both amorphous and crystalline ASR products do not swell upon uptake of water, rather alternative mechanisms seem responsible for ASR expansion as well as their suppression by Li, indicating an urgent need for clarifying the real cause of ASR expansion.

3.2.3 Formation of a Physical Barrier

Another mechanism of ASR mitigation suggested for lithium is that these products serve as physical barrier preventing the further dissolution and reaction of reactive silica. This mechanism was first suggested by Lawrence and Vivian (1961), who reported that the lithium silicates formed had low solubility producing a coating effectively protecting the reactive aggregates from further participation in ASR. This observation has been supported by many later studies (Kawamura and Fuwa, 2003; Mitchell et al., 2004; Feng et al., 2010; Leemann et al., 2014; Leemann et al., 2015; Kim and Olek, 2016; Guo et al., 2019). Leemann et al. (2015) observed that the mitigating efficiency of $LiNO_3$ lessens with increasing the specific surface area of the reactive aggregates, due to the increased area to be covered by the lithium products. Based on this finding, Kawamura (2017) assumed that the mitigating effects of lithium on ASR affected structures may be related to the amount of ASR products already formed. Few studies reported that only the Li products containing Ca could serve a physical barrier. Zhou et al. (2018) observed that quartz glass slices immersed in solution containing both $LiNO_3$ and $Ca(OH)_2$ were well protected by the precipitation of a dense layer, while samples were seriously damaged in the solution with only $LiNO_3$ or $Ca(OH)_2$. In contrast, Tremblay et al. (2010) considered the formation of physical barriers unlikely based on detail analysis of the surface and suggested an increased chemical stability of silica due to a presently unknown mechanism as the probable cause.

3.2.4 Other Mechanisms

Several additional mechanisms for the ASR mitigation of lithium have been proposed. Prezzi et al. (1997) introduced an electrical double layer (EDL) theory to explain the suppressive effect of lithium on ASR expansion. ASR gels are negatively charged (Krattiger et al., 2021), and are thus surrounded by a positively charged electrical double layer where cations accumulate. Theoretically, cations with the same valence but smaller hydrated ionic radii will result in a thinner double layer, which would cause based on the swelling theory less gel expansion. As the hydrated radius increases in the order $K^+ < Na^+ < Li+$ (Conway, 1981), this would mean that Li would result in higher expansion, which is contradictory to the results generally observed in expansion testing, and thus also to the explanation suggested by (Prezzi et al., 1997). It was also proposed that presence of lithium may reduce the repulsive forces between colloidal ASR gel particles (Mohd et al., 2017). Bian et al. (1996) proposed that the suppressive effect of cations on ASR expansion depended on the ionic surface charge density. The higher value of surface charge density, the stronger the bonding between the cation and anions in the gels, the less tendency to expand. Others (McCormick et al., 1989; Gaboriaud et al., 1999) studied the mitigating mechanisms based on sol-gel principles, they observed that presence of lithium enhanced the formation of large silicate species in solution, which took longer time to destabilize (Gaboriaud et al., 1998).

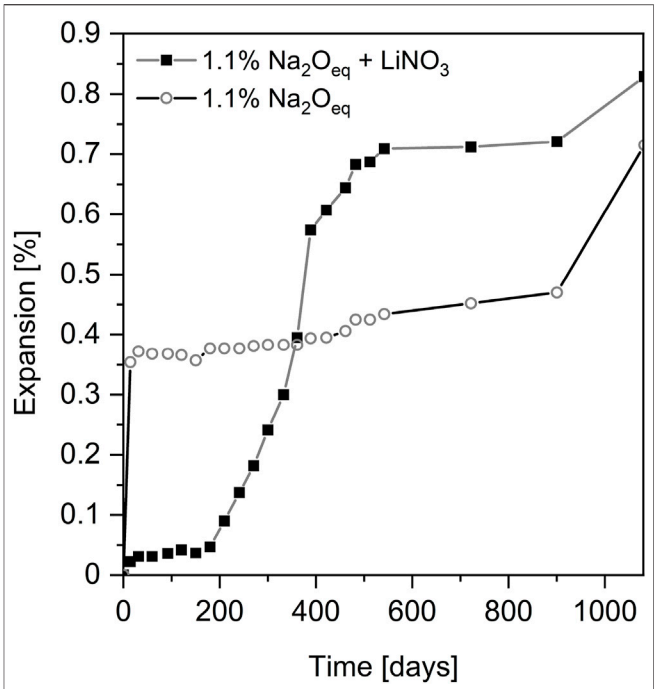

FIGURE 7 | Mortar bar expansion determined according to ASTM C227. Data from (Zapała-Sławeta and Owsiak, 2017).

Based on the literature reviewed above it becomes clear, that the presence of some Ca as well as of sufficient Li are prerequisites for an effective mitigation by Li. Different mechanism such as blocking of dissolution, formation of a non-expansive solid, prevention of swelling due to other reasons have been suggested, however the findings reported in literature are contradictory and the experimental evidence pointing in any direction is circumstantial and inconclusive. This may not be surprising as also the mechanism of ASR expansion itself is under debate since recent investigations have suggested that the swelling theory does not agree with the observed changes in the ASR product (Shi et al., 2019; Leemann et al., 2020; Shi et al., 2020a; Geng et al., 2021).

3.3 Pore Solution Observations

Analysis of the pore solution of the samples containing lithium can also provide valuable information about the reaction of Li with Si. The addition of some lithium salts (LiF and Li_2CO_3) can increase the pore solution pH through reaction with $Ca(OH)_2$ forming insoluble $CaCO_3$ or CaF_2, while Li^+ and OH^- remain in solution. However, the pore solution pH is not affected by $LiNO_3$ (Diamond, 1999). Several studies (Sakaguchi et al., 1989; Collins et al., 2004b; Tremblay et al., 2008; Tremblay et al., 2010;

Leemann et al., 2014) reported that the Li concentration of the extracted pore solution decreased with time, while the concentration of K and Na remained unchanged. In contrast, the samples without Li showed a decrease of K and Na concentrations (Sakaguchi et al., 1989). Diamond and Ong (1992) reported that even in the samples without reactive aggregates, 40% of Li was absorbed by the cement hydrates after 1 day of hydration, while only 25% NaOH and 20% KOH were incorporated in the C-S-H phase. Similarly (Bérubé et al., 2004), reported that only 35% of the original quantity of lithium left in pore solution in contrast to 55 and 80% for Na and K respectively. Kim and Olek (2015) found that 50% of added lithium is not available in the pore solution but incorporated into cement hydrates. These observations suggest the precipitation of a solid phase containing Li and a stronger interaction of Si with Li than with K and Na.

3.4 Long-Term Effectiveness and Cautions to Potential Risk

Only few studies have investigated the long-term effectiveness of lithium salts to inhibit ASR. Mo et al. (2003) studied the long-term effectiveness of LiOH in mitigating ASR by applying a rigorous experimental condition for the mortars, i.e., cured at 80°C for 3 years after being autoclaved for 24 h at 150°C. Under this condition, they found that LiOH was able to inhibit long-term ASR expansion effectively at Li/Na ratio above 0.3 or 0.6, depending on the alkali dosage of cements, i.e., 2.5% or 3.0%. A 6-years experimental study (Ekolu et al., 2017) also showed that $LiNO_3$ with Li/(K + Na) molar ratio of 0.74 is effective in long-term control of delayed ettringite formation (DEF) or combined ASR-DEF mechanism in concretes. However, other researchers (Zapała-Sławeta and Owsiak, 2017) observed that, $LiNO_3$ used at the molar ratio of Li/(K + Na) = 1.0, mitigated ASR only for a limited period of time as shown in **Figure 7**. A significant increase of expansion was observed from 180 to 540 days. Microscopic observation from this study confirmed that large amount of ASR products were formed with indication of multiple exudations in the presence of $LiNO_3$ at long term. Additionally, DEF was also observed in this study, which possibly contribute the boost expansion after 900 days. Slower DEF than ASR was also observed in (Ekolu et al., 2017). The mechanism for the post formation of ASR products within this period remains unclear, but the authors stated that the ASR products formed seemed to be less viscous. Recently, Liu et al. (2019) showed that high concentration of $LiNO_3$ only inhibit ASR at early stages, and suggested that formation of $LiSiO_3$ could cause expansion and cracking of concrete after long period of time.

4 SYNERGETIC EFFECT BETWEEN AL AND LI

In some cases, the use of Al-rich SCMs alone may not be able to fully control the ASR. Therefore, combination of Al-rich SCMs with small dosage of lithium salts to mitigate ASR has also gained some interests. Thomas et al. (2001) studied the efficacy of

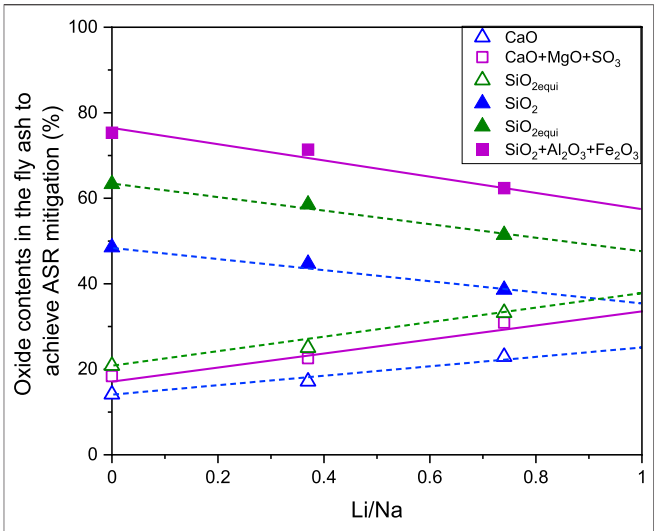

FIGURE 8 | Correlation of chemical contents of fly ash and lithium dosage required to achieve ASR mitigation at 25% fly ash replacement level. Data reproduced from (Venkatanarayanan and Rangaraju, 2014).

combinations of fly ash and lithium salts for preventing ASR. Their results indicated that the beneficial effects of lithium and fly ash are cumulative when the materials are combined and, in some cases, there is a synergistic effect. Drimalas et al. (2012) reported that both single use of either 30% class C fly ash or $LiNO_3$ with a Li/(K + Na) molar ratio 0.56 are effective in reducing ASR expansion of concrete containing a highly reactive fine aggregate from Texas. The combinations of lithium and fly ash have shown synergistically beneficial but also detrimental effects (i.e., no synergistic effect and even increase of ASR expansion) may occur. A mixture containing both $LiNO_3$ and 30% class C fly ash showed only a 50% of reduction of the ASR expansion compared to single use of 30% class C fly ash after 3,500 days of outdoor exposure. Venkatanarayanan and Rangaraju (2014) conducted a quantitative analysis of the combined effects of fly ash and lithium admixture in mitigating ASR in mortars containing Spratt aggregate. A linear correlation between the minimum oxide contents (for ASR inhibiting oxides: SiO_2, SiO_{2equi}, and $SiO_2+Al_2O_3+Fe_2O_3$) or maximum oxide contents (for ASR promoting oxides: CaO, CaO_{equi}, and CaO + MgO + SO_3) and the lithium dosage needed to achieve effective ASR mitigation was established as shown in **Figure 8**. The results show that use of lithium nitrate is not needed for mortars containing fly ashes with less than 14.40% CaO. It was expected that the correlation could be used to optimize the lithium dosage as a function of fly ash composition to provide an economic solution for ASR mitigation.

5 SUMMARY AND PERSPECTIVES

The efficiency of Al in mitigating ASR expansion has been directly confirmed by replacing Portland cement with 20%

$Al(OH)_3$ following ASTM C1293 or 10% γ-Al_2O_3 following ASTM C 1260 or ASTM C227. The presence of Al leads to a slower SiO_2 dissolution and thus a slower formation of reaction products. Sorption of $Al(OH)_4^-$ on the surface of silica and the slowing down of silica dissolution silica is more distinct at intermediate pH values (<12), while at pH 13 and above the sorption of $Al(OH)_4^-$ on silica becomes weak resulting in only feeble suppression of the dissolution rate. As the sorption of $Al(OH)_4^-$ on SiO_2 only slows down, but does not prevent silica dissolution, although the presence of $Al(OH)_3$ or Al-rich SCMs seems to prevent ASR completely up to 700 days, additional not yet well-understood effects could play an important role.

Uptake of alkalis by C-S-H is not significantly increased in the presence of Al, such that the mechanism of significantly increased alkali fixation by C-A-S-H with subsequent pH reduction can be excluded.

The structure and composition of ASR products are not affected by the presence of Al at ambient conditions, while at higher temperature such as 80°C, formation of alkali alumino-silicates or zeolites could lower the potential to form ASR products. However, the formation of alkali alumino-silicate and zeolite is under most conditions expected to be too slow to be relevant in suppressing ASR formation in field concretes.

Different lithium salts, such as $LiNO_3$, $LiNO_2$, Li_2CO_3, LiF, LiOH, $LiOH{\cdot}H_2O$, Li_2SiO_3, Li_2SO_4, LiCl, LiBr, and LiH_2PO_4, have been found to be effective in mitigating ASR at a certain dosage. The use of some lithium salt such as Li_2CO_3 and LiF as well as LiOH results an increase of pore solution pH. Preferably, $LiNO_3$ and $LiNO_2$ are used due to their high solubility and good compatibility with other admixtures. $LiNO_2$ can have in addition a positive effect on preventing rebar corrosion.

The effective dosage of lithium depends on the type of lithium salts, alkali content of the cements and reactivity of the aggregates. Lithium salts are more effective in mitigating ASR for the highly reactive aggregates than for the less reactive aggregates. Generally, high alkali content in the cement result in high effective Li dosages needed. A linear correlation between the effective lithium dosage and the difference between total alkali content and threshold alkali level of the aggregates has been established by some authors, while others did not find a correlation between alkali reactivity of the aggregates and effective lithium dosage. More investigations will be needed to clarify those effects.

$LiNO_3$ was found to be effective at both low (38°C) and high (150°C) temperatures, while Li_2CO_3 was only effective at 38°C, due to unknown reasons. In laboratory studies, lithium salts are often used as an admixture, while in practice they are rather applied to already ASR-affected structures. The transferability from pre-treatment laboratory results to post-exposure treatment on concrete structure will also need further research.

Various mechanisms have been proposed to explain why lithium salts mitigate ASR. Lithium might somewhat accelerate SiO_2 dissolution, but only in the absence of calcium, while in the presence of Ca and Li a clear decrease of the silica dissolution has been observed which might contribute together with other factors to the lower the expansion observed for Li containing concretes. Li can replace Ca, K and Na in ASR products, thus alter their composition and structure although it remains unclear how that affects expansion. In addition, Li can also react with Si to form amorphous and/or crystalline lithium silicates. Different mechanism such as blocking of dissolution, formation of a non-expansive solid, prevention of swelling due to other reasons have been suggested, however the findings reported in literature are contradictory and the experimental evidences are not conclusive, indicating more systematic research will be needed.

The combination of Al-rich SCMs such as fly ash and lithium could be very efficient in preventing ASR. A correlation of the CaO content of fly ash and the required lithium dosage could be established. Such relationships could be used to optimize the lithium dosage as a function of fly ash composition to provide an economic solution for ASR mitigation.

AUTHOR CONTRIBUTIONS

ZS and BL contributed to the conception and design of the review. ZS wrote the first draft of the manuscript. BL contributed with writing, reviewing and editing of the manuscript.

FUNDING

The partial financial contribution of SNF Sinergia project: alkali-silica reaction in concrete (ASR), grant number CRSII5_17108; is gratefully acknowledged.

REFERENCES

Aquino, W., Lange, D. A., and Olek, J. (2001). The Influence of Metakaolin and Silica Fume on the Chemistry of Alkali-Silica Reaction Products. *Cem. Concr. Compos.* 23 (6), 485–493. doi:10.1016/s0958-9465(00)00096-2

Avet, F., and Scrivener, K. (2018). Investigation of the Calcined Kaolinite Content on the Hydration of Limestone Calcined Clay Cement (LC3). *Cem. Concr. Res.* 107, 124–135. doi:10.1016/j.cemconres.2018.02.016

Bagheri, M., Lothenbach, B., Shakoorioskooie, M., and Scrivener, K. (2022). Effect of Different Ions on Dissolution Rates of Silica and Feldspars at High pH. *Cem. Concr. Res* 152, 106644. doi:10.1016/j.cemconres.2021.106644

Bagheri, M., Lothenbach, B., Shakoorioskooie, M., Leemann, A., and Scrivener, K. (2021). Use of Scratch Tracking Method to Study the Dissolution of alpine Aggregates Subject to Alkali Silica Reaction. *Cem. Concr. Compos.* 124, 104260. doi:10.1016/j.cemconcomp.2021.104260

Bérubé, M. A., Tremblay, C., Fournier, B., Thomas, M. D., and Stokes, D. B. (2004). Influence of Lithium-Based Products Proposed for Counteracting ASR on the Chemistry of Pore Solution and Cement Hydrates. *Cem. Concr. Res.* 34 (9), 1645–1660. doi:10.1016/j.cemconres.2004.03.025

Berra, M., Mangialardi, T., and Paolini, A. E. (2003). Use of Lithium Compounds to Prevent Expansive Alkali-Silica Reactivity in concrete. *Adv. Cem. Res.* 15 (4), 145–154. doi:10.1680/adcr.2003.15.4.145

Bian, Q., Nishibayashi, S., Kuroda, T., Wu, X., and Tang, M. (1996). "Various Chemicals in Suppressing Expansion Due to Alkali–Silica Reaction," in Proceedings of the 10th International Conference on Alkali–Aggregate Reaction, Melbourne, Australia, August 18–24, 1996 (CSIRO Division of Building Construction and Engineering), 868.

Bickmore, B. R., Nagy, K. L., Gray, A. K., and Brinkerhoff, A. R. (2006). The Effect of Al(OH)4− on the Dissolution Rate of Quartz. *Geochim. Cosmochim. Acta* 70 (2), 290–305. doi:10.1016/j.gca.2005.09.017

Chappex, T., and Scrivener, K. (2012a). Alkali Fixation of C-S-H in Blended Cement Pastes and its Relation to Alkali Silica Reaction. *Cem. Concr. Res.* 42 (8), 1049–1054. doi:10.1016/j.cemconres.2012.03.010

Chappex, T., and Scrivener, K. L. (2012b). The Influence of Aluminium on the Dissolution of Amorphous Silica and its Relation to Alkali Silica Reaction. *Cem. Concr. Res.* 42 (12), 1645–1649. doi:10.1016/j.cemconres.2012.09.009

Collins, C. L., Ideker, J. H., and Kurtis, K. E. (2004a). Laser Scanning Confocal Microscopy for *In Situ* Monitoring of Alkali-Silica Reaction. *J. Microsc.* 213 (2), 149–157. doi:10.1111/j.1365-2818.2004.01280.x

Collins, C. L., Ideker, J. H., Willis, G. S., and Kurtis, K. E. (2004b). Examination of the Effects of LiOH, LiCl, and LiNO3 on Alkali-Silica Reaction. *Cem. Concr. Res.* 34 (8), 1403–1415. doi:10.1016/j.cemconres.2004.01.011

Conway, B. E. (1981). *Ionic Hydration in Chemistry and Biophysics*. Amsterdam, Netherlands: Elsevier Scientific Publishing.

Demir, İ., and Arslan, M. (2013). The Mechanical and Microstructural Properties of Li2SO4, LiNO3, Li2CO3 and LiBr Added Mortars Exposed to Alkali-Silica Reaction. *Constr. Build. Mater.* 42, 64–77. doi:10.1016/j.conbuildmat.2012.12.059

Demir, İ., Sevim, Ö., and Kalkan, İ. (2018). Microstructural Properties of Lithium-Added Cement Mortars Subjected to Alkali–Silica Reactions. *Sādhanā* 43 (7), 1–10. doi:10.1007/s12046-018-0901-3

Deschner, F., Winnefeld, F., Lothenbach, B., Seufert, S., Schwesig, P., Dittrich, S., et al. (2012). Hydration of Portland Cement with High Replacement by Siliceous Fly Ash. *Cem. Concr. Res.* 42 (10), 1389–1400. doi:10.1016/j.cemconres.2012.06.009

Diamond, S., and Ong, S. (1992). "The Mechanism of Lithium Effects on ASR," in Proc. of 9th International Conference on Alkali-Aggregate Reaction, Westminster, London, July 27–31, 269–278.

Diamond, S. (1981). Effects of Two Danish Flyashes on Alkali Contents of Pore Solutions of Cement-Flyash Pastes. *Cement Concrete Res.* 11 (3), 383–394. doi:10.1016/0008-8846(81)90110-1

Diamond, S. (1992). "The Mechanisms of Lithium Effects on ASR," in Proc. of 9th International Conference on Alkali-Aggregate Reaction, Westminster, London, July 27-31, 269.

Diamond, S. (1999). Unique Response of LiNO3 as an Alkali Silica Reaction-Preventive Admixture. *Cem. Concr. Res.* 29 (8), 1271–1275. doi:10.1016/s0008-8846(99)00115-5

Dove, P. M., and Nix, C. J. (1997). The Influence of the Alkaline Earth Cations, Magnesium, Calcium, and Barium on the Dissolution Kinetics of Quartz. *Geochim. Cosmochim. Acta* 61 (16), 3329–3340. doi:10.1016/s0016-7037(97)00217-2

Dove, P. M. (1999). The Dissolution Kinetics of Quartz in Aqueous Mixed Cation Solutions. *Geochim. Cosmochim. Acta* 63 (22), 3715–3727. doi:10.1016/s0016-7037(99)00218-5

Drimalas, T., Ideker, J. H., Bentivegna, A. F., Folliard, K. J., Fournier, B., and Thomas, M. D. A. (2012). The Long-Term Monitoring of Large-Scale Concrete Specimens Containing Lithium Salts to Mitigate Alkali-Silica Reaction. *Spec. Publ.* 289, 1–17.

Duchesne, J., and Bérubé, M.-A. (2001). Long-term Effectiveness of Supplementary Cementing Materials against Alkali-Silica Reaction. *Cem. Concr. Res.* 31 (7), 1057–1063. doi:10.1016/s0008-8846(01)00538-5

Durand, B. (2000). "More Results about the Use of Lithium Salts and mineral Admixtures to Inhibit ASR in concrete," in Proceedings of the 11th International Conference on Alkali–Aggregate Reaction, Quebec, Canada, June 11–16.

Ekolu, S., Rakgosi, G., and Hooton, D. (2017). Long-term Mitigating Effect of Lithium Nitrate on Delayed Ettringite Formation and ASR in Concrete - Microscopic Analysis. *Mater. Charact.* 133, 165–175. doi:10.1016/j.matchar.2017.09.025

Feng, X., Thomas, M. D. A., Bremner, T. W., Balcom, B. J., and Folliard, K. J. (2005). Studies on Lithium Salts to Mitigate ASR-Induced Expansion in New concrete: a Critical Review. *Cem. Concr. Res.* 35 (9), 1789–1796. doi:10.1016/j.cemconres.2004.10.013

Feng, X., Thomas, M. D. A., Bremner, T. W., Folliard, K. J., and Fournier, B. (2010). New Observations on the Mechanism of Lithium Nitrate against Alkali Silica Reaction (ASR). *Cem. Concr. Res.* 40 (1), 94–101. doi:10.1016/j.cemconres.2009.07.017

Fernandes, I., Noronha, F., and Teles, M. (2007). Examination of the concrete from an Old Portuguese Dam: Texture and Composition of Alkali–Silica Gel. *Mater. Charact.* 58 (11–12), 1160–1170. doi:10.1016/j.matchar.2007.04.007

Fernandes, I. (2009). Composition of Alkali-Silica Reaction Products at Different Locations within concrete Structures. *Mater. Charact.* 60 (7), 655–668. doi:10.1016/j.matchar.2009.01.011

Folliard, K. J., Thomas, M. D. A., and Kurtis, K. E. (2003). *Guidelines for the Use of Lithium to Mitigate or Prevent ASR*. Washington, DC: US Department of Transportation, Federal Highway Administration (FHWA).

Folliard, K. J., Thomas, M. D. A., Fournier, B., Kurtis, K. E., and Ideker, J. H. (2006). *Interim Recommendations for the Use of Lithium to Mitigate or Prevent Alkali-Silica Reaction (ASR)*. United States: Federal Highway AdministrationOffice of Infrastructure.

Gaboriaud, F., Chaumont, D., Nonat, A., Hanquet, B., and Craeivich, A. (1998). Study of the Influence of Alkaline Ions (Li, Na and K) on the Structure of the Silicate Entities In Silico Alkaline Sol and on the Formation of the Silico-Calco-Alkaline Gel. *J. Sol-Gel Sci. Technol.* 13 (1–3), 353–358. doi:10.1023/a:1008644405473

Gaboriaud, F., Nonat, A., Chaumont, D., Craievich, A., and Hanquet, B. (1999). 29Si NMR and Small-Angle X-ray Scattering Studies of the Effect of Alkaline Ions (Li+, Na+, and K+) In Silico-alkaline Sols. *J. Phys. Chem. B* 103 (12), 2091–2099. doi:10.1021/jp984074x

Geng, G., Barbotin, S., Shakoorioskooie, M., Shi, Z., Leemann, A., Sanchez, D. F., et al. (2021). An *In-Situ* 3D Micro-XRD Investigation of Water Uptake by Alkali-Silica-Reaction (ASR) Product. *Cem. Concr. Res.* 141, 106331. doi:10.1016/j.cemconres.2020.106331

Guo, S., Dai, Q., Sun, X., Xiao, X., Si, R., and Wang, J. (2018). Reduced Alkali-Silica Reaction Damage in Recycled Glass Mortar Samples with Supplementary Cementitious Materials. *J. Clean. Prod.* 172, 3621–3633. doi:10.1016/j.jclepro.2017.11.119

Guo, S., Dai, Q., and Si, R. (2019). Effect of Calcium and Lithium on Alkali-Silica Reaction Kinetics and Phase Development. *Cem. Concr. Res.* 115, 220–229. doi:10.1016/j.cemconres.2018.10.007

Hagelia, P., and Fernandes, I. (2012). "On the AAR Susceptibility of Granitic and Quartzitic Aggregates in View of Petrographic Characteristics and Accelerated Testing," in The 14th International Conference on Alkali-Aggregate Reactions in Concrete, Austin, Texas, USA, May 20–25, 10.

Hong, S.-Y., and Glasser, F. P. (2002). Alkali Sorption by C-S-H and C-A-S-H Gels. *Cem. Concr. Res.* 32 (7), 1101–1111. doi:10.1016/s0008-8846(02)00753-6

Hünger, K.-J. (2007). The Contribution of Quartz and the Role of Aluminum for Understanding the AAR with Greywacke. *Cem. Concr. Res.* 37 (8), 1193–1205. doi:10.1016/j.cemconres.2007.05.009

Iler, R. K. (1973). Effect of Adsorbed Alumina on the Solubility of Amorphous Silica in Water. *J. Colloid Interf. Sci.* 43 (2), 399–408. doi:10.1016/0021-9797(73)90386-x

Iler, K. R. (1979). *The Chemistry of Silica. Solubility, Polymerization, Colloid and Surface Properties and Biochemistry of Silica*. John Wiley & Sons.

Islam, M. S., and Ghafoori, N. (2016). Experimental Study and Empirical Modeling of Lithium Nitrate for Alkali-Silica Reactivity. *Constr. Build. Mater.* 121, 717–726. doi:10.1016/j.conbuildmat.2016.06.026

Kandasamy, S., and Shehata, M. H. (2014). The Capacity of Ternary Blends Containing Slag and High-Calcium Fly Ash to Mitigate Alkali Silica Reaction. *Cem. Concr. Compos.* 49, 92–99. doi:10.1016/j.cemconcomp.2013.12.008

Katayama, T. (2012a). "Late-expansive ASR in a 30-year Old PC Structure in Eastern Japan,". Paper in Proc. 14th International Conference on Alkali-Aggregate Reaction (ICAAR), Austin, Texas, USA, May 20–25, 862–873.

Katayama, T. (2012b). "ASR Gels and Their Crystalline Phases in concrete—universal Products in Alkali–Silica, Alkali–Silicate and Alkali–Carbonate Reactions," in Proceedings of the 14th International

Conference on Alkali Aggregate Reactions (ICAAR), Austin, Texas, May 20–25, 1–12.

Kawamura, M., and Fuwa, H. (2003). Effects of Lithium Salts on ASR Gel Composition and Expansion of Mortars. *Cem. Concr. Res.* 33 (6), 913–919. doi:10.1016/s0008-8846(02)01092-x

Kawamura, M., Takeuchi, K., and Sugiyama, A. (1994). Mechanisms of Expansion of Mortars Containing Reactive Aggregate in NaCl Solution. *Cem. Concr. Res.* 24 (4), 621–632. doi:10.1016/0008-8846(94)90186-4

Kawamura, M. (2017). A Discussion of the Paper "ASR Prevention - Effect of Aluminum and Lithium Ions on the Reaction Products" by Andreas Leemann, Laetitia Bernard, Salaheddine Alahrache, Frank Winnefeld. *Cem. Concr. Res.*, 102, 225–226. doi:10.1016/j.cemconres.2017.05.012

Kim, T., and Olek, J. (2015). Modeling of Early Age Loss of Lithium Ions from Pore Solution of Cementitious Systems Treated with Lithium Nitrate. *Cem. Concr. Res.* 67, 204–214. doi:10.1016/j.cemconres.2014.10.010

Kim, T., and Olek, J. (2016). The Effects of Lithium Ions on Chemical Sequence of Alkali-Silica Reaction. *Cem. Concr. Res.* 79, 159–168. doi:10.1016/j.cemconres.2015.09.013

Kirkpatrick, R. J., Kalinichev, A. G., Hou, X., and Struble, L. (2005). Experimental and Molecular Dynamics Modeling Studies of Interlayer Swelling: Water Incorporation in Kanemite and ASR Gel. *Mat. Struct.* 38 (4), 449–458. doi:10.1007/bf02482141

Kobayashi, K., and Takagi, Y. (2020). Penetration of Pressure-Injected Lithium Nitrite in concrete and ASR Mitigating Effect. *Cem. Concr. Compos.* 114, 103709. doi:10.1016/j.cemconcomp.2020.103709

Krattiger, N., Lothenbach, B., and Churakov, S. V. (2021). Sorption and Electrokinetic Properties of ASR Product and C-S-H: A Comparative Modelling Study. *Cem. Concr. Res.* 146, 106491. doi:10.1016/j.cemconres.2021.106491

Kurihara, T., and Katawaki, K. (1989). "Effects of Moisture Control and Inhibition on Alkali Silica Reaction," in Proc., 8th Int. Conf. on Alkali Aggregate Reaction in Concrete, Kyoto, Japan, July 17–20, 629–634.

Kurtis, K. E., and Monteiro, P. J. M. (2003). Chemical Additives to Control Expansion of Alkali-Silica Reaction Gel: Proposed Mechanisms of Control. *J. Mater. Sci.* 38 (9), 2027–2036. doi:10.1023/a:1023549824201

Kurtis, K. E., Monteiro, P. J. M., and Meyer-Ilse, W. (2000). *Examination of the Effect of LiCl on ASR Gel Expansion*. California: Ernest Orlando Lawrence Berkeley National Lab.

L'Hôpital, E., Lothenbach, B., Scrivener, K., and Kulik, D. A. (2016). Alkali Uptake in Calcium Alumina Silicate Hydrate (CASH). *Cem. Concr. Res.* 85, 122–136. doi:10.1016/j.cemconres.2016.03.009

Lane, D. S., and Board, V. C. T. (2002). *Laboratory Investigation of Lithium-Bearing Compounds for Use in concrete*. Charlottesville, VA: Virginia Transportation Research Council.

Lane, D. S. (2000). "Preventive Measures for ASR Used in Virginia, USA," in Proceedings of the 11th International Conference on Alkali–Aggregate Reaction, Quebec, Canada, June 11–16 (Quebec: Centre de Recherche Interuniversitaire Sur Le Beton), 693.

Lawrence, M., and Vivian, H. E. (1961). Reactions of Various Alkalis with Silica. *Aust. J. Appl. Sci.* 12, 96–103.

Leemann, A., and Lothenbach, B. (2008). The Influence of Potassium-Sodium Ratio in Cement on concrete Expansion Due to Alkali-Aggregate Reaction. *Cem. Concr. Res.* 38 (10), 1162–1168. doi:10.1016/j.cemconres.2008.05.004

Leemann, A., and Lura, P. (2013). E-modulus of the Alkali-Silica-Reaction Product Determined by Micro-Indentation. *Constr. Build. Mater.* 44, 221–227. doi:10.1016/j.conbuildmat.2013.03.018

Leemann, A., Lörtscher, L., Bernard, L., Le Saout, G., Lothenbach, B., and Espinosa-Marzal, R. M. (2014). Mitigation of ASR by the Use of LiNO3-Characterization of the Reaction Products. *Cem. Concr. Res.* 59, 73–86. doi:10.1016/j.cemconres.2014.02.003

Leemann, A., Bernard, L., Alahrache, S., and Winnefeld, F. (2015). ASR Prevention - Effect of Aluminum and Lithium Ions on the Reaction Products. *Cem. Concr. Res.* 76, 192–201. doi:10.1016/j.cemconres.2015.06.002

Leemann, A., Shi, Z., Wyrzykowski, M., and Winnefeld, F. (2020). Moisture Stability of Crystalline Alkali-Silica Reaction Products Formed in concrete Exposed to Natural Environment. *Mater. Des.* 195, 109066. doi:10.1016/j.matdes.2020.109066

Leemann, A. (2017). Raman Microscopy of Alkali-Silica Reaction (ASR) Products Formed in concrete. *Cem. Concr. Res.* 102, 41–47. doi:10.1016/j.cemconres.2017.08.014

Leemann, A. (2021). "Impact of Different Added Alkalis on concrete Expansion Due to ASR," in Proceedings of the 16th International Conference on Alkali-Aggregate Reaction in Concrete. Editors A. Lopes Batista, A. Santos Silva, I. Fernandes, L. Oliveira Santos, J. Custódio, and C. Serra, 175–184.

Liu, J., Yu, L., and Deng, M. (2019). Effect of LiNO3 on Expansion of Alkali-Silica Reaction in Rock Prisms and Concrete Microbars Prepared by Sandstone. *Materials* 12 (7), 1150. doi:10.3390/ma12071150

Lothenbach, B., Bernard, E., and Mäder, U. (2017). Zeolite Formation in the Presence of Cement Hydrates and Albite. *Phys. Chem. Earth, Parts A/B/C* 99, 77–94. doi:10.1016/j.pce.2017.02.006

Lumley, J. S. (1997). ASR Suppression by Lithium Compounds. *Cem. Concr. Res.* 27 (2), 235–244. doi:10.1016/s0008-8846(97)00003-3

McCormick, A. V., Bell, A. T., and Radke, C. J. (1989). Evidence from Alkali-Metal NMR Spectroscopy for Ion Pairing in Alkaline Silicate Solutions. *J. Phys. Chem.* 93 (5), 1733–1737. doi:10.1021/j100342a013

McCoy, W. J., and Caldwell, A. G. (1951). New Approach to Inhibiting Alkali-Aggregate Expansion. *J. Proc.* 47 (5), 693–706.

Mitchell, L. D., Beaudoin, J. J., and Grattan-Bellew, P. (2004). The Effects of Lithium Hydroxide Solution on Alkali Silica Reaction Gels Created with Opal. *Cem. Concr. Res.* 34 (4), 641–649. doi:10.1016/j.cemconres.2003.10.011

Mo, X., Yu, C., and Xu, Z. (2003). Long-term Effectiveness and Mechanism of LiOH in Inhibiting Alkali-Silica Reaction. *Cem. Concr. Res.* 33 (1), 115–119. doi:10.1016/s0008-8846(02)00934-1

Mo, X., Jin, T., Li, G., Wang, K., Xu, Z., and Tang, M. (2005). Alkali-aggregate Reaction Suppressed by Chemical Admixture at 80 °C. *Constr. Build. Mater.* 19 (6), 473–479. doi:10.1016/j.conbuildmat.2004.07.012

Mo, X. (2005). Laboratory Study of LiOH in Inhibiting Alkali-Silica Reaction at 20 °C: a Contribution. *Cem. Concr. Res.* 35 (3), 499–504. doi:10.1016/j.cemconres.2004.06.003

Mohd, I., Yasutaka, S., Hidenori, H., and Yamamoto, D. (2017). An Experimental Study on Mitigating Alkali Silica Reaction by Using Lithium Hydroxide Monohydrate. *AIP Conf. Proc.* 1903 (1), 30005. doi:10.1063/1.5011512

Nicoleau, L., Schreiner, E., and Nonat, A. (2014). Ion-specific Effects Influencing the Dissolution of Tricalcium Silicate. *Cement Concrete Res.* 59, 118–138. doi:10.1016/j.cemconres.2014.02.006

Oey, T., La Plante, E. C., Falzone, G., Hsiao, Y.-H., Wada, A., Monfardini, L., et al. (2020). Calcium Nitrate: A Chemical Admixture to Inhibit Aggregate Dissolution and Mitigate Expansion Caused by Alkali-Silica Reaction. *Cem. Concr. Compos.* 110, 103592. doi:10.1016/j.cemconcomp.2020.103592

Ohama, Y., Demura, K., and Kakegawa, M. (1989). "Inhibiting ASR with Chemical Admixtures," in Proceedings of the 8th International Conference of Alkali–Aggregate Reaction, Kyoto, Japan, July 17–20.

Olafsson, H. (1986). "The Effect of Relative Humidity and Temperature on Alkali Expansion of Mortar Bars," in Proc., 7th Int. Conf. on Alkali Aggregate Reaction in Concrete, Ottawa, Canada, August, 461–465.

Plettinck, S., Chou, L., and Wollast, R. (1994). Kinetics and Mechanisms of Dissolution of Silica at Room Temperature and Pressure. *Mineral. Mag.* 58A (2), 728–729. doi:10.1180/minmag.1994.58a.2.116

Prezzi, M., Monteiro, P. J. M., and Sposito, G. (1997). The Alkali–Silica Reaction: Part I. Use of the Double-Layer Theory to Explain the Behavior of Reaction-Product Gels. *ACI Mater. J.* 94 (1), 10–17.

Qinghan, B., Nishibayashi, S., Xuequan, W., Yoshino, A., Hong, Z., Tiecheng, W., et al. (1995). Preliminary Study of Effect of LiNO2 on Expansion of Mortars Subjected to Alkali-Silica Reaction. *Cem. Concr. Res.* 25 (8), 1647–1654. doi:10.1016/0008-8846(95)00161-1

Rajabipour, F., Giannini, E., Dunant, C., Ideker, J. H., and Thomas, M. D. A. (2015). Alkali-Silica Reaction: Current Understanding of the Reaction Mechanisms and the Knowledge Gaps. *Cem. Concr. Res.* 76, 130–146. doi:10.1016/j.cemconres.2015.05.024

Ramlochan, T., Thomas, M. D. A., and Hooton, R. D. (2004). The Effect of Pozzolans and Slag on the Expansion of Mortars Cured at Elevated Temperature: Part II: Microstructural and Microchemical

Investigations. *Cem. Concr. Res.* 34 (8), 1341–1356. doi:10.1016/j.cemconres.2003.12.026

Šachlová, Š., Přikryl, R., and Pertold, Z. (2010). Alkali-Silica Reaction Products: Comparison between Samples from concrete Structures and Laboratory Test Specimens. *Mater. Charact.* 61 (12), 1379–1393. doi:10.1016/j.matchar.2010.09.010

Saito, M., Kitagawa, A., and Hasaba, S. (1992). Effectiveness of Lithium Nitrite in Suppressing Alkali-Aggregate Expansion. *J. Soc. Mater. Sci. Jpn.* 41 (468), 1375–1381. doi:10.2472/jsms.41.1375

Sakaguchi, T., Takakura, M., Kitagawa, A., Hori, T., Tomozawa, F., and Abe, M. (1989). "The Inhibiting Effect of Lithium Compounds on Alkali-Silica Reaction," in 8th International Conference on Alkali-Aggregate Reaction, Kyoto, Japan, July 17–20, 229–234.

Sand, L. B., Sacco, A., Jr, Thompson, R. W., and Dixon, A. G. (1987). Large Zeolite Crystals: Their Potential Growth in Space. *Zeolites* 7 (5), 387–392. doi:10.1016/0144-2449(87)90001-7

Schneider, J. F., Hasparyk, N. P., Silva, D. A., and Monteiro, P. J. M. (2008). Effect of Lithium Nitrate on the Alkali-Silica Reaction Gel. *J. Am. Ceram. Soc.* 91 (10), 3370–3374. doi:10.1111/j.1551-2916.2008.02638.x

Shafaatian, S. M. H., Akhavan, A., Maraghechi, H., and Rajabipour, F. (2013). How Does Fly Ash Mitigate Alkali-Silica Reaction (ASR) in Accelerated Mortar Bar Test (ASTM C1567)? *Cem. Concr. Compos.* 37, 143–153. doi:10.1016/j.cemconcomp.2012.11.004

Shi, Z., and Lothenbach, B. (2020). The Combined Effect of Potassium, Sodium and Calcium on the Formation of Alkali-Silica Reaction Products. *Cem. Concr. Res.* 127, 105914. doi:10.1016/j.cemconres.2019.105914

Shi, Z., Shi, C., Zhang, J., Wan, S., Zhang, Z., and Ou, Z. (2018). Alkali-silica Reaction in Waterglass-Activated Slag Mortars Incorporating Fly Ash and Metakaolin. *Cem. Concr. Res.* 108, 10–19. doi:10.1016/j.cemconres.2018.03.002

Shi, Z., Geng, G., Leemann, A., and Lothenbach, B. (2019). Synthesis, Characterization, and Water Uptake Property of Alkali-Silica Reaction Products. *Cem. Concr. Res.* 121, 58–71. doi:10.1016/j.cemconres.2019.04.009

Shi, Z., Leemann, A., Rentsch, D., and Lothenbach, B. (2020a). Synthesis of Alkali-Silica Reaction Product Structurally Identical to that Formed in Field concrete. *Mater. Des.* 190, 108562. doi:10.1016/j.matdes.2020.108562

Shi, Z., Park, S., Lothenbach, B., and Leemann, A. (2020b). Formation of Shlykovite and ASR-P1 in concrete under Accelerated Alkali-Silica Reaction at 60 and 80 °C. *Cem. Concr. Res.* 137, 106213. doi:10.1016/j.cemconres.2020.106213

Shi, Z., Ma, B., and Lothenbach, B. (2021). Effect of Al on the Formation and Structure of Alkali-Silica Reaction Products. *Cem. Concr. Res.* 140, 106311. doi:10.1016/j.cemconres.2020.106311

Sims, I., and Poole, A. B. (2017). *Alkali-Aggregate Reaction in Concrete: A World Review*. CRC Press. doi:10.1201/9781315708959

Souza, L. M. S., Polder, R. B., and Çopuroğlu, O. (2017). Lithium Migration in a Two-Chamber Set-Up as Treatment against Expansion Due to Alkali-Silica Reaction. *Constr. Build. Mater.* 134, 324–335. doi:10.1016/j.conbuildmat.2016.12.052

Stark, D., Morgan, B., and Okamoto, P. (1993). *Eliminating or Minimizing Alkali-Silica Reactivity*. Issue SHRP-C-343.

Stark, D. (1991). The Moisture Condition of Field concrete Exhibiting Alkali-Silica Reactivity. *Spec. Publ.* 126, 973–988.

Stark, D. C. (1992). "Lithium Salt Admixtures--An Alternative Method to Prevent Expansive Alkali-Silica Reactivity," in The 9th International Conference on Alkali-Aggregate Reactions in Concrete, Westminster, London, July 27–31, 1017–1025.

Sun, G. K., Young, J. F., and Kirkpatrick, R. J. (2006). The Role of Al in C-S-H: NMR, XRD, and Compositional Results for Precipitated Samples. *Cem. Concr. Res.* 36 (1), 18–29. doi:10.1016/j.cemconres.2005.03.002

Szeles, T., Wright, J., Rajabipour, F., and Stoffels, S. (2017). Mitigation of Alkali-Silica Reaction by Hydrated Alumina. *Transp. Res. Rec.* 2629 (1), 15–23. doi:10.3141/2629-04

Tambelli, C. E., Schneider, J. F., Hasparyk, N. P., and Monteiro, P. J. M. (2006). Study of the Structure of Alkali-Silica Reaction Gel by High-Resolution NMR Spectroscopy. *J. Non-Cryst. Sol.* 352 (32–35), 3429–3436. doi:10.1016/j.jnoncrysol.2006.03.112

Tapas, M. J., Sofia, L., Vessalas, K., Thomas, P., Sirivivatnanon, V., and Scrivener, K. (2021). Efficacy of SCMs to Mitigate ASR in Systems with Higher Alkali Contents Assessed by Pore Solution Method. *Cem. Concr. Res.* 142, 106353. doi:10.1016/j.cemconres.2021.106353

Thomas, M., Hooper, T., and Stokes, D. (2000). "Use of Lithium Containing Compounds to Control Expansion in Concrete Due to Alkali-Silica Reaction," in Proc. of 11th International Conference on Alkali-Aggregate Reaction, Quebec, Canada, June 11–16 (Quebec: Centre de Recherche Interuniversitaire Sur Le Beton), 783.

Thomas, M., Baxter, S., Stokes, D., and Hill, R. (2001). "The Combined Use of Fly Ash and Lithium Nitrate for Controlling Expansion Due to Alkali-Silica Reaction," in International Center for Aggregates Research 9th Annual Symposium: Aggregates-Concrete, Bases and FinesInternational Center for Aggregates Research (ICAR), Austin, Texas, April 22–25 (University of Texas at Austin; Texas A&M University System; Aggregates Foundation for Technology, R, Final Draft).

Thomas, M. D. A., Fournier, B., Folliard, K. J., Ideker, J. H., and Resendez, Y. (2007). *The Use of Lithium to Prevent or Mitigate Alkali-Silica Reaction in concrete Pavements and Structures*. Virginia: Turner-Fairbank Highway Research Center.

Thomas, M. (2011). The Effect of Supplementary Cementing Materials on Alkali-Silica Reaction: A Review. *Cem. Concr. Res.* 41 (12), 1224–1231. doi:10.1016/j.cemconres.2010.11.003

Tremblay, C., Bérubé, M. A., Fournier, B., and Thomas, M. D. A. (2004a). "Performance of Lithium-Based Products against ASR: Effect of Aggregate Type and Reactivity, and Reaction Mechanisms,". Suppl. Papers in Proceedings of the Seventh CANMET/ACI International Conference on Recent Advances in Concrete Technology, Las Vegas, USA, 26–29 May, 247–267.

Tremblay, C., Bérubé, M. A., Fournier, B., Thomas, M. D. A., and Stokes, D. B. (2004b). "Performance of lithium-based products against ASR: application to Canadian reactive aggregates, reaction mechanisms and testing," in Proceedings of the 12th International Conference on Alkali-Aggregate Reaction (AAR) in Concrete, Beijing (China). Editors M. Tang and Deng (October 15–19: International Academic Publishers, Beijing World Publishing Corp), 668–677.

Tremblay, C., Bérubé, M.-A., Fournier, B., Thomas, M. D. A., and Folliard, K. J. (2007). Effectiveness of Lithium-Based Products in concrete Made with Canadian Natural Aggregates Susceptible to Alkali-Silica Reactivity. *ACI Mater. J.* 104 (2), 195–205.

Tremblay, C., Bérubé, M. A., Fournier, B., Thomas, M. D., Folliard, K. J., and Nkinamubanzi, P. C. (2008). Use of the Accelerated Mortar Bar Test to Evaluate the Effectiveness of LiNO 3 against Alkali-Silica Reaction—Part 2: Comparison with Results from the concrete Prism Test. *J. ASTM Int.* 5 (8), 1–21. doi:10.1520/JAI101352

Tremblay, C., Bérubé, M. A., Fournier, B., Thomas, M. D., and Folliard, K. J. (2010). Experimental Investigation of the Mechanisms by Which LiNO3 Is Effective against ASR. *Cem. Concr. Res.* 40 (4), 583–597. doi:10.1016/j.cemconres.2009.09.022

Venkatanarayanan, H. K., and Rangaraju, P. R. (2014). Effectiveness of Lithium Nitrate in Mitigating Alkali-Silica Reaction in the Presence of Fly Ashes of Varying Chemical Compositions. *J. Mater. Civil Eng.* 26 (7), 4014021. doi:10.1061/(asce)mt.1943-5533.0000908

Vollpracht, A., Lothenbach, B., Snellings, R., and Haufe, J. (2016). The Pore Solution of Blended Cements: a Review. *Mater. Struct.* 49 (8), 3341–3367. doi:10.1617/s11527-015-0724-1

Wang, H., Stokes, D. B., and Tang, F. (1996). "Compatibility of Lithium-Based Admixtures with Other concrete Admixtures," in Proceedings of the 10th International Conference on Alkali–Aggregate Reaction, Melbourne, Australia, August 18–23 (CSIRO Division of Building Construction and Engineering), 884–891.

Wijnen, P. W. J. G., Beelen, T. P. M., De Haan, J. W., Rummens, C. P. J., Van de Ven, L. J. M., and Van Santen, R. A. (1989). Silica Gel Dissolution in Aqueous Alkali Metal Hydroxides Studied by 29Si NMR. *J. Non-Cryst. Sol.* 109 (1), 85–94. doi:10.1016/0022-3093(89)90446-8

Yokoyama, T., Kinoshita, S., Wakita, H., and Tarutani, T. (1988). 27Al NMR Study on the Interaction between Aluminate and Silicate Ions in Alkaline Solution. *Bcsj* 61 (3), 1002–1004. doi:10.1246/bcsj.61.1002

Zapała-Sławeta, J., and Owsiak, Z. (2017). Effect of Lithium Nitrate on the Reaction between Opal Aggregate and Sodium and Potassium Hydroxides in concrete over a Long Period of Time. *Bull. Polish Acad. Sci. Tech. Sci.* 65, 773–778. doi:10.1515/bpasts-2017-0085

Zapała-Sławeta, J., and Owsiak, Z. (2018). The Use of Lithium Compounds for Inhibiting Alkali-Aggregate Reaction Effects in Pavement Structures. *MSE&E* 356 (1), 12008. doi:10.1088/1757-899x/356/1/012008

Zhou, B., Mao, Z., and Deng, M. (2018). Reaction of Quartz Glass in Lithium-Containing Alkaline Solutions with or without Ca. *R. Soc. Open Sci.* 5 (9), 180797. doi:10.1098/rsos.180797

Zhou, J., Zheng, K., Liu, Z., Chen, L., and Lippiatt, N. (2019). Use of γ-Al2O3 to Prevent Alkali-Silica Reaction by Altering Solid and Aqueous Compositions of Hydrated Cement Paste. *Cem. Concr. Res.* 124, 105817. doi:10.1016/j.cemconres.2019.105817

Zhou, J., Chen, L., Liu, Z., He, F., and Zheng, K. (2022). Effect of Transitional Aluminas on Portland Cement Hydration, Phase Assemblage and the Correlation to ASR Preventing Effectiveness. *Cem. Concr. Res.* 151, 106622. doi:10.1016/j.cemconres.2021.106622

Conflict of Interest: ZS was employed by Global R&D, HeidelbergCement AG.

The remaining author declares that the research was conducted in the absence of any commercial or financial relationships that could be construed as a potential conflict of interest.

frontiers in Materials

REVIEW
published: 06 January 2022
doi: 10.3389/fmats.2021.791296

Deep Learning for Photonic Design and Analysis: Principles and Applications

Bing Duan[1†], Bei Wu[2†], Jin-hui Chen[2,3], Huanyang Chen[2] and Da-Quan Yang[1]**

[1]State Key Laboratory of Information Photonics and Optical Communications, School of Information and Communication Engineering, Beijing University of Posts and Telecommunications, Beijing, China, [2]Institute of Electromagnetics and Acoustics and Fujian Provincial Key Laboratory of Electromagnetic Wave Science and Detection Technology, Xiamen University, Xiamen, China, [3]Shenzhen Research Institute of Xiamen University, Shenzhen, China

Innovative techniques play important roles in photonic structure design and complex optical data analysis. As a branch of machine learning, deep learning can automatically reveal the inherent connections behind the data by using hierarchically structured layers, which has found broad applications in photonics. In this paper, we review the recent advances of deep learning for the photonic structure design and optical data analysis, which is based on the two major learning paradigms of supervised learning and unsupervised learning. In addition, the optical neural networks with high parallelism and low energy consuming are also highlighted as novel computing architectures. The challenges and perspectives of this flourishing research field are discussed.

Keywords: optics and photonics, deep learning, photonic structure design, optical data analysis, optical neural networks

OPEN ACCESS

Edited by:
Lingling Huang,
Beijing Institute of Technology, China

Reviewed by:
Ying Li,
Zhejiang University, China
Yuanmu Yang,
Tsinghua University, China

***Correspondence:**
Da-Quan Yang
ydq@bupt.edu.cn
Jin-hui Chen
jimchen@xmu.edu.cn

†These authors have contributed equally to this work

Specialty section:
This article was submitted to Metamaterials, a section of the journal Frontiers in Materials

Received: *08 October 2021*
Accepted: *08 December 2021*
Published: *06 January 2022*

Citation:
Duan B, Wu B, Chen J-h Chen H and Yang D-Q (2022) Deep Learning for Photonic Design and Analysis: Principles and Applications. Front. Mater. 8:791296. doi: 10.3389/fmats.2021.791296

1 INTRODUCTION

Over the past few decades, photonics, as an important field of fundamental research, has been penetrating into various domains, such as life science and information technology (Vukusic and Sambles, 2003; Bigio and Sergio, 2016; Ravì et al., 2016). In particular, the advances of photonic devices, optical imaging and spectroscopy techniques have further accelerated the wide applications of photonics (Török and Kao, 2007; Ntziachristos, 2010; Dong et al., 2014; Jiang et al., 2021). For example, the creation of metasurfaces/metamaterials have promoted the development of holography and superlenses (Zhang and Liu, 2008; Yoon et al., 2018), while the optical spectroscopy and imaging have deep utility in medical diagnosis (Chan and Siegel, 2019; Lundervoldab and Lundervoldacd, 2019) and biological study (Török and Kao, 2007). However, for sophisticated photonic devices, the initial design relies on the electromagnetic modelling, which is largely determined by human experience gained from the physical intuition and previous (Ma W. et al., 2021). The specific structure parameters are determined by means of trial-and-error, and their parametric space is limited by simulation power and time. Besides, the optical data generated from optical measurements are becoming more and more complicated. For instance, when applying optical spectroscopy to characterize various analytes (e.g., malignant tumor tissue and bacterial pathogens) in complex biological environments, it is challenging to extract the fingerprint due to the large spectral overlap from the common bonds in the analytes (Rickard et al., 2020; Fang et al., 2021). The traditional analysis methods are mainly based on the physical intuition and prior-experiences, which are time-consuming and susceptive to human error.

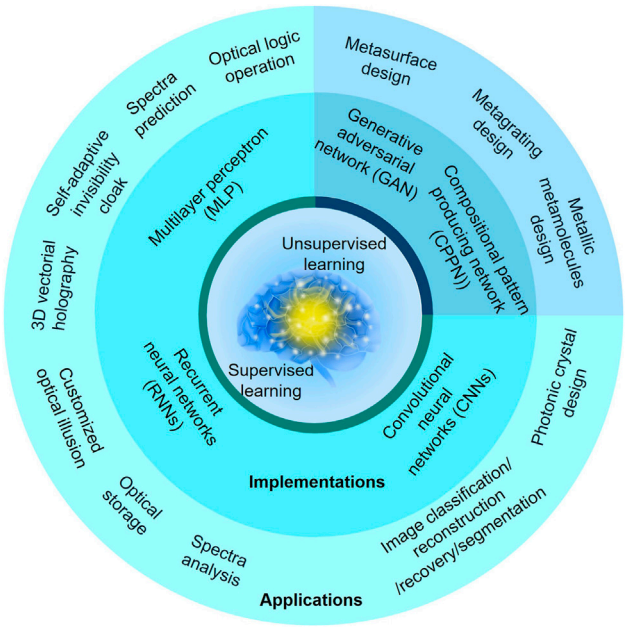

FIGURE 1 | Applications of the deep learning in optical structure design and data analysis.

Recently, the booming field of artificial intelligence has accelerated the pace of technological progresses (Goodfellow et al., 2016). Particularly, deep learning, as a data-driven method, can automatically reveal the inherent connections behind the data by using hierarchically structured layers. It has been widely exploited in the field of computer visions (Luongo et al., 2021), image analysis (Barbastathis et al., 2019), robotic controls (Abbeel et al., 2010), driverless cars (Karmakar et al., 2021) and language translations (Wu et al., 2016; Popel et al., 2020). In the photonics applications, deep learning provides a new perspective for device design and optical data analysis (Anjit et al., 2021). It is capable of searching the nonlinear physical correlations, such as the relationship between photonic structures and their electromagnetic response (Wiecha and Muskens, 2019; Li et al., 2020). The cross-discipline of deep learning and photonics enables researchers to design photonic devices and decode optical data without explicitly modeling the underlying physical processes or manually manipulating the models (Chen et al., 2020). Particular areas of success include the materials and structures design (Malkiel et al., 2018; Ma et al., 2019), optical spectroscopy and image analysis (Ghosh et al., 2019; Moen et al., 2019), data storage (Rivenson et al., 2019; Liao et al., 2019), and optical communications (Khan et al., 2019), as shown in **Figure 1**. The deep neural networks used for these applications are mainly tested and trained in electronic computing systems. Compared with the conventional electronic platforms, the photonic systems have attracted increasing attention due to the low energy consuming, multiple interconnections and high parallelism (Sui et al., 2020; Goi et al., 2021). Recently, various optical neural network (ONN) architectures have been used for high-speed data analysis, such as optical interferometric neural network (Shen et al., 2017) and diffractive optical neural network (Lin et al., 2018).

In this article, we focus on the merging of photonics and deep learning for the optical structures design and data analysis. In **Section 2**, we introduce the typical deep learning algorithms, including supervised learning and unsupervised learning. In **Section 3**, we present the deep learning-assisted photonic structure design and optical data analysis. The optical neural networks are highlighted as novel computing architectures in **Section 4**. In **Section 5**, we discuss the outlook of this flourishing field accompanied with a short conclusion.

2 PRINCIPLES OF TYPICAL NEURAL NETWORKS

In this section, we will introduce several typical deep learning algorithms, and elucidate their working principles for the cross-discipline optical applications. Basically, the algorithms can be divided into supervised learning and unsupervised learning.

In supervised learning, the input training data are accompanied with "correct answer" labels. During the training process, supervised learning compares the predicted results with the ground-true labels in the datasets, and constantly optimizes the network to achieve desired performance. Specifically, it can learn the correlations between photonic structures and optical properties, so as to perform special optical functions. Supervised learning includes multiple artificial neural networks (LeCun et al., 2015), such as multilayer perceptron (MLP), convolutional neural networks (CNNs) and recurrent neural networks (RNNs), as shown in **Figures 2A–C**.

2.1 Multilayer Perceptron

MLP is a fundamental model from which all other artificial neural networks are developed, so it is usually considered as the beginning of deep learning. MLP is composed of a series of hidden layers, which are the link between the inputs and outputs. The neurons in the upper and lower layers are connected to each other through a nonlinear activation function. This model determines a large number of optimizable parameters, which provides high capability to learn the complex and nonlinear relationships in the optical data. In a typical MLP training process, we need to pre-define a cost function by the variance or cross entropy between the predicted and actual values. During the optimization, the weights of the neurons are adjusted by the back propagation algorithm to minimize the cost function. Later, the target optical functions such as the scattering spectra are imported into the network, and the predicted photonic structures are obtained (Wu et al., 2021). Intuitively, with the increase of hidden layers in MLP, the neural network learns more features and realizes higher training accuracy at the cost of training time. Noting that too many hidden layers are prone to cause over-fitting results, thus the appropriate hidden-layer numbers are preferred. To solve the universally non-uniqueness problems, the tandem network model is proposed by cascading an inverse-design network with a forward-modeling network (Liu et al., 2018).

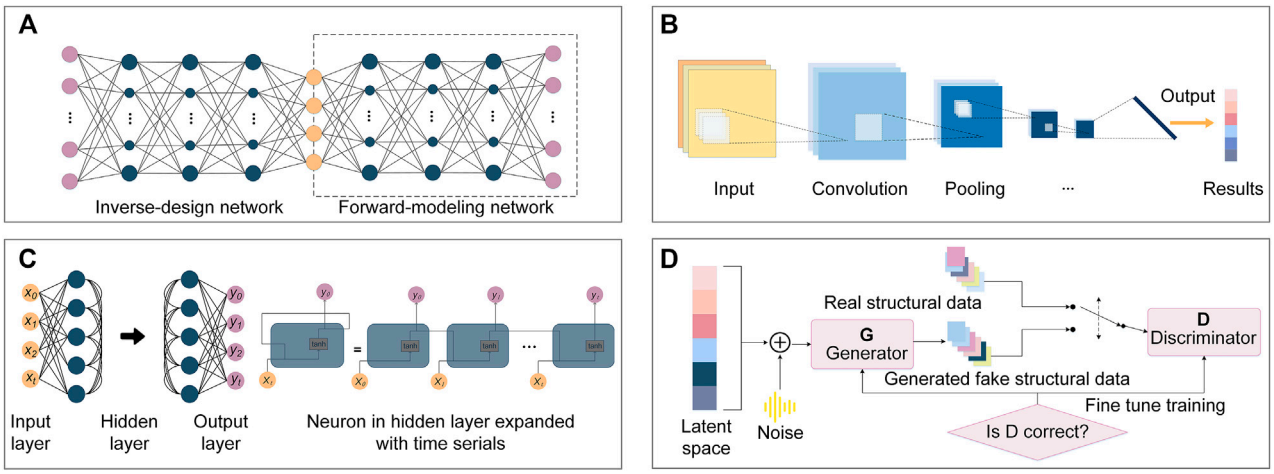

FIGURE 2 | Schematic illustration of typical deep learning models. (A) Multilayer perceptron, (B) Convolutional neural networks, (C) Recurrent neural networks, (D) Generative adversarial network.

2.2 Convolutional Neural Networks

CNNs are specially designed for image classification (Li et al., 2014; Guo et al., 2017) and recognition (Hijazi et al., 2015; Fu et al., 2017), and their performance on special tasks such as image recognition can even surpass humans (Lundervoldab and Lundervoldacd, 2019). The reason why CNNs can effectively process high-dimensional data such as images, is that they can automatically learn the features from large-scale data and generalize them to the same type of unknown data. Generally, CNNs consist of four parts: 1) The convolution layers extract the features of the input images; 2) The activation layers realize nonlinear mapping; 3) The pooling layers aggregate features in different regions to reduce the data dimension; 4) The full connection layer outputs the final classification results. The convolution layers usually contain several convolution kernels, which are also known as filters, and they sequentially extract the features of the input image just like the human brain. In the past years, various derivative networks, such as LeNet (Lecun et al., 1998), AlexNet (Krizhevsky et al., 2012), ZFNet (Zeiler and Fergus, 2014), VGG (Simonyan and Zisserman, 2014), GoogleNet (Szegedy et al., 2015), ResNet (He et al., 2016) and SENet (Hu et al., 2018) are developed on the basic components of CNNs. The network accuracy is improved by manipulating the layer numbers and connection modes. CNNs exhibit two important characteristics: First, the neurons in the neighboring layers are connected locally, which is different from the fully connected neurons in MLP. Second, the weight array in a region is shared to reduce the number of parameters, and it accelerates the convergence of network. Since the complexity of the model is reduced, the over-fitting problem can be released. Theoretically, CNNs are prominent to solve problems relevant to the images, such as optical illusion custom and super-resolution imaging. The network can automatically extract image features, including color, texture, shape and topology, which increases the robustness and operation efficiency in image processing. Recently, CNNs have been applied in photonic crystal (Asano and Noda, 2018) design. By optimizing the positions of air holes in a base nanocavity with CNNs, the extremely high Q-factor of 1.58×10^9 was successfully obtained.

2.3 Recurrent Neural Networks

Just like human beings can better understand the world by virtue of their memory effects, RNNs have certain memory for the past processed information. The output of RNNs is related not only to the current input, but also to the previous inputs. Thus, RNNs are prevalently used to simulate continuous sequential optical signal in the time domain. Since the networks memorize all information in the same way, they usually occupy a lot of memory and reduce the computational efficiency. The long short-term memory network, as a derivative RNNs, can selectively memorize the important information and forget the unimportant information by controlling the gate states (Ochreiter and Schmidhuber, 1997). Moreover, it solves the problem of gradient disappearance and gradient explosion for the long sequence training.

Unsupervised learning is fed with unlabeled training data, which denotes having no standard answer in the training process. Consequently, unsupervised systems are capable of discovering new patterns in the training datasets, some of which can even go beyond prior knowledge and scientific intuition. Moreover, the unsupervised learning focuses on extracting important features from data, rather than directly predicting the optical response, thus it does not need massive data to train the network. In this way, it removes the burden of creating massive labeled data.

2.4 Generative Adversarial Network

GAN is proposed by Goodfellow et al. (2014) to solve unsupervised learning problems. It contains two independent networks as shown in **Figure 2D**, which fight against each other to complete a zero-sum game. The discriminator network distinguishes whether the input structure data is real or fake. The generator network generates fake structure data by selecting and combining elements in the latent space with superposed noise. In the training process, the discriminator receives data from both the real and fake structure data, and judges which category it belongs to. Specifically, if the discriminator is right, adjust the generator to make the fake structure data more real to deceive

TABLE 1 | Comparison of deep learning algorithms.

Algorithms	Unique features	Advantages	Disadvantages	Optical applications
Multilayer perceptron	Full connected neurons, simple structure	High reliability, low latency	Difficult to handle high dimensional data	Nanoparticle simulation(Peurifoy etal., 2018), self-adaptive invisibility cloak(Qian et al., 2020), 3D vectorial holography(Ren et al., 2020)
Convolutional neural networks	Local receptive fields, shared weights	High dimensional data processing	Ignore global and local correlations	Spectra analysis(Fan et al., 2019), optical communications(Fan et al., 2020), data storage(Wiecha e tal., 2019), optical image processing(Buggenthin et al., 2017)
Recurrent neural networks	Intra-layer neurons connected, shared parameters at different cycles	Memorable, sequential information processing	Long-term dependencies, gradient disappearance	Optical character recognition(Singh, 2013), transient electromagnetic modeling(Sharmaand and Zhang, 2005)
Generative model	With two different networks, gradient updated from discriminator rather than training data	Fast convergence speed, incomplete datasets processing	Unsuitable for discrete data, error-prone	Metallic metamolecules design(Liu et al., 2020)

the discriminator; otherwise, adjust the discriminator to avoid making similar mistakes again. The continuous training will reach a balanced state, and a generator with high quality and discriminator with strong judgment ability is achieved. After training, the generator is capable of producing target photonic structures quickly, and the discriminator can accurately judge whether a new input structure matches the target optical response or not.

The typical characteristics of deep learning algorithms including MLP, CNNs, RNNs and generative model are summarized in **Table 1**. Note that MLP and CNNs have been widely used in the photonic devices design and optical data analysis. Further research of RNNs and generation models for photonics applications needs to be explored.

In the inverse design of photonic devices, there have been various optimization algorithms including the classic machine learning approaches (e.g., regularization algorithms, ensemble algorithms, or decision tree algorithms) and the traditional optimization approaches (e.g. topology optimization, adjoint methods or genetic algorithms) to efficiently search the target in large design space. By involving more data, deep learning can usually improve the computing accuracy efficiently, but this method has almost no effect on the conventional machine learning approaches. Moreover, the transfer learning technology enables the well-trained deep learning models to be applied to other scenarios, making it adaptable and easy to transform. In contrast, machine learning can only be applied to a single scene and is weak in transportability. Traditional optimization approaches search the maximal solution iteratively, which modify the searching strategy according to the intermediate results. This strategy consumes huge computational resources and is difficult to be applied for complex designs. People interested in these algorithms can refer to the recent review for more information (Ma L. et al., 2021).

3 PHOTONIC APPLICATIONS OF DEEP LEARNING

In this section, we briefly introduce the deep learning-based applications from photonic structure design to data analysis.

3.1 Deep Learning for Photonic Structure Design

In the past decades, the photonics have developed rapidly, and show a strong capability in tailoring light-matter interactions. Recently, this field has been revolutionized by the data-driven deep learning method. The method can search for the intricate relationship between the photonic structures and the optical responses after training on large samples, which circumvents the time-consuming iterative numerical simulations in photonic structure designs. Moreover, unlike traditional optimization algorithms, which requires repeated iterative training for each computation, data collection and network training for deep learning are only one-time costs. Such data-driven model can serve as a powerful tool for the on-demand design of photonic devices.

3.1.1 Inverse Design of Optical Nanoparticles

Core-shell nanoparticles can exhibit intriguing phenomena, such as multifrequency superscattering (Qin et al., 2021), directional scattering and Fano-like resonance, but its higher degree-of-freedom makes designing difficult. Peurifoy et al. (2018) applied MLP to predict the scattering cross-section of a nanoparticle with silicon dioxide/titanium dioxide multilayered structures, as shown in **Figure 3A**. In this work, MLP was trained on 50,000 scattering cross-section spectra obtained by the transfer matrix method. They achieved dual functions of forward modeling and inverse design. Specifically, MLP was used to approximate the scattering cross section of the core-shell nanoparticle for the input layer parameters. Besides, with the target scattering spectra, MLP would expeditiously output the corresponding structural parameters of the nanoparticle. The results show that MLP is able to calculate spectra accurately even the input structure goes beyond the training data. It suggests that MLP is not just simply fitting the data, but instead discovering some underlying patterns and structures of the input and output data. Note that this model architecture can not achieve the inverse design of materials, and there are certain restrictions on design freedom. So et al. (2019) took a step forward and inversely designed optical material and structural thickness simultaneously by realizing the classification and regression at the same time, as shown in **Figure 3B**. They

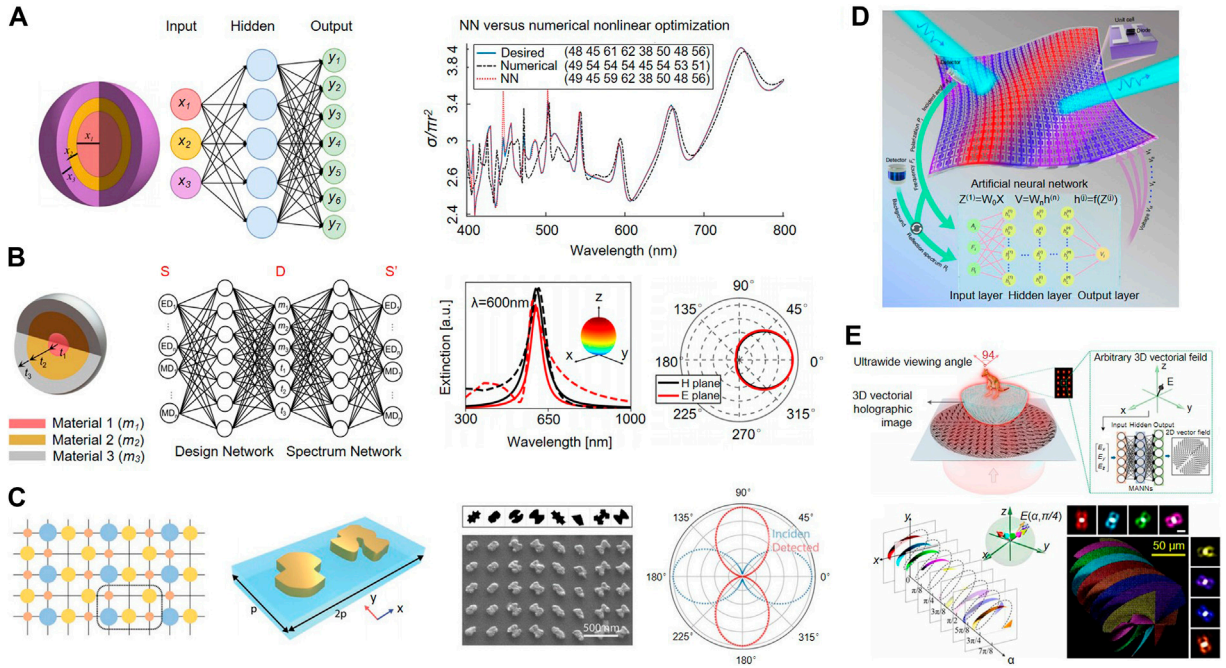

FIGURE 3 | Photonic designs enabled by deep learning models. **(A)** Nanophotonic particle scattering simulation. Reproduced from Peurifoy et al. (2018) with permission from American Association for the Advancement of Science. **(B)** Simultaneous design of material and structure of nanosphere particles. Reproduced from So et al. (2019) with permission from American Chemical Society. **(C)** Inverse design of metallic metamolecules. Reproduced from Liu et al. (2020) with permission from the WILEY-VCH Verlag GmbH & Co. KGaA, Weinheim. **(D)** Self-adaptive invisibility cloak. Reproduced from Qian et al. (2020) with permission from Springer Nature. **(E)** Optical vectorial hologram design of a 3D-kangaroo projection. Reproduced from Ren et al. (2020) with permission from American Association for the Advancement of Science.

used classification to determine what materials were used for each layer, and regression to predict the thickness. The loss function was defined as weighted average of spectrum and design losses. The spectrum loss was calculated by mean squared error of target spectra and predicted response by deep learning, and the design loss was weighted average of material and structural losses. As a result, the material and thickness of the core-shell nanoparticle are designed simultaneously and accurately.

3.1.2 Inverse Design of Metasurface

Over the past 2 decades, the explorations of metasurfaces have led to the discovery of exotic light–matter interactions, such as anomalous deflection (Yu and Capasso, 2014; Wang et al., 2018), asymmetric polarization conversion (Schwanecke et al., 2008; Pfeiffer et al., 2014) and wave-front shaping (Pu et al., 2015; Zhang et al., 2017; Raeker and Grbic, 2019).

From individual nanoparticles to collective meta-atoms metasurfaces, the structural degree of freedom and flexibility are increased drastically. Liu et al. (2020) proposed a hybrid framework, i.e. compositional pattern-producing networks (CPPN) and cooperative coevolution (CC) algorithm, to design metamolecules with significantly increased training efficiency, as shown in **Figure 3C**. The CPPN as a generative network composes high-quality nanostructure patterns, and CC divides the target metamolecule into the independent meta-atoms. The metallic metamolecules for arbitrary manipulation of the polarization and wavefront of light were demonstrated in the hybrid framework. This work provides a promising way to automatically construct the large-scale metasurfaces with high efficiency. Note that the proposed framework is assumed with weak-coupled meta-atoms, the strong coupling and nonlinear optical effects are expected to be involved for the future development. The nature of three-dimensional (3D) vector optical field is crucial to understand the light-matter interaction, which plays a significant role in imaging, holographic optical trapping and high-capacity data storage. Hence, using deep learning to manipulate the complex 3D vector optical fields in photonic structures such as spin and orbital momentum, topology and anisotropic vector fields are ready to be explored. For instance, Ren et al. (2020) designed an optical vectorial hologram of a 3D-kangaroo projection by MLP, as shown in **Figure 3E**. The phase hologram and a 2D vector-field distribution were served as state vector and label vector, respectively, and they were used to train the network model to reconstruct a stereo optical image. This work achieves the lensless reconstruction of a 3D-image with an ultra-wide viewing angle of 94°and a high diffraction efficiency of 78%, which shows great potentials in multiplexed displays and encryption.

Following the pioneering works on the static manipulation of optical field, there is an increasing interest to dynamically manipulate the optical filed, such as the design of invisibility cloak. The invisibility cloak is an intriguing device with great applications in various fields, however, the conventional cloak could not fit into the ever-changing environment. Qian et al.

(2020) used MLP to design a self-adaptive cloak with millisecond response time to the dynamic incident wave and surrounding environment, as shown in **Figure 3D**. To this end, the optical response of each element inside the metasurface was independently tuned by feeding different bias voltages across a loaded varactor diode. With deep learning, the integrated system could exploit the intricate relationship between incident waves, reflection spectra and bias voltages for each individual meta-atom. Thereafter, the proposed intelligent cloak with bandwidth of 6.7–9.2 GHz was realized. The concept of demonstration can be potentially extended to the visible spectra with ingredients of gate-tunable conducting oxide (e.g. indium tin oxide) (Huang et al., 2016) or phase-change materials (e.g., vanadium dioxide) (Cormier et al., 2017).

Deep learning technology exhibits the huge potential in photonic structure design, material optimization, and even the optimization of the entire optical system. Besides the aforementioned work, it has been used for various intricate devices design, such as multi-mode converters (Liu et al., 2019; Zheng et al., 2021), metagratings (Inampudi and Mosallaei, 2018; Jiang et al., 2019), chiral metamaterials (Ma et al., 2018) and photonic crystals (Hao et al., 2019).

3.2 Deep Learning for Optical Data Analysis

The optical techniques have been widely implemented in various fields. Large optical data will be generated when applying optical spectroscopy and imaging to medical diagnosis, information storage and optical communication. The conventional analysis of optical data is often based on the prior experiences and physical intuition. Yet it is time-consuming and error-prone when processing huge amount of the complex optical data, such as optical spectra and images. To tackle this challenge, various deep neural networks have been exploited. In the following part, some important work of deep learning in optical data analysis are introduced.

3.2.1 Complex Spectra Analysis

The optical spectroscopy is the study of interaction between matter and light radiation as a function of the wavelength or frequency. From the spectral analysis, the chemical compositions and relative contents of the target analytes can be deduced. Deep learning provides an alternative way for a better extraction of the encoded information from the massive and complex spectra. For example, Fan et al. (2019) implemented a CNN to analyze the Raman spectra and identify the components of mixtures, as shown in **Figure 4A**. The training datasets contained the spectra of 94 ternary mixtures of methanol, acetonitrile and distilled water. The identification accuracy of CNN was up to 99.9% and the detected volume percentage of methanol was as low as 4%, which went beyond the conventional models, such as k-nearest neighbor. The proposed component identification algorithm is suitable for complex mixtures sensing and is potential for rapid disease diagnosis.

The optical memory provides an intriguing solution for "big data" due to the high information capacity and longevity. However, the diffraction limit of light inevitably restricts the bit density in optical information storage. Wiecha et al. (2019) encoded multiple bits of information in the subwavelength dielectric nanostructures by using a CNN and MLP, as illustrated in **Figure 4B**. The scattering spectra were identified to extract the bit sequence. In the network training, the scattering spectra data propagated forward through the network, and the outputs of highly activated neurons indicated the encoded bit sequence (**Figure 4C**). In this way, they efficiently improved the bit density up to 9-bits with quasi-error-free readout accuracy, which was of 40% higher information density than that of the Blu-ray. Furthermore, they simplified the readout process by probing few wavelengths of nanostructure scattering, i.e., the scattered RGB values of the dark-field microscopy images. This study provides a promising solution for high-density optical information storage based on the planar nanostructures.

3.2.2 Nonlinear Signal Processing

The long-haul optical communications face the fundamental bottlenecks, such as the fiber Kerr nonlinearity and chromatic dispersion. Deep learning, as a powerful tool, has been applied to fiber nonlinearity compensation in optical communications. Fan et al. (2020) utilized the deep learning-based digital back-propagation (DBP) architecture for nonlinear optical signal processing, as shown in **Figure 4E**. For a single-channel 28-GBaud 16-quadrature amplitude modulation system, the developed method demonstrated a 0.9-dB quality factor gain. This architecture was further extended to polarization-division-multiplexed (PDM) and wavelength-division-multiplexed (WDM). The quality factor gain of modified DBP were 0.6 and 0.25 dB for the single channel PDM and WDM system, respectively. This work shows that deep learning provides an effective tool for theoretical understanding of the nonlinear fiber transmission.

In addition, deep learning has promoted the development of intelligent systems in fiber optic communication, such as eye map analyzers. Wang et al. (2017) proposed an intelligent eye-diagram analyzer based on CNNs to achieve the modulation format recognition and optical signal-to-noise rate estimation in optical communications. Four commonly used optical signals by the simulations were obtained, which were then detected by the photodetectors. They collected 6,400 eye-diagram images from the oscilloscope as training sets. Each image in the training datasets had a 20-bits label vector. During the training process, CNNs gradually extracted the effective features of the input images and the back-propagation algorithm was exploited to optimize the kernel parameters. Consequently, the estimation accuracy nearly reached 100%.

3.2.3 Optical Images Processing

Optical imaging technology, such as fluorescence microscopy and super resolution imaging, have been considered as powerful tools in various areas. For example, image classification has been widely used for the medical image recognition. Buggenthin et al. (2017) established a classifier by combining CNNs and RNNs for directly identifying differentiated cells. With massive bright-field images input, the convolutional layers extracted the local features and the concatenation layer combined the highest-level spatial features with cell displacement in differentiation process. The extracted features were fed into the RNNs to

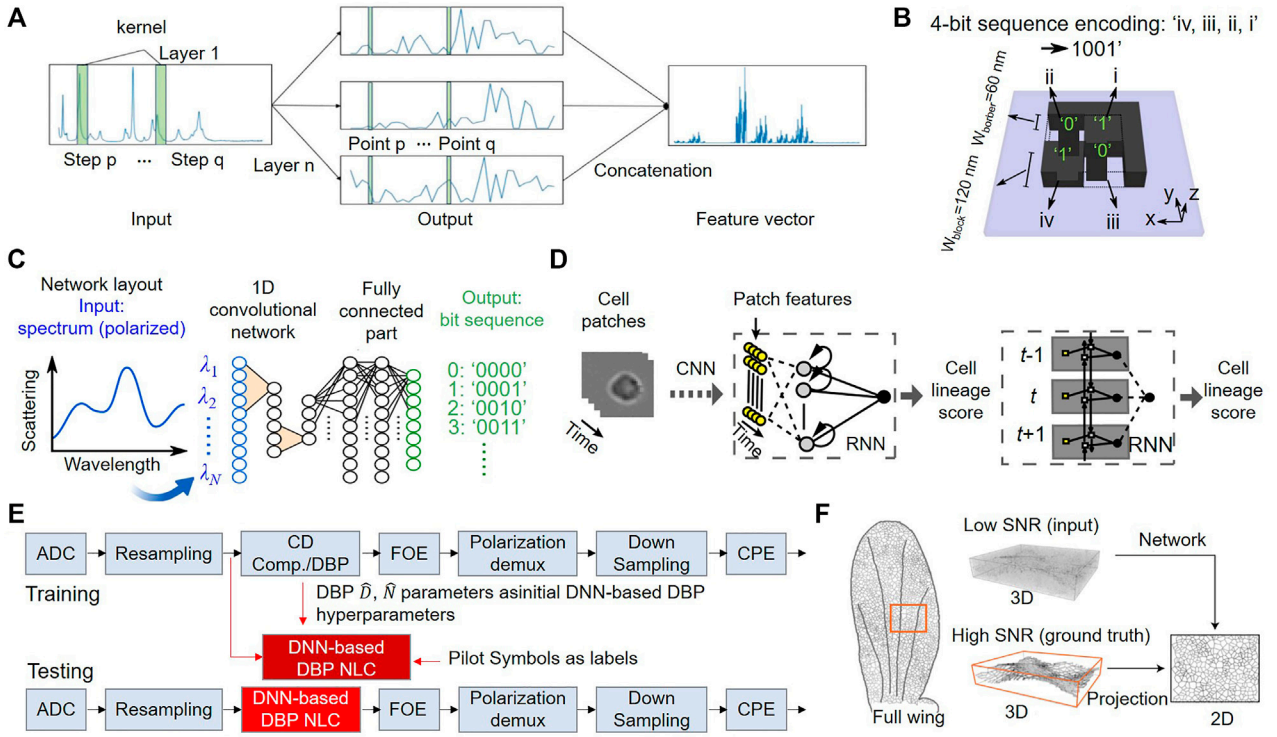

FIGURE 4 | Deep learning for optical data analysis. **(A)** Working principle of CNN used in spectral analysis. Reproduced from Fan et al. (2019) with permission from the Royal Society of Chemistry. **(B)** Schematic of 4-bit nanostructure geometry. **(C)** Illustration of CNN applied for information storage. Reproduced from Wiecha et al. (2019) with permission from Springer Nature. **(D)** Schematic of CNN used for classification of differentiated cells. Reproduced from Buggenthin et al. (2017) with permission from Springer Nature. **(E)** DNN-based DBP architecture. FOE: frequency-offset estimation, CPE: carrier-phase estimation. Reproduced from Fan et al. (2020) with permission from Springer Nature. **(F)** The proposed CARE for image restoration. Reproduced from Weigert et al. (2018) with permission from Springer Nature.

exploit the temporal information of the single-cell tracks for cells lineage prediction, as shown in **Figure 4D**. They achieved the label-free identification of cells with differentially expressed lineage-specifying genes, and the lineage choice could be detected up to three generations. The model allows for analyzing the cell differentiation processes with high robustness and rapid prediction.

In the fluorescence microscopy, the observable phenomena of fluorescence microscopy is limited by the chemistry of fluorophores, and the maximum photon exposure that the sample can withstand. The cross-discipline of deep learning and bio-imaging provides an opportunity to overcome this tackle. For instance, Weigert et al. (2018) proposed a content-aware image restoration (CARE) method to restore the microscopy images with enhanced performance. In **Figure 4F**, the CNN architecture was trained on the well-registered pairs of images: a low signal-to-noise ratio (SNR) image as input and high SNR one as output. The CARE networks could maintain the microscopy images of high SNR even if the 60-fold light dosage was decreased. Besides, the isotropic resolution could be realized with the tenfold fewer axial slices. Impressively, they achieved the imaging speed by CARE of 20-times faster than that of the state-of-the-art reconstruction methods. The proposed CARE networks can extend the range of biological phenomena observable by microscopy, and can be automatically adapted to various image contents.

4 OPTICAL NEURAL NETWORKS

Integrated circuit chip is the mainstream hardware carrier, such as graphical processing units, central processing units and application-specific integrated circuits (Misra and Saha, 2010). However, the conventional electronic computing systems on von Nemumann architectures are insufficient for training and testing neural networks (Neumann, 2012). It is because that they separate the data space from the program space, and the tidal data load is generated between the computing unit and the memory. Photons exhibit the unique abilities of realizing multiple interconnections and simultaneously parallel calculations at the speed of light (Xu et al., 2021). Thus, the optical neural networks (ONNs) constructed by the photonic devices, have opened a new road to achieving orders-of-magnitude improvements in both computation speed and energy consumption over the existing solutions (Cardenas et al., 2009; Yang et al., 2013). The ONNs have shown the potential for addressing the ever-growing demand of high-speed data analysis in complex applications, such as medical diagnosis, autonomous

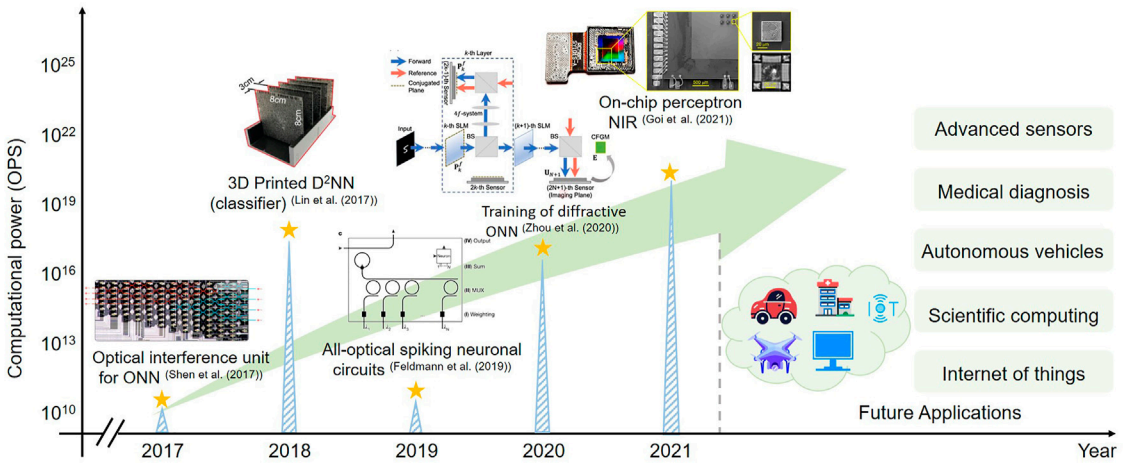

FIGURE 5 | Development of photonic chip computing power and their representative application.

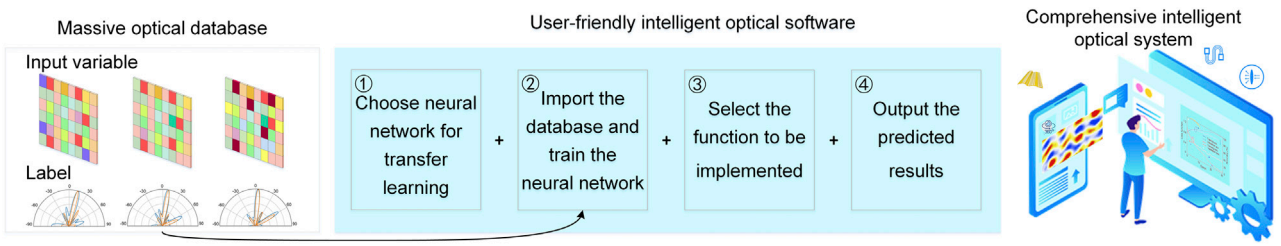

FIGURE 6 | An conceived user-friendly software system for photonic structure design.

driving, and high-performance computing, as shown in **Figure 5**. The platforms to achieving ONNs mainly include photonic circuits and optical diffractive layers as discussed following.

Recently, Shen et al. (2017) experimentally demonstrated an ONN by using a cascaded array of 56 programmable Mach-Zehnder interferometers on an integrated chip. Theoretically, they estimated that the proposed ONN could achieve 10^{11} N-dimension matrix-vector multiplications per second, which was two orders of magnitude faster than the state-of-the-art electronic devices. To test the performance, they verified the utility in vowel recognition with measured accuracy of 76.7%. They claimed that the system could achieve a correctness of 90% with calibrations to reduce the thermal cross-talk, which was comparable to conventional 64-bits computer with accuracy of 91.7%. Noted that the optical nonlinearity unit by a saturable absorber was only modelled on a computer, and the power dissipation of data movement was significant in the current ONNs. There is still a long way to exploring the optical interconnects and optical computing units to realize the supremacy of ONNs.

In addition to the photonic integrated circuit, the physical diffractive layers also provides a method for implementing neural networks algorithms. The optical diffraction of planar structures is mathematically a convolutional processing of input modulated fields and propagation functions. Thus the diffractive layers can be intuitively used to train ONNs. Lin et al. (2018) pioneered the study of all-optical diffractive deep neural network (D^2NN) architectures. The learning framework was based on multiple layers of 3D-printed diffractive surfaces, which was designed through a computer. They demonstrated that the trained D^2NN could achieve the automated classification of handwritten digits (accuracy of 93.39%) and complex images datasets (Fashion MNIST, accuracy of 86.6%) with the 10 diffractive layers and 0.4 million neurons. The proposed D^2NN shows the ability to operates at the speed of light, and it can be easily extended to billions of neurons and connections (Lin et al., 2018).

5 OUTLOOK AND CONCLUSION

Deep learning usually needs large amounts of data support. However, it is impractical to collect massive databases by either physical simulations or experimental measurements. There are mainly two approaches to solving this problem. First, transfer learning allows migrating the knowledge of neural network trained from a certain physical process to other similar cases (Torrey and Shavlik, 2010). Specifically, the

neural network pre-trained on high-quality datasets shows strong generalization ability, which can solve new problems with small datasets. Thus the data collection can be substantially reduced. Second, the burden of massive data collection can also be relieved by combining deep learning model with basic physical rules. For example, deep learning can be used as an intermediate step to effectively solve the Maxwell's equations (So et al., 2020), rather than to directly find a mapping of optical structures and properties.

In the past few years, intelligent photonics has made great progress benefited from the interdisciplinary collaborations from researchers in the field of computer science and physical optics. To relieve the researchers from tedious and complex algorithm programming, a user-friendly system is highly on demand. This system should basically contain two parts: open-source resources and user-friendly interface, as shown in **Figure 6**. Inspired by computer-science community, researchers are encouraged to share their datasets and neural networks to establish a comprehensive optical open-source community. Furthermore, the abundant open-source networks enable transfer learning to solve the various problems. The basic idea is to migrate data characteristics from related domains to improve the learning effect of the target tasks. Thereafter, when a deep learning network is needed to train and solve a specific photonic problem, we can directly call the relative database and well-trained neural networks from the open-source resources, which avoids the ab initio building of data collection.

In the context of photonic structures, people are not only interested in some specific designs and their performances, but also in the general mechanism or principle that leads to the functionalities. The neural networks are considered as black-box models, which fit the training sets to directly provide the expected results. There is relentless effort for researchers to study the interpretability of neural networks. For instance, Zhou et al. (2016) proved that by using global average pooling, CNNs could retain remarkable localization ability, which exposed the implicit attention of CNNs on image-level labels. The remarkable localization ability are probably transferred to physical interpretability of the photonic devices design.

In this review, we have surveyed the recent development of deep learning in the field of photonics, including photonic structure design and optical data analysis. Optical neural networks are also emerging to reform the conventional electronic-circuit architecture for deep learning with high computational power and low energy consumption. We have witnessed the interactions between the deep learning and photonics, and look forward to more exciting works in the interdisciplinary field.

AUTHOR CONTRIBUTIONS

Conceptualization, D-QY and J-hC; methodology, BD and BW; original draft preparation, BD, BW and J-hC; writing-review and editing, D-QY, J-hC and HC. All authors have read and agreed to the submitted version of the manuscript.

FUNDING

The authors would like to thank the support from National Natural Science Foundation of China (11974058, 62005231); Beijing Nova Program (Z201100006820125) from Beijing Municipal Science and Technology Commission; Beijing Natural Science Foundation (Z210004); State Key Laboratory of Information Photonics and Optical Communications (IPOC2021ZT01), BUPT, China; Fundamental Research Funds for the Central Universities (20720200074, 20720210045); Guangdong Basic and Applied Basic Research Foundation (2021A1515012199).

REFERENCES

Abbeel, P., Coates, A., and Ng, A. Y. (2010). Autonomous Helicopter Aerobatics through Apprenticeship Learning. *Int. J. Robotics Res.* 29, 1608–1639. doi:10.1177/0278364910371999

Anjit, T. A., Benny, R., Cherian, P., and Mythili, P. (2021). Non-iterative Microwave Imaging Solutions for Inverse Problems Using Deep Learning. *Pier M* 102, 53–63. doi:10.2528/pierm21021304

Asano, T., and Noda, S. (2018). Optimization of Photonic crystal Nanocavities Based on Deep Learning. *Opt. Express* 26, 32704–32717. doi:10.1364/OE.26.032704

Barbastathis, G., Ozcan, A., and Situ, G. (2019). On the Use of Deep Learning for Computational Imaging. *Optica* 6, 921–943. doi:10.1364/OPTICA.6.000921

Bigio, I., and Sergio, F. (2016). *Quantitative Biomedical Optics: Theory, Methods, and Applications*. Cambridge: Cambridge University Press.

Buggenthin, F., Buettner, F., Hoppe, P. S., Endele, M., Kroiss, M., Strasser, M., et al. (2017). Prospective Identification of Hematopoietic Lineage Choice by Deep Learning. *Nat. Methods* 14, 403–406. doi:10.1038/nmeth.4182

Cardenas, J., Poitras, C. B., Robinson, J. T., Preston, K., Chen, L., and Lipson, M. (2009). Low Loss Etchless Silicon Photonic Waveguides. *Opt. Express* 17, 4752–4757. doi:10.1364/OE.17.004752

Chan, S., and Siegel, E. L. (2019). Will Machine Learning End the Viability of Radiology as a Thriving Medical Specialty? *Bjr* 92, 20180416. doi:10.1259/bjr.20180416

Chen, X., Wei, Z., Li, M., and Rocca, P. (2020). A Review of Deep Learning Approaches for Inverse Scattering Problems (Invited Review). *Pier* 167, 67–81. doi:10.2528/PIER20030705

Cormier, P., Son, T. V., Thibodeau, J., Doucet, A., Truong, V.-V., and Haché, A. (2017). Vanadium Dioxide as a Material to Control Light Polarization in the Visible and Near Infrared. *Opt. Commun.* 382, 80–85. doi:10.1016/j.optcom.2016.07.070

Dong, P., Chen, Y.-K., Duan, G.-H., and Neilson, D. T. (2014). Silicon Photonic Devices and Integrated Circuits. *Nanophotonics* 3, 215–228. doi:10.1515/nanoph-2013-0023

Fan, Q., Zhou, G., Gui, T., Lu, C., and Lau, A. P. T. (2020). Advancing Theoretical Understanding and Practical Performance of Signal Processing for Nonlinear Optical Communications through Machine Learning. *Nat. Commun.* 11, 3694. doi:10.1038/s41467-020-17516-7

Fan, X., Ming, W., Zeng, H., Zhang, Z., and Lu, H. (2019). Deep Learning-Based Component Identification for the Raman Spectra of Mixtures. *Analyst* 144, 1789–1798. doi:10.1039/C8AN02212G

Fang, J., Swain, A., Unni, R., and Zheng, Y. (2021). Decoding Optical Data with Machine Learning. *Laser Photon. Rev.* 15, 2000422. doi:10.1002/lpor.202000422

Fu, J., Zheng, H., and Mei, T. "Look Closer to See Better: Recurrent Attention Convolutional Neural Network for fine-grained Image Recognition," in Proceedings of the IEEE Conference on Computer Vision and Pattern Recognition, Honolulu, HI, USA, July 2017, 4438–4446.

Ghosh, K., Stuke, A., Todorović, M., Jørgensen, P. B., Schmidt, M. N., Vehtari, A., et al. (2019). Deep Learning Spectroscopy: Neural Networks for Molecular Excitation Spectra. *Adv. Sci.* 6, 1801367. doi:10.1002/advs.201801367

Goi, E., Chen, X., Zhang, Q., Cumming, B. P., Schoenhardt, S., Luan, H., et al. (2021). Nanoprinted High-Neuron-Density Optical Linear Perceptrons Performing Near-Infrared Inference on a CMOS Chip. *Light Sci. Appl.* 10, 1–11. doi:10.1038/s41377-021-00483-z

Goodfellow, I. J., Bengio, Y., and Courville, A. (2016). *Deep Learning*. Cambridge, Massachusetts: MIT press.

Goodfellow, I., Pouget-Abadie, J., Mirza, M., Xu, B., Warde-Farley, D., Ozair, S., et al. (2014). Generative Adversarial Nets. *Adv. Neural Inf. Process. Syst.* 27 [, 2014 arXiv:1406.2661].

Guo, T., Dong, J., Li, H., and Gao, Y. "Simple Convolutional Neural Network on Image Classification," in 2017 IEEE 2nd International Conference on Big Data Analysis (ICBDA), Beijing, China, March 2017, 721–724.

Hao, J., Zheng, L., Yang, D., and Guo, Y. "Inverse Design of Photonic Crystal Nanobeam Cavity Structure via Deep Neural Network," in Proceedings of the Asia Communications and Photonics Conference, ed. M4A.296 (Optical Society of America), Chengdu, China, November 2019, 1597–1600.

He, K., Zhang, X., Ren, S., and Sun, J. "Deep Residual Learning for Image Recognition," in Proceedings of the IEEE Conference on Computer Vision and Pattern Recognition, June 2016Las Vegas, NV, USA, 770–778.

Hijazi, S., Kumar, R., and Rowen, C. (2015). *Using Convolutional Neural Networks for Image Recognition*. San Jose, CA, USA: Cadence Design Systems Inc., 1–12.

Hochreiter, S., and Schmidhuber, J. (1997). Long Short-Term Memory. *Neural Comput.* 9, 1735–1780. doi:10.1162/neco.1997.9.8.1735

Hu, J., Shen, L., and Sun, G. "Squeeze-and-excitation Networks," in Proceedings of the IEEE Conference on Computer Vision and Pattern Recognition, Salt Lake City, UT, USA, June 2018, 7132–7141.

Huang, Y.-W., Lee, H. W. H., Sokhoyan, R., Pala, R. A., Thyagarajan, K., Han, S., et al. (2016). Gate-tunable Conducting Oxide Metasurfaces. *Nano Lett.* 16, 5319–5325. doi:10.1021/acs.nanolett.6b00555

Inampudi, S., and Mosallaei, H. (2018). Neural Network Based Design of Metagratings. *Appl. Phys. Lett.* 112, 241102. doi:10.1063/1.5033327

Jiang, J., Chen, M., and Fan, J. A. (2021). Deep Neural Networks for the Evaluation and Design of Photonic Devices. *Nat. Rev. Mater.* 6, 679–700. doi:10.1038/s41578-020-00260-1

Jiang, J., Sell, D., Hoyer, S., Hickey, J., Yang, J., and Fan, J. A. (2019). Free-form Diffractive Metagrating Design Based on Generative Adversarial Networks. *ACS Nano* 13, 8872–8878. doi:10.1021/acsnano.9b02371

Karmakar, G., Chowdhury, A., Das, R., Kamruzzaman, J., and Islam, S. (2021). Assessing Trust Level of a Driverless Car Using Deep Learning. *IEEE Trans. Intell. Transport. Syst.* 22, 4457–4466. doi:10.1109/TITS.2021.3059261

Khan, F. N., Fan, Q., Lu, C., and Lau, A. P. T. (2019). An Optical Communication's Perspective on Machine Learning and its Applications. *J. Lightwave Technol.* 37, 493–516. doi:10.1109/JLT.2019.2897313

Krizhevsky, A., Sutskever, I., and Hinton, G. E. (2012). Imagenet Classification with Deep Convolutional Neural Networks. *Adv. Neural Inf. Process. Syst.* 25, 1097–1105. doi:10.1145/3065386

LeCun, Y., Bengio, Y., and Hinton, G. (2015). Deep Learning. *Nature* 521, 436–444. doi:10.1038/nature14539

Lecun, Y., Bottou, L., Bengio, Y., and Haffner, P. (1998). Gradient-based Learning Applied to Document Recognition. *Proc. IEEE* 86, 2278–2324. doi:10.1109/5.726791

Li, J., Li, Y., Cen, Y., Zhang, C., Luo, T., and Yang, D. (2020). Applications of Neural Networks for Spectrum Prediction and Inverse Design in the Terahertz Band. *IEEE Photon. J.* 12, 1–9. doi:10.1109/JPHOT.2020.3022053

Li, Q., Cai, W., Wang, X., Zhou, Y., Feng, D. D., and Chen, M. "Medical Image Classification with Convolutional Neural Network," in Proceedings of the 2014 13th International Conference on Control Automation Robotics & Vision (ICARCV), Singapore, December 2014, 844–848.

Liao, Z., Zhang, R., He, S., Zeng, D., Wang, J., and Kim, H.-J. (2019). Deep Learning-Based Data Storage for Low Latency in Data center Networks. *IEEE Access* 7, 26411–26417. doi:10.1109/ACCESS.2019.2901742

Lin, X., Rivenson, Y., Yardimci, N. T., Veli, M., Luo, Y., Jarrahi, M., et al. (2018). All-optical Machine Learning Using Diffractive Deep Neural Networks. *Science* 361, 1004–1008. doi:10.1126/science.aat8084

Liu, D., Tan, Y., Khoram, E., and Yu, Z. (2018). Training Deep Neural Networks for the Inverse Design of Nanophotonic Structures. *ACS Photon.* 5, 1365–1369. doi:10.1021/acsphotonics.7b01377

Liu, Y., Xu, K., Wang, S., Shen, W., Xie, H., Wang, Y., et al. (2019). Arbitrarily Routed Mode-Division Multiplexed Photonic Circuits for Dense Integration. *Nat. Commun.* 10, 3263. doi:10.1038/s41467-019-11196-8

Liu, Z., Zhu, D., Lee, K. T., Kim, A. S., Raju, L., and Cai, W. (2020). Compounding Meta-Atoms into Metamolecules with Hybrid Artificial Intelligence Techniques. *Adv. Mater.* 32, 1904790. doi:10.1002/adma.201904790

Lundervold, A. S., and Lundervold, A. (2019). An Overview of Deep Learning in Medical Imaging Focusing on MRI. *Z. für Medizinische Physik* 29, 102–127. doi:10.1016/j.zemedi.2018.11.002

Luongo, F., Hakim, R., Nguyen, J. H., Anandkumar, A., and Hung, A. J. (2021). Deep Learning-Based Computer Vision to Recognize and Classify Suturing Gestures in Robot-Assisted Surgery. *Surgery* 169, 1240–1244. doi:10.1016/j.surg.2020.08.016

Ma, L., Li, J., Liu, Z., Zhang, Y., Zhang, N., Zheng, S., et al. (2021a). Intelligent Algorithms: New Avenues for Designing Nanophotonic Devices. *China Opt. Express* 19, 011301. doi:10.3788/COL202119.011301

Ma, W., Cheng, F., and Liu, Y. (2018). Deep-learning-enabled On-Demand Design of Chiral Metamaterials. *ACS Nano* 12, 6326–6334. doi:10.1021/acsnano.8b03569

Ma, W., Cheng, F., Xu, Y., Wen, Q., and Liu, Y. (2019). Probabilistic Representation and Inverse Design of Metamaterials Based on a Deep Generative Model with Semi-Supervised Learning Strategy. *Adv. Mater.* 31, 1901111. doi:10.1002/adma.201901111

Ma, W., Liu, Z., Kudyshev, Z. A., Boltasseva, A., Cai, W., and Liu, Y. (2021b). Deep Learning for the Design of Photonic Structures. *Nat. Photon.* 15, 77–90. doi:10.1038/s41566-020-0685-y

Malkiel, I., Mrejen, M., Nagler, A., Arieli, U., Wolf, L., and Suchowski, H. (2018). Plasmonic Nanostructure Design and Characterization via Deep Learning. *Light Sci. Appl.* 7, 60. doi:10.1038/s41377-018-0060-7

Misra, J., and Saha, I. (2010). Artificial Neural Networks in Hardware: a Survey of Two Decades of Progress. *Neurocomputing* 74, 239–255. doi:10.1016/j.neucom.2010.03.021

Moen, E., Bannon, D., Kudo, T., Graf, W., Covert, M., and Van Valen, D. (2019). Deep Learning for Cellular Image Analysis. *Nat. Methods* 16, 1233–1246. doi:10.1038/s41592-019-0403-1

Neumann, J. V. (2012). *The Computer and the Brain*. New Haven, Connecticut: Yale University Press.

Ntziachristos, V. (2010). Going Deeper Than Microscopy: the Optical Imaging Frontier in Biology. *Nat. Methods* 7, 603–614. doi:10.1038/nmeth.1483

Peurifoy, J., Shen, Y., Jing, L., Yang, Y., Cano-Renteria, F., DeLacy, B. G., et al. (2018). Nanophotonic Particle Simulation and Inverse Design Using Artificial Neural Networks. *Sci. Adv.* 4, eaar4206. doi:10.1126/sciadv.aar4206

Pfeiffer, C., Zhang, C., Ray, V., Guo, L. J., and Grbic, A. (2014). High Performance Bianisotropic Metasurfaces: Asymmetric Transmission of Light. *Phys. Rev. Lett.* 113, 023902. doi:10.1103/PhysRevLett.113.023902

Popel, M., Tomkova, M., Tomek, J., Kaiser, Ł., Uszkoreit, J., Bojar, O., et al. (2020). Transforming Machine Translation: a Deep Learning System Reaches News Translation Quality Comparable to Human Professionals. *Nat. Commun.* 11, 4381. doi:10.1038/s41467-020-18073-9

Pu, M., Li, X., Ma, X., Wang, Y., Zhao, Z., Wang, C., et al. (2015). Catenary Optics for Achromatic Generation of Perfect Optical Angular Momentum. *Sci. Adv.* 1, e1500396. doi:10.1126/sciadv.1500396

Qian, C., Zheng, B., Shen, Y., Jing, L., Li, E., Shen, L., et al. (2020). Deep-learning-enabled Self-Adaptive Microwave Cloak without Human Intervention. *Nat. Photon.* 14, 383–390. doi:10.1038/s41566-020-0604-2

Qin, Y., Xu, J., Liu, Y., and Chen, H. (2021). Multifrequency Superscattering Pattern Shaping. *China Opt. Express* 19, 123601. doi:10.3788/col202119.123601

Raeker, B. O., and Grbic, A. (2019). Compound Metaoptics for Amplitude and Phase Control of Wave Fronts. *Phys. Rev. Lett.* 122, 113901. doi:10.1103/PhysRevLett.122.113901

Ravì, D., Wong, C., Deligianni, F., Berthelot, M., Andreu-Perez, J., Lo, B., et al. (2017). Deep Learning for Health Informatics. *IEEE J. Biomed. Health Inform.* 21, 4–21. doi:10.1109/JBHI.2016.2636665

Ren, H., Shao, W., Li, Y., Salim, F., and Gu, M. (2020). Three-dimensional Vectorial Holography Based on Machine Learning Inverse Design. *Sci. Adv.* 6, eaaz4261. doi:10.1126/sciadv.aaz4261

Rickard, J. J. S., Di-Pietro, V., Smith, D. J., Davies, D. J., Belli, A., and Oppenheimer, P. G. (2020). Rapid Optofluidic Detection of Biomarkers for Traumatic Brain Injury via Surface-Enhanced Raman Spectroscopy. *Nat. Biomed. Eng.* 4, 610–623. doi:10.1038/s41551-019-0510-4

Rivenson, Y., Wang, H., Wei, Z., de Haan, K., Zhang, Y., Wu, Y., et al. (2019). Virtual Histological Staining of Unlabelled Tissue-Autofluorescence Images via Deep Learning. *Nat. Biomed. Eng.* 3, 466–477. doi:10.1038/s41551-019-0362-y

Schwanecke, A. S., Fedotov, V. A., Khardikov, V. V., Prosvirnin, S. L., Chen, Y., and Zheludev, N. I. (2008). Nanostructured Metal Film with Asymmetric Optical Transmission. *Nano Lett.* 8, 2940–2943. doi:10.1021/nl801794d

Sharma, H., and Zhang, Q. "Transient Electromagnetic Modeling Using Recurrent Neural Networks," in Proceedings of the IEEE MTT-S International Microwave Symposium Digest, 2005, Long Beach, CA, USA, June 2005, 1597–1600.

Shen, Y., Harris, N. C., Skirlo, S., Prabhu, M., Baehr-Jones, T., Hochberg, M., et al. (2017). Deep Learning with Coherent Nanophotonic Circuits. *Nat. Photon* 11, 441–446. doi:10.1038/nphoton.2017.93

Simonyan, K., and Zisserman, A. (2014). Very Deep Convolutional Networks for Large-Scale Image Recognition. *arXiv*, 1097–1105. preprint arXiv:1409.1556.

Singh, S. (2013). Optical Character Recognition Techniques: a Survey. *J. emerging Trends Comput. Inf. Sci.* 4, 545–550. doi:10.1142/S0218001491000041

So, S., Badloe, T., Noh, J., Bravo-Abad, J., and Rho, J. (2020). Deep Learning Enabled Inverse Design in Nanophotonics. *Nanophotonics* 9, 1041–1057. doi:10.1515/nanoph-2019-0474

So, S., Mun, J., and Rho, J. (2019). Simultaneous Inverse Design of Materials and Structures via Deep Learning: Demonstration of Dipole Resonance Engineering Using Core-Shell Nanoparticles. *ACS Appl. Mater. Inter.* 11, 24264–24268. doi:10.1021/acsami.9b05857

Sui, X., Wu, Q., Liu, J., Chen, Q., and Gu, G. (2020). A Review of Optical Neural Networks. *IEEE Access* 8, 70773–70783. doi:10.1109/ACCESS.2020.2987333

Szegedy, C., Liu, W., Jia, Y., Sermanet, P., Reed, S., Anguelov, D., et al. "Going Deeper with Convolutions," in Proceedings of the IEEE Conference on Computer Vision and Pattern Recognition, Boston, MA, June 2015, 1–9.

Török, P., and Kao, F. J. (2007). *Optical Imaging and Microscopy: Techniques and Advanced Systems*. New York: Springer.

Torrey, L., and Shavlik, J. (2010). "Transfer Learning," in *Handbook of Research on Machine Learning Applications and Trends: Algorithms, Methods, and Techniques (IGI Global)*. Editors E. S. Olivas, J. D. M. Guerrero, M. M. Sober, J. R. M. Benedito, and A. J. S. Lopez (Hershey, PA: IGI Publishing), 242–264. doi:10.4018/978-1-60566-766-9.ch011

Vukusic, P., and Sambles, J. R. (2003). Photonic Structures in Biology. *Nature* 424, 852–855. doi:10.1038/nature01941

Wang, D., Zhang, M., Li, Z., Li, J., Fu, M., Cui, Y., et al. (2017). Modulation Format Recognition and OSNR Estimation Using CNN-Based Deep Learning. *IEEE Photon. Technol. Lett.* 29, 1667–1670. doi:10.1109/LPT.2017.2742553

Wang, S., Wu, P. C., Su, V.-C., Lai, Y.-C., Chen, M.-K., Kuo, H. Y., et al. (2018). A Broadband Achromatic Metalens in the Visible. *Nat. Nanotech* 13, 227–232. doi:10.1038/s41565-017-0052-4

Weigert, M., Schmidt, U., Boothe, T., Müller, A., Dibrov, A., Jain, A., et al. (2018). Content-aware Image Restoration: Pushing the Limits of Fluorescence Microscopy. *Nat. Methods* 15, 1090–1097. doi:10.1038/s41592-018-0216-7

Wiecha, P. R., Lecestre, A., Mallet, N., and Larrieu, G. (2019). Pushing the Limits of Optical Information Storage Using Deep Learning. *Nat. Nanotechnol.* 14, 237–244. doi:10.1038/s41565-018-0346-1

Wiecha, P. R., and Muskens, O. L. (2019). Deep Learning Meets Nanophotonics: a Generalized Accurate Predictor for Near fields and Far fields of Arbitrary 3D Nanostructures. *Nano Lett.* 20, 329–338. doi:10.1021/acs.nanolett.9b03971

Wu, B., Hao, Z.-L., Chen, J.-H., Bao, Q.-L., Liu, Y.-N., and Chen, H.-Y. (2022). Total Transmission from Deep Learning Designs. *J. Electron. Sci. Technol.* 20, 100146. doi:10.1016/j.jnlest.2021.100146

Wu, Y., Schuster, M., Chen, Z., Le, Q. V., Norouzi, M., Macherey, W., et al. (2016). Google's Neural Machine Translation System: Bridging the gap between Human and Machine Translation. *arXiv*. preprint arXiv:1609.08144.

Xu, X., Tan, M., Corcoran, B., Wu, J., Boes, A., Nguyen, T. G., et al. (2021). 11 TOPS Photonic Convolutional Accelerator for Optical Neural Networks. *Nature* 589, 44–51. doi:10.1038/s41586-020-03063-0

Yang, L., Zhang, L., and Ji, R. (2013). On-chip Optical Matrix-Vector Multiplier. *Proc. SPIE* 8855. doi:10.1117/12.2028585

Yoon, G., Lee, D., Nam, K. T., and Rho, J. (2018). Pragmatic Metasurface Hologram at Visible Wavelength: the Balance between Diffraction Efficiency and Fabrication Compatibility. *ACS Photon.* 5, 1643–1647. doi:10.1021/acsphotonics.7b01044

Yu, N., and Capasso, F. (2014). Flat Optics with Designer Metasurfaces. *Nat. Mater* 13, 139–150. doi:10.1038/nmat3839

Zeiler, M. D., and Fergus, R. (2014). "Visualizing and Understanding Convolutional Networks," in *European Conference on Computer Vision* (Springer), 818–833. doi:10.1007/978-3-319-10590-1_53

Zhang, F., Pu, M., Li, X., Gao, P., Ma, X., Luo, J., et al. (2017). All-dielectric Metasurfaces for Simultaneous Giant Circular Asymmetric Transmission and Wavefront Shaping Based on Asymmetric Photonic Spin-Orbit Interactions. *Adv. Funct. Mater.* 27, 1704295. doi:10.1002/adfm.201704295

Zhang, X., and Liu, Z. (2008). Superlenses to Overcome the Diffraction Limit. *Nat. Mater* 7, 435–441. doi:10.1038/nmat2141

Zheng, Z.-h., Chen, Y., Chen, H.-y., and Chen, J.-H. (2021). Ultra-compact Reconfigurable Device for Mode Conversion and Dual-Mode DPSK Demodulation via Inverse Design. *Opt. Express* 29, 17718–17725. doi:10.1364/OE.420874

Zhou, B., Khosla, A., Lapedriza, A., Oliva, A., and Torralba, A. "Learning Deep Features for Discriminative Localization," in Proceedings of the IEEE conference on computer vision and pattern recognition, Las Vegas, NV, USA, December 2016, 2921–2929.

Conflict of Interest: The authors declare that the research was conducted in the absence of any commercial or financial relationships that could be construed as a potential conflict of interest.

frontiers in Materials

REVIEW
published: 12 January 2022
doi: 10.3389/fmats.2021.795397

Self-Healing Coatings Based on Stimuli-Responsive Release of Corrosion Inhibitors: A Review

Yue Zhang, Mei Yu, Chao Chen, SongMei Li and JianHua Liu*

School of Materials Science and Engineering, Beihang University, Beijing, China

Corrosion inhibitors loaded in coatings promote the protection performance of coatings, avoid the local corrosion of metal substrates, and endow the self-healing properties of the coatings. The stimuli-responsive release of corrosion inhibitors, which is generally achieved by loading corrosion inhibitors in containers, is key to the self-healing and long-term protection of the coatings. The loading and release methods of corrosion inhibitors are discussed in the article. First, two kinds of loading methods for corrosion inhibitors are reviewed, which are one-step synthetic methods and multistep synthetic methods. Then the released methods of corrosion inhibitors, which can be achieved by intrinsic properties and surface modification of containers, are summarized.

Keywords: self-healing coatings, corrosion inhibitors, containers, loading methods, stimuli-responsive release

OPEN ACCESS

Edited by:
Jinglei Yang,
Hong Kong University of Science and Technology, Hong Kong SAR, China

Reviewed by:
Viswanathan S. Saji,
King Fahd University of Petroleum and Minerals (KFUPM), Saudi Arabia
Wu Junsheng,
University of Science and Technology Beijing, China
Sun Dawei,
Beijing University of Technology, China
Ioannis A. Kartsonakis,
National Technical University of Athens, Greece

****Correspondence:***
Mei Yu
yumei@buaa.edu.cn

Specialty section:
This article was submitted to Smart Materials, a section of the journal Frontiers in Materials

Received: *15 October 2021*
Accepted: *15 December 2021*
Published: *12 January 2022*

Citation:
Zhang Y, Yu M, Chen C, Li S and Liu J (2022) Self-Healing Coatings Based on Stimuli-Responsive Release of Corrosion Inhibitors: A Review. Front. Mater. 8:795397. doi: 10.3389/fmats.2021.795397

INTRODUCTION

Organic coatings on metal surfaces physically isolate the metal substrate from the external corrosion environment, which is one of the most widely used measures in metal corrosion prevention (Abdolah et al., 2016; Zhang et al., 2016). However, traditional organic coatings are susceptible to defects and cracks during use, and it is easy to be infiltrated by corrosive media during service. If not repaired in time, the shielding effect of coatings will be significantly reduced, resulting in metal corrosion. Therefore, in order to prolong the service time of coatings and avoid the local corrosion of the metal substrate caused by coating defects, it is necessary to endow coatings with self-healing protection performance when coatings are damaged or corroded. Self-healing coating is an intelligent protective material, which can self-repair the damage generated in the process of use and has become a research hotspot in the coating field in recent years (Cui et al., 2021). Some articles (Abu-Thabit et al., 2016; Zhang et al., 2018), patents (Keeney et al., 2002; Cho et al., 2018), and books (Li and Meng, 2015; et al., Hosseini, 2016) on self-healing coatings have been published. According to the recent view (Zhang et al., 2018), self-healing coatings are classified into autonomous and non-autonomous healing coatings. The self-repair process can be realized by adding corrosion inhibitors to the coatings shown in **Figure 1**, which is efficient, economical, and convenient, and have become one of the most widely used corrosion protection methods in recent years (Liu et al., 2021).

Adding corrosion inhibitors can obviously inhibit the corrosion electrochemical reaction on the metal surface. However, if corrosion inhibitors are directly added to the coating, they will react with the metal substrate or the material in the coating in advance, so as to prematurely lose the self-healing protection performance and cause adverse effects to coatings (Zhang et al., 2018). The strategy to overcome these drawbacks is encapsulating inhibitors using micro- or nanocontainers (Saji, 2019). Inspired by drug delivery in the medical field, researchers first proposed using nano-/microcapsules to load healing agents and then doped them into coatings. White et al. used capsules to load healing agents (White et al., 2001). When the coating is damaged by external force, the healing agent and

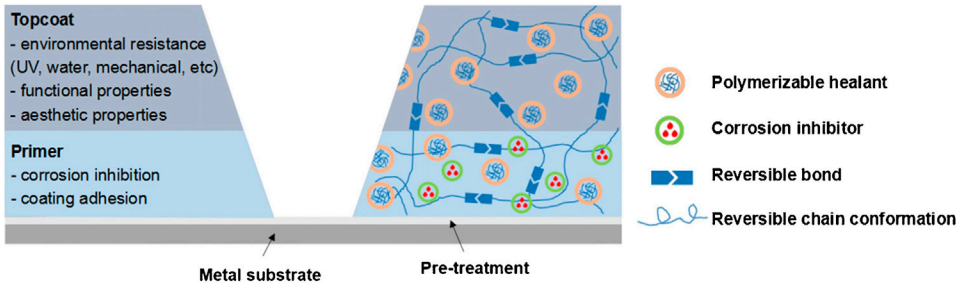

FIGURE 1 | Basic structure and functions of a coating system and major self-healing mechanisms (Zhang et al., 2018).

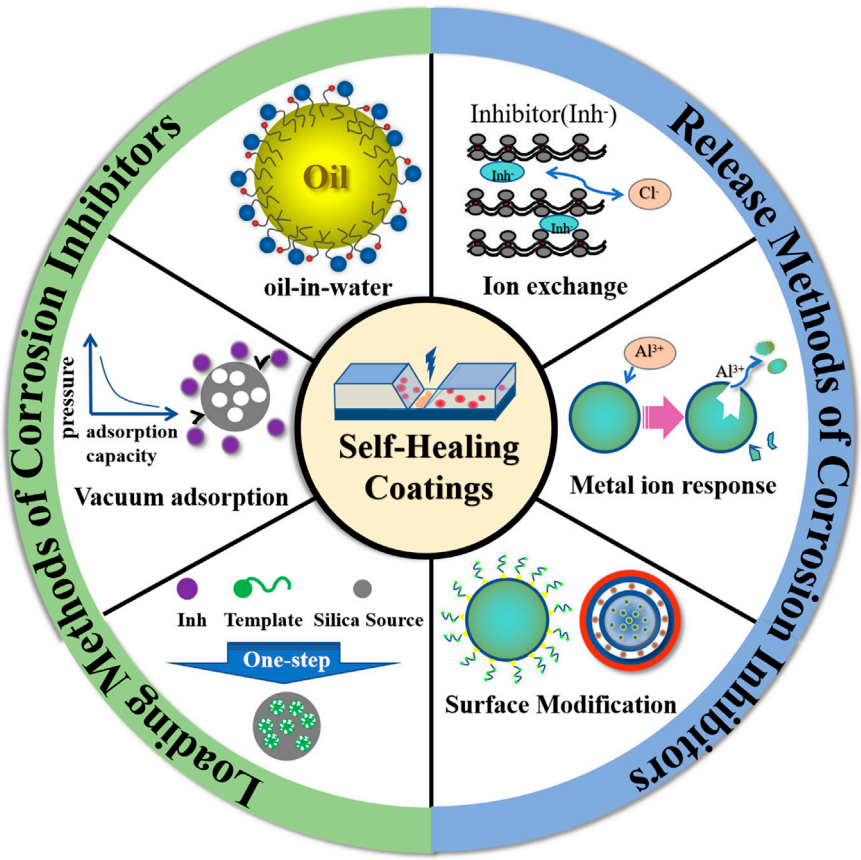

FIGURE 2 | Overview of main loading and release methods of corrosion inhibitors in this review.

catalyst released from ruptured capsules at the mechanical damage caused a cross-linking reaction to repair cracks, and the physical shielding performance of the coating is restored in time. However, in this way, the corrosion inhibitor is released by the mechanical damage of containers, which will result in uncontrollable one-time release of corrosion inhibitors. The self-healing protection performance of coatings will soon disappear and cannot realize long-term service of coatings. In addition, the diameters of microcapsules usually range from dozens of microns to hundreds of microns, and they are not suitable for thin coatings. Also, the weak mechanical properties of microcapsules and incompatibility between microcapsules and matrix destroy the performance of final composites.

The method to overcome this disadvantage is to encapsulate corrosion inhibitors into micro-/nanocontainers, such as mesoporous silica containers (Recloux et al., 2015; Ma et al., 2017; Xu et al., 2018; Wang, et al., 2019; Xiong et al., 2019a), silica nanocapsules (Exbrayat et al., 2019), zeolitic imidazolate framework-8 (ZIF-8) (Xiong et al., 2019b), zeolite (ZEO) (Lv et al., 2021), and layered double hydroxides (LDHs) (Tedim et al.,

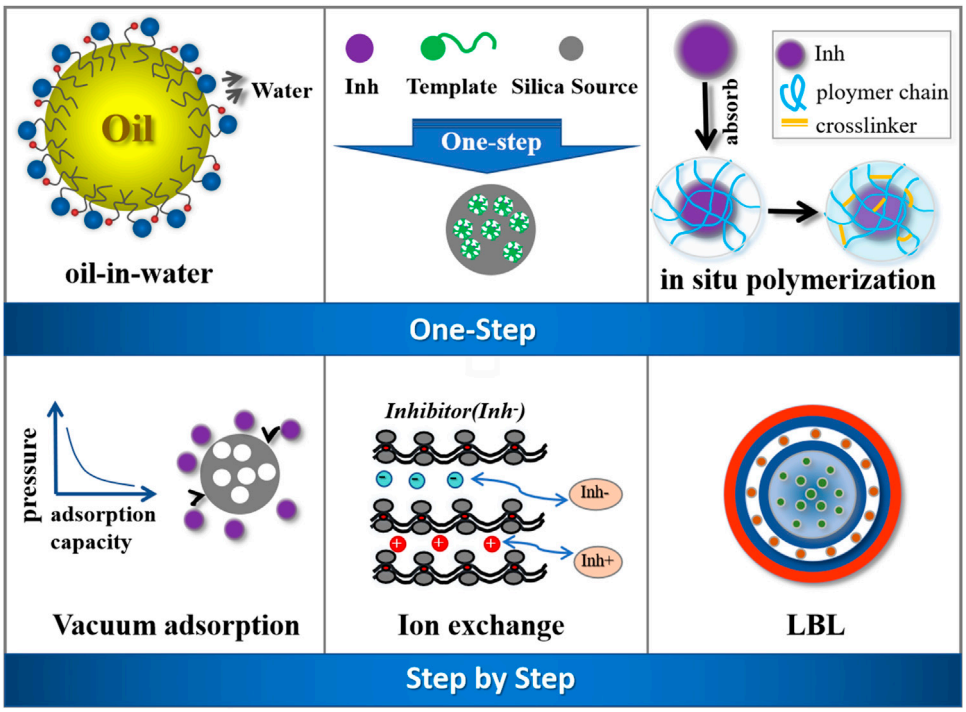

FIGURE 3 | Schematic illustration of common loading methods of corrosion inhibitors.

2016; Alibakhshi et al., 2016). Micro-/nanocontainers have more extensive structure and characteristics. While loading corrosion inhibitors efficiently, it can respond to the external changes in light, heat, pressure, pH, and potential during corrosion occurrence and realize the controllable release of corrosion inhibitors (Shchukin and Moehwald, 2013). Corrosion inhibitors can be released from micro-/nanocontainers only when these internal/external stimuli are triggered. This can prevent corrosion inhibitors from leaking out of coatings and increase the durability of coatings, thereby enhancing the self-healing ability of coatings and preventing corrosion.

Stimuli-responsive self-healing coatings can avoid corrosion inhibitor failure in advance (Zheludkevich et al., 2007) and one-time release leading to loss of self-healing protection performance (White et al., 2001), which is generally achieved by loading corrosion inhibitors in containers, and the critical issue is the loading and release of corrosion inhibitors. In recent works (Crespy et al., 2016; Zhang et al., 2018; Ye K et al., 2020), most of the self-healing coatings are classified according to the type of containers, but the comprehensive investigation of loading and release methods of corrosion inhibitors is rare. Therefore, in this paper, loading and release methods of corrosion inhibitor are reviewed in detail, the main loading and release methods of corrosion inhibitors in this review are shown in **Figure 2**. In the last section, a prospect with critical issues, aiming to provide insights for the further development of self-healing coatings was proposed.

LOADING METHODS OF CORROSION INHIBITORS

The loading methods of corrosion inhibitors are generally divided into two types: one-step method and multistep method. The one-step method refers to the completion of container preparation and corrosion inhibitor loading in one step, usually through oil-in-water, the template method, and *in situ* polymerization. The multistep method refers to the prior preparation of the container and then loading of the corrosion inhibitor (Hu et al., 2011), usually by vacuum adsorption, ion exchange, and layer-by-layer self-assembly. These common loading methods of corrosion inhibitors are shown in **Figure 3**.

One-Step Synthetic

Container preparation and corrosion inhibitor loading are completed in one step. This refers to the direct loading of corrosion inhibitors while preparing containers. In recent years, one-step synthesis of nanocontainers loaded with corrosion inhibitors has attracted attention due to its simple process and economy. The widely used method is oil-in-water microemulsion polymerization. Yi et al. based on the oil-in-water Pickering solution template stabilized by lignin nanoparticles, prepared multilayer composite microcapsules loaded with healing agents and controlled the particle size of microcapsules by changing the lignin content and oil-to-water volume ratio in the Pickering emulsion. When the microcapsules were doped into

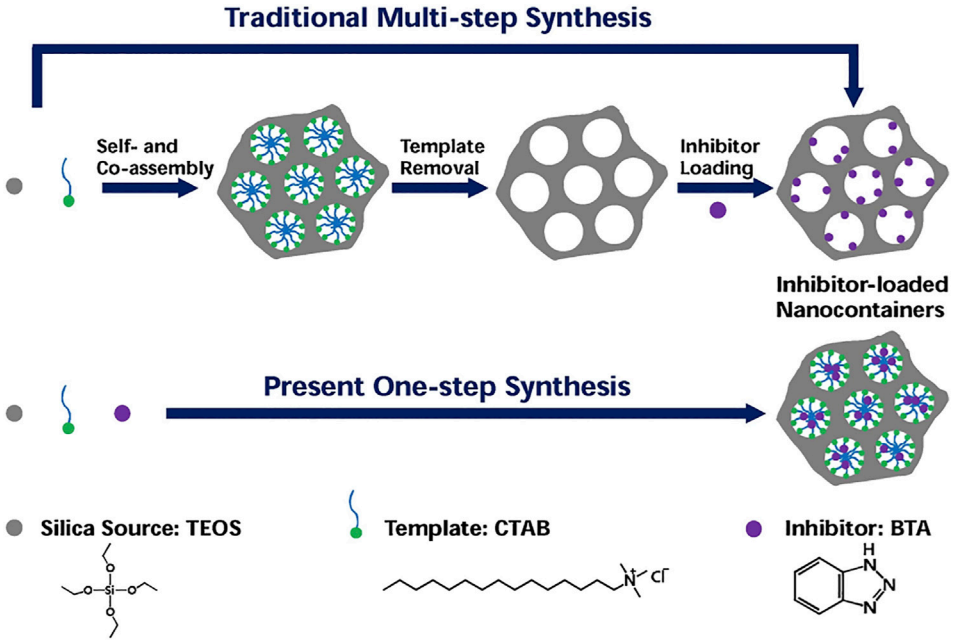

FIGURE 4 | Schematic illustration of MSN loaded with corrosion inhibitors synthesized by traditional multistep method and current one-step methods in this work (Xu et al., 2018).

the epoxy coating, the immersion test showed that the self-healing epoxy coating loaded with microcapsules had good dispersion and a good anticorrosion effect (Yi et al., 2015). However, the particle size obtained by this preparation method is usually at micron level so that the doping may destroy the integrity of the coating and affect its performances. In addition, toxic organic solvents are inevitably used in the preparation of nanocontainers with a diameter less than 150 nm. In this context, it is necessary to study the one-step synthetic method of nanocontainers loaded with corrosion inhibitors for energy conservation and environmental protection.

In various micro-/nanocontainers, mesoporous silica nanoparticles (MSN) have many advantages, such as high stability, large specific surface area, adjustable pore size, and easy surface functionalization, so they are often used as corrosion inhibitors loaded containers in the field of metal corrosion protection. However, traditional methods of loading corrosion inhibitors on MSN include the synthesis of silica template composites, removal of the template by calcination or acid extraction, functionalization of silica nanoparticles, and loading of corrosion inhibitors, which are time-consuming and inefficient. Therefore, it is necessary to develop a simple and effective loading inhibitor method to improve industrial application value. Based on high solubility of organic inhibitors in the template micelle hydrophobic core, Xu et al. prepared the mesoporous silica nanocontainers loaded with corrosion inhibitors by a simple one-step synthetic method, as shown in **Figure 4** (Xu et al., 2018). The MSN loaded with benzotriazole (BTA) and cetyltrimethyl ammonium bromide (CTAB) were prepared without additional steps, such as removing templates or loading corrosion inhibitors, which has H^+ stimulus-response release characteristics. SVET results show that the coatings doped with these nanocontainers exhibit effective corrosion protection performance. The results show that the one-step synthesis method is simple and efficient, and the whole preparation process does not require organic solvents, compared with the traditional multistep preparation method and the one-step synthesis method with toxic organic solvents in the preparation process. It is energy-saving and environmentally friendly and can be applied to a variety of self-healing coatings.

In addition, *in situ* polymerization is also one of the common methods for one-step preparation of micro-/nanocontainers loaded with healing agents, which has the advantages of economy and easy operation. White et al. prepared the urea–formaldehyde resin microcapsules loaded with a polymer-based self-healing material dicyclopentadiene by *in situ* polymerization (White et al., 2001). However, the development of *in situ* polymerization is limited because the preparation time is usually as long as several hours.

Multistep Synthetic

Container preparation and corrosion inhibitor loading are completed by using the multistep synthetic method, which is the most common way to load corrosion inhibitors. After the preparation of micro-/nanocontainers, appropriate methods can be selected according to the properties of containers and corrosion inhibitors. The common corrosion inhibitor loading methods include the vacuum adsorption method, ion exchange method, and layer-by-layer self-assembly technology.

Vacuum Adsorption

The vacuum adsorption method uses decompression (vacuum) to load corrosion inhibitors. Many corrosion inhibitors loaded into containers, such as mesoporous silica, use this method to load corrosion inhibitors.

MSN can be dispersed in the corrosion inhibitor solution and placed in a low-pressure environment to adsorb corrosion inhibitors. Borisova et al. adsorbed BTA as a corrosion inhibitor after the synthesis of MSN and incorporated into a sol-gel coating to protect aluminum alloy (Borisova et al., 2011). Mechanical stability, high specific surface area (1,000 $m^2\ g^{-1}$), and large pore volume (1 ml g^{-1}) of mesoporous silica make its load capacity reach 409 mg BTA/1g SiO_2. SVET is used to simulate the corrosion process. It was found that the newly developed self-healing anticorrosive coating had better corrosion protection performance than control sol-gel coatings.

Ion Exchange

Some micro-/nanocontainers have ion exchange properties, and some corrosion inhibitors are loaded into containers by exchanging with the original ions in the containers. The large specific surface area and porosity of layered silicate materials make it possible to load corrosion inhibitors. Researchers have found that cations (such as Na^+) contained in zeolites have cation exchange properties, which can be exchanged with some cation corrosion inhibitors to incorporate corrosion inhibitors into zeolites.

Rassouli et al. embedded Zn^{2+} into NaX zeolite for corrosion inhibition by ion exchange reaction and doped it into an epoxy coating (Rassouli et al., 2017). Electrochemical tests and surface analysis show that the coating containing NaX zeolite load with corrosion inhibitor Zn^{2+} has better corrosion protection performance than the control group. This is because in the process of corrosion reaction, the zeolite container releases Zn^{2+} by ion exchange with Na^+ in the corrosive medium and forms zinc hydroxide precipitation in the active area, which leads to a decrease in corrosion rate and thus inhibits corrosion. Wang et al. (2016) obtained Ce-MCM-22 zeolite by loading Ce^{3+} corrosion inhibitors into it through the cation exchange reaction of MCM-22 zeolite and added it to the epoxy coating on Mg–Li alloy. Scratch test results show that the epoxy coating containing Ce-MCM-22 zeolite has a self-healing function because during the corrosion process of the Mg–Li alloy substrate, Ce^{3+} is released from MCM-22 zeolite based on the ion exchange of zeolite.

Layer-by-Layer Self-Assembly

Layer-by-layer self-assembly (LBL) technology, which emerged in the 1990s, is a simple, fast, and green multifunctional surface modification method. The most classical principle is the alternate deposition of polyelectrolyte self-assembly multilayers in polyelectrolyte solutions with opposite charges. Common polyelectrolyte multilayers include negatively charged polystyrene sulfonic acid (PSS) and positively charged polyetherimide (PEI). Due to the electrostatic interaction between layers, the polyelectrolyte layer is sensitive to external stimuli such as pH and light, and the active substance encapsulated between layers can be released slowly. Therefore, the controllable release of corrosion inhibitors can be realized when the corrosion environment changes. In this context, layer-by-layer self-assembly technology is often used in the coating field for corrosion inhibitor loading.

Falcón et al. studied the self-repairing and anti-corrosion effects of nanocontainers coated with dodecylamine on carbon steel (Falcón et al., 2014). Researchers used LBL technology to alternately deposit several polyelectrolyte layers (PEI and PSS) and corrosion inhibitor (dodecylamine) layers on the surface of SiO_2 nanoparticles, and the final structure of the obtained nanocontainer is SiO_2/PEI/PSS/dodecylamine/PSS/dodecylamine. The corrosion resistance of coatings at different pH (2.0, 6.2, and 9.0) is evaluated by electrochemical impedance spectroscopy (EIS) and scanning vibrating electrode technique (SVET). The results showed that when the coating contained 10 wt% nanocontainer loaded with dodecylamine, the corrosion inhibition effect was best at pH = 2. At the same time, the salt spray test of carbon steel samples coated with prefabricated scratches shows that the coating with nanocontainers has self-healing performance.

Chen et al. developed a SnO_2 nanocontainer and deposited polypyrrole (PPy), molybdate corrosion inhibitors, and PDA layers using the LBL assembly technology, as shown in **Figure 5** (Chen et al., 2020a). The prepared SnO_2 nanocontainer was incorporated into the epoxy coating of stainless steel, which makes the electrochemical tests of the coating show the best anti-corrosion and self-healing properties. The PDA layer can control the on-demand release of the molybdate corrosion inhibitors and reforms the cracked polymer networks using the dopamine functional group and iron oxide to enhance the self-healing ability of the epoxy coatings.

RELEASE METHODS OF CORROSION INHIBITORS

Natural Release

Loaded in Microcontainers

A large number of studies have shown that compared with the direct doping of healing agents in the coating, whether healing agents are encapsulated into microcapsules or hollow fibers, they can have a better effect. This is because the packaging of healing agents can avoid the adverse reaction with coatings. When coating microcracks form and begin to propagate, microcapsules or hollow fibers at the crack are then ruptured, and healing agents flow out to refill the crack area. This method has high packaging efficiency, strong core material protection ability, and fast response to environmental hazards. **Figure 6** shows its mechanism.

Inspired by the use of capsule-coated drugs for directional delivery in the medical field, White et al. reported the first generation of self-healing systems based on polymer-based self-healing materials, dicyclopentadiene (DCPD), in 2001 (White et al., 2001), which received a strong response in the field of materials. Since then, microcapsule-based self-healing materials have attracted widespread attention and have begun to

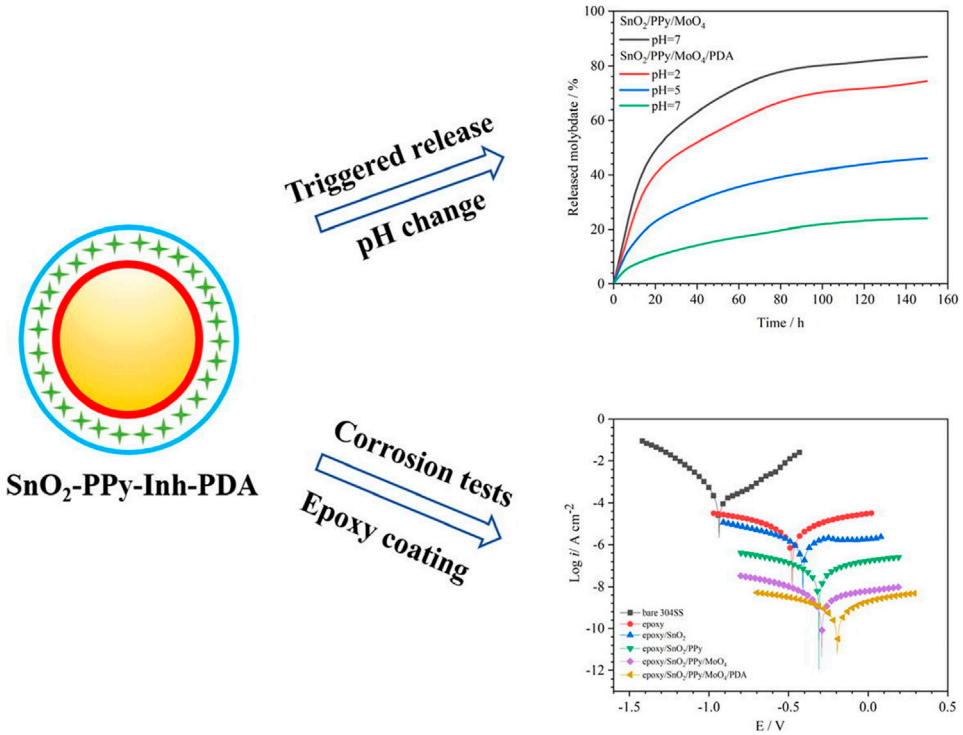

FIGURE 5 | Schematic illustration of SnO_2-ppy-Inh-PDA (Chen et al., 2020a).

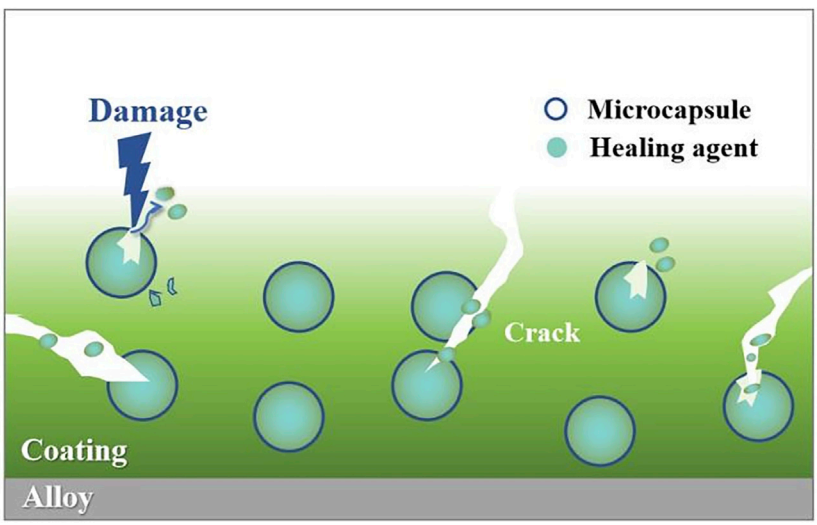

FIGURE 6 | Schematic diagram of natural release method of microcontainers loaded healing agents.

be applied in the field of coatings. They dispersed the microcapsules loaded with a liquid DCPD healing agent and powdered Grubbs catalyst in the epoxy substrate. When microcracks appeared in the substrate and began to propagate, the microcapsules at the crack propagation ruptured, resulting in the release of DCPD and Grubbs catalysts, and contacted at the defect, triggering ring-opening complex decomposition polymerization (ROMP), which led to the formation of cross-linked networks and the healing of damaged areas. The self-healing mechanism is shown in **Figure 7** (White et al., 2001).

In order to optimize the defect that the repair process cannot continue due to the depletion of healing agents in the

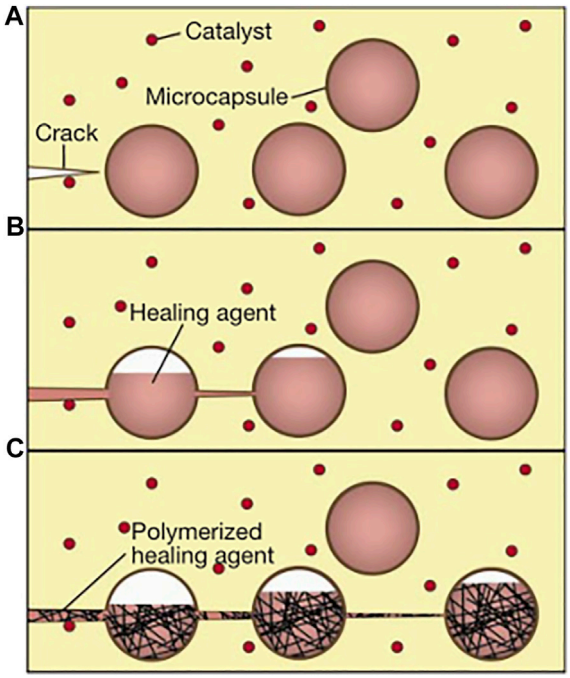

FIGURE 7 | Schematic diagram of autonomic healing concept. **(A)** cracks appeared in the substrate; **(B)** release of the healing agent loaded in microcapsules ruptured by cracks; and **(C)** polymerization reaction between the healing agent and the catalyst (White et al., 2001).

microcapsule model, researchers inspired by the biological vascular system propose the method of encapsulating healing agents and catalysts with hollow fibers, which opens up a new way for the continuous transportation of healing agents and other active substances to the coating defects. Toohey et al. encapsulated DCPD into a three-dimensional capillary network system and embedded it into the coating (Toohey et al., 2007). When the coating is cracked by mechanical force, the fiber pipeline at the "wound" ruptures, the healing agent and the catalyst flow out, and the curing reaction occurs after contact with the coating damage, thus repairing microcracks. The structure is shown in **Figure 8**.

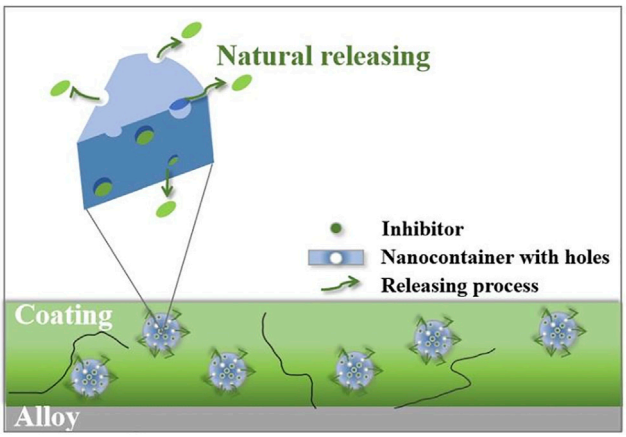

FIGURE 9 | Schematic diagram of natural release method of nanocontainer loaded corrosion inhibitors.

Since then, based on the packaging technology of healing agents, researchers have continued to study the packaging of different types of healing agents, and explore healing agents that can cross-link and cure without additional catalyst or curing agent. For example, the hydrophobic structure is formed by the combination of methylsilyl ester and water in the corrosive environment. Isocyanates can react with water. Some healing agents that polymerize under the stimulation of visible light can also be loaded into microcapsules or hollow fibers, which was developed inspired by human vascular system, which simplifies the process.

Loaded in Nanocontainers

A large number of studies have shown that adding a certain amount of nanocontainers to the coating can fill the original defects in the coating and enhance the physical shielding effect of the coating. At the same time, the corrosion inhibitor loaded in the nanocontainer will slowly release into the coating, enhancing the integrity of the coating and protecting the metal substrate. **Figure 9** shows its mechanism.

Since the microcapsule size is usually between tens and hundreds of microns, it cannot be used for thin coating. And

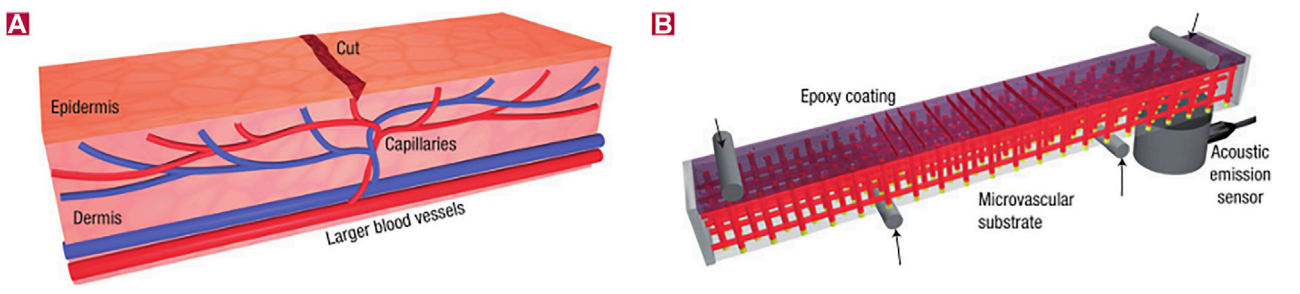

FIGURE 8 | Structure diagram of self-healing materials with 3D microvascular networks. **(A)** Dermal capillary network with a cut in the epidermis layer and **(B)** self-healing structure consisting of a microvascular substrate and an epoxy coating embedded with a catalyst in a four-point bending configuration monitored with an acoustic emission sensor (Toohey et al., 2007).

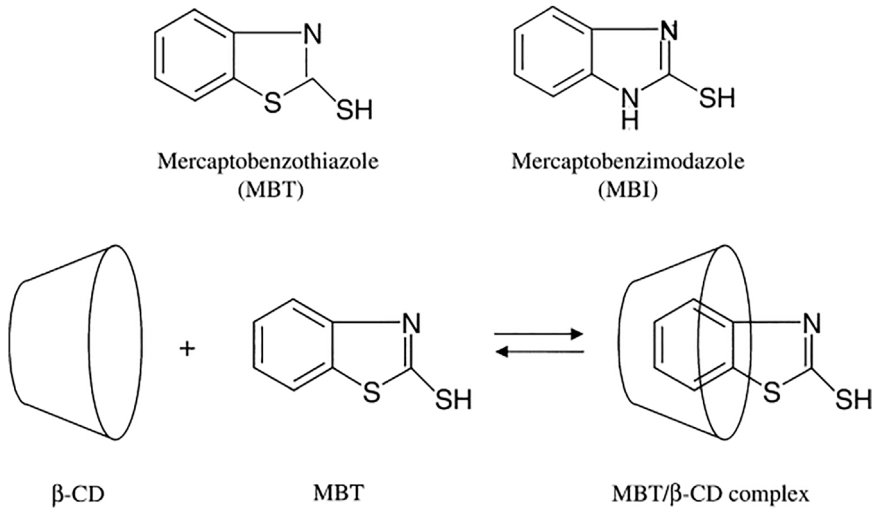

FIGURE 10 | Chemical structures of studied organic corrosion inhibitors MBT and MBI, and schematic of the inclusion complexes formation with b-cyclodextrin (Khramov et al., 2004).

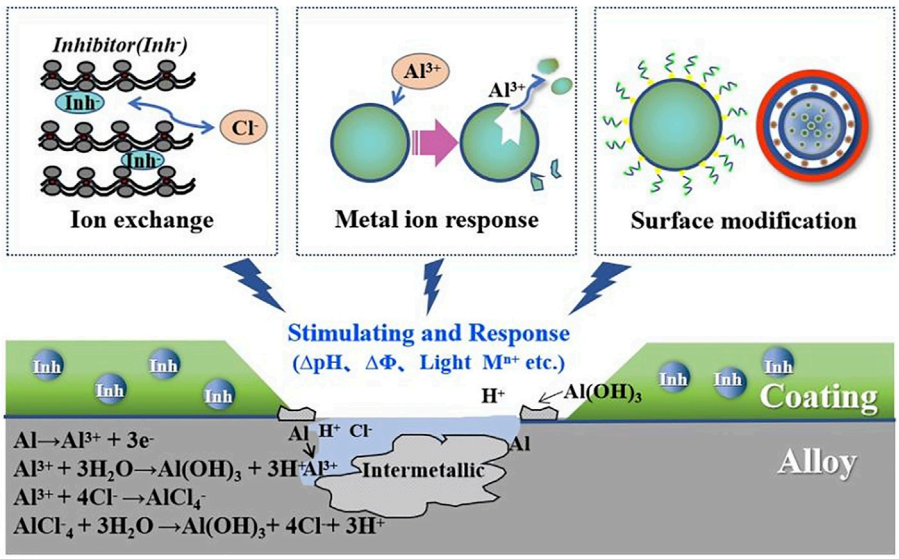

FIGURE 11 | Schematic diagram of the self-healing coating based on stimuli-responsive of corrosion inhibitors.

part of the cavity formed after the rupture of microcapsules will affect the coating stability. In addition to the natural release methods of corrosion inhibitors flowing out of microcapsules or hollow fibers caused by crack propagation, researchers can also realize the slow release of corrosion inhibitors by directly loading the corrosion inhibitor into nanocontainers and adding it into coatings.

Chen et al. loaded molybdate corrosion inhibitors into TiO2 nanotubes, which can slowly release inhibitors into the natural environment (Chen et al., 2020b). Ye et al. loaded corrosion inhibitors of benzotriazole (BTA) into the porous graphene sheets and then embedded into epoxy coating to form composite coating. The spontaneous release of BTA from the graphene-based nanocontainer makes the coating obtain good corrosion resistance (Ye Y et al., 2020). Borisova et al. studied and evaluated using a simplified coating system. They adsorbed BTA under reduced pressure in MSN without additional modification. And then, they added it to the sol-gel coating and coated it on the surface of aluminum alloy (Borisova et al., 2011). The optical images of the bare aluminum alloy substrate, the substrate coated with sol-gel coating, the substrate coated with a sol-gel coating doped with BTA, and the substrate coated with a sol-gel coating doped with MSN loaded with BTA showed that MSN loaded with BTA in the coating has the best corrosion inhibition effect, while the

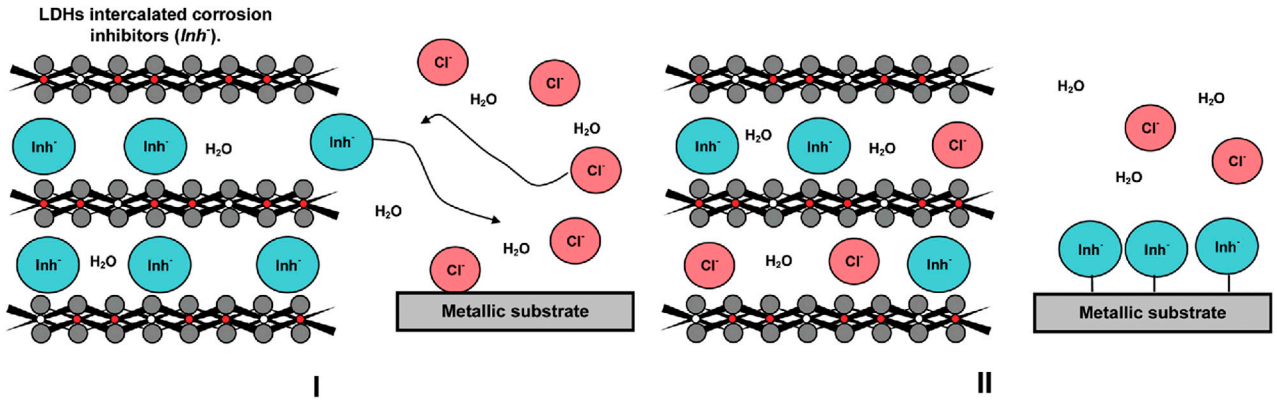

FIGURE 12 | Mechanism diagram of LDHs in corrosion protection (Tedim et al., 2010). (I) Anion (Cl^-) in the solution triggers the release of the inhibitors (Inh^-), and (II) LDHs play a double-role, providing inhibitors to protect the metallic substrates and entrapping aggressive species from the environment.

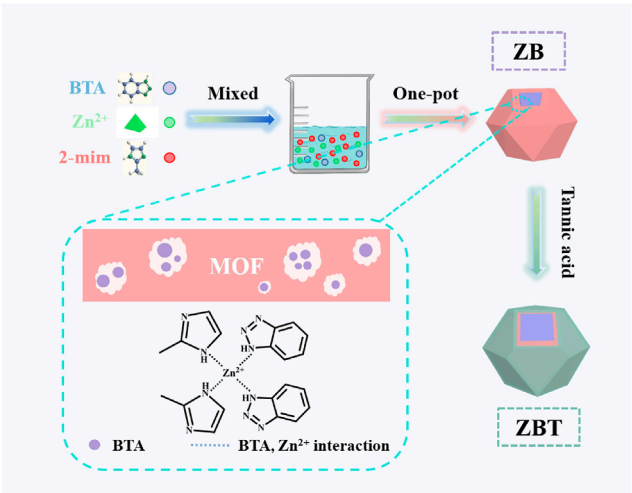

FIGURE 13 | Schematic illustration of the procedure for the synthesis of ZBT nanomaterials (Yang et al., 2021).

long-term corrosion resistance of other control groups is low, and there are many defects and corrosion products. This is due to the uniform distribution of MSN in the coating, filling coating defects, and improving its physical barrier properties. At the same time, corrosion inhibitors are loaded into nanocontainers to prevent their early leakage and reaction with the coating substrate. In addition, MSN can release corrosion inhibitors in the coating, which can inhibit corrosion.

Khramov et al. loaded inhibitors of mercaptobenzimidazole (MBI) and mercaptobenzothiazole (MBT) in the hydrophobic cavity of β-cyclodextrin, as shown in **Figure 10** (Khramov et al., 2004). The container loaded with corrosion inhibitors is added to the silane film and coated on the aluminum alloy surface. SVET test results show that the coating of β-cyclodextrin containers loaded with corrosion inhibitors has the best corrosion resistance performance compared with the coating without corrosion inhibitors and the coating directly doped with corrosion inhibitors, which could be explained that corrosion inhibitors could be continuously and slowly released from β-cyclodextrin and promote the repair of corrosion defects.

Stimuli-Responsive Release

Problems such as premature failure of corrosion inhibitors can be avoided by loading healing agents with microcapsules or hollow fibers or loading corrosion inhibitors in nanocontainers and then adding coatings. The corrosion inhibition effect is enhanced compared with directly doping corrosion inhibitors in coatings. However, these release methods of corrosion inhibitors are natural releases, with low corrosion inhibition efficiency and short service life, which cannot meet the growing demand of industry. Therefore, the study on the controlled release methods of corrosion inhibitors has become a hot issue. The main stimuli-responsive release methods are described in detail in this article.

A large number of studies have shown that when nanocontainers loaded with corrosion inhibitors are doped in coatings, the self-performance or surface modification of nanocontainers can be used to perceive the changes in external conditions (such as light, heat, pressure, potential, pH, and other common variables) when corrosion occurs, and finally, the controllable release of corrosion inhibitors is realized. The controlled release of corrosion inhibitors can greatly improve the corrosion inhibition efficiency and prolong the service time of coatings, which plays an important role in the field of corrosion protection. **Figure 11** shows the mechanism of the process.

Intrinsic Properties of Containers

Some containers have ion exchange properties or are sensitive to some metal ions, such as LDH and MOF. The structure of layered double hydroxides (LDHs) (such as hydrotalcite) includes two parts, which are the layered main body with positive electric property and the interlayer ions with negative electric property and neutral electric property. The two parts are connected by hydrogen bonds, so interlayer ions can move freely so as to replace anions in the environment (Serdechnova et al., 2016).

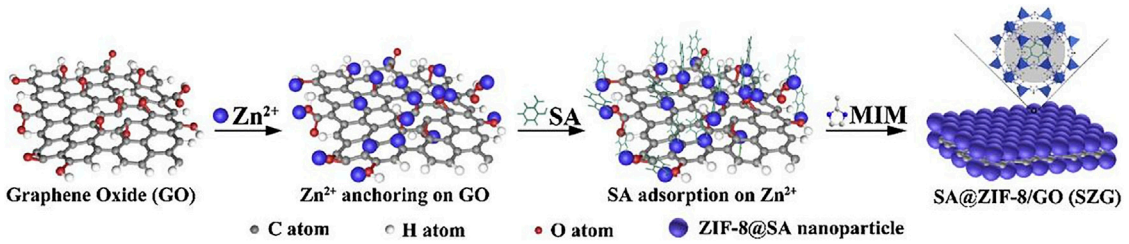

FIGURE 14 | Synthetic procedure illustration of SZG (Xiong et al., 2019b).

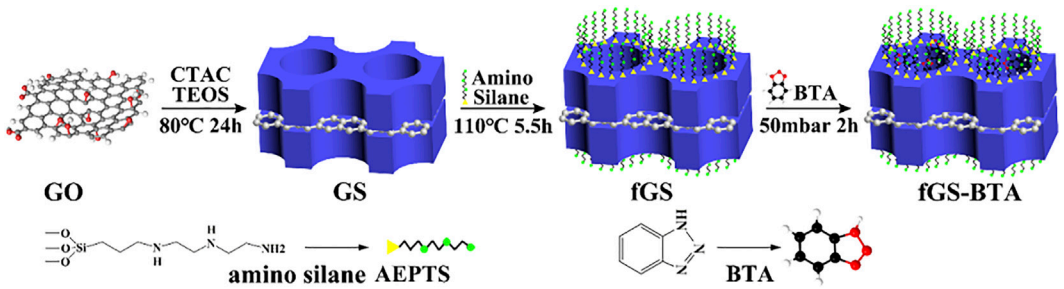

FIGURE 15 | Illustration of the synthetic processes for fGS-BTA nanosheets (Xiong et al., 2019b).

Tedim et al. studied the preparation of LDHs, the load and release of corrosion inhibitors, and their application in corrosion protection (Tedim et al., 2012). They doped Zn–Al LDH intercalated with NO_3^- into organic polymer coatings as containers to absorb Cl^- during corrosion, which can greatly reduce the penetration of corrosive Cl^- in coatings. The spectrophotometric results show that the organic anion NO_3^-in Zn (2)-Al-NO_3 LDH is released due to the presence of Cl^-. The release of $NO_3^-$from LDHs intercalates, and the absorption of Cl^- by LDHs reduces the concentration of Cl^- in the solution, which is controlled by the ion exchange equilibrium. Compared with the unmodified coating, the modified coating significantly reduced the chloride permeability, which proves the protective effect of LDHs on the coating when corrosion occurs and has a good application prospect in the field of self-healing coatings. The mechanism of LDHs releasing anionic corrosion inhibitors and absorbing corrosive anions in the environment is shown in **Figure 12** (Tedim et al., 2010).

The cage-like pore structure of some layered silicates, such as montmorillonite, kaolinite, and zeolite, is formed by the periodic arrangement of tetrahedra such as $SiO_4^{4-}$and AlO_4^{5-}. The isomorphous replacement of Si^{4+} and Al^{3+} makes the main structure negatively charged, so the cation in the pore can be replaced with the cation in the environment.

Thai et al. proposed a new protective coating based on cerium ion corrosion inhibitors for AA2024 corrosion protection (Thai et al., 2020). Cerium cation is inserted into the nanoclay layer by cation exchange reaction to obtain cerium modified montmorillonite (CeMMT). EIS measurement and polarization curves showed that CeMMT had a good corrosion inhibition effect. The corrosion protection performance of AA2024 is improved after the CeMMT is added. Salt spray results of the pre-scratched specimen showed that CeMMT had self-healing performance. UV-Vis spectra showed that the excellent corrosion inhibition performance might be due to the release rate of Ce ions from CeMMT reached 60% in NaCl solution.

When LDHs and some layered silicate containers mentioned earlier have corrosive ions (such as Cl^- or metal ions) in the external environment, the embedded corrosion inhibitor reacts with them by ion exchange, which not only absorbs Cl^- or metal ions in the corrosive environment but also realizes the release of corrosion inhibitors. In addition, the two-dimensional structure of LDHs and chemical stability of layered silicate containers enhance the physical shielding effect of coatings as the carriers of corrosion inhibitors have been favored by industrial production.

In addition, the metal–organic framework (MOF) material is a new type of porous material with broad prospects. The zeolite imidazole ester framework material (ZIF) is a subclass of the MOF. The structure of ZIF-8 is a tetrahedral unit composed of a Zn^{2+} and four imidazole anions, and the large internal space can load corrosion inhibitors. The structure of ZIF-8 will decompose or collapse with the change of some external conditions. For example, ZIF-8 decomposes at pH 5.0–6.0 due to the coordination dissociation of Zn^{2+} and imidazole anions (Zhuang et al., 2014), and ZIF-8 is unstable with divalent and higher valence metal cations. If treated with an Al^{3+} solution, ZIF-8 will completely collapse (Zhang et al., 2011). The corrosion inhibitor loaded in ZIF-8 also released with its structure's decomposition or collapse. In this context, the acidic environment and metal cations can stimulate ZIF-8 to achieve the response release of corrosion inhibitors. Yang et al. loaded with BTA into ZIF-8 by a one-step method and modified it with tannic

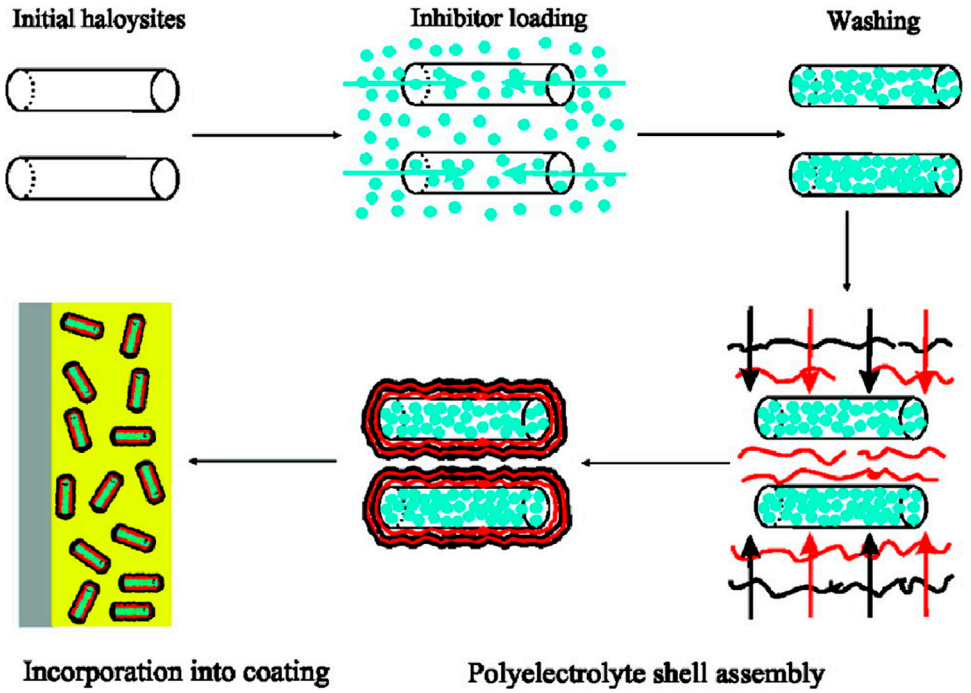

FIGURE 16 | Schematic illustration of the fabrication of 2-mercaptobenzothiazole-loaded halloysite/polyelectrolyte nanocontainers (Shchukin et al., 2008).

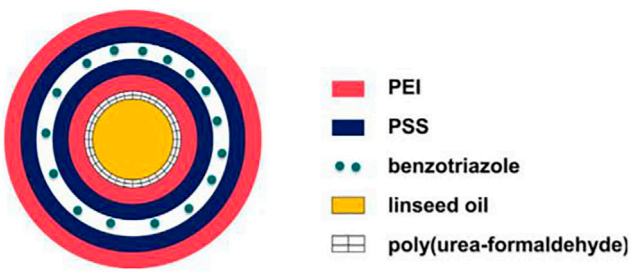

FIGURE 17 | Structure diagram of dual-stimulus responsive microcapsules (Leal et al., 2018).

acid, as shown in **Figure 13** (Yang et al., 2021). The synthesized pH-responsive hydrophilic stimuli-responsive release system TA@ZIF-8@tannic acid (ZBT) based on ZIF-8 was used for epoxy resin coating. EIS and salt spray tests showed that ZBT could significantly inhibit the corrosion of carbon steel and endow the coating with effective self-healing performance. After 20 d of immersion, the impedance modulus of the ZBT/EP composite coating was about two orders of magnitude higher than that of the blank coating.

Xiong et al. used ZIF-8 nanoparticles to load corrosion inhibitor salicylaldehyde (SA) and modified GO to obtain SGZ two-dimensional nanocomposites, as shown in **Figure 14** (Xiong et al., 2019b). When corrosion occurred, under the stimulation of Al^{3+} in the environment, the structure of ZIF-8 collapsed, and SA was released and formed an adsorption layer on the surface of the metal substrate, which prevented the corrosion activity. EIS and immersion tests showed that SGZ effectively improved the protective performance of the PVB coating.

By Surface Modification of Containers

The surface modification of nanocontainers enables some inorganic nanocontainers to combine with some polymer molecular chains with stimulus response characteristics (such as pH, temperature, and light), which can realize the response of containers to external stimuli. At the same time, the grafted molecular chains are expected to enhance the dispersion of inorganic nanocontainers in organic coatings and improve the stability of coatings. Fu et al. used ferrocenyl acid–cucurbituril binary system to modify hollow mesoporous SiO_2 microspheres as pH-responsive valves and loaded caffeine molecules, which realized the controlled release under acidic and alkaline conditions (Fu et al., 2013). Adding nanocontainers loaded with corrosion inhibitors to smart nanocontainers implanted into the self-assembled nanophase particles (SNAP) films on the AA2024 surface, it was found that the composite coating had significant physical shielding and self-healing protection properties. Chen et al. reported a light-responsive self-healing coating loaded with BTA and light-responsive molecular switch azobenzene in MSN (Chen et al., 2015). Azobenzene molecules

close under visible light but open under ultraviolet light, and corrosion inhibitor molecules released from containers. SVET results show that MSN modified by azobenzene molecular switch has excellent light sensitivity and self-healing properties, which can prolong the corrosion protection effect of aluminum alloy.

Wang et al. successfully synthesized hollow MSN modified by a functional polymer poly-(dimethylaminoethyl methacrylate) (PDMAEMA) to load corrosion inhibitors (Wang et al., 2021). Because of its CO_2 response mechanism, it can react with CO_2 corrosion in aqueous solution. In the presence of CO_2 in aqueous solution, the polymer shell PDMAEMA on the surface of the MSN can change from a hydrophobic state to a hydrophilic state to improve the release rate of corrosion inhibitors. Xiong et al. prepared graphene oxide–mesoporous silica nanocomposites (GS) to load the corrosion inhibitor BTA, and nanogates of the GS container were constructed by aminosilane, as shown in **Figure 15** (Xiong et al., 2019a). Aminosilane as a pH-driven "nanogate" inhibits premature leakage of corrosion inhibitors and endows fGS-BTA nanocomposites with stimuli-responsive release characteristics under alkaline conditions. At the same time, aminosilane functionalization significantly enhances its dispersion stability in organic coating. The EIS and scratch tests show that the sol-gel coating filled with fGS-BTA has enhanced barrier performance and self-healing protection performance.

In addition to surface grafting of containers, nanocontainers can also be encapsulated with pH-sensitive polyelectrolyte layers or polymer shells (such as polyphenyl acrylate) by LBL technology. The polyelectrolyte layer is coated outside with microcapsules, and corrosion inhibitors are loaded. When pH changes, the electrostatic adsorption between polyelectrolyte layers changes, thus releasing corrosion inhibitors and realizing the stimulation response to pH. Shchukin et al. loaded corrosion inhibitor 2–mercaptobenzothiazole inside halloysite nanotubes, and polypropylene amine, as shown in Figure 16 (Shchukin et al., 2008). When corrosion occurs, the local pH value changes, resulting in the dissociation of polyelectrolyte layers outside nanocontainers and the release of inhibitors, which makes the corrosion area repaired.

Leal et al. synthesized microcapsules loading flaxseed oil by *in situ* polymerization and used LBL technology to assemble BTA between polyelectrolyte layer polyetherimide (PEI) and polystyrene sulfonate (PSS) outside microcapsules (Leal et al., 2018). The structure is shown in **Figure 17**. The system has two stimuli-responsive mechanisms, which are mechanical stimulation (which controls the release of flaxseed oil) and pH-responsive stimulation (which controls the release of BTA). The EIS results show that the epoxy resin doped with 4.8 wt% dual stimuli-responsive microcapsules is more effective in corrosion protection than the control sample, which is related to the release of flaxseed oil by mechanical stimulation (induced defects) and the release of BTA by pH stimulation.

CONCLUSION AND OUTLOOK

Stimuli-responsive self-healing coatings avoid the one-time release of corrosion inhibitors and the premature failure of self-healing performance, which is generally achieved by loading corrosion inhibitors in containers, and key is the loading and release of corrosion inhibitors.

The adverse reaction between corrosion inhibitors and coatings can also be avoided by loading corrosion inhibitors in micro-/nanocontainers. However, it is found that the micro-/nanocontainers loaded with corrosion inhibitors in coatings may affect the stability of the coating. Therefore, effective loading methods of corrosion inhibitors are important in surface engineering and corrosion protection. The preparation of containers and corrosion inhibitor loading can be completed by a one-step or step-by-step synthetic method. Among them, the loading methods of corrosion inhibitors in micro-/nanocontainers mainly include physical adsorption, ion exchange, and layer-by-layer self-assembly.

Compared with the natural release of corrosion inhibitors from micro-/nanocontainers, the stimuli-responsive release methods increase the inhibition efficiency and service time of coatings, which can be achieved by intrinsic properties or surface modification of containers. For the former, the stimuli-responsive release of corrosion inhibitors is achieved by an ion exchange reaction between corrosion ions and corrosion inhibitors loaded in the containers, or by the collapse of the container structures. For the latter, the stimuli-responsive release of corrosion inhibitors can be achieved by grafting nanocontainers to construct the "nanogate" or by using layer-by-layer self-assembly technology on modified containers.

Self-healing coatings based on the stimuli-responsive release of corrosion inhibitors have potentially broad applications in the future. Although significant progress in the area of self-healing coating has been obtained, many challenges still need to be addressed with a continuous improvement. For example, the efficient encapsulation of these healing agents is critical, since it prolongs the shelf life and endows the coatings with a long-term corrosion inhibition effect. In addition, the containers should be compatible with organic coatings, and their fabrication should be cost-effective for practical applications. Finally, next-generation self-healing coatings will be smarter and multifunctional, for example, the anticorrosion and corrosion sensing. We expect that all these efforts will make a progress in anticorrosion engineering.

AUTHOR CONTRIBUTIONS

YZ made the illustrations and the main analytic and writing work. CC collected the references. MY contributed to the idea and design of the study and participated in the revision of the manuscript with JL and SL. All authors contributed to the article and approved the submitted version.

FUNDING

This work was supported by the Beijing Natural Science Foundation (Grant No. 2172032).

REFERENCES

Abdolah Zadeh, M., van der Zwaag, S., and Garcia, S. J. (2016). Adhesion and Long-Term Barrier Restoration of Intrinsic Self-Healing Hybrid Sol-Gel Coatings. *ACS Appl. Mater. Inter.* 8, 4126–4136. doi:10.1021/acsami.5b11867

Abu-Thabit, N. Y., and Hamdy, A. S. (2016). Stimuli-Responsive Polyelectrolyte Multilayers for Fabrication of Self-Healing Coatings - A Review. *Surf. Coat. Technology.* 303, 406–424. doi:10.1016/j.surfcoat.2015.11.020

Alibakhshi, E., Ghasemi, E., Mahdavian, M., and Ramezanzadeh, B. (2017). A Comparative Study on Corrosion Inhibitive Effect of Nitrate and Phosphate Intercalated Zn-Al- Layered Double Hydroxides (LDHs) Nanocontainers Incorporated into a Hybrid Silane Layer and Their Effect on Cathodic Delamination of Epoxy Topcoat. *Corrosion Sci.* 115, 159–174. doi:10.1016/j.corsci.2016.12.001

Borisova, D., Möhwald, H., and Shchukin, D. G. (2011). Mesoporous Silica Nanoparticles for Active Corrosion Protection. *Acs. Nano.* 5 (3), 1939–1946. doi:10.1021/nn102871v

Chen, T., Chen, R., Jin, Z., and Liu, J. (2015). Engineering Hollow Mesoporous Silica Nanocontainers with Molecular Switches for Continuous Self-Healing Anticorrosion Coating. *J. Mater. Chem. A.* 3 (18), 9510–9516. doi:10.1039/c5ta01188d

Chen, Z., Yang, W., Chen, Y., Yin, X., and Liu, Y. (2020a). Smart Coatings Embedded With Polydopamine-Decorated Layer-By-Layer Assembled SnO2 Nanocontainers for the Corrosion Protection of 304 Stainless Steels. *J. Colloid Interf. Sci.* 579, 741–753. doi:10.1016/j.jcis.2020.06.118

Chen, Z., Yang, W., Yin, X., Chen, Y., Liu, Y., and Xu, B. (2020b). Corrosion Protection of 304 Stainless Steel From a Smart Conducting Polypyrrole Coating Doped with pH-Sensitive Molybdate-Loaded TiO2 Nanocontainers. *Prog. Org. Coat.* 146, 105750. doi:10.1016/j.porgcoat.2020.105750

Cho, C., Kovalev, M., Sakai, N., and Kim, M. (2018). *Anti-Fingerpringing Compositon With Self- Healing Property, Film, Laminate, and Device*. U.S. Patent Application No. 15/889,607. Washington, D.C.: U.S. Patent and Trademark Office.

Crespy, D., Landfester, K., Fickert, J., and Rohwerder, M. (2016). Self-Healing for Anticorrosion Based on Encapsulated Healing Agents. *Adv. Polym. Sci.* 273, 219–245. doi:10.1007/12_2015_342

Cui, M., Njoku, D. I., Li, B., Yang, L., Wang, Z., Hou, B., et al. (2021). Corrosion Protection of Aluminium Alloy 2024 Through an Epoxy Coating Embedded With Smart Microcapsules: The Responses of Smart Microcapsules to Corrosive Entities. *Corrosion Commun.* 1, 1–9. doi:10.1016/j.corcom.2021.06.001

Exbrayat, L., Salaluk, S., Uebel, M., Jenjob, R., Rameau, B., Koynov, K., et al. (2019). Nanosensors for Monitoring Early Stages of Metallic Corrosion. *ACS Appl. Nano Mater.* 2 (2), 812–818. doi:10.1021/acsanm.8b02045

Falcón, J. M., Batista, F. F., and Aoki, I. V. (2014). Encapsulation of Dodecylamine Corrosion Inhibitor on Silica Nanoparticles. *Electrochim. Acta.* 124, 109–118. doi:10.1016/j.electacta.2013.06.114

Fu, J., Chen, T., Wang, M., Yang, N., Li, S., Wang, Y., et al. (2013). Acid and Alkaline Dual Stimuli-Responsive Mechanized Hollow Mesoporous Silica Nanoparticles as Smart Nanocontainers for Intelligent Anticorrosion Coatings. *Acs Nano.* 7 (12), 11397–11408. doi:10.1021/nn4053233

Hosseini, M. (2016). *Industrial Applications for Intelligent Polymers and Coatings*. Switzerland: Springer International Publishing.

Hu, J., Wang, J., Zhang, J., and Cao, C. (2011). *Corrosion of a Metal Surface Loading Methods and Uses*. CN, CN102268709 B. China: Intellectual Property Publishing House.

Keeney, C., Clements, M., Hawkins, J., Yollick, S., and Fader, J. (2002). *Encapsulated Anti-Corrosion Coating*. Washington: U.S. Patent No 6,090,051. US6420052 B1.

Khramov, A. N., Voevodin, N. N., Balbyshev, V. N., and Donley, M. S. (2004). Hybrid Organo-Ceramic Corrosion Protection Coatings With Encapsulated Organic Corrosion Inhibitors. *Thin Solid Films.* 447-448, 549–557. doi:10.1016/j.tsf.2003.07.016

Leal, D. A., Riegel-Vidotti, I. C., Ferreira, M. G. S., and Marino, C. E. B. (2018). Smart Coating Based on Double Stimuli-Responsive Microcapsules Containing Linseed Oil and Benzotriazole for Active Corrosion protection. *Corrosion Sci.* 130, 56–63. doi:10.1016/j.corsci.2017.10.009

Li, G., and Meng, H. (2015). *Recent Advances in Smart Self-Healing Polymers and Composites*. United Kingdom: Woodhead Publishing.

Liu, T., Ma, L., Wang, X., Wang, J., Qian, H., Zhang, D., et al. (2021). Self-Healing Corrosion Protective Coatings Based on Micro/Nanocarriers: a Review. *Corrosion. Commun.* 1, 18–25. doi:10.1016/j.corcom.2021.05.004

Lv, J., Yue, Q.-X., Ding, R., Han, Q., Liu, X., Liu, J.-L., et al. (2021). Construction of Zeolite-Loaded Fluorescent Supramolecular On-Off Probes for Corrosion Detection Based on a Cation Exchange Mechanism. *Nanomaterials.* 11 (1), 169. doi:10.3390/nano11010169

Ma, X., Xu, L., Wang, W., Lin, Z., and Li, X. (2017). Synthesis and Characterisation of Composite Nanoparticles of Mesoporous Silica Loaded With Inhibitor for Corrosion Protection of Cu-Zn alloy. *Corrosion Sci.* 120, 139–147. doi:10.1016/j.corsci.2017.02.004

Rassouli, L., Naderi, R., and Mahdavain, M. (2017). The Role of Micro/Nano Zeolites Doped with Zinc Cations in the Active protection of Epoxy Ester Coating. *Appl. Surf. Sci.* 423, 571–583. doi:10.1016/j.apsusc.2017.06.245

Recloux, I., Mouanga, M., Druart, M.-E., Paint, Y., and Olivier, M.-G. (2015). Silica Mesoporous Thin Films as Containers for Benzotriazole for Corrosion protection of 2024 Aluminium Alloys. *Appl. Surf. Sci.* 346, 124–133. doi:10.1016/j.apsusc.2015.03.191

Saji, V. S. (2019). Supramolecular Concepts and Approaches in Corrosion and Biofouling Prevention. *Corros. Revc.* 37 (3), 187–230. doi:10.1515/corrrev-2018-0105

Serdechnova, M., Salak, A. N., Barbosa, F. S., Vieira, D. E. L., Tedim, J., Zheludkevich, M. L., et al. (2016). Interlayer Intercalation and Arrangement of 2-Mercaptobenzothiazolate and 1,2,3-Benzotriazolate Anions in Layered Double Hydroxides: *In Situ* X-ray Diffraction Study. *J. Solid State Chem.* 233, 158–165. doi:10.1016/j.jssc.2015.10.023

Shchukin, D. G., Lamaka, S. V., Yasakau, K. A., Zheludkevich, M. L., Ferreira, M. G. S., and Möhwald, H. (2008). Active Anticorrosion Coatings With Halloysite Nanocontainers. *J. Phys. Chem. C.* 112 (4), 958–964. doi:10.1021/jp076188r

Shchukin, D., and Möhwald, H. (2013). A Coat of Many Functions. *Science.* 341 (6153), 1458–1459. doi:10.1126/science.1242895

Tedim, J., Bastos, A. C., Kallip, S., Zheludkevich, M. L., and Ferreira, M. G. S. (2016). Corrosion Protection of AA2024-T3 by LDH Conversion Films. Analysis of SVET Results. *Electrochimica Acta.* 210, 215–224. doi:10.1016/j.electacta.2016.05.134

Tedim, J., Kuznetsova, A., Salak, A. N., Montemor, F., Snihirova, D., Pilz, M., et al. (2012). Zn-Al Layered Double Hydroxides as Chloride Nanotraps in Active Protective Coatings. *Corrosion Sci.* 55, 1–4. doi:10.1016/j.corsci.2011.10.003

Tedim, J., Poznyak, S. K., Kuznetsova, A., Raps, D., Hack, T., Zheludkevich, M. L., et al. (2010). Enhancement of Active Corrosion Protection *via* Combination of Inhibitor-Loaded Nanocontainers. *ACS Appl. Mater. Inter.* 2 (5), 1528–1535. doi:10.1021/am100174t

Thai, T. T., Trinh, A. T., and Olivier, M. G. (2020). Hybrid Sol-Gel Coatings Doped with Cerium Nanocontainers for Active Corrosion Protection of AA2024. *Prog. Org. Coat.* 138, 105428. doi:10.1016/j.porgcoat.2019.105428

Toohey, K. S., Sottos, N. R., Lewis, J. A., Moore, J. S., and White, S. R. (2007). Self-Healing Materials With Microvascular Networks. *Nat. Mater.* 6 (8), 581–585. doi:10.1038/nmat1934

Wang, J., Tang, J., Zhang, H., Wang, Y., Wang, H., and Lin, B. (2021). A CO_2-Responsive Anti-Corrosion Ethyl Cellulose Coating Based on the pH-Response Mechanism. *Corros Sci.* 180, 109194. doi:10.1016/j.corsci.2020.109194

Wang, W., Wang, H., Zhao, J., Wang, X., Xiong, C., Song, L., et al. (2019). Self-Healing Performance and Corrosion Resistance of Graphene Oxide-Mesoporous Silicon Layer-Nanosphere Structure Coating Under Marine Alternating Hydrostatic Pressure. *Chem. Eng. J.* 361, 792–804. doi:10.1016/j.cej.2018.12.124

Wang, Y., Zhu, Y., Li, C., Song, D., Zhang, T., Zheng, X., et al. (2016). Smart Epoxy Coating Containing Ce-MCM-22 Zeolites for Corrosion Protection of Mg-Li Alloy. *Appl. Surf. Sci.* 369, 384–389. doi:10.1016/j.apsusc.2016.02.102

White, S. R., Sottos, N. R., Geubelle, P. H., Moore, J. S., Kessler, M. R., Sriram, S. R., et al. (2001). Autonomic Healing of Polymer Composites. *Nature.* 409, 794–797. doi:10.1038/35057232

Xiong, L., Liu, J., Li, Y., Li, S., and Yu, M. (2019a). Enhancing Corrosion protection Properties of Sol-Gel Coating by pH-Responsive Amino-Silane Functionalized Graphene Oxide-Mesoporous Silica Nanosheets. *Prog. Org. Coat.* 135, 228–239. doi:10.1016/j.porgcoat.2019.06.007

Xiong, L., Liu, J., Yu, M., and Li, S. (2019b). Improving the Corrosion protection Properties of Pvb Coating by Using Salicylaldehyde@zif-8/graphene Oxide Two-Dimensional Nanocomposites. *Corrosion Sci.* 146, 70–79. doi:10.1016/j.corsci.2018.10.016

Xu, J.-B., Cao, Y.-Q., Fang, L., and Hu, J.-M. (2018). A One-Step Preparation of Inhibitor-Loaded Silica Nanocontainers for Self-Healing Coatings. *Corrosion Sci.* 140, 349–362. doi:10.1016/j.corsci.2018.05.030

Yang, C., Xu, W. J., Meng, X., Shi, X. L., Shao, L. H., Zeng, X. L., et al. (2021). A pH-Responsive Hydrophilic Controlled Release System Based on Zif-8 for Self-Healing Anticorrosion Application. *Che. Eng. J.* 415, 128985. doi:10.1016/j.cej.2021.128985

Ye, K., Bi, Z., Cui, G., Zhang, B., and Li, Z. (2020). External Self-Healing Coatings in Anticorrosion Applications: A Review. *Corrosion* 76 (3), 279–298. doi:10.5006/3430

Ye, Y., Chen, H., Zou, Y., Ye, Y., and Zhao, H. (2020). Corrosion Protective Mechanism of Smart Graphene-Based Self-Healing Coating on Carbon Steel. *Corrosion Sci.* 174, 108825. doi:10.1016/j.corsci.2020.108825

Yi, H., Yang, Y., Gu, X., Huang, J., and Wang, C. (2015). Multilayer Composite Microcapsules Synthesized by Pickering Emulsion Templates and Their Application in Self-Healing Coating.*J. Mater. Chem. A.* 3 (26), 13749–13757. doi:10.1039/c5ta02288f

Zhang, D., Qian, H., Wang, L., and Li, X. (2016). Comparison of Barrier Properties for a Superhydrophobic Epoxy Coating Under Different Simulated Corrosion Environments. *Corrosion Sci.* 103, 230–241. doi:10.1016/j.corsci.2015.11.023

Zhang, F., Ju, P., Pan, M., Zhang, D., Huang, Y., Li, G., et al. (2018). Self-Healing Mechanisms in Smart Protective Coatings: a Review. *Corrosion Sci.* 144, 74–88. doi:10.1016/j.corsci.2018.08.005

Zhang, L., and Hu, Y. H. (2011). Strong Effects of Higher-Valent Cations on the Structure of the Zeolitic Zn(2-Methylimidazole)2 Framework (ZIF-8). *J. Phys. Chem. C.* 115 (16), 7967–7971. doi:10.1021/jp200699n

Zheludkevich, M. L., Shchukin, D. G., Yasakau, K. A., Möhwald, H., and Ferreira, M. G. S. (2007). Anticorrosion Coatings With Self-Healing Effect Based on Nanocontainers Impregnated with Corrosion Inhibitor. *Chem. Mater.* 19 (3), 402–411. doi:10.1021/cm062066k

Zhuang, J., Kuo, C.-H., Chou, L.-Y., Liu, D.-Y., Weerapana, E., and Tsung, C.-K. (2014). Optimized Metal-Organic-Framework Nanospheres for Drug Delivery: Evaluation of Small-Molecule Encapsulation. *Acs Nano.* 8 (3), 2812–2819. doi:10.1021/nn406590q

Conflict of Interest: The authors declare that the research was conducted in the absence of any commercial or financial relationships that could be construed as a potential conflict of interest.

Publisher's Note: All claims expressed in this article are solely those of the authors and do not necessarily represent those of their affiliated organizations, or those of the publisher, the editors, and the reviewers. Any product that may be evaluated in this article, or claim that may be made by its manufacturer, is not guaranteed or endorsed by the publisher.

frontiers in Materials

REVIEW
published: 10 February 2022
doi: 10.3389/fmats.2022.809226

Capillary Effects in Fiber Reinforced Polymer Composite Processing: A Review

Helena Teixidó[1†], *Jeroen Staal*[1†], *Baris Caglar*[2] *and Véronique Michaud*[1*]

[1]*Laboratory for Processing of Advanced Composites (LPAC), Institute of Materials (IMX), Ecole Polytechnique Fédérale de Lausanne (EPFL), Lausanne, Switzerland,* [2]*Aerospace Manufacturing Technologies, Faculty of Aerospace Engineering, Delft University of Technology, Delft, Netherlands*

Capillarity plays a crucial role in many natural and engineered systems, ranging from nutrient delivery in plants to functional textiles for wear comfort or thermal heat pipes for heat dissipation. Unlike nano- or microfluidic systems with well-defined pore network geometries and well-understood capillary flow, fiber textiles or preforms used in composite structures exhibit highly anisotropic pore networks that span from micron scale pores between fibers to millimeter scale pores between fiber yarns that are woven or stitched into a textile preform. Owing to the nature of the composite manufacturing processes, capillary action taking place in the complex network is usually coupled with hydrodynamics as well as the (chemo) rheology of the polymer matrices; these phenomena are known to play a crucial role in producing high quality composites. Despite its importance, the role of capillary effects in composite processing largely remained overlooked. Their magnitude is indeed rather low as compared to hydrodynamic effects, and it is difficult to characterize them due to a lack of adequate monitoring techniques to capture the time and spatial scale on which the capillary effects take place. There is a renewed interest in this topic, due to a combination of increasing demand for high performance composites and recent advances in experimental techniques as well as numerical modeling methods. The present review covers the developments in the identification, measurement and exploitation of capillary effects in composite manufacturing. A special focus is placed on Liquid Composite Molding processes, where a dry stack is impregnated with a low viscosity thermoset resin mainly via in-plane flow, thus exacerbating the capillary effects within the anisotropic pore network of the reinforcements. Experimental techniques to investigate the capillary effects and their evolution from post-mortem analyses to *in-situ*/rapid techniques compatible with both translucent and non-translucent reinforcements are reviewed. Approaches to control and enhance the capillary effects for improving composite quality are then introduced. This is complemented by a survey of numerical techniques to incorporate capillary effects in process simulation, material characterization and by the remaining challenges in the study of capillary effects in composite manufacturing.

Keywords: capillary effects, composite processing, liquid composite molding, textile preforms, fiber reinforced polymers

OPEN ACCESS

Edited by:
Douglas Soares Galvao, State University of Campinas, Brazil

Reviewed by:
Chung Hae Park, IMT Lille Douai, France
Al Emran Ismail, Universiti Tun Hussein Onn Malaysia, Malaysia
Jinhua Jiang, Donghua University, China

****Correspondence:***
Véronique Michaud
Veronique.michaud@epfl.ch

†These authors have contributed equally to this work and share first authorship

Specialty section:
This article was submitted to Polymeric and Composite Materials, a section of the journal Frontiers in Materials

Received: *04 November 2021*
Accepted: *18 January 2022*
Published: *10 February 2022*

Citation:
Teixidó H, Staal J, Caglar B and Michaud V (2022) Capillary Effects in Fiber Reinforced Polymer Composite Processing: A Review. Front. Mater. 9:809226. doi: 10.3389/fmats.2022.809226

1 INTRODUCTION

Capillary action is defined as the process whereby a fluid flows on a surface, thus displacing air or another immiscible phase present on this solid surface, under no external forces, simply due to the presence of intermolecular forces between the liquid and the solid surface. These forces arise from the presence of the liquid/air surface tension and the interfacial tension between the solid and the liquid phase. A pressure difference is thus created between the pressure in the air and that in the fluid phase, driving fluid flow at the interface between solid, liquid and generally air. For example, these effects help the fluid phase move up against gravity in a capillary tube that was initially filled with air, if the energy balance is favorable when replacing a solid-air interface by a solid-liquid interface. In a circular capillary tube, the capillary pressure drop, ΔP_γ, is written as:

$$\Delta P_\gamma = -\frac{2\sigma_{lv}\cos\theta}{r} \tag{1}$$

where θ is the contact angle between the liquid interface and the tube, σ_{lv} is the surface tension between the fluid and the ambient atmosphere, and r is the radius of the tube. $\Delta P_\gamma > 0$ thus indicates a non-wetting system whereas $\Delta P_\gamma < 0$ indicates a wetting system. Capillary forces play an important role in many physical systems where a fluid invades a network of narrow spaces, ensuring fluid circulation in plants, in the lacrimal ducts, wicks, brushes and towels, heat pipes, fountain pens, and of course they are at the base of hydrogeology and groundwater flow (Bear, 1972; Freeze and Cherry, 1979).

These effects are also found in composite processing, wherever an activated liquid monomer or polymer flows into the initially dry porous network formed by the reinforcing fibers (or powders); they will thus act close to the impregnation flow front, or in regions that are partially impregnated. In most cases, the reinforcing fibers or filaments, which have a diameter in the order of 7–20 μm, are produced in the form of yarns, comprising several thousands of filaments, which are then combined by textile processes into mats, woven, knitted or braided fabrics, as well as non-crimp fabrics or polymer bound tapes. As a result, fiber textiles or preforms used in composite structures exhibit highly anisotropic, in general dual scale pore networks that span from micron scale pores between fibers to millimeter scale pores between fiber yarns (Michaud, 2021). Owing to the nature of the composite manufacturing processes, capillary action is usually coupled with hydrodynamics, since flow is driven by externally applied pressure, as well as with the (chemo)rheology of the polymer matrices; in addition, the matrix material in liquid form is generally much more viscous than water, up to several orders of magnitude, leading to a strong dependence of the mechanisms to the interface velocity. Despite their importance, capillary effects largely remained overlooked in composite processing research. Their magnitude is rather low as compared to hydrodynamic effects, which dominate the flow kinetics. In general, the capillary pressure values found in composite processing are in the range of 1–70 kPa, whereas applied pressures are in the range of 10^2–10^3 kPa. In addition, it is difficult to characterize them due to a lack of adequate monitoring techniques to capture the time and spatial scale on which the capillary effects take place, and to model them, as they require rather advanced fluid flow analysis and the knowledge of the physical phenomena taking place close to the flow front. Interest is nonetheless rapidly increasing, due to a gain in process maturity and thus higher demand for high performance, low porosity composites and to recent advances in experimental techniques as well as numerical modeling methods. The present review addresses these, with particular focus on Liquid Composite Molding (LCM) processes, where a dry fabric stack is impregnated with a low viscosity thermoset resin mainly via in-plane flow, thus exacerbating the capillary effects within the anisotropic pore network of the reinforcements.

2 CAPILLARY EFFECTS IN POROUS MEDIA: PHYSICAL PRINCIPLES

Capillary effects in porous media are directly linked to the wetting of an initially dry porous medium by a fluid phase. Wetting is the ability of a liquid to stay in contact with a solid due to intermolecular interactions, creating a balance between adhesive and cohesive forces. The main parameters controlling capillary effects can be considered based on the different length scales they operate on, from the molecular scale controlling chemical and molecular interactions very close to the solid-liquid-air interface, to the sub-pore and pore scale where surface energy considerations lead to contact angles and menisci, up to the Representative Volume Element (RVE) scale, where macroscopic saturation is observed. The link between the thermodynamic and geometric considerations acting at these length scales has been the subject of intense work with many remaining open questions in the fields related to soil science, as recently reviewed by Armstrong et al. (Armstrong et al., 2021). Although we will consider thermodynamic effects and the possibility to modify the surface of the reinforcement to change wettability, we will mostly focus on the macroscopic or pore scale effects in this review, as these are most relevant in composite manufacturing, due to the presence of additional body forces beyond capillary forces.

As reviewed in Ref. (Michaud, 2016), the patterns found when a fluid displaces another one within a porous medium strongly depend on two parameters, which are the ratio of the invading (η_{resin}) to the displaced (η_{air}) fluid viscosity, $M_v = \frac{\eta_{resin}}{\eta_{air}}$, and the modified capillary number (as commonly referred to in literature on composite processing), a dimensionless number defined in soil science as:

$$Ca^* = \frac{Q}{A}\frac{\eta_{resin}}{\sigma_{lv}\cos\theta} \tag{2}$$

where Q is the invading fluid flow rate, A the cross-sectional area of the porous medium. The value of these two parameters defines a range of infiltration front patterns, from percolation and capillary fingering to viscous fingering, as illustrated in **Figure 1** for the case of a rather homogeneous porous

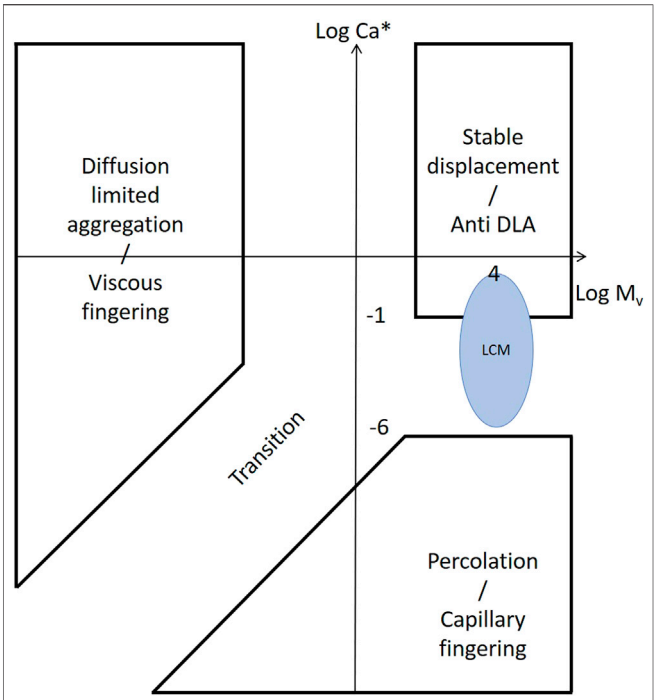

FIGURE 1 | Phase diagram for three types of displacements as a function of the capillary number and viscosity ratio. The blue ellipse schematically represents the location of LCM processes.

medium. In cases typical of LCM, where the invading fluid has a much higher viscosity than the air present in the fibrous preform, M_v is large, and the flow regime can vary from capillary fingering for very low Ca^* to a stable, hydrodynamics dominated plug flow displacement for large Ca^*. Note that for fluids of rather high viscosity as generally found in matrices used in composite manufacturing, as the contact angle strongly depends on the fluid velocity, as will be discussed later, the capillary number is often simply taken as:

$$Ca = \frac{Q}{A}\frac{\eta_{resin}}{\sigma_{lv}} \tag{3}$$

In polymer composite processing, fingering and percolation effects are generally omitted, whereas this approach has been applied to metal matrix composite processing where these effects are observed (Michaud et al., 1994; Léger et al., 2014, Léger et al., 2015; Schneider et al., 2019; Varnavides et al., 2021). Most of the soil science (as well as metal matrix composites) analysis considers a rather homogeneous porous medium without the dual scale and highly localized pore structures observed in polymer composite processing, apart from cases of fractured rocks (Sahimi, 2011), which could be used as an inspiration to the pore network description of textiles. Even the fractured rocks are often considered to contain randomly distributed channels rather than well-organized structures, thus leaving the textiles as a particular case with anisotropic pore networks formed via large inter-tow regions and small intra-tow regions.

As mentioned previously, fibrous reinforcements used in advanced composites generally exhibit a bimodal pore distribution. More specifically, pores present between the fibers in a yarn are referred to as micro-pores and empty space between the yarns are called meso-pores. Irrespective of the manufacturing process, an outcome of this pore characteristic is a matrix/fabric interaction at different scales that generally leads to a dual scale flow during resin infiltration (Bonnard et al., 2017). Hydrodynamic forces resulting from the applied pressure differential drive the impregnation process. However, the viscous drag is significantly higher in micro-pores (i.e., where permeability is lower). In addition, capillary forces are present at the fluid/fiber interface and the coupling between the yarn permeability, overall preform permeability and the capillary effects yield a complex relationship in terms of relative influence of flow within and between tows.

The interplay between different flow modes (micro- and meso-, viscous flow or capillary flow) results in formation of voids that change in shape and location depending on the extent of viscous and capillary driven flows. Void presence in an advanced composite is known to significantly reduce the mechanical performance of these materials and their formation as well as transport and removal has been studied in the literature (Lundström et al., 1993; Binetruy and Hilaire, 1998; Kang et al., 2000; Bréard et al., 2003b; Ruiz et al., 2006; Leclerc and Ruiz, 2008; Park et al., 2011; Abdelwahed et al., 2014; Gueroult et al., 2014; Mehdikhani et al., 2019; Castro et al., 2021). Despite the existence of several sources of void formation such as mechanical air entrapment, nucleation, leakage and cavitation; air entrapment is known to be the most common mechanism in LCM process, originating from the abovementioned dual scale porosity induced flow phenomena (Park and Lee, 2011; Mehdikhani et al., 2019). For a given system, higher Ca indicates dominance of viscous forces over capillary forces and vice versa. In the extremely slow impregnation situations with flow front speeds in the range of few mm/min, micro-flow progresses ahead of the meso-flow and results in entrapment of μm to mm sized spherical voids between tows (as illustrated in **Figure 2**). Similarly, high impregnation rates with typical flow front speeds in the range of several cm/min or higher, results in a delay of impregnation of small spaces between fibers in tows and in return causes formation of elliptically shaped, higher aspect ratio voids in the intra-tow spaces (Leclerc and Ruiz, 2008).

There exists a flow regime where the viscous and capillary forces are in balance which corresponds to an optimum capillary number, also referred to as Ca_{opt} (Leclerc and Ruiz, 2008; Park et al., 2011; LeBel et al., 2014). Void content as a function of Ca has been characterized experimentally (Leclerc and Ruiz, 2008) and numerically (Devalve and Pitchumani, 2013) and is known to follow a "V-shaped" trend as sketched in **Figure 2**. However the range of Ca_{opt} is known to differ for different matrix/fabric systems and as reported by Park (Park and Lee, 2011) and by Michaud (Michaud, 2016), typical values range in the order of 10–3 and in recent studies of Caglar et al. (Caglar et al., 2019) found a value of $1.4{\cdot}10^{-3}$, Lebel et al. (LeBel et al., 2019) a value of $1.5{\cdot}10^{-3}$ and Lystrup et al. (Lystrup et al., 2021) a value of $0.6{\cdot}10^{-3}$. The soil science version of the capillary number (Ca^*), as written

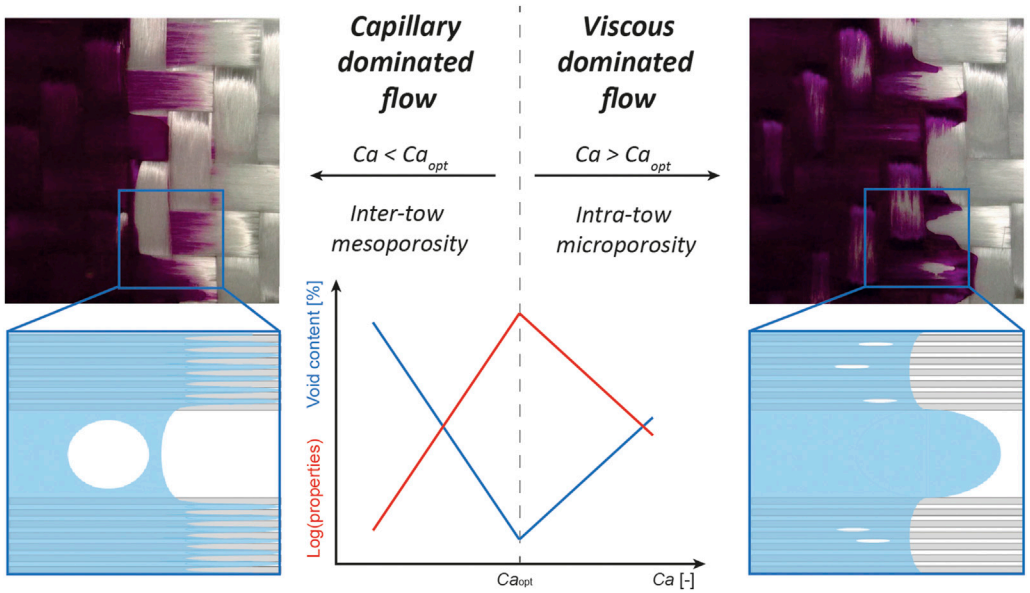

FIGURE 2 | Demonstration of the influence of the capillary number on the void formation and final part properties during infiltration based on fluids paths in a glass twill fabric under capillary- and viscous-dominated flow regimes.

in **Eq. 2**, is preferred in some studies, introducing the static contact angle between the matrix and fibrous reinforcement (θ_0) (Ruiz et al., 2006; Ravey et al., 2014; LeBel et al., 2017).

Alternative approaches have also taken place towards the definition of other non-dimensional numbers as an alternative to *Ca* and their use for identifying the optimal processing conditions, as the so-called Ca_{opt} is merely an intrinsic property of the matrix/fabric system and does not consider the process history (such as spatiotemporal variation of pressure and the formation and transport of voids as a result). Lawrence et al. (Lawrence et al., 2009) and Facciotto et al. (Facciotto et al., 2021) opted for using the so-called capillary ratio ($C = \Delta P_y / P_{inj}$) to account for the changes in the flow velocity over time. Lebel et al. (LeBel et al., 2019) defined a critical capillary number that is required to mobilize a void. In a similar vein, Matsuzaki et al. (Matsuzaki et al., 2015) developed an analytical expression to predict the void formation in anisotropic woven fabrics by decoupling the flow in different domains (meso-flow, transverse and axial micro-flow) and defining criteria for void formation depending on the relation between the required times to fill each domain.

Determination of Ca_{opt} or its modified counterpart (Ca^*_{opt}), as well as the other non-dimensional numbers discussed so far heavily relies on experimental studies with limitations that will be highlighted in the next section, as the current state of research is still far from linking the process conditions and geometrical descriptions of arbitrary matrix/fabric systems to a Ca_{opt} without requiring laborious experiments. Despite the efforts towards achieving flow simulation with ever increasing accuracy and fidelity, the complexity of the underlying physics and the need to account for those at several length scales hinders the developments in the field. The following sections will provide an overview of current developments in the experimental approaches for characterizing the extent of capillary effects in composite manufacturing and their link with residual porosity. Conventional approaches such as post-mortem analysis of composites will be followed by a survey of more advanced methods suitable for translucent reinforcements, mostly glass fibers, and recent developments in experimental approaches to study the capillary phenomena in other types of reinforcements, including but not limited to carbon fibers and natural fibers. Subsequent sections will then present the modeling efforts starting from microscale models to multiscale models that are inspired from the soil science literature to dual-scale models implemented using different numerical solvers and to semi-analytical approaches proposed to overcome the limitations of *Ca*-based residual void prediction.

3 OBSERVATION OF CAPILLARY EFFECTS

3.1 Capillary Wicking

Capillary pressure can be characterized in capillary wicking experiments, allowing for direct quantification from a single experiment. Amico and Lekakou (Amico and Lekakou, 2002) proposed a methodology where a fiber bundle, or a single ply of fibrous reinforcement (Caglar et al., 2019), is partially immersed into a probe liquid, where the capillary pressure was directly derived from the rate of weight gain or height increase. Pucci et al. (Pucci et al., 2015b) proposed a tensiometric method, based on Washburn's method (Washburn, 1921), to characterize capillary wicking of water and n-hexane in stacks of carbon fibrous preforms. By varying the orientation of the fibrous preforms they were able to determine the advancing contact angles in three,

i.e., weft, warp and through-thickness, directions, from which equivalent capillary pressures were derived. With coefficients of variation in the order of 30% this methodology is expected to be less accurate than that proposed by Amico and Lekakou (Amico and Lekakou, 2002) but the possibility to characterize fabric stacks and potentially vary fiber volume fractions makes it a very suitable method to apply in the context of LCM processing. It should be noted that capillary pressures measured in capillary wicking tests are not directly representative of those acting in LCM processes as the typical fluid velocities (hence *Ca*) encountered in these processes are not reached, in contrast to, e.g., direct flow experiments under a given applied pressure or flow rate (Salvatori et al., 2018). Nonetheless, capillary wicking experiments can be a valuable tool to obtain a first indication of capillary pressure in fibrous reinforcements, and to test changes in fiber surface conditions, volume fraction or pore morphology.

3.2 Post-Mortem Analysis

Post-mortem analysis on produced composite parts was the first and a facile method to observe and quantify the role of capillary effects. Post-mortem methods almost uniquely quantify capillary effects via the void content present after final consolidation of the composite, while varying process parameters (Lundström et al., 1993; Lundström and Gebart, 1994; Patel and Lee, 1995; Patel and Lee, 1996; Labat et al., 2001a; Leclerc and Ruiz, 2008) such as the flow rate or injection pressure and thereby the impregnation velocity. It is important to note that for impregnation under constant applied pressure, the velocity of the flow front decreases with the impregnation length. The presence of an optimum *Ca* (Patel and Lee, 1995; Patel and Lee, 1996; Labat et al., 2001a; Leclerc and Ruiz, 2008), where minimum void content is present within the composite, was often reported, while similar consequential observations were made for the resulting tensile modulus and tensile strength (Leclerc and Ruiz, 2008). While bringing the advantage of being an easy method with low equipment costs, post-mortem analysis of capillary effects could lead to large inaccuracies. These arise partially from the methods used for void content analysis such as, in order of increasing accuracy (Little et al., 2012), Archimedes (Kedari et al., 2011), microscopy (Lundström et al., 1993; Lundström and Gebart, 1994; Kedari et al., 2011) and micro-CT (Madra et al., 2014; Sisodia et al., 2016) methods, while part void content is also affected by phenomena occurring after passing of the flow front, e.g., void transport and dissolution into the resin. In spite of the strong assumption that part saturation in a chosen location does not change after passing of the flow front and during the cure/solidification process, these analyses have nonetheless been crucial to highlight the strong influence of capillary effects on part void content, as illustrated in **Figure 2**.

3.3 *In-situ* Analysis

An a priori more accurate method to analyze capillary effects taking place at the flow front is to observe, *in-situ*, the flow front progression and morphology, either very locally at the scale of a few fiber tows, or through the macroscopic analysis of the progressive saturation of the porous medium with the flowing fluid. These analyses usually refer to a saturation term, *S*, which is defined as the ratio of the volume fraction of liquid over the available pore space and is equal to 1 when the porous medium is fully filled with the liquid phase.

3.3.1 Transparent Fiber Reinforced Polymers

In-situ measurements allow for direct observations of capillary effects taking place in polymer composite processing. Optical methods can record impregnating resins in fibrous preforms in a non-intrusive manner and at a high spatial and time resolution with simple equipment, making it an effective and low-cost method for flow characterization (LeBel et al., 2019). Optical imaging is generally limited to translucent fabrics and relies on the matching of refractive indices to distinct phases (Lawrence et al., 2009; Nordlund and Michaud, 2012; LeBel et al., 2019), i.e., refractive indices of epoxy/fiberglass can be very different from that of the air/fiberglass interface and the distinction between the two interfaces can be further enhanced by colorants compatible with the test fluid (Caglar et al., 2018; Salvatori et al., 2018). Recording a linear flow with a conventional camera and subsequent image analysis has allowed Nordlund and Michaud (Nordlund and Michaud, 2012) and Facciotto et al. (Facciotto et al., 2021) to estimate the width of the unsaturated region, which was subsequently modelled with finite difference (Nordlund and Michaud, 2012) and finite element models (Facciotto et al., 2021). Continuous imaging of these regions showed the progressive saturation of the preform, which was quantified from the pixel intensity in the successive pictures. Standard camera imaging however only captures the flow at the surfaces of the mold (in general a glass top surface), which are known to be vulnerable to wall-effects, i.e., race-tracking between the preform and the mold halves, while effects such as nesting are also not well captured (Chen and Chou, 2000; Yousaf et al., 2017).

Visible Light Transmission (VLT), illustrated in **Figure 3A**, has been proposed as an elegant method to overcome this limitation (Lawrence et al., 2009). Placement of a diffuse light source below the transparent mold halves and of a camera above it makes the recorded light intensity an average over the preform thickness. Moreover, the signal is also significantly intensified. Lebel et al. (LeBel et al., 2017; LeBel et al., 2019) employed VLT to characterize the relation between processing conditions, i.e., Ca^*, and saturation of a glass fabric. The increased light intensity allowed them to accurately estimate the local void content after calibration with burn-off composites after consolidation. Distinction of voids allowed them to estimate the optimum Ca^* as well as the onset of pressure-induced void mobility. Further contrast enhancement could be achieved by the addition of fluorophores into the probe liquid. This resulted in strong contrast enhancement, e.g., for visualization of intratow flow (Lebel et al., 2013; LeBel et al., 2014), even enabling the use of optical methods in opaque carbon fibrous preforms (Lystrup et al., 2021). The addition of dyes may however induce changes in resin properties, e.g., wettability, and thereby may affect the apparent *Ca* or Ca^*, making the resulting observations not directly representative of pure resin systems.

Increases in spatial resolution and observations on tow-scale could be achieved with the use of optical microscopy imaging.

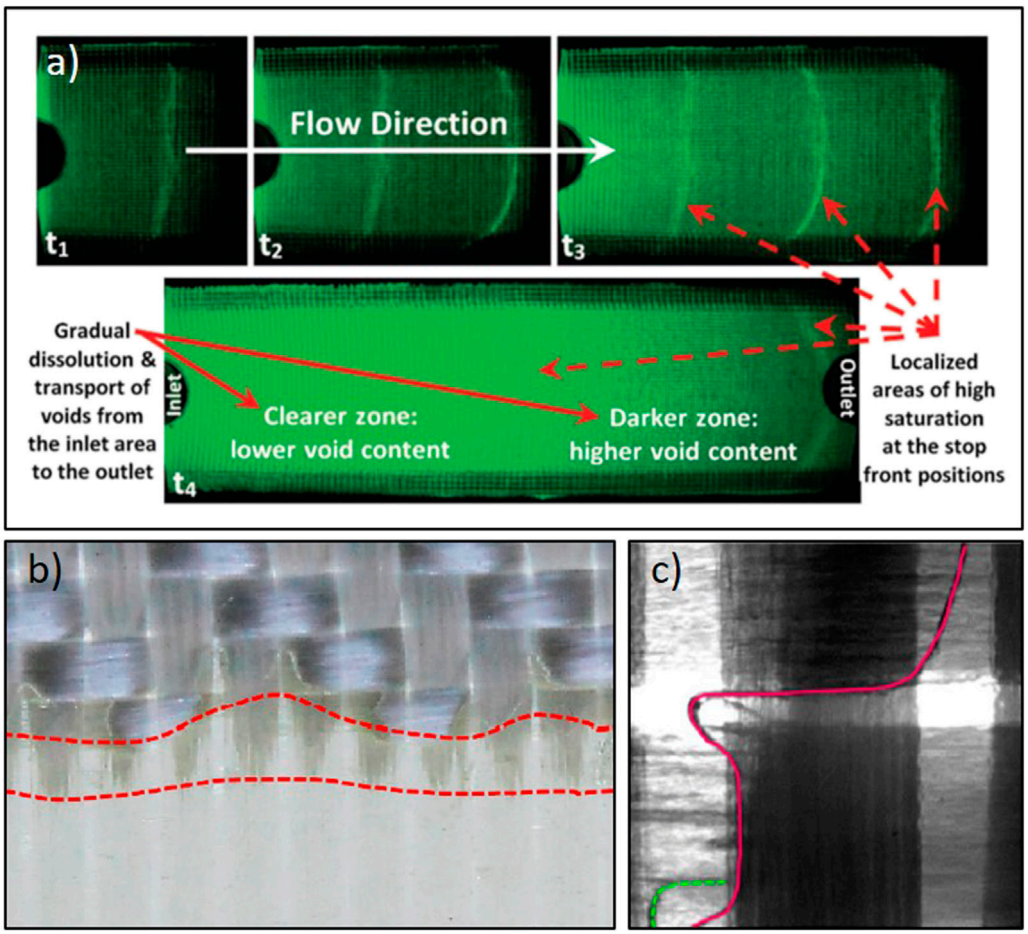

FIGURE 3 | Demonstrations of optical methods for flow characterization at different scales, with increasing resolution: **(A)** Visible Light Transmission on centimetre-scale (Source: (LeBel et al., 2017)), **(B)** UV-flow freezing on millimetre-scale (Source: (Caglar et al., 2019)), **(C)** Microscope imaging on micron-scale (Source: (Yoshihara et al., 2020)).

This increased resolution, however, comes at the cost of the overall field of view, making the method better suited for local detection of voids rather than for the assessment of saturation. Yoshihara et al. (Yoshihara et al., 2020) investigated the role of capillary pressure, varied by the application of different fluorine coatings on the fiber surface, on the dual-scale flow behavior in an optical microscopy setup. This allowed them to observe infusion of a woven fabric on a micron-scale, shown in **Figure 3C**, which were coupled to numerical simulations. Zhao et al. (Zhao et al., 2019) and Matsuzaki et al. (Matsuzaki et al., 2014) followed a similar approach in their studies on void formation and were able to accurately record capillary fingering and void formation upon the impregnation of a woven preform at a range of velocities falling in the capillary-dominated regime. This allowed them to accurately capture the void formation and evolution with the use of *in-situ* optical microscopy. However, flow analysis by means of optical microscopy can typically be applied to single ply fibrous reinforcements if based on light diffusion and suffers from the aforementioned wall effects in reflectance mode, while the upper limit of allowed infusion rates is defined by the maximum imaging rate of the microscope. Caglar et al. (Caglar et al., 2019) proposed an *in-situ* UV flow-freezing method (**Figure 3B**), where infiltrating flows are *in-situ* cured by UV-photopolymerization. This overcomes any constraints in time resolution allowing for visualization of a large range of flow regimes. This method however requires the use of specially designed resin systems and rather thin and transparent samples to avoid inhibiting the cure reaction that is highly dependent on the penetration of UV light.

3.3.2 Non-Transparent Fiber Reinforced Polymers

The opaque nature of many commercially available fibers in polymer composites, e.g., carbon or flax, limits the optical observations of capillary effects in processing to the outer layers, which are susceptible to wall effects as discussed in **Section 3.3.1**. A multitude of methods have been proposed to overcome this limitation, ranging from methods already widely established in other fields, e.g., Magnetic Resonance Imaging (MRI), to more exploratory techniques such as infrared thermography. With no universal agreement on the preferred

technique to elucidate the degree of fluid saturation as a function of time and position, each specific method brings its own advantages and trade-offs between spatial resolution, recording speed and ease of implementation.

One of the proposed methods to track resin front progression and thereby indirectly record progressive saturation and void formation in LCM processing is the inclusion of sensors in or in-between stacked preforms (Konstantopoulos et al., 2014). Methods using conductive sensors typically require a non-conductive fibrous preform to be placed in between two conductive parallel plates. Labat et al. (Labat et al., 2001b) and later Gueroult et al. (Gueroult et al., 2014) infused a glass fiber preform with a conductive liquid and simultaneously recorded the voltage over the preform, which increased with increasing saturation. The first strong increase of the voltage was attributed to the passing of the unsaturated flow front followed by a period of void removal, while the final voltage was directly linked to the saturation and hence the void content in the part. The recorded void contents moreover followed the expected "V-shaped" curve as a function of $Ca^{\star}$. Carlone et al. (Carlone and Palazzo, 2015; Carlone et al., 2018) employed a similar experimental methodology while recording the capacitance over the fabric preforms and correlated the observations to numerical models. This methodology also allowed for impregnation with less conductive resins. Similar saturation curves were obtained and verified in comparison with the void contents in post-mortem optical microscopy images. They moreover compared the accuracy of progressive saturation tracking by dielectric sensors with that recorded by pressure sensors, e.g., as proposed by Refs. (Di Fratta et al., 2013; Chiu et al., 2018), which was found to be significantly higher. The requirement for a non-conductive fibrous preform limits the use of the methods developed by Refs (Labat et al., 2001b; Gueroult et al., 2014; Carlone and Palazzo, 2015; Carlone et al., 2018). with several conventional fabric types. Developments have been made to overcome this issue, e.g., by insulating the sensor with a dielectric material and optimization of the sensor characteristics (Pouchias et al., 2019; Caglar et al., 2021a). However, these types of sensors have not yet been employed to study unsaturated flow phenomena to-date. Alternatively, Villière et al. (Villière et al., 2015) proposed a method based on the saturation-dependence of the thermal behavior of a resin-fiber system. Recording of heat fluxes induced by an electric heater was found to give an accurate representation of the local saturation, which were coupled with mathematical models to fit progressive saturation curves. Implementation of optical micro-flow sensors within tows on the other hand gives the possibility to record capillary pressures, as was demonstrated by He et al. (He et al., 2019) in their study on resin flow in prepreg processing. However, introducing thermal gradients in the fluid induces changes in the viscosity and surface tension characteristics and requires elaborated material characterization next to the experimental analyses.

The discrete nature of sensors limits the observations that can be made in a single impregnation while the spatial resolution of methods making use of integrated sensors is relatively low. Imaging techniques typically possess higher spatial resolution over a larger section of the composite part. Ultrasound techniques are known for their high acquisition rates and have been used to track resin flow in fibrous preforms (Schmachtenberg et al., 2005), in particular for through-thickness resin infusion (Stöven et al., 2003; Thomas et al., 2008; Konstantopoulos et al., 2018). Thomas et al. (Thomas et al., 2008) tracked through-thickness resin flow via acoustic C-scan measurements giving a planar view of the sample. While this method gives an indication of through-thickness saturation of the preform, the limited spatial resolution does not allow for distinction of capillary effects such as localized saturation and void formation. Unsaturated permeability on the other hand was successfully characterized with use of ultrasound, given a microstructure-dependent minimum fiber content is present within the preform (Konstantopoulos et al., 2018).

Magnetic Resonance Imaging (MRI) (Callaghan, 1993) has been investigated as well to observe flow in porous media. While suffering from drawbacks such as large tooling costs and spatial resolutions that are limited to around 0.1 mm due to signal relaxation effects (Endruweit et al., 2011), MRI brings the advantage of an excellent material contrast between constituents of composites, i.e., fibers, polymer and voids, which could be further enhanced by the addition of contrasting agents or by specified measurement sequences (Neacsu et al., 2007). MRI has therefore been used for the characterization of flow in fibrous preforms (Mantle et al., 2001; Bijeljic et al., 2004; Bencsik et al., 2008), with several studies specifically focused on visualizing dual-scale flow behavior. Leisen and Beckham (Leisen and Beckham, 2008) proposed a method of nuclear MRI and subsequent image analysis to quantify inter-yarn voids and their morphologies in saturated woven nylon fabrics, while Neacsu et al. (Neacsu et al., 2007) applied MRI to characterize capillary effects in glass fiber bundles. In the latter case they found fast MRI imaging able to track progressive transversal impregnation within bundles with different volume fractions and were able to use this data to back calculate the driving capillary pressures. Endruweit et al. (Endruweit et al., 2011) carried out an extensive investigation regarding the use of MRI to *in-situ* image the impregnation of dual-scale textiles. Reconstructed 3D images had resolutions of 0.5 mm, visualizing the meso-structure of fibrous preforms. An intermittent injection strategy was used to overcome time resolution limitations, which allowed for imaging of various flow regimes. Resulting images clearly visualized the progressing flow front and the formation of inter-yarn voids, while progressive saturation was tracked by a gradual increase of relative signal intensities.

Intrinsic differences in X-ray absorption coefficients of composite constituents gave rise to a multitude of X-ray-based techniques that were applied to study *in-situ* the role of capillary effects in LCM processing. Bréard et al. (Bréard et al., 1999) continuously tracked through-thickness impregnation of a random mat stack using X-ray radiography. While image resolution was insufficient to capture the fibrous preform, fast imaging allowed for accurate tracking of the infiltrating fluids. Teixidó et al. (Teixidó et al., 2021) used an X-ray phase contrast method *in-operando* to assess saturation of several types of

fibrous preforms. Based on the material-sensitive phase modulation due to interference formed after passing X-rays through a grating, the material contrast, which can be a limiting factor for composites, is significantly enhanced (Gresil et al., 2017). Employing this method allowed them to image progressive saturation of 15 cm × 5 cm non-transparent fabrics over a range of capillary numbers and they were able to extract the thickness-averaged saturation curves from these images, with a time step below 10 s.

The use of X-ray micro computed tomography (μCT) has allowed for the observation of dual-scale flow at an unprecedented resolution. Based on the reconstruction of 3D images from a set of radial X-ray radiographs, X-ray μCT provides the ability to reconstruct through-thickness images of opaque materials (Withers et al., 2021). Features down to sub-μm can be reached, e.g., allowing for accurate imaging of carbon composites and of the void morphology, while image resolutions typically come at a cost of the volume that can be analyzed, and the measurement speed. 4D μCT imaging (3D in space and time), e.g., to study the dual-scale flow behavior, is moreover typically complicated by possible blurring effects occurring, reducing image resolution due to movement of the flow front (Castro et al., 2021). To avoid this, the acquisition time should be short enough to limit the movement to less than 1 voxel per scan (Castro et al., 2021). While some studies have thus aimed at indirect observations of dual-scale flow behavior, e.g., by assessing thickness changes (Hemmer et al., 2018) or image-based computational fluid dynamics simulations (Ali et al., 2019), several investigations aimed at *in-situ* imaging dual-scale flow behavior through a fibrous preform. Vilà et al. (Vilà et al., 2015) were the first to use μCT to study the intra-tow infiltration of a glass fiber bundle in a μCT synchrotron beamline. Infusion was carried out under a capillary-dominated regime and was halted to image the flow front. Images were reconstructed from 900 radiographs taken over a period of 120 min with a voxel size of 2.5 μm^3. At a slightly reduced resolution, Larson et al. (Larson and Zok, 2018; Larson et al., 2019) were able to drastically reduce the imaging time, i.e., to 1.5 min, which allowed them to *in-situ* record impregnation of an enclosed fiber bundle with capillary numbers up to 10^{-3}. They furthermore employed advanced segmentation methods to distinguish local saturated and dry sections. Vilà et al. (Vilà et al., 2015) and Larson et al. (Larson and Zok, 2018; Larson et al., 2019) were both able to observe progressive saturation of the fiber bundle and were able to relate this to local capillary pressures and permeabilities, while the more homogeneous fiber distributions of Larson et al. (Larson and Zok, 2018; Larson et al., 2019) resulted in more homogeneous distributions and magnitudes. They were moreover able to gain insight in the apparent dynamic contact angles and to relate this to fiber displacement. Static contact angles after capillary wicking of a fiber bundle was studied in more detail by Castro et al. (Castro et al., 2020), who employed synchrotron-μCT to produce high resolution images. Image analysis then allowed for an assessment of axial and transverse contact angles.

The resolution requirement to obtain an accurate representation of (carbon) composites with a conventional μCT setup limits the sample size significantly. Castro et al. (Castro et al., 2021) overcame this limitation by making use of so-called synchrotron radiation computed laminography, where significant gains in field of view can be achieved by imaging planar samples at an angle (Helfen et al., 2011; Bull et al., 2013; Fisher et al., 2019). In combination with a fast acquisition rate, i.e., 1.8 min per tomogram, they were the first to *in-situ* image dual-scale flow behavior in woven textiles with micron-scale resolution. Equilibrated flow regimes (**Figure 4A**) were imaged and, although slightly affected by blurring due to movement of the flow front, the images clearly showed the microstructural evolution upon impregnation and the absence of void formation. Slower infusion rates in capillary-dominated regimes (**Figure 4B**) minimized the blurring effect, giving a highly detailed insight on progressive saturation and void formation upon impregnation. Moreover, they were able to segment and analyze both inter- and intra-yarn void distributions as well as gaining novel insights in the void formation mechanisms during LCM.

3.4 The Case of Natural Fiber Reinforced Polymers

Composites made of natural fibers, in general plant-based, are gaining interest for the development of more sustainable and eco-friendly composite materials. Natural fiber reinforced composites still present a large amount of porosity and processing defects mainly due an incomplete understanding of the role of the initial humidity level in the fibers, surface characteristics, depending on the fiber treatment such as alkali treatments, and their complex morphology (illustrated in **Figure 5**). Compared to synthetic fibers, plant based fibers are also known to suffer from extensive resin absorption and swelling due to their microstructure, which highly alter flow characteristics (Francucci et al., 2010; Pucci et al., 2017b; Garat et al., 2020; Salokhe et al., 2021). Moreover, they present irregular and complex morphological and surface properties. Fibers are built-up from elementary cells with a given length and an irregular cross-section, and are composed of a hierarchical sequence of wall layers of different composition and thicknesses around an internal closed cavity called the lumen (Pantaloni et al., 2021). Depending on the extraction conditions, fibers can be present in the fabric as elementary fibers with diameters around 20–40 μm or technical fibers (several elementary fibers bonded together with the middle lamella which acts as matrix) with larger variable sizes in the order of some hundred micrometers (Melelli et al., 2020). The fiber surface roughness together with the composition of lignin, cellulose and hemi-cellulose of the outer layer define the wetting properties of the natural fiber. Given the complexity of the porous network and surface properties of natural reinforcements, the understanding of infiltration and in particular of capillary effects has remained as a very complex issue to-date.

Dual-scale flow behavior and void formation mechanisms in LCM processes have also been observed in the case of natural fiber preforms (Pantaloni et al., 2020), and have received increasing attention over the past decade. Francucci et al. (Francucci et al., 2010) found that natural fibers exhibit capillary pressures that are two or three times higher

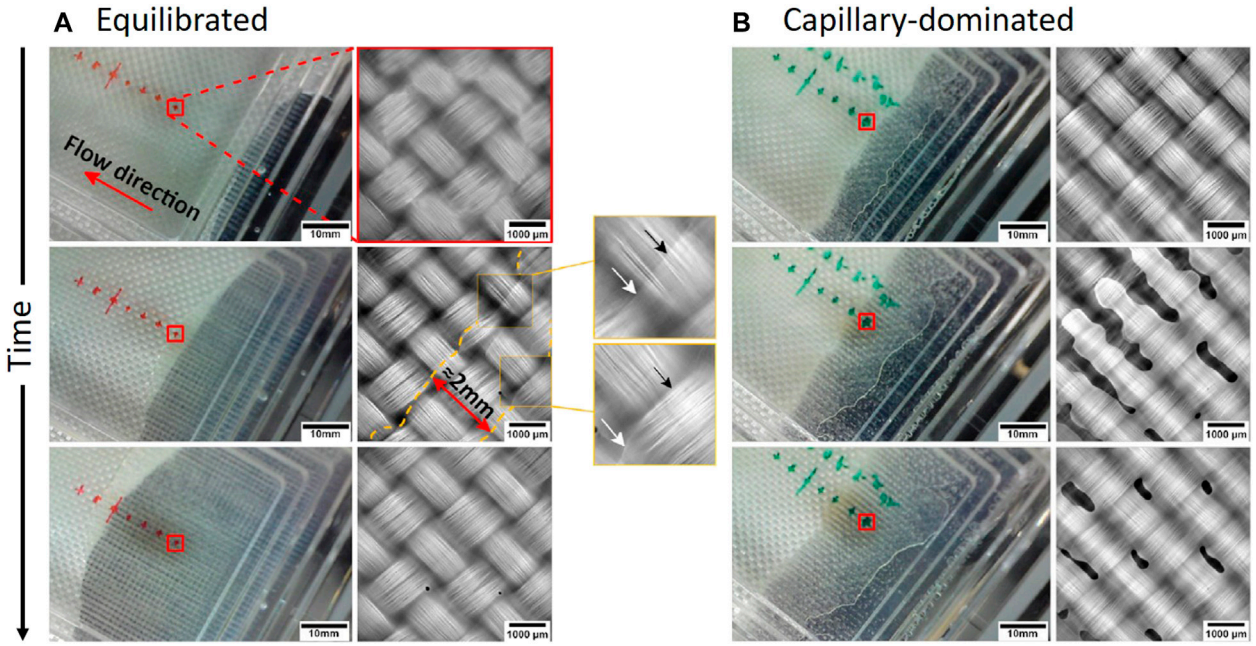

FIGURE 4 | Progressive saturation recorded by synchrotron radiation computed laminography of **(A)** Equilibrated and **(B)** Capillary dominated flow regimes (Source: (Castro et al., 2021)).

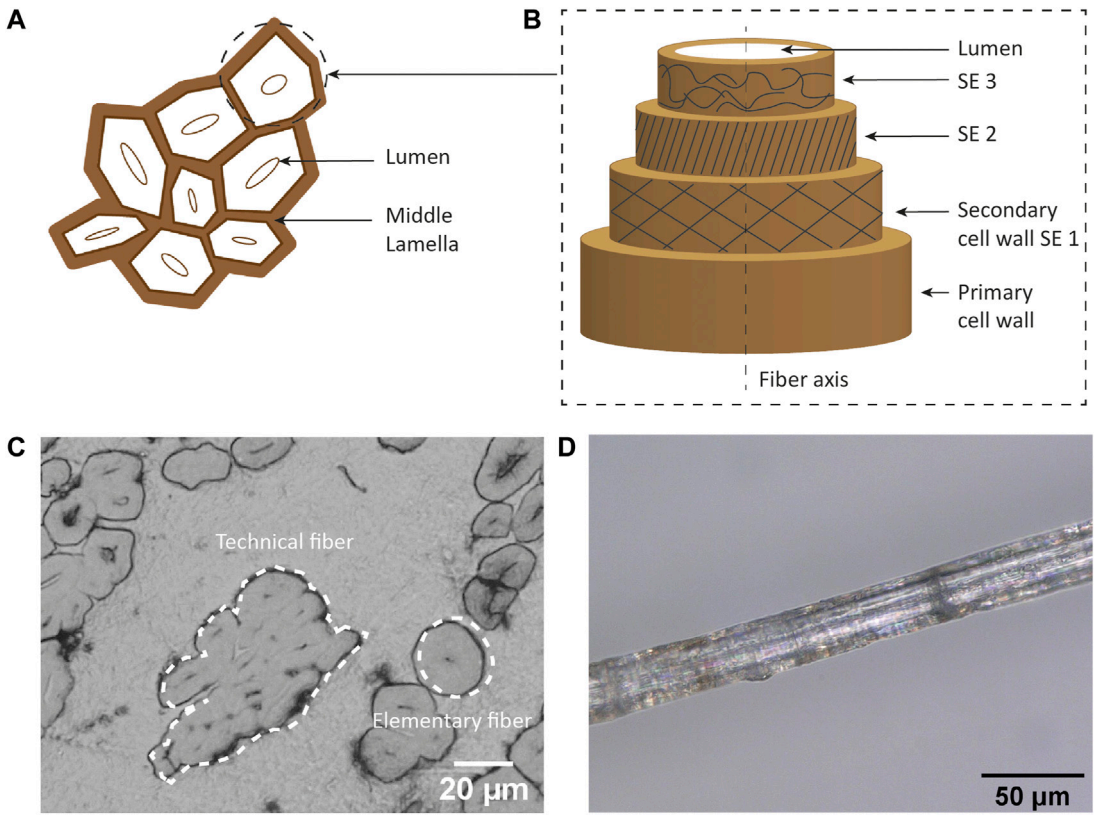

FIGURE 5 | Structure of natural fibers: Schematic representations of **(A)** technical (fiber bundle from the stem) and **(B)** elementary fiber, **(C)** optical microscopy image of technical and elementary fibers in a composite and **(D)** optical microscopy image of an elementary fiber surface.

compared to synthetic fibers, elucidating the relevance of micro-flows and capillary effects occurring during impregnation. Some authors attributed this to the hollow structure of the fibers (Francucci et al., 2010; Yin et al., 2018) however recent studies have shown limited evidence that the resin can impregnate the lumen since it is a closed cavity (Pantaloni et al., 2020). Due to the polar nature of the fibers, the model fluid chosen to carry impregnation measurements highly influences the study of capillary effects. For example, Francucci et al. (Francucci et al., 2010) carried out unidirectional impregnation experiments of woven jute fabrics with a water/glycerin solution and a vinylester resin. They measured the capillary pressure and obtained -25 and 36 kPa with the water-based solution and the resin respectively.

As already said, natural fibers are sensitive to liquid absorption. In consequence, during infiltration, fibers remove liquid from the main stream of infiltrating resin, acting as a sink component, decreasing the velocity of the flow as the fiber cross-section tends to enlarge due to liquid absorption and reduction in permeability during impregnation (Francucci et al., 2010; Testoni et al., 2018). Testoni et al. (Testoni et al., 2018) showed in capillary wicking tests that the swelling of the fibers leads to a reduction of the inter-fiber pores and thus an increase of the capillary pressure. With the aim of predicting and modeling the relation between capillarity and swelling in natural fibers, researchers used a similar approach based on physical wicking experiments coupled to modified Washburn's equations (Pucci et al., 2015a, 2016; Testoni et al., 2018; Vo et al., 2020). In wicking tests, synthetic fibers show a linear trend following Washburn's equation whereas a non-linear trend is usually observed for natural fibers due to swelling. Pucci et al. (Pucci et al., 2016) proposed a modified Washburn's equation, taking into account the change in the porosity due to swelling over time. They assumed a capillary radius decreasing linearly with time, from the initial to the final swollen values, when wicking the fabrics in water. More recently, Vo et al. (Vo et al., 2020) improved their numerical model by defining a dual scale porosity (dual scale capillary radius) of the flax fibers since wicking takes place in between individual yarns and in between elementary fibers. Swelling induced changes in the pore distribution and the effects on the capillary action more complex at high fiber volume fraction (V_f). The proposed method successfully predicted swelling of a flax fabric in water for V_f ranging from 30 to 60%. As recently reviewed by Pantaloni (Pantaloni et al., 2020), flow modelling taking into account both swelling and fluid absorption by the natural fibers could be carried out by modifying the continuity equation accordingly, allowing for changes in both saturation (through a sink term) and porosity over time.

3.5 Role of Sizing and Additional Phases in the Textile Preform

3.5.1 Role of the Fiber Surface Treatment

Commercial fibrous preforms are coated with sizings that form an interphase region between fibers and polymer (Thomason, 2021). Sizings are generally functionalized for compatibility with specific monomer types. Alteration of the surface chemistry of the fiber affects its wettability and thereby the capillary pressures exerted on infiltrating resins, in particular during intra-yarn flow (Palmese and Karbhari, 1995; Thomason, 2021). The wettability of commercial sizings is reported to vary strongly (Bernet et al., 2000) due to differences in the sizing composition, e.g., resin-fiber interactions of glass fibers determining contact angles are sensitive to the silane types (Wei et al., 1993; Araujo et al., 1995) and content present in the sizing (Nishioka, 1990; Karbhari and Palmese, 1997). Hence, the sizing composition could potentially be employed to control local capillary pressures and thereby dual-scale flow in LCM processing, but the confidential nature of commercial sizing compositions has impeded further investigations into the role of sizing compositions on the (intra-yarn) flow behavior. Sharma et al. (Sharma et al., 2009) observed that permeabilities of fibrous preforms, measured with silicon oil and Karo syrup as model fluid phases, are lower in the presence of a compatible sizing. In the absence of capillary effects, saturated permeability decreases due to the stronger resin-fiber interactions experienced by an infiltrating resin in the presence of a dedicated sizing. The decrease in capillary driven unsaturated flow was in agreement with the intra-yarn flow analysis as reported by Wang et al. (Wang et al., 2006) or Palmese and Karbhari (Palmese and Karbhari, 1995; Karbhari and Palmese, 1997) and was attributed to resin-fiber interactions to differences specific surface free energy (Steenkamer et al., 1995; Karbhari and Palmese, 1997). Capillary pressures moreover are reported to be lower for dedicated sizings due to the consequent increase of the contact angle. It should be noted however that dynamic, advancing, contact angles and thereby capillary pressures are highly dependent on the imposed flow rates in LCM (Karbhari and Palmese, 1997), which could potentially explain the decrease in capillary pressure in the presence of a dedicated sizing by increased induced wicking rates.

Surface treatments on sized fabrics have furthermore shown promise to control resin-fiber interactions in LCM processing. Physical treatments comprise electric discharge/plasma treatments, which are extensively employed in polymer composite production (Mittal et al., 2018). Application of electric discharge treatments increases polarity of the fiber surface due to the suggested formation of additional carboxyl and hydroxyl groups (Morent et al., 2008; Sinha and Panigrahi, 2009; Mittal et al., 2018). Caglar et al. (Caglar et al., 2019) assessed the influence of these oxidative treatments on the impregnation of glass fiber textiles. They found that the increased polarity decreased the capillary pressure drop, which subsequently accelerated capillary wicking. Analysis of UV-frozen flow fronts showed that the optimum *Ca* shifted after applying the treatment while the unsaturated region in capillary-dominated flow counterintuitively became smaller. This latter was attributed to a more favorable transverse flow when treated, spreading out the flow front. Application of this surface treatment strongly accelerated impregnation in capillary-dominated regimes, i.e., up to 50%. Further control of surface properties could be achieved by the application of numerous chemical treatments (Mittal et al., 2018). As an example, Yoshihara et al. (Yoshihara et al., 2020) controlled the capillary pressure

by the application of fluorine coatings on glass fiber textiles, which enhanced the capillary effects acting during resin infiltration.

3.5.2 Role of Additional Phases in the Textile Preform

In the search to expand the areas of use of polymer composites, strategies to introduce additional functions have been proposed. Functionalization by the presence of second phase particles in the polymer matrix could improve the overall mechanical, thermal and electrical performance of the resulting composite. Examples of second phases include capsules for self-healing behavior (Kessler et al., 2003; Cohades et al., 2018), hollow microspheres to reduce the composite density (Porfiri and Gupta, 2009; Zhang et al., 2016) and powders to tailor capillary effects in porous structures (Kostornov et al., 2015). The introduction of these particles can however introduce complications in LCM processing. Filtration effects are commonly observed upon the infiltration of nanoparticles (Reia Da Costa et al., 2012; Yum et al., 2016; Zhang et al., 2017), which can even occur at fiber volume fractions of ~40% (Louis et al., 2014). A study by Louis et al. (Louis et al., 2019) showed that the filtration behavior of nanoparticles mainly depends on the particle size and the fiber volume fractions, while the nature, i.e., type of particle is also reported to have a large influence. The role of second phases on the capillary effects taking place in LCM processing is little understood. In their work on the processing of self-healing capsules, Manfredi and Michaud (Manfredi and Michaud, 2014) observed bilinear infusion rates, where, after an initial phase, the unsaturated permeability of the preforms strongly increased compared to that when no capsules were present. This was attributed to increased capillary effects that drive the flow in the presence of capsules, but no correlation between the particle concentration and the in-plane permeability was found. Caglar et al. (Caglar et al., 2017) tried to gain an improved understanding of these effects by a combination of in-plane permeability experiments and computational simulations. They confirmed that permeabilities increased in the presence of spherical glass; this was moreover found to depend on the bead diameter and the concentration in the composite. In a parallel study (Caglar et al., 2016), they reported on the influence of particle size and volume fraction on the capillary effects. They concluded that relatively small particles (40–70 μm and 100–200 μm) at low volume fractions enhanced the capillary effects, whereas an increase in the volume fraction resulted in a more homogenous pore distribution which yielded more balanced flows. On the other hand, large particles (400–800 μm) caused extensive deformation of the fabric layers and formation of new large flow channels resulted in less pronounced capillary flow enhancement.

Hierarchical composites have shown promising enhancements in mechanical, thermal and electrical performance (Thostenson et al., 2002; Yamamoto et al., 2009; Qian et al., 2010b; Chou et al., 2010; Spitalsky et al., 2010) when nanometer-spaced CNTs are grafted onto the fiber surfaces. With capillary pressure being inversely proportional to the channel diameter, strong capillary action (Futaba et al., 2006; Liu et al., 2006; Garcia et al., 2007) is induced in the presence of these nanoporous CNT forests. Garcia et al. (Garcia et al., 2008) observed complete impregnation of their 80 nm-spaced CNT forests grafted on an alumina textile and suggested capillary effects to have contributed to this. Recent investigations by Staal et al. (Staal et al., 2021) on the permeability of the same fabric supported this suggestion. Induced capillary action by the presence of grafted CNTs can further be observed by fast droplet spreading over the surface of a single fiber (Qian et al., 2010a). Alternatively, Lee et al. (Lee et al., 2020) exploited the strong capillary actions induced by nanoporous networks of aligned CNTs for void-removal in Out-of-Autoclave (OoA) prepreg processing. Introduction of a nanoporous network between plies was estimated to increase the pressure gradient at the resin/void interface, i.e., the driving force for void removal, by 57% resulting in a void free composite, while a layup without these networks had a large void content. Moreover, resulting mechanical properties of the OoA-produced composites were like those achieved after conventional autoclave processing.

3.5.3 Capillary Effects in Thermoplastic LCM Processing

Influence of capillary effects in reactive thermoplastics and melt thermoplastics is strongly linked to their viscosity: for the reactive thermoplastics-based monomer (Rijswijk et al., 2009; Han et al., 2020; Obande et al., 2021), it is typically in the same range as or even lower than the viscosity of thermosetting polymers used in LCM processes while melt thermoplastics have a few orders of magnitude higher viscosities (Rijswijk et al., 2009; Salvatori et al., 2019; Han et al., 2020; Obande et al., 2021). In reactive systems, the capillary phenomena and their effects are similar to those found in thermosetting systems, but with enhanced capillary action resulting from the low viscosity of the fluid phase. For instance, Zingraff et al. (Zingraff et al., 2005) experimentally studied the resin transfer molding of a woven fabric with the precursor of an anionically polymerized polyamide 12 and also found an optimum capillary number range (in the order of 10^{-3}) where the void content was minimal. Similarly, Murray et al. (Murray et al., 2020) studied the resin transfer molding of unidirectional stitched glass fabrics with the precursor of *in-situ* polymerized polyamide six and demonstrated the dominance of viscous flow within the bundles as well as the void formation within bundles due to lack of balance between capillary and viscous forces. Melt thermoplastic impregnation is gaining importance in recent years, however capillary effects so far have not been analyzed (Studer et al., 2019; Gomez et al., 2021) as their impregnation is dominated by viscous forces due to the high-pressure differential and/or high viscosity of thermoplastic resins. Research is however ongoing to better capture the role of molecular weight and temperature in the wetting characteristics of polymers (Duchemin et al., 2021).

3.5.4 Capillary Effects in Continuous Composite Manufacturing

Next to LCM processes where the flow lengths can reach up to meters, capillary effects manifest themselves also in continuous composite manufacturing. For instance, resin bath impregnation pultrusion (Strauß et al., 2019; Vedernikov et al., 2020) is a

common technique for manufacturing fiber reinforced profiles of varying cross-sectional complexity. Irfan et al. (Irfan et al., 2017, 2021) modified the resin bath where the rovings are impregnated before entering the mold where they are shaped into the final cross-sectional profile. They demonstrated that in their modified pultrusion process, capillary impregnation was dominant owing to pre-spreading the fibers before entering the resin bath and the extended fluid reservoir promoting the capillary actions under low pressures. Another continuous composite route is the manufacturing of fiber reinforced (typically unidirectional) thermoplastic tapes that are then used in secondary processes such as automated fiber placement, press forming or in autoclave processes. Melt impregnation is generally used for thermoplastic tape manufacturing, as well as powder impregnation. In all cases, as well as in commingled yarns where reinforcement fibers and polymer fibers are intimately mixed, impregnation takes place after the polymer has melt, and capillary effects may again play a role towards local impregnation of the fiber tows. This was for example exploited by Ho et al. (Ho et al., 2011) for improving the quality of their wet powder impregnation approach, and by Bernet et al. (Bernet et al., 1999, 2001) for PA12/Carbon commingled yarns.

4 NUMERICAL MODELLING

Capillary effects play, despite the low magnitude of capillary pressures as compared to applied pressures, a significant role in LCM processing and, while mainly acting on a yarn-scale, largely influence the final part quality on a macroscopic scale. Capillary effects must thus be considered for the development of accurate numerical models that are used to describe and predict flow behavior in LCM. Several approaches have been proposed towards the development of flow simulations over the past decades, describing dual-scale flow behavior and the role of capillary effects at different scales. Most approaches base their estimation of the effects on direct or indirect experimental observation of flow front position, and saturation over time during an infiltration experiment, under no (apart from gravity) or applied external body forces.

4.1 Microscopic Scale Models

At the microscopic scale and under static conditions, the capillary pressure ΔP_γ is described as the pressure jump across the air-fluid interfaces arising from the solid surface and interfacial tensions defined by the Young–Laplace equation as previously described in **Section 2**. In the case of fibrous reinforcements, Ahn et al. (Ahn et al., 1991) and Pillai and Advani (Pillai and Advani, 1996) proposed an analytical expression of the capillary pressure, which was often used in later studies (Amico and Lekakou, 2000, Amico and Lekakou, 2001, Amico and Lekakou, 2002; Matsuzaki et al., 2015; Vilà et al., 2015; Willenbacher et al., 2019; Facciotto et al., 2021). They considered a tow, formed of several fibers with different spacing in size and thus with different capillary diameters impregnated with a unidirectional flow, and defined the capillary pressure as:

$$\Delta P_\gamma = \frac{V_f}{\left(1 - V_f\right)} \frac{F\sigma_{lv}\cos\theta}{D_f} \tag{4}$$

where F is a dimensionless shape factor describing the anisotropy of the tow (in general, F is assumed to be equal to 4 and 2 for longitudinal and transversal flows, respectively) and D_f is the fiber diameter. The term $\frac{V_f}{1-V_f}$ is known as the non-dimensional capillary pressure and represents the effect of the tow microstructure on the capillary pressure within the tow. Similarly, Bayramli and Powell (Bayramli and Powell, 1990) described the capillary pressure as:

$$\Delta P_\gamma = \frac{\sigma_{lv}\cos\left(\theta + \alpha\right)}{D_f\left(1 - \cos\alpha\right) + d} \tag{5}$$

where α is the directional body angle and d half of the minimum distance between two fibers. This model was improved by Foley and Gillespie (Foley and Gillespie, 2005) and later by Neacsu et al. (Neacsu et al., 2006). This equation has been used by Yeager et al. (Yeager et al., 2016; Yeager et al., 2017) and recently by Li et al. (Li et al., 2020) to describe the capillary pressure in their finite element models to simulate the resin moving in-between two fibers and thus model the injection of resin in a dual scale fabric in which the tows are quasi-realistically defined following a realistic model. Counterintuitively, the capillary pressure, which should not depend on the direction of flow, has been experimentally shown and modelled as indicated before as a function of flow direction with respect to the fiber preform. However, this is probably linked to the geometry of the pores and necks as the flow front progresses, indicating the influence of the pore-level scale onto the measurements.

In fluid infiltration, the capillary pressure is used for studying the local wettability between fiber and liquids, quantified by the contact angle θ. As infiltration involves motion, the dynamic contact angle is more accurate to describe the wettability between fluid and fibers. However, due to the complexity of determining it analytically, the static contact angle is usually measured for a first approximation even though it can strongly deviate from dynamic values. To overcome this, empirical laws such as Tanner's law (Tanner, 1979) are proposed in literature to estimate the dynamic contact angle from the static one. The static contact angle can be directly measured from e.g. from sessile drop or droplet-on-fiber measurements (Wu and Dzenis, 2006; Behroozi and Behroozi, 2019). In the case of structural fibers, a tensiometric method coupled to Wilhelmy's equation is usually applied to measure the dynamic contact angle and capillary forces (Pucci et al., 2016; Pucci et al., 2017a; Wang et al., 2017a; Hansen et al., 2017; Pucci et al., 2020). This method measures the force needed to pull or push a fiber or a tow partially submerged in a liquid as a function of the length of the immersed region. It is also possible to evaluate the of the meniscus profile between the fibers and the liquid. Similarly, some researchers performed wicking experiments on single tows (Hamdaoui et al., 2007; Pucci et al., 2015a; Koubaa et al., 2016; Castro et al., 2020) or a single layer of fabric (Lebel et al., 2013; Pucci et al., 2015b, Pucci et al., 2016; Vo et al., 2020) and were able to extract the values of the capillary pressure and the dynamic advancing contact angle using the Lucas-Washburn

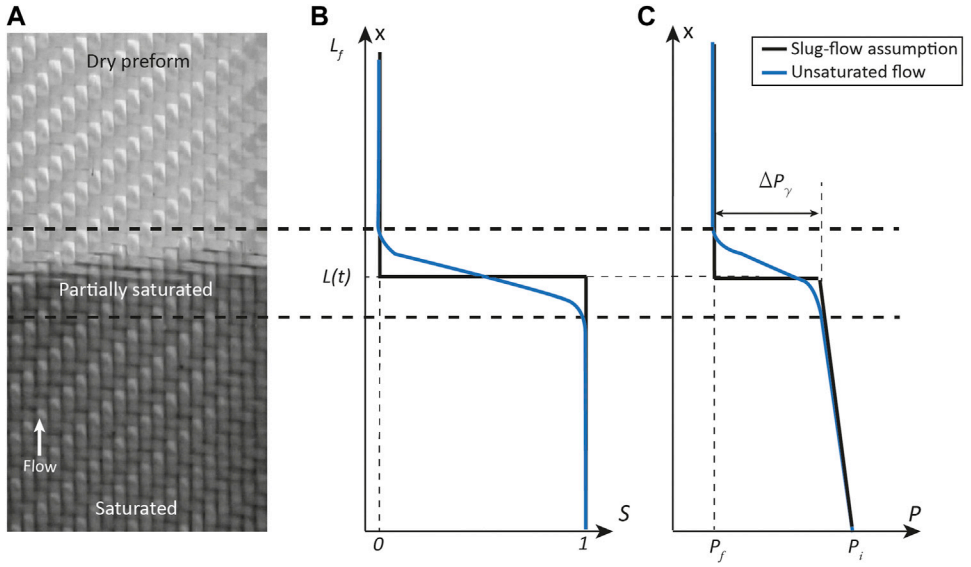

FIGURE 6 | Saturation and slug flow description of an infiltrating flow: **(A)** optical image of flow front **(B)** saturation and **(C)** capillary pressure distributions.

method (Washburn, 1921) which describes the capillary rise of a liquid inside a capillary tube, and by extension into a porous media. However, the Lucas-Washburn approach assumes a constant geometry of the porous medium during the experiment and does not take into account attraction forces between vertical cylinders resulting from elasto-capillary effects and neither the swelling effect in natural fibers which leads to densification phenomenon, this is why some modifications have been proposed over the years (Rieser et al., 2015; Koubaa et al., 2016; Pucci et al., 2016; Vo et al., 2020). Lebel et al. (LeBel et al., 2014) proposed a simple methodology to obtain the optimal flow injection conditions for a given fluid/fabric system based on the Lucas-Washburn imbibition model, which was thereafter used in Refs. (Ravey et al., 2014; Causse et al., 2018; LeBel et al., 2019; Castro et al., 2021).

4.2 Unsaturated Flow Models

Capillary effects are also included in studies at the more macroscopic scale and are regarded as promoters of micro-diffusion inside the tows. Since the dual scale of the fabrics leads to a multiphase flow effect, it is commonly accepted that the fibrous preform is progressively saturated by the liquid, resulting in a nonlinear pressure profile along the unsaturated area (**Figure 6**). Partially saturated regions indeed show a broad distribution of pore channel diameters and thereby capillary forces act at a wide range of scales, therefore in macroscopic studies, the capillary pressure is represented by an average of multiple capillary pressure jumps inside a small region (RVE). Moreover, the progressive saturation is directly linked to a progressive filling of the pores and can be in turn related to void mechanisms during the infiltration (Park and Lee, 2011; LeBel et al., 2017). Two main strategies are commonly adopted to tackle unsaturated flow phenomena: two-phase flow and dual-scale approaches (Michaud, 2016).

The first approach is inspired from soil science and relies on traditional multiphase flow equations for porous media (Panfilov, 2000). Although this approach is commonly used in other branches of engineering, researchers seldom applied it to model composite infiltration processes (Bréard et al., 2003a; Nordlund and Michaud, 2012; Gascón et al., 2015; Villière et al., 2015; Gascón et al., 2016). Resin flow is in this case modelled as a two-phase flow in which the resin invades the porous medium (fabric), displacing and expelling the fluid which saturates the porous medium (air). As already discussed, depending on the fiber/matrix system and the impregnation conditions (fluid velocity), resin and air can be either wetting (*w*) and non-wetting (*nw*). For simplicity, the resin is often considered to be the non-wetting phase, which is often observed to be the case in industrial LCM processing when flow is fast enough that the dynamic contact angle becomes greater than 90°. In the current method, permeability and pressure are dependent on the infiltrating fluid saturation *S* and the sum of the phase's saturations are equal to 1. If the porous medium is assimilated to a random assembly of tubes of various radii, each of these tubes will drain the fluid differently and a strong relationship is created between the saturation and the capillary pressure, defined as the pressure difference between the two phases as:

$$\boldsymbol{\Delta P_\gamma\,(S) = P_{nw} - P_w} \tag{6}$$

There are two main approaches to tackle the modeling. One is the two-pressure formulation which uses mass balance equations and a single-phase Darcy's law to describe the velocity of the two fluids through the same porous material. If the air pressure is assumed to be relatively low, the mass balance equation for the resin can be solved independently and is reduced to Richard's equation (Nordlund and Michaud, 2012). The other approach is the fractional flow method, which considers saturation and

pressure as independent variables. Gravitational and capillary pressures are neglected and saturation is defined by the Buckley-Leverett formulation (which assumes an isotropic medium) (Buckley and Leverett, 1942). Gascón et al. (Gascón et al., 2015; Gascón et al., 2016) more recently proposed a numerical model based on this approach which includes capillary effects and the effect of air residual saturation. In two phase flow modeling, the permeability K is divided into two terms $K = k_r K_{sat}$, where K_{sat} is the saturated permeability and k_r the relative permeability, a dimensionless value between 0 and 1 which is a function of S. The relative permeability is defined for both phases as $k_{r,nw}$ and $k_{r,w}$, and describes how fluid and air phases flow with respect to each other into the porous medium. Two phase flow formulations require constitutive equations between the permeability, the resin saturation and the capillary pressure. Different analytical parameterizations have been proposed to define $k_r(S)$ and $S(P)$, usually defined by a power law such as the functional descriptions of Brooks and Corey (Brooks and Corey, 1964) and Van Genuchten (van Genuchten, 1980), among others (Hassanizadeh and Gray, 1990; Helmig et al., 2007; Gao et al., 2014). These formulations can also be obtained with the help of parametric studies of virtual fibrous microstructures, as proposed by Ashari and Vahedi Tafreshi for thin fibrous sheets (Ashari and Vahedi Tafreshi, 2009). Bréard et al. (Bréard et al., 2003a) introduced a relative permeability law specifically for fibrous reinforcements based on the ratio of unsaturated and saturated permeability R_s which will be introduced thereafter. $S(P)$ curve is known in soil science as the imbibition-drainage curve. Drainage is used to indicate when a non-wetting fluid displaces a wetting fluid whereas imbibition indicates when a wetting fluid displaces a non-wetting fluid. Nordlund et al. (Nordlund and Michaud, 2012) used the semi-empirical expression developed by van Genuchten and Mualem (Mualem, 1978; van Genuchten, 1980) to model the impregnation of a glass preform by a resin; they observed a strong dependence between the saturation curve and flow rate given the dynamic wetting conditions during the impregnation. As a result, they showed that several imbibition-drainage curves may be necessary to model flow over a wider range of velocities. Similarly, Gascón et al. (Gascón et al., 2015; Gascón et al., 2016) used a formulation based on that of Brooks and Corey to model the saturation in a glass fiber reinforcement to predict void formation and transport mechanisms. With this approach, it is not possible to a priori determine the location of voids as a similar degree of saturation could correspond to voids in the tows or in between, nonetheless the dependency of the saturation curve on flow rate may be an indirect indication of a change in void location.

The second approach is more specific to the polymer composite processing field and considers the preform as a dual-scale body, separating the intra- and inter-bundle impregnations by introducing a sink term into fully saturated models (Bréard et al., 2003a; Simacek and Advani, 2003; Gourichon et al., 2006; Wolfrath et al., 2006; Bayldon and Daniel, 2009; Lawrence et al., 2009; Wang et al., 2009; Simacek et al., 2010; Park and Lee, 2011; Tan and Pillai, 2012; Walther et al., 2012; Carlone and Palazzo, 2015; Carlone et al., 2018; Imbert et al., 2018; Patiño-Arcila and Vanegas-Jaramillo, 2018; Wu and Larsson, 2020; Facciotto et al., 2021; Patiño and Nieto-Londoño, 2021). These models consider that viscous forces dominate (non-wetting system) the infiltration and that the flow preferentially fills the inter-tow macro. The bundles upstream are gradually saturated by a delayed secondary micro flow altering the overall pressure as shown in **Figure 7**. The capillary pressure will in this case influence only the time to saturate the tows.

Generally, the length of the partially saturated zone is assumed to be constant. Then, the pressure drop creates an apparent change in the permeability and this delayed effect is considered by adding a sink term $\dot{S}$ into the common equations which represent the liquid saturation or volume rate into the fiber tow. In this approach, tow and overall fabric permeability are usually measured in saturated models. However, for higher accuracy, some researchers proposed to model the permeability in terms of degree of saturation or void content (Lawrence et al., 2009; Simacek et al., 2010). The mass conservation equation can then be written as:

$$\dot{S} = \nabla\left(\frac{K}{\eta_{resin}}\nabla P\right) \tag{7}$$

If the flow front is non-uniform (i.e., intra- or inter-yarn flow is predominant), $\dot{S}$ is not null and the relationship between pressure and time is not linear anymore which in turn influences the overall permeability (Bodaghi et al., 2019). Longitudinal dual-scale flow analysis is usually performed by using a Stokes-Darcy or a Stokes-Brinkman coupling (with the latter one being more common) (Patiño et al., 2017; Lu et al., 2021). The Stokes equation is employed to define the inter-tow flow and the Darcy or Brinkman equations for the intra-tow flow. A coupling condition is developed at the interface to ensure a mass transfer from the inter-to the intra-tow flow. This approach is usually linked to void entrapment and void migration models (Mehdikhani et al., 2019). Given the dual-scale nature of fabrics, some authors worked on the combined interaction between intra- and inter-tow permeability on the global permeability (Bodaghi et al., 2019). Bréard et al. (Bréard et al., 2003a) measured a convex pressure curve profile along the impregnation, explained by the delayed tow saturation. Park and Lee (Park and Lee, 2011) later assimilated a convex and/or concave shape to the pressure curve, depending on the presence of capillary effects as shown in **Figure 8**. If the degree of saturation is lower than 1, unsaturated permeability is lower but close to the saturated permeability, a convex profile is obtained. If the degree of saturation drops and is far from 1, capillary effects are more significant and tow saturation is more prominent.

The Control Volume Finite Element approach has been a preferred route for homogenized simulations to predict the flow evolution, fill times, and has been used for process optimization of RTM and its variants such as VARTM (Correia et al., 2004; Sas et al., 2015; Wang et al., 2016, 2017b; Caglar et al., 2021b; Chai et al., 2021) as well as for purposes such as predicting the formation of macroscale voids (Park et al., 2011; Park and Lee, 2011), predicting the permeability (Lugo et al., 2014; Yun et al., 2017; Caglar et al., 2018; Godbole et al., 2019) and changes in the flow patterns induced by inserts or race-tracking channels

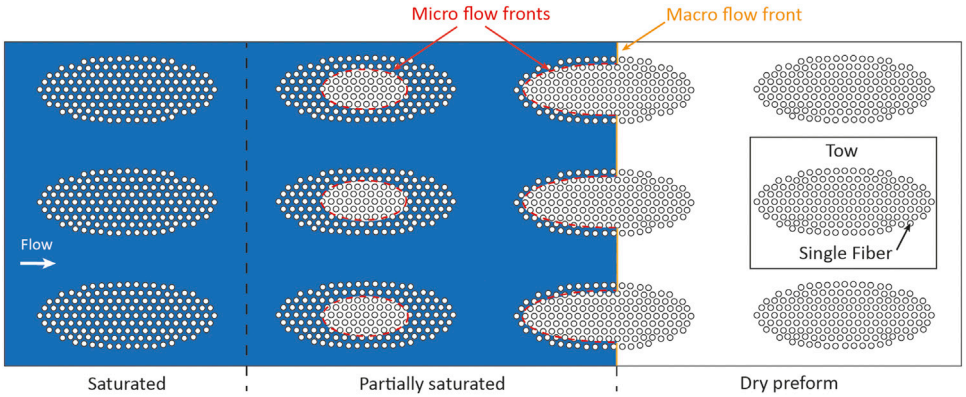

FIGURE 7 | Schematic representation of the dual-phase approach with delayed impregnation yarns.

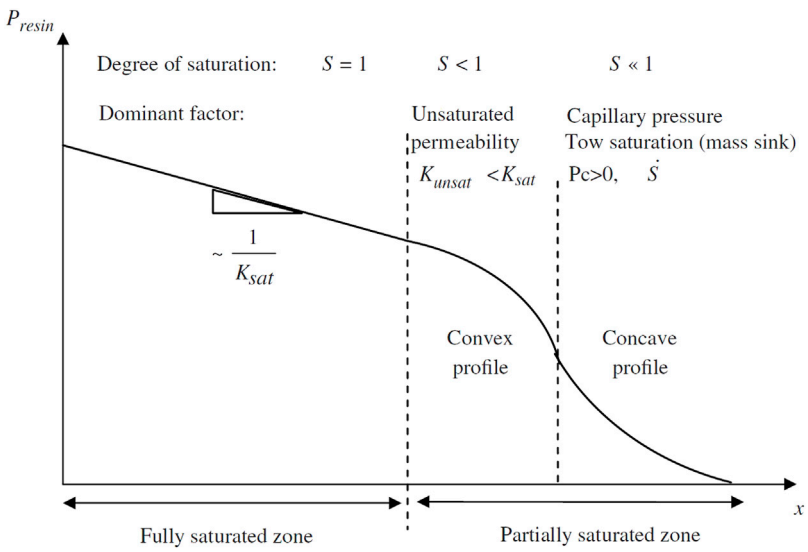

FIGURE 8 | Pressure profile and permeability in saturated and unsaturated areas, convex and concave pressure profiles in a partially saturated zone. (Source (Park and Lee, 2011))

as well as in part manufacturing around inserts (Matsuzaki et al., 2013; Sas et al., 2015; Pierce and Falzon, 2017) and as a predictive tool in active control of these processes (Alms et al., 2011; Matsuzaki et al., 2013). Several works have made use of existing flow simulation software such as LIMS and introduced additional terms to account for the dual scale effects (Schell et al., 2007; Lawrence et al., 2009; Simacek et al., 2010; Facciotto et al., 2021). Similarly, finite element solvers are coupled with level-set for tracking the free surface and enriched for accounting for multiscale effects at the air-liquid-solid interface (Liu et al., 2016; Chevalier et al., 2018; Andriamananjara et al., 2019; Rougier et al., 2021) with capability of modeling wetting and non-wetting systems as well as the transition or to predict the average capillary pressure evolution in between individual fibers (Yeager et al., 2016). In recent years, there has also been interest towards the use of other numerical approaches to account for the dual scale effects using particle based solvers (Yashiro et al., 2019; Yoshihara et al., 2020) or boundary elements (Patiño and Nieto-Londoño, 2021). Recent developments in application of above mentioned in modeling the dual-scale flow with a focus on the introduction of sink effects has been reviewed by Patiño-Arcila and Vanegas-Jaramillo (Patiño-Arcila and Vanegas-Jaramillo, 2018).

4.3 Slug-Flow Assumption

For simplicity, it is often considered that the liquid progresses with a fully saturated front neglecting preferential flow channeling, known as the "slug-flow" assumption. As shown in **Figure 6**, the saturation results in a step function varying between 0 and 1 (the steady-state saturation can be less than one if voids remain entrapped behind the flow front). Although capillary effects arise from local micro-scale geometric and

surface tension mechanisms, they are in this case considered as a macro phenomenon and are lumped in the conventional fluid flow equations as a pressure difference ΔP_γ. This pressure created at the flow front compensates the delayed flow coming from the low permeability of the packed tows (Amico and Lekakou, 2001). The total fluid pressure difference ΔP can be defined as the applied pressure difference ΔP_{app} between the inlet (i) and the outlet (f) considering the capillary forces:

$$\Delta P = P_f - P_i + \Delta P_\gamma = \Delta P_{app} + \Delta P_\gamma \tag{8}$$

The capillary pressure can be expressed as:

$$\Delta P_\gamma = -S_f \sigma_{lv} \cos\theta \tag{9}$$

where S_f is the total surface of matrix-fiber interfaces per unit of volume (Mortensen and Cornie, 1987; Mortensen and Wong, 1990). The capillary pressure drop ΔP_γ can be quantified within an experiment in which the fluid is injected into the preform either at constant pressure or constant flow rate. In unidirectional cases it is possible to track the fluid movement using Darcy's law and the Dupuit-Forchheimer approximation and find the ΔP_γ value from experimental results (Amico and Lekakou, 2001; Zingraff et al., 2005; Verrey et al., 2006; Li et al., 2010; Li et al., 2012). Verrey et al. (Verrey et al., 2006) proved that it is more suitable to measure ΔP_γ in a constant flow rate experiment rather than constant pressure experiment, since in the latter, the velocity changes significantly during impregnation resulting in a decreasing range of capillary numbers.

Intuitively, capillary effects taking place at the flow front can alter the fluid velocity leading to erroneous unsaturated permeability measurements. Although unsaturated (K_{unsat}) and saturated (K_{sat}) permeabilities are respectively measured from the flow front position and the flow rate after filling the textile, they should be theoretically equal as they only depend on the fabric structure. Nevertheless, significant differences between these two values have been reported in literature (Lundström et al., 2000; Bréard et al., 2003a; Pillai, 2004; Kim et al., 2017). Whereas some authors support that the saturated permeability should be higher than the unsaturated permeability because dry tows oppose a certain resistance to the macro-flow, the opposite has also been observed. By using a slug flow approach, one can show that the capillary pressure drop acting at the flow front should be taken into account when estimating the unsaturated permeability, whereas it is generally omitted. As a result, the permeability ratio R_s is also easily expressed as a function of the ratio of capillary over applied pressure (Salvatori et al., 2018):

$$R_s = \frac{K_{unsat}}{K_{sat}} = 1 - \frac{\Delta P_\gamma}{\Delta P_{app}} \tag{10}$$

Since ΔP_γ is directly dependent on the capillary number and thus the dynamic wettability of the system, K_{unsat} turns to be not only fabric architecture dependent, but also relies on the fluid-fabric wettability. Following this approach, if infiltration is carried out under conditions close to the optimal capillary number, capillary effects may be negligible and R_s will be equal to 1. On the contrary, if ΔP_γ is not negligible, the two permeability values will differ. If ΔP_γ is negative, at least when estimated locally close to the tows, the system is wetting and $R_s > 1$ and conversely, if ΔP_γ is positive, the system is non-wetting and $R_s < 1$. The ratio R_s was observed to be generally below 1, considering that the fluid acts with a non-wetting behavior (Bréard et al., 2003a) even though values above 1 have also been observed in the case of slow flow (Lundström et al., 2000). However, it is important to note that the geometric features of the porous medium also have an effect, and optimal Ca flow conditions have been found in cases where ΔP_γ is negative, at least when estimated close to the tows, such that the capillary forces inside the tows compensate for their lower permeability to reach a stable front. This was observed by Gueroult et al. (Gueroult et al., 2014), who proposed an analytical model evaluating the time scales for flow in each of the two regions, tow and inter-tow channels.

Nowadays, the use of K_{unsat} as a measurement of the permeability is still debated since it is influenced by capillary effects. For example, several authors observed that the fiber volume fraction influences R_s due to the increase of tows and micro spaces leading to an increase of capillary phenomena and in turn a change of the unsaturated permeability (Francucci et al., 2010; Caglar et al., 2019; Moudood et al., 2019). The choice of model fluids to measure permeability also becomes highly critical since their surface tension and viscosity should be close enough to those of the resin. Overall, this measurement is fine for comparative purposes if the same fluids and conditions are used, as was demonstrated in the round robin exercise (Vernet et al., 2014).

Salvatori et al. (Salvatori et al., 2018) studied the effect of the fabric architecture on permeability and capillary effects. They showed for a classic woven fabric, that R_s is greater than 1 at low capillary numbers, below 1 for high capillary numbers and around 1 close to the optimal infiltration conditions. For a fabric with large meso-channels, R_s was found to be close to 1 for a wide range of capillary numbers since inter-tow flow dominates the overall flow kinetics and capillary effects are insignificant. They concluded that unsaturated permeability can be used as a permeability measurement for fabrics showing a strong-dual scale nature. Caglar et al. (Caglar et al., 2019) improved the wetting characteristics of a glass fabric by means of corona treatment without altering the permeability. They found similar permeability values for pristine and treated fabrics, however, they proved that the change in the wettability has a strong effect on the R_s. Impregnation of treated fabrics is enhanced by the wettability of the system translated to an increase of K_{unsat} with R_s is higher than 1. Conversely, for the pristine fabrics the system remains non-wetting and R_s is lower than 1. Recently, Staal et al. (Staal et al., 2021) studied the permeability of alumina fiber woven fabrics grafted with aligned carbon nanotubes (CNT). They found R_s values to be higher than 1 in all cases attributed to the capillary wicking happening in the forest areas created by the CNT. In this case, the flow is dragged by capillary forces leading to a strong wetting system. This observation is also consistent with models of wetting on rough surfaces, indicating that wettability can be enhanced when the surface roughness is increased.

In the case of natural fibers, it is usually observed that K_{unsat} is lower than K_{sat}. As already introduced, infiltration is hampered by the fibers absorption behavior which removes fluid from the

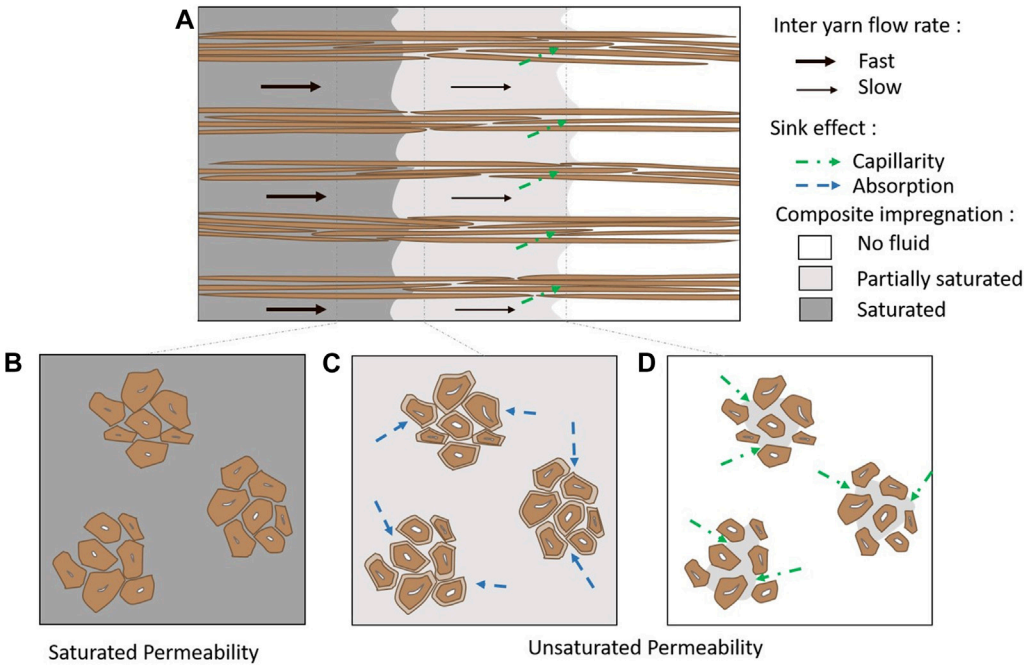

FIGURE 9 | Schematic representation of phenomena occurring during the impregnation of natural fibers: **(A)** infiltration of the preform, **(B)** fiber swelling after saturation, **(C)** resin absorption by fibers and **(D)** capillary flow between fibers. (Source (Pantaloni et al., 2020))

main stream (**Figure 9**), reducing the macro flow velocity and in consequence, directly affecting the unsaturated permeability. Since the sink effect is highly influenced by the nature of the infiltrating fluid, permeability measurements will be highly fluid type dependent (Nguyen et al., 2014; Moudood et al., 2019). Thereupon, fibers will continue to absorb liquid until their saturation leading to fiber swelling and thus changing the fibrous microstructure. Consequently, the fiber volume fraction is increased, reducing the fluid path and directly influencing the saturated permeability. Nguyen et al. (Nguyen et al., 2014) showed that the fiber diameter after swelling is also influenced by liquid nature, in turn, the saturated permeability is also fluid type dependent. Thus, both unsaturated and saturated permeability are reduced due to absorption and swelling respectively, however, it has always been observed that $K_{unsat} > K_{sat}$ absorption thus being more critical than swelling. Nevertheless, researchers showed that at low fiber volume fraction, this behavior is reversed ($K_{unsat} < K_{sat}$) since less amount of fibers are present, less fluid is removed from the stream and the change in the macro flow is insignificant (Francucci et al., 2010; Moudood et al., 2019; Pantaloni et al., 2020).

5 CONCLUSION

Capillary effects operate at several length scales in composite processing, from the molecular scale at the triple line between fluid, solid and air, which can be related to the physical characteristics of the phases, to the scale of the spaces within fiber tows or between tows, which are related to the geometrical features of the reinforcement. They are generally not the main drivers of flow in composite processing, where external pressure or flow rates are imposed on the fluid phase to speed the flow kinetics. However, they have been shown to play a crucial role in determining the part quality; the consensus is now large in our community that there is an optimal flow front velocity to minimize porosity entrapment during impregnation of a fiber reinforcement textile, which corresponds to an optimal capillary number Ca_{opt} ranging between 0.5 and $1.5{\cdot}10^{-3}$ depending on the fabric type and to a minor extent, conditions of experiments. There is also an increasing consensus on the utility to measure unsaturated and saturated permeabilities and to evaluate their ratio to better quantify macro-scale capillary effects, although often using model fluids. Research is very active these days to improve our experimental understanding of these effects thanks to the increasing availability of time- and space-resolved experimental observation tools, and computing power as well as a technological pull to further improve part quality and production robustness. However, modelling is still in progress to link local wetting effects with geometrical pore effects leading to macroscopic volume averaged capillary effects, as also observed in the soil science field, although microscopic and macroscopic effects tend to be independently increasingly well captured.

It is clear to all composite manufacturers that relying only on capillary effects to impregnate a composite is not practical, even if the static contact angle seems very low and the system is wetting, as the flow kinetics would be too low (depending on the fluid viscosity) and the quality poor, due to porosity forming in between the wicking tows. In some cases, when the porous

medium is more uniform or when a very fine porous network is placed between fibers, as in CNT grafted fabrics, enhanced capillary effects may help drive the flow and counteract a reduced overall permeability. This effect could also be taken advantage of when flow takes place at short distance, for example in thermoplastic composite processing from stacked films, fibers or powders.

In most practical cases however, the need to reduce cycle times led to the development of more permeable textiles, with increased dual scale pore space distribution (wider flow channels and more compact tows), and flow takes place well above the optimal capillary number. This often leads to a delay in tow impregnation, with potential porosity remaining within the tows, or the practice to let resin flow out for some time to saturate the fabric. This could possibly be minimized with enhanced local wetting at the tow level if air can find a path to escape ahead of the flow front. As a result, well distributed and optimized sizings could still play a strong role not only for mechanical properties, but also to ensure optimal flow conditions.

AUTHOR CONTRIBUTIONS

All authors listed have made a substantial, direct, and intellectual contribution to the work and approved it for publication.

ACKNOWLEDGMENTS

We acknowledge support from the Swiss National Science Foundation (SNF n° 200021_182669).

REFERENCES

Abdelwahed, M. A. B., Wielhorski, Y., Bizet, L., and Bréard, J. (2014). Bubble Formation and Transport in T-junction for Application to Liquid Composite Molding: Wetting Effect. *J. Compos. Mater.* 48, 37–48. doi:10.1177/0021998312467553

Ahn, K. J., Seferis, J. C., and Berg, J. C. (1991). Simultaneous Measurements of Permeability and Capillary Pressure of Thermosetting Matrices in Woven Fabric Reinforcements. *Polym. Compos.* 12, 146–152. doi:10.1002/pc.750120303

Ali, M. A., Umer, R., Khan, K. A., and Cantwell, W. J. (2019). In-plane Virtual Permeability Characterization of 3D Woven Fabrics Using a Hybrid Experimental and Numerical Approach. *Composites Sci. Techn.* 173, 99–109. doi:10.1016/j.compscitech.2019.01.030

Alms, J. B., Advani, S. G., and Glancey, J. L. (2011). Liquid Composite Molding Control Methodologies Using Vacuum Induced Preform Relaxation. *Composites A: Appl. Sci. Manufacturing* 42, 57–65. doi:10.1016/j.compositesa.2010.10.002

Amico, S. C., and Lekakou, C. (2002). Axial Impregnation of a Fiber Bundle. Part 2: Theoretical Analysis. *Polym. Compos.* 23, 264–273. doi:10.1002/pc.10430

Amico, S., and Lekakou, C. (2001). An Experimental Study of the Permeability and Capillary Pressure in Resin-Transfer Moulding. *Composites Sci. Techn.* 61, 1945–1959. doi:10.1016/S0266-3538(01)00104-X

Amico, S., and Lekakou, C. (2000). Mathematical Modelling of Capillary Micro-flow through Woven Fabrics. *Composites Part A: Appl. Sci. Manufacturing* 31, 1331–1344. doi:10.1016/S1359-835X(00)00033-6

Andriamananjara, K., Moulin, N., Bruchon, J., Liotier, P.-J., and Drapier, S. (2019). Numerical Modeling of Local Capillary Effects in Porous media as a Pressure Discontinuity Acting on the Interface of a Transient Bi-fluid Flow. *Int. J. Mater. Form.* 12, 675–691. doi:10.1007/s12289-018-1442-3

Araujo, Y. C., Toledo, P. G., Leon, V., and Gonzalez, H. Y. (1995). Wettability of Silane-Treated Glass Slides as Determined from X-Ray Photoelectron Spectroscopy. *J. Colloid Interf. Sci.* 176, 485–490. doi:10.1006/jcis.1995.9942

Armstrong, R. T., Sun, C., Mostaghimi, P., Berg, S., Rücker, M., Luckham, P., et al. (2021). Multiscale Characterization of Wettability in Porous Media. *Transp Porous Med.* 140, 215–240. doi:10.1007/s11242-021-01615-0

Ashari, A., and Vahedi Tafreshi, H. (2009). General Capillary Pressure and Relative Permeability Expressions for Through-Plane Fluid Transport in Thin Fibrous Sheets. *Colloids Surf. A: Physicochemical Eng. Aspects* 346, 114–122. doi:10.1016/j.colsurfa.2009.06.001

Bayldon, J. M., and Daniel, I. M. (2009). Flow Modeling of the VARTM Process Including Progressive Saturation Effects. *Composites Part A: Appl. Sci. Manufacturing* 40, 1044–1052. doi:10.1016/j.compositesa.2009.04.008

Bayramli, E., and Powell, R. L. (1990). The normal (Transverse) Impregnation of Liquids into Axially Oriented Fiber Bundles. *J. Colloid Interf. Sci.* 138, 346–353. doi:10.1016/0021-9797(90)90217-C

Bear, J. (1972). *Dynamics of Fluids in Porous Media*. New York, NY: American Elsevier Publishing Company.

Behroozi, F., and Behroozi, P. S. (2019). Reliable Determination of Contact Angle from the Height and Volume of Sessile Drops. *Am. J. Phys.* 87, 28–32. doi:10.1119/1.5078512

Bencsik, M., Adriaensen, H., Brewer, S. A., and McHale, G. (2008). Quantitative NMR Monitoring of Liquid Ingress into Repellent Heterogeneous Layered Fabrics. *J. Magn. Reson.* 193, 32–36. doi:10.1016/j.jmr.2008.04.003

Bernet, N., Bourban, P.-E., and Maånson, J.-A. E. (2000). On the Characterization of Wetting and Adhesion in Glass fiber-PA12 Composites. *J. Thermoplastic Compos. Mater.* 13, 434–450. doi:10.1106/W3B4-CFKP-02VR-OXTE

Bernet, N., Michaud, V., Bourban, P.-E., and Manson, J.-A. E. (1999). Impregnation Model for the Consolidation of Thermoplastic Composites Made from Commingled Yarns. *J. Compos. Mater.* 33. doi:10.1177/002199839903300806

Bernet, N., Michaud, V., Bourban, P. E., and Månson, J. A. E. (2001). Commingled Yarn Composites for Rapid Processing of Complex Shapes. *Compos. - Part. A. Appl. Sci. Manuf.* 32. doi:10.1016/S1359-835X(00)00180-9

Bijeljic, B., D. Mantle, M., J. Sederman, A., F. Gladden, L., and D. Papathanasiou, T. (2004). Slow Flow across Macroscopically Semi-circular Fibre Lattices and a Free-Flow Region of Variable Width-Visualisation by Magnetic Resonance Imaging. *Chem. Eng. Sci.* 59, 2089–2103. doi:10.1016/j.ces.2004.02.007

Binetruy, C., Hilaire, B., and Pabiot, J. (1998). Tow Impregnation Model and Void Formation Mechanisms during RTM. *J. Compos. Mater.* 32, 223–245. doi:10.1177/002199839803200302

Bodaghi, M., Lomov, S. V., Simacek, P., Correia, N. C., and Advani, S. G. (2019). On the Variability of Permeability Induced by Reinforcement Distortions and Dual Scale Flow in Liquid Composite Moulding: A Review. *Composites Part A: Appl. Sci. Manufacturing* 120, 188–210. doi:10.1016/j.compositesa.2019.03.004

Bonnard, B., Causse, P., and Trochu, F. (2017). Experimental Characterization of the Pore Size Distribution in Fibrous Reinforcements of Composite Materials. *J. Compos. Mater.* 51, 3807–3818. doi:10.1177/0021998317694424

Bréard, J., Saouab, A., and Bouquet, G. (1999). Dependence of the Reinforcement Anisotropy on a Three Dimensional Resin Flow Observed by X-Ray Radioscopy. *J. Reinforced Plastics Composites* 18, 814–826. doi:10.1177/073168449901800903

Bréard, J., Henzel, Y., Trochu, F., and Gauvin, R. (2003a). Analysis of Dynamic Flows through Porous media. Part I: Comparison between Saturated and Unsaturated Flows in Fibrous Reinforcements. *Polym. Compos.* 24, 391–408. doi:10.1002/pc.10038

Bréard, J., Saouab, A., and Bouquet, G. (2003b). Numerical Simulation of Void Formation in LCM. *Composites Part A: Appl. Sci. Manufacturing* 34, 517–523. doi:10.1016/S1359-835X(03)00055-1

Brooks, R., and Corey, A. (1964). *Hydraulic Properties of Porous media*. Fort Collins: Colorado State University Hydrology. Papers Available at: http://www.citeulike.org/group/1336/article/711012.

Buckley, S. E., and Leverett, M. C. (1942). Mechanism of Fluid Displacement in Sands. *Trans. AIME* 146, 107–116. doi:10.2118/942107-g

Bull, D. J., Spearing, S. M., Sinclair, I., and Helfen, L. (2013). Three-dimensional Assessment of Low Velocity Impact Damage in Particle Toughened Composite Laminates Using Micro-focus X-ray Computed Tomography and Synchrotron Radiation Laminography. *Composites Part A: Appl. Sci. Manufacturing* 52, 62–69. doi:10.1016/j.compositesa.2013.05.003

Caglar, B., Esposito, W., Nguyen-Dang, T., Laperrousaz, S., Michaud, V., and Sorin, F. (2021a). Functionalized Fiber Reinforced Composites via Thermally Drawn Multifunctional Fiber Sensors. *Adv. Mater. Technol.* 6, 2000957–2000958. doi:10.1002/admt.202000957

Caglar, B., Hancioglu, M., and Sozer, E. M. (2021b). Monitoring and Modeling of Part Thickness Evolution in Vacuum Infusion Process. *J. Compos. Mater.* 55, 1053–1072. doi:10.1177/0021998320963173

Caglar, B., Michaud, V., and Sozer, E. M. (2016). "Experimental Investigation of Textile Permeability in the Presence of Spherical Inclusions," in ECCM 2016 - Proceeding 17th European Conference on Composite Materials, Munich, Germany, June 26–30, 2016, 26–30.

Caglar, B., Orgéas, L., Rolland du Roscoat, S., Sozer, E. M., and Michaud, V. (2017). Permeability of Textile Fabrics with Spherical Inclusions. *Composites Part A: Appl. Sci. Manufacturing* 99, 1–14. doi:10.1016/j.compositesa.2017.03.031

Caglar, B., Salvatori, D., Sozer, E. M., and Michaud, V. (2018). In-plane Permeability Distribution Mapping of Isotropic Mats Using Flow Front Detection. *Composites Part A: Appl. Sci. Manufacturing* 113, 275–286. doi:10.1016/j.compositesa.2018.07.036

Caglar, B., Tekin, C., Karasu, F., and Michaud, V. (2019). Assessment of Capillary Phenomena in Liquid Composite Molding. *Composites Part A: Appl. Sci. Manufacturing* 120, 73–83. doi:10.1016/j.compositesa.2019.02.018

Callaghan, P. T. (1993). *Principles of Nuclear Magnetic Resonance Microscopy*. Oxford: Oxford University Press.

Carlone, P., and Palazzo, G. S. (2015). Unsaturated and Saturated Flow Front Tracking in Liquid Composite Molding Processes Using Dielectric Sensors. *Appl. Compos. Mater.* 22, 543–557. doi:10.1007/s10443-014-9422-3

Carlone, P., Rubino, F., Paradiso, V., and Tucci, F. (2018). Multi-scale Modeling and Online Monitoring of Resin Flow through Dual-Scale Textiles in Liquid Composite Molding Processes. *Int. J. Adv. Manuf. Technol.* 96, 2215–2230. doi:10.1007/s00170-018-1703-9

Castro, J., Sket, F., and González, C. (2020). S-XCT Experimental Determination of Local Contact Angle and Meniscus Shape in Liquid Moulding of Composites. *Composites Sci. Techn.* 199, 108362. doi:10.1016/j.compscitech.2020.108362

Castro, J., Sket, F., Helfen, L., and González, C. (2021). *In Situ* local Imaging and Analysis of Impregnation during Liquid Moulding of Composite Materials Using Synchrotron Radiation Computed Laminography. *Composites Sci. Techn.* 215, 108999. doi:10.1016/j.compscitech.2021.108999

Causse, P., Ravey, C., and Trochu, F. (2018). Capillary Characterization of Fibrous Reinforcement and Optimization of Injection Strategy in Resin Transfer Molding. *J. Compos. Sci.* 2, 19. doi:10.3390/jcs2020019

Chai, B. X., Eisenbart, B., Nikzad, M., Fox, B., Blythe, A., Blanchard, P., et al. (2021). Simulation-based Optimisation for Injection Configuration Design of Liquid Composite Moulding Processes: A Review. *Composites Part A: Appl. Sci. Manufacturing* 149, 106540. doi:10.1016/j.compositesa.2021.106540

Chen, B., and Chou, T. W. (2000). Compaction of Woven-Fabric Preforms: Nesting and Multi-Layer Deformation. *Compos. Sci. Technol.* 60, 2223–2231. doi:10.1016/S0266-3538(00)00017-8

Chevalier, L., Bruchon, J., Moulin, N., Liotier, P.-J., and Drapier, S. (2018). Accounting for Local Capillary Effects in Two-phase Flows with Relaxed Surface Tension Formulation in Enriched Finite Elements. *Comptes Rendus Mécanique* 346, 617–633. doi:10.1016/j.crme.2018.06.008

Chiu, T.-H., Li, J.-B., Yao, Y., Wang, C.-W., Sun, S.-P., Hsu, C.-H., et al. (2018). Estimation of Local Permeability/porosity Ratio in Resin Transfer Molding. *J. Taiwan Inst. Chem. Eng.* 91, 32–37. doi:10.1016/j.jtice.2018.05.040

Chou, T.-W., Gao, L., Thostenson, E. T., Zhang, Z., and Byun, J.-H. (2010). An Assessment of the Science and Technology of Carbon Nanotube-Based Fibers and Composites. *Composites Sci. Techn.* 70, 1–19. doi:10.1016/j.compscitech.2009.10.004

Chung Hae Park, C. H., and Woo, L. (2011). Modeling Void Formation and Unsaturated Flow in Liquid Composite Molding Processes: A Survey and Review. *J. Reinforced Plastics Composites* 30, 957–977. doi:10.1177/0731684411411338

Cohades, A., Branfoot, C., Rae, S., Bond, I., and Michaud, V. (2018). Progress in Self-Healing Fiber-Reinforced Polymer Composites. *Adv. Mater. Inter.* 5, 1800177. doi:10.1557/mrs2008.16410.1002/admi.201800177

Correia, N. C., Robitaille, F., Long, A. C., Rudd, C. D., Šimáček, P., and Advani, S. G. (2004). Use of Resin Transfer Molding Simulation to Predict Flow, Saturation, and Compaction in the VARTM Process. *J. Fluids Eng. Trans. ASME* 126, 210–215. doi:10.1115/1.1669032

Devalve, C., and Pitchumani, R. (2013). Simulation of Void Formation in Liquid Composite Molding Processes. *Composites Part A: Appl. Sci. Manufacturing* 51, 22–32. doi:10.1016/j.compositesa.2013.03.016

Di Fratta, C., Klunker, F., and Ermanni, P. (2013). A Methodology for Flow-Front Estimation in LCM Processes Based on Pressure Sensors. *Composites Part A: Appl. Sci. Manufacturing* 47, 1–11. doi:10.1016/j.compositesa.2012.11.008

Duchemin, B., Cazaux, G., Gomina, M., and Bréard, J. (2021). Temperature-dependence of the Static Contact Angle: A Transition State Theory Approach. *J. Colloid Interf. Sci.* 592, 215–226. doi:10.1016/j.jcis.2021.02.059

Endruweit, A., Glover, P., Head, K., and Long, A. C. (2011). Mapping of the Fluid Distribution in Impregnated Reinforcement Textiles Using Magnetic Resonance Imaging: Application and Discussion. *Composites Part A: Appl. Sci. Manufacturing* 42, 1369–1379. doi:10.1016/j.compositesa.2010.11.01210.1016/j.compositesa.2011.05.020

Facciotto, S., Simacek, P., Advani, S. G., and Middendorf, P. (2021). Modeling of Anisotropic Dual Scale Flow in RTM Using the Finite Elements Method. *Composites B: Eng.* 214, 108735. doi:10.1016/j.compositesb.2021.108735

Fisher, S. L., Holmes, D. J., Jørgensen, J. S., Gajjar, P., Behnsen, J., Lionheart, W. R. B., et al. (2019). Laminography in the Lab: Imaging Planar Objects Using a Conventional X-ray CT Scanner. *Meas. Sci. Technol.* 30, 035401. doi:10.1088/1361-6501/aafcae

Foley, M. E., and Gillespie, J. W. (2005). Modeling the Effect of Fiber Diameter and Fiber Bundle Count on Tow Impregnation during Liquid Molding Processes. *J. Compos. Mater.* 39, 1045–1065. doi:10.1177/0021998305048739

Francucci, G., Rodríguez, E. S., and Vázquez, A. (2010). Study of Saturated and Unsaturated Permeability in Natural Fiber Fabrics. *Composites Part A: Appl. Sci. Manufacturing* 41, 16–21. doi:10.1016/j.compositesa.2009.07.012

Freeze, R. A., and Cherry, J. A. (1979). *Groundwater*. Englewood Cliffs, NJ: Prentice Hall, Inc.

Futaba, D. N., Hata, K., Yamada, T., Hiraoka, T., Hayamizu, Y., Kakudate, Y., et al. (2006). Shape-engineerable and Highly Densely Packed Single-Walled Carbon Nanotubes and Their Application as Super-capacitor Electrodes. *Nat. Mater* 5, 987–994. doi:10.1038/nmat1782

Gao, H., Yu, B., Duan, Y., and Fang, Q. (2014). Fractal Analysis of Dimensionless Capillary Pressure Function. *Int. J. Heat Mass Transfer* 69, 26–33. doi:10.1016/j.ijheatmasstransfer.2013.10.006

Garat, W., Le Moigne, N., Corn, S., Beaugrand, J., and Bergeret, A. (2020). Swelling of Natural Fibre Bundles under Hygro- and Hydrothermal Conditions: Determination of Hydric Expansion Coefficients by Automated Laser Scanning. *Composites Part A: Appl. Sci. Manufacturing* 131, 105803. doi:10.1016/j.compositesa.2020.105803

García, E. J., Hart, A. J., Wardle, B. L., Slocum, A. H., García, E. J., Hart, A. J. J., et al. (2007). Fabrication of Composite Microstructures by Capillarity-Driven Wetting of Aligned Carbon Nanotubes with Polymers. *Nanotechnology* 18, 165602. doi:10.1088/0957-4484/18/16/165602

Garcia, E., Wardle, B., Johnhart, A., and Yamamoto, N. (2008). Fabrication and Multifunctional Properties of a Hybrid Laminate with Aligned Carbon Nanotubes Grown *In Situ*. *Composites Sci. Techn.* 68, 2034–2041. doi:10.1016/j.compscitech.2008.02.028

Gascón, L., García, J. A., LeBel, F., Ruiz, E., and Trochu, F. (2016). A Two-phase Flow Model to Simulate Mold Filling and Saturation in Resin Transfer Molding. *Int. J. Mater. Form.* 9, 229–239. doi:10.1007/s12289-015-1225-z

Gascón, L., García, J. A., Lebel, F., Ruiz, E., and Trochu, F. (2015). Numerical Prediction of Saturation in Dual Scale Fibrous Reinforcements during Liquid Composite Molding. *Composites Part A: Appl. Sci. Manufacturing* 77, 275–284. doi:10.1016/j.compositesa.2015.05.019

Godbole, M. G., Purandare, R., Harshe, R., Hood, A., Gururaja, S., Joshi, M., et al. (2019). Influence of Filament Distribution on Transverse Tow Permeability: Model Predictions and Experimental Validation. *Composites Part A: Appl. Sci. Manufacturing* 118, 150–161. doi:10.1016/j.compositesa.2018.12.024

Gomez, C., Salvatori, D., Caglar, B., Trigueira, R., Orange, G., and Michaud, V. (2021). Resin Transfer Molding of High-Fluidity Polyamide-6 with Modified Glass-Fabric Preforms. *Composites Part A: Appl. Sci. Manufacturing* 147, 106448. doi:10.1016/j.compositesa.2021.106448

Gourichon, B., Binetruy, C., and Krawczak, P. (2006). A New Numerical Procedure to Predict Dynamic Void Content in Liquid Composite Molding. *Composites Part A: Appl. Sci. Manufacturing* 37, 1961–1969. doi:10.1016/j.compositesa.2005.12.017

Gresil, M., Revol, V., Kitsianos, K., Kanderakis, G., Koulalis, I., Sauer, M.-O., et al. (2017). EVITA Project: Comparison between Traditional Non-destructive Techniques and Phase Contrast X-Ray Imaging Applied to Aerospace Carbon Fibre Reinforced Polymer. *Appl. Compos. Mater.* 24, 513–524. doi:10.1007/s10443-016-9540-1

Gueroult, S., Lebel-Lavacry, A., Park, C. H., Bizet, L., Saouab, A., and Bréard, J. (2014). Analytical Modeling Andin Situmeasurement of Void Formation in Liquid Composite Molding Processes. *Adv. Compos. Mater.* 23, 31–42. doi:10.1080/09243046.2013.862383

Hamdaoui, M., Fayala, F., and Nasrallah, S. B. (2007). Dynamics of Capillary Rise in Yarns: Influence of Fiber and Liquid Characteristics. *J. Appl. Polym. Sci.* 104, 3050–3056. doi:10.1002/app.25642

Han, N., Baran, I., Zanjani, J. S. M., Yuksel, O., An, L., and Akkerman, R. (2020). Experimental and Computational Analysis of the Polymerization Overheating in Thick glass/Elium Acrylic Thermoplastic Resin Composites. *Composites Part B: Eng.* 202, 108430. doi:10.1016/j.compositesb.2020.108430

Hansen, D., Bomholt, N., Jeppesen, J. C., and Simonsen, A. C. (2017). Contact Angle Goniometry on Single Micron-Scale Fibers for Composites. *Appl. Surf. Sci.* 392, 181–188. doi:10.1016/j.apsusc.2016.09.018

Hassanizadeh, S. M., and Gray, W. G. (1990). Mechanics and Thermodynamics of Multiphase Flow in Porous media Including Interphase Boundaries. *Adv. Water Resour.* 13, 169–186. doi:10.1016/0309-1708(90)90040-B

He, Y., Li, Y., Hao, X., zhou, J., and Liu, S. (2019). Micro-flow Sensor for Continuous Resin Fluidity Monitoring between Fibers. *Sensors Actuators B: Chem.* 282, 177–186. doi:10.1016/j.snb.2018.11.022

Helfen, L., Myagotin, A., Mikulík, P., Pernot, P., Voropaev, A., Elyyan, M., et al. (2011). On the Implementation of Computed Laminography Using Synchrotron Radiation. *Rev. Scientific Instr.* 82, 063702. doi:10.1063/1.3596566

Helmig, R., Weiss, A., and Wohlmuth, B. I. (2007). Dynamic Capillary Effects in Heterogeneous Porous media. *Comput. Geosci.* 11, 261–274. doi:10.1007/s10596-007-9050-1

Hemmer, J., Burtin, C., Comas-Cardona, S., Binetruy, C., Savart, T., and Babeau, A. (2018). Unloading during the Infusion Process: Direct Measurement of the Dual-Scale Fibrous Microstructure Evolution with X-ray Computed Tomography. *Composites Part A: Appl. Sci. Manufacturing* 115, 147–156. doi:10.1016/j.compositesa.2018.09.013

Ho, K. K. C., Shamsuddin, S. R., Riaz, S., Lamorinere, S., Tran, M. Q., Javaid, A., et al. (2011). Wet Impregnation as Route to Unidirectional Carbon Fibre Reinforced Thermoplastic Composites Manufacturing. *Plastics, Rubber and Composites* 40, 100–107. doi:10.1179/174328911X12988622801098

Imbert, M., Comas-Cardona, S., Abisset-Chavanne, E., and Prono, D. (2018). Experimental Investigation of Intra-tow Fluid Storage Mechanisms in Dual-Scale Fiber Reinforcements. *Composites Part A: Appl. Sci. Manufacturing* 107, 70–82. doi:10.1016/j.compositesa.2017.12.015

Irfan, M., Harris, D., Paget, M., Ma, T., Leek, C., Machavaram, V., et al. (2021). On-site Evaluation of a Modified Pultrusion Process: Fibre Spreading and Resin Injection-Based Impregnation. *J. Compos. Mater.* 55, 77–93. doi:10.1177/0021998320943268

Irfan, M. S., Shotton-Gale, N., Paget, M. A., Machavaram, V. R., Leek, C., Wootton, S., et al. (2017). A Modified Pultrusion Process. *J. Compos. Mater.* 51, 1925–1941. doi:10.1177/0021998316666653

Kang, M., Lee, W. Il., and Hahn, H. T. (2000). Formation of Microvoids during Resin-Transfer Molding Process. *Compos. Sci. Technol.* 60, 2427–2434. doi:10.1016/S0266-3538(00)00036-1

Karbhari, V. M., and Palmese, G. R. (1997). Sizing Related Kinetic and Flow Considerations in the Resin Infusion of Composites. *J. Mater. Sci.* 32, 5761–5774. doi:10.1023/A:1018626002895

Kedari, V. R., Farah, B. I., and Hsiao, K.-T. (2011). Effects of Vacuum Pressure, Inlet Pressure, and Mold Temperature on the Void Content, Volume Fraction of Polyester/e-Glass Fiber Composites Manufactured with VARTM Process. *J. Compos. Mater.* 45, 2727–2742. doi:10.1177/0021998311415442

Kessler, M. R., Sottos, N. R., and White, S. R. (2003). Self-healing Structural Composite Materials. *Composites Part A: Appl. Sci. Manufacturing* 34, 743–753. doi:10.1016/S1359-835X(03)00138-6

Kim, S. H., Jung, J. W., Li, M. X., Choi, S. W., Lee, W. I., and Park, C. H. (2017). Unsaturated Flow Behavior in Double-Scale Porous Reinforcement for Liquid Composite Molding Processes. *J. Reinforced Plastics Composites* 36, 85–97. doi:10.1177/0731684416671422

Konstantopoulos, S., Fauster, E., and Schledjewski, R. (2014). Monitoring the Production of FRP Composites: A Review of In-Line Sensing Methods. *Express Polym. Lett.* 8, 823–840. doi:10.3144/expresspolymlett.2014.84

Konstantopoulos, S., Grössing, H., Hergan, P., Weninger, M., and Schledjewski, R. (2018). Determination of the Unsaturated Through-Thickness Permeability of Fibrous Preforms Based on Flow Front Detection by Ultrasound. *Polym. Compos.* 39, 360–367. doi:10.1002/pc.23944

Kostornov, A. G., Moroz, A. L., Shapoval, A. A., Kabov, O., Strizhak, P., and Legros, J. C. (2015). Composite Structures with Gradient of Permeability to Be Used in Heat Pipes under Microgravity. *Acta Astronautica* 115, 52–57. doi:10.1016/j.actaastro.2015.04.022

Koubaa, S., Burtin, C., and Le Corre, S. (2016). Investigation of Capillary Impregnation for Permeability Prediction of Fibrous Reinforcements. *J. Compos. Mater.* 50, 1417–1429. doi:10.1177/0021998315593797

Labat, L., Bréard, J., Pillut-Lesavre, S., and Bouquet, G. (2001a). Void Fraction Prevision in LCM Parts. *Eur. Phys. J. AP* 16, 157–164. doi:10.1051/epjap:2001104

Labat, L., Grisel, M., Breard, J., and Bouquet, G. (2001b). Original Use of Electrical Conductivity for Void Detection Due to Injection Conditions of Composite Materials. *Comptes Rendus de l'Académie des Sci. - Ser. IIB - Mech.* 329, 529–534. doi:10.1016/S1620-7742(01)01363-0

Larson, N. M., Cuellar, C., and Zok, F. W. (2019). X-ray Computed Tomography of Microstructure Evolution during Matrix Impregnation and Curing in Unidirectional Fiber Beds. *Composites Part A: Appl. Sci. Manufacturing* 117, 243–259. doi:10.1016/j.compositesa.2018.11.021

Larson, N. M., and Zok, F. W. (2018). Insights from *In-Situ* X-ray Computed Tomography during Axial Impregnation of Unidirectional Fiber Beds. *Composites Part A: Appl. Sci. Manufacturing* 107, 124–134. doi:10.1016/j.compositesa.2017.12.024

Lawrence, J. M., Neacsu, V., and Advani, S. G. (2009). Modeling the Impact of Capillary Pressure and Air Entrapment on Fiber Tow Saturation during Resin Infusion in LCM. *Composites Part A: Appl. Sci. Manufacturing* 40, 1053–1064. doi:10.1016/j.compositesa.2009.04.013

Lebel, F., Fanaei, A. E., Ruiz, E., and Trochu, F. (2013). Experimental Characterization by Fluorescence of Capillary Flows in Dual-Scale Engineering Fabrics. *Textile Res. J.* 83, 1634–1659. doi:10.1177/0040517512471742

LeBel, F., Fanaei, A. E., Ruiz, É., and Trochu, F. (2014). Prediction of Optimal Flow Front Velocity to Minimize Void Formation in Dual Scale Fibrous Reinforcements. *Int. J. Mater. Form.* 7, 93–116. doi:10.1007/s12289-012-1111-x

LeBel, F., Ruiz, É., and Trochu, F. (2017). Experimental Study of Saturation by Visible Light Transmission in Dual-Scale Fibrous Reinforcements during Composite Manufacturing. *J. Reinforced Plastics Composites* 36, 1693–1711. doi:10.1177/0731684417725187

LeBel, F., Ruiz, É., and Trochu, F. (2019). Void Content Analysis and Processing Issues to Minimize Defects in Liquid Composite Molding. *Polym. Compos.* 40, 109–120. doi:10.1002/pc.24609

Leclerc, J. S., and Ruiz, E. (2008). Porosity Reduction Using Optimized Flow Velocity in Resin Transfer Molding. *Composites Part A: Appl. Sci. Manufacturing* 39, 1859–1868. doi:10.1016/j.compositesa.2008.09.008

Lee, J., Kessler, S. S., and Wardle, B. L. (2020). Void-Free Layered Polymeric Architectures via Capillary-Action of Nanoporous Films. *Adv. Mater. Inter.* 7, 1901427. doi:10.1002/admi.201901427

Léger, A., Molina-Jordá, J. M., Weber, L., and Mortensen, A. (2014). Percolation and Universal Scaling in Composite Infiltration Processing. *Mater. Res. Lett.* 3, 7–15. doi:10.1080/21663831.2014.948692

Léger, A., Weber, L., and Mortensen, A. (2015). Influence of the Wetting Angle on Capillary Forces in Pressure Infiltration. *Acta Materialia* 91, 57–69. doi:10.1016/j.actamat.2015.03.002

Leisen, J., and Beckham, H. W. (2008). Void Structure in Textiles by Nuclear Magnetic Resonance, Part I. Imaging of Imbibed Fluids and Image Analysis by Calculation of Fluid Density Autocorrelation Functions. *J. Textile Inst.* 99, 243–251. doi:10.1080/00405000701404122

Li, C., Cantarel, A., and Gong, X. (2020). A Study on Resin Infusion and Effects of Reinforcement Structure at Dual Scales by a Quasi-Realistic Numerical Simulation Method. *J. Compos. Mater.* 54, 4157–4171. doi:10.1177/0021998320926707

Li, M., Wang, S.-K., Gu, Y.-Z., Li, Y.-X., Potter, K., and Zhang, Z.-G. (2012). Evaluation of Through-Thickness Permeability and the Capillary Effect in Vacuum Assisted Liquid Molding Process. *Composites Sci. Techn.* 72, 873–878. doi:10.1016/j.compscitech.2012.02.014

Li, M., Wang, S., Gu, Y., Zhang, Z., Li, Y., and Potter, K. (2010). Dynamic Capillary Impact on Longitudinal Micro-flow in Vacuum Assisted Impregnation and the Unsaturated Permeability of Inner Fiber Tows. *Composites Sci. Techn.* 70, 1628–1636. doi:10.1016/j.compscitech.2010.06.004

Little, J. E., Yuan, X., and Jones, M. I. (2012). Characterisation of Voids in Fibre Reinforced Composite Materials. *NDT E Int.* 46, 122–127. doi:10.1016/j.ndteint.2011.11.011

Liu, H., Zhai, J., and Jiang, L. (2006). Wetting and Anti-wetting on Aligned Carbon Nanotube Films. *Soft Matter* 2, 811–821. doi:10.1039/b606654b

Liu, Y., Moulin, N., Bruchon, J., Liotier, P.-J., and Drapier, S. (2016). Towards Void Formation and Permeability Predictions in LCM Processes: A Computational Bifluid-Solid Mechanics Framework Dealing with Capillarity and Wetting Issues. *Comptes Rendus Mécanique* 344, 236–250. doi:10.1016/j.crme.2016.02.004

Louis, B. M., Maldonado, J., Klunker, F., and Ermanni, P. (2014). "Measurement of Nanoparticle Distribution in Composite Laminates Produced by Resin Transfer Molding," in 16th European Conference on Composite Materials ECCM 2014, Seville, Spain, June 22–26, 2014, 22–26.

Louis, B. M., Maldonado, J., Klunker, F., and Ermanni, P. (2019). Particle Distribution from In-Plane Resin Flow in a Resin Transfer Molding Process. *Polym. Eng. Sci.* 59, 22–34. doi:10.1002/pen.24860

Lu, J. G., Lee, S. B., Lundström, T. S., and Hwang, W. R. (2022). Numerical Simulation on Void Formation and Migration Using Stokes-Brinkman Coupling with Effective Dual-Scale Fibrous Porous media. *Composites Part A: Appl. Sci. Manufacturing* 152, 106683. doi:10.1016/j.compositesa.2021.106683

Lugo, J., Simacek, P., and Advani, S. G. (2014). Analytic Method to Estimate Multiple Equivalent Permeability Components from a Single Rectilinear experiment in Liquid Composite Molding Processes. *Composites Part A: Appl. Sci. Manufacturing* 67, 157–170. doi:10.1016/j.compositesa.2014.08.031

Lundström, T. S., and Gebart, B. R. (1994). Influence from Process Parameters on Void Formation in Resin Transfer Molding. *Polym. Compos.* 15, 25–33. doi:10.1002/pc.750150105

Lundström, T. S., Gebart, B. R., and Lundemo, C. Y. (1993). Void Formation in RTM. *J. Reinforced Plastics Composites* 12, 1339–1349. doi:10.1177/073168449301201207

Lundström, T. S., Stenberg, R., Bergström, R., Partanen, H., and Birkeland, P. A. (2000). In-plane Permeability Measurements: a Nordic Round-Robin Study. *Composites Part A: Appl. Sci. Manufacturing* 31, 29–43. doi:10.1016/S1359-835X(99)00058-5

Lystrup, C., George, A., Zobell, B., Boster, K., Childs, C., Girod, H., et al. (2021). Optical Measurement of Voids *In Situ* during Infusion of Carbon Reinforcements. *J. Compos. Mater.* 55, 775–786. doi:10.1177/0021998320959820

Madra, A., Hajj, N. E., and Benzeggagh, M. (2014). X-ray Microtomography Applications for Quantitative and Qualitative Analysis of Porosity in Woven Glass Fiber Reinforced Thermoplastic. *Composites Sci. Techn.* 95, 50–58. doi:10.1016/j.compscitech.2014.02.009

Manfredi, E., and Michaud, V. (2014). Packing and Permeability Properties of E-Glass Fibre Reinforcements Functionalised with Capsules for Self-Healing Applications. *Composites Part A: Appl. Sci. Manufacturing* 66, 94–102. doi:10.1016/j.compositesa.2014.07.006

Mantle, M. D., Bijeljic, B., Sederman, A. J., and Gladden, L. F. (2001). MRI Velocimetry and Lattice-Boltzmann Simulations of Viscous Flow of a Newtonian Liquid through a Dual Porosity Fibre Array. *Magn. Reson. Imaging* 19, 527–529. doi:10.1016/S0730-725X(01)00285-5

Matsuzaki, R., Kobayashi, S., Todoroki, A., and Mizutani, Y. (2013). Flow Control by Progressive Forecasting Using Numerical Simulation during Vacuum-Assisted Resin Transfer Molding. *Composites Part A: Appl. Sci. Manufacturing* 45, 79–87. doi:10.1016/j.compositesa.2012.09.014

Matsuzaki, R., Seto, D., Todoroki, A., and Mizutani, Y. (2014). Void Formation in Geometry-Anisotropic Woven Fabrics in Resin Transfer Molding. *Adv. Compos. Mater.* 23, 99–114. doi:10.1080/09243046.2013.832829

Matuzaki, R., Seto, D., Naito, M., Todoroki, A., and Mizutani, Y. (2015). Analytical Prediction of Void Formation in Geometrically Anisotropic Woven Fabrics during Resin Transfer Molding. *Composites Sci. Techn.* 107, 154–161. doi:10.1016/j.compscitech.2014.12.013

Mehdikhani, M., Gorbatikh, L., Verpoest, I., and Lomov, S. V. (2019). Voids in Fiber-Reinforced Polymer Composites: A Review on Their Formation, Characteristics, and Effects on Mechanical Performance. *J. Compos. Mater.* 53, 1579–1669. doi:10.1177/0021998318772152

Melelli, A., Arnould, O., Beaugrand, J., and Bourmaud, A. (2020). The Middle Lamella of Plant Fibers Used as Composite Reinforcement: Investigation by Atomic Force Microscopy. *Molecules* 25, 632. doi:10.3390/molecules25030632

Michaud, V. (2016). A Review of Non-saturated Resin Flow in Liquid Composite Moulding Processes. *Transp Porous Med.* 115, 581–601. doi:10.1007/s11242-016-0629-7

Michaud, V. J., Compton, L. M., and Mortensen, A. (1994). Capillarity in Isothermal Infiltration of Alumina Fiber Preforms with Aluminum. *Mmta* 25, 2145–2152. doi:10.1007/bf02652315

Michaud, V. (2021). "Permeability Properties of Composite Reinforcements," in *Composite Reinforcements for Optimum Performance* (Sawston: Woodhead Publishing). Editor P. Boisse. Second Edition, 443–472. doi:10.1016/B978-0-12-819005-0.00014-9

Mittal, G., Rhee, K. Y., Mišković-Stanković, V., and Hui, D. (2018). Reinforcements in Multi-Scale Polymer Composites: Processing, Properties, and Applications. *Composites Part B: Eng.* 138, 122–139. doi:10.1016/j.compositesb.2017.11.028

Morent, R., De Geyter, N., Verschuren, J., De Clerck, K., Kiekens, P., and Leys, C. (2008). Non-thermal Plasma Treatment of Textiles. *Surf. Coat. Techn.* 202, 3427–3449. doi:10.1016/j.surfcoat.2007.12.027

Mortensen, A., and Cornie, J. A. (1987). On the Infiltration of Metal Matrix Composites. *Mta* 18, 1160–1163. doi:10.1007/BF02668570

Mortensen, A., and Wong, T. (1990). Infiltration of Fibrous Preforms by a Pure Metal: Part III. Capillary Phenomena. *Mta* 21, 2257–2263. doi:10.1007/BF02647888

Moudood, A., Rahman, A., Öchsner, A., Islam, M., and Francucci, G. (2019). Flax Fiber and its Composites: An Overview of Water and Moisture Absorption Impact on Their Performance. *J. Reinforced Plastics Composites* 38, 323–339. doi:10.1177/0731684418818893

Mualem, Y. (1978). Hydraulic Conductivity of Unsaturated Porous media: Generalized Macroscopic Approach. *Water Resour. Res.* 14, 325–334. doi:10.1029/WR014i002p00325

Murray, J. J., Robert, C., Gleich, K., McCarthy, E. D., and Ó Brádaigh, C. M. (2020). Manufacturing of Unidirectional Stitched Glass Fabric Reinforced Polyamide 6 by Thermoplastic Resin Transfer Moulding. *Mater. Des.* 189, 108512. doi:10.1016/j.matdes.2020.108512

Neacsu, V., Abu Obaid, A., and Advani, S. G. (2006). Spontaneous Radial Capillary Impregnation across a Bank of Aligned Micro-cylinders - Part I: Theory and Model Development. *Int. J. Multiphase Flow* 32, 661–676. doi:10.1016/j.ijmultiphaseflow.2006.02.006

Neacsu, V., Leisen, J., Beckham, H. W., and Advani, S. G. (2007). Use of Magnetic Resonance Imaging to Visualize Impregnation across Aligned Cylinders Due to Capillary Forces. *Exp. Fluids* 42, 425–440. doi:10.1007/s00348-007-0251-0

Nguyen, V. H., Lagardère, M., Park, C. H., and Panier, S. (2014). Permeability of Natural Fiber Reinforcement for Liquid Composite Molding Processes. *J. Mater. Sci.* 49, 6449–6458. doi:10.1007/s10853-014-8374-1

Nishioka, G. M. (1990). Interaction of Organosilanes with Glass Fibers. *J. Non-Crystalline Sol.* 120, 102–107. doi:10.1016/0022-3093(90)90195-r

Nordlund, M., and Michaud, V. (2012). Dynamic Saturation Curve Measurement for Resin Flow in Glass Fibre Reinforcement. *Composites Part A: Appl. Sci. Manufacturing* 43, 333–343. doi:10.1016/j.compositesa.2011.12.001

Obande, W., Ó Brádaigh, C. M., and Ray, D. (2021). Continuous Fibre-Reinforced Thermoplastic Acrylic-Matrix Composites Prepared by Liquid Resin Infusion -

A Review. *Composites Part B: Eng.* 215, 108771. doi:10.1016/j.compositesb.2021.108771

Palmese, G. R., and Karbhari, V. M. (1995). Effects of Sizings on Microscopic Flow in Resin Transfer Molding. *Polym. Compos.* 16, 313–318. doi:10.1201/9781003064886-310.1002/pc.750160408

Panfilov, M. (2000). in *Theory and Applications of Transport in Porous Media*. Editor T. N. S. Majid Hassanizadeh (Utrecht, Netherlands: Department of Earth Sciences, Utrecht University). Utrecht and Founding Springer Available at: doi:10.1007/978-3-319-72826-1

Pantaloni, D., Bourmaud, A., Baley, C., Clifford, M. J., Ramage, M. H., and Shah, D. U. (2020). A Review of Permeability and Flow Simulation for Liquid Composite Moulding of Plant Fibre Composites. *Materials* 13, 4811–4823. doi:10.3390/ma13214811

Pantaloni, D., Rudolph, A. L., Shah, D. U., Baley, C., and Bourmaud, A. (2021). Interfacial and Mechanical Characterisation of Biodegradable Polymer-Flax Fibre Composites. *Composites Sci. Techn.* 201, 108529. doi:10.1016/j.compscitech.2020.108529

Park, C. H., Lebel, A., Saouab, A., Bréard, J., and Lee, W. I. (2011). Modeling and Simulation of Voids and Saturation in Liquid Composite Molding Processes. *Composites Part A: Appl. Sci. Manufacturing* 42, 658–668. doi:10.1016/j.compositesa.2011.02.005

Patel, N., and Lee, L. J. (1995). Effects of Fiber Mat Architecture on Void Formation and Removal in Liquid Composite Molding. *Polym. Compos.Compos* 16, 386–399. doi:10.1002/pc.750160507

Patel, N., and Lee, L. J. (1996). Modeling of Void Formation and Removal in Liquid Composite Molding. Part I: Wettability Analysis. *Polym. Compos.* 17, 96–103. doi:10.1002/pc.10594

Patiño, I. D., and Nieto-Londoño, C. (2021). Boundary Element Techniques for Multiscale Filling Simulations in Dual-Scale Fibrous Reinforcements Using Two Lumped Approaches. *Comput. Mech.* 68, 1223–1266. Springer Berlin Heidelberg. doi:10.1007/s00466-021-02066-6

Patiño, I. D., Power, H., Nieto-Londoño, C., and Flórez, W. F. (2017). Stokes-Brinkman Formulation for Prediction of Void Formation in Dual-Scale Fibrous Reinforcements: a BEM/DR-BEM Simulation. *Comput. Mech.* 59, 555–577. doi:10.1007/s00466-016-1360-5

Patiño-Arcila, I. D., and Vanegas-Jaramillo, J. D. (2018). Modeling and Simulation of Filling in Dual-Scale Fibrous Reinforcements: State of the Art and New Methodology to Quantify the Sink Effect. *J. Compos. Mater.* 52, 1915–1946. doi:10.1177/0021998317734038

Pierce, R. S., and Falzon, B. G. (2017). Simulating Resin Infusion through Textile Reinforcement Materials for the Manufacture of Complex Composite Structures. *Engineering* 3, 596–607. doi:10.1016/J.ENG.2017.04.006

Pillai, K. M., and Advani, S. G. (1996). Wicking across a Fiber-Bank. *J. Colloid Interf. Sci.* 183, 100–110. doi:10.1006/jcis.1996.0522

Pillai, K. M. (2004). Modeling the Unsaturated Flow in Liquid Composite Molding Processes: A Review and Some Thoughts. *J. Compos. Mater.* 38, 2097–2118. doi:10.1177/0021998304045585

Porfiri, M., and Gupta, N. (2009). Effect of Volume Fraction and wall Thickness on the Elastic Properties of Hollow Particle Filled Composites. *Composites Part B: Eng.* 40, 166–173. doi:10.1016/j.compositesb.2008.09.002

Pouchias, A., Cunningham, P. R., Stein, J., and Kazilas, M. (2019). Development of a Flexible Dielectric Sensor for Flow Monitoring of the Liquid Resin Infusion Process. *Sensors* 19, 5292. doi:10.3390/s19235292

Pucci, M. F., Duchemin, B., Gomina, M., and Bréard, J. (2020). Dynamic Wetting of Molten Polymers on Cellulosic Substrates: Model Prediction for Total and Partial Wetting. *Front. Mater.* 7. doi:10.3389/fmats.2020.00143

Pucci, M. F., Liotier, P.-J., and Drapier, S. (2015a). Capillary Effects on Flax Fibers - Modification and Characterization of the Wetting Dynamics. *Composites Part A: Appl. Sci. Manufacturing* 77, 257–265. doi:10.1016/j.compositesa.2015.03.010

Pucci, M. F., Liotier, P.-J., and Drapier, S. (2015b). Capillary Wicking in a Fibrous Reinforcement - Orthotropic Issues to Determine the Capillary Pressure Components. *Composites Part A: Appl. Sci. Manufacturing* 77, 133–141. doi:10.1016/j.compositesa.2015.05.031

Pucci, M. F., Liotier, P.-J., and Drapier, S. (2016). Capillary Wicking in Flax Fabrics - Effects of Swelling in Water. *Colloids Surf. A: Physicochemical Eng. Aspects* 498, 176–184. doi:10.1016/j.colsurfa.2016.03.050

Pucci, M. F., Liotier, P.-J., and Drapier, S. (2017a). Tensiometric Method to Reliably Assess Wetting Properties of Single Fibers with Resins: Validation on Cellulosic Reinforcements for Composites. *Colloids Surf. A: Physicochemical Eng. Aspects* 512, 26–33. doi:10.1016/j.colsurfa.2016.09.047

Pucci, M. F., Liotier, P.-J., Seveno, D., Fuentes, C., Van Vuure, A., and Drapier, S. (2017b). Wetting and Swelling Property Modifications of Elementary Flax Fibres and Their Effects on the Liquid Composite Molding Process. *Composites Part A: Appl. Sci. Manufacturing* 97, 31–40. doi:10.1016/j.compositesa.2017.02.028

Qian, H., Bismarck, A., Greenhalgh, E. S., and Shaffer, M. S. P. (2010a). Carbon Nanotube Grafted Silica Fibres: Characterising the Interface at the Single Fibre Level. *Composites Sci. Techn.* 70, 393–399. doi:10.1016/j.compscitech.2009.11.014

Qian, H., Greenhalgh, E. S., Shaffer, M. S. P., and Bismarck, A. (2010b). Carbon Nanotube-Based Hierarchical Composites: A Review. *J. Mater. Chem.* 20, 4751–4762. doi:10.1039/c000041h

Ravey, C., Ruiz, E., and Trochu, F. (2014). Determination of the Optimal Impregnation Velocity in Resin Transfer Molding by Capillary Rise Experiments and Infrared Thermography. *Composites Sci. Techn.* 99, 96–102. doi:10.1016/j.compscitech.2014.05.019

Reia Da Costa, E. F., Skordos, A. A., Partridge, I. K., and Rezai, A. (2012). RTM Processing and Electrical Performance of Carbon Nanotube Modified Epoxy/fibre Composites. *Composites Part A: Appl. Sci. Manufacturing* 43, 593–602. doi:10.1016/j.compositesa.2011.12.019

Rieser, J. M., Arratia, P. E., Yodh, A. G., Gollub, J. P., and Durian, D. J. (2015). Tunable Capillary-Induced Attraction between Vertical Cylinders. *Langmuir* 31, 2421–2429. doi:10.1021/la5046139

Rijswijk, K. v., Teuwen, J. J. E., Bersee, H. E. N., and Beukers, A. (2009). Textile Fiber-Reinforced Anionic Polyamide-6 Composites. Part I: The Vacuum Infusion Process. *Composites Part A: Appl. Sci. Manufacturing* 40, 1–10. doi:10.1016/j.compositesa.2008.03.018

Rougier, V., Cellier, J., Gomina, M., and Bréard, J. (2021). Slip Transition in Dynamic Wetting for a Generalized Navier Boundary Condition. *J. Colloid Interf. Sci.* 583, 448–458. doi:10.1016/j.jcis.2020.09.015

Ruiz, E., Achim, V., Soukane, S., Trochu, F., and Bréard, J. (2006). Optimization of Injection Flow Rate to Minimize Micro/macro-Voids Formation in Resin Transfer Molded Composites. *Composites Sci. Techn.* 66, 475–486. doi:10.1016/j.compscitech.2005.06.013

Sahimi, M. (2011). *Flow and Transport in Porous Media and Fractured Rock: From Classical Methods to Modern Approaches*. 2nd ed. Weinheim, Germany: Wiley VCH. doi:10.1002/9783527636693

Salokhe, S., Rahmati, M., and Masoodi, R. (2021). Numerical Modelling of the Flow in a Swelling Preform during LCM Mould Filling. *J. Reinforced Plastics Composites* 40, 490–504. doi:10.1177/0731684420975197

Salvatori, D., Caglar, B., and Michaud, V. (2019). 3D Spacers Enhance Flow Kinetics in Resin Transfer Molding with Woven Fabrics. *Composites Part A: Appl. Sci. Manufacturing* 119, 206–216. doi:10.1016/j.compositesa.2019.01.023

Salvatori, D., Caglar, B., Teixidó, H., and Michaud, V. (2018). Permeability and Capillary Effects in a Channel-wise Non-crimp Fabric. *Composites Part A: Appl. Sci. Manufacturing* 108, 41–52. doi:10.1016/j.compositesa.2018.02.015

Sas, H. S., Šimáček, P., and Advani, S. G. (2015). A Methodology to Reduce Variability during Vacuum Infusion with Optimized Design of Distribution media. *Composites Part A: Appl. Sci. Manufacturing* 78, 223–233. doi:10.1016/j.compositesa.2015.08.011

Schell, J. S. U., Deleglise, M., Binetruy, C., Krawczak, P., and Ermanni, P. (2007). Numerical Prediction and Experimental Characterisation of Meso-Scale-Voids in Liquid Composite Moulding. *Composites Part A: Appl. Sci. Manufacturing* 38, 2460–2470. doi:10.1016/j.compositesa.2007.08.005

Schmachtenberg, E., Schulte Zur Heide, J., and Töpker, J. (2005). Application of Ultrasonics for the Process Control of Resin Transfer Moulding (RTM). *Polym. Test.* 24, 330–338. doi:10.1016/j.polymertesting.2004.11.002

Schneider, G., Weber, L., and Mortensen, A. (2019). Reactive Pressure Infiltration of Cu-46at.Pct. Si into Carbon. *Acta Materialia* 177, 9–19. doi:10.1016/j.actamat.2019.07.010

Sharma, S., Siginer, D. A., Dukipatti, R. K., and Soschinske, K. A. (2009). Effect of Fiber Sizing - Test Fluid Interaction on the Unsaturated and Saturated Flow in the VARTM Process. *J. Compos. Mater.* 43, 1589–1601. doi:10.1177/0021998308337898

Simacek, P., and Advani, S. G. (2003). A Numerical Model to Predict Fiber Tow Saturation during Liquid Composite Molding. *Composites Sci. Techn.* 63, 1725–1736. doi:10.1016/S0266-3538(03)00155-6

Simacek, P., Neacsu, V., and Advani, S. G. (2010). A Phenomenological Model for Fiber Tow Saturation of Dual Scale Fabrics in Liquid Composite Molding. *Polym. Compos.* 31, 1881–1889. doi:10.1002/pc.20982

Sinha, E., and Panigrahi, S. (2009). Effect of Plasma Treatment on Structure, Wettability of Jute Fiber and Flexural Strength of its Composite. *J. Compos. Mater.* 43, 1791–1802. doi:10.1177/0021998309338078

Sisodia, S. M., Garcea, S. C., George, A. R., Fullwood, D. T., Spearing, S. M., and Gamstedt, E. K. (2016). High-resolution Computed Tomography in Resin Infused Woven Carbon Fibre Composites with Voids. *Composites Sci. Techn.* 131, 12–21. doi:10.1016/j.compscitech.2016.05.010

Spitalsky, Z., Tasis, D., Papagelis, K., and Galiotis, C. (2010). Carbon Nanotube-Polymer Composites: Chemistry, Processing, Mechanical and Electrical Properties. *Prog. Polym. Sci.* 35, 357–401. doi:10.1016/j.progpolymsci.2009.09.003

Staal, J., Caglar, B., Hank, T., Wardle, B. L., Gorbatikh, L., Lomov, S. V., et al. (2021). In-series Sample Methodology for Permeability Characterization Demonstrated on Carbon Nanotube-Grafted Alumina Textiles. *Composites Part A: Appl. Sci. Manufacturing* 150, 106631. doi:10.1016/j.compositesa.2021.106631

Steenkamer, D. A., McKnight, S. H., Wilkins, D. J., and Karbhari, V. M. (1995). Experimental Characterization of Permeability and Fibre Wetting for Liquid Moulding. *J. Mater. Sci.* 30, 3207–3215. doi:10.1007/BF01209239

Stöven, T., Weyrauch, F., Mitschang, P., and Neitzel, M. (2003). Continuous Monitoring of Three-Dimensional Resin Flow through a Fibre Preform. *Composites Part A: Appl. Sci. Manufacturing* 34, 475–480. doi:10.1016/S1359-835X(03)00059-9

Strauß, S., Senz, A., and Ellinger, J. (2019). Comparison of the Processing of Epoxy Resins in Pultrusion with Open bath Impregnation and Closed-Injection Pultrusion. *J. Compos. Sci.* 3, 87. doi:10.3390/jcs3030087

Studer, J., Dransfeld, C., Jauregui Cano, J., Keller, A., Wink, M., Masania, K., et al. (2019). Effect of Fabric Architecture, Compaction and Permeability on through Thickness Thermoplastic Melt Impregnation. *Composites Part A: Appl. Sci. Manufacturing* 122, 45–53. doi:10.1016/j.compositesa.2019.04.008

Tan, H., and Pillai, K. M. (2012). Multiscale Modeling of Unsaturated Flow in Dual-Scale Fiber Preforms of Liquid Composite Molding I: Isothermal Flows. *Composites Part A: Appl. Sci. Manufacturing* 43, 1–13. doi:10.1016/j.compositesa.2010.12.013

Tanner, L. H. (1979). The Spreading of Silicone Oil Drops on Horizontal Surfaces. *J. Phys.-D.* 12, 1473–1484. doi:10.1088/0022-3727/12/9/009

Teixidó, H., Caglar, B., Revol, V., and Michaud, V. (2021). In-operando Dynamic Visualization of Flow through Porous Preforms Based on X-ray Phase Contrast Imaging. *Composites Part A: Appl. Sci. Manufacturing* 149, 106560. doi:10.1016/j.compositesa.2021.106560

Testoni, G. A., Kim, S., Pisupati, A., and Park, C. H. (2018). Modeling of the Capillary Wicking of Flax Fibers by Considering the Effects of Fiber Swelling and Liquid Absorption. *J. Colloid Interf. Sci.* 525, 166–176. doi:10.1016/j.jcis.2018.04.064

Thomas, S., Bongiovanni, C., and Nutt, S. R. (2008). *In Situ* estimation of Through-Thickness Resin Flow Using Ultrasound. *Composites Sci. Techn.* 68, 3093–3098. doi:10.1016/j.compscitech.2008.07.012

Thomason, J. L. (2021). "Sizing Chemistry of Glass Fibers," in *Fiberglass Science and Technology* (Switzerland AG, Cham: Springer Nature). Editor H. Li, 259–321. doi:10.1007/978-3-030-72200-510.1007/978-3-030-72200-5_4

Thostenson, E. T., Li, W. Z., Wang, D. Z., Ren, Z. F., and Chou, T. W. (2002). Carbon Nanotube/carbon Fiber Hybrid Multiscale Composites. *J. Appl. Phys.* 91, 6034–6037. doi:10.1063/1.1466880

van Genuchten, M. T. (1980). A Closed-form Equation for Predicting the Hydraulic Conductivity of Unsaturated Soils. *Soil Sci. Soc. America J.* 44, 892–898. doi:10.2136/sssaj1980.03615995004400050002x

Varnavides, G., Mortensen, A., and Carter, W. C. (2021). Simulating Infiltration as a Sequence of Pinning and De-pinning Processes. *Acta Materialia* 210, 116831. doi:10.1016/j.actamat.2021.116831

Vedernikov, A., Safonov, A., Tucci, F., Carlone, P., and Akhatov, I. (2020). Pultruded Materials and Structures: A Review. *J. Compos. Mater.* 54, 4081–4117. doi:10.1177/0021998320922894

Vernet, N., Ruiz, E., Advani, S., Alms, J. B., Aubert, M., Barburski, M., et al. (2014). Experimental Determination of the Permeability of Engineering Textiles: Benchmark II. *Composites Part A: Appl. Sci. Manufacturing* 61, 172–184. doi:10.1016/j.compositesa.2014.02.010

Verrey, J., Michaud, V., and Månson, J.-A. E. (2006). Dynamic Capillary Effects in Liquid Composite Moulding with Non-crimp Fabrics. *Composites Part A: Appl. Sci. Manufacturing* 37, 92–102. doi:10.1016/j.compositesa.2005.04.011

Vilà, J., Sket, F., Wilde, F., Requena, G., González, C., and LLorca, J. (2015). An *In Situ* Investigation of Microscopic Infusion and Void Transport during Vacuum-Assisted Infiltration by Means of X-ray Computed Tomography. *Composites Sci. Techn.* 119, 12–19. doi:10.1016/j.compscitech.2015.09.016

Villière, M., Guéroult, S., Sobotka, V., Boyard, N., Bréard, J., and Delaunay, D. (2015). Dynamic Saturation Curve Measurement in Liquid Composite Molding by Heat Transfer Analysis. *Composites Part A: Appl. Sci. Manufacturing* 69, 255–265. doi:10.1016/j.compositesa.2014.11.024

Vo, H. N., Pucci, M. F., Corn, S., Le Moigne, N., Garat, W., Drapier, S., et al. (2020). Capillary Wicking in Bio-Based Reinforcements Undergoing Swelling - Dual Scale Consideration of Porous Medium. *Composites Part A: Appl. Sci. Manufacturing* 134, 105893. doi:10.1016/j.compositesa.2020.105893

Walther, J., Simacek, P., and Advani, S. G. (2012). The Effect of Fabric and Fiber Tow Shear on Dual Scale Flow and Fiber Bundle Saturation during Liquid Molding of Textile Composites. *Int. J. Mater. Form.* 5, 83–97. doi:10.1007/s12289-011-1060-9

Wang, B. C., Huang, Y. D., and Liu, L. (2006). Effects of Fibre Surface Silanisation on Silica Fibre/phenolics Composites Produced by Resin Transfer Moulding Process. *Mater. Sci. Techn.* 22, 206–212. doi:10.1179/174328406X91078

Wang, J., Fuentes, C. A., Zhang, D., Wang, X., Van Vuure, A. W., and Seveno, D. (2017a). Wettability of Carbon Fibres at Micro- and Mesoscales. *Carbon* 120, 438–446. doi:10.1016/j.carbon.2017.05.055

Wang, J., Simacek, P., and Advani, S. G. (2016). Use of Centroidal Voronoi Diagram to Find Optimal Gate Locations to Minimize Mold Filling Time in Resin Transfer Molding. *Composites Part A: Appl. Sci. Manufacturing* 87, 243–255. doi:10.1016/j.compositesa.2016.04.026

Wang, J., Simacek, P., and Advani, S. G. (2017b). Use of Medial axis to Find Optimal Channel Designs to Reduce Mold Filling Time in Resin Transfer Molding. *Composites Part A: Appl. Sci. Manufacturing* 95, 161–172. doi:10.1016/j.compositesa.2017.01.003

Wang, Y., Moatamedi, M., and Grove, S. M. (2009). Continuum Dual-Scale Modeling of Liquid Composite Molding Processes. *J. Reinforced Plastics Composites* 28, 1469–1484. doi:10.1177/0731684408089533

Washburn, E. W. (1921). Note on a Method of Determining the Distribution of Pore Sizes in a Porous Material. *Proc. Natl. Acad. Sci.* 7, 115–116. doi:10.1073/pnas.7.4.115

Wei, M., Bowman, R. S., Wilson, J. L., and Morrow, N. R. (1993). Wetting Properties and Stability of Silane-Treated Glass Exposed to Water, Air, and Oil. *J. Colloid Interf. Sci.* 157, 154–159. doi:10.1006/jcis.1993.1170

Willenbacher, B., May, D., and Mitschang, P. (2019). Out-of-plane Capillary Pressure of Technical Textiles. *Composites Part A: Appl. Sci. Manufacturing* 124, 105495. doi:10.1016/j.compositesa.2019.105495

Withers, P. J., Bouman, C., Carmignato, S., Cnudde, V., Grimaldi, D., Hagen, C. K., et al. (2021). X-ray Computed Tomography. *Nat. Rev. Methods Primers* 1, R29–R43. doi:10.1038/s43586-021-00015-4

Wolfrath, J., Michaud, V., Modaressi, A., and Månson, J.-A. E. (2006). Unsaturated Flow in Compressible Fibre Preforms. *Composites Part A: Appl. Sci. Manufacturing* 37, 881–889. doi:10.1016/j.compositesa.2005.01.008

Wu, D., and Larsson, R. (2020). A Shell Model for Resin Flow and Preform Deformation in Thin-Walled Composite Manufacturing Processes. *Int. J. Mater. Form.* 13, 923–937. doi:10.1007/s12289-019-01517-z

Wu, X.-F., and Dzenis, Y. A. (2006). Droplet on a Fiber: Geometrical Shape and Contact Angle. *Acta Mechanica* 185, 215–225. doi:10.1007/s00707-006-0349-0

Yamamoto, N., Wicks, S. S., Guzman, R., Ishiguro, K., and Steiner, S. A. (2009). "Mechanical, Thermal, and Electrical Properties of Woven Laminated Advanced Composites Containing Aligned Carbon Nanotubes," in ICCM: 17th Conference on Composite Materials, Edinburgh, United Kingdom, July 27–31, 2009.

Yashiro, S., Nakashima, D., Oya, Y., Okabe, T., and Matsuzaki, R. (2019). Particle Simulation of Dual-Scale Flow in Resin Transfer Molding for Process Analysis.

Composites Part A: Appl. Sci. Manufacturing 121, 283–288. doi:10.1016/j.compositesa.2019.03.038

Yeager, M., Hwang, W. R., and Advani, S. G. (2016). Prediction of Capillary Pressure for Resin Flow between Fibers. *Composites Sci. Techn.* 126, 130–138. doi:10.1016/j.compscitech.2016.02.014

Yeager, M., Simacek, P., and Advani, S. G. (2017). Role of Fiber Distribution and Air Evacuation Time on Capillary Driven Flow into Fiber Tows. *Composites Part A: Appl. Sci. Manufacturing* 93, 144–152. doi:10.1016/j.compositesa.2016.11.016

Yin, T., Li, Y., and Yuan, B. (2018). The Multi-Scale Flow Behaviors of Sisal Fiber Reinforced Composites during Resin Transfer Molding Process. *Sci. China Technol. Sci.* 61, 1925–1934. doi:10.1007/s11431-018-9343-5

Yoshihara, K., Kamei, Y., Mizuno, A., Ohgaki, H., Hori, T., and Ueno, I. (2020). Effect of Wettability on Viscous Fluid Impregnation in Single-Layer Woven-Fibre Bundles Driven by Pressure Difference. *Composites Part A: Appl. Sci. Manufacturing* 138, 106049. doi:10.1016/j.compositesa.2020.106049

Yousaf, Z., Potluri, P., and Withers, P. J. (2017). Influence of Tow Architecture on Compaction and Nesting in Textile Preforms. *Appl. Compos. Mater.* 24, 337–350. doi:10.1007/s10443-016-9554-8

Yum, S. H., Lee, W. I., and Kim, S. M. (2016). Particle Filtration and Distribution during the Liquid Composite Molding Process for Manufacturing Particles Containing Composite Materials. *Composites Part A: Appl. Sci. Manufacturing* 90, 330–339. doi:10.1016/j.compositesa.2016.07.016

Yun, M., Sas, H., Simacek, P., and Advani, S. G. (2017). Characterization of 3D Fabric Permeability with Skew Terms. *Composites Part A: Appl. Sci. Manufacturing* 97, 51–59. doi:10.1016/j.compositesa.2016.12.030

Zhang, H., Liu, Y., Huo, S., Briscoe, J., Tu, W., Picot, O. T., et al. (2017). Filtration Effects of Graphene Nanoplatelets in Resin Infusion Processes: Problems and Possible Solutions. *Composites Sci. Techn.* 139, 138–145. doi:10.1016/j.compscitech.2016.12.020

Zhang, X., Wang, P., Zhou, Y., Li, X., Yang, E.-H., Yu, T. X., et al. (2016). The Effect of Strain Rate and Filler Volume Fraction on the Mechanical Properties of Hollow Glass Microsphere Modified Polymer. *Composites Part B: Eng.* 101, 53–63. doi:10.1016/j.compositesb.2016.06.079

Zhao, C., Yang, B., Wang, S., Ma, C., Wang, S., and Bi, F. (2019). Three-Dimensional Numerical Simulation of Meso-Scale-Void Formation during the Mold-Filling Process of LCM. *Appl. Compos. Mater.* 26, 1121–1137. doi:10.1007/s10443-019-09770-w

Zingraff, L., Michaud, V., Bourban, P.-E., and Månson, J.-A. E. (2005). Resin Transfer Moulding of Anionically Polymerised Polyamide 12. *Composites Part A: Appl. Sci. Manufacturing* 36, 1675–1686. doi:10.1016/j.compositesa.2005.03.023

Conflict of Interest: The authors declare that the research was conducted in the absence of any commercial or financial relationships that could be construed as a potential conflict of interest.

Publisher's Note: All claims expressed in this article are solely those of the authors and do not necessarily represent those of their affiliated organizations, or those of the publisher, the editors, and the reviewers. Any product that may be evaluated in this article, or claim that may be made by its manufacturer, is not guaranteed or endorsed by the publisher.

frontiers in Materials

REVIEW
published: 24 February 2022
doi: 10.3389/fmats.2022.812984

Recent Progress in Crystallographic Characterization, Magnetoresponsive and Elastocaloric Effects of Ni-Mn-In-Based Heusler Alloys—A Review

Hai-Le Yan[1]*, *Xiao-Ming Huang*[1] *and Claude Esling*[2]*

[1]Key Laboratory for Anisotropy and Texture of Materials (Ministry of Education), School of Material Science and Engineering, Northeastern University, Shenyang, China, [2]Laboratoire d'Étude des Microstructures et de Mécanique des Matériaux (LEM3), CNRS UMR 7239, Université de Lorraine, Metz, France

Ni-Mn-In-based magnetic shape memory alloys have promising applications in numerous state-of-the-art technologies, such as solid-state refrigeration and smart sensing, resulting from the magnetic field-induced inverse martensitic transformation. This paper aims at presenting a comprehensive review of the recent research progress of Ni-Mn-In-based alloys. First, the crystallographic characterization of these compounds that strongly affects functional behaviors, including the crystal structure of modulated martensite, the self-organization of martensite variants and the strain path during martensitic transformation, are reviewed. Second, the current research progress in functional behaviors, including magnetic shape memory, magnetocaloric and elastocaloric effects, are summarized. Finally, the main bottlenecks hindering the technical development and some possible solutions to overcome these difficulties are discussed. This review is expected to provide some useful insights for the design of novel advanced magnetic shape memory alloys.

Keywords: NiMnIn, modulated martensite, martensitic transformation, magnetocaloric effect, elastocaloric effect

OPEN ACCESS

Edited by:
Vincent G. Harris,
Northeastern University, United States

Reviewed by:
Durga Paudyal,
Iowa State University, United States
Francesca Casoli,
Italian National Research Council, Italy

***Correspondence:**
Hai-Le Yan
yanhaile@mail.neu.edu.cn
Claude Esling
claude.esling@univ-lorraine.fr

Specialty section:
This article was submitted to Smart Materials, a section of the journal Frontiers in Materials

Received: *11 November 2021*
Accepted: *31 January 2022*
Published: *24 February 2022*

Citation:
Yan H-L, Huang X-M and Esling C (2022) Recent Progress in Crystallographic Characterization, Magnetoresponsive and Elastocaloric Effects of Ni-Mn-In-Based Heusler Alloys—A Review. Front. Mater. 9:812984. doi: 10.3389/fmats.2022.812984

1 INTRODUCTION

In 1996, a large magnetic-field-induced strain, i.e., 0.2% under a magnetic field of 0.8 T realized by the rearrangement of martensite variants driven by the magnetocrystalline anisotropy energy, was first reported in the stoichiometric Heusler-type Ni_2MnGa alloys by K. Ullakko and collaborators (Ullakko et al., 1996). Compared with the magnetostrictive materials, such as Terfenol-D, and conventional shape memory alloys, such as Ni-Ti, the magnetic-field-induced strain in Ni_2MnGa has both fast responsive frequency and large output strain, and thus is considered to have huge potential in the fields of smart actuators and sensors. From then on, the Heusler-type NiMnGa alloy has aroused widespread attention (Zheludev et al., 1996; Mañosa et al., 1997; Planes et al., 1997; Ullakko et al., 1997; Brown et al., 1999). About 10 years later, Y. Sutou and R. Kainuma et al. fabricated a series of nonstoichiometric Ni(Co)MnZ (Z = In, Sn and Sb) Heusler-type alloys by the replacement of the *p-block* type Ga by Z (Z = In, Sn or Sb) (Sutou et al., 2004a). Although Ga ($4s^2p^1$) and In ($5s^2p^1$) belong to the same main-group elements (IIIA) and their positions in the elemental periodic table are adjacent, the magnetic properties and the resultant functional behaviors of NiMnGa and NiMnIn are significantly different.

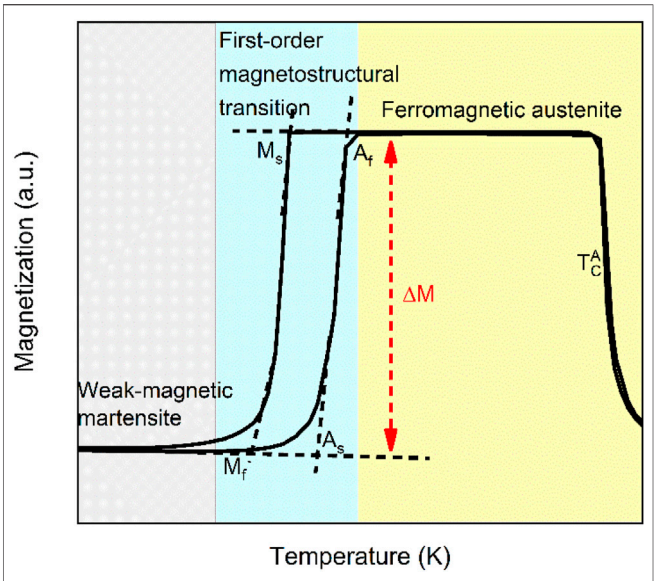

FIGURE 1 | Typical temperature dependence of magnetization (M-T curve) for the NiMnIn-based alloys.

Specifically, the magnetization of martensite and austenite are similar in NiMnGa, while the magnetization of martensite in the NiMnIn is much weaker than that of austenite, as shown in **Figure 1**. In other words, for the NiMnIn-based alloys, there is a significant change in magnetism during the martensitic transformation, and thus this transition is also termed the magnetostructural transition. As a result, the Zeeman energy ($E_{Zeeman} = -\mu_0 \int MHdV$) of austenite, i.e., the potential energy of a magnetized body having magnetization M and a volume of V in an external magnetic field H, should be much lower than that of martensite. Thus, the magnetic field should stabilize the strong magnetic austenite phase. This feature of the NiMnIn alloy provides an extra stimulus, apart from thermal and mechanical fields, to drive the inverse martensitic transformation. To be specific, when a magnetic field is applied to the martensite of the NiMnIn alloy, the sample tends to transform to the austenite state, i.e., the magnetic-field-induced inverse martensite transformation, under the driving force of the Zeeman energy difference $\mu_0 H\Delta M$ of these two phases.

If a pre-strain is applied to the martensite before the application of a magnetic field, during the magnetic-field-induced inverse martensite transformation, the sample tends to recover its original shape, which is termed as the metamagnetic shape-memory effect (Kainuma et al., 2006). Different from NiMnGa, in which the output stress (a few MPa) is limited by the magnetocrystalline anisotropy energy, the output stress of Ni(Co)MnIn can reach a large value (~100 MPa) since the Zeeman energy continues to increase with the elevated magnetic field (Karaca et al., 2006; Karaca et al., 2009). In addition, since the total entropy and the electric resistance of austenite and martensite have great differences, when an external magnetic field is applied, a huge change of total entropy (termed as the magnetocaloric effect) and electric resistance (termed as the magnetoresistance effect) may occur during the magnetic-field-induced inverse martensite transformation. Thus, the Ni(Co)MnIn alloys possess excellent magnetoresponsive performances (Han et al., 2006; Han et al., 2008; Kustov et al., 2009; Liu et al., 2012; Kihara et al., 2014), including magnetocaloric, magnetoresistance, and exchange bias effects. Besides, like the conventional shape memory alloy in which the martensitic transformation can be driven by thermal and mechanical fields, the Ni(Co)MnIn alloys also exhibit the thermal-induced shape memory, superelasticity, and elastocaloric effects (Mañosa et al., 2010; Lu et al., 2014; Moya et al., 2014; Liu et al., 2017; Manosa and Planes, 2017; Kabirifar et al., 2019).

During the past 15 years, scientists from all over the world have conducted continuous and in-depth research on NiMnIn-based alloys (Kainuma et al., 2008; Hu et al., 2013; Bachaga et al., 2019). Numerous systematic and in-depth research results covering crystal structure, morphological and crystallographic features of microstructure, martensitic transformation, multifunctional behaviors, etc., have been reported in the literature. Therefore, a systematical overview of the current findings is of great significance to the development of this compound. To date, the metamagnetic shape memory, magnetocaloric, and elastocaloric effects of NiMnIn alloy have been briefly summarized and compared with other competitors in different review papers, such as the review paper about magnetic shape memory alloy by Kainuma et al. (2008), the paper focused on caloric materials by Moya et al. (2014), the review about mechanocaloric effect by Manosa and Planes (2017) and the paper focused on magnetic elastocaloric materials by Liu et al. (2017), and the review about magnetic refrigeration materials by Gottschall et al. (2019). Nevertheless, to the best of the authors' knowledge, there is still a lack of review articles focusing on the NiMnIn-based alloy in the literature.

This paper aims at presenting a comprehensive review of the research progress of Ni-Mn-In-based alloys. First, the crystallographic characterizations, including the crystal structure of austenite and modulated martensite (**Section 2**), the self-organization microstructure of modulated martensite (**Section 3**), and the transformation strain path of martensitic transformation (**Section 4**), are reviewed. Then, the current research progress in functional behaviors, including magnetic shape memory (**Section 5**), magnetocaloric (**Section 6**), and mechanocaloric (**Section 7**) effects, are summarized. For each topic, the main bottlenecks hindering the technical development and some possible solutions for overcoming these difficulties are discussed.

2 CRYSTAL STRUCTURE

The crystal structure is one of the most fundamental information of crystalline materials. In general, the determination of crystal structure is the first step to understanding the physical or mechanical properties of materials (Ravel et al., 2002b). Since the magnetostructural transition was discovered in the NiMnIn-based alloys, many state-of-the-art modern characterization

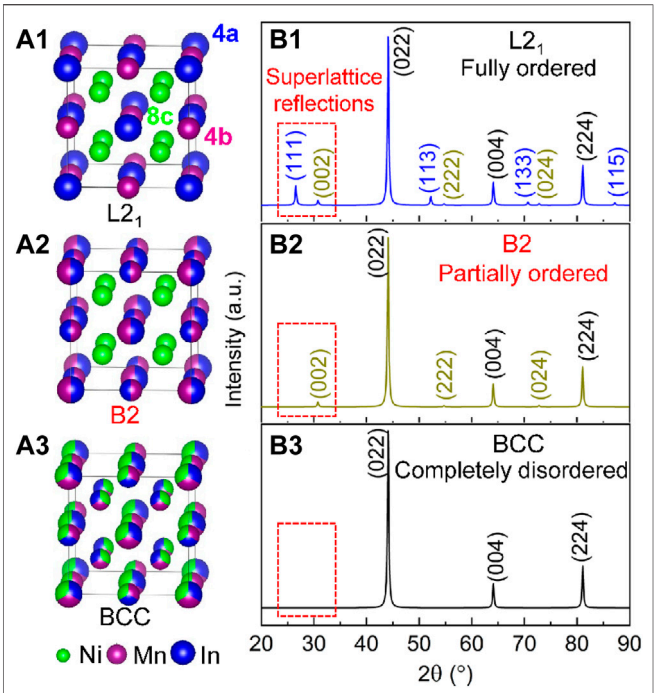

FIGURE 2 | Illustration of crystal structural models of $L2_1$ **(A_1)**, B2 **(A_2)**, and BCC **(A_3)** of NiMnIn alloy and their corresponding Cu Kα-radiation X-ray diffraction patterns **(B_1–B_3)**. To keep consistency with the $L2_1$ structure **(A_1)**, for the B2 **(A_2)** and the BCC **(A_3)** structures, the superstructural models containing 8 unit cells are illustrated. The main reflections in **(B_1–B_3)** are labeled with the black indices, while the superlattice reflections generated due to the B2 and the $L2_1$ types of stacking order of Ni, Mn, and In atoms are highlighted in olive and blue, respectively.

techniques, such as X-ray diffraction (XRD) (Liu et al., 2008; Feng et al., 2009; Zhang et al., 2014; Crouigneau et al., 2015; Paramanik and Das, 2016), synchrotron high-energy XRD (Karaca et al., 2009; Huang et al., 2016), neutron diffraction (Yan et al., 2015), high-resolution transmission electron microscope (HRTEM) (Yan et al., 2016c), selected area electron diffraction (SAED) (Ito et al., 2007; Ito et al., 2008; Liu et al., 2009a), high angle annular dark-field (HAADF) imaging of spherical aberration-corrected high-resolution scanning transmission electron microscope (Yang et al., 2020), have been used to characterize crystal structure of the compounds.

2.1 Austenite

2.1.1 Stoichiometric Ni_2MnIn

NiMnIn-based alloys belong to the Heusler-type alloys. The austenite phase of this compound has a typical structure of 2:1:1 full Heusler alloy, that is, a highly ordered cubic Cu_2MnAl-type $L2_1$ structure (space group: $Fm\bar{3}m$) (Heusler, 1934). **Figures $2A_1$,B_1** display the $L2_1$ structural model and a typical X-ray diffraction pattern, respectively. It is seen that the $L2_1$ structure is composed of four interpenetrated face-centered-cubic (FCC) sublattices, i.e., In: *4a* (0 0 0), Mn: *4b* (0.5 0.5 0.5), and Ni: *8c* (0.25 0.25 0.25) and (0.75 0.75 0.75). Theoretically, under 2θ ranging from 20° to 90°, there are three main reflections (labeled with the black indices), i.e., (022), (004) and (224), and seven satellite reflections (labeled with the blue and olive indices) due to the orderly stacking of Ni, Mn and In atoms, i.e., (111), (002), (113), (222), (133), (024) and (115), as shown in **Figure $2B_1$**.

As is known, the ordering degree of crystal structure significantly affects both mechanical and functional properties in the Heusler-type alloy (Ravel et al., 2002a; Raphael et al., 2002; Harris and Chen, 2015). For the NiMn-based alloys, the order degree of austenite is sensitive to the fabrication process and chemical composition (Krenke et al., 2006). When the alloy is quenched from a high temperature with a high cooling rate (such as melt-spinning technique), the austenite of NiMnIn alloy could exhibit the B2 type structure, as illustrated in **Figure $2A_2$**. The difference between the $L2_1$ and the B2 structures is that In and Mn atoms are orderly located at *4a* and *4b* sites in the former, whereas these two elements occupy the *4a* and *4b* sites randomly in the latter. Owing to the reduction of ordering degree, as shown in **Figure $2B_2$**, the number of satellite reflections decreases from 7 (the $L2_1$ structure) to 3 (the B2 structure), i.e., (002), (222), and (024). When the ordering degree further decreases, the B2 structure may turn to be the body-centered cubic (BCC) type. In this case, as shown in **Figure $2A_3$**, all Ni, Mn, and In atoms randomly occupy the *4a*, *4b*, and *8c* sites. For the XRD spectrum, the fully random occupations of Ni, Mn, and In atoms lead to the disappearance of all satellite diffraction peaks (**Figure $2B_3$**). Generally, the ordering degree of the austenite of the NiMnIn-based alloys can be evaluated by examining the number of satellite reflections at 2θ ranging from 25° to 35° (Cu Kα-radiation), as indicated in the red dashed boxes in **Figures $2A_1$–A_3**. Two (**Figure $2A_1$**), one (**Figure $2A_2$**), or zero (**Figure $2A_3$**) reflections suggest the austenite has the $L2_1$, the B2, or the BCC structure.

First-principles calculations showed that the exchange energy for In (*4a*) and Mn (*4b*) is around 70 meV/atom (Liu et al., 2020), which is smaller than that for Ni (*8c*) and Mn (*4b*) (around 85 meV/atom) (Liang et al., 2021). This result implies that the possibility of the occurrence of *4a*-*4b* disorder should be larger than that of *4a* (*4b*)-*8c* disorder, which explains the experimental results that the B2 structure is observed easier than the BCC structure. Moreover, from **Figures $2A_1$–A_3**, it is seen that even though the $L2_1$ structure is usually classified to be the face-centered cubic (FCC) structure from the point of view of crystallographic symmetry (Yan et al., 2016a; Lin et al., 2016), the atom stacking manner of the NiMnIn-based alloys mostly follows the characteristics of the BCC structure (with a different degree of ordering) rather than FCC. Thus, the typical structure characteristic parameters of the NiMnIn-based alloy, such as close-packed crystal plane, close-packed crystal direction, stacking density, coordination number, are the same as those of the BCC structure.

2.1.2 Non-stoichiometric NiMnIn Alloys

Unlike the NiMnGa alloys, where the stoichiometric case, i.e., Ni_2MnGa, undergoes a displacive structural transition at around 210 K (Wirth et al., 1997; Brown et al., 2002), the stoichiometric Ni_2MnIn is thermodynamically stable even when the temperature drops toward 0 K (Kurfiß et al., 2005; Krenke et al., 2006). Thus, the investigations on the NiMnIn-

based alloys are mostly focused on the nonstoichiometric compositions, especially the Mn-enriched Ni_2Mn(In, Mn) systems. Rietveld refinement of the high-resolution neutron diffraction data (Yan et al., 2015) showed that the extra-Mn prefers to directly substitute In at the 4a site. For the NiMnIn-based alloys, the magnetoresponsive behaviors are originated from the magnetic-field induced inverse martensitic transformation owing to the significant change of magnetization between austenite (ferromagnetism) and martensite (antiferromagnetism). Numerous studies suggested that the antiferromagnetism comes from the first-neighbored Mn (*4a*)-Mn(*4b*) coupling (Şaşıoğlu et al., 2004; Liu et al., 2006), which can be easily realized in the Mn-enriched Ni_2Mn(In, Mn) system since the extra-Mn tends to occupy the *4a* sites while the normal Mn is located at the *4b* sites (**Figure 2A$_2$**). This could be the reason why the fruitful magnetoresponsive behaviors of the NiMnIn-based alloys mostly exist in the Mn-enriched systems. By using the first-principles calculations, it is revealed that at the *4b* site, the extra-Mn atoms prefer to be dispersed from one another (Yan et al., 2015).

2.2 Martensite

For the martensite of the NiMnIn-based alloys, numerous studies showed that there exist two kinds of crystal structures, i.e., the non-modulated (NM) martensite and modulated martensite (Krenke et al., 2006). Note that even though the partial substitution of Co for Ni can significantly enhance the ferromagnetism of the NiMn-based alloys and thus improve their magnetoresponsive performances, this substitution will not change the type of crystal structure. Moreover, with the addition of Co, it is difficult to obtain a pure single-phase martensite powder sample, even if the testing temperature is far below the finishing temperature of martensitic transformation M_f measured by the DSC technique (Abematsu et al., 2014; Yan et al., 2015; Yan et al., 2016b). The reason could be attributed to the large specific surface area of the powder sample, which tends to stabilize the austenite and suppress the occurrence of martensitic transformation (Yan et al., 2021a). Thus, it is more convenient to determine the crystal structure of martensite with Co-free NiMnIn samples. X-ray diffraction studies showed that for the ternary Mn-enriched $Ni_{50}Mn_{50-x}In_x$ ($0 \le x \le 25$) alloys, the NM martensite structure exists in the alloys with a relatively low In content ($x \le 10$) (Yang et al., 2016). When $10 < x \le 16$, the martensite has a modulated structure. When the content of In continues to increase, the martensite transformation is arrested (Sutou et al., 2004b).

2.2.1 Non-modulated Martensite

For the $Ni_{50}Mn_{50-x}In_x$ alloys with a relatively low In content, it can be considered as In doped NiMn alloys. Actually, the crystal structure of the martensite of the $Ni_{50}Mn_{50-x}In_x$ ($x \le 10$) alloys is indeed the same as that of the stochiometric NiMn (Yang et al., 2016), i.e., the tetragonally distorted B2 structure. Nevertheless, to keep consistency with the $L2_1$ structure of austenite, as an equivalent structural model of the distorted B2 structure, the double $L1_0$ tetragonal cell proposed by J. Pons and coworkers (Pons et al., 2000) was extensively used in the literature to describe the non-modulated structure of martensite, as shown in **Figure 3A**. The space group of the double $L1_0$ tetragonal structure is I4/mmm (group number: 139). The atomic fractional coordinates of the different constituent elements in the NiMnIn alloys are as follows: Ni: *4d* (0, 0.5, 0.25); Mn and In: *2a* (0, 0, 0) and *2b* (0, 0, 0.5). The typical X-ray diffraction pattern of the non-modulated martensite is displayed in **Figure 3B**. Note that in this figure, the reflections are indexed based on the double $L1_0$ structural model rather than the distorted B2 model.

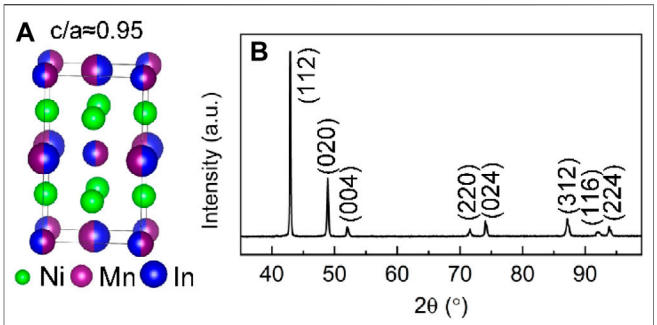

FIGURE 3 | Double $L1_0$ tetragonal structural model **(A)** and typical X-ray diffraction pattern **(B)** of the non-modulated martensite of the NiMnIn-based alloys.

2.2.2 Modulated Martensite

With the increase of In content in the $Ni_{50}Mn_{50-x}In_x$ alloys, the crystal structure of martensite no longer follows the structure of NiMn (non-modulated double $L1_0$ tetragonal structure) and exhibits a long periodic layered modulated structure (Yang et al., 2016). For the NiMnIn-based alloys, the excellent magnetoresponsive performance mainly exists in the alloy systems with a modulated structure. Therefore, the accurate determination of the crystal structure for the modulated martensite is of significant importance for understanding and optimizing magnetoresponsive behaviors. Measured by neutron diffraction and synchrotron high-energy X-ray diffraction, and analyzed using the (3+1) dimensional superspace theory in combination with the Rietveld full-profile fitting method, the crystal structure of the modulated martensite of the NiMnIn alloys was determined with the $Ni_{50}Mn_{36}In_{14}$ alloy as a model material (Yan et al., 2015), as shown in **Figure 4A**. The basic idea of superspace theory is that by increasing the dimension of space, as shown in **Figure 4B**, the aperiodic structure can be mathematically transformed into a periodic one (Van Smaalen, 1995). Then, a unit cell can be defined in a higher-dimensional space and can thus be determined by fitting the diffraction data.

The determination process in Ref. (Yan et al., 2015) is as follows: 1) Construct the average crystal structure model of modulated martensite (ignoring atomic position modulation). Based on the crystal structure of austenite, combined with the splitting characteristics of neutron diffraction peaks during the martensitic transformation, the space group, the lattice constants, and the atom occupation information of the average crystal structure of the modulated martensite were determined.

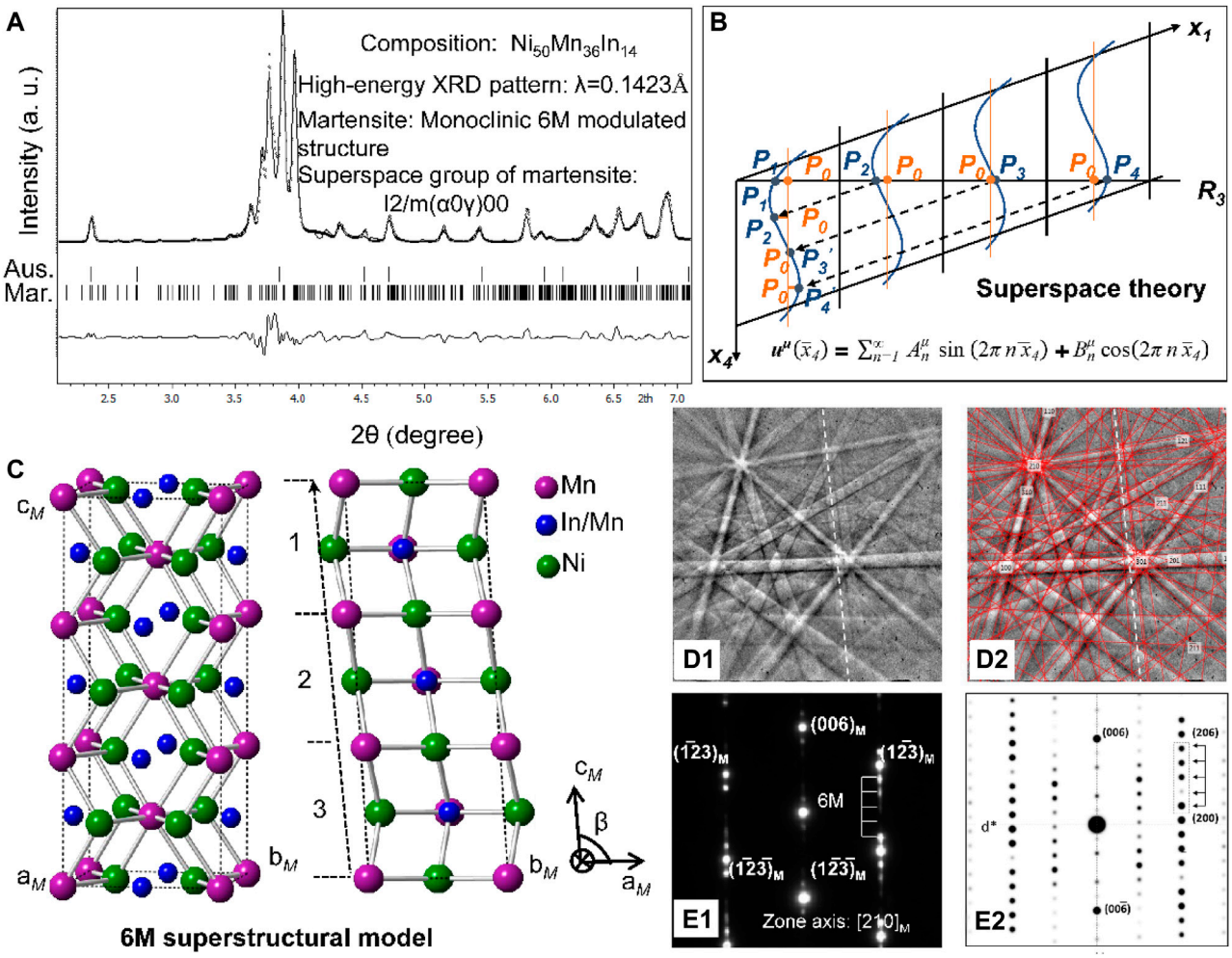

FIGURE 4 | (A) Rietveld full-profile refinement of high-energy synchrotron XRD pattern of the $Ni_{50}Mn_{36}In_{14}$ alloy by using the (3 + 1)-dimensional theory (Yan et al., 2015). **(B)** Basic idea of superspace theory, i.e., mathematically transforming the aperiodic structure to a periodic representation by increasing the dimension of space (x_4). **(C)** Established the three-dimensional 6M superstructural model with three consecutive averaging cells along the ***c*** axis. Measured **(D_1,E_1)** and simulated **(D_2,E_2)** SEM/EBSD Kikuchi and TEM selected area electron diffraction patterns (Yan et al., 2015). Reproduced with the permission of Elsevier Publisher.

2) Estimate the modulation wave vector ***q*** representing the modulation periodicity using the peak position of the satellite reflections caused by the periodic modulation of atom position. 3) Refine all structure information, including the coefficients of atom position modulation function, the lattice parameters, etc., with the high energy synchrotron X-ray diffraction pattern by means of the Rietveld method in the frame of the (3+1) dimensional superspace theory. 4) Analyze the rationality of the determined crystal structure information. 5) Build a three-dimensional superstructure model. A three-dimensional periodic superstructure model was established to approximately represent the determined modulated structure since many theoretical and experimental studies require the crystal structure information in the three-dimensional space.

Refinement showed that the modulated martensite has a monoclinic 6M modulated crystal structure and the space group is I2/m(α0γ)00, the lattice parameters of the average 1crystal structure are a = 4.3919 (4) Å, b = 5.6202 (1) Å, c = 4.3315 (7) Å, and β = 93.044 (1)°, and the modulation wave vector ***q*** = 0.343 (7) ***c**** (Yan et al., 2015). Since the coefficient of modulation wave vector ***q*** [0.343 (7)] is irrational, the structure should be incommensurate. The modulation wave vector can be described as ***q*** = 1/3(1+δ)***c**** , where δ (0.0312) represents the incommensurability. As δ is very small, the determined incommensurable 6M modulated structure can be approximately described using a superstructural model containing three average crystal structure cells along the ***c*** axis, as shown in **Figure 4C**. The space group of the established superstructural model is P2/m, and the lattice constants are a = 4.3919 (4) Å, b = 5.6202 (1) Å, c = 12.9947 (1) Å and β = 93.044 (1)°. For the detailed atomic occupation information, the readers can refer to Ref. (Yan et al., 2015). It is seen from **Figure 4C** that the shuffling character of the atomic layers is the same as that of the $(2\bar{1})_2$ Zhdanov sequence. To verify the accuracy of the established superstructure model, the EBSD Kikuchi pattern and the TEM selected area electron diffraction

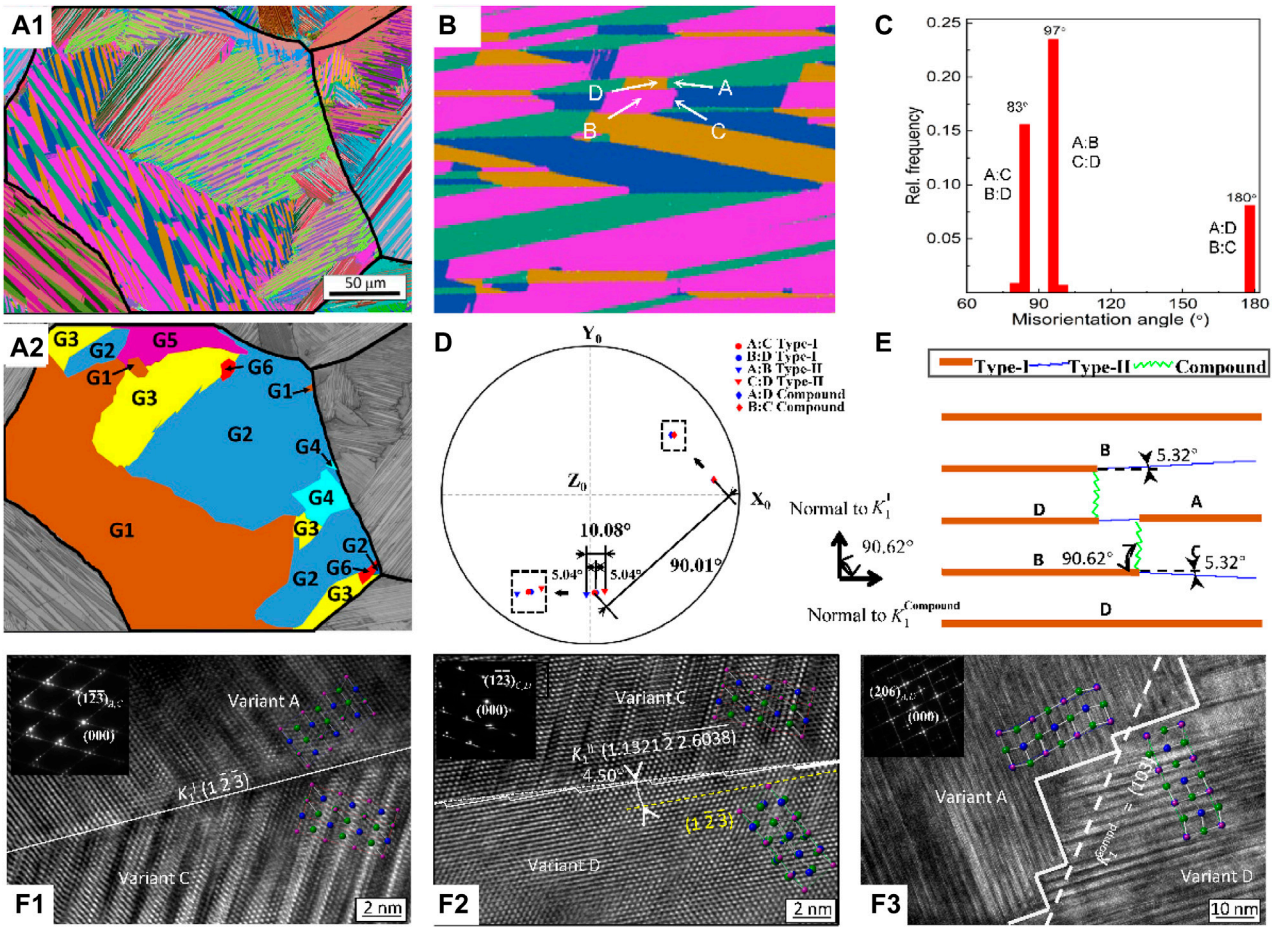

FIGURE 5 | Crystallographic orientation **(A_1)** and variant-group distribution **(A_2)** maps of the 6M modulated martensite of the NiMnIn-based alloys at room temperature measured using SEM/EBSD. The bold black line represents the initial austenite grain. **(B)** Variant organization within the martensite variant group. **(C)** Minimum misorientation angles of different variant pairs. **(D)** Stereographic projections of twinning plane K_1 of different variant pairs. **(E)** 2D illustration of variant organization. High-resolution TEM images of the type-I **(F_1)**, the type-II **(F_2)**, and the compound **(F_3)** twin interfaces (Yan et al., 2016b). Reproduced with the permission of Elsevier Publisher.

(SAED) pattern were acquired and simulated using the determined crystal structure data, as shown in **Figures 4D,E**. It can be seen that both the main and satellite reflections are accurately represented with the established superstructural model.

Recently, by means of synchrotron and neutron diffraction, using the (3+1) dimensional superspace theory, P. Devi et al. also reported that the $Ni_2Mn_{1.4}In_{0.6}$ alloy possesses a 6M incommensurate structure (Devi et al., 2018). It is worth emphasizing that the type of modulated martensite in the NiMn-based alloy is very sensitive to external stress and the sample state. Based on the TEM SAED method, 5M, 7M, and 8M modulated structures (Ito et al., 2007; Liu et al., 2008; Karaca et al., 2009; Erkartal et al., 2012; Huang et al., 2016; Paramanik and Das, 2016) were also observed in the NiMnIn-based alloys. Nevertheless, for the stress-free powder sample investigated by neutron and X-ray diffraction, so far, only the 6M modulated martensite has been evidenced in the Ni(Co)MnIn based alloys.

2.3 Perspectives

(1) The formation mechanism of modulated martensite is still unclear. For the $Ni_2Mn_{1+x}In_{1-x}$ alloy, the martensite has a non-modulated double $L1_0$ structure when the In content is low, while the structure of martensite transforms into a complex long periodic layered 6M modulated structure when the In content is high. Moreover, the NiMnGa-based alloys have 5M and 7M structures, and NiMnSn and NiMnSb alloys possess 4O structure, but only 6M structure is observed in the NiMnIn-based alloys at the stress-free state. As mentioned above, structural modulation often brings excellent magnetoresponsive properties. However, so far, the formation mechanism of modulated structure is still an open issue.

(2) The relationship between the modulated martensite and the functional properties in the NiMn-based alloy is not clear yet. The excellent magnetoresponsive performances of the NiMn-based alloys often only exist in alloys with a modulated martensite structure. However, the quantitative

TABLE 1 | Twining elements of the type-I, the type-II, and the compound twins for the 6M modulated martensite of the NiMnIn alloys (Yan et al., 2016a). K_1, K_2, η_1, η_2, s, and P represent the twinning plane, the conjugate twinning plane, the twinning direction, the conjugate twinning direction, the shear magnitude and the shear plane, respectively. $\omega/\boldsymbol{d}$ indicates the minimum misorientation angle/the corresponding rotation axis, respectively. Reproduced with permission of the International Union of Crystallography.

Twinning elements	Type-I twin A: C, B: D	Type-II twin A: B, C: D	Compound twin A: D, B: C
K_1	$\{1\bar{2}3\}_M$	$\{1.13\,\bar{2}\,\bar{2.60}\}_M$	$\{103\}_M$
K_2	$\{\bar{1}.13\,\bar{2}\,2.60\}_M$	$\{\bar{1}2\bar{3}\}_M$	$\{\bar{1}03\}_M$
η_1	$<\bar{3}.34\,\bar{3}\,0.88>_M$	$<\bar{3}3\bar{1}>_M$	$<\bar{3}01>_M$
η_2	$<3\bar{3}\bar{1}>_M$	$<3.34\,\bar{3}\,\bar{0.88}>_M$	$<301>_M$
P	$\{1\,\bar{0}.12\,3.36\}_M$	$\{1\,0.12\,3.36\}_M$	$\{010\}_M$
s	0.27	0.27	0.03
$\omega/\boldsymbol{d}$	82.40°/ $<301>_M$	97.60°/Normal of $\{103\}_M$	180°/ $<\bar{3}01>_M$

relationship between the modulated structure and the properties has yet to be established.

3 MICROSTRUCTURE OF 6M MODULATED MARTENSITE

3.1 Variant Organization

Based on the established superstructural model (**Figure 4C**), by using the SEM/EBSD technique combined with the orientation analysis method, the morphological and the crystallographic characters of the 6M modulated martensite microstructure of the NiMnIn alloys were characterized in detail (Yan et al., 2015; Yan et al., 2016b; Yan et al., 2016c; Yan et al., 2021b). Experiments showed that the 6M modulated martensite is in a plate shape and self-organized in colonies, as shown in **Figure 5A$_1$**. Within one initial austenite grain, a maximum of 6 orientation-independent variant colonies (**Figure 5A$_2$**) and a total of 24 orientation-independent variants can be generated. The formation mechanism of the microstructure will be discussed with the transformation strain path in **Section 4**. In each martensite colony, as shown in **Figure 5B**, there are four orientation variants, i.e., A, B, C, and D.

Misorientation examinations showed that the four variants within the martensite colony are twin-related. In total, there exist three types of twins, i.e., type-I (A: C and B: D), type-II (A: B and C: D), and compound (A: D and B: C) twins (Yan et al., 2016b). The twinning elements of K_1, K_2, η_1, η_2, s, and P for different types of twins, determined with the method proposed by Zhang et al. (2010), are listed in **Table 1**. It is seen that the shear magnitudes of the type-I and the type-II twins are the same (0.27), which is around one order of magnitude larger than that of the compound twin (0.03). Misorientation calculations showed that for the 6M NiMnIn modulated martensite, the theoretical angle/axis pair ($\omega/\boldsymbol{d}$) for the type-I, the type-II, and the compound twins are 82.4°/ $<301>_M$, 97.6°/normal of $\{103\}_M$ and 180°/ $<\bar{3}01>_M$ (Yan et al., 2016c), respectively, which is in good agreement with the experimental measurements (**Figure 5C**).

3.2 Twin Interface Structure

Twin boundary is a key material parameter that significantly affects both the physical and mechanical properties of materials. For the 6M modulated martensite of the NiMnIn alloys, using the indirect two-trace method (Zhang et al., 2007), the interface indices between different variants within the martensite colony are found to coincide with their twinning plane K_1 in the mesoscale (Yan et al., 2016a). Within one martensite colony, as shown in **Figure 5D**, there is only one kind of type-I (indicated by the solid circle) and compound twin (indicated by the solid diamond) boundaries. In other words, the two boundaries between the type-I twin related variants A: C and B: D (or the compound twin related variants A: D and B: C) are parallel to each other. In addition, the interface between the type-I twin related variants is almost perpendicular to the interface between the compound twin related variants. In contrast, the two boundaries between the type-II twin related variants (indicated by the inverted triangle), i.e., the interfaces between A: B and C: D, are separated. It is seen from **Figure 5D** that the two kinds of type-II twin interfaces are distributed on the two sides of the type-I twin interfaces with an angle of around 5°. The orientation characters of various interfaces within one martensite colony are illustrated in **Figure 5E**.

High-resolution TEM characterization showed that at the atomic scale, the type-I twin interface possesses a straight boundary, whereas the type-II twin boundary has a "stepped" interface (Yan, et al., 2016a). This difference leads to much smaller detwinning stress of the type-II twin with respect to that of the type-I twin, although the shear magnitudes of these two twins are exactly the same. For the compound twin, even though its twinning plane is rational, i.e., $\{103\}_M$, it also has a "stepped" interface at the atomic scale. Compared with the type-II twin, the step of the compound twin is much larger and shows an irregular distribution feature. The irregularly stepped interface structure and the small shear of the compound twin account for its high mobility (Yan et al., 2016a).

3.3 Perspectives

The reason for the difference in detwining stress of different twin systems is still unclear. For the modulated martensite, there are huge differences in the detwining stresses for type-I, type-II, and compound twin systems. At present, we can only speculate that this phenomenon is related to the magnitude of the shear and the structure of the interface. However, the underlying physical mechanism still needs to be explored.

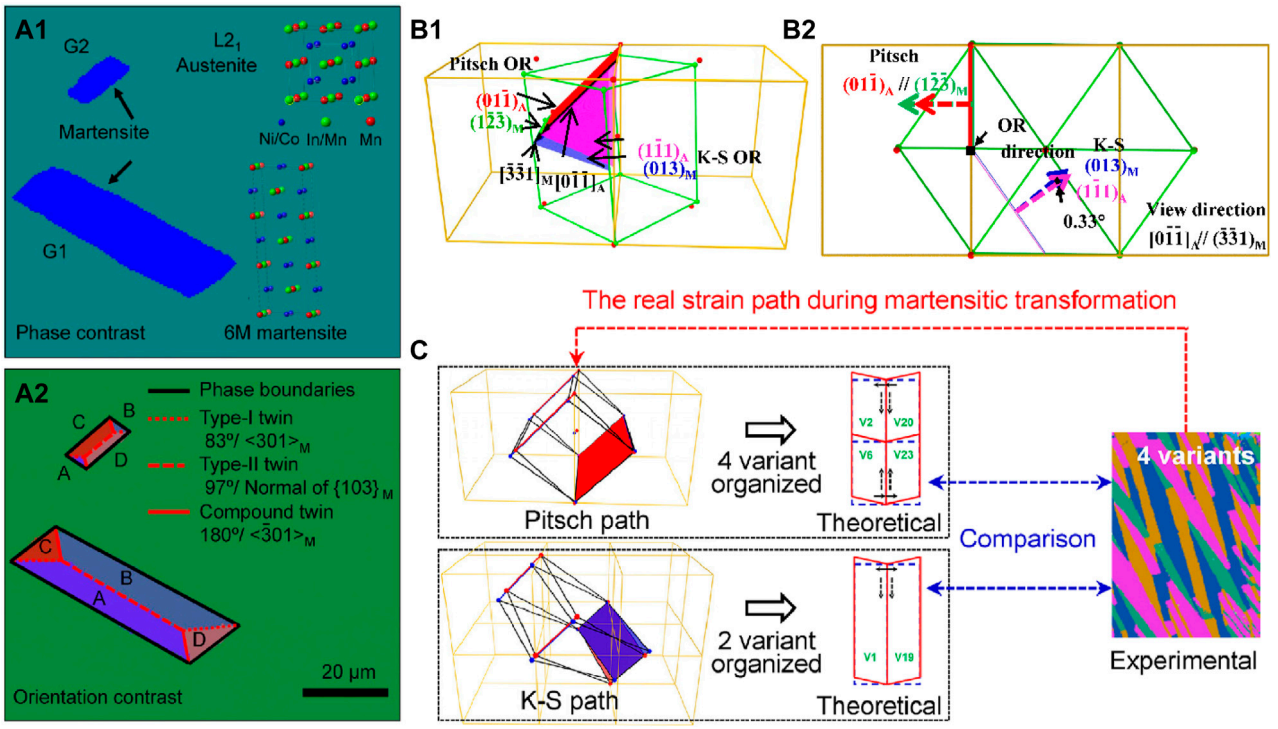

FIGURE 6 | Phase contrast **(A_1)** and crystallographic orientation **(A_2)** maps of the dual-phase $Ni_{45}Co_5Mn_{36.8}In_{13.2}$ alloy measured by using the SEM/EBSD technique at room temperature. **(B_1)** Geometrical relation between the K-S and the Pitsch orientation relationships (ORs). **(B_2)** is the projection of (B_1) along the OR direction. **(C)** Basic idea of determining transformation strain path based on the variant organization of martensite variants. Reproduced with the permission of Elsevier Publisher.

4 CRYSTALLOGRAPHY OF MARTENSITIC TRANSFORMATION

The magnetoresponsive behaviors of the NiMnIn-based alloys are closely related to the magnetic field-induced inverse martensitic transformation. It is thus greatly meaningful to clarify the crystallographic characteristics of martensitic transformation, including transformation orientation relationship (OR), transformation strain path, etc., to understand the formation mechanism of microstructure and magnetoresponsive behaviors.

4.1 Transformation Orientation Relationship

Transformation OR describes the geometrical relation between the crystal lattices of austenite and martensite. Generally, the transformation OR is represented by plane and in-plane direction correspondences, i.e., $\{hkl\}_A//\{hkl\}_M$ and $<uvw>_A//<uvw>_M$ where the subscript "A" and "M" represent austenite and martensite, respectively. By composition design, a dual-phase $Ni_{45}Co_5Mn_{36.8}In_{13.2}$ alloy at room temperature was fabricated, and the accurate crystallographic orientations of the two coexisting phases were measured by using the SEM/EBSD technique (Yan et al., 2021a), as shown in **Figure 6A**. With the orientation information of the co-existing austenite and martensite, the reported ORs in the literature, including the Bain (Bain and Dunkirk, 1924), the Nishiyama-Wassermann (N-W) (Nishiyama, 1934), the Kurdjumov-Sachs (K-S) (Kurfib and Schultz, 1930), and the Pitsch (Pitsch, 1962) ORs were examined one by one. Results showed that the deviations of the measured misorientation between austenite and martensite Δg^{exp} from the theoretical Δg^{OR} of the Bain, the N-W, the K-S, and the Pitsch ORs are 3.73°, 1.27°, 0.70°, and 0.63° (Yan et al., 2021a), respectively.

For the Bain and the N-W ORs, the deviation angles are the largest (>1°), and thus these two ORs can be excluded. In contrast, for both the K-S and the Pitsch OR, the deviation angles are both the smallest and are close to the angular resolution of current EBSD technology (±0.5°). Thus, it is difficult to discriminate which is the valid OR or to determine that both are valid. It is worth emphasizing that such a dual OR occasion is not a unique occurrence in the studied $Ni_{45}Co_5Mn_{36.8}In_{13.2}$ alloy nor in the NiMnIn-based alloys. This dual-OR phenomenon widely exists in many other NiMn-based ferromagnetic shape memory alloys with modulated martensite, such as $Ni_{50}Mn_{30}Ga_{20}$ (Li Z. B. et al., 2011) with 7M modulated martensite, $Ni_{50}Mn_{28}Ga_{22}$ (Li Z. et al., 2011) with 5M modulated martensite and $Ni_{50}Mn_{38}Sb_{12}$ (Zhang et al., 2016) alloy with 4O modulated martensite.

In order to reveal the difference between the K-S and the Pitsch OR in the NiMnIn-based alloys, the correspondent crystalline planes and crystalline directions of these two ORs are outlined in the austenite (orange) and the martensite (green) lattices that strictly obey the Pitsch OR, as shown in **Figure 6B$_1$**. It

is seen that the OR directions of the K-S and the Pitsch relations are exactly the same. The difference between these two ORs lies in the OR planes. For the K-S relation, the OR plane pair is $\{111\}_A//\{013\}_{6M}$, while the OR plane pair of Pitsch relation is $\{101\}_A//\{1\overline{2}3\}$. **Figure 6B$_2$** is a projection of **Figure 6B$_1$** along the OR direction (the black arrow), i.e., $[0\overline{1}1]_A$. The normal of the OR plane in **Figure 6B$_2$** is indicated by the dotted line. It is seen from **Figure 6B$_2$** that when the Pitsch OR is strictly satisfied, for the K-S relation, the deviation between the OR planes of austenite and martensite is just 0.33° away. From the point of view of geometry, this is the difference between the K-S and the Pitsch OR. The reason that the K-S and the Pitsch OR are almost simultaneously satisfied could be related to the special lattice parameters of austenite and martensite in the NiMn-based alloys. The underlying physical mechanism still needs to be further studied.

4.2 Transformation Strain Path

By definition, the transformation OR of martensitic transformation describes the geometric relation between the crystal lattices of austenite and martensite. Nevertheless, considering that the martensitic transformation involves a shear process and the atomic displacement during this process is far less than one atomic spacing, the OR plane $\{hkl\}_A$ and OR direction vector $[uvw]_A$ of austenite should not rotate (distortion is allowed) during the lattice distortion of phase transformation. Thus, OR can be used to describe the transformation strain path of martensitic transformation, that is, the OR plane $\{hkl\}_A$ of austenite shears along the OR direction $<uvw>_A$. It is worth emphasizing that the OR plane of austenite $\{hkl\}_A$ is not the so-called habit plane since both rotation and distortion are not allowed for the habit plane, but only rotation is forbidden for the OR plane. During the lattice distortion of martensitic transformation, the OR plane {hkl} and the OR direction <uvw> can be distorted to realize the change of crystal structure.

Normally, the transformation strain path can be easily obtained from the transformation OR. However, for the NiMnIn-based alloys, both the K-S and the Pitsch ORs can be approximately satisfied. Thus, the commonly utilized method to determine the transformation strain path through the relevant orientation relationship is no longer applicable. For the NiMnIn-based alloys, from the viewpoint of transformation OR, the conclusion that can be drawn is that the two transformation strain paths, i.e., the K-S type $\{1\ \overline{1}\ 1\}_A<0\ \overline{1}1>$ and the Pitsch type $\{01\ \overline{1}\}_A<0\ \overline{1}1>$ (**Figure 6C**) may occur. Previous studies showed that the martensitic transformation occurs at the speed of sound (Bunshah and Mehl, 1953; Mukherjee, 1968), so the direct determination of the transformation strain path is difficult even by using modern physical characterization techniques.

Usually, the resultant behaviors of phase transition are greatly affected by the transformation process. Thus, one can assume that the microstructure characters of martensite produced by different transformation strain paths are likely to be different. Based on this assumption, a strategy of determining the transformation strain path was proposed, i.e., deducing the transformation strain path according to the microstructural features of martensite (Yan et al., 2021b). With this strategy, the transformation strain path of NiMnIn alloy was determined successfully. To satisfy the criterion of the minimum interface and elastic strain energies, combined with the stress and the strain compatibility conditions, theoretically, the K–S path produces two variants as a self-accommodated variant group, whereas the Pitsch path produces four variants as a self-accommodated variant group, as shown in **Figure 6C**. The details are referred to Ref. (Yan et al., 2021a). For the NiMnIn-based alloy, as shown in **Figure 5B** and **Figure 6A**, the self-accommodated variant group is composed of 4 orientation variants. Thus, the Pitsch strain path, $\{01\ \overline{1}\}_A<0\ \overline{1}1>_A$, was evidenced to be the real one that governs the lattice distortion during martensitic transformation.

Moreover, it is found that the 4 self-accommodated martensite variants within the variant group are transformed on the same transformation plane $\{01\ \overline{1}\}_A$ (Yan et al., 2021b). For example, all 4 self-accommodated martensitic variants A, B, C, and D in **Figure 6A$_2$** are transformed mainly by shear deformations on the same $(10\ \overline{1})_A$ plane. The transformation strain paths for these 4 variants lies just by permutating the signs (positive or negative) of the transformation plane and direction. For instance, the specific transformation strain paths for A, B, C, and D are $(10\ \overline{1})_A[101]_A$, $(\overline{1}\ 01)_A[101]_A$, $(10\ \overline{1})_A[\overline{1}\ 0\ \overline{1}]_A$, and $(\overline{1}\ 01)_A[\overline{1}\ 0\ \overline{1}]_A$, respectively. During the martensitic transformation process, the 4 self-accommodated variants gradually grow and develop into a martensite variant group. For cubic structure, owing to the crystal symmetry, there are 6 equivalent Pitsch-type transformation planes $\{01\ \overline{1}\}_A$, i.e., $(01\ \overline{1})_A$, $(011)_A$, $(10\ \overline{1})_A$, $(101)_A$, $(1\ \overline{1}0)_A$, and $(110)_A$. Therefore, theoretically, an austenite grain can form a maximum of 6 independent variant groups and in total 24 orientation-independent variants. This result is consistent with the experimental observation (**Figure 5A**) and explains well the formation mechanism of the self-accommodated microstructure of 6M modulated martensite of the NiMnIn alloys.

4.3 Perspectives

The underlying physical mechanism why the K-S and the Pitsch transformation orientation relations are almost simultaneously satisfied in the NiMn-based alloys is still unclear. The shuffling path of the different $(001)_M$ atomic layers during the martensitic transformation is still unclear. The Pitsch-type transformation strain path can only reveal the shear mode of the average lattice of modulated martensite. However, in addition to the Pitsch-type lattice distortion, the shuffling of the $(001)_M$ atomic layer is also needed to form the modulated martensite. The physical mechanism of this process is still unclear.

5 MAGNETIC SHAPE MEMORY EFFECT

NiMnIn-based alloys can achieve the shape memory effect *via* the magnetic-field-induced inverse martensitic transformation from the weak-magnetic martensite to the ferromagnetic austenite, which is called the magnetic shape memory effect (MSME). The mechanism of MSME of the NiMnIn-based alloys is illustrated in **Figure 7**. When the pre-deformed martensite of a NiMnIn alloy is exposed in a magnetic field, at the condition that the driving force

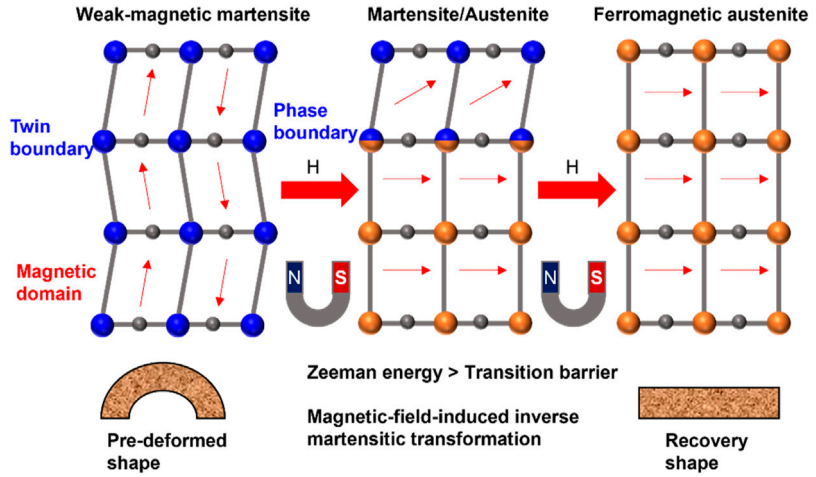

FIGURE 7 | Schematic diagram of magnetic shape memory effect (MSME) from the weak-magnetic martensite to the strong-magnetic austenite.

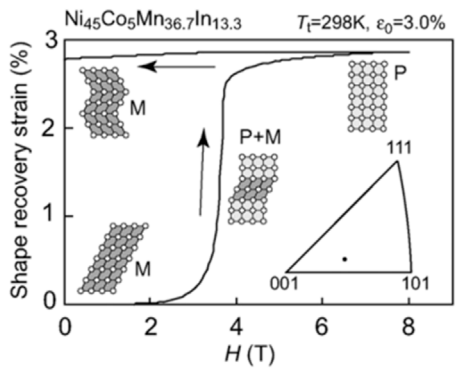

FIGURE 8 | Magnetic shape memory effect (MSME) in the single-crystalline $Ni_{45}Co_5Mn_{36.7}In_{13.3}$ alloy measured at room temperature (Kainuma et al., 2008). Reproduced with the permission of Royal Society of Chemistry Publisher.

for the inverse martensitic transformation (the Zeeman energy difference, $\mu_0 H\Delta M$) exceeds the energy barrier of structural transition, the new phase of austenite nucleates and grows, and thus resulting in the shape recovery (Karaca et al., 2007). Compared with the conventional thermally-induced SME that is limited by the low heat conduction rate, the MSME of the NiMnIn-based alloys shows the advantages of fast response, easy control, and high stability. Moreover, different from NiMnGa in which the magnetic output work (magneto-stress) is limited by the magnetocrystalline anisotropy energy (Karaca et al., 2006; Karaca et al., 2007), the magneto-stress of the NiMnIn-based alloys continuously increases with the strength of magnetic field as there is no limit for the Zeeman Energy (Karaca et al., 2009; Turabi et al., 2016).

In 2006, for the first time, R. Kainuma et al. reported the MSME in a Co-doped $Ni_{45}Co_5Mn_{36.7}In_{13.3}$ single-crystalline sample (Kainuma et al., 2006). They observed that a pre-strain of 3% can almost be recovered by the magnetic field-induced inverse martensitic transformation in the $Ni_{45}Co_5Mn_{36.7}In_{13.3}$ single-crystalline sample, as shown in **Figure 8**. Based on the Clausius–Clapeyron relation, the output magneto-stress generated during the transformation was estimated to be about 108 MPa under a magnetic field of 7 T (Kainuma et al., 2006), which is about 50 times larger than that of NiMnGa (2 MPa) (Murray et al., 2000). Later, under a pulsed magnetic field of 70 kOe, a 3% recoverable strain was obtained in the $Ni_{45}Co_5Mn_{36.7}In_{13.3}$ single-crystalline sample at room temperature (Sakon et al., 2007). Since then, the MSME of the NiMnIn-based alloys has attracted more and more attention.

For the MSME, in view of practical applications, a large magnetic-field-induced strain (MFIS) is desirable (Jiang et al., 2013; Barua et al., 2018). For the NiMnIn-based alloys, owing to the high energy barrier, the magnitude of MFIS is closely associated with the transformed volume under an external magnetic field, which is greatly affected by the sensitivity of transformation temperature to the magnetic field, i.e., $\Delta T/\Delta H$. Normally, under a given magnetic field, a large $\Delta T/\Delta H$ tends to increase the transformed volume and thus the magnitude of the MFIS. Besides, a large $\Delta T/\Delta H$ can expand the operating temperature window of the MSME. Based on the Clausius–Clapeyron relation (**Eq. 1**),

$$\frac{\Delta T}{\Delta H} = \frac{\Delta M}{\Delta S} \tag{1}$$

where ΔM and ΔS represent the magnetization difference and the entropy change during the martensitic transformation, respectively, it is clear that a large ΔM value is favorable to promote a high magnetic-field sensitivity of transformation temperature ($\Delta T/\Delta H$). So far, for the NiMnIn-based alloys, the most successful strategy of increasing ΔM is the partial substitution of Co for Ni. Thus, the MSME of the Co-doped NiCoMnIn alloys has been intensively studied (Karaca et al., 2009; Monroe et al., 2012; Turabi et al., 2016; Bruno et al., 2017).

5.1 NiCoMnIn

Like the conventional shape memory alloy, for the single crystal sample, since the counteraction of transformation strains generated by different austenite grains with distinct orientations is avoided, the transformation strain is much larger than that of the polycrystalline sample. Thus, studies on the MFIS in the NiMnIn-based alloys were first focused on single crystals. Under a magnetic field of 18 T and bias stress of 125 MPa, J.A. Monroe and cooperators observed a fully recoverable transformation strain of 3.1% in the <100> oriented $Ni_{45}Co_5Mn_{36.5}In_{13.5}$ single crystal (Monroe et al., 2012). For this sample, an output work of 1 MJ m^{-3} T^{-1} (Karaca et al., 2009) and a magneto-stress of 71 MPa at a magnetic field of 9 T (Turabi et al., 2016) were obtained. Both of them are one order of magnitude higher than those in NiMnGa. The theoretical magneto-stress along [100], [123], [011], and [111] were 26.5, 42.2, 50.4, 143.4 MPa T^{-1}, respectively, which are much larger than the corresponding values in NiMnGa (2–5 MPa T^{-1}). Along the [111] direction, a transformation strain of ~1.2% was observed. N. M. Bruno et al. found that the magneto-mechanical training can significantly reduce the critical magnetic field required for the inverse martensitic transformation from 8.3 T to 1.3 T in the single-crystalline $Ni_{45}Co_5Mn_{36.6}In_{13.4}$ alloy (Bruno et al., 2017). After the magneto-mechanical training, under a magnetic field of 3 T, an MFIS of 5.6% was obtained.

Apart from single crystals, owing to the simple preparation process and the low cost, the MSME of the NiMnIn-based polycrystalline alloys were also studied (Krenke et al., 2007; Liu et al., 2009a; Sharma et al., 2010a; Li et al., 2010; Acet et al., 2011; Yu et al., 2014; Yu et al., 2016), although the magnitude of the MFIS of polycrystalline sample is generally smaller than those of single crystals. In 2007, by using *in-situ* X-ray diffraction technology, Y. D. Wang et al. evidenced the occurrence of magnetic-field-induced reversible martensitic transformation in the $Ni_{45}Co_5Mn_{36.6}In_{13.4}$ polycrystalline sample under a uniaxial compressive stress of 50 MPa and a magnetic field of 5 T (Wang et al., 2007). In 2009, J. Liu et al. studied the MFIS of the textured $Ni_{45.2}Mn_{36.7}In_{13}Co_{5.1}$ polycrystalline sample during two magnetic-field cycles at 310 K (Liu et al., 2009b). They found that magnetic training was able to enhance the magnitude of magnetostrain from 0.2% (the first magnetic cycle) to 0.25% (the second magnetic cycle). After the magnetic training, the critical magnetic field of transformation is reduced from 1.6 T to 1.2 T. In 2010, Z. Li et al. found that the non-prestrained $Ni_{45}Co_5Mn_{37}In_{13}$ polycrystalline alloy possesses a reversible MFIS of 0.4% and exhibits a large two-way MSME without applying a pre-strain (Li et al., 2010). Moreover, the two-way MSME was still reproducible even after three magnetic-field cycles at 320 K.

5.2 Other NiMnIn-Based Alloys

Apart from the Co-doped NiCoMnIn, the MSME of undoped (Krenke et al., 2007), Cu-doped (Sharma et al., 2010b), Sb-doped (Yu et al., 2014), and Ga-doped (Yu et al., 2016) NiMnIn-based polycrystalline samples were also studied. In 2007, T. Krenke and collaborators obtained an MFIS of 0.12% under a magnetic field of 5 T in the ternary $Ni_{50}Mn_{34}In_{16}$ polycrystalline sample (Krenke et al., 2007). Later, S. Y. Yu et al. found that the transformation strain increases rapidly with the doping by Sb (Yu et al., 2014). Under a magnetic field of 10 T, an MFIS of 1.7% was obtained in the non-prestrained $Ni_{50}Mn_{36}In_8Sb_6$ alloy (Yu et al., 2014). Unfortunately, the critical magnetic field in this alloy is as large as ~ 6 T, and there is almost no shape recovery after removing the magnetic field. Besides, by using the directional solidification technique, S. Y. Yu et al. obtained an MFIS of −0.28% along (and 0.49% perpendicular to) the solidification direction in the polycrystalline $Ni_{50}Mn_{33}In_{13}Ga_4$ alloy (Yu et al., 2016).

5.3 Perspectives

For the NiMnIn-based alloys, both the single-crystal and the polycrystalline samples have excellent MSME, which makes this compound a potential candidate for smart sensors and actuators. However, in view of commercial application, there are still some thorny problems that need to be solved:

High critical magnetic field required to drive reversible transformation. Usually, the critical magnetic field required to drive a completely reversible transformation in the NiMnIn-based alloys is as large as ~ 3 T (Kainuma et al., 2006; Li et al., 2010; Huang et al., 2021), which greatly limits the application range of this compound. For instance, the critical magnetic fields for the inverse martensitic transformation in the $Ni_{45}Co_5Mn_{37}In_{13}$ alloy at 320 K and 310 K are as large as 5 T and 7 T, respectively (Li et al., 2010).

Large thermal hysteresis ΔT_{hys} and transition interval ΔT_{int} during martensitic transformation. The large thermal hysteresis ΔT_{hys} and transition interval ΔT_{int} may lead to the retain of partial austenite after removing the magnetic field and ultimately reduce the transformed volume fraction. For instance, due to the existence of thermal hysteresis, the value of MFIS in the $Ni_{50}Mn_{36}In_8Sb_6$ alloy becomes irreversible after removing the magnetic field (Yu et al., 2014).

Based on the previous studies, for the NiMnIn-based alloys, the critical magnetic field, thermal hysteresis, and transition interval could be optimized in the following ways:

a) External field training to reduce the critical magnetic field. The external field training methods, such as mechanical, magnetic, and thermo-mechanical training, can reduce the number of martensite variants. After that, the number of unfavorable variants is reduced by the process of detwinning (Yan et al., 2016a), and thus the critical magnetic field driving the inverse martensitic transformation can be reduced.
b) Applying mechanical or thermal field to reduce thermal hysteresis and critical magnetic field. Generally speaking, for the NiMnIn-based alloys, the mechanical field stabilizes the martensite, and the thermal field stabilizes the austenite. Applying the mechanical or the thermal field reasonably to assist transformation can reduce the thermal hysteresis and the critical magnetic field of MSME.
c) Increasing geometrical compatibility between austenite and martensite to reduce thermal hysteresis. Adjusting the lattice parameters of austenite and martensite by tailoring the

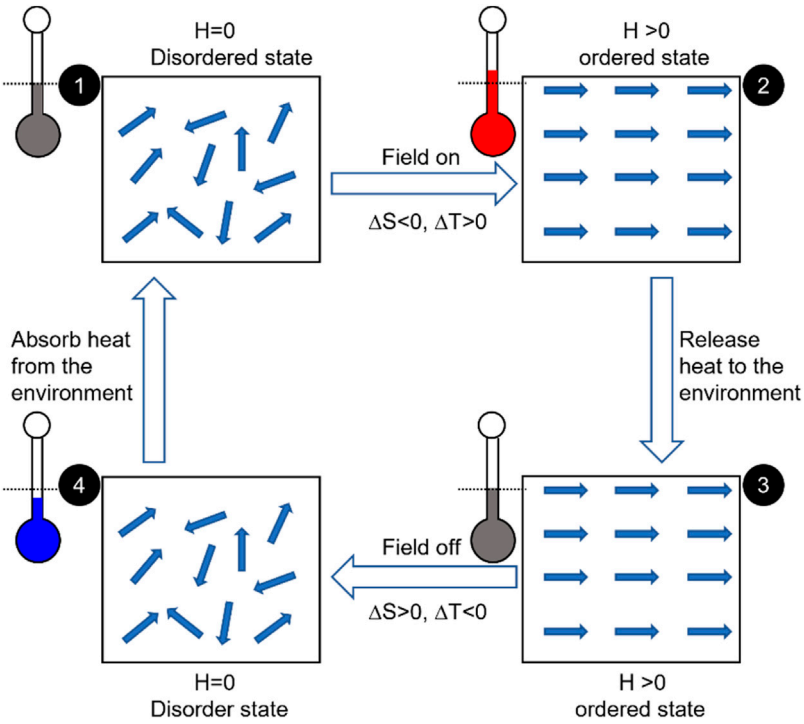

FIGURE 9 | Schematic diagram of magnetocaloric effect for the conventional materials.

chemical composition to increase the geometric compatibility between austenite and martensite can reduce the thermal hysteresis.

d) Tailoring microstructural features to control thermal hysteresis. The microstructure characteristics, including grain boundary, point defect, and phase constituent, play important roles in the nucleation and growth of martensite. Thus, the hysteresis can also be tuned by microstructure modification.

Reasonably utilizing the above-mentioned strategies, it is possible to significantly improve the MSME of the NiMnIn-based alloys and thus promote the practical application of this compound in the field of smart sensors and actuators.

6 MAGNETOCALORIC EFFECT

The magnetocaloric effect (MCE) refers to the temperature change ΔT of a material when exposed to an external magnetic field (Wiedemann, 1889; Moya et al., 2014). Nowadays, the magnetocaloric refrigeration technique has been successfully applied in the low and extremely low-temperature refrigeration fields, such as physical property measurement, superconducting environment, and cryogenic physics, and shows the potential of entering the conventional room-temperature refrigeration market (Yu et al., 2010; Kitanovski and Egolf, 2009), such as conditioner, refrigerator, and food freezer. Generally, the MCE is characterized by the isothermal magnetic entropy change ΔS_M or the adiabatic temperature change ΔT_{ad}. The mechanism of MCE in the conventional materials is shown in **Figure 9**. When a magnetic material is exposed to a magnetic field, the magnetic moment tends to be parallel to the direction of the applied magnetic field, resulting in a decrease in magnetic entropy and thus a rise in temperature. By heat exchange, the heat of the MCE material releases into the environment. When the magnetic field is removed, the magnetic moments of magnetic atoms tend to be disordered again due to the thermal vibration, resulting in an increase in magnetic entropy and a decrease in temperature. In 1933, by using the thermal-magnetic cycle illustrated in **Figure 9**, W. F. Giauque and D. P. Macdougall successfully realized an ultra-low temperature of 0.25 K by using the paramagnetic salt $Gd_2(SO_4)_3{\cdot}8H_2O$ (Giauque and Macdougall, 1933). Subsequently, a variety of excellent low-temperature magnetic refrigerants have been discovered, such as $Gd_2(SO_4)_3{\cdot}8H_2O$ (Giauque and Macdougall, 1933), GGG ($Gd_3Ga_5O_{12}$) (McMichael et al., 1993), and RAl_2 (R = Er, Ho, Dy, $Dy_{0.5}Ho_{0.5}$, Dy_xEr_{1-x}, Gd and Pd) (Hashimoto et al., 1987). After the development of the low-temperature magnetic refrigerants for half a century, in 1976, G. V. Brown observed a room-temperature MCE effect in Gd (Brown, 1976). At this time, both the low-temperature and the room-temperature MCE effects were realized at around the temperature of the second-order Cuire magnetic transition.

A breakthrough came in 1997. In this year, V. K. Pecharsky and K. A. Gschneidner et al. reported a first-order phase transition related room-temperature magnetocaloric material

$Gd_5Si_2Ge_2$ (Pecharsky and Gschneidner, 1997). In this material, a giant ΔS_M of about 18 J kg^{-1} K^{-1} under a magnetic field of 5 T was obtained at 280 K, which is about twice larger than that of Gd. Further investigations showed that this large ΔS_M comes from the magnetic-field-induced transformation from the paramagnetic monoclinic phase to the ferromagnetic orthorhombic phase. From then on, the magnetocaloric materials associated with the first-order phase transition attracted great attention based on this work.

For the NiMnIn-based alloys, as mentioned above, the martensitic transformation is accompanied by significant changes in magnetism, which is similar to the case of $Gd_5Si_2Ge_2$ (Pecharsky and Gschneidner, 1997). Thus, since the discovery of NiMnIn alloy, the magnetocaloric effect of this compound has attracted increasing attention. By the Maxwell relation, R. Kainuma et al. found that the $Ni_{45}Co_5Mn_{36.7}In_{13.3}$ single-crystal exhibits a large ΔS_M of 28.4 J kg^{-1} K^{-1} at 292 K under a magnetic field of 7 T (Kainuma et al., 2006). This value of ΔS_M is comparable to the famous room-temperature rare-earth-based MCE refrigerant, such as $Gd_5Si_2Ge_2$, MnAsSb, and La(Fe, Si)13. Besides, since the critical temperature of first-order martensitic transformation can be easily tailored by composition modification, the NiMnIn-based alloy has adjustable refrigeration working temperature, as well as relatively low cost, compared with the second-order Cuire transition associated rare-earth-based MCE materials, such as Gd, RAl_2 (R = Er, Ho, Dy, $Dy_{0.5}Ho_{0.5}$, Dy_xEr_{1-x}, Gd and Pd), RE-TM (RE = Nd, Ho, Er, and Tm; TM = Zn and Ga) and RETMX (RE = Tb, Dy, Ho, and Er; TM = Fe, Co, and Pt; X = Al, Mg, and C) (Luo and Wang, 2009; Nirmala et al., 2015; Li and Yan, 2020). Moreover, different from the conventional MCE refrigerants in which the temperature is increased upon the application of magnetic field, the temperature of the NiMnIn-based alloys is decreased when a magnetic field is applied. For the NiMnIn-based alloys, when a magnetic field is applied, the heat absorbed from the structural transition from the low-entropy martensite phase to high-entropy austenite is larger than the heat released from the alignment of magnetic moments during the process of the inverse martensitic transformation. Therefore, the temperature of the sample decreases during the process of the magnetic-field induced inverse martensitic transformation. Clearly, the MCE in the NiMnIn-based alloys is different from the above-mentioned conventional magnetocaloric effect, which thus is termed as the inverse magnetocaloric effect (Tegus et al., 2002; Krenke et al., 2005).

For the MCE refrigerant, the following requirements should be satisfied: 1) the value of isothermal magnetic entropy change ΔS_M (or adiabatic temperature change ΔT_{ad}) should be as large as possible as it directly decides the refrigeration efficiency; 2) the transition thermal hysteresis ΔT_{hys} accompanied with the magnetostructural transformation should be as small as possible since the existence of large thermal hysteresis will greatly reduce the cooling efficiency and may further cause the functional fatigue after several cycles; 3) the refrigeration temperature window δT_{FWHM} should be as wide as possible. Aimed at improving the above-mentioned three parameters, the MCE of the NiMnIn-based alloys has been extensively studied during the past 15 years. Next, the main progress related to the improvement of ΔS_M (or ΔT_{ad}), ΔT_{hys}, and δT_{FWHM} in the NiMnIn-based alloys will be briefly reviewed.

6.1 Isothermal magnetic Entropy Change

As mentioned above, the isothermal magnetic entropy change ΔS_M (or adiabatic temperature change ΔT_{ad}) is the key parameter to decide the refrigeration capacity for the MCE refrigerants. Thus, to improve ΔS_M or ΔT_{ad}, several strategies, including increasing transformed volume fraction *via* enlarging the driving force of magnetic-field-induced inverse martensitic transformation, reducing the negative contribution of magnetic entropy change ΔS_{mag} to transformation entropy change ΔS_{tr} and exploiting multicaloric effect, have been proposed.

a) Increasing transformed volume fraction *via* increasing the driving force of magnetic-field-induced inverse martensitic transformation. For the NiMnIn-based alloys, one of the critical issues is the high magnetic field requirement to induce a completely inverse martensitic transformation. This results in a limited volume of inverse martensitic transformation under a relatively low magnetic field. In this case, the corresponding MCE performance is significantly reduced compared with that of a complete transformation. This is why the reported MCEs of the NiMnIn-based alloys in the literature were mostly measured with high magnetic field strength, usually 5T (Liu et al., 2009b; Wang et al., 2020; Yang et al., 2020; Bai et al., 2021). It is known that the maximum magnetic field produced by the ordinary permanent magnets is around 2T. This value is much lower than the magnetic field required to induce a complete inverse martensitic transformation in the NiMnIn alloys. Thus, increasing transformed volume under a relatively low magnetic field should be the most efficient method to increase the MCE refrigeration efficiency.

For the NiMnIn-based alloys, the driving force of magnetic-field induced inverse martensitic transformation comes from the giant magnetization difference between austenite and martensite, i.e., Zeeman energy, $\mu_0 H\Delta M$. Thus, under a constant magnetic field, increasing the magnetization difference between austenite and martensite ΔM can greatly elevate the Zeeman energy and thus increase the transformed volume. For the NiMnIn-based alloys, the magnetization of martensite is very small, and thus ΔM is mainly decided by the magnetization of austenite. Therefore, the most effective method to increase ΔM is to enhance the magnetism of austenite.

So far, the most successful method of enhancing the magnetism of austenite in the NiMnIn alloys is the partial substitution of Co for Ni (Kainuma et al., 2006; Liu Z. H. et al., 2009; Pathak et al., 2010; Guillou et al., 2012; Li et al., 2018; Wang et al., 2020; Yang et al., 2020; Bai et al., 2021). In the Co-doped $Ni_{45.2}Mn_{36.7}In_{13}Co_{5.1}$ alloy, J. Liu et al. realized a ΔT_{ad} of −6.2 K under a relatively low magnetic field of 1.9 T at 317 K (Liu et al., 2012). Besides, by using a pulsed magnetic field of 15 T, T. Kihara and collaborators realized a giant ΔT_{ad} of −12.8 K in the $Ni_{45}Co_5Mn_{36.7}In_{13.3}$ alloy (Kihara et al., 2014). Apart from the

doping with Co, Z. H. Liu et al. reported that the addition of Sb can also enhance the ferromagnetism of austenite, thus improving $\Delta T/\Delta H$ (Liu et al., 2009b). In the $Ni_{48.3}Mn_{36.1}In_{10.1}Sb_{5.5}$ alloy, an ΔS_M of 21 J kg^{-1} K^{-1} was obtained at a magnetic field of 5 T (Liu et al., 2009a). Different from the strategy of increasing magnetism of austenite, V. Sánchez-Alarcos reported that the magnetization of martensite can be reduced with the addition of Ti, which further results in an enhancement of MCE (Sánchez-Alarcos et al., 2015).

b) Reducing the negative contribution of magnetic entropy change during the magnetostructural transition. For the MCE associated with the first-order phase transition, the upper-limit of the isothermal magnetic entropy change ΔS_M is the transformation entropy change ΔS_{tr} during phase transition. Thus, a large ΔS_{tr} is a prerequisite to realizing a significant MCE performance. Theoretically, the transformation entropy change ΔS_{tr} comes from three contributions, i.e., the lattice vibration entropy change ΔS_{vib}, the magnetic entropy change ΔS_{mag} and the electronic entropy change ΔS_{elec} (Recarte et al., 2010; Recarte et al., 2012; Wang et al., 2017). For the NiMnIn-based alloys, during the process of magnetic-field induced inverse martensitic transformation from low-entropy martensite to high-entropy austenite, the lattice vibration entropy change ΔS_{vib} is increased. This term makes the highest contribution to ΔS_{tr}. Nevertheless, since the austenite has a highly ordered magnetic structure while martensite has a disordered magnetic structure, ΔS_{mag} is decreased during the process of magnetic-field induced inverse martensitic transformation. Clearly, the sign of ΔS_{mag} is opposite to ΔS_{vib} and ΔS_{tr}. Thus, in the NiMnIn-based alloy, ΔS_{mag} plays a negative contribution to ΔS_{tr}. For the contribution of electronic structure change on ΔS_{tr}, since both austenite and martensite exhibit the conductivity of metal in the reported NiMnIn alloys, ΔS_{elec} usually makes a negligible contribution to ΔS_{tr}. For example, ΔS_{tr} of the $Ni_{45}Co_5Mn_{36.5}In_{13.5}$ alloy was determined to be ~23 J kg^{-1} K^{-1}, where ΔS_{vib}, ΔS_{mag}, and ΔS_{elec} were about 51, −29, and 1.2 J kg^{-1} K^{-1}, respectively (Kihara et al., 2014). From the above analyses, under the condition of constant ΔS_{vib}, decreasing the negative contribution of ΔS_{mag} should be the most effective method to improve ΔS_{tr} and then ΔS_M (or ΔT_{ad}).

Intuitively, the most direct way to decrease the negative contribution of ΔS_{mag} is to reduce the magnetization difference between austenite and martensite ΔM. However, as discussed in the first half of this section, a remarkable ΔM, directly related to the Zeeman energy ($\mu_0 H\Delta M$), is the prerequisite of the occurrence of magnetic-field induced martensitic transformation. Therefore, from the perspective of the MCE performance, a moderate ΔM is appropriate. In experiments, the most utilized strategy to reduce ΔS_{mag} is to reduce the temperature distance between the magnetostructural transition T_M and the Curie temperature of austenite T_C^A, i.e., $T_C^A - T_M$. Specifically, this is achieved by elevating T_M to make it approach T_C^A. During this process, on the one hand, the magnetization difference between austenite and martensite ΔM is decreased, and then the negative contribution of ΔS_{mag} is weakened. On the other hand, ΔM still possesses a relatively large value since T_M is still lower than T_C^A, which guarantees a remarkable Zeeman energy to ensure the occurrence of the magnetic field-induced reverse martensitic transformation. Thus, one of the key issues of weakening ΔS_{mag} is to adjust T_M.

Different from mechanical properties that are strongly dependent on microstructure, T_M belongs to the inherent property of materials and thus is mainly determined by the chemical composition. Aimed at reducing ΔS_{mag} by tailoring T_M, for the ternary NiMnIn alloys, several alloying methods including changing relative contents of different elements of the alloy and adding the fourth alien elements, such as Cu (Li et al., 2019a; Yan et al., 2021a; Huang et al., 2021), Cr (Sharma et al., 2010a; Sharma et al., 2011), Fe (Chen et al., 2012; Feng et al., 2012), Ga (Paramanik and Das, 2016) and Pd (Li et al., 2015), have been utilized. For instance, under the guidance of valence electron concentration (e/a) criteria of T_M, i.e., a larger e/a corresponds to a higher T_M (Wei et al., 2016), Feng et al. elevated T_M of $Ni_{50}Mn_{34}In_{16}$ from 250 K to 303 K *via* the partial substitution of a low valence electron number (VEN) element of In ($5s^2p^1$, VEN = 3) by a high VEN element of Fe ($3d^64s^2$, VEN = 8) (Feng et al., 2012). In the Fe-doped $Ni_{50}Mn_{34}In_{14}Fe_2$ alloy, T_M almost coincides with T_C^A, and a ΔS_M of 53.6 J kg^{-1} K^{-1} was realized under an 8 T magnetic field at 303 K. In addition, under the guidance of lattice volume effect of T_M, i.e., a contracted lattice tends to elevate T_M (Paramanik and Das, 2016), Sharma et al. shifted T_M of $Ni_{50}Mn_{34}In_{16}$ to a higher temperature (Sharma et al., 2010b). In the $Ni_{50}Mn_{33.66}Cr_{0.34}In_{16}$ alloy, a ΔS_M of 17.7 J kg^{-1} K^{-1} was obtained under a magnetic field of 8T at 270 K.

For the Co-doped NiCoMnIn alloys, compared with ternary NiMnIn alloys, the negative contribution of ΔS_{mag} to ΔS_{tr} is more pronounced as the addition of Co greatly enhances the magnetism of austenite and then the value of ΔM (Li et al., 2019a; Yang et al., 2020). The strategy of weakening ΔS_{mag} in the NiCoMnIn alloy is the same as that of NiMnIn, i.e., elevating T_M to make it close to T_C^A by doping a fifth alien element, such as Cu (Li et al., 2019b; Yan et al., 2021a; Huang et al., 2021), Fe (Chen et al., 2012), Ga (Paramanik and Das, 2016), Pd (Li et al., 2015). With respect to the ternary NiMnIn alloys, in these cases, two elements, i.e., Co and a fifth element, are doped. Thus, this alloying method was sometimes termed as co-doping (Li et al., 2019c). Compared with doping with a single element, the improvement of the MCE performance by the co-doping is usually more prominent. For instance, by co-doping with Co and Cu, Z. B. Li and collaborators realized a large ΔT_{ad} up to −4.8 K under a low-field change of 1.5 T in the $Ni_{46}Co_3Mn_{35}Cu_2In_{14}$ alloy at 272 K (Li et al., 2019a).

c) Utilizing multicaloric effect. As discussed above, the incompleteness of magnetic field-induced inverse martensitic transformation due to the high critical magnetic field required for a full transformation is a critical issue that restricts the MCE performance of the NiMnIn-based alloys.

Inspired by the fact that apart from the magnetic field, the martensitic transformation of NiMnIn alloy can also be triggered by mechanical field, an idea of improving MCE by simultaneously or sequentially applying mechanical and magnetic fields was proposed. Owing to the existence of multiple stimuli, the caloric effect generated in this process is termed as the multicaloric effect (Stern-Taulats et al., 2018). Compared with the caloric response when subjected to a single stimulus, the multicaloric effect generally has a much higher refrigeration capacity (Gràcia-Condal et al., 2020). In the $Ni_{50}Mn_{35.5}In_{14.5}$ alloy, by applying a magnetic field of 4 T and a mechanical field of 40 MPa, a multicaloric effect with an entropy change of 25.2 $J\,kg^{-1}\,K^{-1}$ and an adiabatic temperature change of 5.9 K was realized at room temperature. These values obviously exceed that of single magnetocaloric and elastocaloric effects.

6.2 Thermal/Magnetism Hysteresis

In application, to realize a real MCE refrigeration, the magnetic field needs to be repeatedly applied to the MCE refrigerant (around 10^7 times), which requires that the MCE effect possess a good cyclability. Unfortunately, different from MCE around the second-order Curie transition, MCE originated from the first-order magnetostructural transition is inevitably accompanied with the transitional thermal hysteresis ΔT_{Hys}. Theoretically, ΔT_{Hys} caused by the energy barrier between austenite and martensite is closely related to the transitional stress layer between the two phases. During the cyclic transformation, the stress in the transitional layer could induce certain irreversible processes, such as the formation of dislocations and the nucleation of microcracks, which further lead to functional degradation and failure (Song et al., 2013). Thus, for the practical applications, it is greatly meaningful to reduce ΔT_{Hys} and improve the reversibility of magnetostructural transition of the NiMnIn alloys. Until now, several strategies have been proposed, aimed at reducing ΔT_{Hys}, such as improving geometric compatibility between austenite and martensite, applying extra stimuli, etc.

a) Enhancing geometrical compatibility between austenite and martensite: As mentioned above, the degradation of cyclability is associated with the transitional stress layer between austenite and martensite. Thus, reducing the transition layer will be able to fundamentally decrease ΔT_{Hys} and improve the functional stability. According to the crystallographic theory of martensitic transformation (Nishiyama, 1978; Christian, 2002), the transitional stress layer is closely related to the geometrical compatibility between austenite and martensite, which can be described quantitatively by the middle eigenvalue of transformation stretch tensor λ_2 and the more strict cofactor condition (Chen et al., 2013; Song et al., 2013; Della Porta, 2019). A thinner transitional layer corresponds to better geometrical compatibility. For the geometrical compatibility between austenite and martensite, it is purely determined by the lattice parameters of these two phases, which can be adjusted by tailoring the chemical composition of the alloy. This provides an effective method to reduce ΔT_{Hys}.

For the ternary NiMnIn alloys, it is reported that the substitution of Cu for Mn is a valid method to improve the geometrical compatibility and thus decreases ΔT_{Hys} (Zhao et al., 2017a). For instance, D. W. Zhao et al. achieved a small ΔT_{Hys} of 3K and an excellent phase transition stability over 10^5 magnetic field cycles in the Cu-doped $Ni_{50}Mn_{31.5}In_{16}Cu_{2.5}$ alloy (Zhao et al., 2017b). They attributed the low ΔT_{Hys} and the exceptional cyclic stability to the fact that in this compound, λ_2 (0.99281) is fairly close to 1 and the (011) type-I/II twins, together with the (100) compound twins, closely satisfy the co-factor conditions simultaneously (Zhao et al., 2017a).

For the NiCoMnIn alloys, even though the addition of Co can enhance the magnetism of austenite and further significantly improve the magnetoresponsive behaviors, unfortunately, this alloying leads to a significant increase in hysteresis and phase transition irreversibility. For example, ΔT_{hys} of the ternary NiMnIn alloys is around 5–12 K, while with the addition of Co the value of ΔT_{hys} abruptly elevates to 10–30 K (Yan et al., 2021a). Thus, for the NiCoMnIn alloys, the harm caused by the thermal hysteresis and the irreversibility of phase transition is more severe compared with that in the ternary NiMnIn alloys. Until now, apart from Co, several fifth alloying elements were co-added to the NiMnIn alloys aimed at optimizing the hysteresis behavior, such as Co & Fe (Chen et al., 2012), Co & Si (Li et al., 2019b), Co & Cu (Li et al., 2019c; Yan et al., 2021b; Huang et al., 2021). Z. B. Li et al. reported that the Cu substitution for Mn can effectively reduce ΔT_{Hys} of the NiCoMnIn alloys from 17.5 K ($Ni_{46}Co_3Mn_{36}Cu_1In_{14}$) to 9 K ($Ni_{46}Co_3Mn_{34}Cu_3In_{14}$) (Li et al., 2019a). In the Co and Cu co-doped $Ni_{46}Co_3Mn_{35}Cu_2In_{14}$ alloy, they achieved a reversible ΔS_M of 16.4 $J\,kg^{-1}\,K^{-1}$ under a magnetic field of 5 T and a reversible ΔT_{ad} of 2.5 K under a magnetic field of 1.5 T (Li et al., 2019b).

Nevertheless, this alloying strategy of Cu, i.e., replacing Mn, will inevitably lead to the reduction of magnetism, since the magnetic moment of the Ni–Mn-based alloys is mainly provided by Mn (~85%) (Yan et al., 2020a; Yan et al., 2020b). To avoid the negative influence on magnetism caused by Cu doping, the co-alloying strategy with Cu replacing In and Co replacing Mn was studied (Yan et al., 2021a). In the $Ni_{45}Co_5Mn_{36}In_{13.3}Cu_{0.7}$ alloy, a reversible isothermal magnetic entropy change of 13.8 $J\,kg^{-1}\,K^{-1}$ and a refrigeration capacity of 270.2 $J\,kg^{-1}$ were obtained. Moreover, when the geometrical compatibility between austenite and martensite is improved by adjusting lattice parameters via tailoring the chemical composition, the volume variation ratio $\Delta V/V_0$ during the transition that is closely related to the transformation entropy change will inevitably be changed. The alloying strategy of improving geometrical compatibility and keeping remarkable $\Delta V/V_0$ meanwhile is still an open issue.

b) Applying extra stimulus fields: For the NiMnIn based alloys, owing to the strong coupling between magnetism and crystal lattice, the magnetostructural transformation is sensitive to both magnetic field and stress/strain field. This provides another way to tailor the hysteresis behavior of MCE, i.e., the stress/strain-assisted transformation. J. Liu et al. reported that the application of bias stress can greatly reduce or even eliminate the magnetic hysteresis during the

cycle of the magnetic field-induced inverse martensitic transformation (Liu et al., 2012; Zhao et al., 2017a). They observed that if the sample is magnetized without bias stress but is demagnetized under a low external hydrostatic pressure of 1.3 kbar, the isothermal magnetization and demagnetization curves of the NiCoMnIn alloy almost coincide (Liu et al., 2012).

By utilizing the bias stress, T. Gottschall et al. proposed a multicaloric cooling cycle to eliminate the negative influence of hysteresis on the reversibility of phase transition (Gottschall et al., 2018). The key idea of this method is to apply uniaxial stress to assist the transformation of the ferromagnetic austenite phase locked by large hysteresis into the martensite phase. The caloric effect is expected to be reproducible under the following sequence: 1) a decrease in temperature when the NiMnIn-based alloys are adiabatically magnetized; 2) the reverse transition does not happen due to the existence of thermal hysteresis during demagnetization; 3) absorbing heat from surroundings in the absence of a magnetic field; 4) applying uniaxial stress to assist the transformation from austenite to martensite; 5) removing stress; 6) expelling heat to the surroundings. By alternately applying a magnetic field (1.8T) and a stress field (80 MPa), they obtained a reversible ΔT_{ad} of −1.2 K in the $Ni_{49.6}Mn_{35.6}In_{14.8}$ alloy (Gottschall et al., 2018).

Apart from bias stress, Z. Z. Li et al. reported that the existence of the internal stress introduced by the pre-deformation can also improve the MCE cyclability (Li et al., 2018). They found that by applying pre-deformation, the reversible ΔT_{ad} of the $Ni_{45.3}Co_{5.1}Mn_{36.1}In_{13.5}$ alloy increases to 1.1 K from 0.8 K (the stress-free state). Besides, Y.-Y. Gong et al. reported that the strain-assisted transformation can also effectively tailor the hysteresis behavior of the NiCoMnIn alloy (Gong et al., 2015). They found that the strain generated by the PMN-PT piezoelectric ceramics can decrease ΔT_{Hys} from 25.5 to 21.6 K with an electric field varying from 0 to 8 kV cm^{-1}.

c) Other methods: Apart from tailoring geometrical compatibility and applying external stress/strain stimuli, the microstructure of MCE refrigerant was also reported to have an important influence on hysteresis. J. Liu et al. found that for the $Ni_{45}Mn_{37}In_{13}Co_5$ ribbons sample, the annealing can reduce the thermal hysteresis from 25 K to 20 K (Liu et al., 2009b). They attributed the reduction of ΔT_{ad} to the increased grain size and decreased defect density. Besides, T. Gottschall et al. proposed that the transformation performed in a minor loop instead of a complete transformation can improve the MCE stability (Gottschall et al., 2015). With this method, they obtained a cyclic ΔT_{ad} of −3 K at the magnetic field of 1.95 T in the $Ni_{45.7}Mn_{36.6}In_{13.5}Co_{4.2}$ alloy (Gottschall et al., 2015).

6.3 Working Temperature Window

For the NiMnIn-based alloys, different from the conventional giant MCE which occurs around the second-order Curie transition, the excellent MCE in these compounds is originated from the first-order magnetostructural transition. During the second-order Curie transition, the order parameter, i.e., magnetization, experiences a continuous transition in a relatively wide temperature change (40–50 K). In contrast, the first-order martensitic transformation occurs in a burst manner at speed close to that of the sound. The difference in the transformation speed of the first-order and the second-order phase transition results in a large difference in the operating temperature window of the corresponding MCE. An example comparing the MCE operating temperature window widths of the first-order and second-order transitions is illustrated in **Figure 10**. It is seen that the operating temperature range δT_{FWHM} defined as the full width at half maximum of $\Delta S_M(T)$ curve of Gd (second-order Curie transition) is around 47 K, which is about 6 times wider than that of $Gd_5Si_2Ge_2$ (first-order magnetostructural transition) (Pecharsky and Gschneidner, 1997). For the MCE, the refrigeration capacity (RC) is determined by the product of isothermal magnetic entropy change ΔS_M and the operating temperature window δT_{FWHM}. Thus, a narrow δT_{FWHM} will lead to a significant reduction in refrigeration capacity. So far, numerous strategies have been proposed to expand the operating temperature window of the MCE, such as enhancing the magnetic field sensitivity of magnetostructural transition temperature T_M, preparing composite material containing the MCE refrigerants with different T_M, and combining different caloric responses (magnetocaloric and elastocaloric).

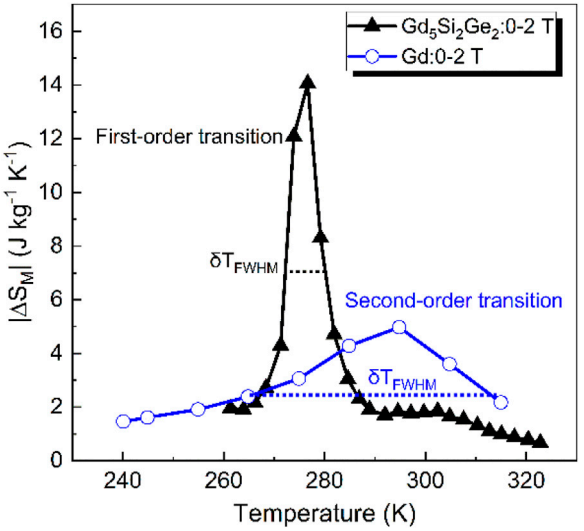

FIGURE 10 | Isothermal magnetic entropy change of the $Gd_5Si_2Ge_2$ between 240 and 325 K for a magnetic field change from 0 to 2 T, compared with that of pure Gd as determined from magnetization measurement (Pecharsky and Gschneidner Jr., 1997).

a) Enhancing the magnetic field sensitivity of magnetostructural transition temperature ΔT/ΔH: Fundamentally, for the MCE associated with the first-order magnetostructural transition, the width of the operating temperature window is decided by the magnetic field sensitivity of magnetostructural transition temperature ΔT/ΔH. Under a certain magnetic field, a higher ΔT/ΔH value will lead to a larger shift of magnetostructural

transition temperature, further resulting in a wider operating temperature window δT_{FWHM}. Based on the Clausius-Clapeyron equation, as discussed previously, the $\Delta T/\Delta H$ value can be increased by enlarging the magnetization difference between austenite and martensite ΔM, which can be achieved by the partial substitution of Co for Ni. For instance, by introducing Co, the value of δT_{FWHM} increases from 24 K ($Mn_{50}Ni_{39}In_9Co_2$) to 32 K ($Mn_{50}Ni_{37}In_9Co_4$) (Yang et al., 2020). However, as mentioned earlier, the substitution of Co will increase ΔT_{hys}. To weaken the negative effect on ΔT_{hys}, L. M. Wang proposed a low content of Co alloying method aiming at simultaneously realizing a wide $\Delta T/\Delta H$ and low ΔT_{hys} (Wang et al., 2020). In the $Ni_{48}Co_1Mn_{37}In_{14}$ alloy, a working temperature range of 34 K and an effective refrigeration capacity of 284 J kg^{-1} were realized under a magnetic field of 5 T.

b) Combining different caloric responses: For the NiMnIn-based alloys, apart from the inverse MCE associated with the first-order magnetostructural transition, it also exhibits the elastocaloric effect (see details in **Section 7**) and the conventional MCE around the second-order Curie transition of austenite. As is known, the magnetic field tends to stabilize the phase with strong magnetism, i.e., austenite, while the mechanical field stabilizes martensite preferentially. Therefore, the transitional temperature of martensitic transformation T_M tends to shift towards an opposite direction when the magnetic field and the stress field are applied, respectively. As a result, although both inverse MCE and elastocaloric effects are associated with martensitic transformation, typically, the working temperature ranges for the inverse MCE and the elastocaloric effect are, respectively, lower and higher than T_M. This characteristic of the NiMnIn-based alloys provides a novel route to widen the working temperature range, i.e., combining the different caloric responses with adjacent temperature ranges. Moreover, by composition design, MCE associated with the second-order Curie temperature can also be adjusted near the magnetostructural transition. In this situation, the inverse MCE, the elastocaloric effect, and the conventional MCE can be combined and further expand the refrigeration temperature region.

In 2017, Y. Hu et al. proposed the method of widening the operating temperature window by combining elastocaloric and MCE effects. By using this method, they realized a broad refrigeration temperature region of around 120 K in the $Ni_{49.5}Mn_{28}Ga_{22.5}$ alloy (Hu et al., 2017). In the $Ni_{50}Mn_{35}In_{15}$ alloy, Z. B. Li et al. realized a broad refrigeration temperature region ranging from 270 K to 380 K *via* the combination of successive MCE and elastocaloric effects (Li et al., 2020). Recently, P. T. Cheng et al. realized a refrigeration temperature range of 250–340 K in the $Ni_{45}Co_5Mn_{37}In_{13}$ alloy by using the same strategy (Cheng et al., 2021).

c) Utilizing the intermediate martensitic transformation: In some NiMnIn-based alloys, an intermediate martensitic transformation has been observed, i.e., the martensitic transformation occurs in multiple stages. By using the multi-stage phase transition characteristics, the operating temperature window of MCE can be extended if different stages of martensite transformation occur in an adjacent temperature range. For example, S. Dwevedi et al. reported a two-step martensitic transformation in the Sn-doped Ni–Mn–In-based alloys, which leads to the double peak behavior of ΔS_M and widens the operating temperature range (Dwevedi and Tiwari, 2012). With a two-step martensitic transformation, an operating temperature window δT_{FWHM} of around 46.5 K was realized in the $Ni_{50}Mn_{34}In_8Sn_8$ alloy that greatly exceeds the typical δT_{FWHM} value of the single-stage martensitic transformation (~10 K at a magnetic field of 2 T).

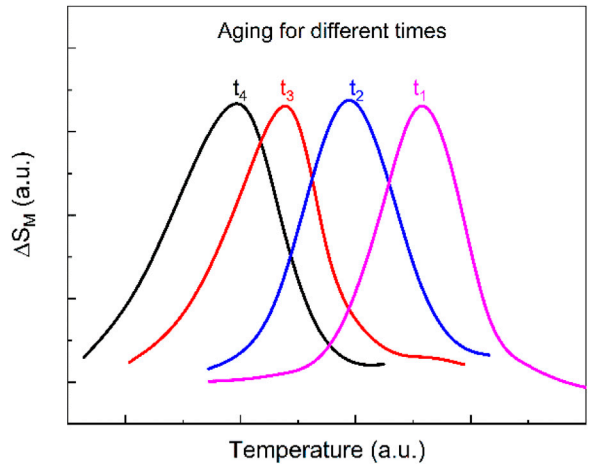

FIGURE 11 | Realizing a wide operating temperature window by combining various samples with different aging times.

d) Fabricating composite material containing the MCE refrigerants with different T_M: For the MCE associated with the first-order magnetostructural transition, the operating temperature is around the temperature of magnetostructural transition. Thus, fabricating a series of MCE refrigerants with different T_M and compositing them will allow to greatly expand the operating temperature range. Using this strategy, J. Liu et al. proposed a method of stacking a series of alloys with different annealing times to successfully expand the operating temperature window of the NiCoMnIn alloy(Liu et al., 2012). For the NiCoMnIn alloys, with the prolongation of aging time, the martensitic transformation is gradually shifted to the lower temperatures, whereas the transformation entropy change remains unchanged. Thus, for the composite containing a series of alloys aged at different times, the operating temperature window is greatly enlarged, as illustrated in **Figure 11**. Later, J.-P. Camarillo et al. reported that a reversible ΔS_M of 7.5 J kg^{-1} K^{-1} was obtained over a broad temperature range of 30 K by assembling a composite specimen in a NiMnInCu alloy (Camarillo et al., 2016).

6.4 Perspectives

From the above discussion, the high magnetic moment of austenite, which usually brings about a large magnetization difference ΔM between austenite and martensite, is a double-edged sword for the MCE performance. On the one hand, a remarkable ΔM is a prerequisite for the magnetic field-induced inverse martensitic transformation. On the other hand, a higher ΔM makes a larger negative contribution of ΔS_{mag} to ΔS_{tr}. Thus, for the optimized MCE performance, ΔM should be neither too big nor too small. For the multicaloric effect, it is indeed possible to improve refrigeration efficiency. Unfortunately, compared with the single stimulus, the multiple stimuli significantly increase the complexity of machine construction and equipment cost. More efforts focused on optimizing the structure of the equipment are required. Apart from the above-mentioned strategies, in our opinion, the methods of improving lattice vibration entropy change ΔS_{vib} and electronic entropy change ΔS_{elec} may open new ways to improve the MCE performance. Since ΔS_{tr} is mainly decided by ΔS_{vib}, the method of enlarging ΔS_{vib} could greatly improve the MCE performance. In addition, even though in the known NiMnIn-based alloys, ΔS_{elec} plays a negligible positive role on ΔS_{tr}, it might be possible to obtain a large ΔS_{elec} by tailoring the electronic structure of martensite from metal to semiconductor state. The semiconducting state is not uncommon in the 2:1:1 type Heusler alloys. Recently, J. C. Lin et al. found that ΔS_{elec} plays a key role on ΔS_{tr} in the $Ni_{1-x}Fe_xS$ alloy during the study of barocaloric effect (Lin et al., 2020), which evidenced that it is feasible to utilize ΔS_{elec} to improve ΔS_{tr}.

Through the above-mentioned strategies, the thermal/magnetic hysteresis of the Ni(Co)MnIn alloys has been greatly optimized. However, the cyclic stability of the MCE performance of the Ni(Co)MnIn alloys yet cannot meet the needs for practical applications. For instance, in the state-of-the-art Co and Cu co-doped $Ni_{46}Co_3Mn_{35}Cu_2In_{14}$ alloy, the maximum ΔT_{ad} is up to −4.8 K under the magnetic field of 1.5 T at the first cycle, while this value rapidly drops to −2.5 K at the second cycle (Li et al., 2019c). So far, there is still a lack of satisfactory alloying methods, which can substantially improve the geometrical compatibility of the alloy without degrading other parameters required for MCE. One of the difficulties is that the geometrical compatibility rule is a posteriori criterion. Specifically, the geometrical compatibility factors can only be calculated with the measured lattice parameters of austenite and martensite after the alloy is fabricated. This method is inefficient and cannot be directly used to guide the design of alloy composition. So far, the direct relation between alloy composition and geometrical compatibility is unknown. High throughput experimental or computational methods and machine learning may provide a feasible way to find the correlation and then promote the design of low-hysteresis NiMnIn alloys.

7 ELASTOCALORIC EFFECT

Elastocaloric effect (eCE) refers to the caloric response of material when external uniaxial stress is applied (Brown, 1981). Compared with the MEC and the electrocaloric effect, the elastocaloric effect is of high work efficiency, environmental friendliness, and low cost. Therefore, the elastocaloric refrigeration technique has been considered to be the most promising alternative to replace traditional vapor compression technology for room-temperature refrigeration (Goetzler et al., 2014), such as air conditioners and fridges. Besides, owing to the convenience of mechanical loading, the elastocaloric effect also exhibits promising potential application in the field of micro- or nano-refrigeration, such as the microelectronic chip. In recent years, some significant progress has been made in the design and development of elastocaloric refrigeration devices (Schmidt et al., 2015; Tušek et al., 2016; Kabirifar et al., 2019).

At present, the discovered elastocaloric material includes natural rubber, shape memory alloy, ion or molecular compound, and rare-earth-based compound. Among them, the shape memory alloy possesses a remarkable refrigeration capacity with the adiabatic temperature change of 3–30 K (Mañosa et al., 2010; Lu et al., 2014; Moya et al., 2014; Liu et al., 2017; Manosa and Planes, 2017; Kabirifar et al., 2019), which is much larger than those of ion or molecular compounds and rare earth compounds, such as 0.42 K for $Ce_{0.85}(La_{0.95}Y_{0.05})_{0.15}Sb$ and 0.4 K for HoAs (Nikitin, 2011; Cazorla, 2019; Zhang et al., 2020). Moreover, the constituent elements of shape memory alloy are relatively abundant and cheap compared with the rare-earth-based compounds. Among numerous shape memory alloys, NiMnIn-based magnetic shape memory alloys represent a special category owing to the relatively low critical driving stress (100–300 MPa) (Lu et al., 2014; Huang et al., 2019; Li et al., 2020).

For shape memory alloy materials, the large elastocaloric effect is originated from the process of stress-induced martensitic transformation. During the loading-unloading cycle, the release and the absorption of the latent heat are used to achieve refrigeration, as illustrated in **Figure 12**. When uniaxial stress is applied to austenite, at the condition that the applied stress exceeds the critical stress to drive martensitic transformation σ_M^S, the alloy will transform from a high-temperature austenite phase to a low-temperature martensite phase (stage ② in **Figure 12A**). During this process, the latent heat of phase transition will be released, leading to a rise in the temperature of the refrigerant (stage ② in **Figure 12B**). When the load is removed, the sample experiences a process of inverse martensitic transformation and returns to the austenitic state (stage ⑥ in **Figure 12A**). In the process, the refrigerant absorbs heat from the environment, leading to a decrease in the temperature of the sample (stage ⑥ in **Figure 12B**).

Like MCE, eCE is characterized by the isothermal entropy change ΔS_{iso} and adiabatic temperature change ΔT_{ad}. For the NiMnIn alloys, eCE was first reported by Lu et al. (2014). In the textured $Ni_{45.7}Mn_{36.6}In_{13.3}Co_{5.1}$ polycrystalline sample, they observed a reversible ΔT_{ad} of 3.5 K under uniaxial stress of 100 MPa at room temperature. Later, Y. J. Huang et al. realized a ΔT_{ad} of −4 K in the ternary $Ni_{48}Mn_{35}In_{17}$ directionally solidified alloy (Huang et al., 2015). Among various known eCE refrigerants, the required critical stress for martensitic transformation σ_M^S is relatively small (~100 MPa) in

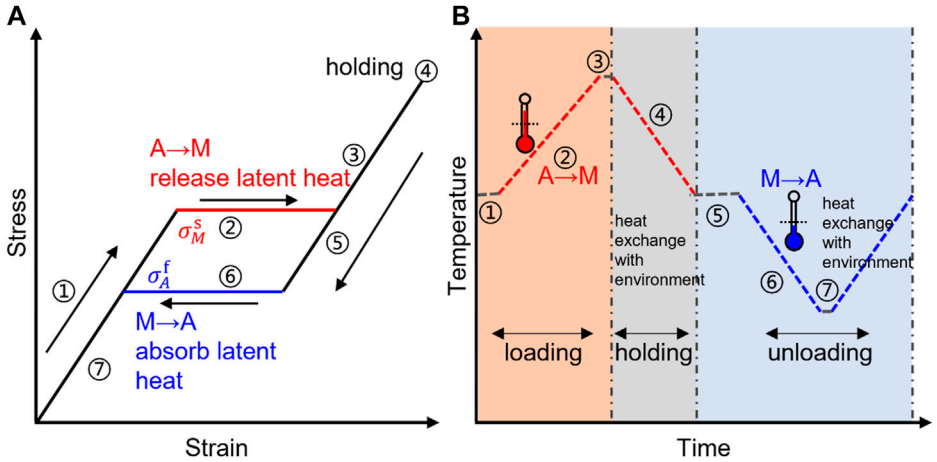

FIGURE 12 | Schematic diagram of **(A)** stress-strain curve and **(B)** corresponding temperature change for eCE of shape memory alloys. The temperature variations of ① to ⑦ in **(B)** exactly correspond to the stages of ① to ⑦ in the stress-strain curve of **(A)**.

TABLE 2 | Research progress of elastocaloric effect in the NiMnIn-based alloys.

Year	Reference	Alloy composition (at%)	Sample state	eCE			Stress	Test temperature
				ΔS_{iso} J kg^{-1} K^{-1}	ΔT K	COP	MPa	K
2014	Lu et al. (2014)	$Ni_{45.7}Mn_{36.6}In_{13.3}Co_{5.1}$	Oriented polycrystalline		−3.5		100	300
2015	Huang et al. (2015)	$Ni_{48}Mn_{35}In_{17}$	Oriented polycrystalline	10.3	−4		300	313.3
2015	Lu et al. (2015)	$Ni_{45}Mn_{36.4}In_{13.6}Co_5$	Bulk Polycrystalline		−4		150	296
2016	Shen et al. (2017)	$Ni_{51.4}Mn_{34}In_{15.6}Tb_{0.4}$	Bulk Polycrystalline		−5.1		622	291
2017	Zhao et al. (2017b)	$Ni_{45}Mn_{36.5}In_{13.5}Co_5$	Oriented polycrystalline		+8.6		260	298
2017	Lu and Liu (2017)	$Ni_{45}Mn_{36.4}In_{13.6}Co_5$	Bulk Polycrystalline		−3		135	293
		$Ni_{45}Mn_{36}In_{14}Co_5$			−2		340	287
		$Ni_{45}Mn_{36.2}In_{13.8}Co_5$			−3.1		225	room temperature
2017	Yang et al. (2017)	$(Ni_{51.5}Mn_{33}In_{15.5})_{99.7}B_{0.3}$	Bulk Polycrystalline	20	−6.2	18	550	303
2017	Zhao et al. (2017a)	$Ni_{50}Mn_{31.5}In_{16}Cu_{2.5}$	Oriented polycrystalline	−23.1	+13		280	room temperature
2017	Camarillo et al. (2017)	$Ni_{51.4}Mn_{33.6}In_{12.1}Ga_{2.9}$	Bulk Polycrystalline	25	−4.9		100	room temperature
2018	Henández-Navarro et al. (2018)	$Ni_{50}Mn_{32}In_{16}Cr_2$	Bulk Polycrystalline		−3.9		100	room temperature
2018	Shen et al. (2018)	$Ni_{45}Mn_{36}In_{13}Co_5Cr$	Bulk Polycrystalline		−5.8		300	323
2019	Huang et al. (2019)	$Ni_{50}Mn_{34.8}In_{15.2}$	Oriented polycrystalline	–	−7.6	–	345	room temperature
2019	Tang et al. (2019)	$(Ni_{52}Mn_{31}In_{16}Cu_1)B_{0.2}$	Bulk Polycrystalline		−9.5		220	room temperature
2019	Yang et al. (2019)	$(Ni_{51}Mn_{33}In_{14}Fe_2)_{99.4}B_{0.6}$	Bulk Polycrystalline		+5.6		350	304
2019	Li et al. (2019c)	$Ni_{44.9}Co_{4.9}Mn_{36.9}In_{13.3}$	Oriented polycrystalline		+14.7		650	390
2020	Huang et al. (2020)	$Ni_{50}(Mn_{31.7}Cu_{2.5}B_{0.3})In_{15.5}$	Oriented polycrystalline	–	−12.8	–	500	room temperature
2020	Li et al. (2020)	$Ni_{50}Mn_{35}In_{15}$	Oriented polycrystalline		−19.7		350	320
2021	Cheng et al. (2021)	$Ni_{45}Co_5Mn_{37}In_{13}$	Oriented polycrystalline	10	−6		200	303

the NiMnIn-based alloys (Lu et al., 2014; Huang et al., 2019; Cheng et al., 2021), which makes this kind of compounds have broad prospects in the fields of micro- and nano-refrigeration, such as microelectronic chips. From then on, the eCE of the NiMnIn-based alloys has been attracting more and more attention. Some representative work associated with eCE of the NiMnIn-based alloys are summarized in **Table 2**.

Until now, the studies on the eCE of the NiMnIn-based alloys were mainly focused on the following two aspects: 1) elevating adiabatic temperature change ΔT_{ad} that is directly linked to the refrigeration capacity. A large ΔT_{ad} is a constant pursuit to improve the energy conversion efficiency; 2) improving mechanical properties. Different from the MCE, the eCE has a much higher requirement on the mechanical properties of a refrigerant since the refrigeration material must bear a large mechanical load during work. Unfortunately, owing to the strong covalent *p-d* hybridization between the *p* valence electrons of the *p-block* element of In and the *3d* valence electrons of Ni (and Mn) (Bechtold et al., 2012; Qian et al., 2015; Liu et al., 2017), the NiMnIn-based alloys are intrinsically brittle, which will introduce structural fatigue and do harm to cyclic stability of eCE. Next, the main progress related to these two aspects of the Ni–Mn–In-based alloys will be briefly reviewed.

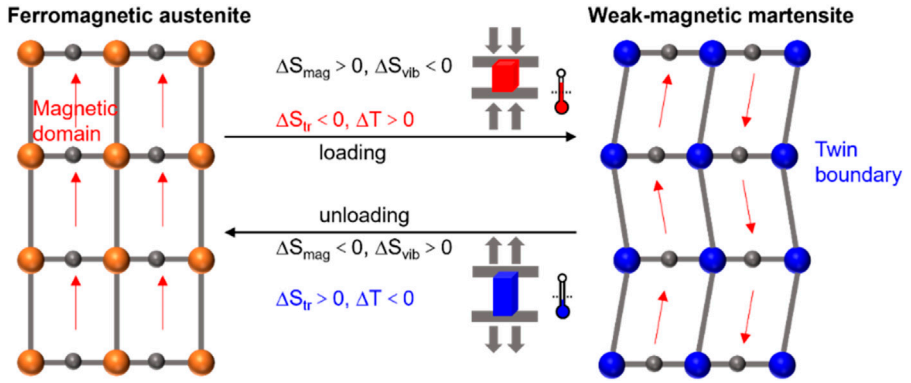

FIGURE 13 | Schematic diagram of the entropy change of magnetostructural transition in NiMnIn-based alloys.

7.1 Adiabatic Temperature Change

Like the isothermal magnetic entropy change ΔS_M of the MCE, the upper limit of isothermal entropy change ΔS_{iso} (or adiabatic temperature change ΔT_{ad}) of eCE is determined by the transformation entropy change ΔS_{tr}. As discussed in **Section 6**, for the NiMnIn-based alloys, the sign of magnetic entropy change ΔS_{mag} is opposite to the total transformation entropy change ΔS_{tr} (**Figure 13**). Therefore, one of the critical issues of increasing ΔS_{tr} is to reduce the negative contribution of magnetic entropy change ΔS_{mag}. To optimize the eCE of the NiMnIn-based alloys by means of weakening ΔS_{mag}, as illustrated in **Figure 14**, several methods have been proposed, including (a) elevating the temperature of magnetostructural transition T_M to make it close (or above) the Curie temperature of austenite, (b) increasing the testing temperature T_{Test} to make it close (or above) the Curie temperature of austenite, and (c) reducing the magnetism of austenite.

a) Elevating the temperature of magnetostructural transition T_M to (or above) the Curie temperature of austenite: As utilized in improving the MCE performance, as illustrated in **Figure 14A**, ΔT_{ad} of the eCE can also be optimized by elevating the temperature of magnetostructural transition T_M to or above the Curie temperature of austenite to reduce the negative contribution of ΔS_{mag} on ΔS_{tr}. By the partial substitution of Cu for Mn, D. W. Zhao et al. elevated the finish temperature of inverse martensitic transformation (A_f) from 235.0 K of $Ni_{50}Mn_{34}In_{16}$ to 279.8 K of $Ni_{50}Mn_{31.5}In_{16}Cu_{2.5}$. With this substitution, the ΔT_{ad} values of +13 K and −10 K in a directionally solidified $Ni_{50}Mn_{31.5}In_{16}Cu_{2.5}$ sample were obtained during loading and unloading at room temperature, respectively (Zhao et al., 2017b). As can be seen from **Table 2**, this ΔT_{ad} belongs to the relatively high value of room-temperature eCE in the NiMnIn-based alloys. Z. Yang et al. reported that by Fe doping, A_f of 304 K of the $Ni_{51.5}Mn_{33}In_{15.5}$ alloy (e/a = 7.93) is shifted to 319 K in the $Ni_{51}Mn_{33}In_{14}Fe_2$ alloy (e/a = 7.99) (Yang et al., 2019). Under this substitution, ΔT_{ad} was increased from 3 K of $Ni_{51.5}Mn_{33}In_{15.5}$ to 5.7 K of $Ni_{51}Mn_{33}In_{14}Fe_2$ under 350 MPa.

b) Increasing testing temperature T_{Test} to (or above) the Curie temperature of austenite: For the eCE, the temperature at which the structural transition occurs, i.e., the temperature of stress-induced martensitic transformation, is determined by the testing temperature T_{Test}, rather than the temperature of martensitic transformation under zero-field (T_M). Thus, as a conjugate way by T_M, the negative contribution of ΔS_{mag} can be reduced by increasing testing temperature T_{Test} to or above the Curie temperature of austenite, as illustrated in **Figure 14B**. For instance, Z. Z. Li et al. reported that as the test temperature increased from 320 to 390 K under 650 MPa, ΔT_{ad} of the $Ni_{44.9}Co_{4.9}Mn_{36.9}In_{13.3}$ alloy increased from 8.3 to 14.7 K due to the decreased ΔS_{mag} (Li et al., 2019c). Similar to this temperature enhanced eCE, as T_{Test} increased from 310 to 320 K under 350 MPa, ΔT_{ad} of the $Ni_{50}Mn_{35}In_{15}$ alloy increased from −15 to −19.7 K (Li et al., 2020). In addition, as T_{Test} increased from 290 to 314 K under 250 MPa, ΔS_{iso} increased from 15 to 47.8 J kg^{-1} K^{-1} (Li et al., 2020).

c) Reducing the magnetism of austenite: For the MCE performance, as discussed in **Section 6**, the magnetism of austenite is a double-edged sword. On the one hand, a strong magnetism of austenite will lead to a remarkable ΔM and then a large driving force for inverse martensitic transformation; on the other hand, a strong magnetism will bring about a large ΔS_{mag}, which is harmful to the MCE refrigeration capacity. However, for the eCE in which the martensitic transformation is driven by a mechanical field rather than a magnetic field, the magnetism of austenite seems to be a purely harmful factor. Thus, for the eCE performance, the most effective and fundamental method to weaken the negative contribution of ΔS_{mag} is to reduce the magnetism of austenite, as illustrated in **Figure 14C**.

For the Ni–Mn-based alloys, the adiabatic temperature change realized at room temperature is only 3–15 K (Lu et al., 2014; Zhao et al., 2017a; Huang et al., 2020), which is smaller than those of non-magnetic NiTi (10–25 K) (Cui et al., 2012; Pataky et al., 2015; Tušek et al., 2015) and NiMnTi (20–30 K) (Cong et al., 2019; Yan et al., 2019). One of the possible reasons might be associated with

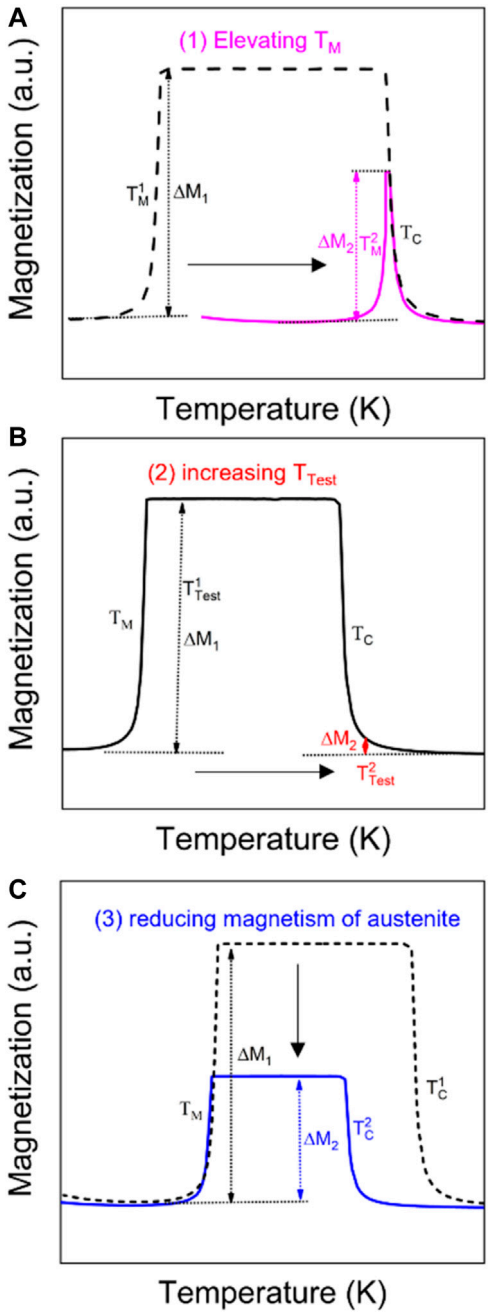

FIGURE 14 | Schematic diagrams of weakening ΔS_{mag} by **(A)** elevating the temperature of magnetostructural transition T_M to make it close (or above) the Curie temperature of austenite, **(B)** increasing the test temperature T_{Test} to make it close (or above) the Curie temperature of austenite, and **(C)** reducing the magnetism of austenite.

the large negative contribution of magnetic entropy change ΔS_{mag}. It is known that the magnetic moment of the Ni–Mn-based alloys is mainly originated from the Mn element. Therefore, decreasing the concentration of Mn, substituted by non-magnetic elements, allows to dramatically reduce the ferromagnetism of austenite and further eliminate the negative contribution of ΔS_{mag}. By using this strategy, with the co-substitution of Cu and B for Mn, X. M. Huang et al. successfully reduced the value of ΔM from 82 to 42 emu g^{-1} and realized a large ΔT_{ad} of −12.8 K in the $Ni_{50}(Mn_{31.7}Cu_{2.5}B_{0.3})In_{15.5}$ directionally solidified alloy (Huang et al., 2020).

7.2 Mechanical Properties and Cyclic Stability

To realize a real application of eCE refrigeration, the number of cyclic loading-unloading around 10^7 times (Chluba et al., 2015) of uniaxial stress to the eCE refrigerant is necessary, which requires that the eCE refrigerant be mechanically stable. As discussed above, the NiMnIn-based alloys are intrinsically brittle due to the high covalency in chemical bonds, which greatly reduces the fatigue fracture resistance of the material and thus is detrimental to the cyclic stability of the eCE. Aimed at improving the mechanical properties of the NiMnIn-based alloys, several methods have been proposed to enhance the mechanical properties, such as grain refinement (Yang et al., 2017; Yang et al., 2019; Huang et al., 2020), grain boundary strengthening (Huang et al., 2015; Zhao et al., 2017b; Huang et al., 2019), introducing coarse columnar crystals with strong texture (Huang et al., 2015; Zhao et al., 2017a; Huang et al., 2019), and introducing a soft second-phase (Yang et al., 2015; Shen et al., 2018).

a) Grain refinement: For the NiMnIn-based polycrystalline alloys, since the transformation strain ε_{trans} is strongly orientation-dependent (**Section 4.2**), the strain discontinuity would inevitably occur near the grain boundary of the austenite with different orientations, especially at triple junctions. Thus, cracks may nucleate at the grain boundaries of austenite and propagate along the grain boundaries due to the relative weakness of the grain boundary with respect to the grain interior in intermetallics. For the refined samples, the reduced grain size leads to the decrease of the difference of cumulative transformation displacements $d{\cdot}\varepsilon trans$ between two austenite grains. Thus, the nucleation and the propagation of the crack might be suppressed. As a result, the strength and toughness of the material will be improved.

V. Sánchez-Alarcos et al. reported that the Ti doping can refine the grain size from 1160 μm ($Ni_{50}Mn_{33.5}In_{16.5}$) to 40 μm [$(Ni_{50}Mn_{33.5}In_{16.5})_{98}Ti_2$] (Sánchez-Alarcos et al., 2015). For their studied $(Ni_{50}Mn_{33.5}In_{16.5})_{100-x}Ti_x$ (x = 0, 0.5, 1, and 2) alloys, they found that the Vickers hardness and yield strength increase with the increasing Ti concentration, with an increase of around 10% for $(Ni_{50}Mn_{33.5}In_{16.5})_{98}Ti_2$ compared with the undoped alloy. Q. Shen et al. reported that the Tb doping can reduce the grain size from 50 μm ($Ni_{50}Mn_{34}In_{15.7}Tb_{0.3}$) to 5 μm ($Ni_{50}Mn_{34}In_{15.6}Tb_{0.4}$) (Shen et al., 2017). The compressive strength of $Ni_{50}Mn_{34}In_{15.6}Tb_{0.4}$ increases to 622 MPa from 372 MPa ($Ni_{50}Mn_{34}In_{15.7}Tb_{0.3}$).

b) Grain boundary strengthening: As discussed above, for the NiMnIn compounds, the nucleation and the propagation of

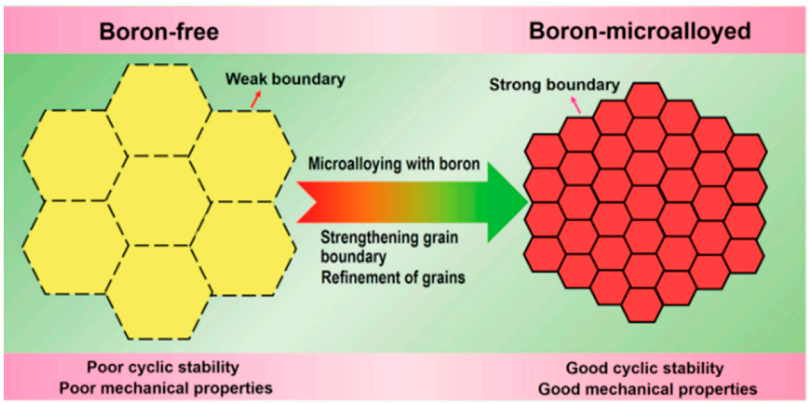

FIGURE 15 | Effects of the B microalloying on the microstructure of a NiMnIn alloy (Yang et al., 2019).

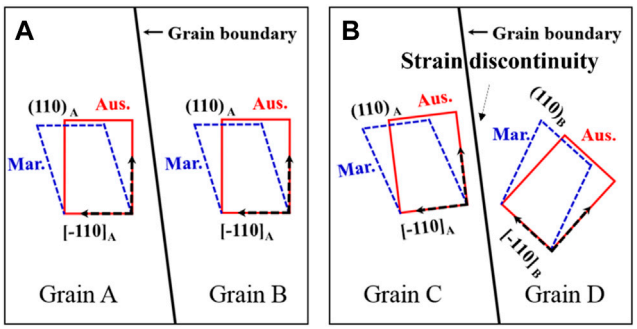

FIGURE 16 | Texture effect on the compatibility of transformation strain around grain boundary. **(A)** strong texture and **(B)** random texture (Huang et al., 2019). Reproduced with the permission of Elsevier Publisher.

cracks mostly occur near grain boundaries of austenite. Thus, elevating the strength of grain boundaries could significantly improve the mechanical properties. Until now, the most effective method known for increasing the cohesion of grain boundary is microalloying with boron (Yang et al., 2017; Yang et al., 2019). Z. Yang et al. reported that by microalloying with boron, as illustrated in **Figure 15**, the grain boundary cohesion can be increased; meanwhile, the grain size can be refined (Yang et al., 2017). With this microstructure modification, the mechanical properties and the eCE cyclic stability of the NiMnIn alloy can be prominently improved. For instance, the eCE of 2 K remains stable with almost no degradation for more than 150 cycles in $(Ni_{51.5}Mn_{33}In_{15.5})_{99.7}B_{0.3}$ (Yang et al., 2017). Later, they realized an ultrahigh cyclability of eCE in the $(Ni_{51}Mn_{33}In_{14}Fe_2)_{99.4}B_{0.6}$ polycrystalline alloy, i.e., a ΔT_{ad} of 5.6 K at 2700 loading-unloading cycles (Yang et al., 2019). With the 3D atom probe tomography (ATP) technique, they reported that the addition of B promotes the formation of NiBH cluster, which may act as the H trapping to reduce the hydrogen diffusion along the grain boundary and thus suppresses the hydrogen embrittlement, leading to an improvement of the grain boundary strength. X. M. Huang et al. found that with the addition of B, the compressive strength σ_{comp} and strain ε_{comp} was significantly improved from 630 MPa to 9.3% of $Ni_{50}Mn_{34.5}In_{15.5}$ alloy to 1142 MPa and 12.3% of $Ni_{50}(Mn_{31.7}Cu_{2.5}B_{0.3})In_{15.5}$ alloy (Huang et al., 2020).

c) Introducing crystallographic texture: The crack nucleation in the NiMnIn alloys is closely related to the discontinuity of transformation strain near the grain boundary regions of austenite with different orientations. Thus, introducing crystallographic texture could effectively reduce the discontinuity of transformation strain at grain boundaries, as illustrated in **Figure 16** (Huang et al., 2019), and thus improve the fracture resistance and the eCE cyclic stability of the NiMnIn alloys. Unlike the conventional metals (such as Al, Cu and Ti) for which the texture can be introduced by severe plastic deformation and heat treatment (Kocks et al., 1998; Yan et al., 2014), the texture of brittle intermetallics can just be introduced at the solidification process, such as the directional solidification and the melt-spinning techniques. Considering the convenience of mechanical loading, the directional solidification technique was widely used to introduce texture for the studies of eCE of the NiMnIn alloys (Huang et al., 2015; Huang et al., 2020).

X. M. Huang et al. systematically studied the influence of microstructural characters on mechanical properties and cyclic stability of eCE using $Ni_{50}Mn_{34.8}In_{15.2}$ as an example material (Huang et al., 2019). By applying arc-melting, suction casting, and directional solidification techniques, three samples with different microstructural features, i.e., arc-melted (columnar-shape grains with the long axis of 1–2 mm and the wide axis of 100–500 μm; random texture), suction cast (grain size less than 200 μm; random texture) and directionally solidified (coarse columnar-shaped grains of several mm; strong <001> texture) samples, were fabricated. The compressive strength and strain of the directionally solidified sample were 991 MPa and 11.9%, respectively, which are obviously higher than the arc-melted (451 MPa and 9.4%) and suction cast (341 MPa and 7%)

samples. Moreover, the cyclic stability of the directionally solidified sample (>40) is much higher than the arc melted and the suction cast samples (<10). These results suggest that the microstructure of the directionally solidified sample, i.e., strong texture and coarse grain, is conducive to obtaining excellent mechanical properties. The improved mechanical properties of the directionally solidified sample are attributed to the reduced strain incompatibility near grain boundaries owing to the strong texture.

d) Introducing a soft second phase: Introducing a soft second phase was also reported to be an effective method to increase the mechanical properties of the NiMnIn-based alloys (Yang et al., 2015; Shen et al., 2018). A. Shen et al. reported that the undoped $Ni_{45}Mn_{37}In_{13}Co_5$ sample with no precipitates could only withstand maximum compressive stress and strain of 155 MPa and 3%. Furthermore, the fracture strength and strain of $Ni_{45}Mn_{36}In_{13}Co_5Cr_1$ with a small amount of the second phase precipitates along grain boundaries increased to 407 MPa and 5% (Shen et al., 2018).

7.3 Perspectives

For the eCE refrigerants, one of the key parameters measuring refrigeration efficiency is ΔT_{ad} or ΔS_{iso}. At present, as discussed in **Section 7.1**, most of the work is focused on reducing the negative contribution of ΔS_{mag} to improve ΔT_{ad}. Apart from the magnetism contribution ΔS_{mag}, ΔT_{ad} is also closely related to the contributions of lattice vibration ΔS_{vib} and electron structure ΔS_{elec}, especially ΔS_{vib}. Thus, increasing ΔS_{vib} could significantly improve the total entropy change ΔS_{str} and further eCE ΔT_{ad}. It is now understood that ΔS_{vib} is associated with the volume change of crystal lattice $\Delta V/V_0$ during martensitic transformation. Thus, elevating $\Delta V/V_0$ would be an effective method to increase eCE ΔT_{ad}. Recently, D. Y. Cong et al. confirmed that a large $\Delta V/V_0$ corresponds to a high value of eCE ΔT_{ad} in the *all-d-metal* NiMnTi alloys (Cong et al., 2019). However, the key materials factors affecting $\Delta V/V_0$ are unknown for certain eCE refrigerants. In addition, for the cyclic stability of eCE, apart from mechanical properties, stress hysteresis is also a critical influencing factor. Generally, a large stress hysteresis is harmful to both the refrigeration efficiency and the functional stability of eCE. However, the key materials factors affecting stress hysteresis also remain unclear. High-throughput experimental techniques, high-throughput first-principle calculations, and machine learning algorithms would provide powerful tools to find the key factors determining ΔV/V0 and stress hysteresis and thus improve the performance of the NiMnIn alloys.

8 SUMMARY

In the past 15 years, stimulated by the potential applications in the fields of smart sensors and solid-state refrigeration, the NiMnIn-based metamagnetic shape memory alloys have attracted increasing attention from both communities of materials science and solid-state physics. Scientists from all over the world have conducted systematic research on the NiMnIn alloy covering from the crystal structure, microstructure, martensitic transformation to metamagnetic shape memory, magnetocaloric, and elastocaloric effects.

The austenite of NiMnIn alloy has a highly ordered cubic $L2_1$ structure. The martensite has a non-modulated (NM) tetragonal or a monoclinic modulated (6M) structure based on the chemical composition. 6M martensite possesses a self-accommodated microstructure with six distinct martensite colonies in one austenite grain. In each colony, there exist four twin-related martensite variants. The Pitsch strain path, $\{01\bar{1}\}_A<0\bar{1}1>_A$, is the real strain path that governs the lattice distortion during martensitic transformation. The progress of metamagnetic shape memory effect was summarized from two aspects of NiCoMnIn and other NiMnIn-based alloys. The magnetocaloric effect was reviewed in the focus of increasing isothermal magnetic entropy change, reducing thermal/magnetism hysteresis, and expanding the operating temperature window. For the elastocaloric effect, the main progress was summarized from two aspects of increasing adiabatic temperature change and improving cyclic stability.

Until now, there are still many fundamental scientific issues to be resolved, including 1) the formation mechanism of modulated martensite structure, 2) the key materials factors that determine the modulation type of martensite, 3) the quantitative relationship between the modulated martensite and functional properties, 4) the reason for the huge difference in detwining stress for different twinning systems, 5) the underlying physical mechanism that the K-S and the Pitsch orientation relations are almost simultaneously satisfied and 6) the shuffling path of the $(001)_M$ atomic layer during the martensitic transformation. To realize practical applications of the fruitful magnetoresponsive and elastocaloric effects, more effective methods to 1) reduce the critical driving field of magnetic-field induced inverse martensitic transformation, 2) decrease the transitional thermal/magnetic/stress hysteresis, and 3) improve mechanical properties and cyclic stability are still in great need.

In recent years, the rapid development of advanced computational characterization methods such as high-throughput first-principles calculations based on quantum mechanics, spherical aberration-corrected TEM electron microscopes, *in-situ* high-resolution TEM electron microscopes, high-throughput experimental methods, and machine learning methods based on big data analyses provide powerful tools for solving the issues mentioned above. The resolution of these issues will definitely promote the development of the NiMn-based magnetic shape memory alloys and the numerous related practical applications.

AUTHOR CONTRIBUTIONS

H-LY and CE conceived and designed the structure of the review. H-LY and X-MH wrote the manuscript. All authors contributed to the discussion and commented on the manuscript.

ACKNOWLEDGMENTS

We would like to thank Dr. Habil. Yudong Zhang for her critical reading and helpful suggestions. The author also thankfully acknowledges the National Natural Science Foundation of China (Grant No. 51801020), the Fundamental Research Funds for the Central Universities (Grant No. N2002005, N2002021), the 111 Project of China (Grant No. BP0719037, B20029), Analytical and Testing Center, Northeastern University, China, LEM3 laboratory, UMR CNRS 7239, Metz, Université de Lorraine, France, and the Heinz Maier-Leibnitz Zentrum, Garching, Germany.

REFERENCES

Abematsu, K., Umetsu, R. Y., Kainuma, R., Kanomata, T., Watanabe, K., and Koyama, K. (2014). Structural and Magnetic Properties of Magnetic Shape Memory Alloy $Ni_{46}Mn_{41}In_{13}$ under Magnetic Fields. *Mater. Trans.* 55, 477–481. doi:10.2320/matertrans.M2013372

Acet, M., Mañosa, L., and Planes, A. (2011). Magnetic-Field-Induced Effects in Martensitic Heusler-Based Magnetic Shape Memory Alloys. *Handbook Magn. Mater.* 19, 231–289. doi:10.1016/b978-0-444-53780-5.00004-1

Bachaga, T., Zhang, J., Khitouni, M., and Sunol, J. J. (2019). NiMn-based Heusler Magnetic Shape Memory Alloys: a Review. *Int. J. Adv. Manuf. Technol.* 103, 2761–2772. doi:10.1007/s00170-019-03534-3

Bai, J., Liu, D., Gu, J., Jiang, X., Liang, X., Guan, Z., et al. (2021). Excellent Mechanical Properties and Large Magnetocaloric Effect of Spark Plasma Sintered Ni-Mn-In-Co alloy. *J. Mater. Sci. Tech.* 74, 46–51. doi:10.1016/j.jmst.2020.10.011

Bain, E. C., and Dunkirk, N. (1924). The Nature of Martensite. *Trans. AIME* 70, 25–47.

Barua, R., Taheri, P., Chen, Y., Koblischka-Veneva, A., Koblischka, M., Jiang, L., et al. (2018). Giant Enhancement of Magnetostrictive Response in Directionally-Solidified $Fe_{83}Ga_{17}Er_x$ Compounds. *Materials* 11, 1039. doi:10.3390/ma11061039

Bechtold, C., Chluba, C., Lima de Miranda, R., and Quandt, E. (2012). High Cyclic Stability of the Elastocaloric Effect in Sputtered TiNiCu Shape Memory Films. *Appl. Phys. Lett.* 101, 091903. doi:10.1063/1.4748307

Brown, G. V. (1976). Magnetic Heat Pumping Near Room Temperature. *J. Appl. Phys.* 47, 3673–3680. doi:10.1063/1.323176

Brown, L. C. (1981). The Thermal Effect in Pseudoelastic Single Crystals of β-CuZnSn. *Mta* 12, 1491–1494. doi:10.1007/bf02643695

Brown, P. J., Bargawi, A. Y., Crangle, J., Neumann, K.-U., and Ziebeck, K. R. A. (1999). Direct Observation of a Band Jahn-Teller Effect in the Martensitic Phase Transition of Ni_2MnGa. *J. Phys. Condens. Matter* 11, 4715–4722. doi:10.1088/0953-8984/11/24/312

Brown, P. J., Crangle, J., Kanomata, T., Matsumoto, M., Neumann, K.-U., Ouladdiaf, B., et al. (2002). The crystal Structure and Phase Transitions of the Magnetic Shape Memory Compound Ni_2MnGa. *J. Phys. Condens. Matter* 14, 10159–10171. doi:10.1088/0953-8984/14/43/313

Bruno, N. M., Wang, S., Karaman, I., and Chumlyakov, Y. I. (2017). Reversible Martensitic Transformation under Low Magnetic Fields in Magnetic Shape Memory Alloys. *Sci. Rep.* 7, 40434. doi:10.1038/srep40434

Bunshah, R., and Mehl, R. (1953). Rate of Propagation of Martensite. *Trans. Am. Inst. Mining Metallurgical Eng.* 197, 1251–1258.

Camarillo, J.-P., Aguilar-Ortiz, C.-O., Flores-Zúñiga, H., Ríos-Jara, D., Soto-Parra, D.-E., Stern-Taulats, E., et al. (2017). Large and Reversible Elastocaloric Effect Near Room Temperature in a Ga-doped Ni-Mn-In Metamagnetic Shape-Memory alloy. *Funct. Mater. Lett.* 10, 1740007. doi:10.1142/s1793604717400070

Camarillo, J.-P., Stern-Taulats, E., Mañosa, L., Flores-Zúñiga, H., Ríos-Jara, D., and Planes, A. (2016). Expanding the Magnetocaloric Operation Range in Ni-Mn-In Heusler Alloys by Cu-Doping. *J. Phys. D: Appl. Phys.* 49, 125006. doi:10.1088/0022-3727/49/12/125006

Cazorla, C. (2019). Novel Mechanocaloric Materials for Solid-State Cooling Applications. *Appl. Phys. Rev.* 6, 041316. doi:10.1063/1.5113620

Chen, L., Hu, F. X., Wang, J., Bao, L. F., Sun, J. R., Shen, B. G., et al. (2012). Magnetoresistance and Magnetocaloric Properties Involving strong Metamagnetic Behavior in Fe-Doped $Ni_{45}(Co_{1-x}Fe_x)_5Mn_{36.6}In_{13.4}$ Alloys. *Appl. Phys. Lett.* 101, 957. doi:10.1063/1.4732525

Chen, X., Srivastava, V., Dabade, V., and James, R. D. (2013). Study of the Cofactor Conditions: Conditions of Supercompatibility between Phases. *J. Mech. Phys. Sol.* 61, 2566–2587. doi:10.1016/j.jmps.2013.08.004

Cheng, P., Zhou, Z., Chen, J., Li, Z., Yang, B., Xu, K., et al. (2021). Combining Magnetocaloric and Elastocaloric Effects in a $Ni_{45}Co_5Mn_{37}In_{13}$ alloy. *J. Mater. Sci. Tech.* 94, 47–52. doi:10.1016/j.jmst.2021.02.071

Chluba, C., Ge, W., Lima de Miranda, R., Strobel, J., Kienle, L., Quandt, E., et al. (2015). Ultralow-fatigue Shape Memory alloy Films. *Science* 348, 1004–1007. doi:10.1126/science.1261164

Christian, J. W. (2002). *The Theory of Transformations in Metals and Alloys*. London: Pergamon Press.

Cong, D., Xiong, W., Planes, A., Ren, Y., Mañosa, L., Cao, P., et al. (2019). Colossal Elastocaloric Effect in Ferroelastic Ni-Mn-Ti Alloys. *Phys. Rev. Lett.* 122, 255703. doi:10.1103/PhysRevLett.122.255703

Crouïgneau, G., Porcar, L., Courtois, P., Pairis, S., Mossang, E., Eyraud, E., et al. (2015). Annealing Effect on the Magnetic Induced Austenite Transformation in Polycrystalline Freestanding Ni-Co-Mn-In Films Produced by Co-sputtering. *J. Appl. Phys.* 117, 035302. doi:10.1063/1.4906224

Cui, J., Wu, Y., Muehlbauer, J., Hwang, Y., Radermacher, R., Fackler, S., et al. (2012). Demonstration of High Efficiency Elastocaloric Cooling with Large ΔT Using NiTi Wires. *Appl. Phys. Lett.* 101, 073904. doi:10.1063/1.4746257

Della Porta, F. (2019). On the Cofactor Conditions and Further Conditions of Supercompatibility between Phases. *J. Mech. Phys. Sol.* 122, 27–53. doi:10.1016/j.jmps.2018.08.012

Devi, P., Singh, S., Dutta, B., Manna, K., D'Souza, S. W., Ikeda, Y., et al. (2018). Adaptive Modulation in the $Ni_2Mn_{1.4}In_{0.6}$ Magnetic Shape-Memory Heusler alloy. *Phys. Rev. B* 97, 224102. doi:10.1103/PhysRevB.97.224102

Dwevedi, S., and Tiwari, B. (2012). Martensitic Transformations and Magnetocaloric Effect in Sn-Doped NiMnIn Shape Memory alloy. *J. Alloys Comp.* 540, 16–20. doi:10.1016/j.jallcom.2012.06.057

Erkartal, B., Duppel, V., Niemann, R., Schultz, L., Fähler, S., Schürmann, U., et al. (2012). Structure and Composition of Magnetocaloric Ni-Mn-In-Co Thin Films on the Nanoscale-A TEM Study. *Adv. Eng. Mater.* 14, 710–715. doi:10.1002/adem.201200072

Feng, Y., Sui, J. H., Gao, Z. Y., Dong, G. F., and Cai, W. (2009). Microstructure, Phase Transitions and Mechanical Properties of $Ni_{50}Mn_{34}In_{16-y}Co_y$ Alloys. *J. Alloys Comp.* 476, 935–939. doi:10.1016/j.jallcom.2008.09.149

Feng, Y., Sui, J. H., Wang, H. B., and Cai, W. (2012). Reversible Magnetic-Field-Induced Phase Transformation and Magnetocaloric Effect above Room Temperature in a Ni-Mn-In-Fe Polycrystal. *J. Magnetism Magn. Mater.* 324, 1982–1984. doi:10.1016/j.jmmm.2012.01.041

Giauque, W. F., and Macdougall, D. P. (1933). Attainment of Temperatures below 1° Absolute by Demagnetization of $Gd_2(SO_4)_3{\cdot}8H_2O$. *Phys. Rev.* 43, 768. doi:10.1103/physrev.43.768

Goetzler, W., Zogg, R., Young, J., and Johnson, C. (2014). *Energy Savings Potential and RD&D Opportunities for Non-vapor-compression HVAC Technologies*. USA: US Department of Energy, Office of Energy Efficiency and Renewable Energy, Building Technologies Office.

Gong, Y.-Y., Wang, D.-H., Cao, Q.-Q., Liu, E.-K., Liu, J., and Du, Y.-W. (2015). Electric Field Control of the Magnetocaloric Effect. *Adv. Mater.* 27, 801–805. doi:10.1002/adma.201404725

Gottschall, T., Gràcia-Condal, A., Fries, M., Taubel, A., Pfeuffer, L., Mañosa, L., et al. (2018). A Multicaloric Cooling Cycle that Exploits thermal Hysteresis. *Nat. Mater* 17, 929–934. doi:10.1038/s41563-018-0166-6

Gottschall, T., Skokov, K. P., Fries, M., Taubel, A., Radulov, I., Scheibel, F., et al. (2019). Making a Cool Choice: The Materials Library of Magnetic Refrigeration. *Adv. Energ. Mater.* 9, 1901322. doi:10.1002/aenm.201901322

Gottschall, T., Skokov, K. P., Frincu, B., and Gutfleisch, O. (2015). Large Reversible Magnetocaloric Effect in Ni-Mn-In-Co. *Appl. Phys. Lett.* 106, 021901. doi:10.1063/1.4905371

Gràcia-Condal, A., Gottschall, T., Pfeuffer, L., Gutfleisch, O., Planes, A., and Mañosa, L. (2020). Multicaloric Effects in Metamagnetic Heusler Ni-Mn-In under Uniaxial Stress and Magnetic Field. *Appl. Phys. Rev.* 7, 041406. doi:10.1063/5.0020755

Guillou, F., Courtois, P., Porcar, L., Plaindoux, P., Bourgault, D., and Hardy, V. (2012). Calorimetric Investigation of the Magnetocaloric Effect in $Ni_{45}Co_5Mn_{37.5}In_{12.5}$. *J. Phys. D: Appl. Phys.* 45, 255001. doi:10.1088/0022-3727/45/25/255001

Han, Z. D., Wang, D. H., Zhang, C. L., Tang, S. L., Gu, B. X., and Du, Y. W. (2006). Large Magnetic Entropy Changes in the $Ni_{45.4}Mn_{41.5}In_{13.1}$ Ferromagnetic Shape Memory alloy. *Appl. Phys. Lett.* 89, 182507. doi:10.1063/1.2385147

Han, Z. D., Wang, D. H., Zhang, C. L., Xuan, H. C., Zhang, J. R., Gu, B. X., et al. (2008). The Phase Transitions, Magnetocaloric Effect, and Magnetoresistance in Co Doped Ni-Mn-Sb Ferromagnetic Shape Memory Alloys. *J. Appl. Phys.* 104, 053906. doi:10.1063/1.2975146

Harris, V. G., and Chen, Y. (2015). Equilibrium Chemical Disorder at the Surface of a Single-Crystal $C1_b$ NiMnSb Half-Heusler Alloy: Implications for Spintronics. *IEEE Magn. Lett.* 6, 1–4. doi:10.1109/lmag.2015.2476778

Hashimoto, T., Kuzuhara, T., Matsumoto, K., Sahashi, M., Inomata, K., Tomokiyo, A., et al. (1987). Investigation of the Magnetic Refrigerant for the Ericsson Magnetic Refrigerator. *Jpn. J. Appl. Phys.* 26, 1673. doi:10.7567/jjaps.26s3.1673

Henández-Navarro, F., Camarillo-Garcia, J. P., Aguilar-Ortiz, C. O., Flores-Zúñiga, H., Ríos, D., González, J. G., et al. (2018). The Influence of Texture on the Reversible Elastocaloric Effect of a Polycrystalline $Ni_{50}Mn_{32}In_{16}Cr_2$ alloy. *Appl. Phys. Lett.* 112, 164101.

Heusler, O. (1934). Kristallstruktur und Ferromagnetismus der Mangan-Aluminium-Kupferlegierungen. *Ann. Phys.* 411, 155–201. doi:10.1002/andp.19344110205

Hu, F.-X., Shen, B.-G., and Sun, J.-R. (2013). Magnetic Entropy Change Involving Martensitic Transition in NiMn-Based Heusler Alloys. *Chin. Phys. B* 22, 037505. doi:10.1088/1674-1056/22/3/037505

Hu, Y., Li, Z., Yang, B., Qian, S., Gan, W., Gong, Y., et al. (2017). Combined Caloric Effects in a Multiferroic Ni-Mn-Ga alloy with Broad Refrigeration Temperature Region. *APL Mater.* 5, 046103. doi:10.1063/1.4980161

Huang, L., Cong, D. Y., Ma, L., Nie, Z. H., Wang, Z. L., Suo, H. L., et al. (2016). Large Reversible Magnetocaloric Effect in a Ni-Co-Mn-In Magnetic Shape Memory alloy. *Appl. Phys. Lett.* 108, 032405. doi:10.1063/1.4940441

Huang, X.-M., Wang, L.-D., Liu, H.-X., Yan, H.-L., Jia, N., Yang, B., et al. (2019). Correlation between Microstructure and Martensitic Transformation, Mechanical Properties and Elastocaloric Effect in Ni-Mn-Based Alloys. *Intermetallics* 113, 106579. doi:10.1016/j.intermet.2019.106579

Huang, X.-M., Zhao, Y., Yan, H.-L., Jia, N., Tang, S., Bai, J., et al. (2020). A Multielement Alloying Strategy to Improve Elastocaloric and Mechanical Properties in Ni-Mn-Based Alloys via Copper and boron. *Scripta Materialia* 185, 94–99. doi:10.1016/j.scriptamat.2020.04.001

Huang, X.-M., Zhao, Y., Yan, H.-L., Jia, N., Yang, B., Li, Z., et al. (2021). Giant Magnetoresistance, Magnetostrain and Magnetocaloric Effects in a Cu-Doped-Textured $Ni_{45}Co_5Mn_{36}In_{13.2}Cu_{0.8}$ Polycrystalline alloy. *J. Alloys Comp.* 889, 161652. doi:10.1016/j.jallcom.2021.161652

Huang, Y. J., Hu, Q. D., Bruno, N. M., Chen, J.-H., Karaman, I., Ross, J. H., et al. (2015). Giant Elastocaloric Effect in Directionally Solidified Ni-Mn-In Magnetic Shape Memory alloy. *Scripta Materialia* 105, 42–45. doi:10.1016/j.scriptamat.2015.04.024

Ito, W., Imano, Y., Kainuma, R., Sutou, Y., Oikawa, K., and Ishida, K. (2007). Martensitic and Magnetic Transformation Behaviors in Heusler-type NiMnIn and NiCoMnIn Metamagnetic Shape Memory Alloys. *Metall. Mat Trans. A.* 38, 759–766. doi:10.1007/s11661-007-9094-9

Ito, W., Nagasako, M., Umetsu, R. Y., Kainuma, R., Kanomata, T., and Ishida, K. (2008). Atomic Ordering and Magnetic Properties in the $Ni_{45}Co_5Mn_{36.7}In_{13.3}$ Metamagnetic Shape Memory alloy. *Appl. Phys. Lett.* 93, 232503. doi:10.1063/1.3043456

Jiang, L., Yang, J., Hao, H., Zhang, G., Wu, S., Chen, Y., et al. (2013). Giant Enhancement in the Magnetostrictive Effect of FeGa Alloys Doped with Low Levels of Terbium. *Appl. Phys. Lett.* 102, 222409. doi:10.1063/1.4809829

Kabirifar, P., Žerovnik, A., Ahčin, Ž., Porenta, L., Brojan, M., and Tušek, J. (2019). Elastocaloric Cooling: State-Of-The-Art and Future Challenges in Designing Regenerative Elastocaloric Devices. *SV-JME* 65, 615–630. doi:10.5545/sv-jme.2019.6369

Kainuma, R., Imano, Y., Ito, W., Sutou, Y., Morito, H., Okamoto, S., et al. (2006). Magnetic-field-induced Shape Recovery by Reverse Phase Transformation. *Nature* 439, 957–960. doi:10.1038/nature04493

Kainuma, R., Oikawa, K., Ito, W., Sutou, Y., Kanomata, T., and Ishida, K. (2008). Metamagnetic Shape Memory Effect in NiMn-Based Heusler-type Alloys. *J. Mater. Chem.* 18, 1837. doi:10.1039/b713947k

Karaca, H. E., Karaman, I., Basaran, B., Lagoudas, D. C., Chumlyakov, Y. I., and Maier, H. J. (2007). On the Stress-Assisted Magnetic-Field-Induced Phase Transformation in Ni_2MnGa Ferromagnetic Shape Memory Alloys. *Acta Materialia* 55, 4253–4269. doi:10.1016/j.actamat.2007.03.025

Karaca, H. E., Karaman, I., Basaran, B., Ren, Y., Chumlyakov, Y. I., and Maier, H. J. (2009). Magnetic Field-Induced Phase Transformation in NiMnCoIn Magnetic Shape-Memory Alloys-A New Actuation Mechanism with Large Work Output. *Adv. Funct. Mater.* 19, 983–998. doi:10.1002/adfm.200801322

Karaca, H., Karaman, I., Basaran, B., Chumlyakov, Y., and Maier, H. (2006). Magnetic Field and Stress Induced Martensite Reorientation in NiMnGa Ferromagnetic Shape Memory alloy Single Crystals. *Acta Materialia* 54, 233–245. doi:10.1016/j.actamat.2005.09.004

Kihara, T., Xu, X., Ito, W., Kainuma, R., and Tokunaga, M. (2014). Direct Measurements of Inverse Magnetocaloric Effects in Metamagnetic Shape-Memory alloy NiCoMnIn. *Phys. Rev. B* 90, 214409. doi:10.1103/PhysRevB.90.214409

Kitanovski, A., and Egolf, P. W. (2009). Application of Magnetic Refrigeration and its Assessment. *J. Magnetism Magn. Mater.* 321, 777–781. doi:10.1016/j.jmmm.2008.11.078

Kocks, U. F., Tome, C. N., Wenk, H. R., and Mecking, H. (1998). *Texture and Anisotropy: Preferred Orientations in Polycrystals and Their Effect on Materials Properties*. Cambridge University Press.

Krenke, T., Acet, M., Wassermann, E. F., Moya, X., Mañosa, L., and Planes, A. (2006). Ferromagnetism in the Austenitic and Martensitic States ofNi–Mn–Inalloys. *Phys. Rev. B* 73. doi:10.1103/PhysRevB.73.174413

Krenke, T., Duman, E., Acet, M., Wassermann, E. F., Moya, X., Mañosa, L., et al. (2007). Magnetic Superelasticity and Inverse Magnetocaloric Effect in Ni-Mn-In. *Phys. Rev. B* 75, 4414. doi:10.1103/physrevb.75.104414

Krenke, T., Duman, E., Acet, M., Wassermann, E. F., Moya, X., Mañosa, L., et al. (2005). Inverse Magnetocaloric Effect in Ferromagnetic Ni-Mn-Sn Alloys. *Nat. Mater* 4, 450–454. doi:10.1038/nmat1395

Kurfiß, M., and Schultz, F. (1930). *Over the Mechanisms of Steel Hardening*, 290–291.

Kurfiß, M., Schultz, F., Anton, R., Meier, G., von Sawilski, L., and Kötzler, J. (2005). Structural and Magnetic Properties of Ni_2MnIn Heusler alloy Films. *J. Magnetism Magn. Mater.* 290, 591–594. doi:10.1016/j.jmmm.2004.11.272

Kustov, S., Corró, M. L., Pons, J., and Cesari, E. (2009). Entropy Change and Effect of Magnetic Field on Martensitic Transformation in a Metamagnetic Ni-Co-Mn-In Shape Memory alloy. *Appl. Phys. Lett.* 94, 191901. doi:10.1063/1.3130229

Li, L., and Yan, M. (2020). Recent Progresses in Exploring the Rare Earth Based Intermetallic Compounds for Cryogenic Magnetic Refrigeration. *J. Alloys Comp.* 823, 153810. doi:10.1016/j.jallcom.2020.153810

Li, Z. B., Zhang, Y. D., Esling, C., Zhao, X., and Zuo, L. (2011a). Determination of the Orientation Relationship between Austenite and Incommensurate 7M Modulated Martensite in Ni-Mn-Ga Alloys. *Acta Materialia* 59, 2762–2772. doi:10.1016/j.actamat.2011.01.015

Li, Z., Dong, S., Li, Z., Yang, B., Liu, F., Sánchez-Valdés, C. F., et al. (2019a). Giant Low-Field Magnetocaloric Effect in Si Alloyed Ni-Co-Mn-In Alloys. *Scripta Materialia* 159, 113–118. doi:10.1016/j.scriptamat.2018.09.029

Li, Z., Jing, C., Zhang, H. L., Yu, D. H., Chen, L., Kang, B. J., et al. (2010). A Large and Reproducible Metamagnetic Shape Memory Effect in Polycrystalline $Ni_{45}Co_5Mn_{37}In_{13}$ Heusler alloy. *J. Appl. Phys.* 108, 113908. doi:10.1063/1.3516487

Li, Z., Li, Z., Li, D., Yang, J., Yang, B., Hu, Y., et al. (2020). Achieving a Broad Refrigeration Temperature Region through the Combination of Successive Caloric Effects in a Multiferroic $Ni_{50}Mn_{35}In_{15}$ alloy. *Acta Materialia* 192, 52–59. doi:10.1016/j.actamat.2020.03.043

Li, Z., Li, Z., Li, D., Yang, J., Yang, B., Wang, D., et al. (2019c). Influence of Austenite Ferromagnetism on the Elastocaloric Effect in a $Ni_{44.9}Co_{4.9}Mn_{36.9}In_{13.3}$ Metamagnetic Shape Memory alloy. *Appl. Phys. Lett.* 115, 083903. doi:10.1063/1.5114997

Li, Z., Li, Z., Yang, B., Zhao, X., and Zuo, L. (2018). Giant Low-Field Magnetocaloric Effect in a Textured $Ni_{45.3}Co_{5.1}Mn_{36.1}In_{13.5}$ alloy. *Scripta Materialia* 151, 61–65. doi:10.1016/j.scriptamat.2018.03.043

Li, Z., Xu, K., Yang, H. M., Zhang, Y. L., and Jing, C. (2015). Magnetostrain and Magnetocaloric Effect by Field-Induced Reverse Martensitic Transformation for Pd-Doped $Ni_{45}Co_5Mn_{37}In_{13}$ Heusler alloy. *J. Appl. Phys.* 117, 223904. doi:10.1063/1.4922579

Li, Z., Yang, J., Li, D., Li, Z., Yang, B., Yan, H., et al. (2019b). Tuning the Reversible Magnetocaloric Effect in Ni-Mn-In-Based Alloys through Co and Cu Co-Doping. *Adv. Electron. Mater.* 5, 1800845. doi:10.1002/aelm.201800845

Li, Z., Zhang, Y., Esling, C., Zhao, X., and Zuo, L. (2011b). Determination of the Orientation Relationship between Austenite and 5M Modulated Martensite in Ni-Mn-Ga Alloys. *J. Appl. Cryst.* 44, 1222–1226. doi:10.1107/S0021889811043366

Liang, X., Bai, J., Guan, Z., Gu, J., Yan, H., Zhang, Y., et al. (2021). Revealing the Role of Site Occupation in Phase Stability, Magnetic and Electronic Properties of Ni-Mn-In Alloys by Ab Initio Approach. *J. Mater. Sci. Tech.* 83, 90–101. doi:10.1016/j.jmst.2020.12.040

Lin, C., Yan, H., Zhang, Y., Esling, C., Zhao, X., and Zuo, L. (2016). Crystal Structure of Modulated Martensite and Crystallographic Correlations between Martensite Variants of $Ni_{50}Mn_{38}Sn_{12}$ alloy. *J. Appl. Cryst.* 49, 1276–1283. doi:10.1107/S1600576716010372

Lin, J., Tong, P., Zhang, X., Wang, Z., Zhang, Z., Li, B., et al. (2020). Giant Room-Temperature Barocaloric Effect at the Electronic Phase Transition in $Ni_{1-x}Fe_xS$. *Mater. Horiz.* 7, 2690–2695. doi:10.1039/C9MH01976F

Liu, G. D., Dai, X. F., Yu, S. Y., Zhu, Z. Y., Chen, J. L., Wu, G. H., et al. (2006). Physical and Electronic Structure and Magnetism of Mn_2NiGa: Experiment and Density-Functional Theory Calculations. *Phys. Rev. B* 74. doi:10.1103/physrevb.74.054435

Liu, J., Aksoy, S., Scheerbaum, N., Acet, M., and Gutfleisch, O. (2009a). Large Magnetostrain in Polycrystalline Ni–Mn–In–Co. *Appl. Phys. Lett.* 95, 1746. doi:10.1063/1.3249585

Liu, J., Gottschall, T., Skokov, K. P., Moore, J. D., and Gutfleisch, O. (2012). Giant Magnetocaloric Effect Driven by Structural Transitions. *Nat. Mater* 11, 620–626. doi:10.1038/nmat3334

Liu, J., Scheerbaum, N., Hinz, D., and Gutfleisch, O. (2008). Magnetostructural Transformation in Ni-Mn-In-Co Ribbons. *Appl. Phys. Lett.* 92, 162509. doi:10.1063/1.2913162

Liu, J., Woodcock, T. G., Scheerbaum, N., and Gutfleisch, O. (2009b). Influence of Annealing on Magnetic Field-Induced Structural Transformation and Magnetocaloric Effect in Ni-Mn-In-Co Ribbons. *Acta Materialia* 57, 4911–4920. doi:10.1016/j.actamat.2009.06.054

Liu, J., Zhao, D., and Li, Y. (2017). Exploring Magnetic Elastocaloric Materials for Solid-State Cooling. *Shap. Mem. Superelasticity* 3, 192–198. doi:10.1007/s40830-017-0118-z

Liu, X., Raulot, J.-M., Esling, C., Zhao, X., and Zuo, L. (2020). Investigation on the Preference of the Martensitic Structure in Off-Stoichiometric Ni-Mn-In Alloys by First-Principle Calculations. *J. Magnetism Magn. Mater.* 514, 167194. doi:10.1016/j.jmmm.2020.167194

Liu, Z. H., Aksoy, S., and Acet, M. (2009c). Influence of Sb on the Magnetic and Magnetocaloric Properties of Ferromagnetic Shape Memory alloy NiMnIn. *J. Appl. Phys.* 105, 033913. doi:10.1063/1.3075821

Lu, B., and Liu, J. (2017). Elastocaloric Effect and Superelastic Stability in Ni-Mn-In-Co Polycrystalline Heusler Alloys: Hysteresis and Strain-Rate Effects. *Sci. Rep.* 7, 1–11. doi:10.1038/s41598-017-02300-3

Lu, B., Xiao, F., Yan, A., and Liu, J. (2014). Elastocaloric Effect in a Textured Polycrystalline Ni-Mn-In-Co Metamagnetic Shape Memory alloy. *Appl. Phys. Lett.* 105, 161905. doi:10.1063/1.4899147

Lu, B., Zhang, P., Xu, Y., Sun, W., and Liu, J. (2015). Elastocaloric Effect in $Ni_{45}Mn_{36.4}In_{13.6}Co_5$ Metamagnetic Shape Memory Alloys under Mechanical Cycling. *Mater. Lett.* 148, 110–113. doi:10.1016/j.matlet.2015.02.076

Luo, Q., and Wang, W. H. (2009). Rare Earth Based Bulk Metallic Glasses. *J. Non-Crystalline Sol.* 355, 759–775. doi:10.1016/j.jnoncrysol.2009.02.006

Mañosa, L., González-Alonso, D., Planes, A., Bonnot, E., Barrio, M., Tamarit, J.-L., et al. (2010). Giant Solid-State Barocaloric Effect in the Ni-Mn-In Magnetic Shape-Memory alloy. *Nat. Mater* 9, 478–481. doi:10.1038/nmat2731

Mañosa, L., Gonzalez-Comas, A., Obradó, E., Planes, A., Chernenko, V., Kokorin, V., et al. (1997). Anomalies Related to the TA_2-Phonon-Mode Condensation in the Heusler Ni_2MnGa alloy. *Phys. Rev. B* 55, 11068.

Mañosa, L., and Planes, A. (2017). Materials with Giant Mechanocaloric Effects: Cooling by Strength. *Adv. Mater.* 29, 1603607. doi:10.1002/adma.201603607

McMichael, R. D., Ritter, J. J., and Shull, R. D. (1993). Enhanced Magnetocaloric Effect in $Gd_3Ga_{5-x}Fe_xO_{12}$. *J. Appl. Phys.* 73, 6946–6948. doi:10.1063/1.352443

Monroe, J. A., Karaman, I., Basaran, B., Ito, W., Umetsu, R. Y., Kainuma, R., et al. (2012). Direct Measurement of Large Reversible Magnetic-Field-Induced Strain in Ni-Co-Mn-In Metamagnetic Shape Memory Alloys. *Acta Materialia* 60, 6883–6891. doi:10.1016/j.actamat.2012.07.040

Moya, X., Kar-Narayan, S., and Mathur, N. D. (2014). Caloric Materials Near Ferroic Phase Transitions. *Nat. Mater* 13, 439–450. doi:10.1038/nmat3951

Mukherjee, K. (1968). On the Dynamics of Martensitic Transformation. *Trans. Met. Soc. AIME* 242, 1494–1501.

Murray, S. J., Marioni, M., Allen, S. M., O'Handley, R. C., and Lograsso, T. A. (2000). 6% Magnetic-Field-Induced Strain by Twin-Boundary Motion in Ferromagnetic Ni–Mn–Ga. *Appl. Phys. Lett.* 77, 886–888.

Nikitin, S. A. (2011). Magnetoelastic and Elastocaloric Effects in Rare-Earth Metals, Their Alloys and Compounds in the Region of Magnetic Phase Transitions, *Mosc. Univ. Phys.*, 66. 519–533. Their Alloys and Compounds in the Region of Magnetic Phase Transitions. doi:10.3103/s0027134911060130

Nirmala, R., Morozkin, A. V., and Malik, S. K. (2015). Magnetocaloric Effect in Rare-Earth Intermetallics: Recent Trends. *Pramana - J. Phys.* 84, 977–985. doi:10.1007/s12043-015-1000-1

Nishiyama, Z. (1978). *Martensitic Transformation*. New York: Academic Press.

Nishiyama, Z. (1934). X-ray Investigation of the Mechanism of the Transformation from Face Centered Cubic Lattice to Body Centered Cubic. *Sci. Rep. Tohoku Univ.* 23, 637.

Paramanik, T., and Das, I. (2016). Near Room Temperature Giant Magnetocaloric Effect and Giant Negative Magnetoresistance in Co, Ga Substituted Ni-Mn-In Heusler alloy. *J. Alloys Comp.* 654, 399–403. doi:10.1016/j.jallcom.2015.09.096

Pataky, G. J., Ertekin, E., and Sehitoglu, H. (2015). Elastocaloric Cooling Potential of NiTi, Ni_2FeGa, and CoNiAl. *Acta Materialia* 96, 420–427. doi:10.1016/j.actamat.2015.06.011

Pathak, A. K., Dubenko, I., Pueblo, C., Stadler, S., and Ali, N. (2010). Magnetism and Magnetocaloric Effects in $Ni_{50}Mn_{35-x}Co_xIn_{15}$ Heusler Alloys. *J. Appl. Phys.* 107, 09A907. doi:10.1063/1.3335893

Pecharsky, V. K., and Gschneidner, Jr., K. A., Jr. (1997). Giant Magnetocaloric Effect in $Gd_5(Si_2Ge_2)$. *Phys. Rev. Lett.* 78, 4494–4497. doi:10.1103/PhysRevLett.78.4494

Pitsch, W. (1962). Der orientierungszusammenhang zwischen zementit und austenit. *Acta Metallurgica* 10, 897–900. doi:10.1016/0001-6160(62)90108-6

Planes, A., Obradó, E., Gonzàlez-Comas, A., and Mañosa, L. (1997). Premartensitic Transition Driven by Magnetoelastic Interaction in Bcc Ferromagnetic Ni_2MnGa. *Phys. Rev. Lett.* 79, 3926–3929. doi:10.1103/PhysRevLett.79.3926

Pons, J., Chernenko, V. A., Santamarta, R., and Cesari, E. (2000). Crystal Structure of Martensitic Phases in Ni-Mn-Ga Shape Memory Alloys. *Acta Materialia* 48, 3027–3038. doi:10.1016/s1359-6454(00)00130-0

Qian, S., Ling, J., Hwang, Y., Radermacher, R., and Takeuchi, I. (2015). Thermodynamics Cycle Analysis and Numerical Modeling of Thermoelastic Cooling Systems. *Int. J. Refrigeration* 56, 65–80. doi:10.1016/j.ijrefrig.2015.04.001

Raphael, M. P., Ravel, B., Huang, Q., Willard, M. A., Cheng, S. F., Das, B. N., et al. (2002). Presence of Antisite Disorder and its Characterization in the Predicted Half-metal Co_2MnSi. *Phys. Rev. B* 66, 104429. doi:10.1103/physrevb.66.104429

Ravel, B., Cross, J. O., Raphael, M. P., Harris, V. G., Ramesh, R., and Saraf, L. V. (2002a). Atomic Disorder in Heusler Co_2MnGe Measured by Anomalous X-ray Diffraction. *Appl. Phys. Lett.* 81, 2812–2814. doi:10.1063/1.1513216

Ravel, B., Raphael, M. P., Harris, V. G., and Huang, Q. (2002b). EXAFS and Neutron Diffraction Study of the Heusler alloy Co_2MnSi. *Phys. Rev. B* 65, 184431. doi:10.1103/physrevb.65.184431

Recarte, V., Pérez-Landazábal, J. I., Gómez-Polo, C., Sánchez-Alarcos, V., Cesari, E., and Pons, J. (2010). Vibrational and Magnetic Contributions to the Entropy Change Associated with the Martensitic Transformation of Ni-Fe-Ga

Ferromagnetic Shape Memory Alloys. *J. Phys. Condens. Matter* 22, 416001. doi:10.1088/0953-8984/22/41/416001

Recarte, V., Pérez-Landazábal, J. I., Sánchez-Alarcos, V., Zablotskii, V., Cesari, E., and Kustov, S. (2012). Entropy Change Linked to the Martensitic Transformation in Metamagnetic Shape Memory Alloys. *Acta Materialia* 60, 3168–3175. doi:10.1016/j.actamat.2012.02.022

Sakon, T., Yamazaki, S., Kodama, Y., Motokawa, M., Kanomata, T., Oikawa, K., et al. (2007). Magnetic Field-Induced Strain of Ni-Co-Mn-In Alloy in Pulsed Magnetic Field. *Jpn. J. Appl. Phys.* 46, 995–998. doi:10.1143/jjap.46.995

Sánchez-Alarcos, V., Pérez-Landazábal, J. I., Recarte, V., and Urdiaín, A. (2015). Effect of Ti Addition on the Mechanical Properties and the Magnetocaloric Effect of Ni-Mn-In Metamagnetic Shape Memory Alloys. *J. Phys. D: Appl. Phys.* 48, 445006. doi:10.1088/0022-3727/48/44/445006

Şaşıoğlu, E., Sandratskii, L. M., and Bruno, P. (2004). First-principles Calculation of the Intersublattice Exchange Interactions and Curie Temperatures of the Full Heusler alloys Ni_2MnX(X=Ga,In,Sn,Sb). *Phys. Rev. B* 70, 024427. doi:10.1103/PhysRevB.70.024427

Schmidt, M., Schütze, A., and Seelecke, S. (2015). Scientific Test Setup for Investigation of Shape Memory alloy Based Elastocaloric Cooling Processes. *Int. J. Refrigeration* 54, 88–97. doi:10.1016/j.ijrefrig.2015.03.001

Sharma, V. K., Chattopadhyay, M. K., Khandelwal, A., and Roy, S. B. (2010a). Martensitic Transition Near Room Temperature and the Temperature- and Magnetic-Field-Induced Multifunctional Properties of $Ni_{49}CuMn_{34}In_{16}$ alloy. *Phys. Rev. B* 82, 172411. doi:10.1103/PhysRevB.82.172411

Sharma, V. K., Chattopadhyay, M. K., and Roy, S. B. (2010b). Large Magnetocaloric Effect in $Ni_{50}Mn_{33.66}Cr_{0.34}In_{16}$ alloy. *J. Phys. D: Appl. Phys.* 43, 225001. doi:10.1088/0022-3727/43/22/225001

Sharma, V. K., Chattopadhyay, M. K., Sharath Chandra, L. S., and Roy, S. B. (2011). Elevating the Temperature Regime of the Large Magnetocaloric Effect in a Ni-Mn-In alloy towards Room Temperature. *J. Phys. D: Appl. Phys.* 44, 145002. doi:10.1088/0022-3727/44/14/145002

Shen, A., Sun, W., Zhao, D., and Liu, J. (2018). Influence of Cr on Microstructure and Elastocaloric Effect in Ni-Mn-In-Co-Cr Polycrystalline Alloys. *Phys. Lett. A* 382, 2876–2879. doi:10.1016/j.physleta.2018.06.022

Shen, Q., Zhao, D., Sun, W., Li, Y., and Liu, J. (2017). The Effect of Tb on Elastocaloric and Mechanical Properties of Ni-Mn-In-Tb Alloys. *J. Alloys Comp.* 696, 538–542. doi:10.1016/j.jallcom.2016.11.290

Song, Y., Chen, X., Dabade, V., Shield, T. W., and James, R. D. (2013). Enhanced Reversibility and Unusual Microstructure of a Phase-Transforming Material. *Nature* 502, 85–88. doi:10.1038/nature12532

Stern-Taulats, E., Castán, T., Mañosa, L., Planes, A., Mathur, N. D., and Moya, X. (2018). Multicaloric Materials and Effects. *MRS Bull.* 43, 295–299. doi:10.1557/mrs.2018.72

Sutou, Y., Imano, Y., Koeda, N., Omori, T., Kainuma, R., Ishida, K., et al. (2004a). Magnetic and Martensitic Transformations of NiMnX(X=In,Sn,Sb) Ferromagnetic Shape Memory Alloys. *Appl. Phys. Lett.* 85, 4358. doi:10.1063/1.1808879

Sutou, Y., Imano, Y., Koeda, N., Omori, T., Kainuma, R., Ishida, K., et al. (2004b). Magnetic and Martensitic Transformations of NiMnX(X=In,Sn,Sb) Ferromagnetic Shape Memory Alloys. *Appl. Phys. Lett.* 85, 4358–4360. doi:10.1063/1.1808879

Tang, X., Feng, Y., Wang, H., and Wang, P. (2019). Enhanced Elastocaloric Effect and Cycle Stability in B and Cu Co-doping Ni-Mn-In Polycrystals. *Appl. Phys. Lett.* 114, 033901. doi:10.1063/1.5080762

Tegus, O., Brück, E., Zhang, L., Dagula, K., Buschow, K. H. J., and de Boer, F. R. (2002). Magnetic-phase Transitions and Magnetocaloric Effects. *Physica B: Condensed Matter* 319, 174–192. doi:10.1016/S0921-4526(02)01119-5

Turabi, A. S., Karaca, H. E., Tobe, H., Basaran, B., Aydogdu, Y., and Chumlyakov, Y. I. (2016). Shape Memory Effect and Superelasticity of NiMnCoIn Metamagnetic Shape Memory Alloys under High Magnetic Field. *Scripta Materialia* 111, 110–113. doi:10.1016/j.scriptamat.2015.08.027

Tušek, J., Engelbrecht, K., Eriksen, D., Dall'Olio, S., Tušek, J., and Pryds, N. (2016). A Regenerative Elastocaloric Heat Pump. *Nat. Energ.* 1. doi:10.1038/nenergy.2016.134

Tušek, J., Engelbrecht, K., Mikkelsen, L. P., and Pryds, N. (2015). Elastocaloric Effect of Ni-Ti Wire for Application in a Cooling Device. *J. Appl. Phys.* 117, 124901. doi:10.1063/1.4913878

Ullakko, K., Huang, J. K., Kantner, C., O'Handley, R. C., and Kokorin, V. V. (1996). Large Magnetic-field-induced Strains in Ni_2MnGa Single Crystals. *Appl. Phys. Lett.* 69, 1966–1968. doi:10.1063/1.117637

Ullakko, K., Huang, J. K., Kokorin, V. V., and O'Handley, R. C. (1997). Magnetically Controlled Shape Memory Effect in Ni_2MnGa Intermetallics. *Scripta Materialia* 36, 1133–1138. doi:10.1016/s1359-6462(96)00483-6

Van Smaalen, S. (1995). Incommensurate crystal Structures. *Crystallogr. Rev.* 4, 79–202. doi:10.1080/08893119508039920

Wang, J., Yu, Q., Xu, K., Zhang, C., Wu, Y., and Jiang, C. (2017). Large Room-Temperature Elastocaloric Effect of $Ni_{57}Mn_{18}Ga_{21}In_4$ alloy Undergoing a Magnetostructural Coupling Transition. *Scripta Materialia* 130, 148–151. doi:10.1016/j.scriptamat.2016.11.024

Wang, L., Li, Z., Yang, J., Yang, B., Zhao, X., and Zuo, L. (2020). Large Refrigeration Capacity in a $Ni_{48}Co_1Mn_{37}In_{14}$ Polycrystalline alloy with Low thermal Hysteresis. *Intermetallics* 125, 106888. doi:10.1016/j.intermet.2020.106888

Wang, Y. D., Ren, Y., Huang, E. W., Nie, Z. H., Wang, G., Liu, Y. D., et al. (2007). Direct Evidence on Magnetic-Field-Induced Phase Transition in a NiCoMnIn Ferromagnetic Shape Memory alloy under a Stress Field. *Appl. Phys. Lett.* 90, 101917. doi:10.1063/1.2712509

Wei, Z. Y., Liu, E. K., Li, Y., Han, X. L., Du, Z. W., Luo, H. Z., et al. (2016). Magnetostructural Martensitic Transformations with Large Volume Changes and Magneto-Strains in All-D-Metal Heusler Alloys. *Appl. Phys. Lett.* 109, 071904. doi:10.1063/1.4961382

Wiedemann, G. (1889). Magnetische Untersuchungen. *Ann. Phys.* 273, 610–628. doi:10.1002/andp.18892730806

Wirth, S., Leithe-Jasper, A., Vasil, A. N. E., and Coey, J. M. D. (1997). Structural and Magnetic Properties of Ni_2MnGa. *J. Magn. Magn. Mater.* 167. doi:10.1016/S0304-8853(96)00745-7

Yan, H.-L., Huang, X.-M., Yang, J.-H., Zhao, Y., Fang, F., Jia, N., et al. (2021a). A Strategy of Optimizing Magnetism and Hysteresis Simultaneously in Ni-Mn-Based Metamagnetic Shape Memory Alloys. *Intermetallics* 130, 107063. doi:10.1016/j.intermet.2020.107063

Yan, H.-L., Liu, H.-X., Huang, X.-M., Zhang, M.-J., Jia, N., Bai, J., et al. (2020a). First-principles Investigation of Mg Substitution for Ga on Martensitic Transformation, Magnetism and Electronic Structures in Ni_2MnGa. *J. Alloys Comp.* 843, 156049. doi:10.1016/j.jallcom.2020.156049

Yan, H.-L., Wang, L.-D., Liu, H.-X., Huang, X.-M., Jia, N., Li, Z.-B., et al. (2019). Giant Elastocaloric Effect and Exceptional Mechanical Properties in an All-D-Metal Ni-Mn-Ti alloy: Experimental and Ab-Initio Studies. *Mater. Des.* 184, 108180. doi:10.1016/j.matdes.2019.108180

Yan, H.-L., Zhang, Y., Esling, C., Zhao, X., and Zuo, L. (2021b). Determination of Strain Path during Martensitic Transformation in Materials with Two Possible Transformation Orientation Relationships from Variant Self-Organization. *Acta Materialia* 202, 112–123. doi:10.1016/j.actamat.2020.10.054

Yan, H.-L., Zhao, Y., Liu, H.-X., Zhang, M.-J., Zhang, H.-F., Bai, J., et al. (2020b). Ab-initio Revelation on the Origins of Ti Substitution for Ga, Mn and Ni on Ferromagnetism, Phase Stability and Elastic Properties in Ni_2MnGa. *J. Alloys Comp.* 821, 153481. doi:10.1016/j.jallcom.2019.153481

Yan, H., Yang, B., Zhang, Y., Li, Z., Esling, C., Zhao, X., et al. (2016a). Variant Organization and Mechanical Detwinning of Modulated Martensite in Ni-Mn-In Metamagnetic Shape-Memory Alloys. *Acta Materialia* 111, 75–84. doi:10.1016/j.actamat.2016.03.049

Yan, H., Yang, B., Zhang, Y., Li, Z., Esling, C., Zhao, X., et al. (2016b). Variant Organization and Mechanical Detwinning of Modulated Martensite in Ni-Mn-In Metamagnetic Shape-Memory Alloys. *Acta Materialia* 111, 75–84. doi:10.1016/j.actamat.2016.03.049

Yan, H., Zhang, C., Zhang, Y., Wang, X., Esling, C., Zhao, X., et al. (2016c). Crystallographic Insights into Ni-Co-Mn-In Metamagnetic Shape Memory Alloys. *J. Appl. Cryst.* 49, 1585–1592. doi:10.1107/s1600576716012140

Yan, H., Zhang, Y., Xu, N., Senyshyn, A., Brokmeier, H.-G., Esling, C., et al. (2015). Crystal Structure Determination of Incommensurate Modulated Martensite in Ni-Mn-In Heusler Alloys. *Acta Materialia* 88, 375–388. doi:10.1016/j.actamat.2015.01.025

Yan, H., Zhao, X., Jia, N., Zheng, Y., and He, T. (2014). Influence of Shear Banding on the Formation of Brass-type Textures in Polycrystalline Fcc Metals with Low Stacking Fault Energy. *J. Mater. Sci. Tech.* 30, 408–416. doi:10.1016/j.jmst.2013.11.010

Yang, S. Y., Liu, Y. D., Wang, C. P., Lu, Y., Wang, J. M., Shi, Z., et al. (2015). Microstructure and Functional Properties of Two-phase Ni-Mn-Fe-In Shape

Memory Alloys with Small Transformation Hysteresis Width. *J. Alloys Comp.* 619, 498–504. doi:10.1016/j.jallcom.2014.09.079

Yang, Y., Li, Z., Sánchez-Valdés, C. F., Sánchez Llamazares, J. L., Yang, B., Zhang, Y., et al. (2020). Phase Transformation and Magnetocaloric Effect of Co-doped Mn-Ni-In Melt-Spun Ribbons. *J. Appl. Phys.* 128, 055110. doi:10.1063/5.0014883

Yang, Z., Cong, D. Y., Huang, L., Nie, Z. H., Sun, X. M., Zhang, Q. H., et al. (2016). Large Elastocaloric Effect in a Ni-Co-Mn-Sn Magnetic Shape Memory alloy. *Mater. Des.* 92, 932–936. doi:10.1016/j.matdes.2015.12.118

Yang, Z., Cong, D. Y., Sun, X. M., Nie, Z. H., and Wang, Y. D. (2017). Enhanced Cyclability of Elastocaloric Effect in boron-microalloyed Ni-Mn-In Magnetic Shape Memory Alloys. *Acta Materialia* 127, 33–42. doi:10.1016/j.actamat.2017.01.025

Yang, Z., Cong, D., Yuan, Y., Wu, Y., Nie, Z., Li, R., et al. (2019). Ultrahigh Cyclability of a Large Elastocaloric Effect in Multiferroic Phase-Transforming Materials. *Mater. Res. Lett.* 7, 137–144. doi:10.1080/21663831.2019.1566182

Yu, B., Liu, M., Egolf, P. W., and Kitanovski, A. (2010). A Review of Magnetic Refrigerator and Heat Pump Prototypes Built before the Year 2010. *Int. J. Refrigeration* 33, 1029–1060. doi:10.1016/j.ijrefrig.2010.04.002

Yu, S. Y., Gu, A. J., Kang, S. S., Hu, S. J., Li, Z. C., Ye, S. T., et al. (2016). Large Reversible Magnetostrain in Polycrystalline $Ni_{50}Mn_{33}In_{17-x}Ga_x$. *J. Alloys Comp.* 681, 1–5. doi:10.1016/j.jallcom.2016.04.249

Yu, S. Y., Wei, J. J., Kang, S. S., Chen, J. L., and Wu, G. H. (2014). Large Temperature and Magnetic Field Induced Strain in Polycrystalline $Ni_{50}Mn_{36}In_{14-x}Sb_x$ Alloys. *J. Alloys Comp.* 586, 328–332. doi:10.1016/j.jallcom.2013.10.072

Zhang, C., Yan, H., Zhang, Y., Esling, C., Zhao, X., and Zuo, L. (2016). Crystal Structure and Crystallographic Characteristics of Martensite in $Ni_{50}Mn_{38}Sb_{12}$ Alloys. *J. Appl. Cryst.* 49, 513–519. doi:10.1107/S1600576716002296

Zhang, J., Xu, Y., An, S., Sun, Y., Li, X., and Li, Y. (2020). Giant Mechanocaloric Materials for Solid-State Cooling*. *Chin. Phys. B* 29, 076202. doi:10.1088/1674-1056/ab8a40

Zhang, X.-x., Miao, S.-p., and Sun, J.-f. (2014). Magnetocaloric Effect in Ni-Mn-In-Co Microwires Prepared by Taylor-Ulitovsky Method. *Trans. Nonferrous Met. Soc. China* 24, 3152–3157. doi:10.1016/s1003-6326(14)63454-3

Zhang, Y. D., Esling, C., Zhao, X., and Zuo, L. (2007). Indirect Two-Trace Method to Determine a Faceted Low-Energy Interface between Two Crystallographically Correlated Crystals. *J. Appl. Cryst.* 40, 436–440. doi:10.1107/s0021889807014331

Zhang, Y., Li, Z., Esling, C., Muller, J., Zhao, X., and Zuo, L. (2010). A General Method to Determine Twinning Elements. *J. Appl. Cryst.* 43, 1426–1430. doi:10.1107/s0021889810037180

Zhao, D., Liu, J., Chen, X., Sun, W., Li, Y., Zhang, M., et al. (2017a). Giant Caloric Effect of Low-Hysteresis Metamagnetic Shape Memory Alloys with Exceptional Cyclic Functionality. *Acta Materialia* 133, 217–223. doi:10.1016/j.actamat.2017.05.020

Zhao, D., Liu, J., Feng, Y., Sun, W., and Yan, A. (2017b). Giant Elastocaloric Effect and its Irreversibility in [001]-oriented $Ni_{45}Mn_{36.5}In_{13.5}Co_5$ Meta-Magnetic Shape Memory Alloys. *Appl. Phys. Lett.* 110, 021906. doi:10.1063/1.4973965

Zheludev, A., Shapiro, S. M., Wochner, P., and Tanner, L. E. (1996). Precursor Effects and Premartensitic Transformation in Ni_2MnGa. *Phys. Rev. B* 54, 15045–15050. doi:10.1103/physrevb.54.15045

Conflict of Interest: The authors declare that the research was conducted in the absence of any commercial or financial relationships that could be construed as a potential conflict of interest.

Publisher's Note: All claims expressed in this article are solely those of the authors and do not necessarily represent those of their affiliated organizations, or those of the publisher, the editors and the reviewers. Any product that may be evaluated in this article, or claim that may be made by its manufacturer, is not guaranteed or endorsed by the publisher.

frontiers in Materials

REVIEW
published: 14 March 2022
doi: 10.3389/fmats.2022.810575

Progress in the Use of Biosourced Phenolic Molecules for Electrode Manufacturing

Javier Quílez-Bermejo, Sara Pérez-Rodríguez, Alain Celzard and Vanessa Fierro**

Centre National de La Recherche Scientifique (CNRS), Institut Jean Lamour (IJL), Université de Lorraine, Épinal, France

In the era of renewable technologies and clean processes, carbon science must adapt to this new model of a green society. Carbon materials are often obtained from petroleum precursors through polluting processes that do not meet the requirements of sustainable and green chemistry. Biomass is considered the only renewable source for the production of carbon materials, as the carbon in biomass comes from the consumption of carbon dioxide from the atmosphere, resulting in zero net carbon dioxide emissions. In addition to being a green source of carbon materials, biomass has many advantages such as being a readily available, large and cheap feedstock, as well as the ability to create unique carbon-derived structures with well-developed porosity and heteroatom doping. All these positive aspects position biomass-derived carbon materials as attractive alternatives in multiple applications, from energy storage to electrocatalysis, *via* adsorption and biosensors, among others. This review focuses on the application of phenolic resins to the production of electrodes for energy storage and the slow but inexorable movement from petroleum-derived phenolic compounds to biosourced molecules (*i.e.*, lignins, tannins, etc.) as precursors for these carbon materials. Important perspectives and challenges for the design of these biosourced electrodes are discussed.

Keywords: biosourced, phenolic molecules, electrodes, carbon, energy storage

OPEN ACCESS

Edited by:
Liming Dai,
Case Western Reserve University, United States

Reviewed by:
Jun Maruyama,
Osaka Research Institute of Industrial Science and Technology, Japan
Noriko Yoshizawa,
National Institute of Advanced Industrial Science and Technology (AIST), Japan

****Correspondence:***
Vanessa Fierro
vanessa.fierro@univ-lorraine.fr
Javier Quílez-Bermejo
javier.quilez-bermejo@univ-lorraine.fr

Specialty section:
This article was submitted to Carbon-Based Materials, a section of the journal Frontiers in Materials

Received: *22 November 2021*
Accepted: *31 January 2022*
Published: *14 March 2022*

Citation:
Quílez-Bermejo J, Pérez-Rodríguez S, Celzard A and Fierro V (2022) Progress in the Use of Biosourced Phenolic Molecules for Electrode Manufacturing. Front. Mater. 9:810575. doi: 10.3389/fmats.2022.810575

INTRODUCTION

Most countries have signed the Paris Agreement on climate change, with the intention of avoiding a global temperature increase of 1.5°C above pre-industrial levels (Paris Agreement to the United Nations Framework Convention on Climate Change, 2015). According to the IPCC report (IPCC, 2021: Climate Change 2021), the risk of not being able to slow the rate of temperature increase would threaten human life and environmental health worldwide. This fact encourages society toward a governmental and social movement that involves net zero emissions in the coming years. This movement should also be accompanied by the growth of clean and renewable energy technologies. In this context, multiple green technologies have been presented as attractive alternatives to replace fossil fuel-based energy (Du and Li, 2019). Electrochemistry is at the forefront of this renewable movement since most of these technologies are based on electrochemical processes and reactions (Ganiyu and Martínez-Huitle, 2020). Fuel cells (Ganiyu and Martínez-Huitle, 2020; Sazali et al., 2020; Neatu et al., 2021), supercapacitors (Muzaffar et al., 2019; Pomerantseva et al., 2019; Poonam et al., 2019), batteries (Mauger et al., 2019; Xu et al., 2020; Liu et al., 2021) and electrolyzers (Abbasi et al., 2019; Brauns and Turek, 2020), among others, are electrochemical devices that are among the most innovative suppliers of energy and chemicals.

Carbon materials have been proposed as excellent low-cost electrodes for all these electrochemical devices due to their unique properties, such as high availability, large developed porosity, wide variety of pore size distributions, tunability of surface chemistry, high conductivity, excellent chemical and thermal stability, etc. (Quílez-Bermejo et al., 2020a; Castro-Gutierrez et al., 2020; Wu et al., 2020; Yin et al., 2020). Nevertheless, carbon materials chemistry, and carbon science in general, must adapt immediately to the rapid changes facing our society. Traditional methods of preparing carbon materials are often based on thermal processing of petrochemical precursors (Liu W.-J. et al., 2015; Titirici et al., 2015; Yahya et al., 2015; Ma et al., 2017; Lan et al., 2021). This is a huge problem because, despite their use in renewable technologies, most of the carbon electrodes in these devices are still produced from fossil fuels, which does not solve the problematic issue of polluting emissions. If the ultimate goal is to use technologies with fully environmentally friendly equipment, the renewable production of carbon materials is mandatory.

A branch of carbon science and technology involves the preparation of carbon materials from phenolic resins (Effendi et al., 2008; Celzard and Fierro, 2020; Szczesniak et al., 2020; Torres et al., 2021). Phenolic resins are synthetic polymeric compounds that are obtained from the condensation reaction of phenolic molecules with or without a crosslinking agent (Sarika et al., 2020). Such resins are excellent precursors for carbon materials since the selection of phenolic molecules and crosslinkers allows excellent control of the properties of the resulting carbon materials. Nevertheless, it is worth noting that phenolic precursors and crosslinkers are commonly obtained from petrochemical precursors that involve polluting processes (European Chemicals Agency, 2021a; European Chemicals Agency, 2021c; European Chemicals Agency, 2021d). Due to the high levels of pollution in recent years, new renewable alternatives have been proposed to replace petroleum precursors to produce carbon materials derived from phenolic molecules (Nieuwenhove et al., 2020; Sarika et al., 2020; Sternberg et al., 2021).

Biomass-derived carbon precursors are considered the only renewable carbon source since the carbon emissions released during thermal processing of biomass were previously consumed from the atmosphere during biomass growth (Forest Research 2021). This means that biomass absorbs anthropic carbon dioxide emissions while growing and releases them back into the atmosphere during carbon materials production. Therefore, the carbon cycle remains closed with zero net emissions while synthesizing a value-added product. This closed cycle can be very useful for preparing carbon materials derived from phenolic resins since the phenolic and crosslinking components can be found in nature as biomass feedstocks (Foyer et al., 2016; Nieuwenhove et al., 2020; Sarika et al., 2020; Sternberg et al., 2021). Biomass represents a large amount of natural reservoirs of carbon, including agricultural crops, plants, forest residues or materials, and industrial or domestic biowastes, among others. The nature, composition, structure and other features of these biosourced precursors have been widely detailed in extensive reviews (Jian et al., 2018; Li et al., 2019; Szczesniak et al., 2020).

In this review, we aim to summarize the most fundamental advances in the preparation of carbon electrodes from biosourced phenolic molecules in the quest for the non-dependence on fossil fuels. This review does not provide a detailed overview but shows the extensive possibilities of carbon materials derived from biosourced phenolic molecules as electrodes for energy storage and conversion applications.

Biosourced Precursors of Phenolic-Based Resins

Phenolic resins, of which the best known are phenol-formaldehyde resins, are primarily based on two main components: phenolic and aldehyde structural units. The phenolic units react with the crosslinkers in *ortho-* or *para-*position, leading to a condensed product, the phenolic resin, whose characteristics depend on phenol/aldehyde ratio, the phenol and aldehyde precursors and the synthesis conditions, in particular the pH (Grenier-Loustalot et al., 1994; Effendi et al., 2008). Regarding phenolic and aldehyde precursors, it is important to emphasize that phenol and formaldehyde are the most common raw materials for the preparation of phenolic resins.

The reaction mechanisms for the formation of phenol-formaldehyde resins have been extensively studied in the literature since their discovery in 1907, and multiple works can be found regarding the proposed mechanisms (Yeddanapalli and Francis, 1962; Grenier-Loustalot et al., 1994; Pilato, 2013). The first step of the mechanism is attributed to the formaldehyde substitution in *ortho-* or *para-*positions in the phenolic ring, leading to the possible formation of *mono-*, *di-*, and *tri-*functionalized phenol monomer, which is thought to be mainly related to the phenol/formaldehyde ratio during synthesis. Then, the second step of the mechanism involves polymeric reactions between the monomeric products through condensation processes. Such processes have been shown to be highly dependent on pH (Pizzi and Stephanou, 1994). Under alkaline conditions, the bonds between the monomers are based on methylene-type ($-CH_2-$) bridging bonds, while in neutral or acid environments, ether-type ($-CH_2-O-CH_2-$) bridging bonds can also be found.

All the parameters that influence the synthesis are of paramount importance to adapt the properties of phenolic resins. The high process tunability (pH, temperature, precursor ratios, etc.) makes them of prime interest for a wide range of applications: aerospace industry, adhesives, coatings, and high-yield precursors for the preparation of carbon materials, among others (Celzard and Fierro, 2020). However, one of the main concerns about phenolic resins is their production from petrochemical feedstocks (European Chemicals Agency, 2021a; European Chemicals Agency, 2021c; European Chemicals Agency, 2021d). On the one hand, 95% of the world's phenol production is based on the cumene process (Zakoshansky, 2007), which involves the partial oxidation of benzene and propylene to obtain phenol and acetone. Benzene and propylene are highly

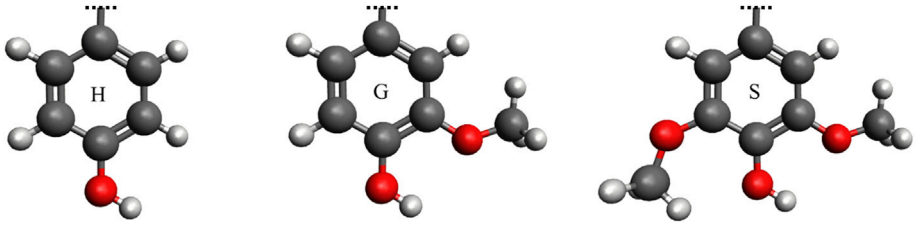

FIGURE 1 | Structural units of lignin monomers: p-hydroxyphenyl (H), guaiacyl (G) and syringyl (S).

polluting petrochemical raw materials (European Chemicals Agency, 2021b; European Chemicals Agency. Propene). On the other hand, although crosslinker-free resins exist (Celzard and Fierro, 2020), the most common preparation of carbon materials from phenolic molecules involves the reaction between the phenolic groups and formaldehyde (Grenier-Loustalot et al., 1994; Zhang et al., 2015; Foyer et al., 2016). Unfortunately, formaldehyde is also considered a pollutant since it is obtained from hydrocarbons such as methanol (European Chemicals Agency, 2021a). The presence of formaldehyde in the air can have dangerous consequences for human health (European Chemicals Agency, 2021a).

Biosourced precursors of phenolic resins have been explored over the last decades in the search for fully green technologies. This section reviews the most common bio-based precursors of phenolic molecules (lignin and tannins), including structure, properties and role in bio-resins. Moreover, crosslinker-free resins and bio-based crosslinker components will also be studied in this section.

Lignin

Lignin is an amorphous 3D phenolic polymer composed mainly of three structural units: p-hydroxyphenyl (H), guaiacyl (G) and syringyl (S) (**Figure 1**). Lignin is one of the largest components of plant matter, along with cellulose and hemicellulose. However, unlike the other two, lignin is the only component with aromatic properties and carbon contents above 60 wt%, making it desirable for the development of carbon materials (Fierro et al., 2005, 2006). Lignin is a highly heterogeneous polymer that plants naturally produce through the consumption of carbon dioxide followed by the formation of carbohydrates through the photosynthesis (Hu, 2002).

As commented above, phenol-formaldehyde resins do not necessarily involve the use of pure phenol as the phenolic component. Lignin can serve as a substitute for phenol molecules in these resins (Sellers et al., 2004; Hu et al., 2011; Nieuwenhove et al., 2020). The structural units of lignin are based on phenol-like moieties, which can interact with aldehydes in a form similar to phenol-formaldehyde resins (**Figure 1**). Assuming that lignin-aldehyde resins are formed through the same mechanism and that the *para*- positions of phenolic rings in lignin are occupied, the reaction can only take place through the *ortho*- position of H and G moieties of lignin *via* methylene or ether bridging bonds. At the same time, S-type groups would not be able to interact in such crosslinking reactions (Xu and Ferdosian, 2017; Wang Y.-Y. et al., 2020).

The main problem with lignin as a phenol-type component in phenolic resins is its considerable molecular weight and complex, stable structure, which results in low reactivity of the lignin feedstock. In order to increase the reaction rate, lignin is often purified and chemically modified by methylolation (Peng et al., 1993; Vázquez et al., 1997), phenolation (Jiang et al., 2018) and demethylation (Song et al., 2016; Wang et al., 2019) reactions. Without applying modifications to the non-reactive raw structure, the use of lignin as a phenolic component is severely hampered. After these chemical modifications, large amounts of phenol [up to 100% of lignin-based resins (Kalami et al., 2017)] were successfully substituted by lignin components in phenol-formaldehyde resins (Zhang et al., 2013; Kalami et al., 2017). Interestingly, lignin has also been shown to react with glyoxal (as a crosslinker) to form lignin-based phenolic resins without using phenol and formaldehyde in the formulation (Kumar et al., 2021).

Tannin and Raw Materials Derived From Tannin

Tannins are complex polyphenolic biomolecules found in plant materials, especially in dicotyledonous plants. After lignin, tannins are the second most abundant aromatic compound in biomass, with a high carbon content. However, tannin

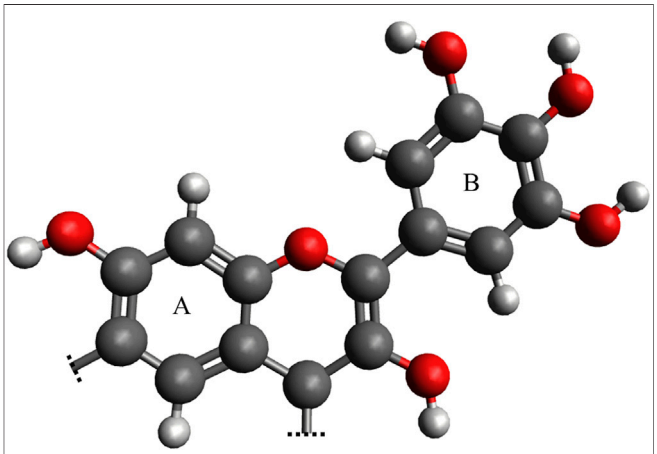

FIGURE 2 | Chemical structure of the flavonoid unit.

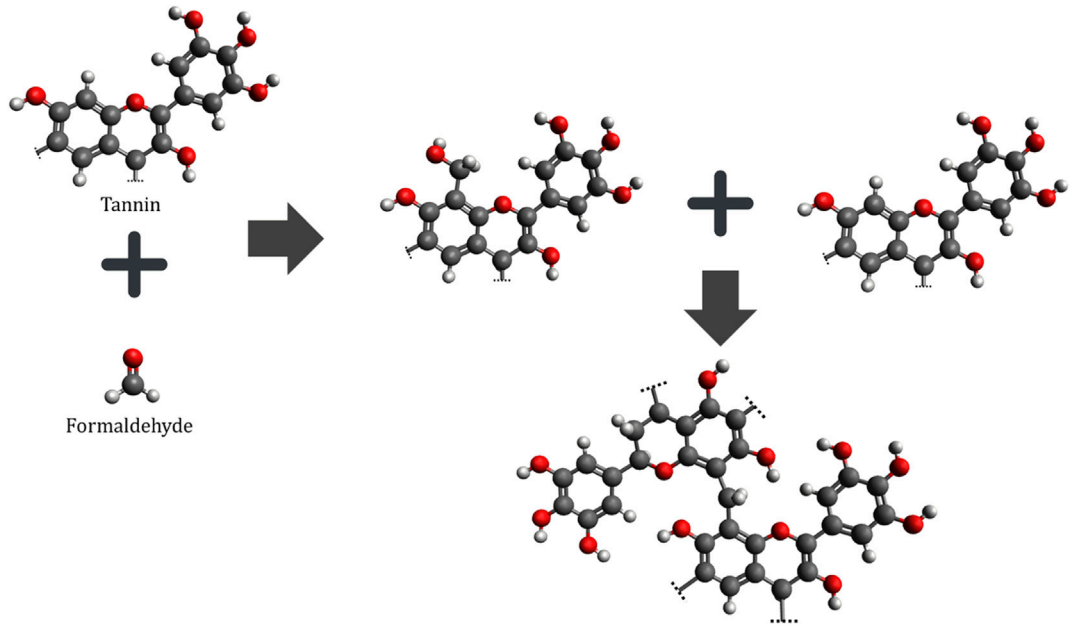

FIGURE 3 | Reaction mechanism between flavonoid units of tannin and formaldehyde.

composition highly depends on the plant source. High tannin concentration has been reported in mimosa, quebracho, pine and chestnut. Nevertheless, despite the heterogeneous nature of tannins, these can be classified into three different groups according to their structural units; 1) hydrolysable tannins, 2) condensed tannins and 3) complex tannins (Gross, 1999; Kahnbabaee and Van-Ree, 2001).

Condensed tannins (also known as flavan-3,4-diol-derived tannins) are another important renewable substitute for phenol in phenolic resins. The monomers of condensed tannins is based on flavonoid units, which are formed by a heterocyclic ring linking two phenolic rings: the A ring and the B ring (**Figure 2**).

The use of tannin as a phenolic-type component has been widely demonstrated in the scientific literature through the formation of multiple tannin-formaldehyde resins (Amaral-Labat et al., 2013; Pizzi et al., 2013; Lagel et al., 2014; Li et al., 2016). Due to their phenolic moieties, these tannin-derived substances indeed undergo the same kind of reaction mechanisms with aldehydes. Such reactions are mainly based on the polymerization of flavonoid units with formaldehyde through -C-C- and -C-O-C bridging bonds (**Figure 3**) (Gross, 1999; Kahnbabaee and Van-Ree, 2001), similar to the original phenol-formaldehyde resins.

Not only that, many different derivatives can be obtained through organic reactions between condensed tannins and other compounds. Tannins have proven to be able to react with amines to obtain polycondensed resins (Delgado-Sánchez et al., 2017). Some recent work shows that in alkaline or acidic solution, the reaction mechanism proceeds through 1) the reaction of the amine and the phenolic-type component and 2) the formation of ionic bonds between the protonated amino groups and the hydroxyl groups of the flavonoid structure of the tannin (Santiago-Medina et al., 2017). Biosourced tannin resins have also been obtained from the reaction between tannin and furfuryl alcohol with glyoxal, a crosslinker that is much less toxic and much less volatile than formaldehyde (Lacoste et al., 2013).

However, one of the most exciting tannin-based preparation is the one obtained by the self-condensation of these organic molecules (Pizzi et al., 1995; Pizzi, 2008; Basso et al., 2014). Unlike simple phenolic molecules, condensed tannins are also prone to self-condensation reactions through methylene or ether bridging bonds in alkaline and acids (Pizzi et al., 1995). The mechanism of self-condensation is well-known; tannins react through three different reactions that are: 1) degradation of tannins to lower molecular weight compounds, such as catechin, 2) condensation reaction by hydrolysis of aromatic rings, and 3) formation and reaction of free radicals in the presence of air. This feature makes tannins one of the few phenolic-type molecules capable of producing phenolic resins without the presence of additional crosslinkers, leading to tannin-only resins.

Crosslinkers

Lignin and tannins are the main substitutes for phenol in phenol-formaldehyde resins. In the case of aldehyde components, hydroxymethylfurfural (HMF) represents the main biosourced alternative to replace formaldehyde (Sarika et al., 2020). HMF is an aromatic aldehyde found in sugars, fruits, coffee, flavoring agents and other carbohydrate polymers. It is usually synthesized from cellulose and lignocellulose using ionic liquids and/or organic solvents (Stahlberg et al., 2011; Zakrzewska et al., 2011).

HMF has proven to be an effective substitute for formaldehyde in the manufacture of "green" phenolic resins, in which the

production of polluting formaldehyde emissions is avoided (Zhang et al., 2016a). The use of HMF in fully "green" resins have already been demonstrated: phenol was replaced by lignin derivatives, while formaldehyde was substituted by HMF, resulting in a green phenolic resin with interesting properties in terms of thermal stability and mechanical strength (Zhang et al., 2016b). Nevertheless, HMF is not the only biosourced crosslinker. Other formaldehyde substitutes have proven to be helpful for the formation of phenolic resin with excellent properties. Among all the aldehyde-type alternatives, the role of furfural (Oliveira et al., 2008; Zhang et al., 2020), furfuryl alcohol (Cheng et al., 2018), glyoxal (Ramires et al., 2010) and vanillin (Foyer et al., 2016) should be highlighted. If readers are looking for more details on biosourced precursors to phenolic resins, we encourage them to read the following scientific literature (Sarika et al., 2020).

FROM PHENOLIC MOLECULES TO CARBON MATERIALS

The high carbon content and low cost of biosourced phenolic molecules and the resultant phenolic resins make them an attractive alternative to petrochemical compounds for producing carbon materials. The variety of phenolic and crosslinking precursors (if used) and their extensive properties make them a potential material for the production of carbons with different chemical and structural properties, such as porosity, carbon and oxygen content, heteroatom doping, electrical conductivity or thermal stability. The following section briefly summarizes the most common methodologies for producing carbon materials from phenolic compounds and resins.

Carbonization

The most widely used method for the production of carbon materials is based on high-temperatures heat treatment of precursors in an oxygen-free atmosphere. These high temperatures promote condensation reactions of chains of phenolic molecules or resins (Meng et al., 2006; Muylaert et al., 2012). Prior to carbonization processes, a standard methodology for increasing the carbonization yield is a well-known curing process (Meng et al., 2006; Muylaert et al., 2012). The curing process uses heat treatments at moderate temperatures in an air atmosphere to promote crosslinking reactions of the phenolic structure. After the pre-treatment, high-temperature carbonization is applied (Meng et al., 2006; Muylaert et al., 2012). This procedure consists of the thermal degradation of carbon precursors by heating in an inert atmosphere at temperatures above 300°C, leading to the conversion of the phenolic matrix into highly disordered carbon (Ko et al., 2000). Such conversion involves multiple reactions at high temperature: crosslinking, dehydration, isomerization and condensation (Trick and Saliba, 1995). The mechanism of pyrolysis of phenolic resins is well established: 1) formation of additional crosslinks, 2) scission of these crosslinks, and 3) polycyclic aromatization (Jiang et al., 2012). As a result of phenolic resin decomposition, water vapor, hydrogen, methane and carbon monoxide emissions are produced during thermal processing (Trick and Saliba, 1995).

The properties of the carbon material depend on the heat-treatment temperature, heating rate, residence time, flow rate, and phenolic and crosslinking precursors. As with other biomass precursors, to achieve high carbonization yields, a rather slow heating rate is preferable. Otherwise, rapid carbonization leads to volatilization of most of the biomass and production of bio-oils, and thus to low carbonization yields (Szczesniak et al., 2020).

With respect to the previously mentioned biosourced phenolic resins, it is worth noting that tannin-derived carbon materials have been prepared extensively through the carbonization of self-condensed tannins and tannin-aldehyde resins (Celzard and Fierro, 2020). The properties of such carbons have been tailored through heating temperature, heating rate, etc., but the non-graphitizable structure remains present regardless of the carbonization parameters. Moreover, tannins alone have been shown to be a promising precursor for obtaining carbon materials with excellent properties in terms of porosity (S_{NLDFT} = 770 $m^2 g^{-1}$), without requiring any additional crosslinking procedures, thereby avoiding any additional steps related to the formation of phenolic resins (Jagiello et al., 2019). In the case of lignin, the properties of lignin-derived carbon materials are also highly dependent on carbonization conditions. Lignin has been used as a phenolic substitute in resins for subsequent carbon materials (Simitzis and Sfyrakis, 1993; Guo et al., 2015; Zhang et al., 2018; Castro-Díaz et al., 2019). The heat-treatment temperature was found to be of paramount importance in the apparent surface area of carbon materials since the same lignin precursor shows 496 $m^2 g^{-1}$ at 500°C and 278 $m^2 g^{-1}$ at 900°C at a heating rate of 10°C·min^{-1} (Rodríguez-Mirasol et al., 1993a; 1993b). This effect of the temperature is related to the constriction of micropores when increasing the treatment temperature at such a high heating rate (Rodríguez-Mirasol et al., 1993a; 1993b). However, treatment at the same temperatures at a heating rate of 2.5°C·min^{-1} shows the opposite trend. The higher the treatment temperature, the higher the apparent surface area of the carbon materials (Xie et al., 2009), which also highlights the relevance of the heating rate.

Hydrothermal Carbonization

Hydrothermal carbonization, also known as aqueous carbonization or wet pyrolysis, is an alternative method for producing carbon materials from phenolic resins under milder conditions. The most common hydrothermal carbonization is done under subcritical conditions, which involves thermal treatment of a carbon precursor at temperatures between 150 and 350°C in a pressure vessel in the presence of water (or other aqueous solvents). In this temperature and pressure range, ionization of water occurs, which promotes hydrolysis of organic compounds. Besides, this process can be further accelerated by the presence of acids in the solution. The reaction mechanisms of hydrothermal carbonization are still contradictory because they seem to depend strongly on the carbon precursor. Nevertheless, there is a general consensus

that hydrothermal carbonization involves dehydration, decarboxylation, aromatization and condensation reactions, which govern the structural arrangement of the resultant carbon materials, also called hydrochars (Mohamed et al., 2017; Nizamuddin et al., 2017).

This methodology for producing carbon materials from phenolic resins is less standard than conventional carbonization. Nevertheless, there is a large number of publications reporting phenolic resins-derived carbon nanospheres (Xu and Guo, 2013), fibers (Fei et al., 2015), ordered mesoporous carbons (Yu and So, 2019), etc., obtained by hydrothermal method.

It is also worth mentioning that lignin and tannins are widely used to prepare carbon materials by hydrothermal carbonization without prior formation of phenolic resins, as these two kinds of organic molecules can produce carbon materials with excellent properties. Tannins are especially attractive for the preparation of carbon materials by hydrothermal methods because they are soluble in water. This facilitates condensation and dehydration reactions in hot pressurized water, leading to high hydrothermal yields near 60% (Braghiroli et al., 2014). Furthermore, this methodology is desirable for doping with heteroatoms since heteroatom precursors can also be introduced in the hydrothermal equipment. Following this approach, apparent surface areas of 500 $m^2 g^{-1}$ and nitrogen content above 8 at% were obtained in tannin-derived hydrothermal carbons (Braghiroli et al., 2015). In hydrothermal carbons derived from biomass under mild conditions, the most common nitrogen species are edge-type functionalities, such as imines and amines. However, more aggressive conditions are needed to obtain heterocyclic-type nitrogen groups, such as pyridines, pyrroles and graphitic nitrogen (Zhuang et al., 2018). The same principle of nitrogen doping can be used to complex transition metals and, therefore, to form metal-carbon hybrids.

On the other hand, lignin-based carbons have also been obtained by hydrothermal carbonization (Kang et al., 2013), with promising hydrothermal pyrolysis yields up to 66 wt% (Li et al., 2021). Carbon dots with photoluminescence emissions were obtained from hydrothermal carbonization of lignin in the presence of a small amount of hydrogen peroxide at 180°C. H_2O_2 act as an oxidizing agent that functionalizes the lignin-derived carbon domains during hydrothermal treatment (Chen et al., 2016). The functionalization involves the formation of oxygen groups and the creation of defects on the surface of the carbon dots. These can act as excitation energy traps, which may be responsible for the photoluminescence behavior (Chen et al., 2016).

Activation

Activation processes are not strictly speaking synthetic routes to produce carbon materials, but a promising pathway to modulate the microporosity and nanostructure of carbon materials derived from phenolic compounds. There are two types of activation processes: 1) chemical activation, and 2) physical activation (Marsh and Rodríguez-Reinoso, 2006).

Chemical activations involve the use of chemical activating agents, such as KOH, NaOH, and H_3PO_4 (Marsh and Rodríguez-Reinoso, 2006; Pérez-Mayoral et al., 2021; Pérez-Rodríguez et al., 2021). These activating agents are mixed with the carbon precursors, followed by thermal treatment at temperatures of 350–900°C. The mechanisms of chemical activation with KOH and NaOH have been widely studied. KOH (or NaOH) reacts with carbon materials at about 400°C to form K_2CO_3 (Lillo-Rodenas et al., 2003). At temperatures above 700°C, potassium (or sodium) carbonate decomposes into K_2O (or Na_2O) and CO_2. At this high temperature, CO_2 can also interact with the carbon matrix through oxidation of the carbon material to produce two CO molecules. In addition, K_2O or K_2CO_3 can also be reduced by the carbon network to produce metallic K, leading to the removal of carbon atoms.

Besides alkaline agents, acidic solvents can also be used during the activation process. Although many acidic agents have been used (Legrouri et al., 2004; Sanchez et al., 2006; Liu et al., 2011; Gao et al., 2020), the most widely used acidic activation agent is H_3PO_4 (Molina-Sabio et al., 1996; Jagtoyen and Derbyshite, 1998; Puziy et al., 2003). H_3PO_4 operates by different mechanisms than NaOH and KOH. The carbon material and acid solution are mixed and subjected to heat treatment at temperatures between 350 and 700°C. The proposed mechanism of acid activation is as follows: evaporation of the acidic agent leads to depolymerization and dehydration reactions of the polymeric materials. Then, the volatile by-products of the reaction between H_3PO_4 and the carbon material decompose, releasing cavities and pores (Gao et al., 2020). Chemical activations with acidic agents of biosourced phenolic molecules have generated significant developments of microporosity in carbon materials, reaching surface areas of nearly 3,000 $m^2 g^{-1}$ (Fierro et al., 2008). Nevertheless, by regulating the acid concentration, many surface areas can also be obtained (Gao et al., 2020).

On the other hand, physical activation consists of a two-step process: 1) carbonization of the carbon precursor, and 2) high-temperature treatment (500–900°C) in the presence of oxidizing agents, such as air, water vapor or CO_2 (Marsh and Rodríguez-Reinoso, 2006; Din et al., 2017; Heidarinejad et al., 2020; Pérez-Mayoral et al., 2021). These gases consume the carbon material creating microchannels in the carbonaceous structure. Carbons subjected to physical activation develop a large surface area due to the formation of micropores. Depending on the physical agent, the microporosity can be modulated. The use of CO_2 results in narrower micropores, whereas the use of steam leads to a broader pore size distribution with a lower content of micropores (Pérez-Mayoral et al., 2021).

Among all activating agents, CO_2 is by far the most common in physical activations, whose reaction mechanisms have been widely explained according to the following reaction:

$$CO_2 + C \rightarrow 2\,CO$$

This means that the carbon material reduces the CO_2 molecule while the carbon material is oxidized, producing two carbon monoxide molecules and eliminating one carbon atom from the surface. Such physical activation has been widely applied to obtain carbon materials from biosourced phenolic molecules (Doney et al., 2009; Xue et al., 2011).

Template Methods

The main limitation of the above carbonization processes is the lack of control over the porosity of the resultant carbon materials. Carbonization in the presence of templates is a powerful strategy to produce carbon materials with accurate control of pore structure and size distribution. In order to prepare carbon materials with a well-defined pore structure, one attractive strategy, known as hard-templating, is to replicate a template material that already has a well-ordered structure (Muylaert et al., 2012; Wang H. et al., 2020; Xie et al., 2020; Díez et al., 2021). Thus, the carbon precursor is deposited chemically (Jun et al., 2009) or electrochemically (Quílez-Bermejo et al., 2020b) as the inverse template structure, filling the pores of the pristine template structure. For carbon materials derived from phenolic resins, the template cannot only be added during carbonization but also during the formation of the phenolic resins (Muylaert et al., 2012). Therefore, porosity control can be overcome early in resin production or during pyrolysis of carbon precursors. This approach has been widely applied to obtain ordered mesoporous carbons (OMCs) from biosourced phenolic compounds (Fierro et al., 2013; Salinas-Torres et al., 2016; Xi et al., 2020). The main limitation of this approach is the need for an additional step to remove the template from the composition of the material, which often involves the use of hazardous and toxic chemicals, such as hydrofluoric acid or high concentrations of sodium hydroxide.

The second template method, known as soft-templating, involves cooperative assembly between an amphiphilic templating agent and the carbon precursor. This is the most common method for obtaining carbon materials of phenolic origin (Szczesniak et al., 2020). In general, in soft-templating, the templating agent consists of surfactants or copolymers and the carbon precursor is based on phenolic precursors. The mixture of the components and a solvent leads to a mesophase that is heated to produce well-ordered carbon materials. At the same time, the templating agent is removed by heat treatment (Muylaert et al., 2012; Nita et al., 2016; Choma et al., 2020). Compared to hard-templating, the main advantage of this methodology is the lack of need for corrosive compounds to remove the template from the final carbon material. After pyrolysis at temperatures above 400°C, the soft template is completely eliminated, releasing the porosity of the resultant carbons.

In soft-template methods for the formation of phenolic-derived carbons, some factors are of paramount importance, especially the effect of pH (Meng et al., 2006; Huang et al., 2009; Xie et al., 2011; Renda and Bertholdo, 2018). In a basic medium, phenolic moieties are deprotonated by the action of the OH^- anions, which leads to the formation of phenolate anions. Then, these anions interact with the surfactant. The resultant polymer has large amounts of hydroxyl groups that strengthen the template-resin interaction through hydrogen bonding.

These hard- and soft-templating methodologies have been widely applied to bio-based phenolic resins. Furthermore, carbon materials by templating directly from biosourced phenolic molecules have proven to be an effective way to produce well-ordered carbon materials, especially from tannins (**Figure 4**) and triblock copolymers such as Pluronic® (Castro-Gutierrez et al., 2018, 2021a; Sanchez-Sanchez et al., 2018). These ordered carbon materials show outstanding properties not only for electrochemical applications (Celzard and Fierro, 2020), as discussed in the next section, but also for adsorption (Nelson et al., 2016; Canevesi et al., 2020; Zhao et al., 2020), hydrogen storage (Schaefer et al., 2016) or even molecular sieving of alkanes (Castro-Gutierrez et al., 2021b). Lignin-derived ordered carbon materials obtained by template methods have also shown excellent properties in catalysis (Gan et al., 2019; Wang X. et al., 2020) or adsorption (Xie et al., 2019).

Mechanosynthesis

Mechanosynthesis has emerged in recent years as a promising methodology to simplify all the above-mentioned synthetic protocols (Suryanarayana, 2001; James et al., 2012). Mechanochemical synthesis has the advantage of using mechanical forces to produce the reaction instead of using hazardous chemicals or high temperatures and pressures as in conventional procedures (**Figure 5**).

Mechanosynthesis is based on milling processes in which the mechanical energy of motion is transferred to the precursor through abundant collisions (Margetic and Strukil, 2016). Depending on the mechanical forces, elastic or plastic deformation can be achieved (**Figure 5**) (Xu et al., 2015). If the mechanical forces are not strong enough, the kinetics transferred to the reagents only provides energy to reduce the size of the carbon particles. However, if the energy is high enough, the organic reactants can be chemically altered through the cleavage of chemical bonds (**Figure 5**) (James et al., 2012; Margetic and Strukil, 2016). This leads to the formation of new bonds between reactants and, consequently, the formation of new materials with significantly different chemical properties. Although it is a technique primarily used for the formation of metallic alloys, metal oxides and co-crystals, the use of mechanosynthesis for the preparation of carbon materials has been increasing significantly in recent years (Friscic, 2012; Margetic and Strukil, 2016; Zhang P. et al., 2017). This is particularly remarkable in the use of biosourced phenolic molecules and resins. In recent years, a few very relevant works can be found on this hot topic for lignin (Zhang J. et al., 2017; Liang et al., 2018; Liu et al., 2019) and tannins (Zhang P. et al., 2017; Castro-Gutierrez et al., 2018). Tannin, a templating agent (Pluronic® F127), and a small amount of water were ball-milled at room temperature. Interestingly, despite the absence of aldehyde, this synthetic methodology produces a structured mesophase through the self-condensation of tannin monomers due to the considerable energy provided by this novel technique without the need for hazardous solutions or compounds (Castro-Gutierrez et al., 2018). Moreover, this synthetic procedure has proven to be very versatile since multiple mesostructures can be found by modifying the amount of water, surfactant, and energy applied to the mechanochemical process. After heat treatment of the carbon mesophase, the well-ordered homogeneous pore size distribution was still observed (Castro-Gutierrez et al., 2018).

Nevertheless, mechanosynthesis is still in the early stages of carbon science. It holds promising prospects for the future of phenolic resins and carbon materials. However, more

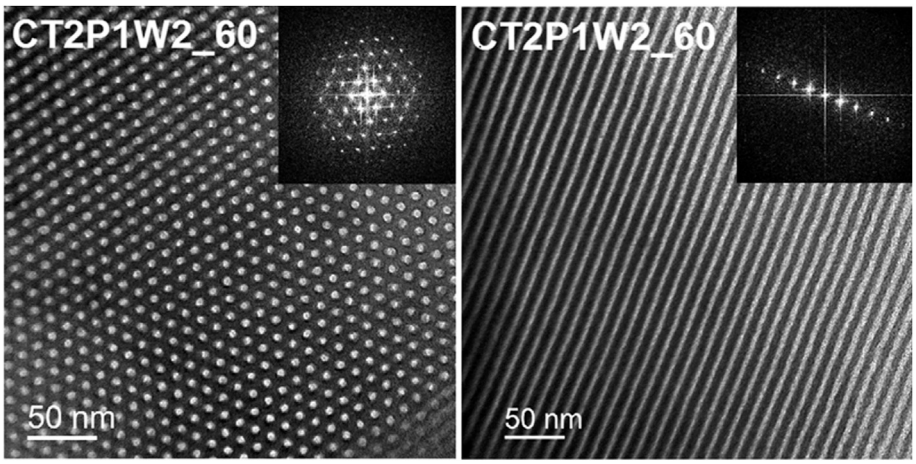

FIGURE 4 | Bright-field TEM micrographs of transverse and longitudinal views of well-ordered mesoporous carbon materials obtained by soft-templating of tannins [Reprinted with permission from (Castro-Gutierrez et al., 2018)].

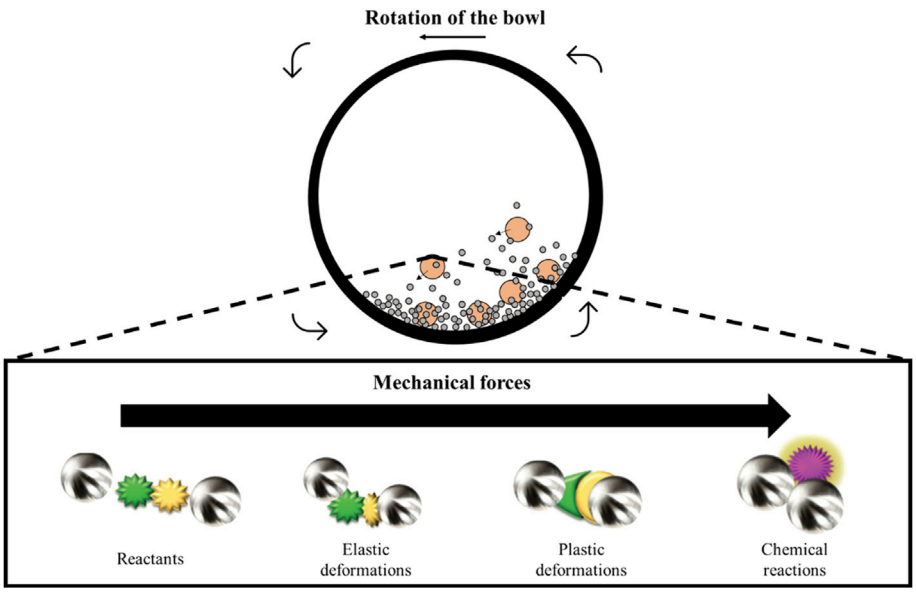

FIGURE 5 | Schematic representation of the ball motion inside the ball-milling and illustration of deformation and reaction in mechanochemical processes (Xu et al., 2015).

fundamental and applicative studies are still necessary to go further in its realization and understanding.

ELECTROCHEMICAL APPLICATIONS

Carbon materials, whose most important characteristics are high availability, tunable porosity and chemical nature, easy of processing, inexpensive synthesis, and intrinsic heteroatom doping, can be found in almost every aspect and branch of materials science, such as membranes, water treatment, optics, aerospace industry, biosensors, energy storage and energy conversion (Ruoff, 2018). Considering all the properties already mentioned, carbon materials have proven to be an excellent way to improve performance in electrochemical applications, in the form of electrodes for electrochemical energy storage and conversion.

This review section will focus on the significant findings and advances in the different electrochemical applications of carbon materials obtained from "green" phenolic compounds. This will cover their use as electrodes in supercapacitors and rechargeable batteries for energy storage.

Supercapacitors

Supercapacitors (SCs), also known as electrochemical capacitors or ultracapacitors, have attracted significant attention in the energy storage field due to their superior rate capability, high power density, fast charge/discharge rates, and long-term durability (Sharma and Bhatti, 2010; Xing et al., 2014). These unique properties of SCs bridge the gap between batteries and traditional capacitors. SCs consist of two electrodes electrically isolated by an ion-permeable separator containing an electrolyte, where energy storage occurs by charge accumulation at the electrode-electrolyte interface. Among the various parameters influencing the performance of SCs, the porous structure of the active electrodes, i.e., the pore size and specific surface area, is of critical importance. Carbons with well-developed porosity obtained from fossil precursors (such as mesoporous carbons, carbon gels, nanostructured materials, etc.) have been widely explored as electrodes for SCs. Nowadays, the fabrication of cost-effective and high energy density electrodes using environmentally friendly resources remains a challenge facing material scientists worldwide.

Lignin and other natural phenolic compounds, especially tannin and tannin-related molecules (such as phloroglucinol), have been investigated in the reaction with an aldehyde for the production of porous carbons derived from phenolic resins with outstanding electrochemical performance when used as SC electrodes (Liu M. et al., 2015; Miao et al., 2017; Vinodh et al., 2020; Sima et al., 2021). In this regard, hierarchical structured pore materials, incorporating ultramicropores, supermicropores and mesopores in a carbon network, were successfully synthesized by solvothermal polymerization of phloroglucinol and terephthaldehyde in dioxane, followed by carbonization (Miao et al., 2017; Vinodh et al., 2020). In these reaction systems, dioxane acts as both a solvent and a template to produce mesoporous domains, whereas the polymeric phloroglucinol/terephthaldehyde units serve as self-template to generate micropores during pyrolysis. Interestingly, the authors (Miao et al., 2017) reported the production of porous carbons with a high specific surface area (up to 1,003 $m^2 g^{-1}$) by this strategy. The developed porosity, together with the micro-mesopore network, provides the resultant SC electrodes adequate specific capacitance (214 $F g^{-1}$ at 1 $A g^{-1}$) in 6M KOH aqueous electrolyte, high-rate capability (154 $F g^{-1}$ at 50 $A g^{-1}$), and long-term cycling stability (with a capacitance retention of 95.5% after 10,000 cycles) (Miao et al., 2017).

Further efforts in the eco-friendly synthesis of carbon electrodes for SCs from greener, non-toxic phenolic resins have been made by replacing formaldehyde with glyoxylic acid or glyoxal as crosslinkers (Moussa et al., 2018; Herou et al., 2019). For example, the synthesis of sustainable ordered mesoporous carbons (OMCs) by self-assembly of a phloroglucinol/lignin mixture (phenolic precursor) and glyoxal (crosslinker) in the presence of a soft template (Pluronic® F127) has been recently reported (Herou et al., 2019). The influence of phloroglucinol/lignin mass ratio on the electrochemical performance of the resultant OMC-based electrodes was investigated. The bio-based electrode derived from 50 wt% lignin + 50 wt% phloroglucinol showed optimal behavior with an enhanced volumetric capacitance (90 $F cm^{-3}$), twice as high as the material prepared with phloroglucinol alone.

Self-condensation of tannins in the absence of crosslinkers has emerged over the past decade as an environmentally friendly approach to fabricate carbon materials with outstanding capacitive properties and high-rate capability (Castro-Gutierrez et al., 2019; 2021a). This particular route paves the way for the production of green, phenolic resin-derived carbon materials for energy storage applications with zero formaldehyde emissions. Several micro-mesoporous carbon materials obtained from the self-condensation of tannins by different synthetic routes have been explored as SC electrodes with promising results. Nano-cast OMCs based on tannin-related polyphenols (phloroglucinol, gallic acid, catechin or Mimosa tannin) have been investigated for electrochemical double-layer capacitors (Sanchez-Sanchez et al., 2017a). The synthesis route consists of a one-step impregnation of the hard template (SBA-15 silica) with the natural phenolic molecule in ethanol, which avoids the use of toxic solvents. The pyrolyzed carbon material achieved specific capacitances up to 277 $F g^{-1}$ (at 0.5 $mV s^{-1}$) in 1M H_2SO_4 aqueous electrolyte, which is in the range of OMCs with comparable textural parameters (Jurewicz et al., 2004; Tanaka et al., 2015) but obtained from petrochemical carbon precursors, and which require additional post-oxidation treatment to introduce oxygenated functionalities. These surface oxygen-containing groups increase the specific capacitance through: 1) pseudocapacitive contributions (quinone-hydroquinone redox reactions), and 2) improved carbon wettability and hence, increased electrochemical active area.

Although the nanocasting approach provides good control of the surface area and pore size of the resultant carbon electrodes, it requires the use of harsh acids (e.g., HF) to remove the hard silica template, which prevents the scaling-up of this methodology. A subsequent work showed successful soft-templating synthesis of OMCs by self-assembly of Mimosa tannin with Pluronic® F127 under mild conditions (30°C, pH 3) (Sanchez-Sanchez et al., 2018). An additional CO_2 activation step led to highly porous carbons (specific surface area up to 1,152 $m^2 g^{-1}$) with a gravimetric capacitance of 286 $F g^{-1}$ (at 0.5 $mV s^{-1}$) and better capacitance retention compared to the non-activated electrode. Although this strategy free of phenol and formaldehyde avoids the acid leaching step (essential for hard-templating routes), long polymerization times (three days) are needed, making the methodology time-consuming and limiting its practical application for SC electrode production.

Recently, a versatile water-assisted mechanochemical tannin self-assembly method was reported for the rapid production of phenolic resins (1 h) using Pluronic® F127 as a surfactant. By controlling the mimosa tannin/water/F127 ratio, disordered and perfectly ordered mesoporous carbons (DMC and OMC, respectively) with similar physicochemical properties and differing only in the mesoporous structure were obtained, see **Figure 6A** (Castro-Gutierrez et al., 2018, 2019; 2021a). After physical activation with CO_2, which resulted in a fourfold increase in surface area (from *ca* 500–2000 $m^2 g^{-1}$), the resultant mesoporous carbon electrodes exhibited superior capacitive properties with excellent rate capabilities at high

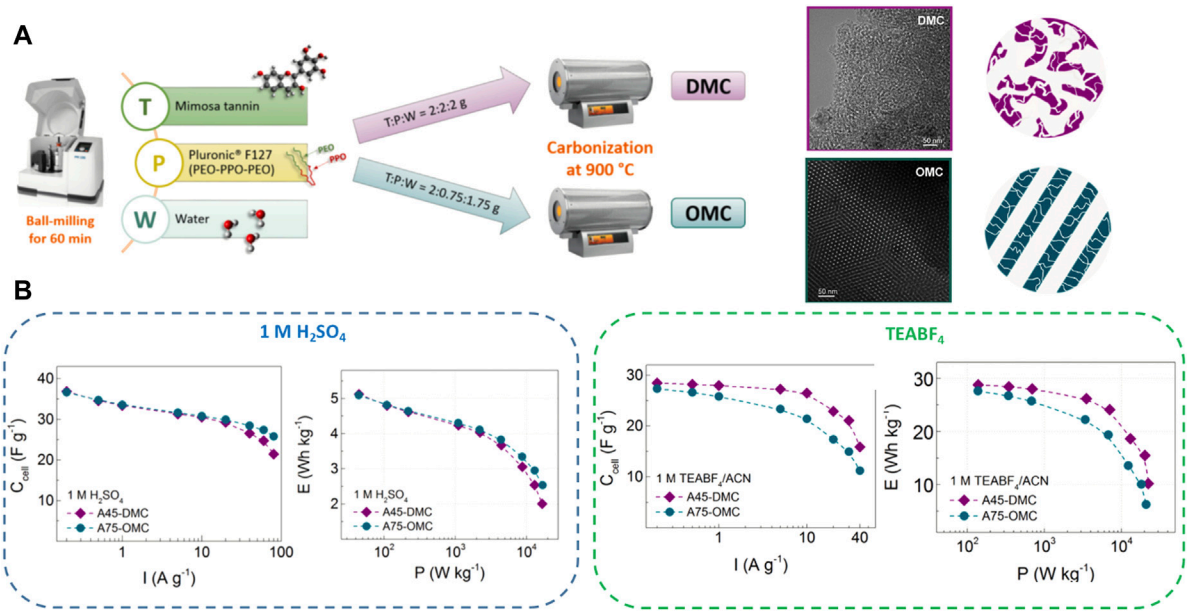

FIGURE 6 | (A) Schematic representations of the synthesis of ordered and disordered mesoporous carbons (OMC and DMC, respectively) by mechanochemical mesostructuration. TEM images and schematic porous structure of the resultant OMC and DMC materials. **(B)** Cell capacitance (C_{cell}) as a function of the applied current and Ragone-like plots in aqueous (1M H_2SO_4) and organic ($TEABF_4$) electrolytes. Adapted with permission from (Castro-Gutierrez et al., 2021a).

current densities and long-term stability in both aqueous (1M H_2SO_4) and organic ($TEABF_4$) electrolytes (**Figure 6B**). By scanning the hysteresis loops of nitrogen adsorption-desorption isotherms, the role of the connectivity of the micro-mesopore structure on the capacitive behavior has been studied (Castro-Gutierrez et al., 2021a). A 15% higher capacitance retention at 40 A g^{-1} in organic electrolyte was obtained with DMC compared to the ordered analog due to the more interconnected porosity of the former material, which allows for better diffusion of large ions. Conversely, the longer diffusion paths for small ions in 1M H_2SO_4 of the disordered mesoporous structure led to a 12% lower capacitance retention at 80 A g^{-1} than that obtained with OMC in the aqueous electrolyte.

As mentioned above, the interfacial capacitance of the materials can be further increased by the introduction of pseudocapacitance, which has been the subject of intensive research in the past decades. In addition to the surface oxygen functionalities, the introduction of other heteroatoms (nitrogen, phosphorous, boron, etc.) in the carbon lattice has been presented as a promising strategy to improve the capacitive performance of carbon electrodes derived from self-condensed-tannin. An innovative approach is the hydrothermal carbonization of aqueous tannin solutions, which benefits from tannin self-condensation under basic or acidic conditions. For example, a highly N- and O-doped carbon was prepared by hydrothermal carbonization (190°C) of pine tannins in ammonia, followed by pyrolysis of the resultant hydrochar at 900°C to develop the porous structure (Sanchez-Sanchez et al., 2017b). This easy, activation-free route to a carbon material with low ultramicroporosity and well-developed mesoporosity, as well as high N + O content (*i.e.*, 24 μmol m^{-2}), resulting in a specific capacitance of 252 F g^{-1} (0.5 mV s^{-1}) in 1M H_2SO_4 and a high energy density (up to ~1,500 mA g^{-1}).

The crucial role of N and O co-doping in carbon materials has been demonstrated to have a positive impact for other electrochemical applications by acting as active sites towards the oxygen reduction reaction in fuel cells or metal-air batteries (Quílez-Bermejo et al., 2017, Quílez-Bermejo et al., 2019; Quílez-Bermejo et al., 2020c). Other works have also revealed the superior capacitive properties of dual heteroatom-doped carbon materials from aminated tannin or tannin-melamine resins using a microwave-assisted carbonization method (Nasini et al., 2014; Bairi et al., 2015). Following this strategy, these authors synthesized phosphorus- and nitrogen- co-doped mesoporous carbons from tannin crosslinked by melamine (N precursor) in the presence of phosphoric acid (as the P source) (Fu et al., 2016). The resultant carbon materials achieved specific capacitances up to 271 F g^{-1} in acidic (1M H_2SO_4) and 236 F g^{-1} in alkaline (6M KOH) aqueous electrolytes, which can be explained by: 1) the developed surface area (up to 855 m^2 g^{-1}), which plays a key role in the electric double layer capacitive behavior; and 2) the modification of the carbon with nitrogen moieties (specially pyridinic-N and quaternary-N), which is responsible for the pseudocapacitance.

In addition to the carbonization of renewable phenolic resins, the direct thermal treatment of lignin and tannin has also been evaluated for the production of advanced carbon electrodes for electrochemical capacitors. A recent work (Pérez-Rodríguez et al., 2021) used biochars obtained as a byproduct of bio-oil production from the fast pyrolysis of pine bark tannin as green and abundant precursors for the fabrication of SC electrodes (**Figure 7A**). After activation of the tannin-derived biochars with KOH at 650°C at different activation

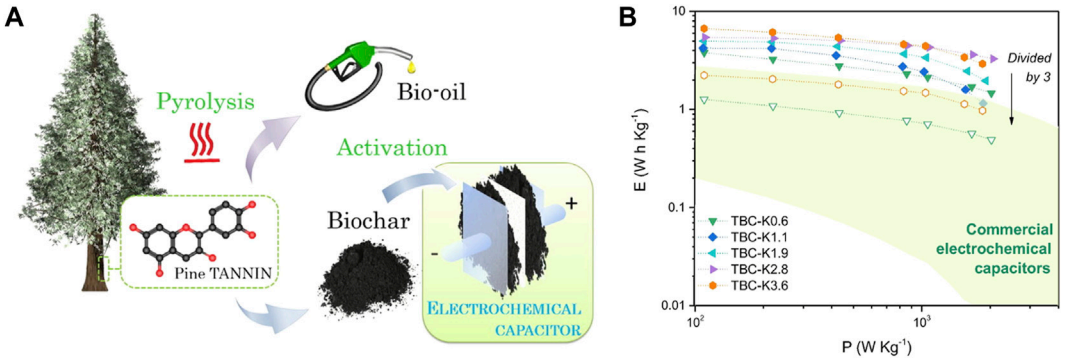

FIGURE 7 | (A) Schematic representations of the upgrading of biochars obtained as a byproduct of bio-oil production from pine bark tannin as precursors for the fabrication of SC electrodes. **(B)** Ragone plots of symmetrical SCs based on tannin biochars (TBCs) activated with different ratios (from 0 to 0.6 g KOH per gram of biochar) (full symbols) and Ragone-like curves of the packaged device extrapolated by dividing the specific energy values by a factor of 3 (empty symbols). Commercial electrochemical capacitor technologies have been included in the green zone. Reprinted with permission from (Pérez-Rodríguez et al., 2021).

ratios (ARs), the resultant microporous activated carbons exhibited highly developed surface areas (up to 2,200 $m^2\ g^{-1}$) and high oxygen content (10–15 wt%). These values explain their excellent capacitive behavior, with a maximum electrode capacitance of 232 $F\ g^{-1}$ (at 0.5 $A\ g^{-1}$, 1M H_2SO_4) and a capacitance retention of 70% at 10 $A\ g^{-1}$ for the most activated carbons, *i.e.*, those obtained at ARs of 2.8 and 3.6 g of KOH per gram of biochar (TBC-K2.8 and TBC-K3.6, respectively). This improved condition for energy storage is also evident in the Ragone-like plots (**Figure 7B**): TBC-K2.8 and TBC-K3.6 presented the highest specific energies with maxima of 5.4 and 6.7 Wh kg^{-1} at 110 W kg^{-1} under standard commercial mass loadings (~10 mg cm^{-2}). From the power-energy curves, the performance of a commercial device was extrapolated by estimating the carbon mass to be 30% of the SC stack (Gogotsi and Simon, 2011; Sevilla et al., 2019). The materials obtained from the upgrading of pine tannin biochars provided similar behavior to that of commercial reference SCs, showing their practical use for energy storage. The tannin-derived activated carbons also exhibited long-term stability, retaining 94% (at 5 $A\ g^{-1}$) of the initial stored charge after 10,000 cycles. Further details of the use of lignin- and tannin-derived carbon materials as advanced electrodes for SCs can be found in the following references (Espinoza-Acosta et al., 2018; Castro-Gutierrez et al., 2020). All these results are comparable or even better than those obtained with other biomass precursors not based on phenolic molecules, such as the 228 $F\ g^{-1}$ achieved in an alkaline electrolyte by using coconut shell as carbon precursor (Mi et al., 2012). This highlights the paramount importance of lignin and tannin as carbon precursors for the preparation of supercapacitor electrodes.

Despite all the above advantages of SCs, the low energy density compared to batteries and fuel cells limits their practical application as autonomous devices. The next section reviews significant progress in the development of carbon electrodes derived from phenolic compounds for rechargeable batteries.

Rechargeable Batteries

Rechargeable batteries (secondary batteries) are older electrochemical energy storage devices than SCs on the market. In particular, batteries are used in a wide range of mid- and short-term storage technologies, such as electric vehicles, portable devices and grid storage. Similar to an SC, a battery also consists of two electrodes and an electrolyte-soaked separator, but the main energy storage mechanism is based on chemical reactions (redox reactions) and not on charge separation as in electrochemical capacitors. Among the different types of batteries, lithium-ion batteries (LIBs) outperform other systems due to their high energy density (180 Wh kg^{-1}), cycle stability, and design flexibility (Tarascon and Armand, 2001). However, the uneven distribution and scarcity of lithium resources limit the large-scale application of

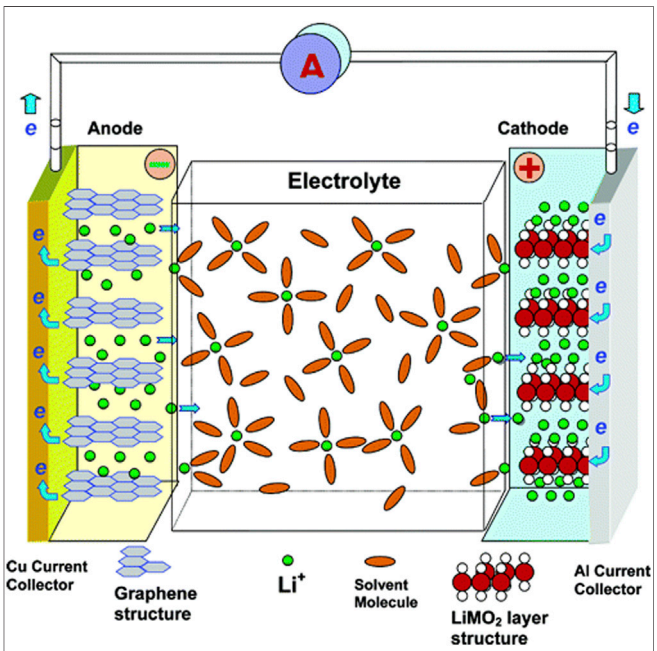

FIGURE 8 | Schematic representations of a lithium-ion battery (in discharge mode of operation) (reprinted with permission from (Xu et al., 2004).

LIBs. Similar technologies, such as sodium-ion batteries (NIBs), have emerged in the recent years as affordable alternatives due to the greater availability and lower cost of sodium comparted to lithium (Hwang et al., 2017).

In commercial LIBs, the negative electrode is typically graphite, where lithium ions are de-intercalated during battery discharge (spontaneous reaction, oxidation semi-reaction at the graphite electrode) and intercalated during the charging process (current is applied, reduction semi-reaction at the graphite electrode) for thousands of cycles (**Figure 8**). While graphite electrodes offer a suitable lithium intercalation capacity (with a theoretical value of 372 mAh g^{-1}), the instability of Na-graphite intercalation compounds (NaC_6 or NaC_8) limits their use in NIBs (Stevens and Dahn, 2001; Yoon et al., 2016).

Motivated by graphite's inability to store sodium ions and the energy transition to a sustainable economy, many groups have focused their research on developing of green, cheap and efficient carbon electrodes for next-generation rechargeable metal-ion batteries. Hard (*i.e.*, non-graphitizable) carbons have attracted special attention as negative electrodes due to their high ability to store more lithium ions than graphite and their suitability for NIBs (Soltani et al., 2021; Xie et al., 2021). Hard carbons are usually obtained from the pyrolysis of biomass waste, sugars, or phenolic resins. Phenolic resins have recently been shown to be more suitable precursors than commercial cellulose or lignin to produce hard carbons for practical use in NIBs due to their high carbon yield and reversible sodium ion insertion capacity (249 mAh g^{-1}) (Irisarri et al., 2018). In this study, however, commercial phenolic resins based on toxic and petrochemical precursors were used. The abundance, low cost, sustainability and non-toxicity of biomass make eco-friendly phenolic resin-derived hard carbons a promising option for metal-ion batteries.

Although the development of hard carbons from green (or partially green) phenolic resins for high-performance metal-ion batteries is an emerging field, a few examples can already be found in the literature involving different biosourced phenolic molecules (tannin, phloroglucinol, lignin, etc.) and crosslinkers (formaldehyde, furfuryl alcohol, glyoxylic acid, glyoxal) (Beda et al., 2018; Sun et al., 2020). Interestingly, a recent work synthesized hard carbons materials from phloroglucinol crosslinked with glyoxylic acid for NIB negative electrodes (Beda et al., 2018). In this environmentally friendly route, glyoxylic acid, containing aldehyde and carboxylic acid functionalities, acts as both a crosslinker and acidic catalyst, which leads to the formation of a phenolic resin with shorter curing times (Ghimbeu et al., 2015). Pyrolysis of the phenolic resin at high temperature (1,100–1700°C) led to the production of hard carbons with low surface area, disordered structure and moderate carbon yields (25–35%). The materials provided a sodium intercalation capacity of 270 mA h g^{-1} at a specific current density of 37.2 mA g^{-1} and good stability for 40 cycles, showing the potential of these green hard carbons for rechargeable metal-ion batteries.

It is also worth mentioning here a very recent work in which a hard carbon powder derived from tannin was tested as an anode material for NIB (Tonnoir et al., 2021). This powder was obtained by milling glassy carbon foam, itself obtained from self-generated foaming of a resin based on tannin and furfuryl alcohol and pyrolyzed at temperatures between 900 and 1,600°C. The hard carbon obtained at the highest temperature showed a high reversible capacity of 306 mAh g^{-1} at C/20 and a high initial Coulombic efficiency of 87%. To the best of our knowledge, these electrochemical performances are among the best reported in the literature for hard carbon derived from biomass.

Other attempts to increase defects (or active sites) and electrical conductivity of hard carbons derived from biophenolics-based polymer networks, and hence, to improve the sodium or lithium storage capabilities, have been made by heteroatom doping (such as nitrogen or sulfur) of carbon structures (Zhang et al., 2018; Huang et al., 2020). Recently, N-doped hard carbons derived from resole and urea have been explored for Na-ion storage (Sun et al., 2020). Porous carbons were obtained by a co-assembly strategy using phloroglucinol/glyoxal as the carbon precursor and urea as the nitrogen source, whereas Pluronic® F123 was used as a soft template. The resultant N-doped carbon electrode exhibited higher ability for sodium intercalation with a stable capacity of 229 mAh g^{-1} (at 100 mA g^{-1}) for 200 cycles, which is almost twice that of the non-doped electrode (123 mAh g^{-1}). The better performance of N-doped carbon materials has been also been proven for LIBs using hard carbons obtained by carbonizing formaldehyde-crosslinked lignin/melamine resins at 1,000°C (Yang et al., 2018). Nickel nitrate was used as a catalyst to induce graphitization, and thus, to enhance the electrical conductivity of the resultant hard carbon. When assembled into lithium-ion batteries, the electrode containing nitrogen moieties delivered a higher reversible lithium insertion capacity (340 mAh g^{-1} at 0.1 A g^{-1}) than the N-free electrode (260 mAh g^{-1}). In addition, the N-doped electrode presented a capacity retention of 69% when the current density increased from 0.1 to 1 A g^{-1}, which is higher than for the non-doped electrode (42%) or the N-doped electrode synthesized in the absence of nickel nitrate (55%). This study also reveals the long-term stability of the N-doped electrode for 300 cycles at 0.5 A g^{-1}. This work shows the potential of both introducing nitrogen-containing species and creating graphitic carbon structures to improve the electrochemical performance for LIBs of hard carbons obtained from phenolic bioresources.

The direct use of lignin (in the absence of any crosslinker) for the production of porous carbon-based electrodes has also been explored for metal-ion batteries and other related storage technologies, for example, as positive electrodes in Li-O_2 batteries or primary batteries. This research field has been the subject of recent reviews and we encourage readers to find more details in the following references (Espinoza-Acosta et al., 2018; Mehta et al., 2020; Baloch and Labidi, 2021).

On the other hand, porous carbons obtained by polymerization of biophenolic molecules (tannin, phloroglucinol, lignin) in the presence of an aldehyde or by crosslinker-free methodologies and subsequent carbonization have been explored for the oxygen reduction reaction (ORR), leading to promising results (Nasini et al., 2013; Bairi et al., 2015; Parthiban et al., 2019). These works pave the way for the production of metal-free carbon electrodes with outstanding catalytic properties when used as cathodes in fuel cells but

also as positive electrodes in metal-air batteries. However, further efforts are required for the design of green and highly active phenolic resin-derived carbon electrocatalysts for ORR with Pt-like performance (state-of-the-art electrodes) and with bi-functional activity for both oxygen reduction and oxygen evolution reactions, which plays a key role in the development of metal-air batteries and regenerative fuel cells.

PERSPECTIVES AND FUTURE RESEARCH

Biosourced phenolic resins represent one of the most promising alternatives to petrochemical feedstocks for the production of carbon materials. The properties of phenolic resins and the resultant carbon materials are highly dependent on the precursor ratios, their nature, synthesis protocols, etc., making phenolic resins a critical and complex branch of materials science. In the quest for green production of carbon materials from phenolic resins, lignin and tannin have proven to be the most realistic substitutes for traditional fossil fuel-based precursors because of their abundance in nature and high carbon content.

Throughout this review, the most essential information has been collected and detailed, from the type of biomass precursors to the methods of obtaining these carbon materials from phenolic resins. Biomass precursors, and especially tannin and lignin, possess tunable characteristics that can further enhance the properties of these carbon electrodes through defects, heteroatom or metal doping. Phenolic-derived carbon materials have received much attention in recent years due to their excellent energy storage properties in supercapacitors and rechargeable batteries, reaching or surpassing the state-of-the-art electrodes. The high surface area and tunability of the surface chemistry by simple functionalization processes make them ideal for combining large surface area electrodes with pseudocapacitive reactions on the surface of the carbon electrodes, which can increase the energy storage in these electrochemical devices.

A deeper understanding on carbon materials derived from phenolic compounds is needed, with a focus on synthetic methods and functionalization processes. Special mention must be made here for mechanosynthesis, which has proven to be a new synthetic route to overcome the limitations of conventional fabrication protocols, but further research is still needed as it is in the early stages of carbon materials preparation.

Supercapacitors and rechargeable batteries are just two devices in which phenolic-derived carbon materials play a crucial role, but these properties are scalable to multiple electrochemical and non-electrochemical devices. The outstanding and tunable properties of these carbons make them an attractive alternative for adsorption, gas storage, fuel cells, electrochemical biosensors, or as electrodes for electrochemical water splitting.

AUTHOR CONTRIBUTIONS

JQ-B compiled, organized the data and wrote the first draft. SP-R contributed to wrote the first draft. AC reviewed the manuscript. VF conceived and reviewed the manuscript. All authors read and approved the submitted version.

FUNDING

This study was partly supported by ANR-15-IDEX-04-LUE and TALiSMAN project (2019- 000214), funded by European Regional Development Fund (ERDF). SPR acknowledges MCIN/AEI/10.13039/501100011033 for her Juan de la Cierva Incorporación research contract (IJC 2019-041874-I).

REFERENCES

Abbasi, R., Setzler, B. P., Lin, S., Wang, J., Zhao, Y., Xu, H., et al. (2019). A Roadmap to Low-Cost Hydrogen with Hydroxide Exchange Membrane Electrolyzers. *Adv. Mater.* 31, 1805876. doi:10.1002/adma.201805876

Amaral-Labat, G., Szczurek, A., Fierro, V., Pizzi, A., and Celzard, A. (2013). Systematic Studies of Tannin-Formaldehyde Aerogels: Preparation and Properties. *Sci. Tech. Adv. Mater.* 14, 015001. doi:10.1088/1468-6996/14/1/015001

Bairi, V. G., Nasini, U. B., Kumar Ramasahayam, S., Bourdo, S. E., and Viswanathan, T. (2015). Electrocatalytic and Supercapacitor Performance of Phosphorous and Nitrogen Co-doped Porous Carbons Synthesized from Aminated Tannins. *Electrochimica Acta* 182, 987–994. doi:10.1016/j.electacta.2015.10.011

Baloch, M., and Labidi, J. (2021). Lignin Biopolymer: the Material of Choice for Advanced Lithium-Based Batteries. *RSC Adv.* 11, 23644–23653. doi:10.1039/d1ra02611a

Basso, M. C., Giovando, S., Pizzi, A., Lagel, M. C., and Celzard, A. (2014). Alkaline Tannin Rigid Foams. *J. Renew. Mater.* 2, 3. doi:10.7569/jrm.2013.634137

Beda, A., Taberna, P.-L., Simon, P., and Matei Ghimbeu, C. (2018). Hard Carbons Derived from green Phenolic Resins for Na-Ion Batteries. *Carbon* 139, 248–257. doi:10.1016/j.carbon.2018.06.036

Braghiroli, F. L., Fierro, V., Izquierdo, M. T., Parmentier, J., Pizzi, A., and Celzard, A. (2014). Kinetics of the Hydrothermal Treatment of Tannin for Producing Carbonaceous Microspheres. *Bioresour. Tech.* 151, 271–277. doi:10.1016/j.biortech.2013.10.045

Braghiroli, F. L., Fierro, V., Izquierdo, M. T., Parmentier, J., Pizzi, A., Delmotte, L., et al. (2015). High Surface - Highly N-Doped Carbons from Hydrothermally Treated Tannin. *Ind. Crops Prod.* 66, 282–290. doi:10.1016/j.indcrop.2014.11.022

Brauns, J., and Turek, T. (2020). Alkaline Water Electrolysis Powered by Renewable Energy: A Review. *Processes* 8, 248. doi:10.3390/pr8020248

Canevesi, R. L. S., Sanchez-Sanchez, A., Gadonneix, P., Celzard, A., and Fierro, V. (2020). Hierarchical Tannin-Derived Carbons as Efficient Tetracycline Adsorbents. *Appl. Surf. Sci.* 533, 147428. doi:10.1016/j.apsusc.2020.147428

Castro-Díaz, M., Vega, M. F., Díaz-Faes, E., Barriocanal, C., and Snape, C. (2019). Evaluation of Demineralized Lignin and Lignin-Phenolic Resin Blends to Produce Biocoke Suitable for Blast Furnace Operation. *Fuel* 258, 116125. doi:10.1016/j.fuel.2019.116125

Castro-Gutiérrez, J., Celzard, A., and Fierro, V. (2020). Energy Storage in Supercapacitors: Focus on Tannin-Derived Carbon Electrodes. *Front. Mater.* 7, 217. doi:10.3389/fmats.2020.00217

Castro-Gutiérrez, J., De Oliveira Jardim, E., Canevesi, R. L. S., Silvestre-Albero, J., Kriesten, M., Thommes, M., et al. (2021b). Molecular Sieving of Linear and Branched C6 Alkanes by Tannin-Derived Carbons. *Carbon* 174, 413–422. doi:10.1016/j.carbon.2020.12.061

Castro-Gutiérrez, J., Díez, N., Sevilla, M., Izquierdo, M. T., Celzard, A., and Fierro, V. (2021a). Model Carbon Materials Derived from Tannin to Assess the

Importance of Pore Connectivity in Supercapacitors. *Renew. Sust. Energ. Rev.* 151, 111600. doi:10.1016/j.rser.2021.111600

Castro-Gutiérrez, J., Díez, N., Sevilla, M., Izquierdo, M. T., Ghanbaja, J., Celzard, A., et al. (2019). High-Rate Capability of Supercapacitors Based on Tannin-Derived Ordered Mesoporous Carbons. *ACS Sust. Chem. Eng.* 7, 17627–17635. doi:10.1021/acssuschemeng.9b03407

Castro-Gutiérrez, J., Sanchez-Sanchez, A., Ghanbaja, J., Díez, N., Sevilla, M., Celzard, A., et al. (2018). Synthesis of Perfectly Ordered Mesoporous Carbons by Water-Assisted Mechanochemical Self-Assembly of Tannin. *Green. Chem.* 20, 5123–5132. doi:10.1039/c8gc02295j

Celzard, A., and Fierro, V. (2020). "Green", Innovative, Versatile and Efficient Carbon Materials from Polyphenolic Plant Extracts. *Carbon* 167, 792–815. doi:10.1016/j.carbon.2020.05.053

Chen, W., Hu, C., Yang, Y., Cui, J., and Liu, Y. (2016). Rapid Synthesis of Carbon Dots by Hydrothermal Treatment of Lignin. *Materials* 9, 184. doi:10.3390/ma9030184

Cheng, Y., Sui, G., Liu, H., Wang, X., Yang, X., and Wang, Z. (2018). Preparation of Highly Phenol Substituted Bio-Oil-Phenol-Formaldehyde Adhesives with Enhanced Bonding Performance Using Furfural as Crosslinking Agent. *J. Appl. Polym. Sci.* 136, 46995. doi:10.1002/app.46995

Choma, J., Zubrowska, A., Górka, J., and Jaroniec, M. (2020). Adsorption Properties of Phenolic Resin-Based Mesoporous Carbons Obtained by Using Mixed Templates of Pluronic F127 and Brij 58 or Brij 78 Polymers. *Adsorption* 16, 377. doi:10.1007/s10450-010-9230-5

Delgado-Sánchez, C., Fierro, V., Li, S., Pasc, A., Pizzi, A., and Celzard, A. (2017). Stability Analysis of Tannin-Based Foams Using Multiple Light-Scattering Measurements. *Eur. Polym. J.* 87, 318–330. doi:10.1016/j.eurpolymj.2016.12.036

Díez, N., Sevilla, M., and Fuertes, A. B. (2021). Synthesis Strategies of Templated Porous Carbons beyond the Silica Nanocasting Technique. *Carbon* 178, 451–476. doi:10.1016/j.carbon.2021.03.029

Din, M. I., Ashraf, S., and Intisar, A. (2017). Comparative Study of Different Activation Treatments for the Preparation of Activated Carbon: a Mini-Review. *Sci. Prog.* 100, 299–312. doi:10.3184/003685017x14967570531606

Doney, S. C., Fabry, V. J., Feely, R. A., and Kleypas, J. A. (2009). Ocean Acidification: The Other CO2 Problem. *Annu. Rev. Mar. Sci.* 1, 169–192. doi:10.1146/annurev.marine.010908.163834

Du, K., and Li, J. (2019). Towards a green World: How Do green Technology Innovations Affect Total-Factor Carbon Productivity. *Energy Policy* 131, 240–250. doi:10.1016/j.enpol.2019.04.033

Effendi, A., Gerhauser, H., and Bridgwater, A. V. (2008). Production of Renewable Phenolic Resins by Thermochemical Conversion of Biomass: A Review. *Renew. Sust. Energ. Rev.* 12, 2092–2116. doi:10.1016/j.rser.2007.04.008

Espinoza-Acosta, J. L., Torres-Chávez, P. I., Olmedo-Martínez, J. L., Vega-Rios, A., Flores-Gallardo, S., and Zaragoza-Contreras, E. A. (2018). Lignin in Storage and Renewable Energy Applications: A Review. *J. Energ. Chem.* 27, 1422–1438. doi:10.1016/j.jechem.2018.02.015

European Chemicals Agency (2021a). *Substance Infocard - Benzene*. https://echa.europa.eu/nl/substance-information/-/substanceinfo/100.000.685 (accessed Aug 28, 2021).

European Chemicals Agency (2021b). *Substance Infocard - Propene*. https://echa.europa.eu/nl/substance-information/-/substanceinfo/100.003.693 (accessed Aug 28, 2021).

European Chemicals Agency (2021c). *Substance Infocard – Formaldehyde*. https://echa.europa.eu/nl/substance-information/-/substanceinfo/100.000.002 (accessed Aug 28, 2021).

European Chemicals Agency (2021d). *Substance Infocard – Phenol*. https://echa.europa.eu/nl/substance-information/-/substanceinfo/100.003.303 (accessed Aug 28, 2021).

Fei, J., Luo, W., Huang, J., Ouyang, H., Wang, H., and Cao, L. (2015). Effect of Hydrothermal Modified Carbon Fiber through Diels-Alder Reaction and its Reinforced Phenolic Composites. *RSC Adv.* 5, 64450–64455. doi:10.1039/c5ra09798c

Fierro, C. M., Górka, J., Zazo, J. A., Rodríguez, J. J., Ludwinowicz, J., and Jaroniec, M. (2013). Colloidal Templating Synthesis and Adsorption Characteristics of Microporous-Mesoporous Carbons from Kraft Lignin. *Carbon* 62, 233–239. doi:10.1016/j.carbon.2013.06.012

Fierro, V., Torné-Fernández, V., and Celzard, A. (2006). Kraft Lignin as a Precursor for Microporous Activated Carbons Prepared by Impregnation with Ortho-Phosphoric Acid: Synthesis and Textural Characterisation. *Microporous Mesoporous Mater.* 92, 243–250. doi:10.1016/j.micromeso.2006.01.013

Fierro, V., Torné-Fernández, V., Montané, D., and Celzard, A. (2008). Adsorption of Phenol onto Activated Carbons Having Different Textural and Surface Properties. *Microporous Mesoporous Mater.* 111, 276–284. doi:10.1016/j.micromeso.2007.08.002

Fierro, V., Torné-Fernández, V., Montané, D., and Celzard, A. (2005). Study of the Decomposition of Kraft Lignin Impregnated with Orthophosphoric Acid. *Thermochim. Acta* 433, 142–148. doi:10.1016/j.tca.2005.02.026

Forest Research (2021). https://www.forestresearch.gov.uk/tools-and-resources/fthr/biomass-energy-resources/general-biomass-information/what-is-biomass/(accessed Aug 28, 2021).

Foyer, G., Chanfi, B.-H., Boutevin, B., Caillol, S., and David, G. (2016). New Method for the Synthesis of Formaldehyde-free Phenolic Resins from Lignin-Based Aldehyde Precursors. *Eur. Polym. J.* 74, 296–309. doi:10.1016/j.eurpolymj.2015.11.036

Friscic, T. (2012). Supramolecular Concepts and New Techniques in Mechanochemistry: Cocrystals, Cages, Rotaxanes, Open Metal–Organic Frameworks. *Chem. Soc. Rev.* 41, 3493–3510.

Fu, Y. a., Huang, Y., Xiang, Z., Liu, G., and Cao, D. (2016). Phosphorous-Nitrogen-Codoped Carbon Materials Derived from Metal-Organic Frameworks as Efficient Electrocatalysts for Oxygen Reduction Reactions. *Eur. J. Inorg. Chem.* 2016, 2100–2105. doi:10.1002/ejic.201500822

Gan, L., Lyu, L., Shen, T., and Wang, S. (2019). Sulfonated Lignin-Derived Ordered Mesoporous Carbon with Highly Selective and Recyclable Catalysis for the Conversion of Fructose into 5-hydroxymethylfurfural. *Appl. Catal. A: Gen.* 574, 132–143. doi:10.1016/j.apcata.2019.02.008

Ganiyu, S. O., and Martínez-Huitle, C. A. (2020). The Use of Renewable Energies Driving Electrochemical Technologies for Environmental Applications. *Curr. Opin. Electrochemistry* 22, 211–220. doi:10.1016/j.coelec.2020.07.007

Gao, Y., Yue, Q., Gao, B., and Li, A. (2020). Insight into Activated Carbon from Different Kinds of Chemical Activating Agents: A Review. *Sci. Total Environ.* 746, 141094. doi:10.1016/j.scitotenv.2020.141094

Ghimbeu, C. M., Vidal, L., Delmotte, L., Meins, J. M. Le., and Vix-Guterl, C. (2015). Catalyst-free Soft-Template Synthesis of Ordered Mesoporous Carbon Tailored Using Phloroglucinol/Glyoxylic Acid Environmentally Friendly Precursors. *Green. Chem.* 16, 3079. doi:10.1039/C4GC00269E

Gogotsi, Y., and Simon, P. (2011). True Performance Metrics in Electrochemical Energy Storage. *Science* 334, 917–918. doi:10.1126/science.1213003

Grenier-Loustalot, M.-F., Larroque, S., Grenier, P., Leca, J.-P., and Bedel, D. (1994). Phenolic Resins: 1. Mechanisms and Kinetics of Phenol and of the First Polycondensates towards Formaldehyde in Solution. *Polymer* 35, 3046–3054. doi:10.1016/0032-3861(94)90418-9

Gross, G. (1999). "Biosynthesis of Hydrolysable Tannins," in *Comprehensive Natural Product Chemistry: Carbohydrates and Their Derivatives Including Tannins, Cellulose and Related Lignings*.

Guo, Z., Liu, Z., Ye, L., Ge, K., and Zhao, T. (2015). The Production of Lignin-Phenol-Formaldehyde Resin Derived Carbon Fibers Stabilized by BN Preceramic Polymer. *Mater. Lett.* 142, 49–51. doi:10.1016/j.matlet.2014.11.068

Heidarinejad, Z., Dehghani, M. H., Heidari, M., Javedan, G., Ali, I., and Sillanpää, M. (2020). Methods for Preparation and Activation of Activated Carbon: a Review. *Environ. Chem. Lett.* 18, 393–415. doi:10.1007/s10311-019-00955-0

Herou, S., Ribadeneyra, M. C., Madhu, R., Araullo-Peters, V., Jensen, A., Schlee, P., et al. (2019). Ordered Mesoporous Carbons from Lignin: a New Class of Biobased Electrodes for Supercapacitors. *Green. Chem.* 21, 550–559. doi:10.1039/c8gc03497d

Hu, L., Pan, H., Zhou, Y., and Zhang, M. (2011). Methods to Improve Lignin's Reactivity as a Phenol Substitute and as Replacement for Other Phenolic Compounds: A Brief Review. *BioRes* 6, 3515–3525. doi:10.15376/biores.6.3.3515-3525

Huang, Q., Hu, J., Wen, S., Zhang, X., Liu, G., Chang, S., et al. (2020). Sulfur-Doped and Bio-Resin-Derived Hard Carbon@rGO Composites as Sustainable Anodes for Lithium-Ion Batteries. *Front. Chem.* 8, 241. doi:10.3389/fchem.2020.00241

Huang, Y., Yang, J., Cai, H., Zhai, Y., Feng, D., Deng, Y., et al. (2009). A Curing Agent Method to Synthesize Ordered Mesoporous Carbons from Linear

Novolac Phenolic Resin Polymers. *J. Mater. Chem.* 19, 6536–6541. doi:10.1039/b908183f

Hwang, J.-Y., Myung, S.-T., and Sun, Y.-K. (2017). Sodium-ion Batteries: Present and Future. *Chem. Soc. Rev.* 46, 3529–3614. doi:10.1039/c6cs00776g

Irisarri, E., Amini, N., Tennison, S., Ghimbeu, C. M., Gorka, J., Vix-Guterl, C., et al. (2018). Optimization of Large Scale Produced Hard Carbon Performance in Na-Ion Batteries: Effect of Precursor, Temperature and Processing Conditions. *J. Electrochem. Soc.* 165, A4058–A4066. doi:10.1149/2.1171816jes

Jagiello, J., Kenvin, J., Celzard, A., and Fierro, V. (2019). Enhanced Resolution of Ultra Micropore Size Determination of Biochars and Activated Carbons by Dual Gas Analysis Using N2 and CO2 with 2D-NLDFT Adsorption Models. *Carbon* 144, 206–215. doi:10.1016/j.carbon.2018.12.028

Jagtoyen, M., and Derbyshire, F. (1998). Activated Carbons from Yellow poplar and white Oak by H3PO4 Activation. *Carbon* 36, 1085–1097. doi:10.1016/s0008-6223(98)00082-7

James, S. L., Adams, C. J., Bolm, C., Braga, D., Collier, P., Friščić, T., et al. (2012). Mechanochemistry: Opportunities for New and Cleaner Synthesis. *Chem. Soc. Rev.* 41, 413–447. doi:10.1039/c1cs15171a

Jiang, H., Wang, J., Wu, S., Yuan, Z., Hu, Z., Wu, R., et al. (2012). The Pyrolysis Mechanism of Phenol Formaldehyde Resin. *Polym. Degrad. Stab.* 97, 1527–1533. doi:10.1016/j.polymdegradstab.2012.04.016

Jiang, L., Sheng, L., and Fan, Z. (2018). Biomass-derived Carbon Materials with Structural Diversities and Their Applications in Energy Storage. *Sci. China Mater.* 61, 133–158. doi:10.1007/s40843-017-9169-4

Jiang, X., Liu, J., Du, X., Hu, Z., Chang, H.-m., and Jameel, H. (2018). Phenolation to Improve Lignin Reactivity toward Thermosets Application. *ACS Sust. Chem. Eng.* 6, 5504–5512. doi:10.1021/acssuschemeng.8b00369

Jun, Y.-S., Hong, W. H., Antonietti, M., and Thomas, A. (2009). Mesoporous, 2D Hexagonal Carbon Nitride and Titanium Nitride/Carbon Composites. *Adv. Mater.* 21, 4270–4274. doi:10.1002/adma.200803500

Jurewicz, K., Vix-Guterl, C., Frackowiak, E., Saadallah, S., Reda, M., Parmentier, J., et al. (2004). Capacitance Properties of Ordered Porous Carbon Materials Prepared by a Templating Procedure. *J. Phys. Chem. Sol.* 65, 287–293. doi:10.1016/j.jpcs.2003.10.024

Kahnbabaee, K., and Van-Ree, T. (2001). Tannins: Classification and Definition. *Nat. Prod. Rep.* 18, 641. doi:10.1039/B101061L

Kalami, S., Arefmanesh, M., Master, E., and Nejad, M. (2017). Replacing 100% of Phenol in Phenolic Adhesive Formulations with Lignin. *Appl. Polym. Sci.* 134, 45124

Kang, S., Li, X., Fan, J., and Chang, J. (2013). Hydrothermal Conversion of Lignin: A Review. *Renew. Sustain. Energ. Rev.* 27, 13. doi:10.1016/j.rser.2013.07.013

Ko, T.-H., Kuo, W.-S., and Chang, Y.-H. (2000). Raman Study of the Microstructure Changes of Phenolic Resin during Pyrolysis. *Polym. Compos.* 21, 745–750. doi:10.1002/pc.10229

Kumar, B., Agumba, D. O., Pham, D. H., Latif, M., DineshKim, H. C., Kim, H. C., et al. (2021). Recent Research Progress on Lignin-Derived Resins for Natural Fiber Composite Applications. *Polymers* 13, 1162. doi:10.3390/polym13071162

Lacoste, C., Basso, M. C., Pizzi, A., Laborie, M.-P., Garcia, D., and Celzard, A. (2013). Bioresourced pine Tannin/furanic Foams with Glyoxal and Glutaraldehyde. *Ind. Crops Prod.* 45, 401–405. doi:10.1016/j.indcrop.2012.12.032

Lagel, M. C., Pizzi, A., Giovando, S., and Celzard, A. (2014). Development and Characterisation of Phenolic Foams with Phenol-Formaldehyde-Chestnut Tannins Resin. *J. Renew. Mater.* 2, 220–229. doi:10.7569/jrm.2014.634113

Lan, G., Yang, J., Ye, R. P., Boyjoo, Y., Liang, J., Liu, X., et al. (2021). Sustainable Carbon Materials toward Emerging Applications. *Small Methods* 5, 2001250. doi:10.1002/smtd.202001250

Legrouri, K., Khouya, E., Ezzine, M., Hannache, H., Denoyel, R., Pallier, R., et al. (2004). Production of Activated Carbon from a New Precursor Molasses by Activation with Sulphuric Acid. *J. Hazard. Mater.* 118, 259–263. doi:10.1016/j.jhazmat.2004.11.004

Li, H., Shi, F., An, Q., Zhai, S., Wang, K., and Tong, Y. (2021). Three-dimensional Hierarchical Porous Carbon Derived from Lignin for Supercapacitors: Insight into the Hydrothermal Carbonization and Activation. *Int. J. Biol. Macromolecules* 166, 923–933. doi:10.1016/j.ijbiomac.2020.10.249

Li, J., Li, C., Wang, W., Zhang, W., and Li, J. (2016). Reactivity of Larch and Valonia Tannins in Synthesis of Tannin-Formaldehyde Resins. *BioResources* 11, 2256–2268. doi:10.15376/biores.11.1.2256-2268

Li, T., Ma, R., Lin, J., Hu, Y., Zhang, P., Sun, S., et al. (2019). The Synthesis and Performance Analysis of Various Biomass-based Carbon Materials for Electric Double-layer Capacitors: A Review. *Int. J. Energ. Res.* 44, 2426–2454. doi:10.1002/er.5061

Liang, J., Zhang, J., Du, G., Feng, S., Xi, X., and Lei, H. (2018). Lignin-based Grinding Wheels with Aluminum Oxide: Synthesis and Characterization. *BioResources* 13, 1388–1400. doi:10.15376/biores.13.1.1388-1400

Lillo-Ródenas, M. A., Cazorla-Amorós, D., and Linares-Solano, A. (2003). Understanding Chemical Reactions between Carbons and NaOH and KOH. *Carbon* 41, 267–275. doi:10.1016/s0008-6223(02)00279-8

Liu, L., Deng, Q.-F., Liu, Y.-P., Ren, T.-Z., and Yuan, Z.-Y. (2011). HNO3-activated Mesoporous Carbon Catalyst for Direct Dehydrogenation of Propane to Propylene. *Catal. Commun.* 16, 81–85. doi:10.1016/j.catcom.2011.09.005

Liu, L., Solin, N., and Inganäs, O. (2019). Scalable Lignin/graphite Electrodes Formed by Mechanochemistry. *RSC Adv.* 9, 39758–39767. doi:10.1039/c9ra07507k

Liu, M., Qian, J., Zhao, Y., Zhu, D., Gan, L., and Chen, L. (2015a). Core-shell Ultramicroporous@microporous Carbon Nanospheres as Advanced Supercapacitor Electrodes. *J. Mater. Chem. A.* 3, 11517–11526. doi:10.1039/c5ta02224j

Liu, W.-J., Jiang, H., and Yu, H.-Q. (2015b). Development of Biochar-Based Functional Materials: Toward a Sustainable Platform Carbon Material. *Chem. Rev.* 115, 12251–12285. doi:10.1021/acs.chemrev.5b00195

Liu, X., Li, Y., Xu, X., Zhou, L., and Mai, L. (2021). Rechargeable Metal (Li, Na, Mg, Al)-Sulfur Batteries: Materials and Advances. *J. Energ. Chem.* 61. doi:10.1016/j.jechem.2021.02.028

López de Letona Sánchez, M., Macías-García, A., Díaz-Díez, M. A., Cuerda-Correa, E. M., Gañán-Gómez, J., and Nadal-Gisbert, A. (2006). Preparation of Activated Carbons Previously Treated with Hydrogen Peroxide: Study of Their Porous Texture. *Appl. Surf. Sci.* 252, 5984–5987. doi:10.1016/j.apsusc.2005.11.022

Ma, Q., Yu, Y., Sindoro, M., Fane, A. G., Wang, R., and Zhang, H. (2017). Carbon-Based Functional Materials Derived from Waste for Water Remediation and Energy Storage. *Adv. Mater.* 29, 1605361. doi:10.1002/adma.201605361

Margetic, D., and Strukil, V. (2016). *Mechanochemical Organic Synthesis*. Elsevier. 978-0-12-802184-2.

Marsh, H., and Rodríguez-Reinoso, F. (2006). *Activated Carbon*. Elsevier. 978-0-08-044463-5.

Mauger, A., Julien, C. M., Paolella, A., Armand, M., and Zaghib, K. (2019). Building Better Batteries in the Solid State: A Review. *Materials* 12, 3892. doi:10.3390/ma12233892

Mayoral, E. P., Matos, I., Bernardo, M., Durán-Valle, C., and Fonseca, I. (2021). Functional Porous Carbons: Synthetic Strategies and Catalytic Application in fine Chemical Synthesis. *Emerging Carbon Mater. Catal.* 601, 299–352. doi:10.1016/b978-0-12-817561-3.00009-3

Mehta, S., Jha, S., and Liang, H. (2020). Lignocellulose Materials for Supercapacitor and Battery Electrodes: A Review. *Renew. Sust. Energ. Rev.* 134, 110345. doi:10.1016/j.rser.2020.110345

Meng, Y., Gu, D., Zhang, F., Shi, Y., Cheng, L., Feng, D., et al. (2006). A Family of Highly Ordered Mesoporous Polymer Resin and Carbon Structures from Organic–Organic Self-Assembly. *Chem. Mater.* 18, 4447–4464. doi:10.1021/cm060921u

Mi, J., Wang, X.-R., Fan, R.-J., Qu, W.-H., and Li, W.-C. (2012). Coconut-Shell-Based Porous Carbons with a Tunable Micro/Mesopore Ratio for High-Performance Supercapacitors. *Energy Fuels* 26, 5321–5329. doi:10.1021/ef3009234

Miao, L., Zhu, D., Zhao, Y., Liu, M., Duan, H., Xiong, W., et al. (2017). Design of Carbon Materials with Ultramicro-, Supermicro- and Mesopores Using Solvent- and Self-Template Strategy for Supercapacitors. *Microporous Mesoporous Mater.* 253, 1–9. doi:10.1016/j.micromeso.2017.06.032

Mohamed, G., El-Shafey, O., and Fathy, N. A. (2017). Preparation of Carbonaceous Hydrochar Adsorbents from Cellulose and Lignin Derived from rice Straw. *Egypt. J. Chem.* 60, 793–804. doi:10.21608/ejchem.2017.1311.1080

Molina-Sabio, M., Rodríguez-Reinoso, F., Caturla, F., and Sellés, M. J. (1996). Development of Porosity in Combined Phosphoric Acid-Carbon Dioxide Activation. *Carbon* 34, 457–462. doi:10.1016/0008-6223(95)00209-x

Moussa, G., Hajjar-Garreau, S., Taberna, P.-L., Simon, P., and Matei Ghimbeu, C. (2018). Eco-Friendly Synthesis of Nitrogen-Doped Mesoporous Carbon for Supercapacitor Application. *C. J. Carbon. Res.* 4, 20. doi:10.3390/c4020020

Muylaert, I., Verberckmoes, A., De Decker, J., and Van Der Voort, P. (2012). Ordered Mesoporous Phenolic Resins: Highly Versatile and Ultra Stable Support Materials. *Adv. Colloid Interf. Sci.* 175, 39–51. doi:10.1016/j.cis.2012.03.007

Muzaffar, A., Ahamed, M. B., Deshmukh, K., and Thirumalai, J. (2019). A Review on Recent Advances in Hybrid Supercapacitors: Design, Fabrication and Applications. *Renew. Sust. Energ. Rev.* 101, 123–145. doi:10.1016/j.rser.2018.10.026

Nasini, U. B., Bairi, V. G., Ramasahayam, S. K., Bourdo, S. E., Viswanathan, T., and Shaikh, A. U. (2014). Phosphorous and Nitrogen Dual Heteroatom Doped Mesoporous Carbon Synthesized via Microwave Method for Supercapacitor Application. *J. Power Sourc.* 250, 257–265. doi:10.1016/j.jpowsour.2013.11.014

Nasini, U. B., Gopal Bairi, V., Kumar Ramasahayam, S., Bourdo, S. E., Viswanathan, T., and Shaikh, A. U. (2013). Oxygen Reduction Reaction Studies of Phosphorus and Nitrogen Co-doped Mesoporous Carbon Synthesized via Microwave Technique. *ChemElectroChem* 1, 573–579. doi:10.1002/celc.201300047

Neatu, S., Neatu, F., Chirica, J. M., Borbath, I., Talas, E., Tompos, A., et al. (2021). Recent Progress in Electrocatalysts and Electrodes for Portable Fuel Cells. *J. Mater. Chem. A.* 9, 17065. doi:10.1039/D1TA03644K

Nelson, K. M., Mahurin, S. M., Mayes, R. T., Williamson, B., Teague, C. M., Binder, A. J., et al. (2016). Preparation and CO2 Adsorption Properties of Soft-Templated Mesoporous Carbons Derived from Chestnut Tannin Precursors. *Microporous Mesoporous Mater.* 222, 94–103. doi:10.1016/j.micromeso.2015.09.050

Nita, C., Bensafia, M., Vaulot, C., Delmotte, L., and Matei Ghimbeu, C. (2016). Insights on the Synthesis Mechanism of green Phenolic Resin Derived Porous Carbons via a Salt-Soft Templating Approach. *Carbon* 109, 227–238. doi:10.1016/j.carbon.2016.08.011

Nizamuddin, S., Baloch, H. A., Griffin, G. J., Mubarak, N. M., Bhutto, A. W., Abro, R., et al. (2017). An Overview of Effect of Process Parameters on Hydrothermal Carbonization of Biomass. *Renew. Sust. Energ. Rev.* 73, 1289–1299. doi:10.1016/j.rser.2016.12.122

Oliveira, F. B., Gardrat, C., Enjalbal, C., Frollini, E., and Castellan, A. (2008). Phenol-furfural Resins to Elaborate Composites Reinforced with Sisal Fibers-Molecular Analysis of Resin and Properties of Composites. *J. Appl. Polym. Sci.* 109, 2291–2303. doi:10.1002/app.28312

Paris Agreement to the United Nations Framework Convention on Climate Change (2015). New York, NY: T.I.A.S. No, 16–1104.

Parthiban, V., Bhuvaneshwari, B., Karthikeyan, J., Murugan, P., and Sahu, A. K. (2019). Fluorine-enriched Mesoporous Carbon as Efficient Oxygen Reduction Catalyst: Understanding the Defects in Porous Matrix and Fuel Cell Applications. *Nanoscale Adv.* 1, 4926–4937. doi:10.1039/c9na00572b

Peng, W., Riedl, B., and Barry, A. O. (1993). Study on the Kinetics of Lignin Methylolation. *J. Appl. Polym. Sci.* 48, 1757–1763. doi:10.1002/app.1993.070481009

Pérez-Rodríguez, S., Pinto, O., Izquierdo, M. T., Segura, C., Poon, P. S., Celzard, A., et al. (2021). Upgrading of pine Tannin Biochars as Electrochemical Capacitor Electrodes. *J. Colloid Inter. Sci.* 601, 836–876. doi:10.1016/j.jcis.2021.05.162

Pilato, L. (2013). Phenolic Resins: 100Years and Still Going strong. *Reactive Funct. Polym.* 73, 270–277. doi:10.1016/j.reactfunctpolym.2012.07.008

Pizzi, A., Meikleham, N., Dombo, B., and Roll, W. (1995). Autocondensation-based, Zero-Emission, Tannin Adhesives for Particleboard. *Holz als Roh-und Werkstoff* 53, 201–204. doi:10.1007/bf02716424

Pizzi, A., Pasch, H., Celzard, A., and Szczurek, A. (2013). Oligomers Distribution at the Gel point of Tannin-Formaldehyde Thermosetting Adhesives for wood Panels. *J. Adhes. Sci. Tech.* 27, 2094–2102. doi:10.1080/01694243.2012.697669

Pizzi, A. (2008). Polyflavonoid Tannins Self-Condensation Adhesives for Wood Particleboard. *J. Adhes.* 85, 57–68.

Pizzi, A., and Stephanou, A. (1994). Phenol-Formaldehyde Wood Adhesives under Very Alkaline Conditions. Part I: Behaviour and Proposed Mechanism. *Holzforschung* 48, 35–40. doi:10.1515/hfsg.1994.48.1.35

Pomerantseva, E., Bonaccorso, F., Feng, X., Cui, Y., and Gogotsi, Y. (2019). Energy Storage: The Future Enabled by Nanomaterials. *Science* 366, 6468. doi:10.1126/science.aan8285

PoonamSharma, K., Arora, A., and Tripathi, S. K. (2019). Review of Supercapacitors: Materials and Devices. *J. Energ. Storage* 21, 801–825. doi:10.1016/j.est.2019.01.010

Puziy, A. M., Poddubnaya, O. I., Martínez-Alonso, A., Suárez-Garcı´a, F., and Tascón, J. M. D. (2003). Synthetic Carbons Activated with Phosphoric Acid III. Carbons Prepared in Air. *Carbon* 41, 1181–1191. doi:10.1016/s0008-6223(03)00031-9

Quílez-Bermejo, J., González-Gaitán, C., Morallón, E., and Cazorla-Amorós, D. (2017). Effect of Carbonization Conditions of Polyaniline on its Catalytic Activity towards ORR. Some Insights about the Nature of the Active Sites. *Carbon* 119, 62–71. doi:10.1016/j.carbon.2017.04.015

Quílez-Bermejo, J., Melle-Franco, M., San-Fabián, E., Morallón, E., and Cazorla-Amorós, D. (2019). Towards Understanding the Active Sites for the ORR in N-Doped Carbon Materials through fine-tuning of Nitrogen Functionalities: an Experimental and Computational Approach. *J. Mater. Chem. A.* 7, 24239–24250. doi:10.1039/c9ta07932g

Quílez-Bermejo, J., Morallón, E., and Cazorla-Amorós, D. (2020a). Metal-free Heteroatom-Doped Carbon-Based Catalysts for ORR: A Critical Assessment about the Role of Heteroatoms. *Carbon* 165, 434–454. doi:10.1016/j.carbon.2020.04.068

Quílez-Bermejo, J., Morallón, E., and Cazorla-Amorós, D. (2020b). Polyaniline-Derived N-Doped Ordered Mesoporous Carbon Thin Films: Efficient Catalysts towards Oxygen Reduction Reaction. *Polymers* 12, 2382. doi:10.3390/polym12102382

Quílez-Bermejo, J., Strutyński, K., Melle-Franco, M., Morallón, E., and Cazorla-Amorós, D. (2020c). On the Origin of the Effect of pH in Oxygen Reduction Reaction for Nondoped and Edge-type Quaternary N-Doped Metal-free Carbon-Based Catalysts. *ACS Appl. Mater. Inter.* 12, 54815–54823. doi:10.1021/acsami.0c17249

Ramires, E. C., Megiatto, J. D., Gardrat, C., Castellan, A., and Frollini, E. (2010). Biobased Composites from Glyoxal-Phenolic Resins and Sisal Fibers. *Bioresour. Tech.* 101, 1998–2006. doi:10.1016/j.biortech.2009.10.005

Renda, C. G., and Bertholdo, R. (2018). Study of Phenolic Resin and Their Tendency for Carbon Graphitization. *J. Polym. Res.* 25, 241. doi:10.1007/s10965-018-1635-y

Rodríguez-Mirasol, J., Cordero, T., and Rodríguez, J. J. (1993a). Activated Carbons from Carbon Dioxide Partial Gasification of eucalyptus Kraft Lignin. *Energy Fuels* 7, 133–138. doi:10.1021/ef00037a021

Rodríguez-Mirasol, J., Cordero, T., and Rodríguez, J. J. (1993b). Preparation and Characterization of Activated Carbons from eucalyptus Kraft Lignin. *Carbon* 31, 87–95. doi:10.1016/0008-6223(93)90160-c

Ruoff, R. S. (2018). A Perspective on Objectives for Carbon Science. *Carbon* 132, 802. doi:10.1016/j.carbon.2018.02.057

Salinas-Torres, D., Ruiz-Rosas, R., Valero-Romero, M. J., Rodríguez- Mirasol, J., Cordero, T., Morallón, E., et al. (2016). Asymmetric Capacitors Using Lignin-Based Hierarchical Porous Carbons. *J. Power Sourc.* 326, 641–651. doi:10.1016/j.jpowsour.2016.03.096

Sanchez-Sanchez, A., Izquierdo, M. T., Ghanbaja, J., Medjahdi, G., Mathieu, S., Celzard, A., et al. (2017a). Excellent Electrochemical Performances of Nanocast Ordered Mesoporous Carbons Based on Tannin-Related Polyphenols as Supercapacitor Electrodes. *J. Power Sourc.* 344, 15–24. doi:10.1016/j.jpowsour.2017.01.099

Sanchez-Sanchez, A., Izquierdo, M. T., Mathieu, S., González-Álvarez, J., Celzard, A., and Fierro, V. (2017b). Outstanding Electrochemical Performance of Highly N- and O-Doped Carbons Derived from pine Tannin. *Green. Chem.* 19, 2653–2665. doi:10.1039/c7gc00491e

Sanchez-Sanchez, A., Izquierdo, M. T., Medjahdi, G., Ghanbaja, J., Celzard, A., and Fierro, V. (2018). Ordered Mesoporous Carbons Obtained by Soft-Templating of Tannin in Mild Conditions. *Microporous Mesoporous Mater.* 270, 129–139. doi:10.1016/j.micromeso.2018.05.017

Santiago-Medina, F.-J., Pizzi, A., Basso, M., Delmotte, L., and Celzard, A. (2017). Polycondensation Resins by Flavonoid Tannins Reaction with Amines. *Polymers* 9, 37. doi:10.3390/polym9020037

Sarika, P. R., Nancarrow, P., Khansaheb, A., and Ibrahim, T. (2020). Bio-Based Alternatives to Phenol and Formaldehyde for the Production of Resins. *Polymers* 12, 2237. doi:10.3390/polym12102237

Sazali, N., Wan Salleh, W. N., Jamaludin, A. S., and Mhd Razali, M. N. (2020). New Perspectives on Fuel Cell Technology: A Brief Review. *Membranes* 10, 99. doi:10.3390/membranes10050099

Schaefer, S., Fierro, V., Izquierdo, M. T., and Celzard, A. (2016). Assessment of Hydrogen Storage in Activated Carbons Produced from Hydrothermally

Treated Organic Materials. *Int. J. Hydrogen Energ.* 41, 12146–12156. doi:10.1016/j.ijhydene.2016.05.086

Sellers, T., McGinnis, G. D., Ruffin, T. M., and Janiga, E. R. (2004). Lignin-modified Phenol-Formaldehyde Resin Development for Fiberboard. *For. Prod. J.* 54, 45–51.

Sevilla, M., Diez, N., Ferrero, G. A., and Fuertes, A. B. (2019). Sustainable Supercapacitor Electrodes Produced by the Activation of Biomass with Sodium Thiosulfate. *Energ. Storage Mater.* 18, 356–365. doi:10.1016/j.ensm.2019.01.023

Sharma, P., and Bhatti, T. S. (2010). A Review on Electrochemical Double-Layer Capacitors. *Energ. Convers. Manage.* 51, 2901–2912. doi:10.1016/j.enconman.2010.06.031

Sima, G., Gan, L., Chang, L., Cui, Y., and Kankala, R. K. (2021). Efficient Fabrication of Ordered Mesoporous Carbon Derived from Lignin via Deep Eutectic Solvent Pretreatment for Supercapacitors. *Microporous Mesoporous Mater.* 323, 111192. doi:10.1016/j.micromeso.2021.111192

Simitzis, J., and Sfyrakis, J. (1993). Pyrolysis of Lignin Biomass-Novolac Resin for the Production of Polymeric Carbon Adsorbents. *J. Anal. Appl. Pyrolysis* 26, 37–52. doi:10.1016/0165-2370(93)85017-s

Soltani, N., Bahrami, A., Giebeler, L., Gemming, T., and Mikhailova, D. (2021). Progress and Challenges in Using Sustainable Carbon Anodes in Rechargeable Metal-Ion Batteries. *Prog. Energ. Combustion Sci.* 87, 100929. doi:10.1016/j.pecs.2021.100929

Song, Y., Wang, Z., Yan, N., Zhang, R., and Li, J. (2016). Demethylation of Wheat Straw Alkali Lignin for Application in Phenol Formaldehyde Adhesives. *Polymers* 8, 209. doi:10.3390/polym8060209

Ståhlberg, T., Fu, W., Woodley, J. M., and Riisager, A. (2011). Synthesis of 5-(Hydroxymethyl)furfural in Ionic Liquids: Paving the Way to Renewable Chemicals. *ChemSusChem* 4, 451–458. doi:10.1002/cssc.201000374

Sternberg, J., Sequerth, O., and Pilla, S. (2021). Green Chemistry Design in Polymers Derived from Lignin: Review and Perspective. *Prog. Polym. Sci.* 113, 101344. doi:10.1016/j.progpolymsci.2020.101344

Stevens, D. A., and Dahn, J. R. (2001). The Mechanisms of Lithium and Sodium Insertion in Carbon Materials. *J. Electrochem. Soc.* 148, A803. doi:10.1149/1.1379565

Sun, S., Zhang, C., Yao, J., Wang, H., Zhao, X., and Shen, X. (2020). Resol and Urea Derived N-Doped Porous Carbon for Na-Ion Storage. *Mater. Chem. Phys.* 254, 123535. doi:10.1016/j.matchemphys.2020.123535

Suryanarayana, C. (2001). Mechanical Alloying and Milling. *Prog. Mater. Sci.* 46, 1–184. doi:10.1016/s0079-6425(99)00010-9

Szczesniak, B., Phuriragpitikhon, J., Choma, J., and Jaroniec, M. (2020). Recent Advances in the Development and Applications of Biomass-Derived Carbons with Uniform Porosity. *J. Mater. Chem. A.* 8, 18464–18491.

Tanaka, S., Fujimoto, H., Denayer, J. F. M., Miyamoto, M., Oumi, Y., and Miyake, Y. (2015). Surface Modification of Soft-Templated Ordered Mesoporous Carbon for Electrochemical Supercapacitors. *Microporous Mesoporous Mater.* 217, 141–149. doi:10.1016/j.micromeso.2015.06.017

Tarascon, J.-M., and Armand, M. (2001). Issues and Challenges Facing Rechargeable Lithium Batteries. *Nature* 414, 359–367. doi:10.1038/35104644

Titirici, M.-M., White, R. J., Brun, N., Budarin, V. L., Su, D. S., del Monte, F., et al. (2015). Sustainable Carbon Materials. *Chem. Soc. Rev.* 44, 250–290. doi:10.1039/c4cs00232f

Tonnoir, H., Huo, D., Canevesi, R. L. S., Fierro, V., Celzard, A., and Janot, R. (2021). Tannin-Based Hard-Carbons as High-Performance Anode Materials for Sodium-Ion Batteries. *Mater. Today Chem.* 23, 100614. doi:10.1016/j.mtchem.2021.100614

Torres, D., Pérez-Rodríguez, S., Cesari, L., Castel, C., Favre, E., Fierro, V., et al. (2021). Review on the Preparation of Carbon Membranes Derived from Phenolic Resins for Gas Separation: From Petrochemical Precursors to Bioresources. *Carbon* 183, 12–33. doi:10.1016/j.carbon.2021.06.087

T. Q. Hu (Editor) (2002). *Chemical Modification, Properties, and Usage of Lignin* (Boston, MA: Springer). 978-1-4613-5173-3.

Trick, K. A., and Saliba, T. E. (1995). Mechanisms of the Pyrolysis of Phenolic Resin in a Carbon/phenolic Composite. *Carbon* 33, 1509–1515. doi:10.1016/0008-6223(95)00092-r

Van Nieuwenhove, I., Renders, T., Lauwaert, J., De Roo, T., De Clercq, J., and Verberckmoes, A. (2020). Biobased Resins Using Lignin and Glyoxal. *ACS Sust. Chem. Eng.* 8, 18789–18809. doi:10.1021/acssuschemeng.0c07227

Vázquez, G., González, J., Freire, S., and Antorrena, G. (1997). Effect of Chemical Modification of Lignin on the Gluebond Performance of Lignin-Phenolic Resins. *Bioresour. Tech.* 60, 191–198. doi:10.1016/s0960-8524(97)00030-8

Vinodh, R., Muralee Gopi, C. V. V., Yang, Z., Deviprasath, C., Atchudan, R., Raman, V., et al. (2020). Novel Electrode Material Derived from Porous Polymeric Organic Framework of Phloroglucinol and Terephthaldehyde for Symmetric Supercapacitors. *J. Energ. Storage* 28, 101283. doi:10.1016/j.est.2020.101283

Wang, H., Eberhardt, T. L., Wang, C., Gao, S., and Pan, H. (2019). Demethylation of Alkali Lignin with Halogen Acids and its Application to Phenolic Resins. *Polymers* 11, 1771. doi:10.3390/polym11111771

Wang, H., Shao, Y., Mei, S., Lu, Y., Zhang, M., Sun, J.-k., et al. (2020a). Polymer-Derived Heteroatom-Doped Porous Carbon Materials. *Chem. Rev.* 120, 9363–9419. doi:10.1021/acs.chemrev.0c00080

Wang, X., Qiu, M., Smith, R. L., Yang, J., Shen, F., and Qi, X. (2020b). Ferromagnetic Lignin-Derived Ordered Mesoporous Carbon for Catalytic Hydrogenation of Furfural to Furfuryl Alcohol. *ACS Sust. Chem. Eng.* 8, 18157–18166. doi:10.1021/acssuschemeng.0c06533

Wang, Y.-Y., Meng, X., Pu, Y., and J. Ragauskas, A. (2020c). Recent Advances in the Application of Functionalized Lignin in Value-Added Polymeric Materials. *Polymers* 12, 2277. doi:10.3390/polym12102277

Wu, M., Liao, J., Yu, L., Lv, R., Li, P., Sun, W., et al. (2020). 2020 Roadmap on Carbon Materials for Energy Storage and Conversion. *Chem. Asian J.* 15, 995–1013. doi:10.1002/asia.201901802

Xi, J., Li, H., Xi, J., Tan, S., Zheng, J., and Tan, Z. (2020). Preparation of High Porosity Biochar Materials by Template Method: a Review. *Environ. Sci. Pollut. Res.* 27, 20675–20684. doi:10.1007/s11356-020-08593-8

Xie, A., Dai, J., Chen, Y., Liu, N., Ge, W., Ma, P., et al. (2019). NaCl-template Assisted Preparation of Porous Carbon Nanosheets Started from Lignin for Efficient Removal of Tetracycline. *Adv. Powder Tech.* 30, 170–179. doi:10.1016/j.apt.2018.10.020

Xie, L., Jin, Z., Dai, Z., Chang, Y., Jiang, X., and Wang, H. (2020). Porous Carbons Synthesized by Templating Approach from Fluid Precursors and Their Applications in Environment and Energy Storage: A Review. *Carbon* 170, 100–118. doi:10.1016/j.carbon.2020.07.034

Xie, L., Tang, C., Bi, Z., Song, M., Fan, Y., Yan, C., et al. (2021). Hard Carbon Anodes for Next-Generation Li-Ion Batteries: Review and Perspective. *Adv. Energ. Mater.* 11, 2101650. doi:10.1002/aenm.202101650

Xie, M., Dong, H., Zhang, D., Guo, X., and Ding, W. (2011). Simple Synthesis of Highly Ordered Mesoporous Carbon by Self-Assembly of Phenol-Formaldehyde and Block Copolymers under Designed Aqueous Basic/acidic Conditions. *Carbon* 49, 2459–2464. doi:10.1016/j.carbon.2011.02.014

Xie, X., Goodell, B., Zhang, D., Nagle, D. C., Qian, Y., Peterson, M. L., et al. (2009). Characterization of Carbons Derived from Cellulose and Lignin and Their Oxidative Behavior. *Bioresour. Tech.* 100, 1797–1802. doi:10.1016/j.biortech.2008.09.057

Xing, T., Zheng, Y., Li, L. H., Cowie, B. C. C., Gunzelmann, D., Qiao, S. Z., et al. (2014). Observation of Active Sites for Oxygen Reduction Reaction on Nitrogen-Doped Multilayer Graphene. *ACS Nano* 8, 6856–6862. doi:10.1021/nn501506p

Xu, K. (2004). Nonaqueous Liquid Electrolytes for Lithium-Based Rechargeable Batteries. *Chem. Rev.* 104, 4303–4418. doi:10.1021/cr030203g

Xu, C., De, S., Balu, A. M., Ojeda, M., and Luque, R. (2015). Mechanochemical Synthesis of Advanced Nanomaterials for Catalytic Applications. *Chem. Commun.* 51, 6698–6713. doi:10.1039/c4cc09876e

Xu, C., and Ferdosian, F. (2017). *Conversion of Lignin into Bio-Based Chemicals and Materials*. Springer.

Xu, C., Zhang, Y., Zhang, N., Liu, X., Yi, J., Liu, X., et al. (2020). 2020 Roadmap on Zinc Metal Batteries. *Chem. Asian J.* 15, 3696–3708. doi:10.1002/asia.202000946

Xu, Z., and Guo, Q. (2013). A Simple Method to Prepare Monodisperse and Size-Tunable Carbon Nanospheres from Phenolic Resin. *Carbon* 52, 464–467. doi:10.1016/j.carbon.2012.09.057

Xue, R., Yan, J., Liu, X., Tian, Y., and Yi, B. (2011). Effect of Activation on the Carbon Fibers from Phenol-Formaldehyde Resins for Electrochemical Supercapacitors. *J. Appl. Electrochem.* 41, 1357–1366. doi:10.1007/s10800-011-0357-1

Yahya, M. A., Al-Qodah, Z., and Ngah, C. W. Z. (2015). Agricultural Bio-Waste Materials as Potential Sustainable Precursors Used for Activated Carbon Production: A Review. *Renew. Sust. Energ. Rev.* 46, 218–235. doi:10.1016/j.rser.2015.02.051

Yang, Z., Guo, H., Li, F., Li, X., Wang, Z., Cui, L., et al. (2018). Cooperation of Nitrogen-Doping and Catalysis to Improve the Li-Ion Storage Performance of Lignin-Based Hard Carbon. *J. Energ. Chem.* 27, 1390–1396. doi:10.1016/j.jechem.2018.01.013

Yeddanapalli, L. M., and Joseph Francis, D. (1962). Kinetics and Mechanism of the Alkali Catalysed Condensation of O- and P-Methylol Phenols by Themselves and with Phenol. *Makromol. Chem.* 55, 74–86. doi:10.1002/macp.1962.020550106

Yin, J., Zhang, W., Alhebshi, N. A., Salah, N., and Alshareef, H. N. (2020). Synthesis Strategies of Porous Carbon for Supercapacitor Applications. *Small Methods* 4, 1900853. doi:10.1002/smtd.201900853

Yoon, G., Kim, H., Park, I., and Kang, K. (2016). Conditions for Reversible Na Intercalation in Graphite: Theoretical Studies on the Interplay Among Guest Ions, Solvent, and Graphite Host. *Adv. Energ. Mater.* 7, 1601519. doi:10.1002/aenm.201601519

Yu, J., and So, J. (2019). Synthesis and Characterization of Nitrogen-Containing Hydrothermal Carbon with Ordered Mesostructure. *Chem. Phys. Lett.* 716, 237–246. doi:10.1016/j.cplett.2018.12.014

Zakoshansky, V. M. (2007). The Cumene Process for Phenol-Acetone Production. *Pet. Chem.* 47, 273–284. doi:10.1134/s096554410704007x

Zakrzewska, M. E., Bogel-Łukasik, E., and Bogel-Łukasik, R. (2011). Ionic Liquid-Mediated Formation of 5-Hydroxymethylfurfural-A Promising Biomass-Derived Building Block. *Chem. Rev.* 111, 397–417. doi:10.1021/cr100171a

Zhang, H., Zhang, W., Ming, H., Pang, J., Zhang, H., Cao, G., et al. (2018). Design Advanced Carbon Materials from Lignin-Based Interpenetrating Polymer Networks for High Performance Sodium-Ion Batteries. *Chem. Eng. J.* 341, 280–288. doi:10.1016/j.cej.2018.02.016

Zhang, J., Liang, J., Du, G., Zhou, X., Wang, H., and Wang, H. (2017a). Performance of Cutting and Grinding Wheel Based on Lignin-Phenolic Resin Matrix and Aluminum Oxide. *BioRes* 12, 9118–9129. doi:10.15376/biores.12.4.9118-9129

Zhang, P., Wang, L., Yang, S., Schott, J. A., Liu, X., Mahurin, S. M., et al. (2017b). Solid-state Synthesis of Ordered Mesoporous Carbon Catalysts via a Mechanochemical Assembly through Coordination Cross-Linking. *Nat. Commun.* 8, 15020. doi:10.1038/ncomms15020

Zhang, W., Ma, Y., Wang, C., Li, S., Zhang, M., and Chu, F. (2013). Preparation and Properties of Lignin-Phenol-Formaldehyde Resins Based on Different Biorefinery Residues of Agricultural Biomass. *Ind. Crops Prod.* 43, 326–333. doi:10.1016/j.indcrop.2012.07.037

Zhang, Y., Li, N., Chen, Z., Ding, C., ZHeng, Q., Xu, J., et al. (2020). Synthesis of High-Water-Resistance Lignin-Phenol Resin Adhesive with Furfural as a Crosslinking Agent. *Polymers* 12, 2805. doi:10.3390/polym12122805

Zhang, Y., Nanda, M., Tymchyshyn, M., Yuan, Z., and Xu, C. (2016a). Mechanical, thermal, and Curing Characteristics of Renewable Phenol-Hydroxymethylfurfural Resin for Application in Bio-Composites. *J. Mater. Sci.* 51, 732–738. doi:10.1007/s10853-015-9392-3

Zhang, Y., Yuan, Z., Mahmood, N., Huang, S., and Xu, C. (2016b). Sustainable Bio-Phenol-Hydroxymethylfurfural Resins Using Phenolated De-polymerized Hydrolysis Lignin and Their Application in Bio-Composites. *Ind. Crops Prod.* 79, 84–90. doi:10.1016/j.indcrop.2015.10.048

Zhang, Y., Yuan, Z., and Xu, C. C. (2015). Engineering Biomass into Formaldehyde-free Phenolic Resin for Composite Materials. *Aiche J.* 61, 1275–1283. doi:10.1002/aic.14716

Zhao, J., Shan, W., Zhang, P., and Dai, S. (2020). Solvent-free and Mechanochemical Synthesis of N-Doped Mesoporous Carbon from Tannin and Related Gas Sorption Property. *Chem. Eng. J.* 381, 122579. doi:10.1016/j.cej.2019.122579

Zhuang, X., Huang, Y., Song, Y., Zhan, H., Yin, X., and Wu, C. (2018). The Transformation Pathways of Nitrogen in Sewage Sludge during Hydrothermal Treatment. *Bioresour. Technol.* 245, 463–470. doi:10.1016/j.biortech.2017.08.195

Conflict of Interest: The authors declare that the research was conducted in the absence of any commercial or financial relationships that could be construed as a potential conflict of interest.

Publisher's Note: All claims expressed in this article are solely those of the authors and do not necessarily represent those of their affiliated organizations, or those of the publisher, the editors and the reviewers. Any product that may be evaluated in this article, or claim that may be made by its manufacturer, is not guaranteed or endorsed by the publisher.

frontiers in Materials

REVIEW
published: 16 March 2022
doi: 10.3389/fmats.2022.818535

Digital Twins for Materials

Surya R. Kalidindi[1]*, *Michael Buzzy*[1], *Brad L. Boyce*[2] *and Remi Dingreville*[2]

[1]Georgia Institute of Technology, Atlanta, GA, United States, [2]Center for Integrated Nanotechnologies, Sandia National Laboratories, Albuquerque, NM, United States

Digital twins are emerging as powerful tools for supporting innovation as well as optimizing the in-service performance of a broad range of complex physical machines, devices, and components. A digital twin is generally designed to provide accurate in-silico representation of the form (i.e., appearance) and the functional response of a specified (unique) physical twin. This paper offers a new perspective on how the emerging concept of digital twins could be applied to accelerate materials innovation efforts. Specifically, it is argued that the material itself can be considered as a highly complex multiscale physical system whose form (i.e., details of the material structure over a hierarchy of material length) and function (i.e., response to external stimuli typically characterized through suitably defined material properties) can be captured suitably in a digital twin. Accordingly, the digital twin can represent the evolution of structure, process, and performance of the material over time, with regard to both process history and in-service environment. This paper establishes the foundational concepts and frameworks needed to formulate and continuously update both the form and function of the digital twin of a selected material physical twin. The form of the proposed material digital twin can be captured effectively using the broadly applicable framework of n-point spatial correlations, while its function at the different length scales can be captured using homogenization and localization process-structure-property surrogate models calibrated to collections of available experimental and physics-based simulation data.

Keywords: artificial intelligence, machine learning, digital twins, computational materials science, materials knowledge systems

OPEN ACCESS

Edited by:
Roberto Brighenti,
University of Parma, Italy

Reviewed by:
Thomas Hammerschmidt,
Ruhr University Bochum, Germany
Xiaoying Zhuang,
Leibniz University Hannover, Germany

***Correspondence:**
Surya R. Kalidindi
surya.kalidindi@me.gatech.edu

Specialty section:
This article was submitted to Computational Materials Science, a section of the journal Frontiers in Materials

Received: *19 November 2021*
Accepted: *18 January 2022*
Published: *16 March 2022*

Citation:
Kalidindi SR, Buzzy M, Boyce BL and Dingreville R (2022) Digital Twins for Materials. Front. Mater. 9:818535. doi: 10.3389/fmats.2022.818535

1 INTRODUCTION

Recent forward-looking roadmaps (Gil and Selman, 2019; Jenks et al., 2020) have identified the development of a fully digital framework that fuses human-subject matter expertise, process and performance modeling, experimental *in-situ* diagnostics, and data science algorithms as one of the most important areas to transform manufacturing and surveillance of components throughput their life cycle. Indeed, the digitization of product lifecycle management (PLM) has led to the emergence and deployment of digital threads (Kapteyn et al., 2021; Niederer et al., 2021; Zeb et al., 2021) in a broad spectrum of manufacturing industries. These digital threads collect, curate, and archive all of the data/information generated from all stages of the product life cycle: conceptualization, design, prototype, manufacturing, operation, and retirement (Singh and Willcox, 2018; Margaria and Schieweck, 2019). Digital threads open multiple new avenues for fostering innovation and improving the in-service performance of a wide range of products. A necessary feature of the digital threads is that they encompass both the in-silico activities (e.g., model-based or virtual engineering) and the physical activities (e.g., measurements made during the different stages of manufacturing, testing, and operation of the product) conducted in the PLM. An important outcome

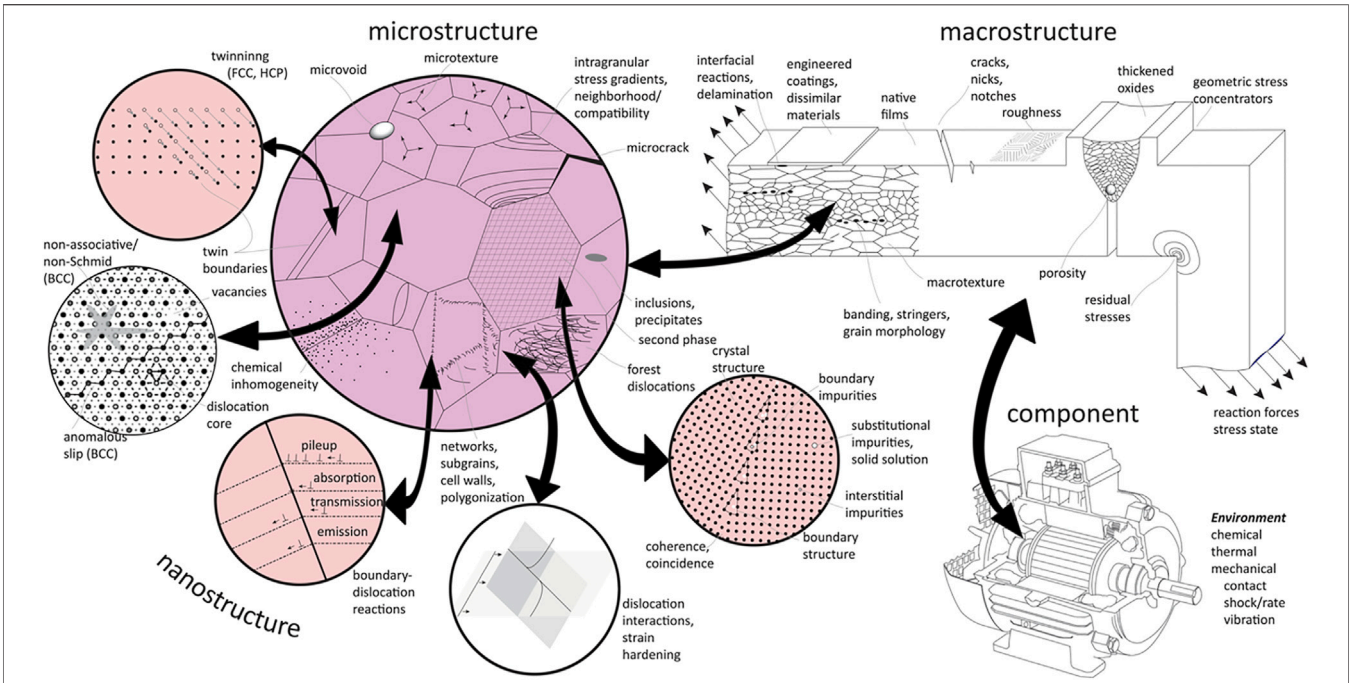

FIGURE 1 | A schematic depiction of the multiscale and multi-physics nature of material systems and their relationship with the component performance. A comprehensive understanding of material performance requires a complete hierarchical representation of structural/chemical features, the relationship between those features and material properties, and the mechanisms that drive their evolution either through processing or service history. All arrows represent scale bridging, i.e., upscaling via homogenization and downscaling via localization.

from the deployment of digital threads is that they have opened new opportunities for the creation and use of in-silico analogues to the physical product. The recent advances in digital and sensor technologies (Mei et al., 2019; Ullo and Sinha, 2020) enable the in-silico objects to co-exist along with their physical counterparts. In addition to mimicking the physical products, the in-silico analogues offer unprecedented potential for consistent change management, allowing the optimization of intentional or unintentional product evolution over time. Therefore, within this context, a digital twin can be defined as a high-fidelity in-silico representation closely mirroring the form (i.e., appearance) and the functional response of a specified (unique) physical twin. Digital twins have thus far been used in the manufacturing and performance evaluation of complex engineered physical systems (e.g., turbine engines) (Tao et al., 2018; Zaccaria et al., 2018; Raj and Surianarayanan, 2020; Lim et al., 2021; Xie et al., 2021) and/or their components, where the focus has been largely on capturing accurately the macroscale geometry and the component-level performance metrics. Current digital twins do not address adequately the capture and archival of the materials data, which typically deals with physical phenomena occurring at the lower material length scales (typically ranging from the atomic to the macroscale). This disconnect is not surprising given the siloed nature of current materials research and product design/manufacturing communities. However, it is abundantly clear that a successful extension of digital twins to include the materials data/information in a comprehensive manner can allow for a holistic co-design of material, manufacturing process, and product in fully integrated innovation cycles, possibly resulting in dramatic improvements in the overall part performance.

Materials, in their own right, represent highly complex multiscale and multi-physics systems. Their production and in-service responses are controlled by a wide range of phenomena occurring at length scales ranging from the atomic to the macroscale and an equally broad range of associated time scales. **Figure 1** depicts schematically the hierarchical nature of materials systems with examples of a wide variety of physical phenomena that occur at the nano- and micro-scales. Clearly, the materials phenomena occurring at the lower material length scales play important roles in controlling the macro- and component-scale performances of the part. In the current research paradigm, the considerations at the component/part scale and the material scale are studied in a mostly de-coupled manner by different groups of researchers. The former are the domain of mechanical designers and manufacturing specialists, while the latter are addressed by materials science and engineering specialists. More specifically, the field of materials science and engineering focuses on understanding how the different processing histories (e.g., thermo-mechanical processing) influence the material structure (includes information on the many aspects of order and disorder seen at different length scales cf. **Figure 1**) and their associated properties. However, understanding and quantifying accurately the underlying process-structure-property (PSP) relationships (Kalidindi, 2015; McDowell and LeSar, 2016) at the different

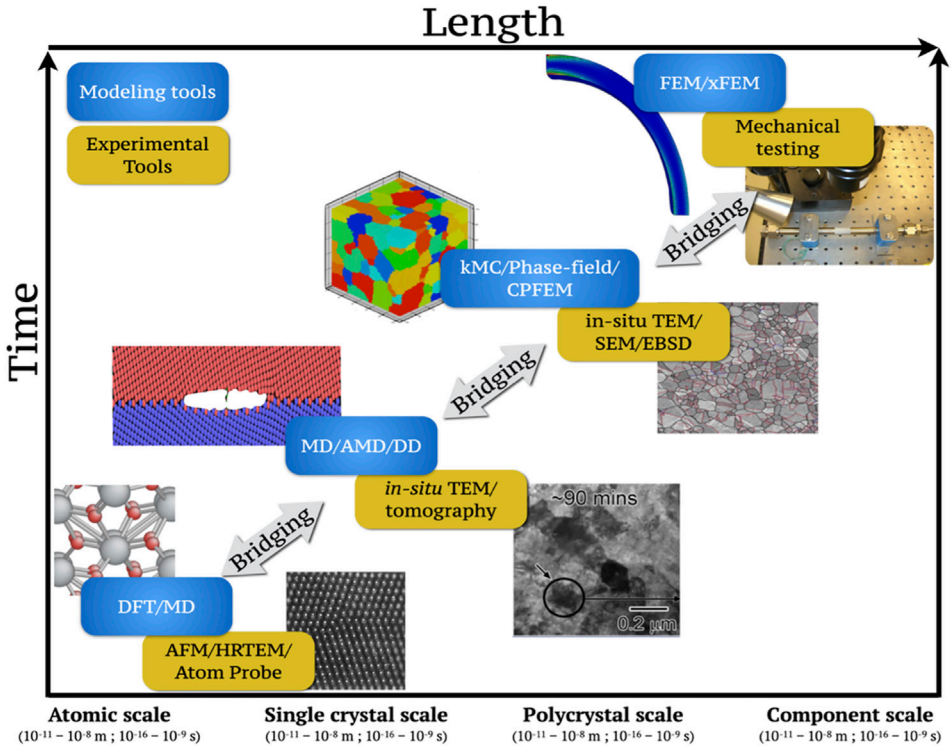

FIGURE 2 | Modeling and experimental tools typically used to obtain relevant materials data at different length and time scales. Example of modeling tools used include Density Functional Theory (DFT), Molecular Dynamics (MD), Accelerated MD (AMD), Dislocation Dynamics (DD), kinetic Monte Carlo (kMC), Crystal Plasticity Finite Element Modeling (CPFEM), FEM, and extended FEM (xFEM). Examples of experimental tools used include Atomic Force Microscopy (AFM), High Resolution Transmission Microscopy (HRTEM), *in situ* TEM, tomography, Scanning Electron Microscopy (SEM), Electron Backscattered Diffraction (EBSD), and mechanical testing.

material length and time scales is quite arduous. This is mainly because the diverse physical phenomena occurring at these scales are necessarily related and co-dependent with one another. Therefore, adopting a systems approach that manages the complex trade-offs between potentially conflicting multifunctional requirements at the different length scales spanning across the complete range of material and product scales would yield significant benefits.

However, this task faces many hurdles. The most significant of these hurdles comes from the fact that the relevant data, even for a selected single material system, is necessarily generated by distributed teams of researchers with the requisite expertise. For example, on the experimental front, materials data comes from a wide range of imaging modalities (e.g., optical microscopy, scanning and transmission electron microscopy, various diffraction and spectroscopic techniques, X-ray tomography, atomic force microscopy) (Belianinov et al., 2018; Polonsky and Pandey, 2021) and property evaluations (e.g., mechanical testing in different modes and at different spatial resolutions, thermal conductivity, diffusivities) (Khosravani et al., 2020:; Khosravani et al., 2021). On the modelling front, the data comes from an equally disparate set of sources that aim to faithfully simulate specific selected sub-phenomena at different material length scales (e.g., density functional theory computations, molecular dynamics, discrete dislocation dynamics, kinetic Monte-Carlo simulations, cellular automata, phase-field simulations, finite element models) (Horstemeyer, 2009; Panchal et al., 2013; Matouš et al., 2017). Although each individual dataset often provides a partial insight, only a systems approach can provide the comprehensive holistic view needed to objectively drive materials innovation in an accelerated manner; this is indeed the goal of many national and international materials research initiatives [e.g., ICME (Allison et al., 2006), MGI (National Science and Technology Council, 2011; de Pablo et al., 2019)].

Figure 2 illustrates the large variety of data sources involved in formulating a systems approach to understanding and optimizing materials for desired combinations of macroscale (effective) properties. As already noted, the datasets collected from any one data source (refers to either a single experimental protocol or a single physics-based simulation tool) often provides incomplete and uncertain insights into the physics controlling the materials phenomena of interest. At a high level, it should be recognized that physics-based simulations are designed to provide predictions of the material response to imposed (thermo-mechanical) environments for user-specified physics. On the other hand, experiments are generally designed to provide observations of material response to specific imposed environments, for as yet unknown (or uncertain) materials physics. Clearly, all individual datasets (from any individual

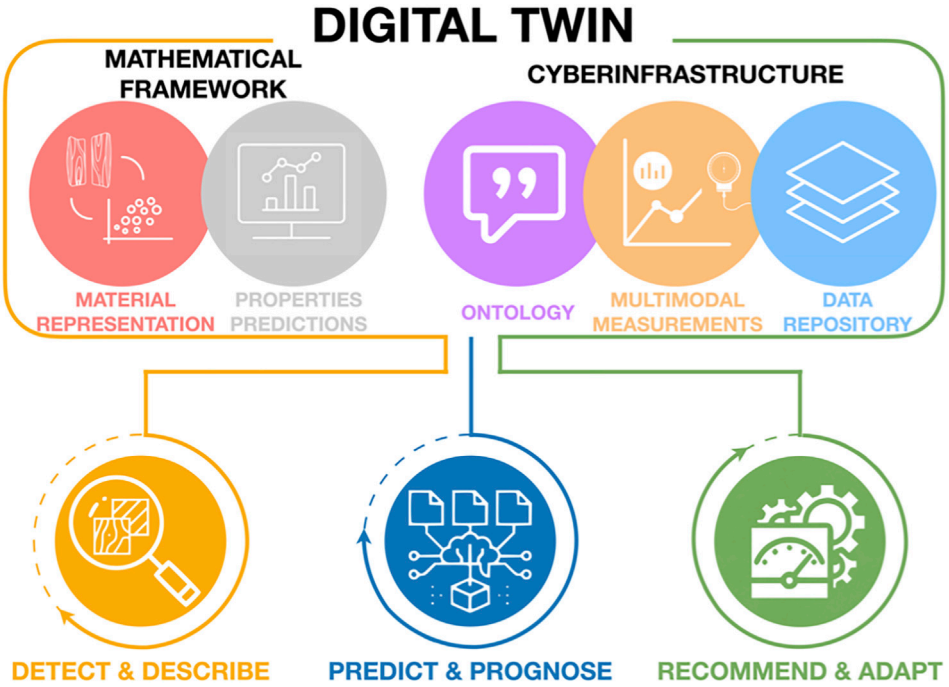

FIGURE 3 | The main components of the proposed roadmap for building digital twins for material systems.

data source) should be treated as being incomplete and/or uncertain. However, if the insights from the datasets collected from the different data sources can be effectively fused in a consistent framework, it is likely to produce much more comprehensive and valuable insights. Currently, there does not yet exist an overarching mathematical framework for such data fusion. The development and utilization of such a framework is likely to open new avenues for major time and effort savings in materials-product co-design and innovation efforts by optimally guiding the effort investment (i.e., objectively identifying the next best steps based on a rigorous statistical analyses of all previously aggregated data).

As already noted, the perspectives presented above build on multiple national and international initiatives. Specifically, ICME (Allison et al., 2006), and MGI (de Pablo et al., 2019) have articulated the need for increased use of computational tools and data sciences [including artificial intelligence/machine learning toolsets (AI/ML)] to accelerate the rate of materials discovery, development, and deployment in advanced technologies. Indeed, much progress has been made in organizing and disseminating materials data (The Minerals, Metals & Materials Society TMS, 2017), and physics-based simulation toolsets (The Minerals, Metals & Materials Society TMS, 2015). There has also been a strong injection of data sciences and AI/ML into materials research, especially in aspects related to data ingestion (e.g., experimental laboratory automation) (Kalidindi et al., 2019), curation (e.g., ontologies) (Morgado et al., 2020; Voigt and Kalidindi, 2021), feature engineering (Kalidindi, 2020; Xiang et al., 2021), and automated generation of surrogate models (Generale and Kalidindi, 2021; Marshall and Kalidindi, 2021). These recent advances in materials research have set the stage for the extension and application of the emerging concept of digital twins described earlier to include the multiscale details of the material. This paper establishes a roadmap for the pursuit of this goal, i.e., the extension of digital twins to include materials data over a hierarchy of length scales. Specifically, we identify the key foundational elements that currently exist and outline the gaps that need to be overcome for success in this endeavor (**Figure 3**).

2 MAIN ELEMENTS OF DIGITAL TWINS FOR MATERIALS SYSTEMS

2.1 Physical Twin of a Material System

Digital twins of macroscale engineered components and machines typically aim to represent a uniquely identified single physical twin. For example, a digital twin might target a specific turbine engine in service on an airplane. However, in building digital twins for a material system, it becomes intractable to consider each individual material sample as the physical twin. This is not only because of the large number of distinct material samples that can be produced for a nominally specified chemical composition and processing history, but also due to the fact that non-destructive characterization techniques are not yet mature for evaluating both the three-dimensional structure of the material as well as its properties of interest. Furthermore, even with the use of destructive techniques for materials characterization, one can only hope to establish distributions that adequately quantify the material structure and properties in a

stochastic framework (i.e., accounting for the significant uncertainty associated with these quantities for any given material sample). Given these considerations, it is readily apparent that the digital twins for materials systems can only be established in a stochastic framework at the present time. In other words, we propose here that digital twins of materials systems should aim to produce multiple instantiations (as many as needed) sampled from the distributions of the possible material structure and their associated properties (with both structure and properties defined over a hierarchy of material length scales). Therefore, in our proposed framework, we will associate the digital twins of the material system to the nominal chemical composition and processing/service history that created the material samples. In doing so, we will implicitly define the material by the controllable details (each of which is identified with aleatoric uncertainty) of the generative process used to create the material samples (i.e., instantiations of the physical twin). This, we believe, will result in a much more pragmatic approach to building digital twins for material systems that will have high value for the design and in-service prognosis of engineered components and devices.

2.2 Mathematical Framework for Digital Twins of Material Systems

The mathematical framework underpinning the digital twins for material systems should address two main needs: (i) the statistical quantification of the material structure over a hierarchy of material length scales[1] and its suitable representation in practically useful low-dimensional forms, and (ii) the reliable prediction of the material properties of interest given information about the material structure and the processing/service history. These tasks indeed correspond to defining the form and the function of the digital twins for material systems. As already noted, both these tasks need to be addressed in a stochastic framework that rigorously tracks the uncertainty associated with all of the available data and propagates it into the predictions of the material properties.

2.2.1 Material Structure Representation and Quantification

The term *material structure* is used here to describe the spatial arrangement of structural and chemical heterogeneities, which constitute a material at a specified instant of time and govern its properties at that instant of time. For a given chemical composition, thermodynamics predicts an equilibrium crystallographic phase (or a multiphase mixture), and at finite temperature, an equilibrium vacancy concentration. Yet materials are rarely in their thermodynamic ground state. Essentially, an overwhelming subset of the material structural features represent metastable or unstable defects created throughout the process history. Conventionally, material structure defects have been classified based on their dimensionality as planar grain boundaries, linear dislocations, and point-wise atomic impurities; these are but the simplest examples of a myriad of complex microstructural features (see **Figure 1**). The material structure is not usually static but evolves when stimulated by exposure to energy (thermal, mechanical, chemical, etc.). Through state-of-the-art processing, the most perfect undoped, isotopically pure silicon single crystals have been produced to purity levels of >99.9999%. On the other hand, the most sophisticated structural alloys benefit from their complex, multiscale arrangement of the lower length scale structural features, reminiscent of the hierarchical nature of biological systems. Hence, the challenge for a digital twin of a material system is to represent the necessary complexity of the inherently high-dimensional material structure features with sufficient fidelity to capture the relevant subset that controls the material response of interest. Complicating matters, no single experimental technique is capable of comprehensively digitizing the material's complete internal structure.

A digital twin of a material system should be able to instantiate a representative volume of the material with sufficient statistical sampling of all the relevant lower length-scale structural features and their spatial arrangements. Given the roughly eight orders of magnitude in length scales (from ~Å to ~ cms) involved, it should become clear that such instantiations cannot be deterministic or unique. Therefore, what is required here is the ability to produce multiple instantiations that reflect as accurately as possible the inherent stochasticity of the material structure for a given nominal composition and process history. Laplace conjectured that by knowing every atom, its position and momentum, we could anticipate the behavior of the material (marquis de Laplace, 1814). While this statement reflects accurately the expected causal relationship between the material structure and its associated properties, it reflects a practically impossible pursuit. Therefore, we take the viewpoint that the digital twin of a material system is intended to be a minimally sufficient reduced-order representation of Laplace's "demon." A tractable digital twin of a material system should therefore utilize a versatile (broadly applicable to all material classes and length scales) low-dimensional representation of the material structure that would allow efficient learning of the functional response of the material system. Based on the earlier discussion, it is also clear that the low-dimensional representation of the material structure can only reflect suitably defined *statistical measures* at different material length scales; henceforth, such salient statistical measures of the material structure will be referred as *features*. Because of our interest in instantiating the material structure in our digital twins, it is important that the selected feature set should produce realistic, sufficiently accurate, instantiations of the material structure that can be subsequently correlated with its functional response. This is not a trivial requirement. For example, most of the conventionally used statistical measures of the material structure, such as the overall alloy composition, phase volume fractions, and the averaged grain sizes are woefully inadequate for producing the required instantiations of the

[1]In PSP linkages, one associates a material structure to an instant of time. The structure is then assumed to be responsible completely for the properties exhibited by the sample. In any imposed process, the structure is assumed to evolve with time. When the structure evolves, its associated properties are also expected to evolve.

multiscale material structure for our digital twins. More advanced approaches involving a richer set of microstructure statistics (e.g., orientation and mis-orientation distributions, grain aspect ratio distributions) have led to concepts such as statistically equivalent representative volume elements (McDowell and LeSar, 2016; Ghosh and Groeber, 2020). Some of these concepts have also been implemented in open-source codes such as DREAM.3D (Groeber and Jackson, 2014; Ghosh and Groeber, 2020).

A comprehensive and systematic framework available today that is capable of providing the requisite feature engineering capabilities for the material structure is the framework of n-point spatial correlations (Torquato and Stell, 1982; Torquato and Haslach, 2002; Fullwood et al., 2010; Niezgoda et al., 2011; Adams et al., 2012; Niezgoda et al., 2013). In recent work, Kalidindi and co-workers (e.g., Kalidindi, 2015) have developed and demonstrated an efficient and broadly applicable computational framework and toolsets for addressing this task. Broadly referred as Materials Knowledge Systems (MKS), this framework takes advantage of the computational efficiency of voxelated representations and Fast Fourier Transform (FFT) algorithms to implement the theoretical framework of n-point spatial correlations. The feasibility and benefits of this approach have been demonstrated on a wide variety of material classes and material structures at different length scales [from the atomic (Gomberg et al., 2017; Kaundinya et al., 2021) to dislocation length scales (Robertson and Kalidindi, 2021a) to microscale (Generale and Kalidindi, 2021)].

At its core, MKS defines and utilizes a material structure function (Kalidindi, 2015) that maps a selected combination of spatial position $\boldsymbol{x} \in \Omega$ (the physical volume of the material domain) and a local material state $\boldsymbol{h} \in \mathrm{H}$ (includes information such as phase identifiers, chemical compositions, lattice orientations, defect densities) to suitable measures (e.g., density) that reflect the intensity of $\boldsymbol{h}$ at $\boldsymbol{x}$. Mathematically, one can express this function as $m(\boldsymbol{h}, \boldsymbol{x})$. Implicit in this definition is the expectation that H needs to be identified suitably to capture the complete set of material states of interest at the different material structure length scales. Features of the material structure can then be defined as expectations of suitably scaled moments of $m(\boldsymbol{h}, \boldsymbol{x})$. For example, the expected value of $m(\boldsymbol{h}, \boldsymbol{x})$ over Ω can provide a set of 1-point features that can be interpreted as the volume fractions of $\boldsymbol{h}$ in Ω (Kalidindi, 2015). Similarly, the expected value of $m(\boldsymbol{h}, \boldsymbol{x})m(\boldsymbol{h}^{'}, \boldsymbol{x}+\boldsymbol{r})$ over Ω can produce a set of 2-point features that can be interpreted as the joint probability of realizing $\boldsymbol{h}$ at $\boldsymbol{x}$ and $\boldsymbol{h}'$ at $\boldsymbol{x}+\boldsymbol{r}$, where $\boldsymbol{r}$ denotes a specified vector separating the two spatial points randomly selected from Ω. Although, one can define higher-order features (e.g., 3-point features), one often finds a sufficiently large number of features in the 2-point feature set, as it includes all permutations of $(\boldsymbol{h}, \boldsymbol{h}')$ over a very large domain of $\boldsymbol{r}$ (this domain includes all distinct set of all vectors of interest that can be placed in Ω). The adequacy of the set of 2-point features in capturing the salient features of the material structure (including the set of features identified in conventional practices in materials science and engineering) has been established for a broad range of material classes (Latypov et al., 2019; Generale and Kalidindi, 2021) as well as the different structure length scales (Fullwood et al., 2010; Robertson and Kalidindi, 2021a; Kaundinya et al., 2021) encountered in them.

The MKS framework described in **Figure 4** produces a very large number of features, even when using only the 2-point feature set. For extracting a low-dimensional feature set, one needs to use a suitable dimensionality reduction technique. Of the various options for this task, principal component analysis (PCA) has been found to be particularly attractive. First, it allows for an unsupervised learning of the salient low-dimensional features based on maximization of captured variance. Therefore, it identifies a consistent set of features that can be used across multiple PSP surrogate models, allowing for full interoperability among collections of such models. In other words, since the salient features are identified without the knowledge of the specific targets (i.e., outputs) of the surrogate model, they can be used for different targets (for example, in the predictions of very different properties of a given material system). Second, the PCA basis can be inspected and interpreted to a limited extent, allowing for the low-dimensional features to be associated with some (limited) physical meaning. Third, since PCA essentially involves a rotational transform of the original space, it preserves distances between datapoints in the original space. Finally, the orthogonal decomposition involved in the PCA allows for practically useful reconstructions of the full feature list, i.e., a reconstruction of the high-dimensional feature list from the low-dimensional feature list. Of course, these reconstructions are approximate because of PC truncation. However, since the PC representations are maximized to capture variance, it is possible to make sure that the approximation introduced by the truncation is within acceptable tolerance. The PC scores obtained from the application of PCA on an ensemble of 2-point feature sets (one set corresponds to one material structure) serve as a highly effective low-dimensional feature set for the material structure in our digital twins. There exist a multitude of other options for dimensionality reduction of the feature space, such as isomap or kernel PCA. However, the nonlinear embeddings employed in these techniques can introduce distortions into the latent space that negate the benefits of PCA identified above (Hu et al., 2022).

As stated earlier in **Section 2.1**, the physical twin is not defined as a single instantiation of a material structure, but rather as the outcome of a stochastic generative process that yields instantiations that we then observe. The MKS framework described above provides a mathematically compact representation using computationally efficient tools. However, many tools (e.g., phase-field simulations, micromechanical finite element models) only take specific instantiations of the material structure as inputs. Therefore, successful creation of digital twins for materials requires the ability to move between statistical representations of material structure and their three-dimensional physical instantiations at low computational cost. While the computation of 2-point spatial correlations from instantiations is relatively easy (Cecen et al., 2016), the inverse computation is not trivial. Very recently, it has been shown that the three-dimensional material structures can be instantiated from their 2-point feature sets with minimal computational cost (Robertson and Kalidindi, 2021b). As a result of the

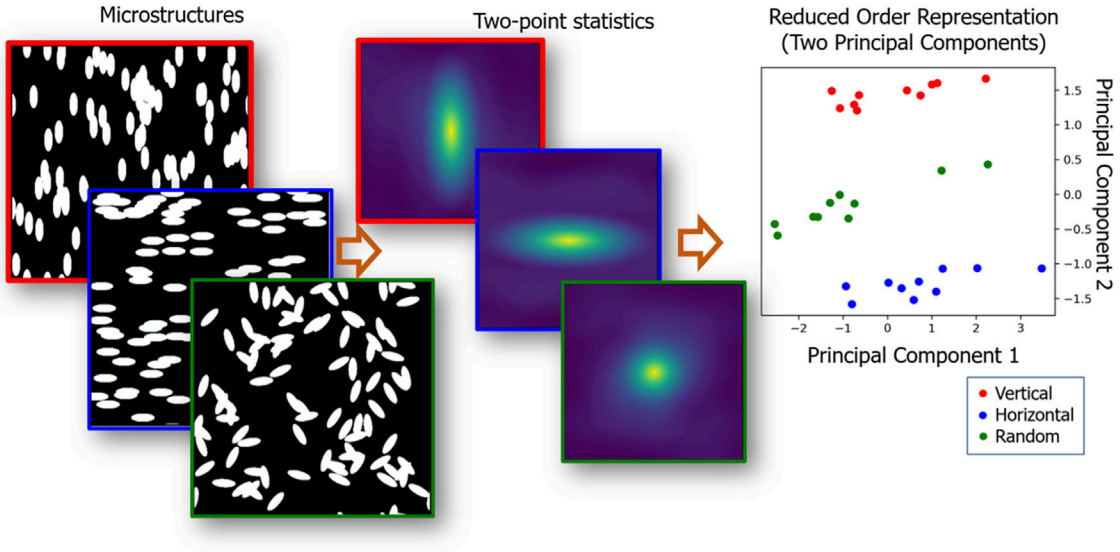

FIGURE 4 | The MKS workflow for feature engineering of material structure. In this example, we start with microstructures belonging to three distinct classes (corresponding to vertical, horizontal, or random ellipses), with one example of each class shown on the left. Their corresponding 2-point features are shown in the middle and reflect a large number of statistics (including volume fractions, size and shape distributions) for each microstructure. The low-dimensional representations of the microstructure statistics are shown on the right, in the subspace of the first two PC scores. The clusters in the PC plots successfully classify the microstructures in the three classes. The intra-class variance between microstructures within each class can also be quantified from the PC representations.

many advantages described above, the MKS framework along with its open-source code repository PyMKS (Brough et al., 2017) offers a powerful, currently available, toolset for addressing the challenges of building digital twins of materials systems.

It is also noted that there are a number of other options based on neural networks that allow one to combine feature engineering and property prediction into a single-step framework. These approaches offer attractive avenues when one is interested in a limited number of properties as targets. If one insists on de-coupling the form and function of the digital twins (as we have argued here), then it is imperative to pursue feature engineering of the material structure independently from establishing property predictors (discussed in the next section). In this context, it should be recognized that the autoencoder-decoder networks (Herr et al., 2019) offer an interesting option. These networks do address the unsupervised feature engineering of the material structure. Therefore, the features identified from such networks can then be input into other neural networks for property predictions. This idea represents an open research avenue that merits further exploration.

2.2.2 Predictions of Material Properties

Reliable prediction of the effective properties of a given material sample is a challenging task. At a high level, the main options are to either measure experimentally the properties of interest or to leverage known physics (often delivered in physics-based simulation packages) to estimate their values. Both approaches face hurdles when one desires to produce a multiscale, digital twin for materials. On the experimental front, the effort and cost involved in measuring all of the properties of interest along with the related information (e.g., anisotropy, variances) over the multiple material length scales of interest are often prohibitive. On the modelling front, there is substantial uncertainty in the model forms and/or parameter values used in the physics-based models. It is therefore clear that neither approach by itself is optimal in getting us the requisite information. In this regard, the recent emergence and successful application of materials data analytics tools has opened up new avenues for addressing these gaps.

Recently (Kalidindi, 2015; Kalidindi, 2020), it has been argued that process-structure-property (PSP) linkages can be defined over different material-structure length scales to capture the core knowledge needed to study multiscale material responses. It is argued here that the same PSP linkages can be utilized to predict the functional response of the material digital twin. This is because the PSP linkages can be used to update both the changes in the multiscale material structure due to the imposed service conditions (using suitably defined process-structure evolution linkages) but also their associated properties (using structure-property linkages). The required PSP linkages need to be formulated using available data that might often be disparate, incomplete and/or uncertain. Most importantly, the framework for predicting the function of the material digital twin should allow easy (and possibly frequent) updates as new data becomes available. It is also likely that one needs to chain together multiple PSP models in order to make the predictions of the function of the material digital twin.

A Bayesian framework has the potential to address scale-bridging with uncertain physics. The proposed Bayesian framework will be described next using the structure-property (SP) linkages as an example. However, they will be formulated such that they can also be easily applied to capturing process-

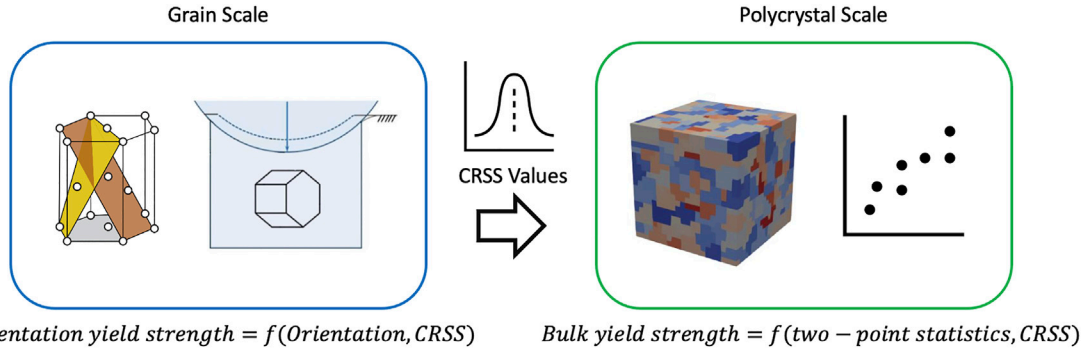

FIGURE 5 | Schematic illustration of the scale-bridging between the response of an individual grain and the response of a polycrystalline aggregate. At the grain scale, the structure-property linkage is formulated to take grain orientation (structure variable) and critical resolved shear strength(s) (CRSS; physics variables) as input and predict the overall property of interest (e.g., indentation yield strength of grains of different orientations). This linkage is used with both experimental and modeling datasets to extract a posterior on the CRSS for a given material system (see **Panel 6** for more details). At the polycrystal scale, the structure-property linkage is formulated to take the 2-point spatial correlations of orientation (structure variables) and CRSS (physics variables) to make a prediction of the bulk (effective) yield strength of the polycrystal (c.f., Paulson et al., 2017).

structure linkages (PS). Typically, SP linkages are formulated to take structure variables as inputs and predict property values as output. The mapping implied in these linkages can be expressed as $P = \mathcal{F}(\boldsymbol{\mu})$, where P is a property variable and $\boldsymbol{\mu}$ denotes a vector of structure features (e.g., the PC scores of the 2-point feature set described in **Section 2.2.1**). Both P and $\boldsymbol{\mu}$ should be treated as stochastic variables. This naïve definition makes the governing physics implicit in the formulation of $\mathcal{F}$. It would be much more desirable for SP linkages to explicitly treat the governing physics as additional input variables to the mapping, i.e., to refine the desired mapping as $P = \mathcal{F}(\boldsymbol{\mu}, \boldsymbol{\varphi})$, where $\boldsymbol{\varphi}$ denotes the governing physics. In practice, $\boldsymbol{\varphi}$ would represent a vector of parameters defining the physical mechanisms controlling the response of the material physical twin (e.g., parameters used in constitutive modeling of the material response). This refinement is advantageous in two ways. Firstly, it allows one to treat $\boldsymbol{\varphi}$ as a stochastic vector variable, which often exhibits a significant amount of uncertainty for a selected material physical twin. Secondly, it allows for the uncertain physics to be passed between linkages. This is particularly useful for the multiscale phenomenon that occur in material systems, as the uncertain physics learned in one length scale can still be utilized at another length scale. An example of this scale-bridging is depicted schematically in **Figure 5**. The first linkage estimates the indentation yield strength (effective property) of a single grain given the grain's orientation (structure variable) and critically resolved shear strengths (physics variables). The second linkage estimates the bulk yield strength (property) given the two-point statistics of the grain orientations (structure variables) and the same critically resolved shear strengths (physics variables). Since the physics variables in these two linkages are the same, the uncertain knowledge of the physics variables extracted in the grain-scale data (could come from experiments and/or simulations) can be upscaled and utilized in making predictions of the effective properties at the polycrystal scale.

In establishing the material physics parameters, one has to exploit all of the available data, collected from disparate sources (e.g., experiments and physics-based simulations). Machine learning of $\boldsymbol{\varphi}$ for a selected material physical twin can be accomplished using a Bayesian update strategy expressed as:

$$p(\boldsymbol{\varphi}|\boldsymbol{E}) \propto p(\boldsymbol{E}|\boldsymbol{\varphi})\, p(\boldsymbol{\varphi}) \tag{1}$$

where $\boldsymbol{E}$ denotes the set of available experimental observations, $p(\boldsymbol{\varphi})$ is the prior (reflecting our best initial guess), $p(\boldsymbol{E}|\boldsymbol{\varphi})$ is the likelihood of realizing the observations in $\boldsymbol{E}$, and $p(\boldsymbol{\varphi}|\boldsymbol{E})$ denotes the updated posterior on $\boldsymbol{\varphi}$. Although **Eq. 1** looks very simple, its practical usage for learning the controlling physics in multiscale material phenomena has been hindered by several factors. First, only the physics-based simulation tools that faithfully mimic the experiments performed to obtain $\boldsymbol{E}$ can allow for the computation of the likelihood term in **Eq. 1**. This is because only these tools allow arbitrary specification of the governing physics $\boldsymbol{\varphi}$. However, a brute-force application of physics-based tools for computing the likelihood is prohibitively expensive because of the extremely large number of simulations one needs to perform to accomplish this task since it entails performing simulations covering a large domain of likely governing physics for all of the experimental observations in $\boldsymbol{E}$. Second, the proportionality in **Eq. 1** implies that one needs to develop and implement a suitable strategy for establishing the proportionality factor. Recent work (Castillo et al., 2021) has demonstrated that it is possible to train AI/ML models on simulation results produced by physics-based models, which can then be used to compute the likelihood term in **Eq. 1**. Furthermore, they would also allow for the implementation of Markov-Chain Metropolis-Hastings (MCMH) approaches for sampling the posterior in **Eq. 1** without explicitly computing the proportionality factor. It is important to note that the posterior estimate of $\boldsymbol{\varphi}$ is not restricted to come from any single source of data. As an example, let us consider the situation where the data becomes available from different test modes (these could be indentation tests and micro-pillar tests for grain-scale

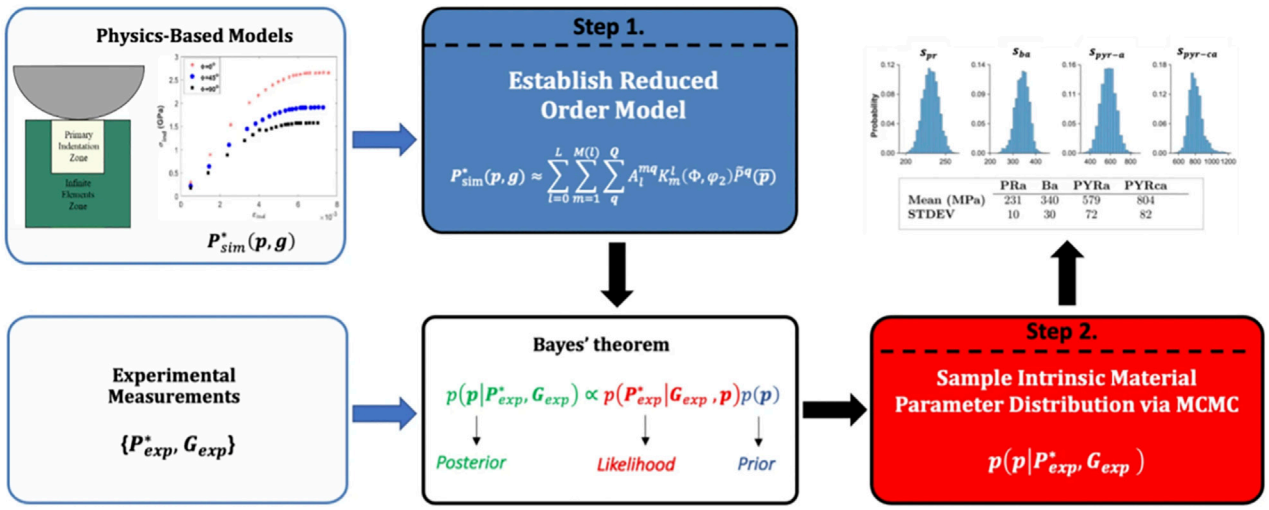

FIGURE 6 | An example application of the Bayesian update strategy for the fusion of experimental and simulation datasets from indentation of a-Ti grains in a polycrystalline sample (Castillo et al., 2021).

mechanical measurements). In such situations, we need to establish different surrogate models for each test mode. Let $P_1 = \mathcal{F}(\boldsymbol{\mu}, \boldsymbol{\varphi})$ and $P_2 = \mathcal{F}(\boldsymbol{\mu}, \boldsymbol{\varphi})$ represent such surrogate models. Since the underlying microstructure and physics variables have the exact same meanings in both models, one can use both models with their respective experimental datasets for sampling a consistent posterior for $\boldsymbol{\varphi}$. Once the posterior is established, one can establish the desired SP linkage in a stochastic framework by marginalizing as:

$$p(\boldsymbol{\mu}|\boldsymbol{E}) = \int f(\boldsymbol{\mu}, \boldsymbol{\varphi}) p(\boldsymbol{\varphi}|\boldsymbol{E}) d\boldsymbol{\varphi} \tag{2}$$

As noted above, the practical implementation of **Eqs 1, 2** needs the establishment of suitable AI/ML surrogates. These usually take the form $\mathcal{F}(\boldsymbol{\mu}, \boldsymbol{\varphi})$, and can be accomplished using Gaussian Process Regression (GPR). The central advantage of the proposed strategy here is that the formulation of the needed AI/ML models is generally a one-time effort. In other words, when these are properly designed to cover large input domains in the space of the controlling physical parameters and the space of relevant material structures, they only need to be performed once [examples can be seen in prior work (Castillo and Kalidindi, 2019; Castillo et al., 2021)]. This feature allows for a relatively low-computational cost update of the surrogate model as new experimental data becomes available. It is also possible to suggest new experiments that maximize the potential for improving the accuracy of the predictions (i.e., reducing the prediction uncertainty). This is most efficiently accomplished using established concepts of information gain such as the posterior predictive variance (Castillo and Kalidindi, 2019; Castillo et al., 2021; Castillo and Kalidindi, 2021), expected improvement (Solomou et al., 2018; Takhtaganov and Müller, 2018; Talapatra et al., 2018; Ghoreishi and Allaire, 2019), and expected information gain (Pandita et al., 2019).

An example application of the proposed Bayesian approach methodology is depicted in **Figure 6**, taken from the work of Castillo et al. (2021). In this example, the information from spherical indentation measurements on individual grains in a polycrystalline sample and the corresponding simulations using crystal plasticity finite element models are combined to establish distributions on the unknown values of the critical resolved shear strengths of four different families of potentially active slip systems in a selected Ti alloy. The approach described in this study resulted in at least one order of magnitude savings in both the overall cost and effort expended, when compared to the conventional approaches that employed small-scale testing to obtain the same information.

2.3 Cyberinfrastructure for Digital Twins of Materials

Cyberinfrastructure supports the acquisition, storage, management, and fusion of data within a collaborative, but distributed, research environment. The creation of a robust cyberinfrastructure is critical to the realization of a digital twin, as digital twins exist at the confluence of multiple disparate data streams (e.g., simulation data, experimental data, real time sensor data). These data streams present challenges in managing both the variety and volume of data ingested, as well as any associated metadata needed to ensure high utility of the data for future use. Challenges in the variety of data come from the *multimodal* nature of materials data, meaning that the data in question stems from a variety of data sources (e.g., different imaging or analysis modalities). For example, materials data can take many forms: scalar parameters (e.g., diffraction line profile), time series (e.g., fatigue response), and spatially resolved (2-D and 3-D) image data (e.g., SEM image, tomography scan), and each modality is accompanied by its own unique forms of

TABLE 1 | Example of energy forms that drive changes in material state and the transducers employed to observe the corresponding exposure history.

Stimuli	Application examples	Sensor examples
Mechanical	Vibration, Shock, Sound/Phonon, Stress, Strain	Strain gauges, piezoelectric, magnetostrictive, eddy current, accelerometer, capacitive
Electrical	Current, magnetic fields	Voltage sensors, current sensors, resistance sensors, power sensors hall-effect sensors, giant magnetoresistance sensors, fluxgate sensor
Radiant Energy	Gamma, X-ray, UV, Infrared, Visible light, Microwave, Radio waves	Photoresistors (LDR), photodiodes, phototransistors, charged-coupled devices, gamma ray detectors, microwave sensors, CMOS detector
Thermal	Convective, conductive, latent	Thermocouples, RTDs, Thermistors, infrared, semiconductor sensors
Chemical	Gases, liquids, solids, ions, isotopesetc.	Hygrometer, gas sensor, pH sensor
Nuclear	Neutron, Beta, Alpha, Proton	Gas-filled proportional detectors, ionization chambers, Geiger-Mueller tubes, scintillators, solid-state detectors
Gravitational	weight	See mechanical sensors

metadata that describe pre-process, in-process, and post-process information. Challenges in the volume of data stem from advancements in acquisition resolution and high-throughput experimental capabilities (hyperspectral imaging, x-ray computed tomography, etc.). For example, it is now commonplace to collect a large ensemble of images with high spatial resolution at a high frame rate using a variety of microscopes (e.g., optical, scanning electron, transmission electron), producing gigabytes-to-terabytes of observations of a single material (Dingreville et al., 2016). Similarly, expanded computational resources and multiscale modeling capabilities can also generate large amounts of data related to a material's response to variety of environments (de Oca Zapiain et al., 2021). The main challenge lies in collecting and curating this large collection of heterogeneous data into the high-value *information* needed for the creation of a digital twin.

2.3.1 Data Sources

Material structure measurements capture the *state* of the material before, during, and after evolution, and material property measurements quantify various *characteristics* of evolution (e.g., resistance to evolution, evolution rates). The constellation of methods used to measure material structure and properties is extensive, and here we only mention two general trends. First, the digital data stream is becoming more entrenched in the instruments used to measure material properties. Just a generation ago, material structures were documented on film and quantification was performed by manual measurements; lab instruments utilized strip-chart recorders that created an analog graphical representation of the data. Now, not only have data streams become digitized, but increasingly, the data collection instruments are networked and remotely accessible. Yet significant concerns remain regarding the cyber vulnerability of both the data and the instrument, and institutional regulations regarding interconnectivity are highly disparate. Second, with the continuing advances in measurement sensors, data transfer, and data storage, the data streams are becoming increasingly dense, requiring thoughtful strategies for intelligent data reduction. Additionally, unconventional datasets, collected with alternative low-cost methods are proving to have utility. Previous trends in measurement science have focused on increases in precision and accuracy of data. Now, the focus is shifting to affordable high-density data streams that can provide similar or complementary information content to the existing suite of ultra-precise measurements.

The external stimuli (e.g., thermo-chemo-mechanical loading) driving material structure evolution need to be tracked through the use of suitable sensors. Sensors generally transduce various forms of energy (**Table 1**) into electrical signals that can be transformed into digital data. The transduction can also involve intermediate forms of energy, e.g., magnetic or optical. All forms of sensing have limits in resolution, range, accuracy, and precision. The fidelity of the digitized resolution of the external stimulus captured by the sensor is limited by the accuracy of the correlation of the electrical signal to the intensity of the imposed stimulus, and the bit-depth of the stored information. The fidelity of an environmental measurement can also be limited by the temporal and spatial resolution of the sensor. Sensor arrays allow for spatial mapping of a field (e.g., temperature field on a sample surface) of interest, with the spatial resolution limited by the spacing between individual sensors in the array. Alternately, one can acquire such information using a single sensor and rapidly scanning a region of interest; this strategy will lead to some degree of temporal disregistry between individual measurements.

2.3.2 Data Management (Ontology, Data Software Platforms)

The high volume and high variety of materials data quickly outpaces rudimentary data organization techniques typically used by humans (project specific folder structures, ad hoc organization or note taking). We therefore require more sophisticated data management tools to manage the storage and organization of the materials data relevant to the digital twin. In their most basic forms data management tools act as *simple data repositories*, centralized locations where data is held and made accessible to others. However, simple data repositories do not necessarily provide a systematic scheme for the organization of the data or metadata therein. Digital twins require the establishment of standards and protocols to catalogue, vet, compare, and use data reliably and credibly in automated (and possibly autonomous) protocols (Kalidindi and De Graef, 2015; Sorkin et al., 2020). Consequently, data management solutions for digital twins should aim to at least meet FAIR data principles: Findability, Accessibility, Interoperability, and Reusability (Wilkinson et al., 2016). FAIR

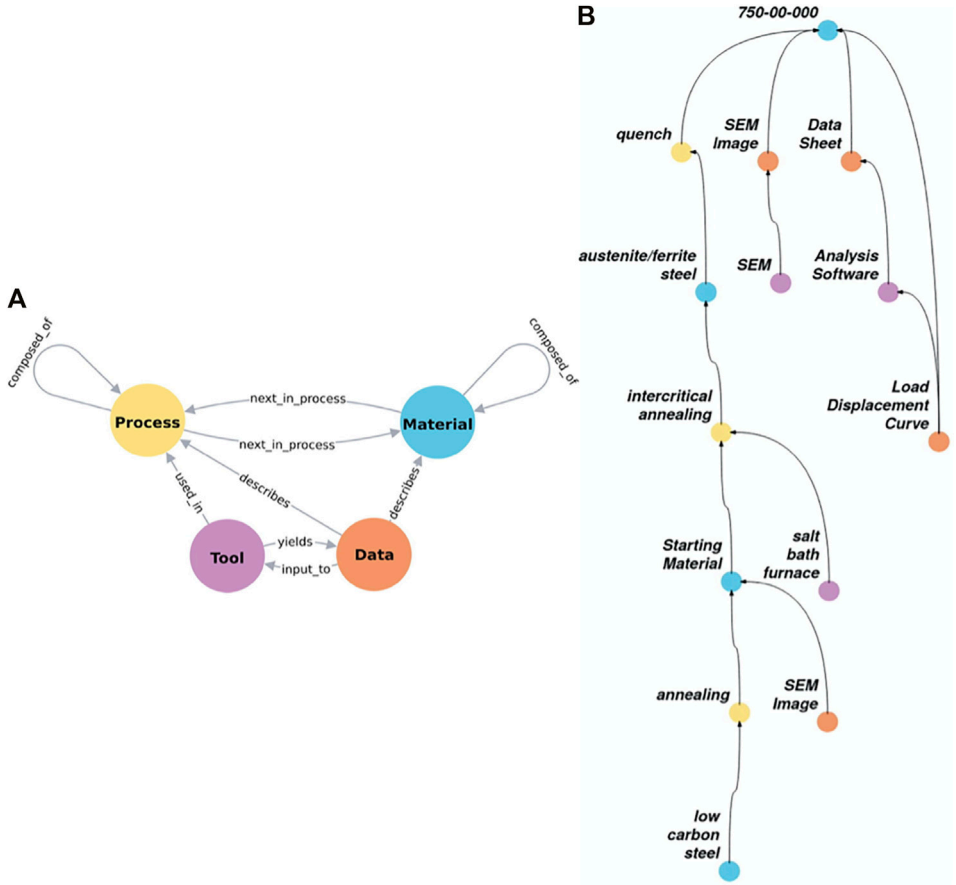

FIGURE 7 | (A) The constitutive elements of a recently proposed materials ontology (Voigt and Kalidindi, 2021). The four main elements are Material (blue), Process (yellow), Tool (purple), and Data (orange) are shown in different colors along with the allowed connections between them. **(B)** An example of a knowledge graph constructed using the ontology.

data should have: (1) globally assigned, rich, searchable metadata with a unique persistent identifier and clear provenance; (2) standardized communication protocols for data storage and retrieval; (3) consistent, widely utilized, non-proprietary standards employed for data formatting. Data repositories generally only meet the most basic aspects of FAIR—namely accessibility. Materials databases progress further towards FAIR principles by providing greater searchability. Databases allow users to construct and carry out complex queries to search for information, and therefore improve searchability. However, their searchability is generally limited to tabular data. Furthermore, databases are also generally limited in their interoperability and reusability. In particular, they are not well suited for the materials data needed for digital twins as there is no natural way to describe the relational connections between disparate materials data (e.g., temporal variations along process paths, nested composition relationships, multimodal data describing single sample).

In order to truly realize FAIR data principles for materials data, we need to adopt emerging software tools in ontologies and linked data. *Ontologies* for data management are an open-world framework where we construct a standardized language to connect and describe objects. There currently exists many standardized languages used to describe ontologies such as OWL (McGuinness and Van Harmelen, 2004), RDF (Lassila and Swick, 1998), or JSONLD (Sporny et al., 2014). These languages all describe data in subject-predicate-object triples where we link the subject and the object through some rule (the predicate). One way to capture this information is through the formation of *knowledge graph* consisting of nodes (subjects, objects) and edges (predicates). Knowledge graphs allow for easily understood visual depictions of metadata, and for the application of emergent graph-based AI toolsets for the automated identification of new connections between aggregated elements of a complex heterogeneous dataset.

A recently proposed materials ontology (Voigt and Kalidindi, 2021) shown in **Figure 7A** can prove valuable in our effort to collect and curate the data needed for a materials digital twin. This ontology consists of four primary classes of entities (denoted by circles) that can serve as subjects or objects: Process, Material, Tool, and Data. A total of nine predicates (denoted by arrows) have been defined to link these objects. Process nodes hold information about process parameters, tool nodes describe the settings and characteristics of machines, and data nodes hold the payloads of interest (images, tabular data, etc). A material node

describes the state of the material along a nominal process. Therefore, every time an action is taken on a material, we produce a new material node. This allows us to easily associate data with a point along a process path. As an example, a given steel (Material) produced after a specified thermo-mechanical processing route (Process) can be studied in a microscope (Tool); the results of the study are captured in a file (Data). **Figure 7B** depicts an example knowledge graph for a steel. The process begins with a generic low carbon steel node (seen at the bottom of the knowledge graph). It then undergoes a standard annealing step to get a uniform starting material, and proceeds through a specialized intercritical annealing and quench steps to its final form (labelled as 750-00-000 in the knowledge graph). Along the processing route shown, we are able to connect the various data/metadata collected. For example, it is seen that both the starting material and the final material have associated SEM images. The final material also has a datasheet generated using a known software package (defined by a Tool node) which took a known load-displacement curve (defined by a Data node) as input. Ontologies allow us to systematically capture interconnected materials data and allow for the context of a dataset to be robustly described and communicated, thus enhancing the reusability of the data.

2.3.3 AI Tools

There currently exist several software packages than can be used to support the mathematical framework proposed in **Section 2.2**. For structure quantification PyMKS (Brough et al.) offers computationally efficient tools for the feature engineering of material internal structures. PyMKS supports various data transformations needed to capture information on a wide range of material local states encountered in different material classes at different material structure length scales. PyMKS utilizes Dask, a distributed framework for developing python applications, to facilitate computations involving large datasets on supercomputers and large clusters (Rocklin, 2015). Subsequent to feature engineering, surrogate model building can be accomplished via a wide variety of popular python packages; examples include Statsmodels (Seabold and Perktold, 2010) for basic statistical models, SKLearn (Pedregosa et al., 2011) for machine learning tools, PyTorch (Paszke et al., 2019) and TensorFlow (Abadi et al., 2016) for neural networks/deep learning tools.

AI tools support digital twins beyond the needs of the mathematical framework alone. AI based segmentation strategies have gained traction, and Bayesian CNNs have recently been used to characterize the segmentation uncertainty in materials images (LaBonte et al., 2020). AI tools have also been effective in fusing multimodal materials data. Multi-input NNs have proven effective in combining data from multiple sources and different data types. For example, numeric and categorical data, assessed via multi-layer perceptron algorithms can be directly combined with image-based convolutional NNs (Azim and Aggarwal, 2014). While data streams are typically experimental, it can sometimes be beneficial to integrate high-fidelity simulation data from traditional high-performance computing approaches (e.g., atomistic modeling, phase-field, finite element) to augment "missing" experimental data or to represent functional dependencies/sensitivities that were not exposed in the experimental datasets. For instance, well-established experimental methods such as diffraction measurements are being implemented into computational models as a complement of the interpretation of experimental results (Coleman et al., 2014; Kunka et al., 2021). Alternatively, researchers have recently used generative machine learning algorithms such as generative adversarial network (GAN) to generate large materials and process libraries (Banko et al., 2020).

3 APPLICATIONS

The ability to use a digital twin to provide an accurate picture of the corresponding physical twin at any given point in time is expected to significantly improve the guidance to subject-matter experts towards rational (and optimized) material/process improvements. Additionally, predictions of component performance can drive upstream changes in design or manufacturing process. To date, the development of detection and prognosis-driven planning strategies has largely focused on tuning individual process parameters such as temperature or materials composition for example, despite the urge to devise efficient strategies for the selection of multiple interdependent variables to substantially accelerate and improve scientific discovery. Digital twins open up new opportunities to enable such strategies and accelerate autonomous experimental design and exploration. Autonomous experiments are emerging in materials research leading to the acceleration of materials design and discovery (Nikolaev et al., 2016; Correa-Baena et al., 2018; Hase et al., 2018; Häse et al., 2019; Pendleton et al., 2019; Gongora et al., 2020). The idea is to integrate automation with some form of machine learning or artificial intelligence framework to accelerate experimentation or to guide and discover the next set of experiments. Most of the work to date is dedicated to materials discovery, *i.e.*, autonomously predict and synthesize materials with targeted properties. For instance, Nikolaev et al. (2016) presented a closed-loop iterative method that automatically analyzes experimental results from carbon nanotubes grown from chemical vapor deposition to design or alter the next set of growth experiments to best reach a designated design target growth. Expanding autonomous loops to encompass more complex workflows will require the integration of the digital twin elements described in **Section 2** with the automation of expert decisions. One interesting direction is to use the digital twins as a tool to autonomously test hypothesis during an experimental design. In this case, the practitioner would simply state the Process, Material, Tool, and Data and have the automation process decide whether the hypothesis is supported or refuted in order to decide on the potential next set of experiments. In this context, each automated trial would be guided by the knowledge collected and curated by the digital twin.

One particular application domain of interest for digital twins is the material/process exploration in additive manufacturing, with origins in rapid prototyping. There are extensive model-

based simulations of the additive manufacturing process, ranging from powder packing through the entire laser-matter interaction and solidification process that can be taken as input into the Bayesian update strategy described in **Section 2.2.2**. The range of physical considerations in this process are daunting. In addition to these process models, there are complementary and similarly extensive set of structure-property models. Currently, a comprehensive digital representation of the entire spectrum of governing equations is beyond the state-of-the-art. A digital twin composed of many surrogate models utilizing the Bayesian update strategy could be formulated to optimize the parameters of these models for use in material design as well as process optimization.

4 CONCLUSION

Digital twins of the components in devices have enabled the in-service monitoring, prognosis, and design of complex systems. This work proposes both the conceptual framework and the cyberinfrastructure required to extend the concept of digital twins to the material level. Digital twins for materials provide a statistical in-silico materials representation of both structure and performance. The proposed framework consists of a materials representation based on n-point spatial correlations and PCA, a performance prediction framework centered around a two-step Bayesian framework, and a cyberinfrastructure that leverages new material ontologies for the management of multimodal materials data. Together, these foundational elements offer new opportunities for the extension of current digital twins to include important details of the material over a multitude of material structure length scales (from the macroscale to the atomistic).

AUTHOR CONTRIBUTIONS

All authors listed have made a substantial, direct, and intellectual contribution to the work and approved it for publication.

FUNDING

MB and SRK acknowledge support from NSF DMREF Award# 2119640. This work was performed, in part, at the Center for Integrated Nanotechnologies, an Office of Science User Facility operated for the U.S. Department of Energy. Sandia National Laboratories is a multimission laboratory managed and operated by National Technology and Engineering Solutions of Sandia, LLC, a wholly owned subsidiary of Honeywell International Inc., for the U.S. Department of Energy's National Nuclear Security Administration under contract DE-NA0003525. This paper describes objective technical results and analysis. Any subjective views or opinions that might be expressed in the paper do not necessarily represent the views of the U.S. Department of Energy or the United States Government.

REFERENCES

Abadi, M., Barham, P., Chen, J., Chen, Z., Davis, A., Dean, J., et al. (2016). "Tensorflow: A System for Large-Scale Machine Learning," in *12th {USENIX} Symposium on Operating Systems Design and Implementation ({OSDI} 16)*, 265–283.

Adams, B. L., Kalidindi, S., and Fullwood, D. T. (2012). *Microstructure Sensitive Design for Performance Optimization*. Butterworth-Heinemann

Allison, J., Backman, D., and Christodoulou, L. (2006). Integrated Computational Materials Engineering: a New Paradigm for the Global Materials Profession. *Jom* 58 (11), 25–27. doi:10.1007/s11837-006-0223-5

Azim, S., and Aggarwal, S. (2014). Hybrid Model for Data Imputation: Using Fuzzy C Means and Multi Layer Perceptron. in IEEE International Advance Computing Conference (IACC), Gurgaon, India, February 21-22, 2014. IEEE, 1281–1285. doi:10.1109/iadcc.2014.6779512

Banko, L., Lysogorskiy, Y., Grochla, D., Naujoks, D., Drautz, R., and Ludwig, A. (2020). Predicting Structure Zone Diagrams for Thin Film Synthesis by Generative Machine Learning. *Commun. Mater.* 1 (1), 1–10. doi:10.1038/s43246-020-0017-2

Belianinov, A., Ievlev, A. V., Lorenz, M., Borodinov, N., Doughty, B., Kalinin, S. V., et al. (2018). Correlated Materials Characterization via Multimodal Chemical and Functional Imaging. *ACS nano* 12 (12), 11798–11818. doi:10.1021/acsnano.8b07292

Brough, D. B., Wheeler, D., and Kalidindi, S. R. (2017). Materials Knowledge Systems in Python-A Data Science Framework for Accelerated Development of Hierarchical Materials. *Integr. Mater. Manuf Innov.* 6 (1), 36–53. doi:10.1007/s40192-017-0089-0

Castillo, A., and Kalidindi, S. R. (2019). A Bayesian Framework for the Estimation of the Single crystal Elastic Parameters from Spherical Indentation Stress-Strain Measurements. *Front. Mater.* 6, 136. doi:10.3389/fmats.2019.00136

Castillo, A. R., and Kalidindi, S. R. (2021). Bayesian Estimation of Single Ply Anisotropic Elastic Constants from Spherical Indentations on Multi-Laminate Polymer-Matrix Fiber-Reinforced Composite Samples. *Meccanica* 56 (6), 1575–1586. doi:10.1007/s11012-020-01154-w

Castillo, A. R., Venkatraman, A., and Kalidindi, S. R. (2021). Mechanical Responses of Primary-α Ti Grains in Polycrystalline Samples: Part II-Bayesian Estimation of Crystal-Level Elastic-Plastic Mechanical Properties from Spherical Indentation Measurements. *Integr. Mater. Manuf Innov.* 10 (1), 99–114. doi:10.1007/s40192-021-00204-9

Cecen, A., Fast, T., and Kalidindi, S. R. (2016). Versatile Algorithms for the Computation of 2-point Spatial Correlations in Quantifying Material Structure. *Integr. Mater. Manuf Innov.* 5 (1), 1–15. doi:10.1186/s40192-015-0044-x

Coleman, S. P., Sichani, M. M., and Spearot, D. E. (2014). A Computational Algorithm to Produce Virtual X-ray and Electron Diffraction Patterns from Atomistic Simulations. *Jom* 66 (3), 408–416. doi:10.1007/s11837-013-0829-3

Correa-Baena, J.-P., Hippalgaonkar, K., van Duren, J., Jaffer, S., Chandrasekhar, V. R., Stevanovic, V., et al. (2018). Accelerating Materials Development via Automation, Machine Learning, and High-Performance Computing. *Joule* 2 (8), 1410–1420. doi:10.1016/j.joule.2018.05.009

de Oca Zapiain, D. M., Stewart, J. A., and Dingreville, R. (2021). Accelerating Phase-Field-Based Microstructure Evolution Predictions via Surrogate Models Trained by Machine Learning Methods. *npj Comput. Mater.* 7 (1), 1–11. doi:10.1038/s41524-020-00471-8

de Pablo, J. J., Jackson, N. E., Webb, M. A., Chen, L. Q., Moore, J. E., Morgan, D., et al. (2019). New Frontiers for the Materials Genome Initiative. *npj Comput. Mater.* 5 (1), 1–23. doi:10.1038/s41524-019-0173-4

Dingreville, R., Karnesky, R. A., Puel, G., and Schmitt, J.-H. (2016). Review of the Synergies between Computational Modeling and Experimental Characterization of Materials across Length Scales. *J. Mater. Sci.* 51 (3), 1178–1203. doi:10.1007/s10853-015-9551-6

Fullwood, D. T., Niezgoda, S. R., Adams, B. L., and Kalidindi, S. R. (2010). Microstructure Sensitive Design for Performance Optimization. *Prog. Mater. Sci.* 55 (6), 477–562. doi:10.1016/j.pmatsci.2009.08.002

Generale, A. P., and Kalidindi, S. R. (2021). Reduced-order Models for Microstructure-Sensitive Effective thermal Conductivity of Woven Ceramic Matrix Composites with Residual Porosity. *Compos. Structures* 274, 114399. doi:10.1016/j.compstruct.2021.114399

Ghoreishi, S. F., and Allaire, D. (2019). Multi-information Source Constrained Bayesian Optimization. *Struct. Multidisc Optim* 59 (3), 977–991. doi:10.1007/s00158-018-2115-z

Ghosh, S., and Groeber, M. A. (2020). Developing Virtual Microstructures and Statistically Equivalent Representative Volume Elements for Polycrystalline Materials. *Methods Theor. Model*, 1631–1656. doi:10.1007/978-3-319-44677-6_13

Gil, Y., and Selman, B. (2019). *A 20-year Community Roadmap for Artificial Intelligence Research in the US*.arXiv preprint arXiv:1908.02624

Gomberg, J. A., Medford, A. J., and Kalidindi, S. R. (2017). Extracting Knowledge from Molecular Mechanics Simulations of Grain Boundaries Using Machine Learning. *Acta Materialia* 133, 100–108. doi:10.1016/j.actamat.2017.05.009

Gongora, A. E., Xu, B., Perry, W., Okoye, C., Riley, P., Reyes, K. G., et al. (2020). A Bayesian Experimental Autonomous Researcher for Mechanical Design. *Sci. Adv.* 6 (15), eaaz1708. doi:10.1126/sciadv.aaz1708

Groeber, M. A., and Jackson, M. A. (2014). DREAM.3D: A Digital Representation Environment for the Analysis of Microstructure in 3D. *Integr. Mater. Manuf Innov.* 3 (1), 56–72. doi:10.1186/2193-9772-3-5

Häse, F., Roch, L. M., and Aspuru-Guzik, A. (2019). Next-generation Experimentation with Self-Driving Laboratories. *Trends Chem.* 1 (3), 282. doi:10.1016/j.trechm.2019.02.007

Häse, F., Roch, L. M., Kreisbeck, C., and Aspuru-Guzik, A. (2018). Phoenics: a Bayesian Optimizer for Chemistry. *ACS Cent. Sci.* 4 (9), 1134–1145. doi:10.1021/acscentsci.8b00307

Herr, J. E., Koh, K., Yao, K., and Parkhill, J. (2019). Compressing Physics with an Autoencoder: Creating an Atomic Species Representation to Improve Machine Learning Models in the Chemical Sciences. *J. Chem. Phys.* 151 (8), 084103. doi:10.1063/1.5108803

Horstemeyer, M. F. (2009). Multiscale Modeling: A Review. *Pract. aspects Comput. Chem*, 87–135. doi:10.1007/978-90-481-2687-3_4

Hu, C., Martin, S., and Dingreville, R. (2022). Accelerating Phase-Field Predictions via Recurrent Neural Networks Learning the Microstructure Evolution in Latent Space. *Comput. Methods Appl. Mech. Eng.*. doi:10.2172/1618267

JenksCynthiaLeeNyung, H., LewisJennifer, P., et al. (2020). *Basic Research Needs for Transformative Manufacturing (Report)*. United States: USDOE Office of Science

Kalidindi, S. R., and De Graef, M. (2015). Materials Data Science: Current Status and Future Outlook. *Annu. Rev. Mater. Res.* 45, 171–193. doi:10.1146/annurev-matsci-070214-020844

Kalidindi, S. R. (2020). Feature Engineering of Material Structure for AI-Based Materials Knowledge Systems. *J. Appl. Phys.* 128 (4), 041103. doi:10.1063/5.0011258

Kalidindi, S. R. (2015). *Hierarchical Materials Informatics: Novel Analytics for Materials Data*. Elsevier.

Kalidindi, S. R., Khosravani, A., Yucel, B., Shanker, A., and Blekh, A. L. (2019). Data Infrastructure Elements in Support of Accelerated Materials Innovation: ELA, PyMKS, and MATIN. *Integr. Mater. Manuf Innov.* 8 (4), 441–454. doi:10.1007/s40192-019-00156-1

Kapteyn, M. G., Pretorius, J. V. R., and Willcox, K. E. (2021). A Probabilistic Graphical Model Foundation for Enabling Predictive Digital Twins at Scale. *Nat. Comput. Sci.* 1 (5), 337–347. doi:10.1038/s43588-021-00069-0

Kaundinya, P. R., Choudhary, K., and Kalidindi, S. R. (2021). Machine Learning Approaches for Feature Engineering of the crystal Structure: Application to the Prediction of the Formation Energy of Cubic Compounds. *Phys. Rev. Mater.* 5 (6), 063802. doi:10.1103/physrevmaterials.5.063802

Khosravani, A., Caliendo, C. M., and Kalidindi, S. R. (2020). New Insights into the Microstructural Changes during the Processing of Dual-phase Steels from Multiresolution Spherical Indentation Stress–Strain Protocols. *Metals* 10 (1), 18. doi:10.3390/met10010018

Khosravani, A., Thadhani, N., and Kalidindi, S. R. (2021). Microstructure Quantification and Multiresolution Mechanical Characterization of Ti-Based Bulk Metallic Glass-Matrix Composites. *JOM*, 1–11. doi:10.1007/s11837-021-04864-y

Kunka, C., Shanker, A., Chen, E. Y., Kalidindi, S. R., and Dingreville, R. (2021). Decoding Defect Statistics from Diffractograms via Machine Learning. *npj Comput. Mater.* 7 (1), 1–9. doi:10.1038/s41524-021-00539-z

LaBonte, T., Martinez, C., and Roberts, S. (2020). *We Know Where We Don't Know: 3D Bayesian CNNs for Uncertainty Quantification of Binary Segmentations for Material Simulations*.osti

Lassila, O., and Swick, R. R. (1998). *Resource Description Framework (RDF) Model and Syntax Specification*. W3C.

Latypov, M. I., Toth, L. S., and Kalidindi, S. R. (2019). Materials Knowledge System for Nonlinear Composites. *Comput. Methods Appl. Mech. Eng.* 346, 180–196. doi:10.1016/j.cma.2018.11.034

Lim, J., Perullo, C. A., Milton, J., Whitacre, R., Jackson, C., Griffin, C., et al. (2021). *The EPRI Gas Turbine [43] Digital Twin–A Platform for Operator Focused Integrated Diagnostics and Performance Forecasting*.

Margaria, T., and Schieweck, A. (2019). "The Digital Thread in Industry 4.0," in *International Conference on Integrated Formal Methods* (Cham: Springer), 3–24. doi:10.1007/978-3-030-34968-4_1

Marquis de Laplace, P. S. (1814). *A Treatise upon Analytical Mechanics: Being the First Book of the Mécanique Céleste*. Boston, Massachusetts: Hilliard, Gray, Little, and Wilkins.

Marshall, A., and Kalidindi, S. R. (2021). Autonomous Development of a Machine-Learning Model for the Plastic Response of Two-phase Composites from Micromechanical Finite Element Models. *JOM*, 1–11. doi:10.1007/s11837-021-04696-w

Matouš, K., Geers, M. G., Kouznetsova, V. G., and Gillman, A. (2017). A Review of Predictive Nonlinear Theories for Multiscale Modeling of Heterogeneous Materials. *J. Comput. Phys.* 330, 192–220.

McDowell, D. L., and LeSar, R. A. (2016). The Need for Microstructure Informatics in Process–Structure–Property Relations. *MRS Bull.* 41 (8), 587–593. doi:10.1557/mrs.2016.163

McGuinness, D. L., and Van Harmelen, F. (2004). OWL Web Ontology Language Overview. *W3C recommendation* 10 (10), 2004.

Mei, H., Haider, M., Joseph, R., Migot, A., and Giurgiutiu, V. (2019). Recent Advances in Piezoelectric Wafer Active Sensors for Structural Health Monitoring Applications. *Sensors* 19 (2), 383. doi:10.3390/s19020383

Morgado, J. F., Ghedini, E., Goldbeck, G., Hashibon, A., Schmitz, G. J., Friis, J., et al. (2020). "Mechanical Testing Ontology for Digital-Twins: a Roadmap Based on EMMO," in *SeDiT@ ESWC*. CEUR Workshop Proceedings.

National Science and Technology Council (Us) (2011). "Materials Genome Initiative for Global Competitiveness," in *Executive Office of the President* (Washington, DC: National Science and Technology Council).

Niederer, S. A., Sacks, M. S., Girolami, M., and Willcox, K. (2021). Scaling Digital Twins from the Artisanal to the Industrial. *Nat. Comput. Sci.* 1 (5), 313–320. doi:10.1038/s43588-021-00072-5

Niezgoda, S. R., Kanjarla, A. K., and Kalidindi, S. R. (2013). Novel Microstructure Quantification Framework for Databasing, Visualization, and Analysis of Microstructure Data. *Integr. Mater. Manuf Innov.* 2 (1), 54–80. doi:10.1186/2193-9772-2-3

Niezgoda, S. R., Yabansu, Y. C., and Kalidindi, S. R. (2011). Understanding and Visualizing Microstructure and Microstructure Variance as a Stochastic Process. *Acta Materialia* 59 (16), 6387–6400. doi:10.1016/j.actamat.2011.06.051

Nikolaev, P., Hooper, D., Webber, F., Rao, R., Decker, K., Krein, M., et al. (2016). Autonomy in Materials Research: a Case Study in Carbon Nanotube Growth. *npj Comput. Mater.* 2 (1), 1–6. doi:10.1038/npjcompumats.2016.31

Panchal, J. H., Kalidindi, S. R., and McDowell, D. L. (2013). Key Computational Modeling Issues in Integrated Computational Materials Engineering. *Computer-Aided Des.* 45 (1), 4–25. doi:10.1016/j.cad.2012.06.006

Pandita, P., Bilionis, I., and Panchal, J. (2019). Bayesian Optimal Design of Experiments for Inferring the Statistical Expectation of Expensive Black-Box Functions. *J. Mech. Des.* 141 (10). doi:10.1115/1.4043930

Paszke, A., Gross, S., Massa, F., Lerer, A., Bradbury, J., Chanan, G., et al. (2019). Pytorch: An Imperative Style, High-Performance Deep Learning Library. *Adv. Neural Inf. Process. Syst.* 32, 8026–8037.

Paulson, N. H., Priddy, M. W., McDowell, D. L., and Kalidindi, S. R. (2017). Reduced-order Structure-Property Linkages for Polycrystalline Microstructures Based on 2-point Statistics. *Acta Materialia* 129, 428–438. doi:10.1016/j.actamat.2017.03.009

Pedregosa, F., Varoquaux, G., Gramfort, A., Michel, V., Thirion, B., Grisel, O., et al. (2011). Scikit-learn: Machine Learning in Python. *J. machine Learn. Res.* 12, 2825–2830.

Pendleton, I. M., Cattabriga, G., Li, Z., Najeeb, M. A., Friedler, S. A., Norquist, A. J., et al. (2019). Experiment Specification, Capture and Laboratory Automation Technology (ESCALATE): a Software Pipeline for Automated Chemical Experimentation and Data Management. *MRS Commun.* 9 (3), 846–859. doi:10.1557/mrc.2019.72

Polonsky, A. T., and Pandey, A. (2021). Advances in Multimodal Characterization of Structural Materials. *JOM*, 1–2. doi:10.1007/s11837-021-04895-5

Raj, P., and Surianarayanan, C. (2020). Digital Twin: the Industry Use casesAdvances in Computers. *Elsevier* 117 (1), 285–320. doi:10.1016/bs.adcom.2019.09.006

Robertson, A. E., and Kalidindi, S. R. (2021a). *Digital Representation and Quantification of Discrete Dislocation Networks*.arXiv preprint arXiv: 2101.03925

Robertson, A. E., and Kalidindi, S. R. (2021b). *Efficient Generation of Anisotropic N-Field Microstructures from 2-Point Statistics Using Multi-Output Gaussian Random Fields*. Rochester, NY: SSRN 3949516

Rocklin, M. (2015). Dask: Parallel Computation with Blocked Algorithms and Task Scheduling. in Proceedings of the 14th python in science conference, Austin, TX, July 6-12, 2009, 130. Austin, TX: SciPy, 136.

Seabold, S., and Perktold, J. (2010). Statsmodels: Econometric and Statistical Modeling with python. in Proceedings of the 9th Python in Science Conference, Pasadena, CA, August 18-23, 2009 (Vol. 57, p. 61).doi:10.25080/majora-92bf1922-011

Singh, V., and Willcox, K. E. (2018). Engineering Design with Digital Thread. *AIAA J.* 56 (11), 4515–4528. doi:10.2514/1.j057255

Solomou, A., Zhao, G., Boluki, S., Joy, J. K., Qian, X., Karaman, I., et al. (2018). Multi-objective Bayesian Materials Discovery: Application on the Discovery of Precipitation Strengthened NiTi Shape Memory Alloys through Micromechanical Modeling. *Mater. Des.* 160, 810–827. doi:10.1016/j.matdes.2018.10.014

Sorkin, B. C., Betz, J. M., and Hopp, D. C. (2020). *Toward FAIRness and a User-Friendly Repository for Supporting NMR Data*. doi:10.1021/acs.joc.0c00800

Sporny, M., Longley, D., Kellogg, G., Lanthaler, M., and Lindström, N. (2014). JSON-LD 1.0. *W3C recommendation* 16, 41.

Takhtaganov, T., and Müller, J. (2018). *Adaptive Gaussian Process Surrogates for Bayesian Inference*. SIAM/ASA Journal on Uncertainty Quantification.arXiv preprint arXiv:1809.10784

Talapatra, A., Boluki, S., Duong, T., Qian, X., Dougherty, E., and Arróyave, R. (2018). Autonomous Efficient experiment Design for Materials Discovery with Bayesian Model Averaging. *Phys. Rev. Mater.* 2 (11), 113803. doi:10.1103/physrevmaterials.2.113803

Tao, F., Zhang, M., Liu, Y., and Nee, A. Y. C. (2018). Digital Twin Driven Prognostics and Health Management for Complex Equipment. *Cirp Ann.* 67 (1), 169–172. doi:10.1016/j.cirp.2018.04.055

The Minerals, Metals & Materials Society Tms (2017). *Building a Materials Data Infrastructure: Opening New Pathways to Discovery and Innovation in Science and Engineering*. Pittsburgh, PA: TMS. Electronic copies available at www.tms.org/mdistudy.

The Minerals, Metals & Materials Society Tms (2015). *Modeling across Scales: A Roadmapping Study for Connecting Materials Models and Simulations across Length and Time Scales*. Warrendale, PA: TMS. Electronic copies available at www.tms.org/multiscalestudy.

Torquato, S., and Haslach, H., Jr (2002). Random Heterogeneous Materials: Microstructure and Macroscopic Properties. *Appl. Mech. Rev.* 55 (4), B62–B63. doi:10.1115/1.1483342

Torquato, S., and Stell, G. (1982). Microstructure of Two-phase Random media. I. The N-point Probability Functions. *J. Chem. Phys.* 77 (4), 2071–2077. doi:10.1063/1.444011

Ullo, S. L., and Sinha, G. R. (2020). Advances in Smart Environment Monitoring Systems Using IoT and Sensors. *Sensors* 20 (11), 3113. doi:10.3390/s20113113

Voigt, S. P., and Kalidindi, S. R. (2021). Materials Graph Ontology. *Mater. Lett.* 295, 129836. doi:10.1016/j.matlet.2021.129836

Wilkinson, M. D., Dumontier, M., Aalbersberg, I. J., Appleton, G., Axton, M., Baak, A., et al. (2016). The FAIR Guiding Principles for Scientific Data Management and Stewardship. *Sci. Data* 3 (1), 160018–160019. doi:10.1038/sdata.2016.18

Xiang, Z., Fan, M., Tovar, G. V., Trehem, W., Yoon, B. J., Qian, X., et al. (2021). Physics-constrained Automatic Feature Engineering for Predictive Modeling in Materials Science. in Proceedings of the AAAI Conference on Artificial Intelligence (Vol. 35, No. 12, pp. 10414–10421). The AAAI Digital Library.

Xie, R., Chen, M., Liu, W., Jian, H., and Shi, Y. (2021). Digital Twin Technologies for Turbomachinery in a Life Cycle Perspective: A Review. *Sustainability* 13 (5), 2495. doi:10.3390/su13052495

Zaccaria, V., Stenfelt, M., Aslanidou, I., and Kyprianidis, K. G. (2018). "Fleet Monitoring and Diagnostics Framework Based on Digital Twin of Aero-Engines," in *Turbo Expo: Power for Land, Sea, and Air* American Society of Mechanical Engineers (ASME), 51128, V006T05A021. doi:10.1115/gt2018-76414

Zeb, S., Mahmood, A., Hassan, S. A., Piran, M. J., Gidlund, M., and Guizani, M. (2021). Industrial Digital Twins at the Nexus of nextG Wireless Networks and Computational Intelligence: A Survey. *Journal of Network and Computer Applications*, 103309. doi:10.1016/j.jnca.2021.103309

Conflict of Interest: The authors declare that the research was conducted in the absence of any commercial or financial relationships that could be construed as a potential conflict of interest.

Publisher's Note: All claims expressed in this article are solely those of the authors and do not necessarily represent those of their affiliated organizations, or those of the publisher, the editors, and the reviewers. Any product that may be evaluated in this article, or claim that may be made by its manufacturer, is not guaranteed or endorsed by the publisher.

frontiers in Materials

REVIEW
published: 21 March 2022
doi: 10.3389/fmats.2022.805131

High Temperature Composites From Renewable Resources: A Perspective on Current Technological Challenges for the Manufacturing of Non-Oil Based High Char Yield Matrices and Carbon Fibers

*Maurizio Natali, Marco Rallini, Luigi Torre and Debora Puglia**

University of Perugia, Civil and Environmental Engineering Department, Materials Engineering Center, Terni, Italy

OPEN ACCESS

Edited by:
Patricia Krawczak, Institut Mines-Télécom, France

Reviewed by:
Mehdi Derradji, Ecole Militaire Polytechnique (EMP), Algeria
Junheng Zhang, South-Central University for Nationalities, China

***Correspondence:**
Debora Puglia
debora.puglia@unipg.it

Specialty section:
This article was submitted to Polymeric and Composite Materials, a section of the journal Frontiers in Materials

Received: *29 October 2021*
Accepted: *02 March 2022*
Published: *21 March 2022*

Citation:
Natali M, Rallini M, Torre L and Puglia D (2022) High Temperature Composites From Renewable Resources: A Perspective on Current Technological Challenges for the Manufacturing of Non-Oil Based High Char Yield Matrices and Carbon Fibers. Front. Mater. 9:805131. doi: 10.3389/fmats.2022.805131

During last decades a plethora of high temperature materials have been developed to work as a Thermal Protection System (TPS). Carbon based materials such as graphite, which possesses low density, high heat capacity and high energy of vaporization, have been used as TPS material. However, graphite has relatively poor mechanical properties, but exhibits low resistance to the thermal shocks. Accordingly, to bypass the limitation of graphite, carbon fibers are typically introduced in a carbon matrix to produce Carbon/Carbon Composites (CCCs). Among the different families of TPS solutions, Polymeric Ablative Materials (PAMs), produced combining high char yield matrices - mainly phenolic resins - and Carbon Fibers (CFs) are used to manufacture Carbon/Phenolic Composites (CPCs) i.e. the most important class of fiber reinforced PAM. Carbon fibers are traditionally produced from Polyacrylonitrile (PAN), Rayon and Pitch. Some limited researches also aimed to use cyanate-esters, bismaleimides, benzoxazines matrices in combination with ex-PAN-CFs, ex-Rayon-CFs, and ex-Pitch-CFs. In our paper, after covering the science and technology of these state-of-the-art fiber reinforced TPS materials, a review of current challenges behind the manufacturing of new, high char yield matrices and carbon fibers derived from alternative precursors will be provided to the reader. In particular, the possibility to produce CFs from precursors different from PAN, Rayon and Pitch will be reported and similarly, the technology of non-oil based phenolics, bismaleimides, cyanate-esters and benzoxazines will be discussed. The effect of the use of nanosized fillers on these matrices will also be reported. More in detail, after a preliminary section in which the state of the art of technologies behind carbon/phenolic composites will be covered, a second part of this review paper will be focused on the most recent development related to non-oil based phenolics and biomass derived carbon fibers. Finally, an outlook focused on the maturity of the lab-scale protocols behind the researches at the base of these non-traditional raw materials from an industrial point of view will conclude this review paper.

Keywords: thermal protection system (TPS), carbon/phenolic composites (CPCs), solid rocket motors (SRMs), traditional and non-oil based high char yield polymers, traditional and non-oil based carbon fibers (CFs)

INTRODUCTION

During last decades, a plethora of high temperature and Thermal Protection System (TPS) materials have been developed and optimized for different applications. TPS materials are used to manufacture propulsion systems, such as liquid rocket engines, Solid Rocket Motors (SRMs) and, more recently, Hybrid Rocket Motors (HRMs) (Sutton and Biblarz, 2000). They are also used to manufacture the heat shields which protect probes and vehicles during the hypersonic flight through an atmosphere (D'Aelio GF, 1971). In addition to Refractory Metals (RMs) and Ultra High Temperature Ceramics (UHTCs), carbon based materials such as graphite, which possesses high heat capacity and high energy of vaporization, have been widely used as TPS material. However, even though graphite has a substantially lower density than RMs and UHTCs, it has the drawback to possess relatively poor mechanical properties and to exhibit problems in terms of resistance to thermal shocks. Accordingly, carbon fibers are typically introduced in a carbon matrix to produce Carbon/Carbon Composites (CCCs) (Fitzer and Manocha, 1998). These materials are used in the throat region of SRMs which is exposed to the harshest conditions generated by modern aluminized propellants and where the heat flux easily exceeds ~1,000 W/cm^2 (Koubek, 1971). Among TPS materials, Polymeric Ablative Materials (PAMs) possess the highest versatility in terms of properties tunability. Ablation is a self-regulating heat and

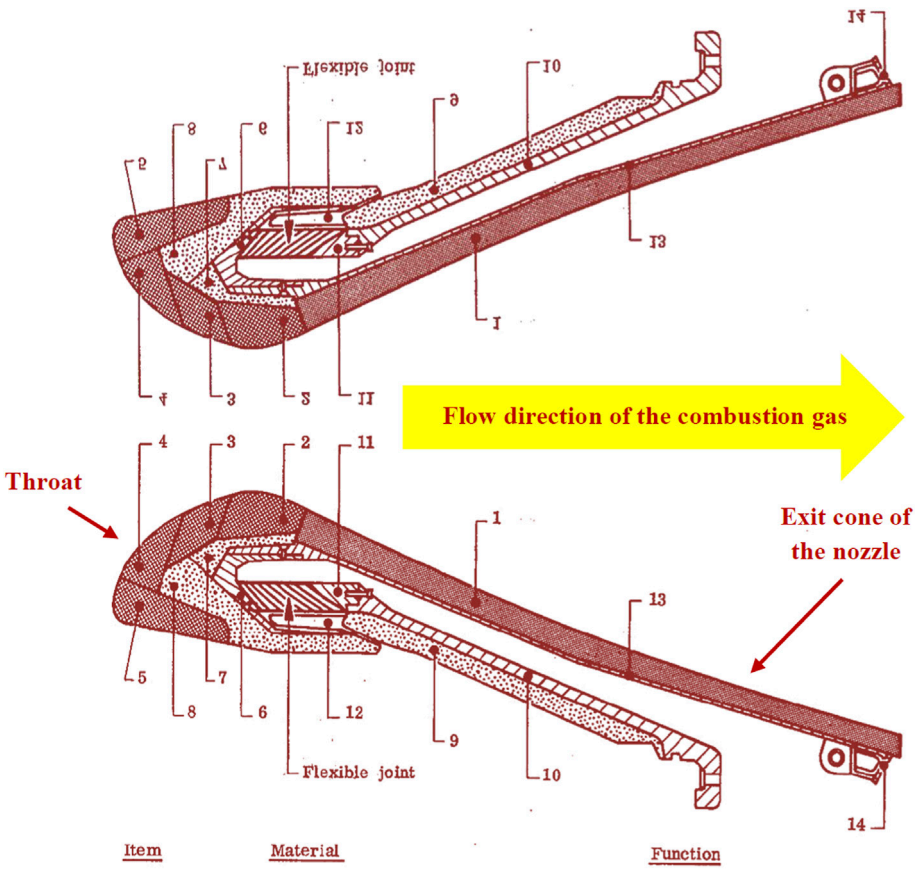

Item	Material	Function
1	Carbon/phenolic tape	Exit thermal liner and insulation
2	Graphite/phenolic tape	Throat insert
3	Graphite/phenolic tape	Throat approach thermal liner
4	Graphite/phenolic rosette	Throat approach thermal liner
5	Graphite/phenolic rosette	Entrance cap
6	Aluminum	Throat and entrance structure
7	Molded Silica/phenolic	Throat insulation
8	Silica/phenolic tape	Entrance insulation, cowl, thermal liner and insulator
9	Silica/phenolic tape	Reentry thermal liner and insulation
10	Aluminum	Reentry structure
11	Aluminum	Seal end ring
12	Silicone rubber	Flexible joint insulation
13	Aluminum	Exit structure
14	Steel	Actuator attach ring

FIGURE 1 | Typical nozzle assembly of a solid rocket motor. In this figure it is possible to see the complex structure of all components of the nozzle assembly of a SLBM Poseidon C-3 first stage. The item indicated in figure as 1-5 are made of carbon/phenolic composites (from Ellis, 1975, credit NASA).

mass transfer process in which the incident thermal energy is dissipated through a sacrificial material which undergoes endothermic degradation reactions.

In general, among PAMs, composite materials are produced combining high char yield matrices with high performance fibers. To this purpose, in order to produce high char yield and performance composite formulations, many researches aimed at use matrices such as cyanate-esters, bismaleimides, benzoxazines in combination with different types of fibers (silica, glass, carbon, etc.). Each type of fiber is optimized to work in a certain hyperthermal environment (Natali et al., 2016). Unfortunately, a series of problems - mainly related to the costs and the processing - tends to hinder the use of these matrices. As a result, the data available on literature on the use of these matrices are very limited. Phenolics are the most important resins used to produce high char yield and performance composite formulations. Consequently, Carbon/Phenolic Composites (CPCs) are the most studied and versatile class of fiber reinforced PAMs. Due to their high mechanical properties, high thermal resistance, low density, Carbon Fibers (CFs) are the most important class of reinforcements for high char yield composites. Carbon/phenolic composites are used to produce many parts of a nozzle (such as the cowl in a submerged configuration or the exit cone) since the erosive phenomena are smaller as compared to the throat region.

Figure 1 reports the exploded view of the Submarine Launched Ballistic Missile (SLBM) UGM-73 Poseidon first stage (Ellis, 1975). It is possible to identify thermoset based PAMs such as the carbon/phenolic composites known as MX-4926 (Natali et al., 2016) that will be discussed in details in **Section 3**. Moreover, through the use of a series of carbonization, graphitization and re-impregnations cycles, carbon/phenolic composites are converted into carbon/carbon composites (Fitzer and Manocha, 1998). Depending on the re-entry or flight conditions, carbon/phenolic composites are also used to manufacture the heat shields of re-entry objects; as an example, a carbon/phenolic composite was used to manufacture the heat shield of the Galileo probe which entered in the Jupiter atmosphere and underwent one of the highest heat flux ever recorded (~30,000 kW/cm^2) (Milos, 1997). For these reasons, carbon/phenolic composites are virtually the most important class of TPS materials. One of the last efforts of NASA to systematically investigate high temperature composites has been done within the Next Generation Launch Vehicle (NGLV) program (Smith, 2019). In this framework, the development of out-of-autoclave processing techniques for carbon/phenolic composites has also been faced. However, for over 60 years, space agencies such as National Aeronautics and Space Administration (NASA) spent millions and substantial efforts to investigate carbon/phenolic composites (Natali et al., 2016). Moreover, hundreds of papers and reports on carbon/phenolic composites have been reported and made readily available mostly through the NASA Technical Reports Server (NTRS). In the next sections we will first provide an introduction to the raw materials used to produce high temperature composites i.e. the matrices - mainly focusing the attention on phenolics - and the carbon fibers (ex-PAN, ex-Rayon, ex-Pitch). Then the efforts of our survey will be focused on non-oil based phenolics and carbon fibers derived from biomass, also highlighting the current limitations and the potential of these renewable raw materials.

AN INTRODUCTION TO TRADITIONAL HIGH CHAR YIELD POLYMERIC MATRICES

Due to the high temperature properties of carbon, the creation of a carbonaceous residue - char - on the surface of the ablated material is essential (Allen, 1958). In fact, carbon possesses a high heat capacity and high energy of vaporization combined with high heat of ablation. In this case, the PAM is based on the use of charring precursors. When the matrix is exposed to a non-oxidizing hyperthermal environment and it is not subjected to mechanical erosion, it is converted into a charred layer obtained from the carbon atoms present in the molecules of the organic precursor (Schmidt, 1968a; Schmidt, 1968b; Schmidt, 1971; D'Aelio GF, 1971; Wen et al., 1971); the carbon based-residue can still partly operate as a binder of the fillers used in the formulation of the ablative. In addition with their superb thermal stability and char yield, phenolics have a remarkable dimensional stability due the high density of highly aromatic rings in the molecular structure of these resins (Schmidt, 1968a; Schmidt, 1968b; Schmidt, 1971; D'Aelio GF, 1971; Wen et al., 1971). Once the polymeric binder is charred it works as thermal insulator for the virgin matrix. Different precursors have been evaluated as binders of PAMs but, among common matrices, phenolics remain the most versatile infiltrants. In fact, in addition to phenolic matrices, other high char yield polymers have been evaluated as binders of high temperature composite (Schmidt, 1971; Pilato et al., 2008; Vincent, 1971; Lurie et al., 1971; Marks and Rubin, 1971; Dickey et al., 1969; Minges, 1971). Among them, it is worth to mention cyanate-esters, bismaleimides, and benzoxazines (Natali et al., 2016). However, when compared to phenolics, they generally tend to exhibit limitations mainly in terms of processability and costs - they are typically one order of magnitude more expensive than phenolics. For these reasons, most of efforts of these review paper on the non-oil based high char yield matrices will be focused on phenolics.

Phenolics

Phenol-formaldehyde resins are synthetic polymers obtained by the reaction of phenol and formaldehyde. The molar ratio between these two organic compounds and the acidity (or basicity) of the environment in which they are allowed to react can lead to various and versatile families of phenolic resins (Gardziella et al., 2013). Heat reactive phenolic resins known as resols are obtained under basic conditions, and the molar ratio between formaldehyde and phenol can vary from equimolar to values in excess of formaldehyde. On the other hand, when less than an equimolar amount of formaldehyde to phenol is maintained under acidic conditions, a novolac resin is obtained. In general, when compared to other polymers in which the chemistry of the cure is based on a single main process, the crosslinking of phenolics is very complex and involves a wide

series of competing reactions which are deeply influenced by experimental conditions. An additional factor that complicates the chemistry of the cure of phenolics is due to the possibility to obtain crosslinking reaction by either or both the ortho- and para-positions of the phenol. As a result, depending on the position of the functional group and as a function of the steric spacing in which the molecules can intertwine, a wide number of isomeric products having different reactivity is created.

Resols are readily cured mainly by acid aiders or thermal conditions. The polymerization is a poly-condensation reaction where the oxygen atom in the formaldehyde molecule reacts with a hydrogen atom on each of two phenol molecules. Water is the product of the reaction. The two phenol molecules are then joined by the residual carbon atom in the formaldehyde (Askeland, 1996). Methylene links connect phenol rings along with methoxy-type ether links produced during the initial reactions that are still present due to shielding from subsequent heating conditions, and phenoxy-type ether links occasionally formed between adjacent phenol hydroxy groups. In both cases, the ether groups are vulnerable to dehydration or oxidation. Post-curing at temperature higher than 200 °C will remove all the ether links as formaldehyde is generated (Lee, 2007). The mechanism of cure for novolac involves benzoxazine intermediates that are converted into benzyl amines, amides/imides, imines, methyl phenol, benzaldehyde. Curing reaction of novolac with hexamine results in a polymer network, especially when sufficient hexamine is available for full cure and reaction of all available novolac sites. Hexamethylenetetramine (HMTA or hexa) is by far the most important curing agent for novolac: typically, about (5–10) % of hexamine is added to novolac. When heat is applied to novolac, the hexamine added to the uncured resin decomposes, enabling the production of methylene bridge bonds to form the crosslinked structure. (Smith and Hashemi. 2006). Complete cure of phenol-formaldehyde resin leads to a polymeric material characterized by high elastic modulus, high crosslink density, moderately high glass transition temperature; the material exhibits excellent moisture, electrical and heat resistance (Smith and Hashemi. 2006; Kim et al., 1997). The dimensional and thermal properties of phenolics are widely covered in (Natali et al., 2016).

Cyanate-Esters

Cyanate esters (CE) matrices consist of a variety of bisphenols as well as phenolic novolac resins with the cyanate (-O-C=N) functional group appended to the phenolic hydroxyl (Hamerton, 2012; Hamerton and Hay, 1998). Chemically speaking, this family of thermo-setting monomers and their prepolymers are prepared by reacting the phenolic containing materials with cyanogen halide to form the resulting cyanate ester in the presence of a base (Hamerton and Hay., 1998). At elevated temperatures cyanate esters convert to a thermoset polymer via cyclotrimerization to form three-dimensional networks of oxygen-linked triazine (or cyanurate) and bisphenyl units called poly (cyanurate) s (Hamerton and Hay, 1998). The cured polymer exhibits high T_g, excellent mechanical properties, heat resistance, low volume shrinkage, and low water absorption (Pilato, 2010).

Bismaleimides

Bismaleimides monomers are usually synthesized from maleic anhydride and an aromatic diamine and then, the resulting bismaleamic acid is cyclo-dehydrated to a bismaleimide resin (Bibin & Reghunadhan Nair, 2014). The double bond of maleimide is very reactive and can promote chain-extension reactions. When bismaleimide is heated above 200°C, a polymerization by an addition mechanism with the formation of a cross-linked network occurs. A basic catalyst such as diazabicyclooctane or 2-methylimidazole can be used to polymerize bismaleimides by an anionic mechanism (Sillion, 1996). or, Bismaleimides can provide a higher service temperature than epoxies maintaining epoxy-like processing glass transition temperatures in excess of 260°C and a continuous-use temperature of 200–230°C. These matrices mainly find applications in high-performance structural adhesives for high temperature application (Bibin & Reghunadhan Nair, 2014).

Benzoxazines

Benzoxazines can be considered as a novel type of phenolic resins, even though they differ from traditional phenolics, because the phenolic moieties are connected through the formation of a cyclic structure from the phenolic hydroxyl to the ortho position [–O–CH_2–N(R)–CH_2–] rather than a methylene [–CH_2–] bridge associated with traditional phenolics (Ning & Ishida, 1994; Takeichi & Agag, 2006; Blyakham et al., 2001; Ghosh et al., 2007). The molecule of monomer consists in oxazine ring (a hetero-cyclic six-membered ring with oxygen and nitrogen atom) attached to a benzene ring. There are several benzoxazine structures that depend on the position of the heteroatoms. Benzoxazines can be readily produced by a combination of a phenolic derivative, formaldehyde, and a primary amine and any combination of them can be used. Like epoxies and cyanate esters, both monomers and oligomeric benzoxazine materials are available by reaction of bisphenols or novolac with primary amines and formaldehyde (Cortopassi, 2012). Polymerization occurs through the ring opening of the cyclic component by heat treatment with or without catalyst and, without the generation of by-products/volatiles. In addition to flame retardant properties and high heat resistance, the material exhibits characteristics that are not showed in traditional phenolic resins, such as low water absorption (Ishida, 2011).

FIBER REINFORCED COMPOSITES AS POLYMERIC ABLATIVE MATERIALS

Many matrices have been tested in PAMs but, among common polymers, phenolics resins still remain the preferred and most widely used charring binders. An important example of a phenolic resin used to produce PAMs is the SC-1008 (Hexion, 2015b). This resin has been used in many of the phenolic based composite formulation. The SC-1008 resin is a resol diluted in isopropyl alcohol whit a solid content close to (60–64) % and a viscosity of (180–300) mPas.

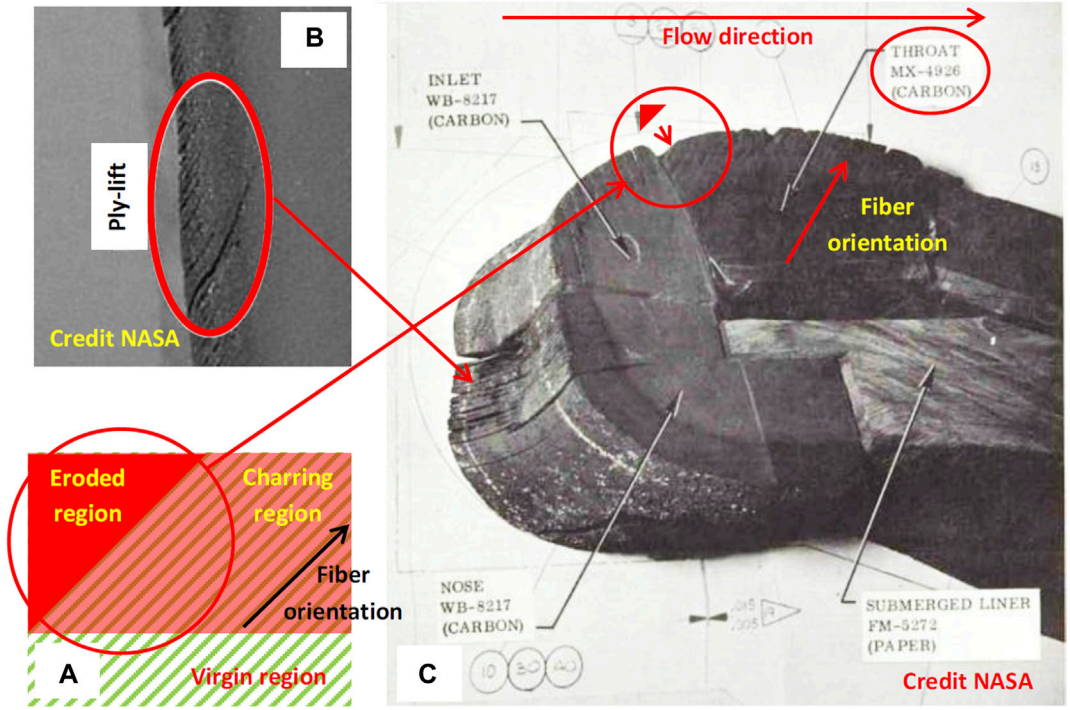

FIGURE 2 | Charring phenomena within the nozzle of a solid rocket motor. **(A)** Ply-lift of a carbon/phenolic composite. **(B)** Post burning appearance of a composite segmented submerged nozzle assembly and phenomena of erosion. **(C)** It is possible to also evidence the portion of the throat made of MX-4926 (image produced starting from an image taken from (Mathis & Laramee, 1970), credit NASA).

Even though matrices such as phenolics possess a carbon yield higher than 50%, the residual char of the polymeric precursor is a relatively weak medium. When the polymer is converted into char a substantial amount of heat is absorbed by the degradation processes and the char works as a heat sink. However, the char i.e. the residue of the organic precursor can be removed by the high pressure and temperature of the combustion products of solid rocket motor propellants or by the interaction with the atmosphere gases during the re-entry flight (Allen, 1958). As a result, since the polymeric matrix needs to be combined with some reinforcement. Once converted into a carbonaceous residue, the retention of the charred matrix is then promoted and consequently the ablation process can proceed effectively - the material can continue to endothermically absorb heat.

When compared to reinforcements made of refractory oxides (such as glass or silica fibers), in not oxidizing conditions, carbon based filaments tend to possess lower density and a substantially higher ablation resistance (Natali et al., 2016). Different precursors have been generally used to produce carbon fibers: CFs are typically produced from Rayon, Polyacrylonitrile (PAN), and Pitch (Rossi & Wong, 1996). Since the introduction of fibers also helps to anchor the charred material on the virgin region which is undergoing pyrolysis, the delamination phenomena tend to be mitigated. A fiber with a high thermal conductivity tends to increase the in-depth penetration of the charring phenomena and consequently a wider degradation of the bonding capability of the virgin matrix. If the pyrolysis gases cannot escape, the fibers can suffer severe in depth de-bonding or pull-out from the matrix (Allen, 1958). In fact, entrapped pyrolysis gases in the charring matrix can cause pore pressure build-up, and also produce a wide series of erosion phenomena such as ply lift, sub-char ply separations, pocketing, etc. (Schmidt. 1968a). These erosion processes can significantly affect the performance of the PAM. Moreover, the reinforcements embedded in the composite material also undergo many endothermic processes. As an example, carbon fibers can also undergo sublimation (Natali et al., 2016). Accordingly, fibers should possess the lowest thermal conductivity and the highest heat capacity.

The virtually most important carbon/phenolic composite used in rocketry and to manufacture nozzle components is Cytec MX-4926 (density 1.45 g/cm^3) (Minges, 1971; Koo, 2006; Cortopassi, 2012; Cortopassi et al., 2009, Hexion, 2015a). It consists of 50 wt% carbon reinforcements, 35 wt% phenolic resin (Hexion SC-1008) and 15 wt% carbon black which help to reduce the shrinkage of the resin pocket, due to the carbonization and loss of volatiles from the matrix. During the firing of the motor (Mathis & Laramee, 1970), the inner layers of the nozzle wall start to char (**Figure 2A**, in red) dramatically reducing the local Inter Laminar Shear Strength (ILSS) (over 90%); as a result, the structural integrity of the nozzle wall is enabled by the virgin portion (**Figure 2A**, in green) of the overlapping fiber layers. The charred part does not contribute to the structural integrity of the nozzle wall which is subjected to ply-lift (**Figure 2B**). Depending on the combustion time, every design and layout of the fibers have to keep into account the fact that a certain portion of the carbon/phenolic composite wall has to be left virgin to avoid the failure of

TABLE 1 | Thermal conductivity values of carbon fibers derived from different precursors. From (Towne, 1989).

Precursor	Thermal conductivity (W/mK)
Rayon derived carbon fibers	~4
"Standard" (T300-like) derived PAN carbon fibers	~22
Low fired derived PAN carbon fibers	~12
"Standard" Pitch derived carbon fibers	~20
High modulus Pitch derived carbon fibers	~120

the nozzle. That's the reason why it is imperative to have carbon/phenolic composites with the highest ILSS and the lower thermal conductivity. The part of throat evidenced in the circular red area of **Figure 2C** is completely charred as compared to other portions of the same part which still possess a certain level of virgin material - as resumed in **Figure 1A**. In **Figure 2C**, the triangular part evidenced in red is the portion that does not possess any virgin material and thus is completely removed.

Moreover, different researchers reported the effect of the use of nanostructured phenolic matrices (Natali et al., 2016; Natali et al., 2012; Rallini at al., 2017; Natali et al., 2011a;, Natali et al., 2011b) on the ablation resistance of the derived carbon/phenolic laminates. Among these researches, some efforts were successfully spent to identify special fillers or chemical modifiers aimed at improve the ILSS of carbon/phenolic composites (Yeh et al., 2006; Lyashenko et al., 2013; Abramovitch et al., 2015; Wang et al., 2006; Wolf et al., 2012; Srikanth et al., 2010).

An Introduction to Carbon Fibers for Polymeric Ablative Materials: Rayon vs. Polyacrylonitrile Precursors

NASA and other US agencies spent decades to study carbon/phenolic composite materials. On the base of these studies, most of the European countries and US allied in the pacific area such as South Korea and Japan set up their corresponding efforts to produce high temperature carbon/phenolic composites. Randy Lee at NASA Marshall Space Flight Center (MSFC) carried out the most comprehensive investigation on the effect of the use of different carbon fibers for carbon/phenolic composites [Lee, 2009; Lee, 2010; Lee, 2014.]. In these papers, the benefits and demerits of ex-Rayon based Carbon Fibers (R-CFs) - which are typically used to produce carbon/phenolic composites and carbon/phenolic composites - and common ex-polyacrylonitrile (PAN) based Carbon Fibers (P-CFs) - i.e., T300-like fibers which are typically used to produce high performance Carbon/Epoxy Composites (CECs) - were highlighted.

Pitch-based CFs were also evaluated as fibers to produce high char yield composites. However, Pitch based carbon fibers possess a thermal conductivity too high so tend to promote in depth charring (i.e. pyrolysis of the resin) and hence are not suitable to produce carbon/phenolic composites (Rossi and Wong, 1996). P-CFs, however, have been evaluated as alternative reinforcement for nozzle insulators for more than 20 years with NASA, Air Force, and Navy funding. Thermal conductivity of P-CFs, a critical performance property, was found to be adjustable by varying the carbonization temperature. A comparison of thermal conductivity for various carbon fibers is reported in **Table 1** (Towne, 1989). By dropping carbonization temperature below 1400°C, P-CFs thermal conductivity values can be reduced to about one-half of standard P-CFs (T300-like), but are still two to three times the value of R-CFs.

Due to the intrinsic properties of Rayon based carbon fibers (Lee, 2010; Lee, 2009; Lee, 2014), the ILSS properties for R-CF-based laminates are much higher than P-CF based counterparts. However, P-CFs represent most of the carbon fiber production worldwide and many suppliers of R-CFs have ceased production, also due to the increasingly stringent environmental constraints [https://parkaerospace.com/our-company]. As a result, over the past 30 years, new cellulose based R-CFs had to be qualified for the production of carbon/phenolic composites (Lee, 2010; Lee, 2009; Lee, 2014). Below, the history of R-CFs in US and Europe will be covered in detail.

Most launch vehicle based on SRMs originally relied on R-CFs produced by North American Rayon Company (NARC) (Mills, 2008). But environmental and economic challenges resulted in NARC stopping the production of Rayon fibers in 1998. In November 2002, Snecma Propulsion Solide (SPS, France) announced that FiberCote (now known as Nelcote, a subsidiary of Park Electrochemical, US) would be SPS's exclusive marketer and distributor of Raycarb C2 carbonized Rayon fabric in North America, Asia and Israel and SPS's global partner for Raycarb C2™ ablative grade prepregs (Berdoyes et al., 2005; Peake et al., 2006; Peake et al., 2007). The new grade R-CFs known as Raycarb C2™ fiber cloth is currently used by large firms in US and France (as an example, in the Ariane and Vega programs). The Raycarb C2™ is stocked in the US and France.

However, since Raycarb C2™ is manufactured in Europe, the launch vehicle systems in the United States depend on foreign sources. It would be helpful to report the text of one Small Business Innovation Research (SBIR) call for proposal released by the US Missile Defense Agency (MDA) in 2016. In particular the topic entitled "Rayon Replacement for High Temperature Materials" (MDA16-020) [https://www.sbir.gov/node/1188777.] reported: "Rayon-based fibers continue as the industry standard for ablative and non-ablative insulators in applications such as nozzles and reentry vehicles. In recent decades, environmental constraints have limited availability since rayon is no longer domestically produced. Many aerospace programs have stockpiled heritage material or utilize foreign sources. This topic focuses on domestically available replacement materials, such as structural or ablative insulators, with performance properties comparable to or exceeding rayon based high temperature composites. In order to address domestic supply issues, many manufacturers have used Polyacrylonitrile (PAN) fibers as reinforcement for high temperature composites. However, PAN based fibers do not have the same thermal properties as rayon based fibers, and some PAN based materials have exhibited aging issues. New fibers, such as cellulose based fiber, have demonstrated properties very

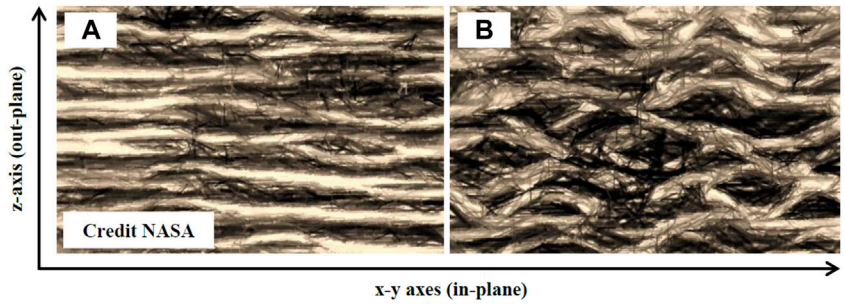

FIGURE 3 | Through section microscopy image of a carbon/phenolic composite based on PAN derived fibers. **(A)** Through section microscopy image of a carbon/phenolic composite based on Rayon derived fibers. **(B)** (from [Nasa Grant NAGS-545, 1988], credit NASA).

similar to rayon in the carbonized form. The thermal conductivity of carbonized rayon fiber is close to 5 W/mK and on the order of 1 W/mK for some rayon based composites. Other precursor fibers may also provide a viable domestic source for high temperature composites. Utilization of new fiber precursors could significantly decrease thermal conductivity of ablative and/or structural insulators. In addition, new fiber based architectures (braids, weaves, etc.) could improve mechanical and thermal properties. Efforts should demonstrate the feasibility of producing either structural or ablative insulator components (valve components, nozzle components, etc.) with improved thermal properties. Process technologies should be appropriate for modest production volumes, be repeatable, and offer significant potential for enhancing performance properties while improving producibility". A careful reader would immediately understand that Department of Defense (DoD) agencies such as the MDA are struggling to overcome the problems due to the procurement of carbon fibers for PAMs. As a result, the US government promoted the evaluation of new cellulose based fibers as a replacement of Raycarb C2™. Lyocell, a cellulose-based fiber like Rayon that is manufactured using an environmentally-friendly process, has been evaluated as a replacement of traditional Rayon derived carbon fiber (Gasch et al., 2016; Gradl & Valentine, 2017). The product, marketed under the trade name Tencel, is produced in Mobile, Alabama and Lenzing, Germany. Lyocell (Wu and Pa, 2002; McCorsley, 1980; Lenz et al., 1994), which has been commercialized under the trademark of Tencel, is a new 100% cellulosic fiber spun from wood or cotton pulp in a closed amine oxide solvent system, a unique, environmentally friendly production process. Lyocell showed to be an excellent candidate for making high performance carbon fibers (Wu & Pa, 2002; McCorsley, 1980). Due to the increasing importance of Lyocell-like fibers in the production of carbon/phenolic composites, section will provide more details on the science and technology of cellulose based carbon fibers.

However, in order to bypass the procurement problems related to R-CFs, some P-CFs were qualified as a replacement of R-CFs (Williams & Murray, 2008). It was noted that P-CFs are readily available and used extensively for composite fabrication in the aircraft industry. These fibers exhibited low erosion, good char integrity, and thermal stability. According to Canfield et al. (Canfield & Koenig, 1989), in general, P-CFs based carbon/phenolic composites erode less, char deeper and weigh more. P-CFs based carbon/phenolic composites are more thermally stable, char cracking and spallation is minimized. P-CFs based carbon/phenolic composites also exhibit low thermal expansion, high purity, and uniform erosion. Because of their good erosion properties, (T300-like) P-CFs should be considered as candidates for high erosion areas, such as the throat and entrance sections. In 2005, Alliant Techsystems (ATK) (now Northrop Grumman Innovation Systems, NGIS) reported a series of delamination issues on one of their program to produce SRM nozzle components based on P-CFs (Orion Stage I Vectorable Nozzle Separations, 2005). Mills and coauthors (Mills, 2008; Mills et al., 2011) indicated that a carbon/phenolic composites made of common (T300-like) P-CFs and a SC-1008 matrix could be manufactured with properties that met the characteristics of the R-CFs based carbon/phenolic formulations, such as MX-4926, thereby establishing a new source of composite materials for ablative nozzle fabrication and/or military applications. This conclusion was reached in part by using the method of photomicrography to compare the micro-crack densities of specimens cut from R-CFs/SC-1008 and P-CFs/SC-1008 composite plates.

Moreover, with the aim to produce a carbon fiber with a reduced thermal conductivity - as compared to the values of standard P-CFs - and consequently, able to mimic the values of R-CFs, special low-fired stretch-broken P-CFs have been developed. In fact, in addition to the low thermal conductivity, due to the intrinsic properties of Rayon-based carbon fibers (Natali et al., 2016; Lee, 2010; Lee, 2009; Lee, 2014) such as high surface roughness, and chemical affinity with phenolics, the Inter Laminar Shear Strength (ILSS) properties of R-CF-based laminates are much higher than P-CF based counterparts (Lee, 2010; Lee, 2009; Lee, 2014). Aerojet's experiences with low-fired stretch-broken P-CFs began in 2001 with a material called Lewcott LR1406 (Williams & Murray, 2008). The test results showed that the Lewcott LR1406 has performance characteristics that are comparable to the R-CFs based carbon/phenolic composites. Other studies confirmed these results (Katzman et al., 1994). Thus, a new generation of carbon/phenolic composites made from the so called Naxeco® 3D reinforcement (Berdoyes et al., 2011), impregnated with a high

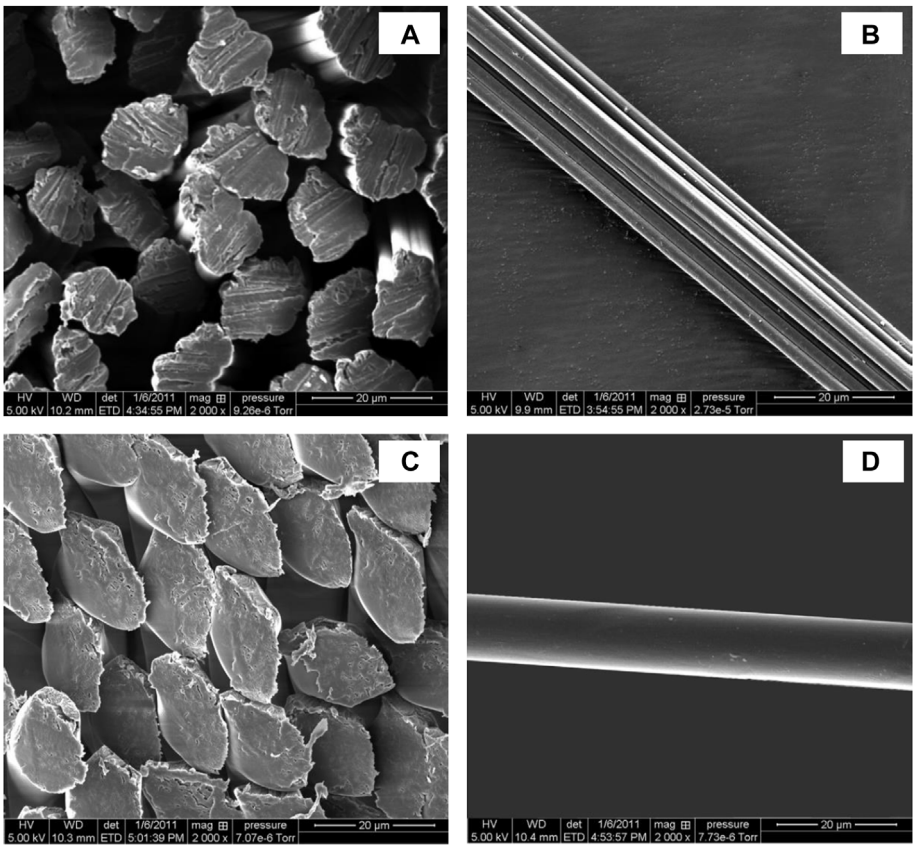

FIGURE 4 | Viscose Rayon fiber cross-sectional view. **(A)** Viscose rayon fiber longitudinal view. **(B)** Lyocell rayon fiber cross-sectional view. **(C)** Lyocell rayon fiber longitudinal view. **(D)** Reprinted with permission from (Chen, 2015).

char yield matrix (a phenolic resin) using the Resin Transfer Molding (RTM) process has been developed and flight validated by SPS in the Ariane five program. Unfortunately, both due to their dual use nature, materials such as the Raycarb C2™ as well as the Naxeco® 3D are available only to the large US and French players. In fact, most of these state-of-the-art aerospace-qualified R-CF-based carbon/phenolic composites (such as the MX-4926) as well as the low thermal conductivity PAN-CF-based-carbon/phenolic composites (such as the LR-1406 (Williams & Murray, 2008; Shields, 1976) or the LR-1750) are restricted under International Traffic in Arms Regulations (ITAR) which controls the export and import of defense-related material (Cortopassi, 2012; Martin, 2013) and so it is extremely difficult to produce a review paper on this topic.

To summarize, at this point of the researches on T300-like P-CFs based carbon/phenolic composites, it can be concluded that most of the problems related to the delamination issues of these high temperature composites can be dramatically mitigated acting on: 1) the composition of the high char yield matrix; 2) the processing parameters of the curing cycle in terms of temperatures, heating rates, length of the plateau, as well as pressure applied during the consolidation of the composite material; 3) the removal of the by-products of the reaction of the phenolic matrix. The following section will help to understand the reason why the difference among PAN derived carbon fibers and Rayon based counterparts can influence the properties of the final carbon/phenolic composites. This section will also help to further understand the reason why many researches are focused on new non-oil based cellulose derived fibers such as the Lyocell.

Carbon Fibers for Polymeric Ablative Materials: Role of the Polymeric Precursors on the Mechanical Properties of Carbon/Phenolic Composites

It has been reported as the longitudinal tensile strength of carbonized P-CFs laminates is in general 4/5 times higher than the corresponding of composites made with R-CFs (Rossi and Wong, 1996; Lee, 2010). Indeed, the tenacity of isolated P-CFs is only 2/3 times higher than R-CFs, but because Rayon derived fibers are crimped along their lengths during the fiber manufacturing process, the tensile strength of the corresponding laminates is then reduced. Moreover, the Young modulus of isolated PAN derived carbon fibers can be 6/10 times higher than the values of R-CFs (Rossi & Wong, 1996; Lee, 2010). As a result, in the in-plane direction, P-CFs-based laminates tend to be significantly stronger and significantly stiffer than R-CFs

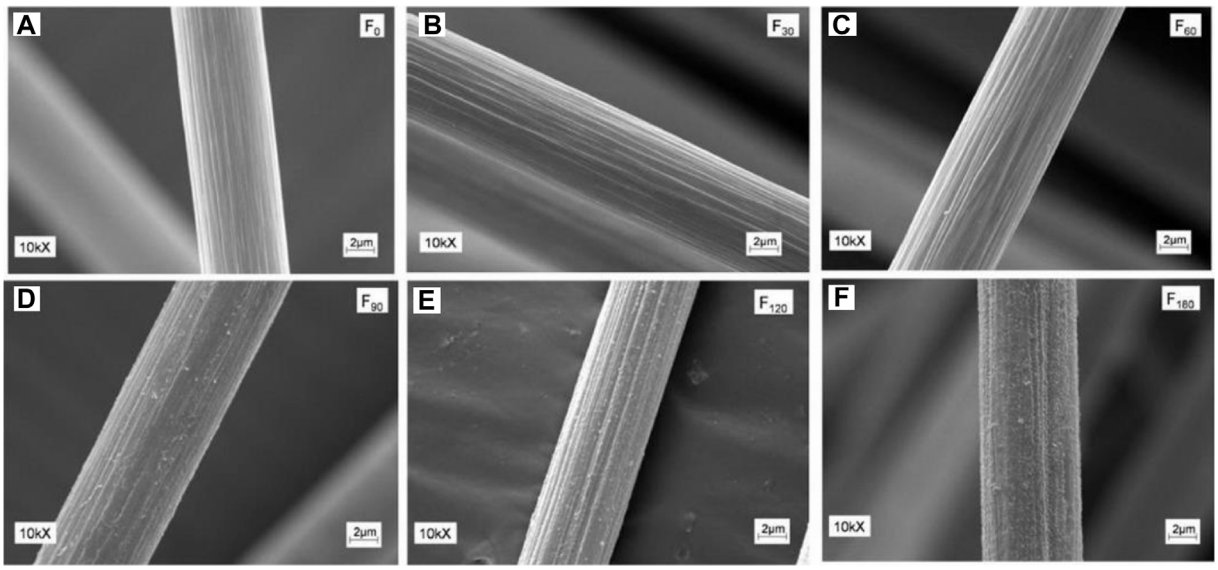

FIGURE 5 | SEM micrographs of untreated and nitric acid treated PAN derived carbon fibers: **(A)** untreated **(B)** 30 **(C)** 60 **(D)** 90 **(E)** 120 **(F)** 180 min of treatment. Reprinted with permission from (Chen, 2015).

counterpart composites. These differences are mainly due to the morphology differences generated during the fiber manufacturing process leading to composite laminates in which the R-CF fabric layers are highly interacting while the P-CF layers are not. Thus, the Rayon laminas are more interacting, but overall, the resulting composite is softer and weaker. P-CF-based laminated tend to fulfill the structural requirements in many regards, but the composite layers are flat, smooth and weakly-interacting leading to out-plane properties. As reported in previous section, due to the widespread use of P-CFs, this issue is of extreme importance and often tops the list of research efforts under pursuit.

One of the principal factors leading to the formation of weak interfaces in laminated composite systems is related to the residual stresses embedded in the laminate during the manufacturing. Two types of stresses are of extreme relevance. Stresses associated with the difference in terms of Coefficient of Thermal Expansion (CTE) between the constituents which develop during thermal processing and those associated with constituent material properties of the mold tooling, especially in presence of complex article geometries.

In the case of composite based on R-CFs, the shape of the fiber is a key factor: crimps and bends are generated along the length of the R-CFs. During the coagulation step the R-CF will develop an inner core of unprecipitated viscose bounded by a peripheral area of fully polymerized and solidified precursor. The shrinking periphery tends to produce patterns - also known as crenulations - around the circumference of the fiber. In **Figure 3** [Nasa Grant NAGS-545, 1988] the straight pattern of PAN derived carbon fibers (a) is evidenced as compared to the longitudinal crimping shape of Rayon based counterparts (b).

As a result, a typical Rayon fiber possesses morphology - both longitudinally and laterally - that traditional P-CFs do not exhibit. These features are key attributes in the distinction between R-CFs and P-CFs in terms of ILSS as well as of interlaminar nesting. Longitudinal crimps and lateral crenulations are unique to Rayon derived fibers, however, the introduction of roughness such as pores and irregularities has been demonstrated, to varying degree, with fibers deriving from PAN (Tiwari & Bijwe, 2014; Yuan et al., 2012). However, in order to maintain the high mechanical properties of PAN derived reinforcements, these etching protocols tend to be detrimental for the final properties of the fiber.

The interlaminar nesting is characterized by the interweaving of fabric features from one layer to the next. The 2D weaving of the fabric determines the pattern of the meshing features across the x-y fabric (in-plane) and along with the 3D z-directional (out-of-plane). The ply-to-ply nesting can also be influenced by the fiber surface roughness. The degree of matrix interaction with the fiber morphology is dependent on several factors. Among them it is worth to mention: 1) the hydrophobicity/hydrophilicity of the fibers, the sizing surfactants coupling and wetting agents; 2) resin viscosity and resin solvent(s); 3) the processing parameters - time/temperature/pressure curing profiles. In terms of manufacturing, the curing profile can influence the degree of nesting and also the level of induced damages. However, an excessively pressures can damage and shift the nesting features of the laminate. Indeed, high pressure cured laminates of both R-CFs and P-CFs have been documented to exhibit reduced interlaminar properties (Lee, 2010). It has been repeatedly showed that the autoclave pressures of less than about 80–100 psi for both R-CF and P-CFs-based laminates produce the optimal mechanical properties (Warga, 1970) and the high ILSS values.

The polymer science at the base of the production of Rayon- and PAN-derived carbon fibers is well documented in literature

(Lee, 2010). Similarly, the manufacturing steps behind the fiber spinning processes for both precursors be documented (Lee, 2010; Morgan, 2005). For wet solution spinning, the raw fiber precursor is dispersed in a proper solvent to create a solution which by means of a spinneret is immersed in a coagulation bath. Rayon fibers are cellulose derivative from wood pulp that is dissolved in a strong acid solution which reacts with carbon disulfide to obtain a viscous liquid called viscose. Once the viscose starts to gel, the outer regions are polymerized and the Rayon fiber starts to form. The fiber is forced to pass through several coagulation baths having decreasing concentrations of sulfuric acid and zinc salt. As a result, the degree of coagulation is the driving force that promotes the creation of the crenulations in the Rayon derived fibers. These lateral and longitudinal features are consequently intrinsically possessed by the Rayon filaments and as a result in the 2D woven fabrics as well as in the carbonization steps. **Figures 4A,B** report the (viscose) Rayon fiber cross-sectional view and also the corresponding fiber longitudinal surface (Chen, 2015).

Relaxation occurs at the end of this process resulting in the formation of sine wave-like crimps along the length of the fiber (**Figure 4B**). In order to bypass the environmental constraints that basically killed the industry of the old Rayon derived carbon fibers, it has been found that cellulosic wood pulp can be effectively dissolved in certain organic solvents (such as N-methylmorpholine N-oxide) leading to the formation of higher tenacity filaments without undesirable waste products (ee, 2010). The most well-known cellulosic fiber product from this method is Lyocell (Morgan, 2005). **Figures 4C,D** report the (viscose) Lyocell fiber cross-sectional view and also the corresponding fiber longitudinal surface (Chen, 2015). One of the major differences between Rayon and PAN is that the initial PAN feedstock is already fully polymerized before the fiber spinning process even begins. Thus, smooth lateral surfaces generally define the predominant morphology of PAN derived carbon fibers.

In terms of microstructure, Lyocell polymers exhibit higher crystal-like order than conventional regenerated Rayon. PAN structures are also expected to show high order due to the extensive nitrile-nitrile interactions. For Rayon derived carbon fibers, bundles (tow) of regenerated polymer fiber are carbonized/graphitized at temperatures in the range (1200–3,000)°C depending on the final desired properties (Morgan, 2005). A protective atmosphere of nitrogen or other inert gases is required in this step of the process. On the other hand, PAN derived fibers are typically spun, stabilized, carbonized, bundled into tow and then woven. A comprehensive review of the manufacturing processes of carbon fibers is provided in (Morgan, 2005). Low temperature processed PAN derived carbon fibers ~(1100–1400) °C exhibit low modulus whilst high modulus, high temperature PAN derived carbon fibers ~(2,200–2,800)°C are more stiff and brittle. Prior to weaving, carbonized PAN fibers are usually exposed to chemical/physical surface treatments. Some of these phases could involve surface etching with reactive gases (such as air or CO_2) and/or strong acids (such as nitric) (Tiwari & Bijwe, 2014; Yuan et al., 2012) that cause the formation of surface morphology features (roughness) along the fiber surfaces as previously described. **Figure 5** reports some PAN derived carbon fibers once treated with nitric acid at different times.

These chemicals not only physically etch the surface, but lead to the formation of active functional groups and allow establishing the principal interface coupling mechanism for matrix-to-fiber chemical bonding in the composite system. Since most of the PAN derived fibers manufactured worldwide are destined for use in epoxy-based composites, they are intentionally treated to contain mostly carboxyl groups, then it is now possible to understand the reason why fiber-to-matrix chemical bonding in carbon/phenolic composites is relatively insignificant. Moreover, PAN derived fibers manufactured worldwide are treated with coupling agents (sizing) aimed at optimize the adhesion with epoxies, evidencing again the reasons why traditional T300-like P-CFs are not simple to be used in the production of carbon/phenolic composites.

AN INTRODUCTION TO THE SYNTHESIS OF NON-OIL BASED HIGH CHAR YIELD MATRICES

As reported in previous sections, high performance and char-yield thermosetting matrices (especially phenolics) are essential in many crucial aerospace applications, which require materials such as carbon/phenolic or carbon/carbon composites. For a series of reasons - mainly related to very severe military standards used to certify these aerospace materials and due to the cost of the qualification of a new product - this industry only relies on well-known and industrially established petroleum-based materials. As an example, the phenolic resin known as SC-1008 has been used for over 50 years to produce the most important American carbon/phenolic composite formulation i.e. the MX-4926. On the other hand, the US government has been forced to spend millions to requalify new materials (such as novel cellulose derived carbon fibers) which are compatible with the environmental constraints.

Nevertheless, the latest developments in the materials science of polymers suggest that sustainable thermosetting polymers can display similar performances than traditional counterparts (Cywar, et al., 2021). Additionally, in order to overcome the problems due to the procurement of raw materials, considering the increasing demand of materials at the base of the space access and of the homeland security activities, the high char yield matrices (and carbon fibers) derived from renewable feedstock have to meet the very specific and stringent requirements of the aerospace industries (Mauck et al., 2017; Derradji et al., 2021; Wan et al., 2020). The purpose of these researchers would be to identify new paths aimed at avoid problems such as the ones found in the production of the Rayon derived carbon fibers which, due to the environmental constraints, has been discontinued by most companies. As a result, in order to satisfy these environmental constraints, the possibility to produce a polymer (and a fiber) partially based on bio raw materials, but also having its mechanical and thermal behavior preserved, has been sought in these researches (Dotan, 2014).

In light of the ever more stringent environmental constraints, a lot of efforts have been spent to advance in the study of materials coming from truly renewable resources. Obviously, these bio based alternative raw materials have to be economically viable and able to produce products with properties comparable to current technologies. The use of renewable resources requires that bio-based compounds with distinct chemical characteristics should be obtained through careful transformations of plant and other non-fossil materials (Liu et al., 2021): in line with this requirement, considerable efforts have been finalized to produce bio-based polymers that could directly substitute those of fossil origin (Cywar et al., 2021; Selvaraj & Raghavarshini, 2021). On the other hand, biomass constituents should be chemically transformed to obtain desired compounds for crosslinked polymers (monomers, oligomers and resins) starting from bio-based phenolic monomers (i.e., vanillin, eugenol, tannins, lignins) and these operations require a series of chemical reactions and purification processes which are also energy intensive and economically not favorable (Paipa-Álvarez et al., 2020; Quirino et al., 2021). In fact, it should be also considered that every additional step brings a decrease in the yield of subsequent product, resulting into higher process costs (Khoo et al., 2016; Mahajan et al., 2020). Following the requirements of the aerospace sector, an overview on the main biosourced thermosetting polymers that could potentially replace the oil based counterparts is reported. It is essential to remark that the following survey will be mostly focused on the experimental routes reported in literature aimed at synthesizing the non-oil based high char yield matrices as well as on their processability, thermal stability and char yield (and of their carbon fiber derived composites). Moreover, the experimental routes reported in literature aimed at synthesizing the non-oil based carbon fibers will also be covered.

Benzoxazines

Polybenzoxazines are high-performance materials possessing exceptional thermomechanical and chemical properties (Kiskan et al., 2011). They are produced by the combination of derivative phenols, primary amines and formaldehyde (Zhang et al., 2019). The ring-opening polymerization of benzoxazines, that take place at high temperature, is able to produce polymers having both phenolic hydroxyl and tertiary amine functionalities (Trejo-Machin et al., 2018). It is reported in the literature that biobased benzoxazines can be prepared from guaiacol (from lignin source), paraformaldehyde (from oxidized biomethanol), and furfurylamine (from furfural). Rising interest has been also originated by the possible use of cardanol, having reactivity similar to phenol, due to the existence of the hydroxyl group in its structure. Vanillin, that brings both para formyl and ortho methoxy group, is industrially obtained from the processing of lignin, and it can be used as a precursor for the synthesis of benzoxazines (Lochab et al., 2021; Froimowicz et al., 2016). Eugenol, due to its availability and low cost, has also attracted much interest, even if, owing to its blocked ortho and para positions, has limited reactivity and consequently low cross-linked networks. Other bio-phenols can be used for the preparation of benzoxazine monomers: examples can be found in the case of coumaric, ferulic and phloretic acid (Comí et al., 2013). Nonetheless, the presence of additive chemical functionality on monomers may also affect the overall processability of monomers and related polymers. For example, position of functional groups, steric hindrance or limited processing window may strongly hinder the processing and polymerization of the benzoxazines. To surpass such difficulties frequently faced in presence of monomers synthetized with bio-based phenols, some research groups reported the synthesis of asymmetric benzoxazines monomers (eugenol/phenol, vanillin/cardanol) (Verge et al., 2017). This methodology is moving the research toward more processable high performance bio-based benzoxazines (Kirubakaran et al., 2020). More recently, even if the majority of the research on bio-based benzoxazine has been dedicated almost entirely to the selection of phenolic and amine compounds, few groups also considered the possibility of synthesizing a fully bio-based benzoxazine in which all three reactants necessary to synthesize it, comprising the aldehyde, are from renewable sources for the first time (Machado et al., 2021).

The intrinsic molecular-design flexibility of benzoxazines, their chemical structures and properties open their use to tailored and dedicated applications, so they have been widely applied in the field of space and military applications due to low moisture absorption, high charring ability, limited shrinkage after polymerization, worthy chemical resistance, and high glass transition temperature. High crosslinking degree, that brings high charring ability, can be promoted, for example, by incorporation of diphenolic acid and furfurylamine (Feng et al., 2020): in the reported paper, the authors found that decarboxylation during heating was effectively blocked by the better cross-linking, in details the char yield at 800°C for PBA film, measured at ~30%, increased to ~43 and about 54%, respectively, for PDA and PDF, due to the enhanced cross-linking density of cured PDA and PDF films, where PBA, PDA and PDF are the cured films of benzoxazine samples based on different combination of diphenolic acid and furfurylamine (**Figure 6A**). Lu et al. (2020) also found that the increasing thermal stability of cross-linked main-chain-type benzoxazine polymers (poly (propylene glycol) bis(2-aminopropyl ether):furfurylamine molar ratio = 3:14 showed ~54% wt. residual weight at 800°C) can be attributed to the participation of furan moiety in the polymerization at high temperatures.

Even if the current common approach to have highly crosslinked polybenzoxazines is related to the selection of bifunctional monomers, monobenzoxazines are simpler to formulate and are more flexible, having the possibility to introduce substituents into their structures giving special properties to final materials: in their research, Martos et al. (2020) described the effect of monobenzoxazines substitution in meta positions on T_g and crosslinking density (**Figure 6B**): the results confirm that higher char yields and increased T_g can be obtained, proposing also the successful incorporation of this type of benzoxazine into other benzoxazine mixtures (as doping material) to increase the final crosslinking network (Wen et al., 2021). Zhang et al. (2021) also found that diamine

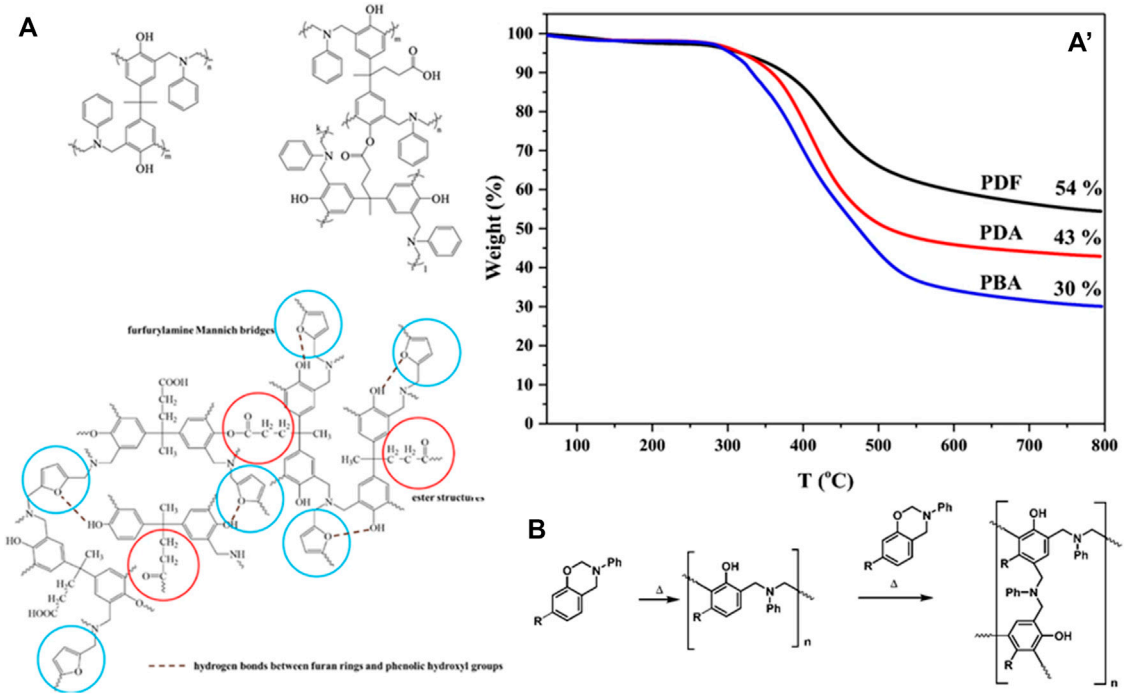

FIGURE 6 | Chemical structures **(A)** and TGA **(A')** curves of PBA, PDA, PDF, cured films of benzoxazine samples DF, DA, and BA **(A)** and proposed crosslinked structures for m-substituted polybenzoxazines derived from monobenzoxazines considering only reactions on the phenolic ring **(B)** *Reprinted with permission from (Feng et al. 2020; Martos et al., 2020)*

derived from furfurylamine (PDFA), when able to react with cardanol/eugenol, had a char yield of ~65% at 850°C.

The thermal stability of highly crosslinked polybenzoxazines can be also enhanced when the biobased matrix is combined with other polymers or specific fillers. As an example (Gao et al., 2019), Gao et al. studied the behavior of a new silicon rubber based composite containing benzoxazine resins and ZrO_2: the limited ablation rate (~0.11 mm/s) of the control sample was reduced to ~0.06 mm/s with a 20% resin formulation. In their work, Subramani et al. (Devaraju et al., 2019), prepared polybenzoxazines-by using cardanol and furfurylamine and further hybridization with silica was considered, by means of thiol-ene click reaction, with the main aim of enhancing thermal stability and fire resistance of the reference material. The same authors also developed hybrid poly (benzoxazine-co-epoxy) composites using cardanol based benzoxazine, commercial bisphenol-F epoxy and functionalized bio-silica (Devaraju et al., 2021). Data acquired from thermal studies confirmed that the bio-silica reinforced hybrid composite showed flexibility, enhanced thermal stability and properties and flame-resistance characteristics.

A comprehensive review on nanostructured natural-sourced polybenzoxazine matrices has been reported by Prof. Ishida (Lyu & Ishida, 2019). In this paper, virtually all the possibilities offered by the combination of benzoxazines with other polymers for the preparation of biobased composites, has been summarized. However, even if it is possible to find papers on the ablation response of nanostructured polybenzoxazine/carbon fiber composites (Rao et al., 2021a) or in general, for high temperature applications (Comer et al., 2019; Wolter et al., 2020), to our knowledge, no papers on the use of non-oil based matrices for the production of high char yield laminates has been documented in literature.

Bismaleimides

Bismaleimide (BMI) resins, that hold outstanding thermal, mechanical and chemical properties, have been considered for many applications, comprehensive of the aerospace sector. Since bismaleimide resins are cured by following polymerization by addition, volatile by-products are produced during the curing process, providing in this way high strength and rigidity to the matrix. (Prasanaa Iyer & Arunkumar, 2020). They can be processed at rather low temperatures (i.e. < 170°C) and then post cured at high temperatures to yield highly cross-linked networks with high glass transition temperatures, but limited toughness is reached in these conditions. Efforts have been spent to overwhelm those problems by incorporating micro sized elastomers or thermoplastic polymers or copolymerizing them with nanomaterials (Jiang et al., 2020) and same energies have been spent to find valuable solutions for the

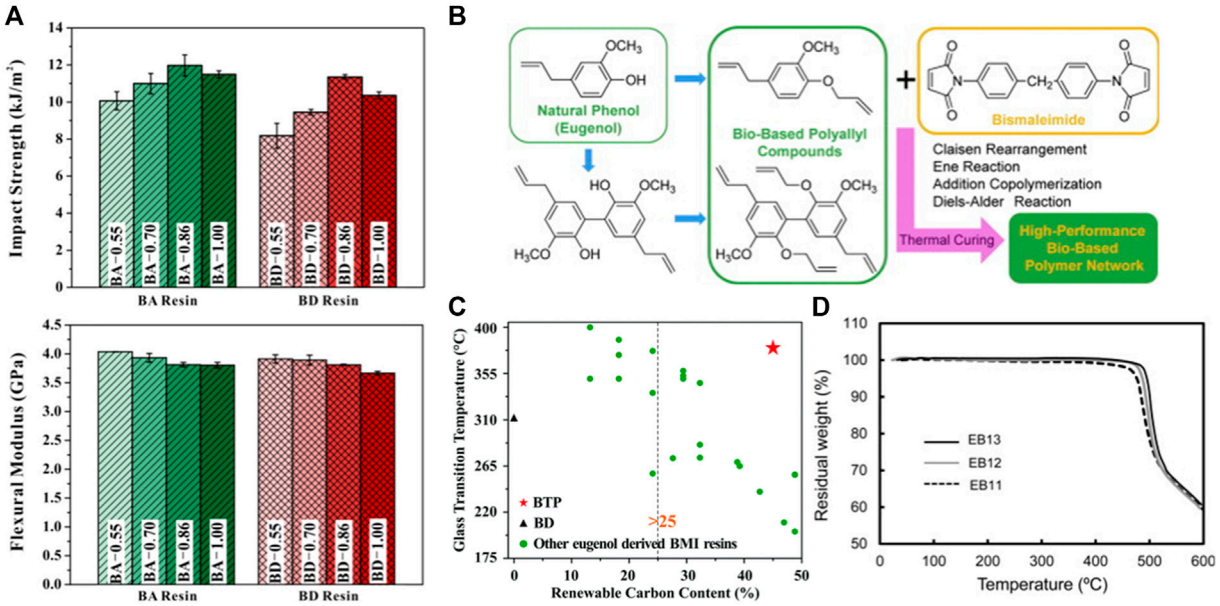

FIGURE 7 | Impact strengths and flexural moduli of BA and BD resin (4,4′-bismaleimidodiphenylmethane (BDM) and renewable bis(5-allyloxy)-4-methoxy-2-methylphenyl) methane (ABE) from bio-based lignin derivative as a function of allyl to imide molar ratio (n) **(A)**; Biobased thermosetting resins based on bismaleimide and allyl-etherified eugenol derivatives **(B)**; T_g and renewable carbon contents of BTP, BD and other eugenol derived BMI resins **(C)**; TGA curves of cured AEG/BMI (EB) (allyl-etherified eugenol prepolymerized with 4,4′-bismaleimidodiphenylmethane, with allyl/maleimide unit ratios of 1/1, 1/2 and 1/3 **(D)** *Reprinted with permission from* (*Neda et al. 2014; Miao et al., 2019; Ge et al., 2017*).

replacement of fossil based monomers with biobased counterparts (Ge et al., 2017) (**Figure 7A**).

Generally, these resins can be synthetized by copolymerizing bismaleimide monomers with 2,2′-diallyl bisphenol A (DBA) in a two reactions mechanism, namely Diels–Alder (DA) and/or ene reactions (Iredale et al., 2016). Shibata and his group have reported the development of biobased BMI (Shibata et al., 2016; Shibata & Hashimoto, 2017), and the literature on these materials essential relies on the attempts they made to replace or modify the DBA fraction with eugenol-based allylphenyl compound (**Figures 7B,C**) (Shibata et al., 2011a; Shibata et al., 2013a), tung oil (Shibata et al., 2011b), difurfurylidenecyclopentanone and dicinnamylidene cyclopentanone (Shibata & Miyazawa, 2016), and cardanol (Shibata et al., 2013b).

Gu's group also prepared a modified BMI resin using a phosphorus-containing allylphenyl compound by linking eugenol to hexachlorocyclotriphosphazene: these BMI resins have demonstrated excellent flame retardancy and high T_g values (~250–270°C) (**Figure 7D**) (Miao et al., 2019). Explorative experiments were also performed to investigate the potential of itaconimides synthesized from itaconic anhydride, confirming that life extension and full recyclability can be achieved with this system (Lejeai & Fischer, 2020).

A series of papers reported the combination of BMIs with carbon fibers (Morgan et al., 1993; Spratt & Akay, 1995; Sun et al., 2011; Li et al., 2019; Yang et al., 2021). Ning et al., 2020 reported the preparation of bio-based BMI resins in combination with carbon fibers. The authors synthesized hydroxymethylated eugenol (MEG) and poly-MEG (PMEG) to modify BMI: carbon-fabric laminate composites based on eugenol/maleimide (1:0.3) had the highest T_g (above ~400°C), high flexural strength (>570 MPa) and modulus (>57 GPa), in the meantime the achieved renewable fraction was the highest (57%) among all the prepared composites. The same authors (Ning et al., 2019) previously considered the preparation of 4,4′-bismaleimidodiphenylmethane (BMI) modified by eugenol and various contents of 4,4′-diphenylmethane diisocyanate (MDI), showing a 5% weight loss temperatures around 300°C and char residue of 42% at 900°C for MDI-EG-BMI resins. However, the limited scientific literature on this subject clearly evidences that the progress on the preparation of bio-based high performance-modified BMI composites is certainly a great challenge.

Cyanate-Esters

Cyanate ester (CE) are obtained by reacting phenols with cyanogen halides to give reactive cyanate groups (-OCN) linked to an aromatic ring. The major part of cyanate esters industrially produced are aromatic polymers with strong rigidity of their cured phase, so blending with other thermosets to improve their processability in the composite industry is needed (Nair et al., 2001; Kandelbauer, 2014). The literature reports the effect of different nanofillers on the cure of CE resin (Amirova et al., 2021), in particular the introduction of silica (Bershtein et al., 2021), POSS (Li et al., 2021) was widely investigated. Combination of carbon fibers and nanofillers for ablative purposes have been recently considered in the paper of Rao et al., 2021b, where the authors studied the effect of organo-

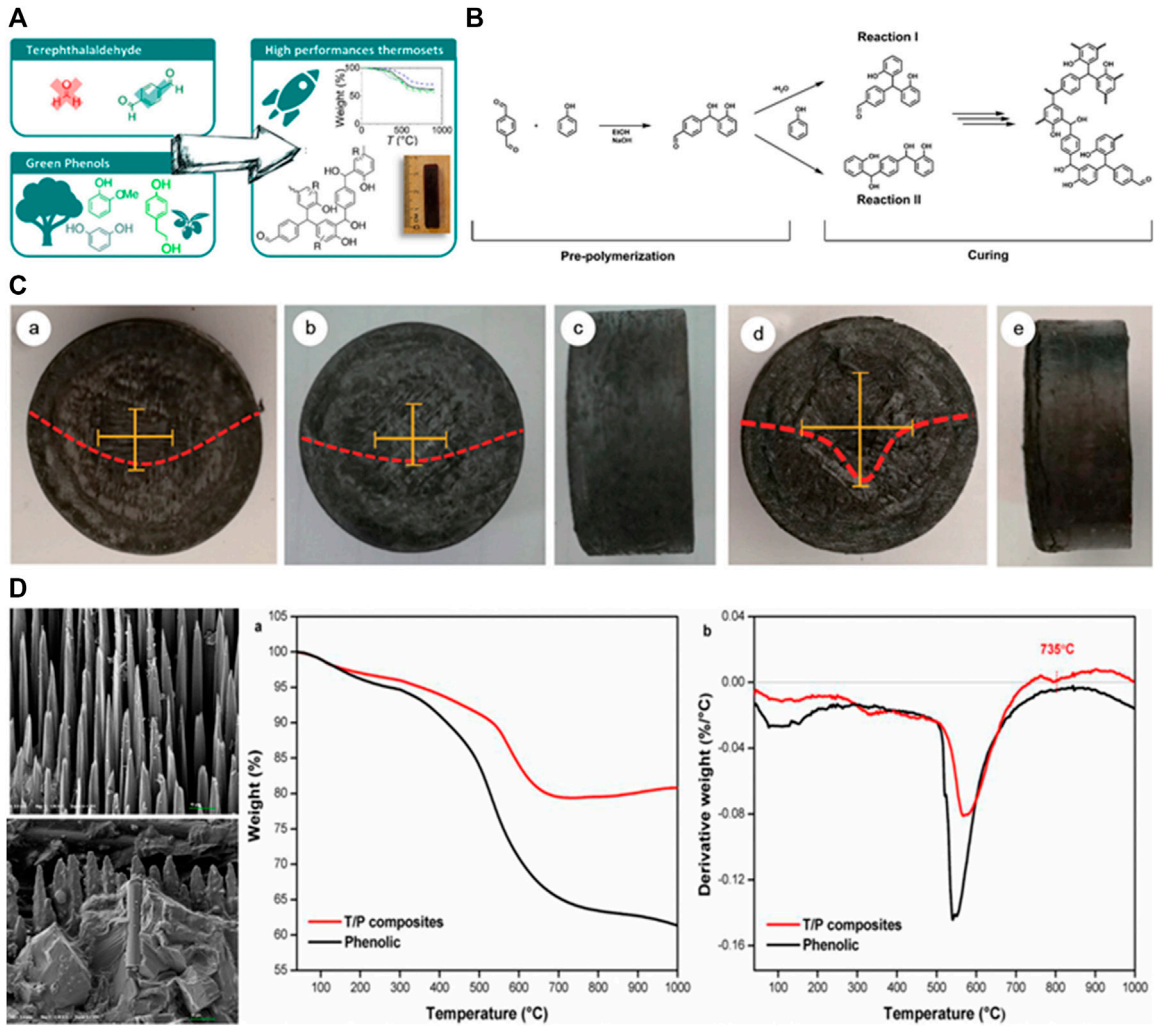

FIGURE 8 | Sustainable alternatives for the synthesis of high thermal performances phenolic networks **(A)**; probable reactions of pre-polymerization and curing between phenol and terephthalaldehyde **(B)**; macroscopic morphologies of the front and side views of **(A)** neat carbon fiber phenolic, **(B,C)** carbon fiber phenolic +0.2% graphitic C3N4 and **(D,E)** carbon fiber phenolic 0.2% wt. of graphene oxide after oxyacetylene flame test. The red parabola represents the ablation depth distribution, while the yellow line represents the ablation central zone **(C)**; SEM fractographs of C-Ph composites and TiBr2/C-Ph composites tested at 1000°C and their TG/DTG curves **(D)** *Reprinted with permission from* (*Granado et al. 2019; Granado et al. 2018*; Ma et al., 2019; Ding et al., 2019).

modified Montmorillonite (o-MMT) addition (0, 1, 2, 4, 6 wt%) on thermal stability of carbon fiber reinforced cyanate ester resin composites, confirming the possibility of using o-MMT for improvement of mechanical properties of CE composites.

In this context, research has moved towards obtaining cyanate ester thermosets by using anethole, resveratrol, vanillin, eugenol, and other lignin derivatives. Harvey and co-workers studied the synthesis of cyanate ester thermosets from vanillin (Meylemans et al., 2013; Harvey et al., 2011), by showing that, even if a decreased thermal stability was observed, vanillin-based resins showed other properties comparable to the petroleum-based commercial counterparts (Llevot et al., 2016). In a recent review, Randani et al. reported about the design and production of biobased cyanate esters from various bioresources, giving a widespread overview of the current advances in the synthesis of these products and discussing their properties and applications (Ramdani et al., 2021). They reported that, in the case of aliphatic bio-precursors, the cyanate ester monomers revealed large processing windows and limited water uptake, while cyanate esters based on aromatic bio-precursors- demonstrated higher thermal properties and stiffness. As in the case of fossil based CE, the introduction of different nanofillers has been considered (Zhan et al., 2011), the available results generally show that the incorporation of reactive fillers can accelerate the initial step of curing process, but decreasing at the same time the final degree of conversion after isothermal curing. On the other hand, no reports have been found on the use of carbon fiber reinforced CE from biobased sources. Actually, the high price requested for chemical modification, limited availability of bio-based raw materials

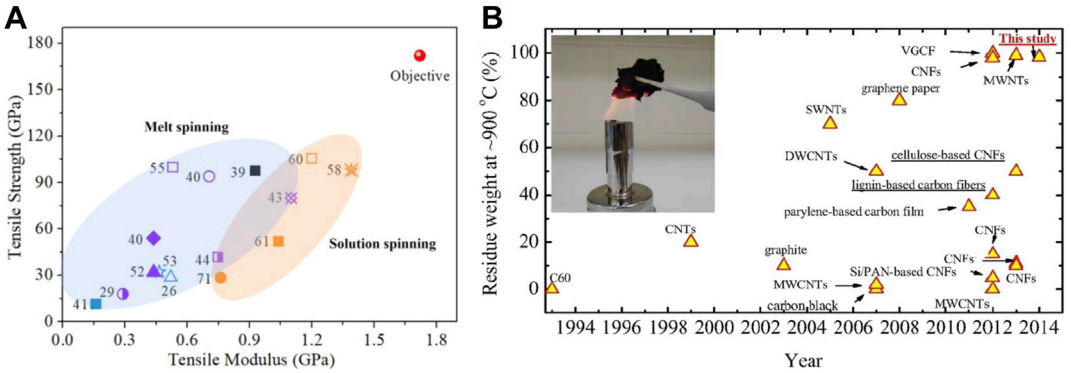

FIGURE 9 | Reported mechanical properties of lignin-based carbon fibers **(A)** and residue weight at 900°C of various carbon materials as reported in literature **(B)**—reprinted with permission from (Wang et al., 2021) (Xu et al., 2014).

for synthesis are some of the crucial problems to be solved before reaching a decent technological maturity.

Phenolics

Phenolic resins (PF) are the result of a step-growth polymerization of a mixture of phenol and formaldehyde using acidic or basic conditions. Phenolic are highly cross-linked and thermally stable thermosets, due to their aromatic structure and high cross-linking densities. As discussed in the previous sections, their high degradation temperatures and high char yields make phenolic thermosets key and ideal materials for aerospace applications (Granado et al., 2019) However, phenolics present several drawbacks that still need to be surpassed. From an environmental perspective, phenol and formaldehyde are hazardous substances: thus in order to develop no-oil based high thermal performance resins, efforts need to be focused on finding alternative strategies to replace both of them, (Sarika et al., 2020). The replacement of formaldehyde is the main challenge. Hydroxymethylfurfural (Zhang et al., 2015; Xu et al., 2019), furfuryl alcohol (Conejo et al., 2017), glyoxal [Van Nieuwenhove et al., 2020] and vanillin (Foyer et al., 2016b) are few of the bio-based precursors that have been considered and investigated for the replacement of formaldehyde in PF resin synthesis.

In light of the high performance required by the aerospace sector, a potential substitute of formaldehyde should show good reactivity and low molecular weight to accomplish with high cross-linking degrees and final densities (**Figure 8A**). Hence, phenolic networks with nontoxic aromatic dialdehydes (Foyer et al., 2016a), such as terephthalaldehyde (TPA), showing the best reactivity, should be considered. TPA can react with phenols (in addition and condensation reactions that can be realized on both aldehyde moieties), yielding highly cross-linked and aromatic dense configurations (Granado et al., 2018) (**Figure 8B**). On the other hand, solutions for phenol substitution in different formulations still have to be found. In order to achieve suitable high charring networks, phenolic blocks must possess high aromatic content and enough activated positions for available reactions. Phenolic blocks can be provided from lignin (Dongre & Bujanovic, 2021), hydrolysable and condensed tannins (Pizzi, 2019), plant oils (Kim, 2015), moreover guaiacol is a possible candidate in the synthesis of phenolic biobased thermosets.

Phenolic resins from biomasses have been indeed developed and studied extensively in recent decades, but the search for biobased alternative to standard phenolic in the specific sector of high charring matrices is still ongoing (Loganathan et al., 2021), even though it is predictable that the properties of resin synthesized from bioresources are lower than the raw material derived from oil (Ipakchi et al., 2020; Ma et al., 2020; Guo et al., 2021; Gruber et al., 2021). One example of nanofiller reinforced phenolic composites for ablative purposes comes from the paper of Ma et al., where the authors found that the addition of graphene oxide or graphitic carbon nitride (**Figure 8C**) (Ma et al., 2019) increased the char yield graphitization level during ablation, helping heat dissipation and thereby increasing the ablation resistance. Other nanoscaled fillers, such as carbon nanotubes, silica, ZrB_2, $ZrSi_2$,TiB_2 (**Figure 8D**) have been also studied (Ding et al., 2019): as a representative result, TiB_2 particles included in carbon–phenolic (T/C-Ph) composites prepared by compression moulding reacted, at high temperature, with oxygen-containing molecules, by coating the residue of phenolic after pyrolysis with glassy B_2O_3, assuring in this way improved mechanical performance at high temperature. Nano-modified carbon fabric represents another opportunity to enhance the ablation behavior of these materials (Xu et al., 2020a; Xu et al., 2020b).

PRODUCTION AND PROPERTIES OF NON-OIL CARBON FIBERS

The current methods for manufacturing carbon fibers are slow and energy-consuming, thus making their production very expensive. Additionally, the high cost of precursors keep CF a niche market with applications restricted essentially to high-performance and structural applications (e.g., aerospace): regardless these assumptions, alternative precursors to reduce

the realization cost for CF and need for no-fossil feedstock have been investigated and are still under exploration (Xu et al., 2020a). These include biomass-derived precursors such as cellulose (Zaitsev et al., 2021), lignin (Wang et al., 2021), lignin/cellulose blends (Byrne et al., 2018; Bengtsson, et al., 2020), glycerol, and lignocellulosic sugars.

Production and properties of carbon fibers obtained by the different biomasses (mainly lignin ad its blends) will be revised: since the precursor of the carbon fiber contributes to about half of the total cost of the final product, some experimental researches on the possibility to use bio-based CFs has been carried out (Ogale et al., 2016; Frank et al., 2014). However, some disadvantages are typical of these fibers: differently from PAN based carbon fibers, biomass typically contains a major amount of ash/minerals, particularly harmful for the tensile strength of the resulting CFs, additionally biomass-based CFs give low carbon yield in carbonization when compared to commercial PAN-based CFs (the maximum theoretical carbonization yield for a cellulose precursor is ~44% (corresponding to the formal loss of five molecules of water per anhydroglucose unit), that decreases to the actual value of 15% without any pre-treatment (oxidative pretreatment, use of a reactive atmosphere, application of carbonization aids, inclusion of catalysts for dehydration and crosslinking reagents).

CF from cellulose (natural or man-made) has been detailed in their manufacturing and properties in the previous sections, while here we will introduce the benefits coming from the selection of lignin biosource. Benefiting of its high intrinsic aromatic content, lignin is certainly attractive for the obtainment of high carbon yield following a high-temperature treatment, conditions which makes lignin a suitable precursor for producing carbon-based materials (Qu et al., 2021). Lignin is an abundant biomass with millions of tons produced every year as a by-product of the pulping industry, its cost is less than PAN, additionally it also shows a significantly theoretical high carbon yield when compared with cellulose (62 vs. 44%) (Frank et al., 2014). However, the current main drawback and limitation for the massive production of carbon fibers by starting from lignin is related to the time-consuming stabilization time, which makes its use largely impractical for industrial production (Bengtsson et al., 2019). Additionally, they have limited mechanical properties, restricting their use to sectors where structural functionality is not stringent (Collins et al., 2019). It has been recently claimed that improvements in mechanical performance can be obtained by means of the optimization of chemical reactions during the stabilization and carbonization processes, through the addition of cross-linkers, miscible thermoplastic biopolymers (Culebras et al., 2019) and optimized thermal processing regimes.

In recent studies, the combination of lignin and cellulose has been considered for the realization of composite fibers, where the main aim was the overcoming of disadvantages typical of cellulose and lignin (low carbon yield and long stabilization time, respectively). Le et al. (2021), Trogen et al. (2021) considered the production of cellulose-lignin fibers with a different weight ratio, stabilized at different temperature, by using organosolv or spruce lignin, revealing that one of the main factors affecting the performance of the CF from lignin is the extraction method and/or source of the biomass. Initial structural differences between lignins cause varying rheological and thermal behavior which need to be studied and optimized to create tailored feedstock appropriate fiber spinning processing windows. It is known that more reactive lignins have a greater tendency to form direct ring-to-ring cross-links and this is very significant for the properties of CF as this leads to higher orientation of graphitic planes and subsequently higher mechanical properties of the final CFs (Demiroğlu Mustafov and Seydibeyoğlu, 2019) (**Figure 9A**).

By changing the reactivity of precursor, the thermal stability of the lignin-based carbon fibers can be also significantly enhanced. Xu et al. [Xu et al., 201491–102] synthesized lignin-based carbon fibers doped with CNTs obtained by catalysis of Fe or Pd: results suggested that the hybrid structure, containing CNTs, showed at 950°C the highest thermal stability when Pd catalyst was considered (~98% residual weight at 950°C), and the residual weights kept to be stable at 90% even after 1 h of isothermal heating at this temperature (Wang et al., 2021) (**Figure 9B**): such nanoparticles were able to convert amorphous carbon to graphitic carbon and enabled the growth of CNTs, while carbon fibers without the presence of metallic nanoparticles showed limited thermal stability, essentially due to the lack of amorphous carbon conversion to a graphitic structure.

It has been concluded that, considering current environmental constraints, lignin precursors show also cost savings over conventional PAN precursors. In particular, it has been estimated that lignin carbon fiber can save $260 per ton from CO_2 environmental impact compared to PAN fibers (Ismail & Akpan, 2019). On the other hand, even though the chemistry of lignin deserves to be further investigated, in terms of performance, the mechanical properties of lignin carbon fibers made with current experimental lab-scale protocols do not meet the requirements of the aerospace industry.

CONCLUSION AND FUTURE OUTLOOK

The access to the space changed our lives in so many ways that it is very difficult to fully grasp the nature of this revolution; considering all the technological returns, new materials, patents, and breakthroughs related to the space activity, then it is practically impossible to draft a comprehensive list. The space sector is also a very profitable market: in "The Space Report 2020" released by The Space Foundation it was estimated that in 2019 the global space economy reached a value of $424 billion worldwide as compared to about $384 billion in 2017. The US Chamber of Commerce reported that this sector will increase from approximately $424 billion of 2019 to at least $1.5 trillion by 2040. As a result, the development of the space economy is intimately related to the space access. Liquid, and especially Solid Rocket Motors (SRMs) provide most of the thrust necessary to reach Low Earth Orbit (LEO). By virtue of their common nature, the materials used for SRMs are also used to manufacture the heat shield which protects the structure, the aerodynamic surfaces, of missiles, probes, and space vehicles from the severe heating encountered during the re-entry flight through the

atmosphere. In fact, due to the interaction of the re-entry item with the atmosphere, its kinetic energy can be dissipated via re-radiation and ablation. Thermal Protection System (TPS) materials such as Carbon/Phenolic Composites (CPCs) and Carbon/Carbon Composites (CCCs) are also essential to enable all homeland security programs. Accordingly, the strategic importance of TPS materials now appears in its full extension.

Among the different families of TPS solutions, Polymeric Ablative Materials (PAMs) such as carbon/phenolic composites possess the highest versatility. As a result, more in general, the combination with high char matrices such as phenolics, bismaleimides, cyanate-esters, benzoxazines with Carbon Fibers (CFs) derived from Polyacrylonitrile (PAN), Rayon and Pitch allow to produce the most advanced high temperature fiber reinforced composites. For a series of reasons - mainly related to very severe military standards used to certify a given aerospace material and due to the cost of the qualification of a new product - this industry only relies on well-known and industrially established petroleum-based materials. In general, in order to be used in a launch vehicle, an SRM and its materials - such as the carbon/phenolic composites - need to be tested for validation of required technical specifications. Any changes in the SRM or its components may have need of supplementary testing and, if the deviations are significant or if there are multiple variations, then the re-testing of the entire launch vehicle could be mandatory and thus, a re-qualification process, very expensive and time-consuming, should be necessary.

In our paper, after covering the science and technology of these state-of-the-art fiber reinforced TPS materials, a review of current challenges behind the manufacturing of new, high char yield matrices and carbon fibers derived from non-oil based precursors has been carried out. As a result, in terms of possibility to replace current raw materials, used to manufacture high temperature composites with non-oil based counterparts, the most relevant conclusions of our review work are the following:

1) The latest developments in the materials science of polymers suggest that, in terms of thermal stability and char yield, the non-oil based thermosetting polymers seem to display comparable properties/performances than traditional counterparts. In line with these requirements, substantial efforts have been invested to produce non-oil based polymers that are chemically identical and could directly replace those from petroleum;
2) In order to address the challenges to minimize supply concerns, considering the increasing demand of high temperature materials for the space access and for to the homeland protection activities - taking into account the efforts aimed at solve the dramatic problems experienced during last 40 years by countries such the US and France related to the possibility to establish a stable and cost effective source of cellulose derived carbon fibers - the new non-oil based high char yield matrices (or fibers) have to depend on renewable feedstock able to meet the ever specific and very stringent demands of these industries;
3) Accordingly, the purpose of the researchers would be to identify new paths aimed at mitigate the problems such as the ones found in the production of the cellulose derived carbon fibers which has been discontinued by most companies due to the environmental constraints. As a result, in order to satisfy the continuously more stringent environmental constraints, the possibility to produce polymer (or fibers) partially based on bio raw materials but also having the mechanical and thermal behavior preserved, has been sought in these researches. Moreover, in light of these ever more stringent environmental constraints, a lot of efforts have to be spent to the development of materials coming from fully renewable resources. Obviously, these bio based alternative raw materials have to be economically viable and able to produce products with properties comparable to the current technologies;
4) With aim to introduce raw materials which can be of real interest for the high tech companies involved in the production of ablative materials, it is necessary to identify more uniform and efficient processes able to ensure the manufacturing of materials having the same quality, repeatability and reproducibility than current counterparts. To make it very short, the Technology Readiness Level (TRL) level of the non-oil based matrices has to match the ones associated with the traditional solutions. Due to the intrinsic limitations related to the use of renewable feedstock, it is also questionable whether or not this TRL level will be reached in future;
5) Finally, due to the dual use of technologies related to high temperature composite materials, and in light of the concerns related to the current geopolitical situation related to the commodities, in order to produce non-oil based materials, which are of real interest for the aerospace and homeland security programs, the renewable raw materials should be obtained from domestically available feedstock.

At the end of our literature survey it is possible to conclude that further researches are worth to be done in some very specific areas. However, in terms of performance, it has been showed that the non-oil based materials made with current experimental lab-scale protocols are not able to meet the extremely demanding technology readiness level required by the aerospace industry. Moreover, in terms of real benefits on the environmental impact of the processing technologies related the these non-oil based materials, mixed or questionable results have also been reported in the available literature (Bilow and Miller, 1969; Cyanate Ester Resins Market, 2018; D' Alelio GF, 1971; Parkaerospace; Rayon Replacement; Nasa Grant NAGS-545, 1988; Van Nieuwenhove et al., 2020; Yongjian Xu et al., 2020).

AUTHOR CONTRIBUTIONS

DP, MR, MN wrote the first draft. LT added notes and revised the manuscript. All authors contributed to the article and approved the submitted version.

REFERENCES

Abramovitch, I., Hoter, N., Levy, H., Gedanken, A., Wolf, A., Eitan, A., et al. (2015). Effects of the 3D Sizing of Polyacrylonitrile Fabric with Carbon Nanotube-SP1 Protein Complex on the Interfacial Properties of Polyacrylonitrile/phenolic Composites. *J. Compos. Mater.* 50 (8), 1031–1036. doi:10.1177/0021998315586080

Allen, H. J. (1958). Hypersonic Flight and the Re-entry Problem: The Twenty-First Wright Brothers Lectureflight and the Re-entry Problem: the Twenty-First Wright Brothers Lecture. *J. Aerospace Sci.* 25 (4), 217–227. doi:10.2514/8.7600

Amirova, L., Brauner, C., Grob, M., Gort, N., Schadt, F., Pantelelis, N., et al. (2021). Online Cure Monitoring and Modelling of Cyanate Ester-Based Composites for High Temperature Applications. *Polymers (Basel)* 13 (8), 3021. doi:10.3390/polym13183021

Askeland, D. R. (1996). "Polymers," in *The Science and Engineering of Materials* (Boston, MA: Springer). doi:10.1007/978-1-4899-2895-5_15

Bengtsson, A., Bengtsson, J., Sedin, M., and Sjöholm, E. (2019). Carbon Fibers from Lignin-Cellulose Precursors: Effect of Stabilization Conditions. *ACS Sust. Chem. Eng.* 7 (9), 8440–8448. doi:10.1021/acssuschemeng.9b00108

Bengtsson, A., Hecht, P., Sommertune, J., Ek, M., Sedin, M., and Sjöholm, E. (2020). Carbon Fibers from Lignin-Cellulose Precursors: Effect of Carbonization Conditions. *ACS Sust. Chem. Eng.* 8 (17), 6826–6833. doi:10.1021/acssuschemeng.0c01734

Berdoyes, M., Broquere, B., Loison, S., and Dauchier, M. (2005). "Sustainable C2 Rayon-Based Carbon Cloth for the Ariane 5 SRM Nozzle," in Proceeding of the 41st AIAA/ASME/SAE/ASEE Joint Propulsion Conference & Exhibit, Tucson, AZ, July 2005, 3795. doi:10.2514/6.2005-3795

Berdoyes, M., Dauchier, M., and Just, C. (2011). "A New Ablative Material Offering SRM Nozzle Design Breakthroughs," in Proceeding of the 47th AIAA/ASME/SAE/ASEE Joint Propulsion Conference & Exhibit, San Diego, California, July - August 2011, 6052.

Bershtein, V. A., Grigoryeva, O. P., Yakushev, P. N., and Fainleib, A. M. (2021). The Nature of the Exceptional Impact of Ultra-low Silica Contents on the Properties of Cyanate Ester Resin-Based Nano- and Subnanocomposites. *Polym. Composites* 42 (12), 6777–6784. doi:10.1002/pc.26338

Bibin, J., and Reghunadhan Nair, C. P. (2014). "Syntactic Foams," in *Handbook of Thermoset Plastics*. Editors H. Dodiuk and S. H. Goodman. Third Edition (William Andrew Publishing), 511–554.

Bilow, N., and Miller, L. J. (1969). Thermosetting Polyphenylene Resin its Synthesis and Use in Ablative Composites. *J. Macromolecular Sci. A - Chem.* 3 (3), 501–525. doi:10.1080/10601326908053825

Blyakhman, Y., Tontisakis, A., Senger, J., and Chaudhari, A. (2001). "Novel High Performance Matrix Systems," in Proceeding of the 46th International SAMPE International Symposium, 533–545.

Byrne, N., De Silva, R., Ma, Y., Sixta, H., and Hummel, M. (2018). Enhanced Stabilization of Cellulose-Lignin Hybrid Filaments for Carbon Fiber Production. *Cellulose* 25 (1), 723–733. doi:10.1007/s10570-017-1579-0

Canfield, A. R., and Koenig, J. (1989). "Development of PAN Precursor Materials for Solid Propellant Rocket Motor Nozzles," in Proceeding of the AIAA/ASME/SAE/ASEE 25th Joint Propulsion Conference, Monterey, CA, July 1989, 2654.

Chen, J. (2015). "Synthetic Textile Fibers," in *Textiles and Fashion Materials, Design and Technology*. Editor R. Sinclair (Woodhead Publishing Series in Textile), 79–95. doi:10.1016/B978-1-84569-931-4.00004-0

Collins, M. N., Nechifor, M., Tanasă, F., Zănoagă, M., McLoughlin, A., Stróżyk, M. A., et al. (2019). Valorization of Lignin in Polymer and Composite Systems for Advanced Engineering Applications - a Review. *Int. J. Biol. Macromolecules* 131, 828–849. doi:10.1016/j.ijbiomac.2019.03.069

Comer, A. J., Ray, D., Clancy, G., Obande, W. O., Rosca, I., McGrail, P. T., et al. (2019). Hydrothermal In-Plane-Shear Strength of Carbon Fibre/benzoxazine Laminates Manufactured Out-Of-Autoclave by Liquid-Resin-Infusion. *Compos. Structures* 213, 261–270. doi:10.1016/j.compstruct.2019.01.069

Comí, M., Lligadas, G., Ronda, J. C., Galià, M., and Cádiz, V. (2013). Renewable Benzoxazine Monomers from "Lignin-like" Naturally Occurring Phenolic Derivatives. *J. Polym. Sci. Part. A: Polym. Chem.* 51 (22), 4894–4903. doi:10.1002/pola.26918

Conejo, L. S., Costa, M. L., Oishi, S. S., and Botelho, E. C. (2017). Degradation Behavior of Carbon Nanotubes/phenol-Furfuryl Alcohol Multifunctional Composites with Aerospace Application. *Mater. Res. Express* 4 (10), 105701. doi:10.1088/2053-1591/aa8f60

Cortopassi, A. C., Boyer, E., and Kuo, K. (2009). "Update: a Subscale Solid Rocket Motor for Characterization of Submerged Nozzle Erosion," in Proceeding of the 45th AIAA/ASME/SAE/ASEE Joint Propulsion Conference & Exhibit, Denver, Colorado, August 2009, 5172. doi:10.2514/6.2009-5172

Cortopassi, A. C. (2012). *Erosion of Carbon-Cloth Phenolic Nozzles in Rocket Motors with Aluminized Solid Propellant*. A Ph.D. dissertation in Mechanical Engineering. The Graduate School, College of Engineering The Pennsylvania State University.

Culebras, M., Geaney, H., Beaucamp, A., Upadhyaya, P., Dalton, E., Ryan, K. M., et al. (2019). Bio-derived Carbon Nanofibres from Lignin as High-Performance Li-Ion Anode Materials. *ChemSusChem* 12 (19), 4516–4521. doi:10.1002/cssc.201901562

Cyanate Ester Resins Market (2018). *Cyanate Ester Resins Market by End-Use Industry (Aerospace & Defense, Electrical & Electronics), Application (Composites, Adhesives), and Region (North America, Europe, APAC, MEA, and South America) - Global Forecast to 2022*. Report ID: 4542902.

Cywar, R. M., Rorrer, N. A., Hoyt, C. B., Beckham, G. T., and Chen, E. Y.-X. (2021). Bio-based Polymers with Performance-Advantaged Properties. *Nat. Rev. Mater.* 7, 83–103. doi:10.1038/s41578-021-00363-3

D'alelio, G. F. (1971). "Structural Design and Thermal Properties of Polymers," in *Ablative Plastics*. (Editors) G. F. D'alelio and J. A. Parker (New York, NY: Marcel Dekker Inc.), 85–123.

Demiroğlu Mustafov, S., and Seydibeyoğlu, M. Ö. (2019). "Surface Treatment of Lignin Sourced Carbon Fibers: Principles, Processes, and Challenges," in *In: Sustainable Lignin for Carbon Fibers: Principles, Techniques, and Applications*. Editors E. Akpan and S. Adeosun (Cham: Springer), 427–439. doi:10.1007/978-3-030-18792-7_10

Derradji, M., Mehelli, O., Liu, W., and Fantuzzi, N. (2021). Sustainable and Ecofriendly Chemical Design of High Performance Bio-Based Thermosets for Advanced Applications. *Front. Chem.* 9, 691117. doi:10.3389/fchem.2021.691117

Devaraju, S., Krishnadevi, K., Sriharshitha, S., and Alagar, M. (2019). Design and Development of Environmentally Friendly Polybenzoxazine-Silica Hybrid from Renewable Bio-Resource. *J. Polym. Environ.* 27 (1), 141–147. doi:10.1007/s10924-018-1327-z

Devaraju, S., Krishnamoorthy, K., Eeda, N., Salendra, S., and Achimuthu, A. K. (2021). Development of Highly Flexible Sustainable Bio-Silica Reinforced Cardanol Based Poly (Benzoxazine-co-epoxy) Hybrid Composites. *J. Macromolecular Sci. A*, 1–7. doi:10.1080/10601325.2021.1981764

Dickey, R. R., Lundell, J. H., and Parker, J. A. (1969). The Development of Polybenzimidazole Composites as Ablative Heat Shields. *J. Macromolecular Sci. Part A - Chem.* 3 (4), 573–584. doi:10.1080/10601326908053830

Ding, J., Sun, J., Huang, Z., and Wang, Y. (2019). Improved High-Temperature Mechanical Property of Carbon-Phenolic Composites by Introducing Titanium Diboride Particles. *Composites B: Eng.* 157, 289–294. doi:10.1016/j.compositesb.2018.08.124

Dongre, P., and Bujanovic, B. (2021). "Lignin-based Thermoset Resins. Chapter 6," in *What to Know about Lignin*. Editor M. González Alriols, et al. (Hauppauge, NY: Nova Science Publishers, Inc.), 249–301.

Dotan, A. (2014). *Handbook of Thermoset Plastics*, 577–622. doi:10.1016/B978-1-4557-3107-7.00015-4Biobased Thermosets

Ellis, R. A. (1975). "Solid Rocket Motor Nozzles," in *NASA Space Vehicle Design Criteria (Chemical Propulsion)* (Washington, D.C.: NASA SP8115).

Feng, Z., Zeng, M., Meng, D., Chen, J., Zhu, W., Xu, Q., et al. (2020). A Novel Bio-Based Benzoxazine Resin with Outstanding thermal and Superhigh-Frequency Dielectric Properties. *J. Mater. Sci. Mater. Electron.* 31 (5), 4364–4376. doi:10.1007/s10854-020-02995-7

Fitzer, W., and Manocha, L. M. (1998). *Carbon Reinforcements and Carbon/carbon Composites*. Springer Science & Business Media. 9783540629337.

Foyer, G., Chanfi, B.-H., Boutevin, B., Caillol, S., and David, G. (2016a). New Method for the Synthesis of Formaldehyde-free Phenolic Resins from Lignin-Based Aldehyde Precursors. *Eur. Polym. J.* 74, 296–309. doi:10.1016/j.eurpolymj.2015.11.036

Foyer, G., Chanfi, B.-H., Virieux, D., David, G., and Caillol, S. (2016b). Aromatic Dialdehyde Precursors from Lignin Derivatives for the Synthesis of

Formaldehyde-free and High Char Yield Phenolic Resins. *Eur. Polym. J.* 77, 65–74. doi:10.1016/j.eurpolymj.2016.02.018

Frank, E., Steudle, L. M., Ingildeev, D., Spörl, J. M., and Buchmeiser, M. R. (2014). Carbon Fibers: Precursor Systems, Processing, Structure, and Properties. *Angew. Chem. Int. Ed.* 53 (21), 5262–5298. doi:10.1002/anie.201306129

Froimowicz, P., R. Arza, C., Han, L., and Ishida, H. (2016). Smart, Sustainable, and Ecofriendly Chemical Design of Fully Bio-Based Thermally Stable Thermosets Based on Benzoxazine Chemistry. *ChemSusChem* 9 (15), 1921–1928. doi:10.1002/cssc.201600577

Gao, J., Li, Z., Li, J., and Liu, Y. (2019). Ablation Behavior of Silicone Rubber-Benzoxazine-Based Composites for Ultra-high Temperature Applications. *Polymers* 11 (11), 1844. doi:10.3390/polym11111844

Gardziella, A., Pilato, L. A., and Knop, A. (2013). *Phenolic Resins: Chemistry, Applications, Standardization, Safety and Ecology*. Berlin: Springer.

Gasch, M., Stackpoole, M., White, S., and Boghozian, T. (2016). "Development of Advanced Conformal Ablative TPS Fabricated from Rayon- and PAN-Based Carbon Felts," in Proceeding of the 57th AIAA/ASCE/AHS/ASC Structures, Structural Dynamics, and Materials Conference, San Diego, CA., January 2016, 1414. doi:10.2514/6.2016-1414

Ge, M., Miao, J.-T., Yuan, L., Guan, Q., Liang, G., and Gu, A. (2017). Building and Origin of Bio-Based Bismaleimide Resins with Good Processability, High thermal, and Mechanical Properties. *J. Appl. Polym. Sci.* 135 (10), 45947. doi:10.1002/app.45947

Ghosh, N. N., Kiskan, B., and Yagci, Y. (2007). Polybenzoxazines-new High Performance Thermosetting Resins: Synthesis and Properties. *Prog. Polym. Sci.* 32 (11), 1344–1391. doi:10.1016/j.progpolymsci.2007.07.002

Gradl, P. R., and Valentine, P. (2017). "Carbon-Carbon Nozzle Extension Development in Support of In-Space and Upper-Stage Liquid Rocket Engines," in Proceeding of the 53rd AIAA/SAE/ASEE Joint Propulsion Conference, Atlanta, GA, July 2017, 5064. doi:10.2514/6.2017-5064

Granado, L., Tavernier, R., Foyer, G., David, G., and Caillol, S. (2018). Comparative Curing Kinetics Study of High Char Yield Formaldehyde- and Terephthalaldehyde-Phenolic Thermosets. *Thermochim. Acta* 667, 42–49. doi:10.1016/j.tca.2018.06.013

Granado, L., Tavernier, R., Henry, S., Auke, R. O., Foyer, G., David, G., et al. (2019). Toward Sustainable Phenolic Thermosets with High Thermal Performances. *ACS Sust. Chem. Eng.* 7 (7), 7209–7217. doi:10.1021/acssuschemeng.8b06286

Gruber, U., Öttinger, O., Baur, W., and Fischer, L. (2021). "12.2 Carbon Fiber Reinforced Carbon*,". *Industrial Carbon and Graphite Materials*. Editors H. Jäger and W. Frohs, Vol. I, 740–824. doi:10.1002/9783527674046.ch12_2

Guo, Z., Xu, Z., Dong, Z., Zhang, M., Chi, Z., Li, M., et al. (2021). High-performance Thermosets with Tailored Properties Derived from Multi-Arm Stared Vanillin and Carbon Fiber Composites. *J. Appl. Polym. Sci.* 138 (25), 50588. doi:10.1002/app.50588

Hamerton, I., and Hay, J. N. (1998). Recent Developments in the Chemistry of Cyanate Esters. *Polym. Int.* 47 (4), 465–473. doi:10.1002/(sici)1097-0126(199812)47:4<465::aid-pi88>3.0.co;2-s

Hamerton, I. (2012). "Introduction to Cyanate Ester Resins," in *Chemistry and Technology of Cyanate Ester Resins*. Editor I. Hamerton (Springer Science & Business Media), 1–6.

Harvey, B. G., Wright, M. E., Compel, S., Guenthner, A. J., Lamison, K., Cambrea, L., et al. (2011). *Cyanate Ester Composite Resins Derived from Renewable Polyphenol Sources, Cyanate Ester Composite Resins Derived from Renewable Polyphenol Sources*. Naval Air Warfare Center Weapons Div China Lake.

Hexion (2015a). *Hexion MX-4926 Datasheet*.

Hexion (2015b). *Hexion SC-1008 Datasheet*.

Ipakchi, H., Shegeft, A., Rezadoust, A. M., Zohuriaan-Mehr, M. J., Kabiri, K., and Sajjadi, S. (2020). Bio-resourced Furan Resin as a Sustainable Alternative to Petroleum-Based Phenolic Resin for Making GFR Polymer Composites. *Iran Polym. J.* 29 (4), 287–299. doi:10.1007/s13726-020-00793-w

Iredale, R. J., Ward, C., and Hamerton, I. (2017). Modern Advances in Bismaleimide Resin Technology: A 21st century Perspective on the Chemistry of Addition Polyimides. *Prog. Polym. Sci.* 69, 1–21. doi:10.1016/j.progpolymsci.2016.12.002

Ishida, H. (2011). "Overview and Historical Background of Polybenzoxazine Research," in *Handbook of Benzoxazine Resins*. Editors H. Ishida and T. Agag (Elsevier), 3–81. doi:10.1016/B978-0-444-53790-4.00046-1

Ismail, S. O., and Akpan, E. I. (2019). "Lignin Carbon Fibres: Properties, Applications and Economic Efficiency," in *Sustainable Lignin for Carbon Fibers: Principles, Techniques, and Applications*. Editors E. Akpan and S. Adeosun (Cham: Springer), 395–426. doi:10.1007/978-3-030-18792-7_9

Jiang, H., Li, Z., Gan, J., Wang, L., and Li, Y. (2020). Improved thermal and Mechanical Properties of Bismaleimide Nanocomposites via Incorporation of a New Allylated Siloxane Graphene Oxide. *RSC Adv.* 10 (60), 36853–36861. doi:10.1039/D0RA06621D

Kandelbauer, A. (2014). "Cyanate Esters," in *Handbook of Thermoset Plastics*, 425–457. doi:10.1016/B978-1-4557-3107-7.00011-7

Katzman, H. A., Adams, P. M., Le, T. D., and Hemminger, C. S. (1994). Characterization of Low Thermal Conductivity Pan-Based Carbon Fibers. *Carbon* 32, 379–391. doi:10.1016/0008-6223(94)90158-9

Khoo, H. H., Ee, W. L., and Isoni, V. (2016). Bio-chemicals from Lignocellulose Feedstock: Sustainability, LCA and the green Conundrum. *Green. Chem.* 18 (7), 1912–1922. doi:10.1039/C5GC02065D

Kim, J-S. (2015). Production, Separation and Applications of Phenolic-Rich Bio-Oil-Aa Review. *Bioresour. Technol.* 178, 90–98. doi:10.1016/j.biortech.2014.08.121

Kim, M., Wu, Y., and Amos, L. W. (1997). Structure of Cured Alkaline Phenol Formaldehyde Resole Resins with Respect to Resin Synthesis Mole Ratio and Oxidative Side Reactions. *Polymer* 38, 5835–5848. doi:10.1002/(SICI)1099-0518(19971115)35:15<3275::AID-POLA21>3.0.CO;2-7

Kirubakaran, R., Sharma, P., Manisekaran, A., Bijwe, J., and Nebhani, L. (2020). Phloretic Acid: a Smart Choice to Develop Low-Temperature Polymerizable Bio-Based Benzoxazine Thermosets. *J. Therm. Anal. Calorim.* 142 (3), 1233–1242. doi:10.1007/s10973-019-09228-y

Kiskan, B., Ghosh, N. N., and Yagci, Y. (2011). Polybenzoxazine-based Composites as High-Performance Materials. *Polym. Int.* 60, 167–177. doi:10.1002/pi.2961

Koo, J. H. (2006). in *Polymer Nanocomposites: Processing, Characterization, and Applications* (McGraw-Hill Professional), 159–176.

Koubek, F. J. (1971). "A Review of Ablative Studies of Interest to Naval Applications," in *Ablative Plastics*. Editors G. F. D'Alelio and J. A. Parker (New York: Marcel Dekker), 69–83.

Le, N.-D., Trogen, M., Ma, Y., Varley, R. J., Hummel, M., and Byrne, N. (2021). Understanding the Influence of Key Parameters on the Stabilisation of Cellulose-Lignin Composite Fibres. *Cellulose* 28 (2), 911–919. doi:10.1007/s10570-020-03583-y

Lee, R. (2007). *Phenolic Resin Chemistry and Proposed Mechanism for Thermal Decomposition*. Washington: NASA Marshall Space Flight Center, 7–13.

Lee, R. (2009). *Fiber Surface Treatments and Matrix Interface Effects*. Huntsville, AL: NASA Marshall Space Flight Center.

Lee, R. (2010). *Interlaminar Factors in Rayon vs. PAN-Based Laminated Composites*. Huntsville, AL: NASA Marshall Space Flight Center.

Lee, R. (2014). *Interlaminar Strengthening Concepts for Polymer Matrix Composites - A Survey of New and Improved Techniques for Advancing the State-Of the Art in Composite Design and Manufacturing*. Huntsville, AL: NASA Marshall Space Flight Center.

Lejeail, M., and Fischer, H. R. (2020). Investigations on the Replacement of Bismaleimide by the Bio-Based Bisitaconimide for Recyclable Thermoset Composites Based on Thermo-Reversible Diels-Alder Cross-Links. *Eur. Polym. J.* 131, 109699. doi:10.1016/j.eurpolymj.2020.109699

Lenz, J., Schurz, J., and Eichinger, D. (1994). Properties and Structure of Lyocell and Viscose-type Fibres in the Swollen State. *Lenzinger Berichte* 74, 19–25.

Li, J., Fan, W., Ma, Y., Xue, L., Yuan, L., Dang, W., et al. (2019). Influence of Reinforcement Structures and Hybrid Types on Inter-laminar Shear Performance of Carbon-Glass Hybrid Fibers/Bismaleimide Composites under Long-Term Thermo-Oxidative Aging. *Polymers* 11 (8), 1288. doi:10.3390/polym11081288

Li, X., Huang, W., Sui, Y., Wang, G., Xiao, L., and Zhang, D. (2021). Curing Behaviors and Thermomechanical Properties of Novolac Cyanate-Polyhedral Oligomeric Silsesquioxane Copolymers. *Composites Commun.* 28, 100932. doi:10.1016/j.coco.2021.100932

Liu, J., Zhang, L., Shun, W., Dai, J., Peng, Y., and Liu, X. (2021). Recent Development on Bio-Based Thermosetting Resins. *J. Polym. Sci.* 59 (14), 1474–1490. doi:10.1002/pol.20210328

Llevot, A., Grau, E., Carlotti, S., Grelier, S., and Cramail, H. (2016). From Lignin-Derived Aromatic Compounds to Novel Biobased Polymers. *Macromol. Rapid Commun.* 37 (1), 9–28. doi:10.1002/marc.201500474

Lochab, B., Monisha, M., Amarnath, N., Sharma, P., Mukherjee, S., and Ishida, H. (2021). Review on the Accelerated and Low-Temperature Polymerization of Benzoxazine Resins: Addition Polymerizable Sustainable Polymers. *Polymers* 13, 1260. doi:10.3390/polym13081260

Loganathan, T. M., Burhan, I., Abdullah, S. K. B., Sultan, M. T. H., Karam Singh, S. S. A. L., et al. (2021). "Physical, Mechanical, Thermal Properties of Bio-Phenolic Based Composites," in *Phenolic Polymers Based Composite Materials, Composites Science and Technology*. Editors M. Jawaid and M. Asim, 169–190. doi:10.1007/978-981-15-8932-4_11

Lu, G., Dai, J., Liu, J., Tian, S., Xu, Y., Teng, N., et al. (2020). A New Sight into Bio-Based Polybenzoxazine: From Tunable Thermal and Mechanical Properties to Excellent Marine Antifouling Performance. *ACS Omega* 5 (7), 3763–3773. doi:10.1021/acsomega.0c00025

Lurie, R. M., D'urso, S. F., and Mullen, C. K. (1969). "Structural Ablative Plastics," in *Ablative Plastics*. Editors G. F. D'Alelio and J. A. Parker (New York: Marcel Dekker), 527–529. doi:10.1080/10601326908053826

Lyashenko, T., Lerman, N., Wolf, A., Harel, H., and Marom, G. (2013). Improved Mode II Delamination Fracture Toughness of Composite Materials by Selective Placement of Protein-Surface Treated CNT. *Composites Sci. Tech.* 85, 29–35. doi:10.1016/j.compscitech.2013.06.001

Lyu, Y., and Ishida, H. (2019). Natural-sourced Benzoxazine Resins, Homopolymers, Blends and Composites: A Review of Their Synthesis, Manufacturing and Applications. *Prog. Polym. Sci.* 99, 101168. doi:10.1016/j.progpolymsci.2019.101168

Ma, Y.-y., Yang, Y., Lu, C.-x., Lu, X.-x., Wu, S.-j., and Yu, Z. (2019). A Comparative Study of the Ablation Properties of Carbon Fiber-Reinforced Phenolic Resin Composites with a Matrix Modified with Graphene Oxide and Graphitic Carbon Nitride[J]. *NEW CARBON MATERIALS* 34 (1), 29–37.

Ma, Y., Du, Y., Zhao, J., Yuan, X., and Hou, X. (2020). Preparation and Characterization of Furan-Matrix Composites Blended with Modified Hollow Glass Microsphere. *Polymers* 12, 1480. doi:10.3390/polym12071480

Machado, I., Hsieh, I., Rachita, E., Salum, M. L., Iguchi, D., Pogharian, N., et al. (2021). A Truly Bio-Based Benzoxazine Derived from Three Natural Reactants Obtained under Environmentally Friendly Conditions and its Polymer Properties. *Green. Chem.* 23, 4051–4064. doi:10.1039/D1GC00951F

Mahajan, J. S., O'Dea, R. M., Norris, J. B., Korley, L. T. J., and Epps, T. H., III (2020). Aromatics from Lignocellulosic Biomass: A Platform for High-Performance Thermosets. *ACS Sust. Chem. Eng.* 8 (40), 15072–15096. doi:10.1021/acssuschemeng.0c04817

Marks, B. S., and Rubin, L. (1969). "Ablative Resins for Hyperthermal Environments," in *Ablative Plastics*. Editors G. F. D'Alelio and J. A. Parker (New York: Marcel Dekker), 555–571. doi:10.1080/10601326908053828

Martin, H. T. (2013). *Assessment of the Performance of Ablative Insulators under Realistic Solid Rocket Motor Operating Conditions*. Ph.D. thesis. State College, PA: The Pennsylvania State University.

Martos, A., Soto, M., Schäfer, H., Koschek, K., Marquet, J., and Sebastián, R. M. (2020). Highly Crosslinked Polybenzoxazines from Monobenzoxazines: The Effect of Meta-Substitution in the Phenol Ring. *Polymers* 12, 254. doi:10.3390/polym12020254

Mathis, J. R., and Laramee, R. C. (19701970). *Development of Low Cost Ablative Nozzles for Solid Propellant Rocket Motors*, Vol. II. Brigham City, Utah: Thiokol Chemical Corporation Wasatch Division. NASA CR-72641.

Mauck, J. R., Yadav, S. K., Sadler, J. M., La Scala, J. J., Palmese, G. R., Schmalbach, K. M., et al. (2017). Preparation and Characterization of Highly Bio-Based Epoxy Amine Thermosets Derived from Lignocellulosics. *Macromol. Chem. Phys.* 218, 1700013. doi:10.1002/macp.201700013

McCorsley, C. C., III (1980). *Shaped Cellulose Article Prepared from a Solution Containing Cellulose Dissolved in a Tertiary Amine N-Oxide Solvent and a Process for Making the Article*. Asheville, NC: U.S. Patent 4416698.

Meylemans, H. A., Harvey, B. G., Reams, J. T., Guenthner, A. J., Cambrea, L. R., Groshens, T. J., et al. (2013). Synthesis, Characterization, and Cure Chemistry of Renewable Bis(cyanate) Esters Derived from 2-Methoxy-4-Methylphenol. *Biomacromolecules* 14, 771–780. doi:10.1021/bm3018438

Miao, J.-T., Yuan, L., Liang, G., and Gu, A. (2019). Biobased Bismaleimide Resins with High Renewable Carbon Content, Heat Resistance and Flame Retardancy via a Multi-Functional Phosphate from Clove Oil. *Mater. Chem. Front.* 3, 78–85. doi:10.1039/C8QM00443A

Mills, V. P., Gilbert, J. A., and Ooi, T. K. (2011). "Quantification of Micro-crack Density for Fiber Based Composites,". *Experimental and Applied Mechanics*. Editor T. Proulx, 6, 218–222. doi:10.1007/978-1-4614-0222-0

Mills, V. P. (2008). *Viable Rayon Composite Replacement Micro-cracking in Polyacrylonitrile-Based Carbon-Phenolic Composites*. Ph.D Dissertation. Huntsville, Alabama.

Milos, F. S. (1997). Galileo Probe Heat Shield Ablation experiment. *J. Spacecraft Rockets* 34, 705–713. doi:10.2514/2.3293

Minges, M. L. (1969). "Thermal Physical Characteristics of High-Performance Ablative Composites," in *Ablative Plastics*. Editors G. F. D'Alelio and J. A. Parker (New York: Marcel Dekker), 613–639. doi:10.1080/10601326908053832

Morgan, P. (2005). *Carbon Fibers and Their Composites, FL 33487-2742*. Boca Raton: Taylor & Francis.

Morgan, R. J., Jurek, R. J., Yen, A., and Donnellan, T. (1993). Toughening Procedures, Processing and Performance of Bismaleimide-Carbon Fibre Composites. *Polymer* 34 (4), 835–842. doi:10.1016/0032-3861(93)90371-G

Nair, C. P. R., Mathew, D., and Ninan, K. N. (2001). "Cyanate Ester Resins, Recent Developments,". *New Polymerization Techniques and Synthetic Methodologies. Advances in Polymer Science* (Berlin, Heidelberg: Springer), Vol 155, 1–99. doi:10.1007/3-540-44473-4_1

Nasa Grant NAGS-545 (1988). *Standardization of the Carbon-Phenolic Materials and Processes*, Vol I. Huntsville, AL: Experimental Studies.

Natali, M., Kenny, J. M., and Torre, L. (2016). Science and Technology of Polymeric Ablative Materials for thermal protection Systems and Propulsion Devices: a Review. *Prog. Mater. Sci.* 84, 192–275. doi:10.1016/j.pmatsci.2016.08.003

Natali, M., Monti, M., Kenny, J., and Torre, L. (2011a). Synthesis and thermal Characterization of Phenolic Resin/silica Nanocomposites Prepared with High Shear Rate-Mixing Technique. *J. Appl. Polym. Sci.* 120, 2632–2640. doi:10.1002/app.33494

Natali, M., Monti, M., Kenny, J. M., and Torre, L. (2011b). A Nanostructured Ablative Bulk Molding Compound: Development and Characterization. *Composites A: Appl. Sci. Manufacturing* 42, 1197–1204. doi:10.1016/j.compositesa.2011.04.022

Natali, M., Monti, M., Puglia, D., Kenny, J. M., and Torre, L. (2012). Ablative Properties of Carbon Black and MWNT/phenolic Composites: A Comparative Study. *Composites Part A: Appl. Sci. Manufacturing* 43, 174–182. doi:10.1016/j.compositesa.2011.10.006

Neda, M., Okinaga, K., and Shibata, M. (2014). High-performance Bio-Based Thermosetting Resins Based on Bismaleimide and Allyl-Etherified Eugenol Derivatives. *Mater. Chem. Phys.* 148 (1-2), 319–327. doi:10.1016/j.matchemphys.2014.07.050

Ning, X., and Ishida, H. (1994). Phenolic Materials via Ring-Opening Polymerization: Synthesis and Characterization of Bisphenol-A Based Benzoxazines and Their Polymers. *J. Polym. Sci. A. Polym. Chem.* 32, 1121–1129. doi:10.1002/pola.1994.080320614

Ning, Y., Li, D. s., Wang, M. c., Jiang, L., and Jiang, L. (2019). Eugenol-Derived Bismaleimide High Performance Resins and Composites Using Diisocyanate as Property Modifier. *Macromol. Mater. Eng.* 304 (4), 1800713. doi:10.1002/mame.201800713

Ning, Y., Li, D. s., Wang, M. c., Chen, Y. c., and Jiang, L. (2020). Bio-based Hydroxymethylated Eugenol Modified Bismaleimide Resin and its High-Temperature Composites. *J. Appl. Polym. Sci* 138, 49631. doi:10.1002/app.49631

Ogale, A. A., Zhang, M., and Jin, J. (2016). Recent Advances in Carbon Fibers Derived from Biobased Precursors. *J. Appl. Polym. Sci* 133, 43794. doi:10.1002/app.43794

Orion Stage I Vectorable Nozzle Separations (2005). *ATK Technical Interchange Meeting, 12 September 2005*.

Paipa-Álvarez, H. O., Alvarado, W. P., and Delgado, B. M. (2020). Biodegradable Thermosets Polymers as an Alternative Solution to Pollution Generated by Plastics. *J. Phys. Conf. Ser.* 1672, 012013. doi:10.1088/1742-6596/1672/1/012013

Peake, S. L., Ellis, R. A., and Broquere, B. (2006). "Update: Sustainable Carbonized Rayon for Solid Rocket Motor Nozzles," in Proceeding of the 42nd AIAA/

ASME/SAE/ASEE Joint Propulsion Conference & Exhibit, Sacramento, California, July 2006, 4598. doi:10.2514/6.2006-4598

Peake, S. L., Ellis, R. A., and Broquere, B. (2007). "Update: Sustainable Carbonized Rayon for SRM Nozzles," in Proceeding of the 43rd AIAA/ASME/SAE/ASEE Joint Propulsion Conference & Exhibit, Cincinnati, OH, July 2007, 5774.

Pilato, L. (2010). in *Resin Chemistry in Phenolic Resins: A Century of Progress*. Editor L. Pilato (Springer-Verlag Berlin Heidelberg), 68–70.

Pilato, L. A., Koo, J. H., Wissler, G. A., and Lao, S. (2008). A Review – Phenolic and Related Resins and Their Nanomodification into Phenolic Resin FRP Systems. *J. Adv. Mater.* 40, 5–16.

Pizzi, A. (2019). Tannins: Prospectives and Actual Industrial Applications. *Biomolecules* 9, 344. doi:10.3390/biom9080344

Prasanaa Iyer, N., and Arunkumar, N. (2020). Review on Fiber Reinforced/modified Bismaleimide Resin Composites for Aircraft Structure Application. *IOP Conf. Ser. Mater. Sci. Eng.* 923, 012051. doi:10.1088/1757-899x/923/1/012051

Qilin Wu, Q., and Ding Pan, . D. (2002). A New Cellulose Based Carbon Fiber from a Lyocell Precursor. *Textile Res. J.* 72, 405–410. doi:10.1177/004051750207200506

Qu, W., Yang, J., Sun, X., Bai, X., Jin, H., and Zhang, M. (2021). Towards Producing High-Quality Lignin-Based Carbon Fibers: A Review of Crucial Factors Affecting Lignin Properties and Conversion Techniques. *Int. J. Biol. Macromolecules* 189, 768–784. doi:10.1016/j.ijbiomac.2021.08.187

Quirino, R. L., Monroe, K., Fleischer, C. H., III, Biswas, E., and Kessler, M. R. (2021). Thermosetting Polymers from Renewable Sources. *Polym. Int.* 70, 167–180. doi:10.1002/pi.6132

Rallini, M., Wu, H., Natali, M., Koo, J., and Torre, L. (2017). Nanostructured Phenolic Matrices: Effect of Different Nanofillers on the thermal Degradation Properties and Reaction to Fire of a Resol. *Fire Mater.* 41, 817–825. doi:10.1002/fam.2425

Ramdani, N., Zaimeche, H., and Derradji, M. (2021). Biobased Thermally-Stable Aromatic Cyanate Ester Thermosets: A Review. *Reactive Funct. Polym.* 168, 105037. doi:10.1016/j.reactfunctpolym.2021.105037

Rao, G. R., Srikanth, I., and Reddy, K. L. (2021a). Mechanical, thermal and Ablative Behavior of Organo Nanoclay Added Carbon Fiber/cyanate Ester Resin Composites and Effect of Heat Flux on its Ablative Performance. *Polym. Polym. Composites* 29, S250–S261. 9_suppl: S250-S261. doi:10.1177/0967391121998833

Rao, G. R., Srikanth, I., and Reddy, K. L. (2021b). Effect of Organo Montmorillonite Nanoclay on Mechanical Properties Thermal Stability and Ablative Rate of Carbon Fiber Polybenzoxazine Resin Composites. *Def. Sc. J.* 71 (5), 682–690. doi:10.14429/dsj.71.16630

Rossi, R. C., and Wong, W. C. (1996). *Availability of Aerospace Rayon for SRM Nozzle Insulators*. Trw Inc San Bernardino Ca: American Institute of Aeronautics and Astronautics, 1–6.

Sarika, P. R., Nancarrow, P., Khansaheb, A., and Ibrahim, T. (2020). Bio-Based Alternatives to Phenol and Formaldehyde for the Production of Resins. *Polymers* 12 (10), 2237. doi:10.3390/polym12102237

Schmidt, D. (1968a). "Hypersonic Atmospheric Flight," in *Environmental Effects on Polymeric Materials, Environments*. Editors D. V. Rosato and R. T. Schwartz (Interscience Publishers), 488–578.

Schmidt, D. (1968b). "Chemical Propulsion Exhaust," in *Environmental Effects on Polymeric Materials, Environments*. Editors D. V. Rosato and R. T. Schwartz (Interscience Publishers), 413–486.

Schmidt, D. (1971). "Ablative Polymers in Aerospace Technology," in *Ablative Plastics*. Editors G. F. D'Alelio and J. A. Parker (New York: Marcel Dekker), 1–35.

Selvaraj, V., and Raghavarshini, T. R. (2021). Development of High-Performance Hybrid Sustainable Bio-Composites from Biobased Carbon Reinforcement and Cardanol-Benzoxazine Matrix. *Polym. Bull.* 78, 4129–4148. doi:10.1007/s00289-020-03232-1

Shibata, M., and Hashimoto, Y. (2017). High Performance Thermosetting Bismaleimide Resins via Thiol-Maleimide "click" Reaction. *Eur. Polym. J.* 93, 561–571. doi:10.1016/j.eurpolymj.2017.06.032

Shibata, M., and Miyazawa, E. (2016). High-performance Bio-Based Thermosetting Bismaleimide Resins Utilizing Difurfurylidenecyclopentanone and Dicinnamylidene Cyclopentanone. *Polym. Bull.* 74 (6), 1949–1963. doi:10.1007/s00289-016-1815-z

Shibata, M., Teramoto, N., and Nakamura, Y. (2011a). High Performance Bio-Based Thermosetting Resins Composed of Tung Oil and Bismaleimide. *J. Appl. Polym. Sci.* 119, 896–901. doi:10.1002/app.32770

Shibata, M., Teramoto, N., Shimasaki, T., and Ogihara, M. (2011b). High-performance Bio-Based Bismaleimide Resins Using Succinic Acid and Eugenol. *Polym. J.* 43, 916–922. doi:10.1038/pj.2011.87

Shibata, M., Itakura, Y., and Watanabe, H. (2013a). Bio-based Thermosetting Resins Composed of Cardanol Novolac and Bismaleimide. *Polym. J.* 45, 758–765. doi:10.1038/pj.2012.195

Shibata, M., Tetramoto, N., Imada, A., Neda, M., and Sugimoto, S. (2013b). Bio-based Thermosetting Bismaleimide Resins Using Eugenol, Bieugenol and Eugenol Novolac. *Reactive Funct. Polym.* 73, 1086–1095. doi:10.1016/j.reactfunctpolym.2013.05.002

Shibata, M., Satoh, K., and Ehara, S. (2016). Thermosetting Bismaleimide Resins Generating Covalent and Multiple Hydrogen Bonds. *J. Appl. Polym. Sci.* 133, a–n. doi:10.1002/app.43121

Shieds, S. (1976). *Scout Nozzle Data Book (No. NASA-CR-145136)*.

Sillion, B. (1989). Polyimides and Other Heteroaromatic Polymers. *Compr. Polym. Sci. Supplements* 30, 499–532. doi:10.1016/B978-0-08-096701-1.00171-3

Smith, J. L. (2019). *Building a Better Booster*. Availablr from: https://www.thespacereview.com/article/3658/1 (accessed on line 10 29, 2021).

Smith, W. F., and Hashemi, J. (2006). *Foundations of Materials Science and Engineering*. McGraw-Hill.

Spratt, G. R., and Akay, M. (1995). High Temperature Stability of Bismaleimide Carbon Fibre Composite Materials. *Kem* 99-100, 3–10. doi:10.4028/www.scientific.net/kem.99-100.3

Srikanth, I., Daniel, A., Kumar, S., Padmavathi, N., Singh, V., Ghosal, P., et al. (2010). Nano Silica Modified Carbon-Phenolic Composites for Enhanced Ablation Resistancefied Carbon-Phenolic Composites for Enhanced Ablation Resistance. *Scripta Materialia* 63, 200–203. doi:10.1016/j.scriptamat.2010.03.052

Sun, P., Zhao, Y., Luo, Y., and Sun, L. (2011). Effect of Temperature and Cyclic Hygrothermal Aging on the Interlaminar Shear Strength of Carbon Fiber/bismaleimide (BMI) Composite. *Mater. Des.* 32, 4341–4347. doi:10.1016/j.matdes.2011.04.007

Sutton, P., and Biblarz, O. (2000). *Rocket Propulsion Elements*. Wiley-IEEE. 0471326429, 9780471326427.

Takeichi, T., and Agag, T. (2006). High Performance Polybenzoxazines as Novel Thermosets. *High Perform. Polym.* 18, 777–797. doi:10.1177/0954008306068254

Tiwari, S., and Bijwe, J. (2014). Surface Treatment of Carbon Fibers - A Review. *Proced. Tech.* 14, 505–512. doi:10.1016/j.protcy.2014.08.064

Towne, M. K. (1989). *Structural and Thermal Properties of Rayon, Pitch and PAN Based Carbon/Graphite Fibers*. El Segundo, CA: Seminar at the Aerospace Corporation.

Trejo-Machin, A., Puchot, L., and Verge, P. (2018). "Design and Synthesis of Bio-Based Benzoxazines," in *Synthetic Resins Publisher: InTechOpen*. Editor L. Zhang. doi:10.5772/intechopen.76104

Trogen, M., Le, N.-D., Sawada, D., Guizani, C., Lourençon, T. V., Pitkänen, L., et al. (2021). Cellulose-lignin Composite Fibres as Precursors for Carbon Fibres. Part 1 - Manufacturing and Properties of Precursor Fibres. *Carbohydr. Polym.* 252, 117133. doi:10.1016/j.carbpol.2020.117133

Van Nieuwenhove, I., Renders, T., Lauwaert, J., De Roo, T., De Clercq, J., and Verberckmoes, A. (2020). Biobased Resins Using Lignin and Glyoxal. *ACS Sust. Chem. Eng.* 8 (51), 18789–18809. doi:10.1021/acssuschemeng.0c07227

Verge, P., Puchot, L., Vancaeyzeele, C., Vidal, F., and Habibi, Y. (2017). "Symmetric versus Asymmetric Di-bz Monomer Design," in *Advanced and Emerging Polybenzoxazine* (Amsterdam, Netherlands: Sci. Technol.), 89–107. doi:10.1016/B978-0-12-804170-3.00007-X

Vincent, D. N. (1971). "Thermal Degradation and Curing of Polyphenylene," in *Ablative Plastics*. Editors G. F. D'Alelio and J. A. Parker (New York: Marcel Dekker), 159–173. doi:10.1080/10601326908053824

Wan, J., Zhao, J., Zhang, X., Fan, H., Zhang, J., Hu, D., et al. (2020). Epoxy Thermosets and Materials Derived from Bio-Based Monomeric Phenols: Transformations and Performances. *Prog. Polym. Sci.* 108, 101287. doi:10.1016/j.progpolymsci.2020.101287

Wang, S., Bai, J., Innocent, M. T., Wang, Q., Xiang, H., Tang, J., et al. (2021). *Lignin-based Carbon Fibers: Formation, Modification and Potential Applications*. Green Energy & Environment. doi:10.1016/j.gee.2021.04.006

Wang, W.-X., Dgany, O., Wolf, S. G., Levy, I., Algom, R., Pouny, Y., et al. (2006). Aspen SP1, an Exceptional Thermal, Protease and Detergent-Resistant Self-Assembled Nano-Particle. *Biotechnol. Bioeng.* 95, 161–168. doi:10.1002/bit.21010

Warga, J. J. (1970). *Low Cost Fabrication Techniques for Solid Rocket Nozzles*. Society of Automotive Engineers.

Wen, R. Y., Sonnabend, L. F., and Eddy, R. (1969). "The Synthesis and Characterization of Some Potential Ablative Polymers," in *Ablative Plastics*. Editors G. F. D'Alelio and J. A. Parker (New York: Marcel Dekker), 471–483. doi:10.1080/10601326908053823

Wen, Z., Bonnaud, L., Mincheva, R., Dubois, P., and Raquez, J.-M. (2021). Development of Low-Viscosity and High-Performance Biobased Monobenzoxazine from Tyrosol and Furfurylamine. *Materials* 14, 440. doi:10.3390/ma14020440

Williams, G., and Murray, J. (2008). "Status on Replacing Rayon Based Carbon Phenolic Ablatives in the MK-104 Motor," in Proceeding of the 44th AIAA/ASME/SAE/ASEE Joint Propulsion Conference e Exhibit, Hartford, CT, July 2008, 5145.

Wolf, A., Buchman, A., Eitan, A., Fine, T., Nevo, Y., Heyman, A., et al. (2012). Improved Adhesives Containing CNT/SP1 Nano Fillers. *J. Adhes.* 88, 435–451. doi:10.1080/00218464.2012.660398

Wolter, N., Beber, V. C., Sandinge, A., Blomqvist, P., Goethals, F., Van Hove, M., et al. (2020). Carbon, Glass and Basalt Fiber Reinforced Polybenzoxazine: The Effects of Fiber Reinforcement on Mechanical, Fire, Smoke and Toxicity Properties. *Polymers* 12, 2379. doi:10.3390/polym12102379

Xu, X., Zhou, J., Jiang, L., Lubineau, G., Payne, S. A., and Gutschmidt, D. (2014). Lignin-based Carbon Fibers: Carbon Nanotube Decoration and superior thermal Stability. *Carbon* 80, 91–102. doi:10.1016/j.carbon.2014.08.042

Xu, Y., Guo, L., Zhang, H., Zhai, H., and Ren, H. (2019). Research Status, Industrial Application Demand and Prospects of Phenolic Resin. *RSC Adv.* 9 (50), 28924–28935. doi:10.1039/C9RA06487G

Xu, F., Zhu, S., Liu, Y., Ma, Z., and Li, H. (2020a). Ablation Behavior and Mechanism of TaSi2-Modified Carbon Fabric-Reinforced Phenolic Composite. *J. Mater. Sci.* 55, 8553–8563. doi:10.1007/s10853-020-04636-0

Xu, F., Zhu, S., Hu, J., Ma, Z., and Liu, Y. (2020b). Ablation Behavior of a Carbon Fabric Reinforced Phenolic Composite Modified by Surface-Decorated ZrB2/SiC. *Materials* 13 (2), 256. doi:10.3390/ma13020256

Yang, T., Zhao, Y., Liu, H., Sun, M., and Xiong, S. (2021). Effect of Sizing Agents on Surface Properties of Carbon Fibers and Interfacial Adhesion of Carbon Fiber/Bismaleimide Composites. *ACS Omega* 6 (36), 23028–23037. doi:10.1021/acsomega.1c01103

Yeh, M.-K., Tai, N.-H., and Liu, J.-H. (2006). Mechanical Behavior of Phenolic-Based Composites Reinforced with Multi-Walled Carbon Nanotubes. *Carbon* 44, 1–9. doi:10.1016/j.carbon.2005.07.005

Yongjian Xu, Y., Liu, Y., Chen, S., and Ni, Y. (2020). Current Overview of Carbon Fiber: Toward Green Sustainable Raw Materials. *BioRes* 15 (3), 7234–7259. doi:10.15376/biores.15.3.xu

Yuan, H., Wang, C., Zhang, S., and Lin, X. (2012). Effect of Surface Modification on Carbon Fiber and its Reinforced Phenolic Matrix Compositefication on Carbon Fiber and its Reinforced Phenolic Matrix Composite. *Appl. Surf. Sci.* 259, 288–293. doi:10.1016/j.apsusc.2012.07.034

Zaitsev, A., Moisan, S., and Poncin-Epaillard, F. (2021). Cellulose Carbon Fiber: Plasma Synthesis and Characterization. *Cellulose* 28, 1973–1988. doi:10.1007/s10570-020-03638-0

Zhan, G., Tang, X., Yu, Y., and Li, S. (2011). Biobased Cyanate Ester Composites with Epoxidized Soybean Oil and *In Situ* Generated Nano-Silica. *Polym. Eng. Sci.* 51 (3), 426–433. doi:10.1002/pen.21842

Zhang, Y., Yuan, Z., and Xu, C. C. (2015). Engineering Biomass into Formaldehyde-free Phenolic Resin for Composite Materials. *Aiche J.* 61 (4), 1275–1283. doi:10.1002/aic.14716

Zhang, K., Han, M., Liu, Y., and Froimowicz, P. (2019). Design and Synthesis of Bio-Based High-Performance Trioxazine Benzoxazine Resin via Natural Renewable Resources. *ACS Sust. Chem. Eng.* 7 (10), 9399–9407. doi:10.1021/acssuschemeng.9b00603

Zhang, S.-M., Zhao, J.-Q., Liu, Y., Liu, Y.-x., and Liu, C.-M. (2021). Renewable Furan-Derived Diamine as Primary Amine Source to Prepare Fully Bio-Based Bis-Benzoxazine Monomer under Solvent-free Condition. *Reactive Funct. Polym.* 165, 104957. doi:10.1016/j.reactfunctpolym.2021.104957

Available from: https://parkaerospace.com/our-company/*History of the Company Park Aerospace Corp*. (accessed on 29/10/2021)

Available from: https://www.sbir.gov/node/1188777*Rayon Replacement for High Temperature Materials*, Topic Number MDA16-020(accessed on 29/10/2021)

Conflict of Interest: The authors declare that the research was conducted in the absence of any commercial or financial relationships that could be construed as a potential conflict of interest.

Publisher's Note: All claims expressed in this article are solely those of the authors and do not necessarily represent those of their affiliated organizations, or those of the publisher, the editors and the reviewers. Any product that may be evaluated in this article, or claim that may be made by its manufacturer, is not guaranteed or endorsed by the publisher.

Advantages of publishing in Frontiers

OPEN ACCESS
Articles are free to read for greatest visibility and readership

FAST PUBLICATION
Around 90 days from submission to decision

HIGH QUALITY PEER-REVIEW
Rigorous, collaborative, and constructive peer-review

TRANSPARENT PEER-REVIEW
Editors and reviewers acknowledged by name on published articles

Frontiers
Avenue du Tribunal-Fédéral 34
1005 Lausanne | Switzerland

Visit us: www.frontiersin.org
Contact us: frontiersin.org/about/contact

REPRODUCIBILITY OF RESEARCH
Support open data and methods to enhance research reproducibility

DIGITAL PUBLISHING
Articles designed for optimal readership across devices

FOLLOW US
@frontiersin

IMPACT METRICS
Advanced article metrics track visibility across digital media

EXTENSIVE PROMOTION
Marketing and promotion of impactful research

LOOP RESEARCH NETWORK
Our network increases your article's readership